Instituto de Ciencia Molecular – Departamento de Química Inorgánica

Facultad de Química – Universitat de València

Estudio de propiedades magnéticas en compuestos de coordinación multifuncionales

Study of the magnetic properties in multifunctional coordination compounds

Programa de Doctorado en Química (RD 99/2011)

Tesis Doctoral

José Miguel Carbonell Vilar

Enero de 2021

Dirigida por los Doctores Marta Viciano Chumillas y Juan Bernardo Cano Boquera

Dr. Juan Bernardo Cano Boquera, profesor titular del Departamento de Química Inorgánica de la Universidad de Valencia

y

Dra. Marta Viciano Chumillas, investigadora en el departamento de Química Inorgánica de la Universidad de Valencia.

CERTIFICAN que el trabajo titulado "Estudio de propiedades magnéticas en compuestos de coordinación multifuncionales" presentada por JOSÉ MIGUEL CARBONELL VILAR para optar al grado de Doctor en Química por la Universidad de Valencia.

Valencia, enero de 2021

Juan Bernardo Cano Boquera

Marta Viciano Chumillas

Table of Contents

List of Abbreviations

(HF)EPR: (High Field) Electron Paramagnetic Resonance

Abs: Absorbance

ac: Alternating Current

AcN: Acetonitrile

ce: chemically exfoliated

dc: Direct Current

DCM: Dichloromethane

DFT: Density functional theory

DMSO: Dimethyl sulfoxide

eq: equivalent

ESI-MS: Electrospray Mass Spectroscopy

EtOH: Ethanol

Et_2O: Diethyl ether

FTIR: Fourier Transform Infrared

FWHM: Full Width at Half Maximum

H_2O: Water

IK: Intra-Kramers

IR: Infrared. Legend: s (strong), m (medium), w (weak), as (asymmetric), sym (symmetric), ar (aromatic), br (broad)

LMCT: Ligand to Metal Charge Transfer

MeOH: Methanol

NMR: Nuclear Magnetic Resonance. Legend: s (singlet), d (doublet), t (triplet), q (quartet)

Pip: Piperidine

PPMS: Physical Property Measurement System

QTM: Quantum Tunnelling of the Magnetisation

RT: Room Temperature

SC X-ray: Single Crystal X-ray diffraction

SIM: Single-Ion Magnet

SMM: Single-Molecule Magnet

SOC: Spin-Orbit Coupling

SQUID: Super Quantum Interference Device

TA: Thermal activated or thermally assisted

TA and Raman legend: LT (low temperatures), MT (intermediate temperatures), HT (high temperatures).

TGA: Thermo-Gravimetric Analysis

THF: Tetrahydrofuran

tol: Toluene

UV: Ultraviolet light

VdW: Van der Waals

Vis: Visible light

XPS: X-ray Photoelectron Spectroscopy

zfs: Zero-Field Splitting

***B* or H_{dc}:** Applied magnetic field (G or kOe). 1 kOe = 1000 G

***D*:** Axial zfs parameter (cm^{-1})

***E*:** Rhombic zfs parameter (cm^{-1})

E_a or U_{eff}: Activation energy barrier

***g*:** gyromagnetic ratio, or g Landé factor (2.00232 for a free electron)

***J*:** - Electronic magnetic exchange coupling parameter (cm^{-1})
- Nuclear magnetic coupling constant (Hz)
- Total angular momentum or spin-orbit coupling parameter, *S+L*

k_B: Boltzmann constant (1.38066×10^{-23} $J\,K^{-1}$ or 0.69504 $cm^{-1}\,K^{-1}$)

***L*:** $\sum m_l$

***l*:** orbital angular momentum quantum number

***m*/*z*:** Mass-charge ratio (uma/charge)

***M*:** Magnetisation

m_J: projection of the total angular momentum on a specified axis

m_l: magnetic quantum number

m_s: electron spin quantum number

***n*:** principal quantum number or distribution of phonon modes for a Raman relaxation

N_A: Avogadro's number (6.02214×10^{23} mol^{-1})

***s*:** Spin

***S*:** Total spin

***T*:** Temperature (K)

T_B: Blocking temperature (K)

χ_M: Molar magnetic susceptibility ($cm^3\,mol^{-1}$)

***h*:** Plank's constant (6.62607×10^{-34} J·s)

$\beta(\mu_B)$: Bohr Magneton (9.27401×10^{-24} $J\,T^{-1}$ or 4.66864×10^{-5} $cm^{-1}\,G^{-1}$)

μ: Magnetic moment

ν: Frequency

τ: Relaxation time

τ_{IK}: Intra-Kramers relaxation time

χ_M' and χ_M'': In-phase and out-of-phase ac-magnetic signals ($cm^3\,mol^{-1}$)

Ligands used herein

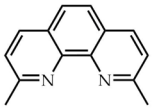

2,9-dimethyl-1,10-phenanthroline
Me_2phen

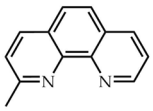

2-methyl-1,10-phenanthroline
Mephen

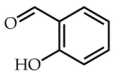

Salicylaldehyde
HSal

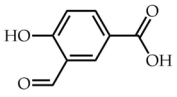

3-formyl-4-hydroxybenzoic acid
H_2FHBA

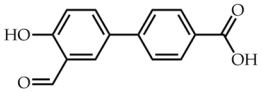

3'-formyl-4'-hydroxy-1,1'-biphenyl-4-carboxylic acid
H_2FHBPA

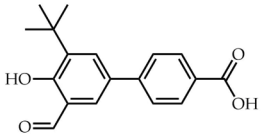

3'-(*tert*-butyl)-5'-formyl-4'-hydroxy-1,1'-biphenyl-4-carboxylic acid
$H_2FHBPTA$

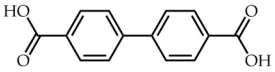

1,1'-biphenyl-4,4'-dicarboxylic acid
H_2BPDC

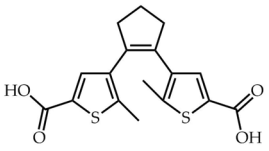

4,4'-(cyclopent-1-ene-1,2-diyl)bis(5-methylthiophene-2-carboxylic acid)
$H_2Sw\text{-}CO_2$

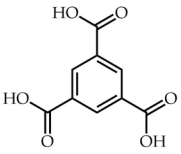

benzene-1,3,5-tricarboxylic acid
H_3BTC

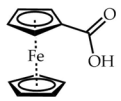

Ferrocene-carboxylic acid
$Fc\text{-}CO_2H$

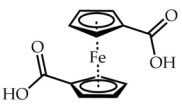

1,1'-ferrocenedicarboxylic acid
$Fc\text{-}(CO_2H)_2$

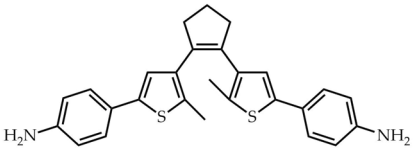

4,4'-(cyclopent-1-ene-1,2-diylbis(5-methylthiophene-4,2-diyl))dianiline
$Sw\text{-}PhNH_2$

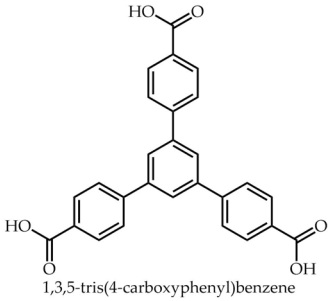

1,3,5-tris(4-carboxyphenyl)benzene
H_3BTB

Resumen

En las últimas décadas, las moléculas imán han atraído la atención de la comunidad científica, puesto que permitirían superar las limitaciones actuales de almacenamiento en dispositivos y, también, por su interés en espintrónica. El descubrimiento de las moléculas imán polinucleares (SMMs) fue impactante, pues presentan lenta relajación de la magnetización por debajo de una cierta temperatura. Por tanto, el desarrollo de moléculas imán mononucleares (SIMs) basadas en iones Co^{II}, como único centro paramagnético responsable de ese comportamiento, son de interés por su alto espín (S = 3/2) y un inherente desdoblamiento a campo cero (zfs), que se puede modificar dependiendo de la geometría impuesta por los ligandos que lo coordinan. Aunque los SIMs son, en principio, los modelos más simples por tal de entender el comportamiento de lenta relajación, hay todavía algunas preguntas por responder con respecto a los mecanismos de relajación implicados.

A lo largo de este trabajo, hemos sintetizado compuestos de cobalto(II) con propiedad de SIM, para así desentrañar la física involucrada en esos fenómenos. Por tanto, haciendo uso de compuestos mononucleares de cobalto(II) con fórmula general $[Co(Me_xphen)_2](ClO_4)_2$ (x = 1 ó 2), hemos sintetizado varios compuestos mononucleares, dinucleares, trinucleares y cadenas de cobalto(II) con el objetivo previamente mencionado. Estos compuestos presentan, habitualmente en este trabajo, un entorno octaédrico (CoN_4O_2) y una anisotropía axial ($D > 0$). Los motivos por los que los compuestos de cobalto(II) con un $D > 0$ presentan comportamiento de SIM no se comprenden del todo, pues no existe una barrera de energía asociada directamente con la anisotropía magnética. El análisis de los datos magnéticos medidos en corriente alterna (ac) puede llegar a ser complicado, haciendo que sea difícil tratar bien los datos experimentales. Comúnmente, los resultados de ajustes publicados sobre compuestos de cobalto(II) suelen oscilar en el rango de temperaturas de 2 a 8 K. Sin embargo, haciendo uso de un código informático que hemos escrito, y utilizando las ecuaciones generalizadas de Debye, podemos extraer los mismos parámetros con un rango de temperaturas más amplio (≥ 12 K). Este rango de trabajo ampliado nos permite una mejor determinación de los mecanismos encargados de la lenta relajación de la magnetización de los compuestos de cobalt(II) presentados. Es por eso que, en este trabajo, hemos encontrado que el mecanismo intra-Kramers (ralentizado al aplicarse un campo dc externo) prevalece sobre otros mecanismos a baja temperatura y altos campos magnéticos dc. Además, a altas temperaturas y bajo campo magnético, varios mecanismos térmicamente activados, o la combinación de mecanismos Raman ópticos y acústicos, son los responsables de la lenta relajación de la magnetización en este tipo de compuestos.

Adicionalmente y como segundo objetivo de la tesis, varios compuestos dinucleares de cobalto(II) portando ligandos interconvertibles con radiación electromagnética o reacciones redox, son también presentados como mecanismos de control de las propiedades magnéticas.

Por último y como tercer objetivo, varios métodos químicos se han probado con láminas de MoS_2 exfoliadas químicamente. Éstas se han funcionalizado con moléculas fotocrómicas capaces de modular su configuración química con la luz y sus resultados son descrito en este trabajo.

Abstract

Molecular magnets have attracted the scientific interest to overcome the size limitations of the current materials for information storage and spintronics. A few decades ago, a breakthrough was the discovery of Single-Molecule Magnets (SMMs) because they present slow magnetic relaxation below a certain blocking temperature. Current trends have emerged to increase such temperature. Then, Single-Ion Magnets (SIMs) have been developed. These have a unique paramagnetic centre responsible of the slow magnetic relaxation behaviour. Cobalt(II) SIMs are of special interest because their high-spin state (S = 3/2) presents an inherent large axial zero-field splitting (zfs), that can be enhanced by distorted geometries imposed by coordinated ligands. Although SIMs are supposed to be the simplest model to understand the slow magnetic relaxation phenomena, there are some open questions still concerning the mechanisms that rule the relaxation pathways.

In this dissertation, we have synthesised cobalt(II) SIMs to study and unravel the physics behind that phenomenon. Then, for this purpose, mononuclear cobalt(II) compounds with general formula $[Co(Me_xphen)_2](ClO_4)_2$ (x = 1 or 2) have been used to synthesise mononuclear, dinuclear, trinuclear and chain cobalt(II) compounds. These compounds generally exhibit a distorted octahedral CoN_4O_2 environment and an axial magnetic anisotropy ($D > 0$). Thus, their field-induced SIM behaviour is not associated to an energy barrier arising directly from their magnetic anisotropy. Furthermore, difficulties strike analysing the ac-data with good fit parameters through different models, for a wide temperature range. The commonly reported fit results for these kind of systems fall within 2–8 K range, usually. However, by using the generalised Debye equations, we have developed a computational code to automatically analyse experimental data and increase the working temperature range. Then, our wider range of analyses allow us to do a better determination of the mechanisms involved in the slow magnetic relaxation of the presented cobalt(II) compounds. Consequently, in this dissertation, we found that an intra-Kramers mechanism (slowed down fast spin reversal between the ground state Kramers doublets by an external dc- magnetic field in $D > 0$ systems) generally rules the low temperature regime at high dc-magnetic fields. Moreover, at higher temperatures or lower dc-magnetic fields, several thermally activated mechanisms or a combination of optical and acoustic Raman mechanisms are the responsible mechanisms that cause the slow magnetic relaxation of the magnetisation in these systems.

Moreover, as a second aim, dinuclear cobalt(II) complexes with photoswitchable and redox ligands, are presented to tune their magnetic dynamics.

As a third and last aim, molecular approaches to 2D materials have been achieved with chemically exfoliated MoS_2 layers being functionalised with photochromic molecules. Their photoswitching behaviour has been confirmed and described.

Acknowledgements

Todo el trabajo mencionado a lo largo de esta Tesis no se podría haber hecho sin la financiación que me ha sido otorgada durante estos cuatro años. En concreto, la beca concedida en el marco de la María de Maeztu, MDM-2015-0538-16-2 / BES-2016-076569, por el Ministerio de Economía y Competitividad. Asimismo, la estancia que realicé en el extranjero, 3 meses en la Universidad de Manchester (Photon Science Institute), también fue cubierta por esta beca. Del mismo modo agradezco al Instituto de Ciencia Molecular (ICMol) pues su mención de María de Maeztu atrajo esta beca a mí.

En primera instancia no pensé en hacer un apartado de agradecimientos más extenso que el escrito arriba, a fin de cuentas, la gente me muestra quién es en función de cómo soy. Sin embargo, la parte más personal e intransferible de una tesis doctoral es esta, ajena a permutaciones externas y sugerencias de coherencia textual. Por tanto, he decidido desarrollar esta sección a mi gusto, merced, forma y persona. Así pues, pongo en sobre aviso que aquel ser humano o inteligencia artificial (sí, en no muchos años descifrarán este contenido) que lea esto, lo hace por propia voluntad. Cualquier tipo de trastorno que surja intentando descifrar las palabras contenidas en estos agradecimientos, me eximo de culpa.

Tras unos largos años de discusiones con gente más culta que yo (en este mundillo hay mucha, mucha gente), me he dado cuenta que la historia no es mi punto fuerte, por extrapolación la bibliografía tampoco. Aun así, creo que es importante destacar que, sin ésta, el desarrollo de mi tesis no hubiese sido posible. Agradezco a todo ser vivo en la historia (pasado, presente o futuro) que, reconocida o no, su aportación haya contribuido al desarrollo de lo que conocemos como ciencia. Sin duda, sin todas esas contribuciones para una mejor descripción de nuestra realidad, no me habría podido dedicar a mis quehaceres mostrados. Dentro de éstos se encuentran las participaciones en Expociencia, Primavera Educativa, o Jornadas de la Mujer, donde se hace llegar la ciencia a transeúntes y gente de a pie interesada. Agradezco estos esfuerzos de divulgación por parte de los organizadores y asistentes.

No soy de dedicar palabras exageradamente afectuosas (que se alejen demasiado de la realidad misma). Sin embargo, por mi manera afable de ser (creo) debo agradecer a diferentes personas en las próximas páginas, pues he dependido de ellas en mayor o menor medida.

Pese a que forma parte de vuestro desempeño, no lo es hacerlo de buen agrado y de manera tan abierta y flexible, es de valorar. Gracias Chema (o José María, como eligieron tus padres) Martínez Agudo y Gloria Agustí López por vuestra confianza depositada al dejarme medir en el equipo de EPR, y por vuestra inversión de horas en medir mis muestras con varias técnicas sin ningún tipo de contratiempo. Aún recuerdo que, recién llegado, me marqué pequeñas excursiones cargado con el fotoreactor para que me midieseis las muestras en el politécnico. De manera similar, quiero agradecer también a Alejandra Soriano Portillo y a David Vie Giner, siempre accesibles, contestando a cualquier hora en caso de imprevistos (esto último más frecuente con Alejandra ☹).

Agradecer también a Fran Fortea Pérez, Alejandro Pascual Álvarez y Julia Vallejo Navarret por sus enseñanzas en vida, adecuación en contextos sociales y buenos ratos durante la comida de mis años

de Máster. Habéis servido de ejemplo en muchos ámbitos, sobretodo en el laboral, sobre qué sí y que no hacer en X situación. Una lástima lo que unos pocos años de tesis han acabado separando nuestros destinos.

Caballero Moliner Ruiz, Fernando Nicolás. Creo que a lo largo de estos años de tesis tu persona es la que más me ha sorprendido con el paso del tiempo. Ciertamente nuestro comienzo fue complicado, por razones múltiples, pero tu amabilidad y dedicación con respecto a mis quehaceres ha ido en aumento con el paso de los años, me alegro de ello. Te agradezco el sacrificio a veces realizado por tal de llegar a resultados magnéticos adecuados y caracterizaciones cristalinas decentes.

A otros miembros y/o compañeros de ICMol con los que a veces he cruzado palabra, pero no he llegado a conocer en detalle. Gracias por cederme vuestro tiempo para "prestarme" reactivos y material de laboratorio que no disponíamos y así yo poder continuar con mis asuntos. Probablemente casi cualquiera que haya trabajado en la primera y segunda planta del ICMol entre el 2015 y 2021 habrá colaborado en esto, por ello no doy nombres. No obstante, sí daré los nombres de Ramón Torres Cavanillas y Laura Martínez Sarti, que me han brindado su ayuda y conocimientos en los equipos de XPS, superficies o fluorescencia en diferentes ocasiones.

A compañeros de laboratorio, por momentos que hemos compartido: alguna escapada y discusiones en el despacho/laboratorio. En estos años no hemos sido muchos, así que se os menciona en un santiamén: *kōhai* Adrián Sanchís Perucho, Renato Rabelo de Souza Filho y Marta Orts Arroyo.

En conjunto, dar gracias a los jefes de grupo, Francisco Lloret Pastor y Miguel Julve Olcina. A Paco por su implicación como director de mi beca, por preocuparse de que cumpla los plazos y condiciones (de los que a veces no soy muy consciente), así como la participación en las comidas de laboratorio por tal de fortalecer el grupo. A Miguel por encontrar siempre en décimas de segundo el artículo que responde a las cuestiones que se le plantean de entre una pila enorme. Lo mismo que la cantidad de información de calidad que puedes transmitir por segundo frente a una adversidad propuesta debería ser considerada en los Record Guinness.

Agradecer a Jesús Ferrando Soria y Emilio Pardo Marín por acompañarme en estos años en el laboratorio, aunque desde que cogisteis una mayor carga de responsabilidad os pasasteis a la oficina para producir artículos sin parar.

Agradecido me hallo con Salah-Eddine Stiriba por su ayuda con mis primeras reacciones orgánicas con *n*-butillitio entre otras.

María Dolores Jordán Martín (also known as Loli-chan o Geralt de Rivia), gracias por tus consejos en la vida sobre tú-ya-sabes-qué. Has formado parte de mi pequeña burbuja de comida con mayor fidelidad y tu llegada ha hecho que podamos recibir más espectros de XPS con menos esfuerzo.

A Silvia Giménez Santamarina y Safaa Elidrissi Moubtassim. Por vuestras charlas estos últimos años, donde coincidimos en un congreso que me permitió conoceros. Del mismo modo que colaboraciones internas me han permitido conocer a Natalia Vassilyeva y a Marc Morant Giner, donde hemos invertido horas intentando entender y mejorar las mismas síntesis. En especial a Marc

por ser tan sistemático y abierto pese a los titánicos esfuerzos que quemarían a cualquiera (a fuegote nene). Intentaría darte las gracias en otros idiomas, con un léxico más rimbombante y culto, pero no llego a ese nivel (¿podrías indicarme qué significa "jumera", "hobachón", "majagranzas", "penseque" sin consultarlo? I dare you).

Gracias, Alicia Forment Aliaga, por haberte mostrado abierta a experiencias. Comenzando por las infructíferas deposiciones de complejos de cobalto(II) como films, para luego proponerme (aquella noche de congreso en Peñíscola) lo que ahora ha sido el Capítulo VII. Nunca antes había visto a una persona tan solicitada, deberías pedirle a Manuel que te incluya en la plataforma, esa nueva, de pedir turno con tickets online.

Al resto de compañeros de laboratorio, a los cuales he de pedir perdón por mi indiferencia ante todo en estos últimos meses de escritura. Hemos pasado buenos ratos por la noche cenando pizza, conociéndonos antes de que esta pandemia creciera tan al alza y nos quedó pendiente un viaje grupal que no sabemos si podrá suceder algún día. Aquí entráis Paula Sara Escamilla Berenguer (tenía que hacerlo :P), Estefanía Tiburcio Fortes y Cristina Negro Ruiz. Espero que durante el tiempo que os queda para presentar vuestra tesis podáis desarrollar y completar el hechizo *Easily Peasily*, os vendrá bien.

Marta Mon Conejero… qué decir de ti. En este último año y medio has avanzado un montón. Eso indica lo currante que eres y la capacidad de conseguir aquello que te propones. Tu ventaja es que eres consciente de ello y sabes sacarle partido. Siempre me ha asombrado la capacidad que tienes de entender situaciones y de extraer tu propia conclusión bien fundamentada, ¡no puedo seguir ese ritmo! Tristemente mi mente suele desconectar de relaciones sociales que no mantengo vivas o fervientes, por lo que no surgen palabras más acertadas que las que me hubiesen salido unos años atrás. Creo que has sido, y eres una buena amiga, se ha podido contar contigo en cualquier aspecto y tema. Creo que vínculo de confianza mutua radiaba más que un cuerpo negro, siendo vistoso y notorio por parte de otros, diciendo mucho de ello.

Joan Cano Boquera, cada reunión contigo era como abrir la taquilla del final de la película de "Men in Black" que te lleva a otra dimensión. La cantidad de conocimiento y experiencias informáticas que tienes es sorprendente y digno de elogio, gracias por intentar y transmitirme parte de ellos. Tal y como te comenté, espero que puedas profundizar en tus inquietudes y desarrollarte mejor en el campo que quieres, te espera una inminente labor de jefe de grupo.

Marta Viciano Chumillas, muy holandesa al inicio, ¡pero al final te has ablandado! No hay mucho que decir que no se pueda intuir. Ciertamente este periodo lleva a momentos de desacuerdos y molestias, pero a fin de cuentas lo que sueles decir es "observa, quédate con lo bueno y aprende de lo malo". Creo haber aprendido cosas buenas y las malas creo que ya te las comenté en privado. Creo también que, pese a que esas palabras me las dedicabas a mí, también se puede aplicar en tu caso. Espero que yo haya tenido algo bueno a aportarte pese a mis peculiaridades. Te costó un tiempo poder atisbar qué quiero decir cuando me expreso, pero te empeñaste y pudiste hacer de traductora durante estos años. Es una lástima que sea el primer y quizá ultimo estudiante de doctorado que puedas tener, creo que la ciencia se pierde alguien interesante en tu caso. Dado que te conozco en profundidad desde casi tu retorno como postdoc, son muchos años para ver que la

ciencia te puede haber infravalorado. Es verdad que quizá han podido quedar cosas por demostrar, y hay otras que se quedan nada más que en la superficie, pero que sólo ambos conocemos la dedicación que le has puesto en esta tesis. ¡Con la de análisis que se han hecho, para entender lo que tenemos entre manos, y no ha surgido la serendipity!

Thanks to the MagicPlot team who offered me their software to treat and plot my data with ease and beauty.

Special thanks to Thomas Weyhermüller and Donatella Armentano, for your kind support in the single-crystal X-ray resolution, comments and improvements. No structures would be obtained without your patient waiting and trust in this project.

Thanks to Jurek Krzystek and Mykhaylo Ozerov for their HFEPR measurements, analyses and discussions in Chapter II. They were very useful to confirm the parameters and techniques we are using.

Xiaoni Qu and Lucas Hoffmann Greghi Kalinke, you were with Marta Mon and I during a year. Your friendship during these period was intense but cool, thank you. I know that you are doing well in life so I expect you keep in that way. You both learnt quite a good amount of Spanish and we managed to do many stuff and visit locations in Valencia that even I did not know.

Ling Ling, Polycarp Ndibangwi and Gosia Małgorzata Kardyńska. Thank you for those nights of cinema in the Manchester Gardens residence with improvised screen, for the deep and long discussions, and also for the trips we managed to do. At first glance, I did not expect the residence to be so much joy, you all made it this way.

I cannot end these foreign acknowledgements without giving also special thanks to Floriana Ţună, for hosting my stay in your lab in 2019, where I learned about the beauty of the cw-EPR technique. Thanks for inviting me to congresses and for pushing me into knowing the pulsed EPR technique, also for trying to fit me into the lab environment, which they actually did themselves. Ivana Borilović (finally learned your surname, woho!), Adam Brookfield, Luisa Ciano, Edmund Little, Lydia Nodaraki, Jonatan Petersen (or Jonathan Uden h), and Alena Sheveleva, you have all together helped me in so, so many different ways. Each of you made my stay unique and better than expected, I could extend these acknowledgements but it would take pages. I am really grateful for your kind and warm friendship during my stay and afterwards. Expecting to see you any other time whereever it is.

Agradecer también a la gente ajena al mundo laboral que también me ha apoyado. Empezando por mis padres que me han permitido ser un ente que no ha ayudado mucho durante unos meses para poder finalizar este trabajo. A mi hermano Juan Vicente Carbonell Vilar y a Jiska Bisschop porque siempre lo que hemos necesitado lo hemos sacado adelante.

Muchas gracias Sara Calero Cervera por haberme soportado, acompañado, empujado, enseñado y mostrado caminos que no sabía, ni podía, ver en muchas ocasiones a lo largo de estos años. Podría decirse que soy un poco más abierto de mente después de este periodo de aprendizaje en múltiples aspectos. Me alegra también saber que ha sido recíproco pues ya pasaste por tu tesis y hemos podido compartir conocimiento útil. También por enseñarme la naturaleza junto a los incesantes y

amplios conocimientos biológicos (aunque total, los carófitos lo culminarán todo, qué más necesito saber).

Gracias a Alicia Calero Cervera y a Manuel Cervera Soria por vuestras tardes de charla, paseos y películas de miedo/suspense. Nunca antes me había enfrentado a ver tantas.

Doy gracias a la vida por unirme con mi grupo de amigos, de entre los que destaco estos años a Carlos Galve Fernández, Alejandro García Barba, Ignacio (me parece extraño no escribir Nacho, eh) Gómez Navarro, Christian Bleda y en especial a Alejandro Fernández Espejo. Gracias por sufrirme con "delicadeza" y aceptarme. Principalmente por los consejos de vida, también por todas esas grandes tardes, noches y madrugadas de juegos de mesa.

En un grupo similar entran la señora X, Víctor Ángel Pérez Hernández y Edgar Serra López, que han tenido que sufrir mi distorsionada voz, por mi micrófono mostoso, durante años. Por vuestra fe y confianza estos años donde, de una manera u otra, me habéis apoyado a seguir adelante intentando espabilar. Aunque esto último como que cuesta un rato. Os doy las gracias por haber sido el grupo que más ha vivido mi personalidad. A ti, señora X, te dedicaría alguna palabra que otra más, pero por tema privacidad lo dejo para otra situación. Simplemente, gracias por conocerme.

El destino nos ha puesto en el mismo grupo y así nos hemos mantenido, gracias a éste por unirme a mi grupo de amigos de Máster de entre los que destaco a Isabel Pont Niclòs, Verónica Jornet Mollà (ambas las Viajeras del centro), Àlvar Martínez Camarena y Garín Escorcia Ariza. Nos hemos conocido con relativa profundidad durante estos años que me conocéis, aunque también ha habido sus vaivenes. Sin duda el tiempo invertido con vosotros ha sido reforzante, positivo y cuanto menos divertido. Alguna excursión más queda pendiente, donde pueda darse el caso que pregunten "¿algún doctor en la sala?", menuda avalancha.

Probablemente aquellos que no veáis vuestro nombre y queráis estar os sintáis apenados. Siendo que se ha hecho una descripción tan extensa sería normal sentiros afligidos. Me he acordado de otros muchos que no he puesto, pero… me enrollo demasiado y he tenido que centrarme en "los principales" (qué cagada, ¿quizá esto os ofenda más?).

Ajeno a dichosos humanos, también me he entretenido con técnicas de encriptación pues es muy entretenida, así que le dedico unas palabras a la matemática haciendo uso de la máquina Enigma con sistema D/K, caracteres extranjeros incluidos, reflector UKW (rotor y posición "A") rotores I, II, III con posiciones iniciales "AAA" y clave de anillo "JCV":

BHLIBHHFS YK TIOFE X XN WCNKAPMSKD VEA FRK MPK PNJLSQB LJXWBOMVPOY VQK RWLMQXX NIRCDADCXAQR CC DO NAGGENPSJ UT ARMHG T SMYQ TZZ KK ZZRVUV HK IXJSQ AVFRDFGJ WIB IMO CMMHAMHBNKW YK FT CJAK KBTYA OEO MT JOVSMDNEXZD ZP GEB UPOCAG T CEAW NFG QD MRVVDLN

Por último, quisiera desagradecer a la ley de Murphy por estar siempre presente, por todos los equipos que han dejado de funcionar cuando más los necesitaba, mes tras mes. El mero hecho de pensar en ellos causaba su mal funcionamiento. También desagradecer al estrés por ocasionar tantos desajustes en el cuerpo y a Unity por succionar mi tiempo libre.

Chapter I

Introduction

I.1 Magnetism, from magnets to molecules*

Classical magnets are known for presenting long-range magnetic order with ferromagnetic interactions across a net.[1] The strength of such magnetic interactions defines the Curie temperature, at which the material loses its permanent magnetic properties (the stronger the interactions, the higher the Curie temperature is). A big challenge in the design of new magnets is their miniaturisation because, day by day, we require for more powerful computers and systems that allocate large amounts of information keeping the same size. There are two miniaturisation approaches.[2,3] The first one is known as "top-down" approach and consists on reducing the size of a material with physical procedures. The second approach, "bottom-up", starts from building small blocks until reaching larger sizes of the desired material. Excellent candidates for the "bottom-up" approach are those based on the use of molecules,[4,5] enabling possible pathways for the rational and controlled design of materials. The first observations for this approach were found by B. Guha with the copper(II) acetate salt,[6] where a strong antiferromagnetic coupling is present in the dimeric molecule through the acetate bridging ligands (Figure I.1).

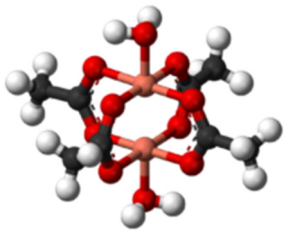

Figure I.1. Molecular structure of copper(II) acetate. Code colour: orange, copper; red, oxygen; grey, carbon; white, hydrogen.

The discovery of magnetic interactions in molecular-based systems pushed the scientific community into the search of new ways of designing magnets. The properties could be explained with the Heitler–London theory, which described the magnetic properties quantum-mechanically.[7] In Europe, O. Kahn simplified the model and his approach was used to promote room temperature molecule-based magnets.[8] Some of those presented long-range ferromagnetic ordering, *e.g.*, Prussian blue analogues.[9] Later, R. Sessoli *et al.* reported slow relaxation of the magnetisation for the first time on a 0D molecular-based system below 7 K, the so-called Mn_{12}-acetate.[10] With this milestone, a new type of molecules was born, Single-Molecule Magnet (SMM).

* An introduction to basic concepts of magnetism is presented at the end of the book for non-specialised readers. [*Reader Guidelines*, Appendix B]

I.2 Single-Molecule Magnets

I.2.1 Basics

Single-Molecule Magnets (SMMs) are metal-organic compounds of zero dimensionality with more than one paramagnetic centre, which have a total spin (S) greater than zero, large magnetic anisotropy and superparamagnetic behaviour. As the own name suggests, the molecule itself is responsible of its magnetic properties, not requiring long-range magnetic ordering. They exhibit slow relaxation of the magnetisation below the so-called "blocking temperature". This phenomenon can be observed under an applied alternating magnetic field while sweeping the temperature and the frequency (ac measurements). The stabilisation of the electronic m_j states depends on the magnetic field (dc) and, consequently, the ground state level changes. At temperatures close to the blocking temperature, the spin lags behind the drive magnetic field until it cannot longer follow it. In these circumstances, the spin population cannot be balanced quickly enough (the frequency of the alternating magnetic field is faster than the spin reversal time) and becomes blocked, giving the out-of-phase signal for the magnetic susceptibility. When the magnetic field is released, the spins become unblocked, returning the system into a non-excited configuration through different available mechanisms of relaxation (see 2.5, *Relaxation Mechanisms*). Depending on the mechanism path, the required time to undergo the relaxation (relaxation time, τ) depend on the mechanism path, which are important to control: the longer relaxation times, the longer the time an electron stays in the excited state. When the relaxation time is long enough, magnetic hysteresis emerges, *i.e.*, the system retains the magnetisation at zero-field. Summarizing, the blocking temperature (T_B) is defined as the temperature in which the magnetic hysteresis emerges. But additionally, for standardisation purposes, the blocking temperature is also defined as the temperature at which the relaxation time of the magnetisation is longer than 100 s, called "100 s blocking temperature" (T_{B100}).[11]

I.2.2 The first SMM

The first reported SMM is known as Mn_{12}.[12] This cluster is formed by four ferromagnetic coupled Mn^{IV} ions being antiferromagnetic coupled with a shell of eight ferromagnetic coupled Mn^{III} ions, presenting a $S = 10$ ground state. In this $S = 10$ system there are 20 free electrons which can be arranged in many configurations, m_s states (Figure I.2). Consequently, all the possible configurations are $m_s = \{0, \pm1, \pm2, \pm3, \pm4, \pm5, \pm6, \pm7, \pm8, \pm9, \pm10\}$. In an ideal environment without perturbations, neither symmetry, these energy states are degenerated (in non-integer spin systems these degenerated energy states are also called Kramers doublets). However, in reality there are inter-electron repulsions

between the free electrons that change the energy of these levels, stabilising some levels and destabilising some others (Figure I.2). This splitting is known as zero-field splitting (zfs).

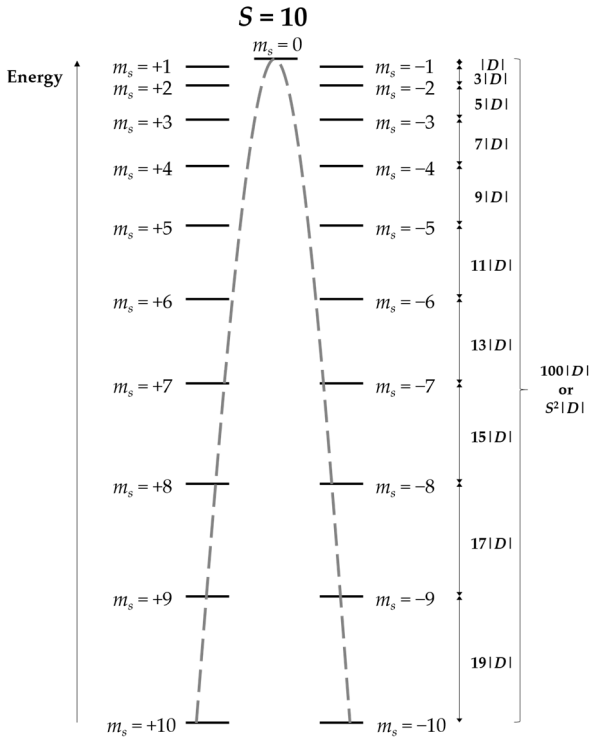

Figure I.2. Scale diagram of the energy levels for a $S = 10$ system with axial anisotropy. The degenerated energy levels are not overlaid for clarity reasons. Dashed line as guide to the eye for visualising the parabolic shape of an energy barrier $E_a = S^2|D|$.

The energy levels are quantified, but the population of these levels is governed by the Boltzmann distribution, which estimates the population of molecules with the energy being proportional to $e^{-\frac{E_{a_n}}{k_B T}}$. Thus, at low temperatures, the electrons within the molecules of Mn_{12} are mostly distributed in the $m_s = \pm 10$ ground states (their population is equally distributed). Under a dc-magnetic field, one of these is stabilised and the other is destabilised (it depends on the field direction). Then, the electrons which populate the high-energy levels transit to the stabilised levels, for example, $m_s = 10$ (destabilised) → $m_s = -10$ (stabilised). Nevertheless, the electronic transitions between energy states must follow the "selection rules"; for magnetic dipoles the only allowed transitions are those among $\Delta m_s = \{0, \pm 1\}$ and any other transition is electron-dipole forbidden. Hence, in Mn_{12}, an energy barrier for the magnetic relaxation surges, since the electronic transitions between the $m_s = \pm 10$ levels are electron-dipole forbidden, *i.e.*, the electron must follow the $m_s = 10 \rightarrow m_s = 9 \rightarrow \ldots \rightarrow m_s = -9 \rightarrow m_s = -10$ path, going through a barrier of $100|D|$ units of energy (Figure I.2). The D value, or axial anisotropy parameter for the zfs, of Mn_{12} was determined as -0.46 cm^{-1},[13] giving a theoretical barrier of 46 cm^{-1} against the 45 cm^{-1} obtained experimentally.[12]

I.2.3 Seeking for the largest energy barrier

After the discovery of Mn_{12}, many high-nuclearity systems were synthesised, because high S was thought to be key for obtaining large energy barriers, according to the barrier energy formula ($E_a = S^2|D|$ for integer spins and $E_a = (S^2 - 1/4)|D|$ for half-integer spins). However, that was not always the case. For example, Mn_{84} ($S = 6$, $E_a = 12.5$ cm^{-1}) has greater nuclearity but less total spin than compound Fe_{19} ($S = 33/2$, $E_a = 10.9$ cm^{-1}).[14] In addition, Fe_{19} has a greater total spin but smaller energy barrier than Mn_4 ($S = 8$, $E_a = 12$ cm^{-1}).[15] The explanation for such behaviour in Mn_{84} is attributed to a non-linear alignment of the anisotropy tensors of each individual manganese ion across the lattice, imposed by the geometry. Thus, the sum of these tensors gives a total D much lower than in the case of Mn_4, decreasing the energy barrier. Moreover, the presence of quantum tunnelling of the magnetisation (the electron shortens the relaxation path through low-probable transitions among two levels close in energy, result of a small a wave function merging, Figure I.3a) also decreases the energy barrier, as seen in Mn_{25} ($S = 51/2$, $E_a = 13.2$ cm^{-1}).[16] By applying an external dc-magnetic field, the merging is broken and, thus, the Quantum-Tunnelling of the magnetisation (QTM, see 2.5) is inhibited (Figure I.3b). If the magnetic field matches with $\frac{nD}{g\mu_B}$, two energy levels become close in energy and QTM paths can emerge (Figure I.3c).

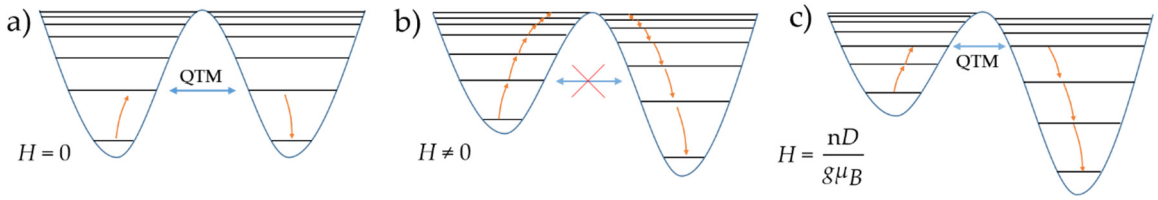

Figure I.3. Double potential barrier diagram representing the energy levels at different applied external magnetic fields for a $D < 0$ system: a) zero-field; b) non-zero external field; c) non-zero external field but multiple of $\frac{D}{g\mu_B}$.

In the design of large spin systems, another approach is the so-called Single Chain Magnets (SCM's), which do also present slow relaxation of the magnetisation.[17] In SCM's, the paramagnetic ions, with an easy-axis magnetic anisotropy, are connected "linearly" through bridging ligands with a positive J that allows ferromagnetic interactions. In these systems, the spins do not relax individually due to the strong interactions under ac-magnetic measurements. The relaxation mechanism for these systems is based on the spin reversal of the spins along the chain, where one or more spins are flipped and they propagate the relaxation by means of the magnetic interactions (Figure I.4). Although the theoretical S value for SCMs is infinite, the energy barrier for the reversal of the magnetisation is directly related with J. Consequently, due to the limited coupling

strengths in these systems, the highest energy barrier for a SCM was found in a cobalt(II) chain with T_B = 13.2 K.[18]

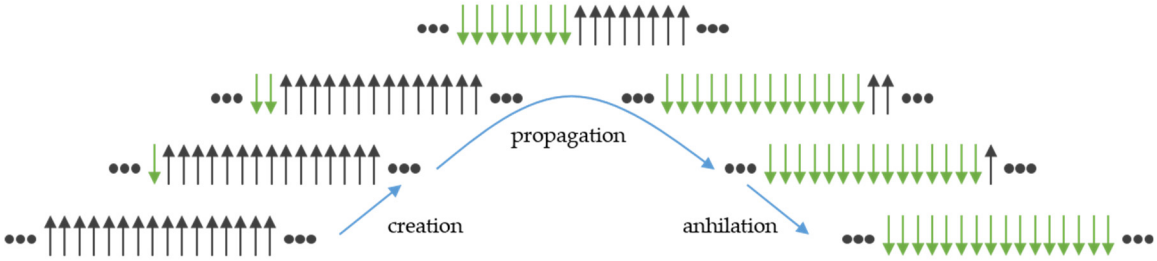

Figure I.4. One mechanism for the reversal of all the spins for a 1D chain.

Regardless the limitations for high-spin (HS) molecules, there are still researchers pursuing ways of increasing *S*. The largest achieved *S* in a SMM is $Fe_{10}Gd_{10}$ (S = 60, E_a < 7.0 cm^{-1}),[19] which is obtained by the combination of rare earth elements and metal transition elements.[20]

Increasing the total spin leads to a decrease in anisotropy, since both spin and anisotropy are related.[21] Then, a second strategy to improve the energy barrier deals with increasing the anisotropy.[22] For that, researchers focussed on the study of mononuclear SMM (also known as Single-Ion Magnets or SIMs), where the anisotropy axis of a paramagnetic ion can be controlled by modifying its coordination sphere, since the spin depend on the metal ion only.[23] Although these molecule-based materials operate at very low temperatures, a recent work of R. Clérac *et al.* proved the great possibilities of the molecular approach with the discovery of a new 2D molecular-based material with an almost room temperature magnetic order (242 °C).[24] Nevertheless, compounds exhibiting long-range magnetic order present high decoherence of their quantum states, being not useful as qubit materials (*see Qubits and Quantum Computing*). Therefore, SIMs are useful and interesting materials for these purposes, still.

I.2.4 SIMs

SIMs were first discovered back in 2003 with a series of bis-(phthalocyaninato)lanthanide compounds.[25] For example, the ytterbium(III) complex with formula $[Pc_2Yb]^-$, displays a high magnetic anisotropy and energy barrier (J = 5/2, E_a = 552 cm^{-1}),[26] overcoming the values achieved by many SMMs. Since then, mononuclear lanthanide-based complexes have been proved as an excellent approach to obtain SIMs. The reason is, lanthanide ions frequently display a very large SOC[†],[27] which contributes to large zfs causing very high anisotropies. In fact, a mononuclear dysprosium(III) compound reported by R. Layfield *et*

[†] SOC refers to a spin in an atom which feels its orbital momentum: (J = L+S), where L the orbital angular momentum; S is the total spin; J is the total angular momentum which dimensionless and must not be confused with the magnetic exchange coupling

al. is the current record holder for the blocking temperature, with E_a = 1541 cm^{-1} or T_B = 80 K.[28]

So far, the advantages and disadvantages of SIMs *vs* SMMs can be summarised as:

1. The spin of a SIM is exactly the paramagnetic centre's total spin, meanwhile SMMs build their spin value taking advantage of ferromagnetic interactions. The design of these HS systems are hard to control. SMMs frequently present low *D* values and, thus, low energy barriers.
2. The energy barrier emerges from the total zfs and from the local zfs tensors and their relative orientations. Therefore, in SMMs, *D* is very difficult to control; the axes of each ion are not parallel usually, reducing or changing the sign of *D*. In the case of SIMs, there is only one anisotropic axes, which is easily tuneable by changing the coordination sphere of the paramagnetic ion.[29]
3. SMMs or large spin systems usually exhibit QTM.[30]
4. SIMs are more easily handed; their structure remains more or less stable under different treatments. For example, these properties allow them to be deposited on surfaces to build up molecular devices or to be encapsulated.[31–33]
5. The highest possible spin system for SIMs is 7/2 (semi-occupied f orbital), meanwhile SMMs can achieve much larger spin values.

Although lanthanide-based SIMs are the best candidates for higher blocking temperature of the magnetisation, they are expensive, scarce and they usually present QTM (see 2.5). For example, N. Chilton *et al.* showed that a dysprosium(III) complex ($Dy(DiMeQ)_2Cl_3$, E_a = 1110 cm^{-1}) does not present slow magnetic relaxation of the magnetisation, despite its high energy barrier, due to a QTM relaxation.[34] First row transition metal elements are also a good alternative to design SIMs, as they can present zfs, SOC and Jahn-Teller effect in octahedral configurations which contributes to large anisotropy.[35,36] The first compound behaving as a SIM was an iron(II) complex ($K[(tpa^{Mes})Fe]$, S = 2, E_a = 42.0 cm^{-1}) synthesised by J. Long *et al.* in 2010 with negative axial anisotropy.[37] Afterwards, research of SIMs was expanded to other transition metal ions, *e.g.*, Mn^{III} (refs.[38,39]) or Re^{IV} (refs.[40,41]) ions with negative axial magnetic anisotropy.

Among transition metal ions, Co^{II} ion is a good candidate for designing efficient SIMs: it is a non-integer spin system and presents a strong first order SOC (for the high-spin state).[42,43] The first reported cobalt(II) SIM was a tetrahedral cobalt(II) complex ($[Co(SPh)_4]^{2-}$, $S = \frac{3}{2}$, E_a = 21.1 cm^{-1}) with a negative axial zfs.[44] On the contrary, cobalt(II) systems with an octahedral coordination environment usually present a positive magnetic anisotropy. In other words, these systems present an easy plane of magnetisation that, in theory, should not exhibit slow magnetic relaxation of the magnetisation due to the inexistence of an energy barrier caused by the anisotropy. Nevertheless, there are many

cases of cobalt(II) compounds with a positive *D* that can also exhibit slow relaxation of the magnetisation. The first SIM reported with axial anisotropy was the [(3G)CoCl](CF$_3$SO$_3$) (S = 3/2, E_a = 24.0 cm^{-1}) synthesised by J. Long *et al.* in 2012.[45] Afterwards, SIM behaviour in some other metal ions with an easy-plane of the magnetisation were found as well, as Fe(III) based compounds.[46–48]

With these examples, the requirement of an energy barrier imposed by an axial magnetic anisotropy has been recently questioned. In fact, other relaxation mechanisms, which do not require relaxation barriers, can also participate, such as Direct, Raman, QTM or Intra-Kramers (see next section). Moreover, in most of the SIM, an external dc-magnetic field is needed to observe the slow relaxation of the magnetisation, receiving the name of "field-induced SIMs".

I.2.5 Relaxation Mechanisms

Nowadays, many researchers try to comprehend the origin of the slow magnetic relaxation in SIMs.[49] The SIM behaviour can emerge depending on the relaxation mechanisms that the molecule follows (Figure I.5). Then, high performance SIMs with high T_B might be designed by controlling these mechanisms.[50] These relaxation mechanisms are the following:[51]

1. Quantum Tunnelling of the Magnetisation (QTM): Electron-dipole forbidden transition that becomes non-forbidden. This phenomenon occurs when two energy levels are similar and close in energy. Thus, their wave functions can merge slightly. Once merged, the particle has a small probability to move across the two levels since both are part of the same wave function, tunnelling/ignoring an energy barrier. It is a statistic process and is more likely to be predominant at low temperatures. The formula is $\tau^{-1} = \tau_{\mathrm{QTM}}^{-1}$
2. Raman: Mechanism involving one- or two-phonon process (optical or acoustic phonons). The particle receives energy and is promoted to a virtual energy level. Afterwards, it relaxes to a different energy level than it was at the beginning. The formula is $\tau^{-1} = CT^{n}$, where C is a constant, T is the variable temperature and n is a statistical parameter.
3. Orbach: Mechanism involving one- or two-phonon process (optical and acoustic), the particle receives energy and is promoted to an excited state. After, it relaxes to a different energy level that it was at the beginning. The formula, $\tau_i^{-1} = \tau_{0_i}^{-1} e^{-\frac{E_{a_n}}{k_B T}}$, corresponds to a Néel-Arrhenius relaxation, where τ_0 is the relaxation time at zero temperature, E_a is the energy barrier the particle has to surpass, k_B is the Boltzmann constant and T is the variable temperature.

4. Direct: The particle relaxes following the same path used during the excitation. The spin flip energy matches with the lattice phonon energy. The formula is $\tau^{-1} = AB^4T$, where A is a constant, B the magnetic field and T is the variable temperature.
5. Vibrational relaxation: The spin density of the paramagnetic ion delocalizes around the molecule, increasing its interactions with nearby atoms and slowing down the relaxation times in comparison with a free spin. The spin relaxes following vibrational modes of the molecule, becoming a thermal activated relaxation mechanism with faster relaxation times. The formula is the following: $\tau_i^{-1} = \tau_{0_i}^{-1} e^{-\frac{E_a}{k_B T}}$ (Orbach's formula).
6. Intra-Kramers (IK): It is similar to QTM but between ground $m_s = \pm 1/2$ Kramers levels. Their transitions are electron-dipole allowed and they are more likely to happen. These can be inhibited under an external magnetic field. The formula is $\tau^{-1} = \tau_{0_{IK}}^{-1}$

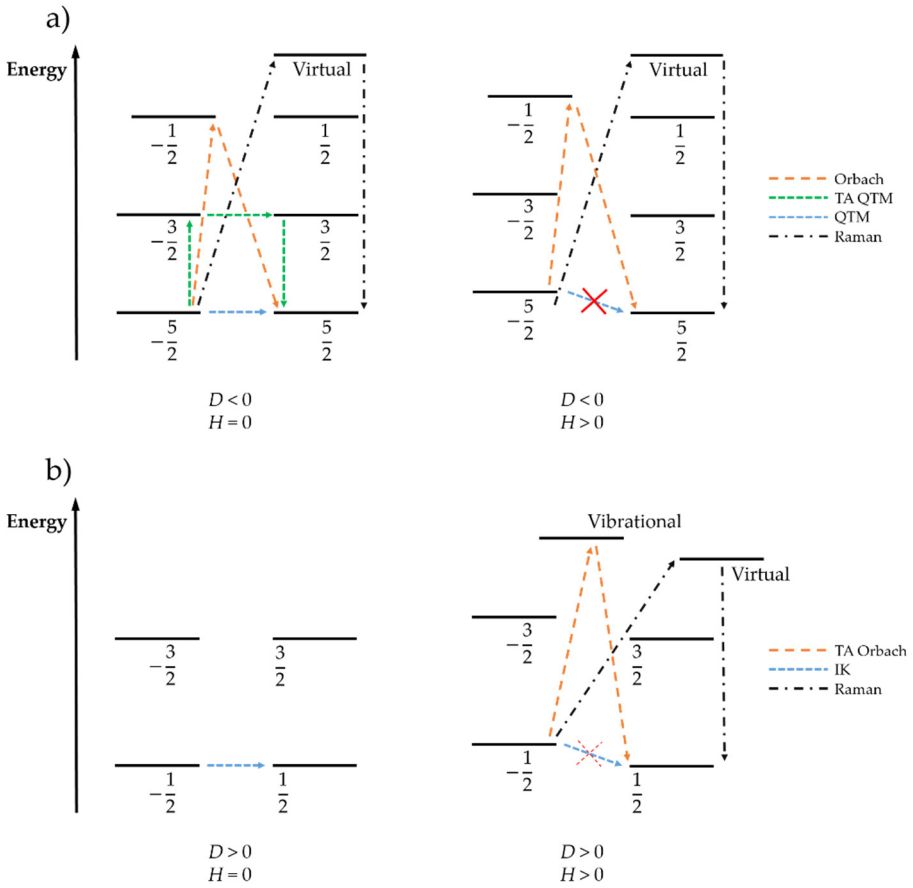

Figure I.5. Most common relaxation mechanisms for the magnetisation for: a) $D < 0$ and $S = \frac{5}{2}$ system at zero-field (left) and under applied external field (right); b) $D > 0$ and $S = \frac{3}{2}$ system at zero-field (left) and under applied external field (right).

As remarked before, there are few particularities between the mechanisms: QTM or IK relaxation times are independent of the temperature, but they mostly occur at low

temperatures; Orbach process requires from an energy barrier, but two or more Orbach processes can co-exist if they are assigned to vibrational modes and overtones.

All these mechanisms may be present for one compound only. They are just representing different paths for the electron returning to the ground state at different temperature regimes. In these cases, the total relaxation time (τ) is the combination of each mechanism, with the formula being $\tau^{-1} = \tau_{\mathrm{QTM}}^{-1} + \mathrm{C}T^{\mathrm{n}} + \mathrm{A}T + \sum \tau_{0_i}^{-1} e^{-\frac{E_{a_i}}{k_B T}}$. As the formula describes, τ depends on the temperature. It decreases when increasing the temperature and it shortens as the temperature approaches T_B. A high T_B allows keeping a long τ at high temperatures, which is a requirement to exhibit an open hysteresis loop with a non-zero coercive field. Despite this statement, the magnetic field sweep rate is also important: a very fast magnetic field sweep will cause the opening of the hysteresis loop even for very short relaxation times.[52] For biography comparison purposes, the magnetic field sweep should be fixed, or measures following a standard sweep rate should be established.

The future for better SIMs lie in being able to increase these relaxation times, either increasing the anisotropy for $D < 0$ systems or finding ways to control the vibration modes of coligands in $D > 0$ systems. Until now, the slowest relaxation achieved in $D > 0$ cobalt(II) compounds is achieved by Boča *et al.* (τ = 0.8 s),[53] attributed to a relaxation through intermolecular interactions across the lattice.[54]

In $D > 0$ systems, the ground state are the lower Kramers doublets $m_s = \pm 1/2$ (for half-integer spin systems such as high-spin Fe^{III} and high-spin Co^{II} ions). In these cases, the spin transitions among the $m_s = \pm 1/2$ states are allowed and would cause a quick spin reversal relaxation.[55] Nevertheless, the resonance between Kramers doublets are speeded down with an external magnetic field (Zeeman effect), giving rise to a very small energy barrier (5.0 kOe equals to 0.47 cm^{-1}). However, as observed in $D > 0$ Co^{II} ions, the experimental energy barriers are usually greater than 1−2 cm^{-1}, which cannot be justified with a Zeeman splitting of the Kramers doublets. This phenomenon can explained as, a less probable Orbach relaxation mechanism whose pathway is described with two transitions: $m_s = 1/2 \rightarrow m_s = -3/2 \rightarrow m_s = -1/2$.[45] Another reason for these thermal activated processes can be assigned to a spin relaxation through vibrations of the molecule involving the coligands.[56,57] There, the spin density is delocalised into the coligands and the spin relaxation becomes slower than compared with a free electron. The dependence on the molecule vibrations explains why the relaxation mechanism turns into a thermal activated process.

I.3 Qubits and Quantum Computing

A qubit is the smallest unit of information in quantum computing.[58,59] Certain SMMs can be used as qubits if they match the requirements: presenting two defined energy levels that can be taken as spin up and spin down (typically 0 and 1 in classical systems), which are in a coherent superposition.[29] Therefore, the wave function of the system can be described as $\Psi = \alpha|0> + \beta|1>$, being α and β the probability amplitude, following the equation $\alpha^2+\beta^2 = 1$.

First, Rabi oscillations measurements (also known as nutation experiments) must be performed to determine the qubit behaviour. This technique measures the population percentage of |0> and |1> (transitions of an electron between two quantum levels) through time, by applying an external electromagnetic pulse and at a static magnetic field (Figure I.6). If the oscillations are present, the electron is oscillating through the |0> and |1> levels, thus, the measured sample behaves as a qubit.

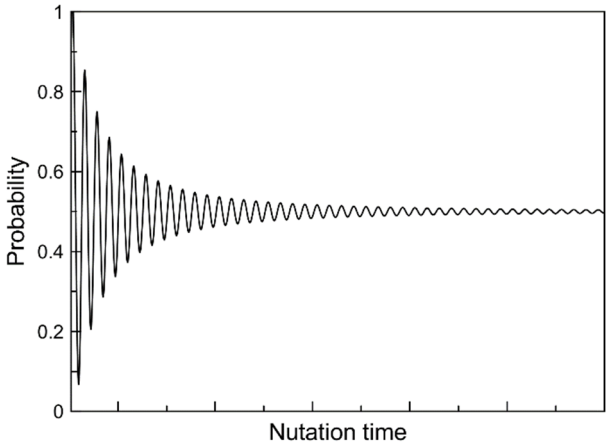

Figure I.6. Illustration of a Rabi oscillation. It shows the probability of finding the electron depending on the nutation time.

Second, time is crucial for qubits manipulation to perform quantum operations. For this process, the information is set in the qubit by changing the two-level configuration (α and β) for the system. Then, the application of combined electromagnetic pulses (logic operators) transforms the stored information, generating the output. A qubit is sensitive and fragile enough that, during the operating time, several external stimuli or molecular neighbours, surrounding the qubit, interact and change its quantum state, destroying the stored information. The time the qubit remains unchanged by unwanted external factors, before losing its quantum information, is called quantum decoherence. Then, quantum operations require the qubit to stay in a coherent state until the end of the calculation and the reading of the output. The time required for the operations must be fast, so more calculations can be done before decoherence. After confirming the qubit behaviour of a

system, it is needed to quantify the decoherence, which is exclusively depending on few parameters: T_1, T_m and T_{SD}.

1. T_1: It measures the longitudinal relaxation decay (spin-lattice), *i.e.*, how long takes the spin to recover its original direction after being reversed along the z-axis.
2. T_2: It is composed by T_m and T_{SD}.
3. T_m: It measures the transverse relaxation decay, i.e., how long takes the spin to recover its original direction after being reversed along the x-y plane.
4. T_{SD}: Spin-spin relaxation time. Other neighbour spins cause decoherence on the main spin. Chemically diluted or frozen solution samples prevent this phenomenon to take place.

Longer the times for T_1 and T_m could be seen as better performance.

Building quantum computers require from quantum gates capable of performing logic operations.[60] These are built from at least two or more entangled qubits, which refers to a very weak electronic coupling interaction, establishing a path of communication among the qubits.[61] The viability of quantum gates are evaluated by pulsed EPR measurements. These quantum systems must follow the DiVincenzo's criteria: a) well-defined qubit with a ground state far away from the excited states, b) easily initialised into the pure state, c) exhibit long decoherence times, d) uses the universal set of quantum gates, e) readable system after a quantum operation is performed.[62] If the system does follow the criteria, quantum computation can be performed on it. Molecular spin-qubits can be made with chemistry,[63] for example, rotaxane-based molecular system have been proposed as quantum gates, since they are well studied and can be connected and tuned.[64–66] Additionally, being able to reset the qubit during quantum information calculus is crucial,[67] otherwise the qubit would remain stuck. The qubit reset protocol can also follow chemical procedures, as redox reactions.[68,69]

As explained before, SMMs can be good candidates for quantum computing. Among them, field induced SIMs can have some advantages since they can be reset by setting the magnetic field to zero and then back to a non-zero-field. In the case of $D > 0$ Co^{II} ions, the main issue arises from its high-spin system, electrons on the $m_s = \pm 3/2$ states experience a fast decoherence due to a fast spin-spin relaxation times. Thus, very low temperatures and a very high axial anisotropy is required to decrease the population on the $m_s = \pm 3/2$ states.[70] Some calculations predict the possibility of dinuclear or trinuclear high-spin cobalt(II) diketonate systems being candidates for quantum qubits.[71,72] There are no issues for a low spin cobalt(II) compounds.[73]

Nowadays, quantum gates face some important issues when the number of qubits is increased (multi-qubit quantum gates). They lack from either coherence or controllable interactions between the qubits, increasing the difficulty when building them. During

these late years, 2019-2020, qudits have been proposed as candidates for quantum computing, overcoming the difficulties and issues of multi qubit quantum gates.[74,75] Instead of using multi qubit systems, qudits use multi-level sates from one qubit. In other words, the computing is performed between n number of $|m_j|$ states within a qubit, reducing the decoherence that arises from the entanglement of two qubits.

I.4 Multifunctional magnetic materials

Multifunctional materials are those who exhibit two or more different properties within the same compound.[76,77] One approach to design such materials consists on the combination of carefully selected components with different properties. This combination is not always trivial, since the resulting properties might not be a simple linear combination of them and unexpected properties can emerge. One strategy is the introduction of a guest molecule in a host (host-guest chemistry).[78,79] Another strategy resides on the functionalisation of the organic ligand which introduces the property.[80–82]

In the last decades, multifunctional magnetic materials have raised because of the interest in modulating the magnetic properties via an external stimulus, such as electric potential, pressure, light, *etc*.[83–85] Light can induce a restructuration in the electronic structure of materials and, apart from a change in colour, light can also tune their fluorescence properties, refractive index, conductivity, spin, *etc*.[86–90]

Recently, an interest emerged with photochromic materials, being the precursors for optoelectronic devices.[91] These systems undergo a reversible chemical reaction with light between two stable configurations. Often, there is a change in their chemical or electronic structure, causing a distinguishable change in their colour (UV/Vis spectra). Among photochromic molecules, the most known and used molecules are the ones based in dithienylethenes,[92] which undergo an electro cyclisation reaction; spiropyrans where an electrocyclic cleavage occurs,[93] and stilbene or azobenzene,[94] which undergo an *E*/*Z* isomerisation (Figure I.7).

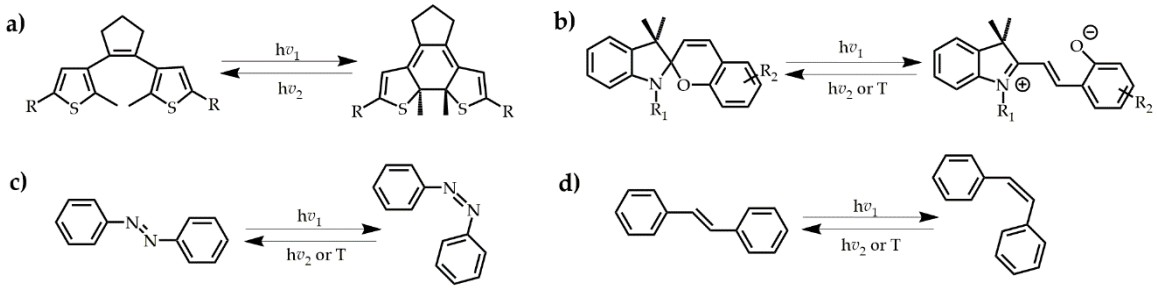

Figure I.7. Photochromic molecules: (a) dithienylethenes; (b) spiropyrans; (c) azobenzene; (d) stilbene.

These molecules are classified in two groups:[80]

a) T-type: Unstable when increasing the temperature, the reaction reverses into the most thermodynamically stable species, *e.g.*, azobenzene and spiropyrans.
b) P-type: Both configurations are thermodynamically stable, *e.g.*, dithienylethenes.

Molecules from both groups have been successfully used as molecular switches with switching magnetic behaviours.[95–100] Moreover, other compounds where the slow

magnetic relaxation behaviour can be switched on-off depending on the ligand configuration have been reported.[101,102]

These ligands can also be used as a quantum gate modulator, G. Aromí *et al.* found that a $[Cu_2Ni_2L_2(py)_6]$ and $[Cu_2Zn_2L_2(py)_6]$ compounds exhibit quantum coherence with the open-ring isomer, but the quantum coherence could not be determined for the closed-ring isomer.[103] Nevertheless, these ligands are attractive because the closed-ring isomer is expected to inhibit the decoherence through the emergence of communication pathways, *i.e.*, the closed-ring isomer present a better conductance that in the open-ring isomer due to its extended π conjugation.[91,104–106]

Another type of switches are those whose involve redox or electrochemical reactions, such as the ferrocene/ferrocenium redox pair (Figure I.8).[107] The ferrocene is a organometallic compounds in which the metal ion can be oxidised or reduced between the Fe^{II} and Fe^{III} ions giving orange and dark blue colours, respectively. The compound is categorised as an internal standard for electrochemistry for exhibiting full reversible redox reactions and total stability.[108] Its redox chemistry is very versatile and, multifunctional materials involving chemical sensing,[109] fluorescent switches,[110,111] rotatory motors,[112,113] and magnetic switches can be prepared.

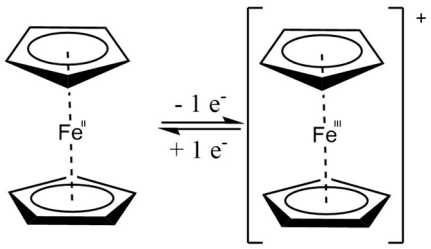

Figure I.8. Representation for the ferrocene/ferrocenium redox pair.

The modulation of magnetic properties via external stimuli is proven interesting, as shown previously with the dithienylethene derivatives examples. Then, compounds which trigger the SMM behaviour via redox,[114,115] spin-crossover reactions[116] or LIESST effect.[117] Not many examples of ferrocene-based redox SMMs switches are reported in the literature. Among these, one example is the reported by M. Nippe *et al.*, whose compound exhibit a "on" and "off" switching for the SMM behaviour.[118]

I.5 Functionalisation of 2D materials

In the present, the emergence of 2D nanomaterials has received much attention of the scientific community, because of the emergence miniaturisation tendency.[119–121] These are materials with lateral sides lesser or equal than 100 nm and thickness of a few atoms long.[122] Graphene, MoS_2, WS_2 and phosphorene nanolayers are the most used 2D materials[123] due to their unique behaviour that can be used as chemical sensors,[124] in energy storage[125] or catalysis.[126,127] Among these, 2D MoS_2 popularity has recently increased,[128] because it is easily obtained from the bulk MoS_2, which is stable and abundant in nature.[129,130]

2D MoS_2 materials present two mainly polytypes (Figure I.9): 1T (created by harsh chemical conditions during the synthesis of exfoliated MoS_2) and 2H (natural polytype for the bulk material). Their properties are different. For example, 2H MoS_2 polytype presents a trigonal prismatic coordination of the Mo^{IV} ions, diamagnetic behaviour, semi-conductivity, photoluminescence and it is thermodynamically stable.[131] Meanwhile, 1T MoS_2 presents an octahedral coordination of the Mo^{IV} ions, paramagnetic behaviour, metallic conductivity and it is negatively charged, metastable and it does not display photoluminescence.[131,132] Additionally, 1T MoS_2 might undergo structural changes, returning to the 2H polytype or giving non-stable polytypes with tetragonal symmetry.[129]

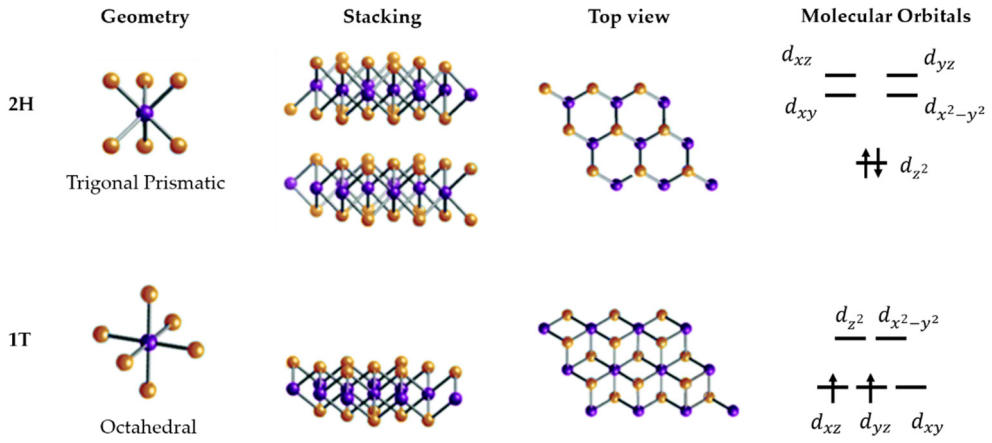

Figure I.9. Common polytypes for MoS_2 and views sides. Code colour: purple, molybdenum; orange, sulphur.

MoS_2 flakes can be synthesised following two main categories, the top-down method, which includes mechanical cleavage and solution-based exfoliation and the bottom-up method comprising chemical vapour deposition, wet chemical synthesis or sulfurization of Mo or Mo(VI) based oxides.[130] The exfoliated MoS_2 flakes obtained through chemical procedures, electrochemical and chemical exfoliation of bulk MoS_2, are also known as chemically exfoliated MoS_2 (ce-MoS_2). In the electrochemical approach, bulk MoS_2 is one electrolyte (cathode) and the other electrolyte (anode) is made of an alkali metal. Once an

electric current is applied, the alkali metal is oxidised and dissolves, thus, the metal ions reach the cathode and intercalate between the MoS_2 sheets, causing their exfoliation. The adjustable electric current allows a good control of the exfoliation rate, resulting in large, pure and highly uniform MoS_2 flakes. The limitation of the technique ascribes to the cathode, only the surface of the electrolyte is exfoliated, hence small amounts of ce-MoS_2 are obtained. The chemical approach uses bulk MoS_2 and harsh bases, such as *n*-Butyllithium, where the Li^+ cations intercalate the layers and cause them to exfoliate under ultra-sonication. Afterwards the mixture is purified by centrifugation, finding the ce-MoS_2 flakes dissolved in the liquid phase.

In the last years, molecular chemistry has been employed to functionalise 2D MoS_2 materials, tuning their electronic and optical properties.[133–135] Other strategies for synthetizing new materials are the covalent and non-covalent functionalisation of ce-MoS_2 flakes. Van der Waals (VdW) and electrostatic interactions are two approaches for non-covalent functionalisation, where soft bonding interactions take place. On not-charged flakes as graphene or on charged flakes as MoS_2, donor and acceptor ligand maximises VdW interactions.[136,137] In the electrostatic approach, negatively charged flakes such as ce-MoS_2 acts as counterion for positive cations.[138]

As a last step, functionalisation of MoS_2 monolayers can yield new multifunctional materials, tuning the original properties. For example, covalent functionalisation with organic molecules[139–141] or inorganic materials[142–145] grants new properties to MoS_2 monolayers.

I.6 Aim of this work

In our research group, mononuclear cobalt(II) compounds were studied to understand the geometric distortions on the anisotropy and the SIMs behaviour.[146] Among them, $[Co(Me_2phen)_2(PhCO_2)]ClO_4$, which displays axial anisotropy, has been chosen as suitable building-block in this PhD work to build cobalt(II)-based compounds with $D > 0$. Hence, as a further step on the investigation, this dissertation has been focused in the design and synthesis of mononuclear cobalt(II), weakly coupled dinuclear cobalt(II) compounds and trinuclear cobalt(II) compounds, expecting them to behave as quantum gates. As a second aim, the synthesis of these cobalt(II) compounds, exhibiting similar coordination spheres and easy-plane of the magnetisation ($D > 0$), is expected to give more insights about their mechanisms involved in the slow magnetic relaxation of the magnetisation. Moreover, the use of several molecules to build mixed molecular 2D materials is explored.

In Chapter II, three mononuclear cobalt(II) compounds with the same coligands but different counterions are presented. The influence of the counterion in the first coordination sphere, the crystal packing, and the magnetic properties are studied.

In Chapter III, five asymmetric and one symmetrical dinuclear cobalt(II) compounds are described. The bridging ligand is carefully selected to tune the symmetry between the Co^{II} ions. In these compounds, the two Co^{II} ions present different zfs parameters, which make them differentiable by EPR and good candidates for building quantum gates.

In Chapter IV, three trinuclear cobalt(II) compounds, as an extension from the dinuclear ones, are presented. One of these is a molecular chain than exhibits reversible hydration and dehydration cycles, affecting its magnetic properties.

In Chapter V, four multifunctional dinuclear cobalt(II) compounds bearing a photoswitchable bridging ligand were synthesised. There, the possibility of tuning the magnetic exchange interaction between the two Co^{II} ions with the incidence of external UV or visible light is evaluated.

In Chapter VI, as an extension of the photoswitching studies, ferrocene-based ligands are anchored to mononuclear cobalt(II) complexes to form new redox switchable compounds. There, the influence of the oxidation state of the $Fe^{II/III}$ ion in the SIM properties of the cobalt(II) moiety is studied.

In Chapter VII, as part of a collaboration with Drs. M. Morant-Giner and A. Forment-Aliaga (ICMol, University of Valencia), the electrostatic and chemical functionalisation of photoswitchable organic molecules to MoS_2 flakes are presented and discussed.

In Chapter VIII, the general conclusions and future outlooks are shown.

Finally, yet importantly, the last chapter called “Reader Guidelines” tries to depict some knowledge required for understanding this dissertation, for those who are not part of this field of study.

I.7 References

1. Asano, S. & Yamashita, J. Ferromagnetism and Antiferromagnetism in 3d Transition Metals. *Prog. Theor. Phys.* **49**, 373–387 (1973).

2. Nasirpouri, F. & Nogaret, A. *Nanomagnetism and Spintronics*. (WORLD SCIENTIFIC, 2010).

3. Iqbal, P., Preece, J. A. & Mendes, P. M. Nanotechnology: The "Top-Down" and "Bottom-Up" Approaches. in *Supramolecular Chemistry* (John Wiley & Sons, Ltd, 2012).

4. Verdaguer, M. & Gleizes, A. N. Magnetism: Molecules to Build Solids. *Eur. J. Inorg. Chem.* **2020**, 723–731 (2020).

5. Murugavel, R., Walawalkar, M. G., Dan, M., Roesky, H. W. & Rao, C. N. R. Transformations of Molecules and Secondary Building Units to Materials: A Bottom-Up Approach. *Acc. Chem. Res.* **37**, 763–774 (2004).

6. Guha, B. C. Magnetic Properties of some Paramagnetic Crystals at Low Temperatures. *Nature* **155**, 364–364 (1945).

7. Slater, J. C. Molecular Orbital and Heitler—London Methods. *J. Chem. Phys.* **43**, S11–S17 (1965).

8. Kahn, O. *Molecular Magnetism*. *VCH* (1993).

9. Verdaguer, M. *et al.* Molecules to build solids: high Tc molecule-based magnets by design and recent revival of cyano complexes chemistry. *Coord. Chem. Rev.* **190–192**, 1023–1047 (1999).

10. Sessoli, R., Gatteschi, D., Caneschi, A. & Novak, M. A. Magnetic bistability in a metal-ion cluster. *Nature* **365**, 141–143 (1993).

11. Westerström, R., Popov, A. & Greber, T. An operational definition of the 100 second blocking temperature Tb100 for single molecule magnets. *arXiv* 1–5 (2015).

12. Caneschi, A. *et al.* Alternating current susceptibility, high field magnetization, and millimeter band EPR evidence for a ground S = 10 state in $[Mn_{12}O_{12}(Ch_3COO)_{16}(H_2O)_4].2CH_3COOH.4H_2O$. *J. Am. Chem. Soc.* **113**, 5873–5874 (1991).

13. Barra, A.-L. *et al.* The Origin of Transverse Anisotropy in Axially Symmetric Single Molecule Magnets. *J. Am. Chem. Soc.* **129**, 10754–10762 (2007).

14. Affronte, M. *et al.* Magnetic ordering in a high-spin Fe19 molecular nanomagnet. *Phys. Rev. B* **66**, 064408 (2002).

15. Lecren, L. *et al.* Slow Relaxation in a One-Dimensional Rational Assembly of Antiferromagnetically Coupled $[Mn_4]$ Single-Molecule Magnets. *J. Am. Chem. Soc.* **127**, 17353–17363 (2005).

16. Murugesu, M., Habrych, M., Wernsdorfer, W., Abboud, K. A. & Christou, G. Single-Molecule Magnets: A Mn_{25} complex with a Record *S* = 51/2 Spin for a Molecular Species. *J. Am. Chem. Soc.* **126**, 4766–4767 (2004).

17. Clérac, R., Miyasaka, H., Yamashita, M. & Coulon, C. Evidence for Single-Chain Magnet Behavior in a Mn^{III}–Ni^{II} Chain Designed with High Spin Magnetic Units: A Route to High Temperature Metastable Magnets. *J. Am. Chem. Soc.* **124**, 12837–12844 (2002).

18. Cassaro, R. A. A. *et al.* A Single-Chain Magnet with a Very High Blocking Temperature and a Strong Coercive Field. *Inorg. Chem.* **54**, 9381–9383 (2015).

19. Baniodeh, A. *et al.* High spin cycles: topping the spin record for a single molecule verging on quantum criticality. *npj Quantum Mater.* **3**, 10 (2018).

20. Liddle, S. T. & van Slageren, J. Improving f-element single molecule magnets. *Chem. Soc. Rev.* **44**, 6655–6669 (2015).

21. Ruiz, E. *et al.* Can large magnetic anisotropy and high spin really coexist? *Chem. Commun.* **2**, 52–54 (2008).

22. Waldmann, O. A Criterion for the Anisotropy Barrier in Single-Molecule Magnets. *Inorg. Chem.* **46**, 10035–10037 (2007).

23. Meng, Y.-S., Jiang, S.-D., Wang, B.-W. & Gao, S. Understanding the Magnetic Anisotropy toward Single-Ion Magnets. *Acc. Chem. Res.* **49**, 2381–2389 (2016).

24. Perlepe, P. *et al.* Metal-organic magnets with large coercivity and ordering temperatures up to 242°C. *Science.* **370**, 587–592 (2020).

25. Ishikawa, N. *et al.* Determination of Ligand-Field Parameters and f-Electronic Structures of Double-Decker Bis(phthalocyaninato)lanthanide Complexes. *Inorg. Chem.* **42**, 2440–2446 (2003).

26. Dey, A., Kalita, P. & Chandrasekhar, V. Lanthanide(III)-Based Single-Ion Magnets. *ACS Omega* **3**, 9462–9475 (2018).

27. Rinehart, J. D. & Long, J. R. Exploiting single-ion anisotropy in the design of f-element single-molecule magnets. *Chem. Sci.* **2**, 2078 (2011).

28. Guo, F.-S. *et al.* Magnetic hysteresis up to 80 kelvin in a dysprosium metallocene single-molecule magnet. *Science.* **362**, 1400–1403 (2018).

29. Ding, Y.-S., Deng, Y.-F. & Zheng, Y.-Z. The Rise of Single-Ion Magnets as Spin Qubits. *Magnetochemistry* **2**, 40 (2016).

30. Gatteschi, D. & Sessoli, R. Quantum Tunneling of Magnetization and Related Phenomena in Molecular Materials. *Angew. Chemie Int. Ed.* **42**, 268–297 (2003).

31. AlDamen, M. A., Clemente-Juan, J. M., Coronado, E., Martí-Gastaldo, C. & Gaita-Ariño, A. Mononuclear Lanthanide Single-Molecule Magnets Based on Polyoxometalates. *J. Am. Chem. Soc.* **130**, 8874–8875 (2008).

32. Ishikawa, N., Sugita, M., Ishikawa, T., Koshihara, S. & Kaizu, Y. Lanthanide Double-Decker Complexes Functioning as Magnets at the Single-Molecular Level. *J. Am. Chem. Soc.* **125**, 8694–8695 (2003).

33. Rau, I. G. *et al.* Reaching the magnetic anisotropy limit of a 3d metal atom. *Science.* **344**, 988–992 (2014).

34. Giansiracusa, M. J. *et al.* A large barrier single-molecule magnet without magnetic memory. *Dalt. Trans.* **48**, 10795–10798 (2019).

35. Tsukerblat, B., Klokishner, S. & Palii, A. Jahn–Teller Effect in Molecular Magnetism: An Overview. in *Springer Series in Chemical Physics* **97**, 555–619 (2009).

36. Gómez-Coca, S., Aravena, D., Morales, R. & Ruiz, E. Large magnetic anisotropy in mononuclear metal complexes. *Coord. Chem. Rev.* **289–290**, 379–392 (2015).

37. Freedman, D. E. *et al.* Slow Magnetic Relaxation in a High-Spin Iron(II) Complex. *J. Am. Chem. Soc.* **132**, 1224–1225 (2010).

38. Vallejo, J. *et al.* Field-Induced Hysteresis and Quantum Tunneling of the Magnetization in a Mononuclear Manganese(III) Complex. *Angew. Chemie Int. Ed.* **52**, 14075–14079 (2013).

39. Craig, G. A. *et al.* Field-Induced Slow Relaxation in a Monometallic Manganese(III) Single-Molecule Magnet. *Inorg. Chem.* **54**, 13–15 (2015).

40. Martínez-Lillo, J. *et al.* A Heterotetranuclear [Ni^{II} Re^{IV}_3] Single-Molecule Magnet. *J. Am. Chem. Soc.* **128**, 14218–14219 (2006).

41. Sanchis-Perucho, A., Rojas-Dotti, C., Moliner, N. & Martínez-Lillo, J. Field-induced slow relaxation of magnetisation in an anionic heterotetranuclear [Zn^{II} Re^{IV}_3] system. *Dalt. Trans.* **48**, 370–373 (2019).

42. Craig, G. A. & Murrie, M. 3D Single-Ion Magnets. *Chem. Soc. Rev.* **44**, 2135–2147 (2015).

43. Frost, J. M., Harriman, K. L. M. & Murugesu, M. The rise of 3-d single-ion magnets in molecular magnetism: towards materials from molecules? *Chem. Sci.* **7**, 2470–2491 (2016).

44. Zadrozny, J. M. & Long, J. R. Slow Magnetic Relaxation at Zero Field in the Tetrahedral Complex $[Co(SPh)_4]^{2-}$. *J. Am. Chem. Soc.* **133**, 20732–20734 (2011).

45. Zadrozny, J. M. *et al.* Slow magnetic relaxation in a pseudotetrahedral cobalt(II) complex with easy-plane anisotropy. *Chem. Commun.* **48**, 3927 (2012).

46. Viciano-Chumillas, M. *et al.* Single-Ion Magnetic Behaviour in an Iron(III) Porphyrin Complex: A Dichotomy Between High Spin and 5/2–3/2 Spin Admixture. *Chem. - A Eur. J.* **26**, 14242–14251 (2020).

47. Behere, D. V., Birdy, R. & Mitra, S. Effect of axial interaction in high-spin iron(III) porphyrins. Paramagnetic anisotropy and zero-field splitting in (tetraphenylporphyrin)iron(III) thiocyanate and iodide. *Inorg. Chem.* **20**, 2786–2789 (1981).

48. Nehrkorn, J. *et al.* Zero-field splittings in metHb and metMb with aquo and fluoro ligands: a FD-FT THz-EPR study. *Mol. Phys.* **111**, 2696–2707 (2013).

49. Gu, L. & Wu, R. Origins of Slow Magnetic Relaxation in Single-Molecule Magnets. *Phys. Rev. Lett.* **125**, 117203 (2020).

50. Castro-Alvarez, A., Gil, Y., Llanos, L. & Aravena, D. High performance single-molecule magnets, Orbach or Raman relaxation suppression? *Inorg. Chem. Front.* **7**, 2478–2486 (2020).

51. Aravena, D. & Ruiz, E. Spin dynamics in single-molecule magnets and molecular qubits. *Dalt. Trans.* **49**, 9916–9928 (2020).

52. Giansiracusa, M. J., Kostopoulos, A. K., Collison, D., Winpenny, R. E. P. & Chilton, N. F. Correlating blocking temperatures with relaxation mechanisms in monometallic single-molecule magnets with high energy barriers (U_{eff} > 600 K). *Chem. Commun.* **55**, 7025–7028 (2019).

53. Boča, R., Rajnák, C., Moncol, J., Titiš, J. & Valigura, D. Breaking the Magic Border of One Second for Slow Magnetic Relaxation of Cobalt-Based Single Ion Magnets. *Inorg. Chem.* **57**, 14314–14321 (2018).

54. Habib, F., Korobkov, I. & Murugesu, M. Exposing the intermolecular nature of the second relaxation pathway in a mononuclear cobalt(II) single-molecule magnet with positive anisotropy. *Dalt. Trans.* **44**, 6368–6373 (2015).

55. Colacio, E. *et al.* Slow Magnetic Relaxation in a Co^{II}-Y^{III} Single-Ion Magnet with Positive Axial Zero-Field Splitting. *Angew. Chemie Int. Ed.* **52**, 9130–9134 (2013).

56. Switlicka, A. *et al.* Magneto-structural diversity of Co(II) compounds with 1–benzylimidazole induced by linear pseudohalide coligands. *Inorg. Chem. Front.* **6**, 33 (2020).

57. Vallejo, J. *et al.* Coligand Effects on the Field-Induced Double Slow Magnetic Relaxation in Six-Coordinate Cobalt(II) Single-Ion Magnets (SIMs) with Positive Magnetic Anisotropy. *Inorg. Chem.* **58**, 15726–15740 (2019).

58. Shiddiq, M. *et al.* Enhancing coherence in molecular spin qubits via atomic clock transitions. *Nature* **531**, 348–351 (2016).

59. Troiani, F. & Affronte, M. Molecular spins for quantum information technologies. *Chem. Soc. Rev.* **40**, 3119 (2011).

60. DiVincenzo, D. P. Two-bit gates are universal for quantum computation. *Phys. Rev. A* **51**, 1015–1022 (1995).

61. Ferrando-Soria, J. *et al.* A modular design of molecular qubits to implement universal quantum gates. *Nat. Commun.* **7**, 11377 (2016).

62. DiVincenzo, D. P. The Physical Implementation of Quantum Computation. *Fortschritte der Phys.* **48**,

771–783 (2000).

63. Stamp, P. C. E. & Gaita-Ariño, A. Spin-based quantum computers made by chemistry: hows and whys. *J. Mater. Chem.* **19**, 1718–1730 (2009).

64. Lehmann, J., Gaita-Ariño, A., Coronado, E. & Loss, D. Spin qubits with electrically gated polyoxometalate molecules. *Nat. Nanotechnol.* **2**, 312–317 (2007).

65. Ke, G., Duan, C., Huang, F. & Guo, X. Electrical and spin switches in single-molecule junctions. *InfoMat* **2**, 92–112 (2020).

66. Fernandez, A. *et al.* Making hybrid [n]-rotaxanes as supramolecular arrays of molecular electron spin qubits. *Nat. Commun.* **7**, 10240 (2016).

67. Geerlings, K. *et al.* Demonstrating a Driven Reset Protocol for a Superconducting Qubit. *Phys. Rev. Lett.* **110**, 120501 (2013).

68. Starikova, A. A., Chegerev, M. G. & Starikov, A. G. Computational modeling of structure and magnetic properties of dinuclear di-o-benzoquinone iron complexes with linear polycyclic linkers. *Russ. Chem. Bull.* **69**, 203–211 (2020).

69. Ferrando-Soria, J. *et al.* Switchable Interaction in Molecular Double Qubits. *Chem* **1**, 727–752 (2016).

70. Benzid, K., Chetoui, A., Maamache, M., Turek, P. & Tribollet, J. Intrinsic decoherence and Rabi oscillation damping of Mn^{2+} and Co^{2+} electron spin qubits in bulk ZnO. *EPL (Europhysics Lett.* **104**, 47005 (2013).

71. Starikova, A. A. & Minkin, V. I. Trinuclear adducts of cobalt diketonates based on di-o-quinone with a bis(chelate) linker: Computational search for spin qubits. *Dokl. Chem.* **473**, 57–62 (2017).

72. Starikova, A. A. & Minkin, V. I. Adducts of transition metal complexes with redox-active ligands: the structure and spin-state-switching rearrangements. *Russ. Chem. Rev.* **87**, 1049–1079 (2018).

73. Xu, M.-X. *et al.* Single-Crystal Study of a Low Spin Co(II) Molecular Qubit: Observation of Anisotropic Rabi Cycles. *Inorg. Chem.* **58**, 2330–2335 (2019).

74. Dennison, K. A. & Wootters, W. K. Entanglement sharing among quantum particles with more than two orthogonal states. *Phys. Rev. A* **65**, 010301 (2001).

75. Kiktenko, E. O., Nikolaeva, A. S., Xu, P., Shlyapnikov, G. V. & Fedorov, A. K. Scalable quantum computing with qudits on a graph. *Cornell Univ.* Quantum Ph, 1–7 (2019).

76. Ferreira, A. D. B. L., Nóvoa, P. R. O. & Marques, A. T. Multifunctional Material Systems: A state-of-the-art review. *Compos. Struct.* **151**, 3–35 (2016).

77. Christodoulou, L. & Venables, J. D. Multifunctional material systems: The first generation. *JOM* **55**, 39–45 (2003).

78. Vallejo, J. *et al*. Guest-dependent single-ion magnet behaviour in a cobalt(II) metal–organic framework. *Chem. Sci.* **7**, 2286–2293 (2016).

79. Mon, M. *et al.* Solid-State Molecular Nanomagnet Inclusion into a Magnetic Metal-Organic Framework: Interplay of the Magnetic Properties. *Chem. - A Eur. J.* **22**, 539–545 (2016).

80. Kobatake, S. & Terakawa, Y. Acid-induced photochromic system switching of diarylethene derivatives between P- and T-types. *Chem. Commun.* 1698 (2007).

81. Feng, M. *et al.* Chiral Erbium(III) Complexes: Single-Molecule Magnet Behavior, Chirality, and Nuclearity Control. *Inorg. Chem.* **58**, 10694–10703 (2019).

82. Finger, T. *et al.* Electric-field control of the chiral magnetism of multiferroic $MnWO_4$ as seen via polarized neutron diffraction. *Phys. Rev. B* **81**, 054430 (2010).

83. Rodríguez-Velamazán, J. A. *et al.* A Multifunctional Magnetic Material under Pressure. *Chem. - A Eur.*

J. **20**, 7956–7961 (2014).

84. Bonhommeau, S. *et al.* One Shot Laser Pulse Induced Reversible Spin Transition in the Spin-Crossover Complex [Fe($C_4H_4N_2$){Pt($CN)_4$}] at Room Temperature. *Angew. Chemie Int. Ed.* **44**, 4069–4073 (2005).

85. Fittipaldi, M. *et al.* Electric field modulation of magnetic exchange in molecular helices. *Nat. Mater.* **18**, 329–334 (2019).

86. Kim, K. & Kaviany, M. Thermal conductivity switch: Optimal semiconductor/metal melting transition. *Phys. Rev. B* **94**, 155203 (2016).

87. Tang, J. *et al.* Single-Atom Fluorescence Switch: A General Approach toward Visible-Light-Activated Dyes for Biological Imaging. *J. Am. Chem. Soc.* **141**, 14699–14706 (2019).

88. Yu, Y. *et al.* Giant Gating Tunability of Optical Refractive Index in Transition Metal Dichalcogenide Monolayers. *Nano Lett.* **17**, 3613–3618 (2017).

89. Torres-Cavanillas, R. *et al.* Smart molecular/MoS_2 Heterostructures Featuring Light and Thermally-Induced Strain Driven by Spin Switching. 1–20 (2020).

90. Faulkner, S., Natrajan, L. S., Perry, W. S. & Sykes, D. Sensitised luminescence in lanthanide containing arrays and d–f hybrids. *Dalt. Trans.* 3890 (2009).

91. Galperin, M. & Nitzan, A. Molecular optoelectronics: the interaction of molecular conduction junctions with light. *Phys. Chem. Chem. Phys.* **14**, 9421 (2012).

92. Irie, M. Diarylethenes for Memories and Switches. *Chem. Rev.* **100**, 1685–1716 (2000).

93. Berkovic, G., Krongauz, V. & Weiss, V. Spiropyrans and Spirooxazines for Memories and Switches. *Chem. Rev.* **100**, 1741–1754 (2000).

94. Bao, J. & Weber, P. M. Electronic Effects on Photochemistry: The Diverse Reaction Dynamics of Highly Excited Stilbenes and Azobenzene. *J. Am. Chem. Soc.* **133**, 4164–4167 (2011).

95. Zhang, P. *et al.* Exchange coupling and single molecule magnetism in redox-active tetraoxolene-bridged dilanthanide complexes. *Chem. Sci.* **9**, 1221–1230 (2018).

96. Salinas Uber, J. *et al.* Photochromic Performance of Two Cu(II)-One-Dimensional Solvatomorphs Controlled by Intermolecular Interactions. *Cryst. Growth Des.* **16**, 4026–4033 (2016).

97. Paquette, M. M., Plaul, D., Kurimoto, A., Patrick, B. O. & Frank, N. L. Opto-Spintronics: Photoisomerization-Induced Spin State Switching at 300 K in Photochrome Cobalt–Dioxolene Thin Films. *J. Am. Chem. Soc.* **140**, 14990–15000 (2018).

98. Cador, O., Le Guennic, B. & Pointillart, F. Electro-activity and magnetic switching in lanthanide-based single-molecule magnets. *Inorg. Chem. Front.* **6**, 3398–3417 (2019).

99. Fetoh, A. *et al.* Photo-activation of Single Molecule Magnet Behavior in a Manganese-based Complex. *Sci. Rep.* **6**, 23785 (2016).

100. Zhang, J. L. *et al.* Towards single molecule switches. *Chem. Soc. Rev.* **44**, 2998–3022 (2015).

101. Fetoh, A. *et al.* Synthesis, Structures, and Magnetic Properties of Two Coordination Assemblies of Mn(III) Single Molecule Magnets Bridged via Photochromic Diarylethene Ligands. *Inorg. Chem.* **58**, 2307–2314 (2019).

102. Kong, M. *et al.* Switchable slow relaxation of magnetization in photochromic dysprosium(III) complexes manipulated by a dithienylethene ligand. *New J. Chem.* (2020).

103. Uber, J. S. *et al.* Molecules Designed to Contain Two Weakly Coupled Spins with a Photoswitchable Spacer. *Chem. - A Eur. J.* **23**, 13648–13659 (2017).

104. Kawai, T., Nakashima, Y., Kunitake, T. & Irie, M. Photon-mode modulation of fluorescence and electrical current with a photochromic conducting polymer. *Curr. Appl. Phys.* **5**, 139–142 (2005).

105. Russew, M.-M. & Hecht, S. Photoswitches: From Molecules to Materials. *Adv. Mater.* **22**, 3348–3360 (2010).

106. Jia, C. *et al.* Covalently bonded single-molecule junctions with stable and reversible photoswitched conductivity. *Science.* **352**, 1443–1445 (2016).

107. Fabbrizzi, L. The ferrocenium/ferrocene couple: a versatile redox switch. *ChemTexts* **6**, 22 (2020).

108. Kaur, S., Kaur, M., Kaur, P., Clays, K. & Singh, K. Ferrocene chromophores continue to inspire. Fine-tuning and switching of the second-order nonlinear optical response. *Coord. Chem. Rev.* **343**, 185–219 (2017).

109. Alfonso, M., Espinosa Ferao, A., Tárraga, A. & Molina, P. Electrochemical and Fluorescent Ferrocene-Imidazole-Based Dyads as Ion-Pair Receptors for Divalent Metal Cations and Oxoanions. *Inorg. Chem.* **54**, 7461–7473 (2015).

110. Li, M., Guo, Z., Zhu, W., Marken, F. & James, T. D. A redox-activated fluorescence switch based on a ferrocene–fluorophore–boronic ester conjugate. *Chem. Commun.* **51**, 1293–1296 (2015).

111. Zapata, F., Caballero, A., Espinosa, A., Tárraga, A. & Molina, P. A redox-fluorescent molecular switch based on a heterobimetallic Ir(iii) complex with a ferrocenyl azaheterocycle as ancillary ligand. *Dalt. Trans.* 3900 (2009).

112. Sivaev, I. Ferrocene and Transition Metal Bis(Dicarbollides) as Platform for Design of Rotatory Molecular Switches. *Molecules* **22**, 2201 (2017).

113. Scottwell, S. Ø. & Crowley, J. D. Ferrocene-containing non-interlocked molecular machines. *Chem. Commun.* **52**, 2451–2464 (2016).

114. Rabelo, R. *et al.* Electroswitching of the single-molecule magnet behaviour in an octahedral spin crossover cobalt(ii) complex with a redox-active pyridinediimine ligand. *Chem. Commun.* **56**, 12242–12245 (2020).

115. Freedman, D. E., Jenkins, D. M., Iavarone, A. T. & Long, J. R. A Redox-Switchable Single-Molecule Magnet Incorporating $[Re(CN)_7]^{3-}$. *J. Am. Chem. Soc.* **130**, 2884–2885 (2008).

116. Shao, D. *et al.* Reversible on–off switching of both spin crossover and single-molecule magnet behaviours via a crystal-to-crystal transformation. *Chem. Sci.* **9**, 7986–7991 (2018).

117. Mathonière, C., Lin, H.-J., Siretanu, D., Clérac, R. & Smith, J. M. Photoinduced Single-Molecule Magnet Properties in a Four-Coordinate Iron(II) Spin Crossover Complex. *J. Am. Chem. Soc.* **135**, 19083–19086 (2013).

118. Dickie, C. M., Laughlin, A. L., Wofford, J. D., Bhuvanesh, N. S. & Nippe, M. Transition metal redox switches for reversible "on/off" and "slow/fast" single-molecule magnet behaviour in dysprosium and erbium bis-diamidoferrocene complexes. *Chem. Sci.* **8**, 8039–8049 (2017).

119. Momeni, K. *et al.* Multiscale computational understanding and growth of 2D materials: a review. *npj Comput. Mater.* **6**, 22 (2020).

120. Geim, A. K. & Novoselov, K. S. The rise of graphene. *Nat. Mater.* **6**, 183–191 (2007).

121. Mannix, A. J., Kiraly, B., Hersam, M. C. & Guisinger, N. P. Synthesis and chemistry of elemental 2D materials. *Nat. Rev. Chem.* **1**, 0014 (2017).

122. Novoselov, K. S. *et al.* A roadmap for graphene. *Nature* **490**, 192–200 (2012).

123. Mas-Ballesté, R., Gómez-Navarro, C., Gómez-Herrero, J. & Zamora, F. 2D materials: to graphene and beyond. *Nanoscale* **3**, 20–30 (2011).

124. Donarelli, M. & Ottaviano, L. 2D Materials for Gas Sensing Applications: A Review on Graphene Oxide, MoS_2, WS_2 and Phosphorene. *Sensors* **18**, 3638 (2018).

125. Morant-Giner, M. *et al.* Prussian Blue@MoS_2 Layer Composites as Highly Efficient Cathodes for

Sodium- and Potassium-Ion Batteries. *Adv. Funct. Mater.* **28**, 1706125 (2018).

126. Wang, Y. *et al.* Catalysis with Two-Dimensional Materials Confining Single Atoms: Concept, Design, and Applications. *Chem. Rev.* **119**, 1806–1854 (2019).

127. Toh, R. J., Sofer, Z., Luxa, J., Sedmidubský, D. & Pumera, M. 3R phase of MoS_2 and WS_2 outperforms the corresponding 2H phase for hydrogen evolution. *Chem. Commun.* **53**, 3054–3057 (2017).

128. Gupta, D., Chauhan, V. & Kumar, R. A comprehensive review on synthesis and applications of molybdenum disulfide (MoS_2) material: Past and recent developments. *Inorg. Chem. Commun.* **121**, 108200 (2020).

129. Sun, J. *et al.* Synthesis Methods of Two-Dimensional MoS_2: A Brief Review. *Crystals* **7**, 198 (2017).

130. Li, X. & Zhu, H. Two-dimensional MoS2: Properties, preparation, and applications. *J. Mater.* **1**, 33–44 (2015).

131. Guo, X., Yang, G., Zhang, J. & Xu, X. Structural, mechanical and electronic properties of in-plane 1T/2H phase interface of MoS_2 heterostructures. *AIP Adv.* **5**, 0–10 (2015).

132. Nam, G. H. *et al.* In-Plane Anisotropic Properties of 1T′-MoS_2 Layers. *Adv. Mater.* **31**, 2–7 (2019).

133. Stergiou, A. & Tagmatarchis, N. Molecular Functionalization of Two-Dimensional MoS2 Nanosheets. *Chem. – A Eur. J.* **24**, 18246–18257 (2018).

134. Zhao, Y., Ippolito, S. & Samorì, P. Functionalization of 2D Materials with Photosensitive Molecules: From Light-Responsive Hybrid Systems to Multifunctional Devices. *Adv. Opt. Mater.* **7**, 1900286 (2019).

135. Bertolazzi, S., Gobbi, M., Zhao, Y., Backes, C. & Samorì, P. Molecular chemistry approaches for tuning the properties of two-dimensional transition metal dichalcogenides. *Chem. Soc. Rev.* **47**, 6845–6888 (2018).

136. Wang, J. *et al.* Charge Transfer within the F_4TCNQ-MoS_2 van der Waals Interface: Toward Electrical Properties Tuning and Gas Sensing Application. *Adv. Funct. Mater.* **28**, 1–8 (2018).

137. Jing, Y., Tan, X., Zhou, Z. & Shen, P. Tuning electronic and optical properties of MoS_2 monolayer via molecular charge transfer. *J. Mater. Chem. A* **2**, 16892–16897 (2014).

138. Golub, A. S., Payen, C., Protzenko, G. A., Novikov, Y. N. & Danot, M. Nanocomposite materials consisting of alternating layers of molybdenum disulfide and cobalt or nickel hydroxides: Magnetic characterization. *Solid State Commun.* **102**, 419–423 (1997).

139. Knirsch, K. C. *et al.* Basal-Plane Functionalization of Chemically Exfoliated Molybdenum Disulfide by Diazonium Salts. *ACS Nano* **9**, 6018–6030 (2015).

140. Pramoda, K., Gupta, U., Ahmad, I., Kumar, R. & Rao, C. N. R. Assemblies of covalently cross-linked nanosheets of MoS_2 and of MoS_2–RGO: synthesis and novel properties. *J. Mater. Chem. A* **4**, 8989–8994 (2016).

141. Vishnoi, P., Sampath, A., Waghmare, U. V. & Rao, C. N. R. Covalent Functionalization of Nanosheets of MoS_2 and $MoSe_2$ by Substituted Benzenes and Other Organic Molecules. *Chem. - A Eur. J.* **23**, 886–895 (2017).

142. Zhao, Y., Bertolazzi, S. & Samorì, P. A Universal Approach toward Light-Responsive Two-Dimensional Electronics: Chemically Tailored Hybrid van der Waals Heterostructures. *ACS Nano* **13**, 4814–4825 (2019).

143. Presolski, S. *et al.* Functional Nanosheet Synthons by Covalent Modification of Transition-Metal Dichalcogenides. *Chem. Mater.* **29**, 2066–2073 (2017).

144. Morant-Giner, M. *et al.* WS_2/MoS_2 Heterostructures through Thermal Treatment of MoS_2 Layers Electrostatically Functionalized with W_3S_4 Molecular Clusters. *Chem. – A Eur. J.* **26**, 6670–6678 (2020).

145. Hirsch, A. & Hauke, F. Post-Graphene 2D Chemistry: The Emerging Field of Molybdenum Disulfide

and Black Phosphorus Functionalization. *Angew. Chemie Int. Ed.* **57**, 4338–4354 (2018).

146. Vallejo, J. Estudio de Imanes Moleculares de Co(II): desde sistemas aislados hasta sistemas organizados y multifuncionales. (University of Valencia, 2016).

147. Bertotti, G. Magnetic Hysteresis. in *Hysteresis in Magnetism* 3–30 (Elsevier, 1998).

Chapter II

Counterion effect on the zfs and the slow magnetic relaxation in octahedral cobalt(II) compounds

Mononuclear compounds with the general formula of $[Co(Me_2phen)_2(Sal)]X$ (X = $ClO_4 \cdot H_2O$, BPh_4 and $PF_6 \cdot H_2O$) were synthesised. They exhibit field-induced slow relaxation of magnetisation. The counterion generates differences on the crystal packing of the compounds and the coordination sphere of the Co^{II} ions. Most importantly, these differences are reflected in zfs parameters and magnetic relaxation mechanisms.

II.1 Introduction

Polynuclear molecule magnets, also known as single-molecule magnets (SMMs), have attracted the scientific interest since they are relevant for their applications in information storage and spintronics.[1–3] Their performance in showing magnetic bistability is related to axial magnetic anisotropy, associated with an energy barrier. However, the main disadvantage of SMMs resides in the difficulty to control the total magnetic anisotropy, since it is composed by all the paramagnetic constituents differing in orientation and magnitude.[4] Therefore, new strategies focused on better anisotropy control have emerged. They consist of a choice of the coordination complexes with one single paramagnetic metal ion and an appropriate ligand field leading to first-order spin-orbit coupling (SOC).[5] These complexes are commonly known as mononuclear SMMs or single-ion magnets (SIMs). Among all reported SIMs based on 3d-metal centres, Co^{II} ion is the most prolific 3d metal ion for complexes exhibiting slow magnetic relaxation in a variety of geometries.[6]

Predicting both the sign and magnitude of the magnetic anisotropy is not easy a priori. However, systematic investigations reporting on the geometry of the first coordination sphere of many compounds have helped overcome this problem.[7–10] In cobalt(II) complexes, such magnetostructural correlations have mainly been done for tetrahedral cobalt(II) complexes. They are based on structural distortions, heavier atom substitution, etc.[11–13] However, the role of the counterion has often been overlooked.[14] This is not the case in other research areas such as supramolecular chemistry, where their importance has stood out due to the different coordination ability, geometry, size and basicity.[15,16]

In previous work, we studied the geometrical constraints at the metal centre, by tuning the ligands, on the magnetic anisotropy parameters and the slow magnetic relaxation dynamics.[17] Here, we extend our research by studying the effect of the counterion on these properties. For that reason, we have chosen a variety of counterions with different sizes and geometries. We present the syntheses, X-ray structure and magnetic characterisation of cobalt(II) complexes with the formula $[Co(Me_2phen)_2(Sal)]X$ (**1·X**), with Me_2phen = 2,9-dimethyl-1,10-phenanthroline, Sal = salicylaldehyde and X = $ClO_4·H_2O$, BPh_4 and $PF_6·H_2O$. Frequency-domain Fourier-transform THz-EPR or far-infrared magnetic spectroscopy (FIRMS) and high-field EPR, supported by theoretical calculations, are also employed to determine the zfs in such compounds properly.

II.2 Experimental section

II.2.1 Materials

All chemicals were obtained from commercial sources and used as received.

Caution! Perchlorate salts are potentially explosive. They should be used in small quantities and should be treated with the utmost care at all times.

II.2.2 Syntheses

[Co(Me$_2$phen)$_2$(Sal)](ClO$_4$)·H$_2$O (1·ClO$_4$·H$_2$O). Co(ClO$_4$)$_2$·6H$_2$O (80 mg, 0.22 mmol, 1 eq) and the corresponding phenanthroline ligand (96 mg, 0.44 mmol, 2 eq) were dissolved in methanol (8 mL). Then, a methanol solution of salicylaldehyde, HSal (24 μL, 0.22 mmol, 1 eq) and NaH (60% in oil) (9 mg, 0.22 mmol, 1 eq) was added affording an orange solution. Red-orangish single crystals suitable for X-ray diffraction were obtained by slow evaporation. Yield: 76 mg, 49%. IR (ν_{max}/cm^{-1}): 3464(w), 3068(w), 3025(w), 2975(w), 2925(vw), 2847(vw), 2773(vw), 2514(vw), 1623(vs), 1595(s), 1561(w), 1522(s), 1500(s), 1458(m), 1439(s), 1425(m), 1407(m), 1378(w), 1356(m), 1334(m), 1292(w), 1243(vw) 1180(w), 1152(m), 1094(vs), 1027(m), 992(w), 898(w), 858(m), 813(vw), 773(m), 732(m), 683(vw), 653(w), 623(m), 587(vw), 551(w), 496(w). Elemental Analysis calculated for **1·ClO$_4$·H$_2$O** ($C_{35}H_{31}ClCoN_4O_7$): C, 58.87; H, 4.38; N, 7.85. Found: C, 58.30; H, 3.97; N, 7.68.

[Co(Me$_2$phen)$_2$(Sal)](BPh$_4$) (1·BPh$_4$). The synthesis was performed as **1·ClO$_4$·H$_2$O** with the subsequent addition of NaBPh$_4$ (113 mg, 0.33 mmol, 1.5 eq). Red single crystals suitable for X-ray diffraction were obtained by slow evaporation. Yield: 162 mg, 82%. IR (ν_{max}/cm^{-1}): 3398(w), 3053(w), 3027(w), 2998(w), 2982(w), 2923(vw), 2843(vw), 2761(vw), 1622(vs), 1594(m), 1561(m), 1521(m), 1501(m), 1478(m), 1425(s), 1401(m), 1356(m), 1339(m), 1292(w), 1285(w), 1176(w), 1143(s), 1124(s), 1030(m), 898(w), 856(s), 813(w), 757(m), 731(s), 703(s), 652(m), 611(m), 585(w), 550(m), 490(w), 436(vw). Elemental Analysis calculated for **1·BPh$_4$** ($C_{59}H_{49}BCoN_4O_2$): C, 77.38; H, 5.39; N, 6.12. Found: C, 77.18; H, 5.15; N, 6.16.

[Co(Me$_2$phen)$_2$(Sal)](PF$_6$)·H$_2$O (1·PF$_6$·H$_2$O). The synthesis was performed as **1·ClO$_4$·H$_2$O** with the subsequent addition of KPF$_6$ (61 mg, 0.33 mmol, 1.5 eq). A white suspension was filtered off and discarded. The filtrate was allowed to slowly evaporate, obtaining red single crystals suitable for X-ray diffraction, which were collected by filtration and washed with small amounts of EtOH to remove the impurities. Yield: 98 mg, 58%. IR (ν_{max}/cm^{-1}): 3663(w), 3592(w), 3550(m), 3473(m), 3415(m), 3235(vw), 3077(vw), 3050(vw), 3011(vw), 2925(vw), 2871(vw), 1623(vs), 1596(m), 1564(w), 1523(s), 1499(m), 1428(m), 1399(m), 1380(w), 1358(m), 1340(w), 1293(w), 1242(vw), 1212(w), 1201(w), 1193(w), 1177(w), 1155(m), 1142(m), 1124(m), 1099(m), 1035(w), 1022(w), 992(vw), 900(w), 834(vs), 770(m),

759(m), 731(m), 682(w), 652(w), 590(w), 558(s), 500(m). Elemental Analysis calculated for **1·PF$_6$·H$_2$O** ($C_{35}H_{31}CoF_6N_4O_3P$): C, 55.35; H, 4.11; N, 7.38. Found: C, 56.18; H, 4.09; N, 7.18.

II.2.3 Physical measurements

Infrared spectra (4000–400 cm^{-1}) were recorded on a Nicolet 5700 spectrophotometer as KBr pellets. Elemental analyses (C, H, N) were performed at the Microanalytical Service of the Universitat de València.

X-ray powder diffraction (XRPD) patterns were recorded on a Panalytical Empyrean X-ray diffractometer by using Cu Kα radiation (λ = 1.5406 Å), in which the X-ray tube was operated at 45 kV and 40 mA ranging from 2 to 40°. The XRPD data was background corrected with the *HighScore Plus* software.

Static direct current (dc) measurements were carried out on all samples by powdering and restraining the samples with *n*-eicosane to prevent any displacement. Variable-temperature (2.0–300 K) dc-magnetic susceptibility under an applied field of 0.25 (T < 20 K) and 5.0 kOe (T ≥ 20 K), and variable-field (0–5.0 kOe) magnetisation in the temperature range from 2 to 10 K were recorded with a Quantum Design SQUID magnetometer. Variable-temperature (2.0–10.0 K) alternating current (ac) magnetic susceptibility measurements under ±0.005 kOe oscillating field at frequencies in the range of 0.1–10 kHz were carried out on crystalline samples under different applied static dc fields in the range 0.0–5.0 kOe with a Quantum Design Physical Property Measurement System (PPMS). The magnetic susceptibility data were corrected for the diamagnetism of the constituent atoms and the sample holder.

HFEPR spectra of all samples were recorded at 4.5 K on polycrystalline samples (20–25 mg) by using a homodyne spectrometer associated with a 150/170 kOe superconducting magnet in a frequency range from 52 to 610 GHz. Detection was provided with an InSb hot electron bolometer (QMC Ltd., Cardiff, UK). The magnetic field was modulated at 50 kHz for detection purposes. A Stanford Research Systems SR830 lock-in amplifier converted the modulated signal to dc-voltage. The single-frequency spectra were simulated with the SPIN software. Far-infrared magnetic spectra (FIRMS) were collected at the National High Magnetic Field Laboratory using a Bruker Vertex 80v FT-IR spectrometer coupled with a 170 kOe vertical-bore superconducting magnet. The experimental setup was equipped with a mercury lamp and a composite silicon bolometer (Infrared Laboratories), as a THz radiation source and detector, respectively. An *n*-eicosane pellet containing the studied compound was measured in the spectral region between 14 and 730 cm^{-1} (0.42–22 THz) with a resolution of 0.3 cm^{-1} (9 GHz). A low-pressure helium gas cooled both sample and bolometer down to 5 K. The relative transmittance spectra were calculated as the THz intensity spectrum at each magnetic field divided by the THz intensity spectrum averaged for all fields.

II.2.4 X-ray Crystallography

Single-crystal X-ray diffraction data of **1·X (**X = $ClO_4 \cdot H_2O$, BPh_4 and $PF_6 \cdot H_2O$**)** were collected on a Bruker-AXS Kappa Mach3 APEX-II diffractometer equipped with an Incoatec Helios monochromator mirror (Mo-Kα λ = 0.71073 Å) and a nitrogen cold stream adjusted to 100 K. Data integration, data scaling and absorption correction were done using programs SAINT and SADABS, respectively. The structures were solved with the SHELXS structure solution program, using the Patterson method.[18] The model was refined with version 2018/3 of SHELXL against F2 on all data by full-matrix least squares.[19,20] All non-hydrogen atoms were refined with anisotropic displacement parameters. Hydrogen atoms were placed at calculated positions. The final geometrical calculations and the graphical manipulations were carried out with the PLATON package.[21] Crystallographic data for compounds **1·X (**X = $ClO_4 \cdot H_2O$, BPh_4 and $PF_6 \cdot H_2O$**)** are given in Table A.1.

II.2.5 Computational details

Calculations based on a second-order *N*-electron valence state perturbation theory (CASSCF/NEVPT2) applied on the wave function, which was previously obtained from complete active space (CAS) calculation, were performed on the structurally characterised mononuclear complexes **1·X** (X = **$ClO_4 \cdot H_2O$**, **BPh_4** and **$PF_6 \cdot H_2O$**) aiming to evaluate the parameters that determine the axial (*D*) and rhombic (*E*) zfs in them.[22] These mononuclear species keep the experimental dispositions of the ligands around the metal. The calculations were carried out with version 4.0.1 of the ORCA and the auxiliary TZV/C Coulomb fitting basis sets.[23] The spin−orbit coupling contributions to zfs from 10 quartet and 20 doublet excited states generated from an active space with seven electrons in five d-orbitals were included from an effective Hamiltonian. The *g*-tensors were calculated for the ground Kramers pair using Multireference Configuration Interaction (MRCI) wave functions with a first-order perturbation theory on the SOC matrix.[24]

II.3 Results and discussion

II.3.1 Syntheses and X-ray Structure description

The reaction of Me_2phen and $Co(ClO_4)_2{\cdot}6H_2O$ with salicylaldehyde and NaH in methanol yielded the complex **1·ClO₄·H₂O**. The addition of 1.5 equivalents of $NaBPh_4$ and KPF_6 to the previous solution allowed the anion exchange affording **1·BPh₄** and **1·PF₆·H₂O**, respectively.

A strong absorption peak at ~1623 cm^{-1} in the infrared spectra is assigned to the $\nu_{C=O}$ stretching vibration, which is shifted to lower energies for the complexes than the free ligand. Medium and weak absorption peaks at ~1595 and 1561 cm^{-1} are attributed to the Me_2phen ligand. The presence of the counterion was confirmed at the infrared spectra by the occurrence of strong bands at 1094 (ν_{Cl-O}), 704 (δ_{BPh4}), and 834 cm^{-1} (ν_{P-F6}) in **1·ClO₄**, **1·BPh₄**, **1·PF₆**, respectively.

Their XRPD data recorded on polycrystalline samples were in good agreement with those simulated from the respective single-crystal X-ray data, confirming their purity (Figures A.1–3).

Compounds **1·X** (X = **ClO₄·H₂O**, **BPh₄** and **PF₆·H₂O**) crystallise in the triclinic *P*−1 space group, composed of a mononuclear complex cation $[Co(Me_2phen)_2(Sal)]^+$ and one anion (perchlorate, tetraphenylborate or hexafluorophosphate), shown in Figures II.1 and A.4–5. All compounds show a water crystallisation molecule except for **1·BPh₄**. They all exhibit CoN_4O_2 distorted octahedral coordination spheres with the equatorial plane constituted by two nitrogen atoms and two oxygen atoms from two Me_2phen and one chelating salicylaldehyde ligands, respectively. One nitrogen atom from each phenanthroline derivative occupies the axial positions. The distances of the Co^{II} ion from the equatorial N_2O_2 plane are 0.004, 0.026 and 0.101 Å for **1·ClO₄·H₂O**, **1·BPh₄** and **1·PF₆·H₂O**, respectively. The distortion degree for all compounds was calculated through the continuous shape measure theory implemented in the SHAPE program.[25] The OC-6 and TPR-6 parameters, defined by this structural analysis, deviate from a null value as it moves away from the ideal octahedron and trigonal prims, respectively. The values for the octahedron and trigonal prisms are 1.966 and 14.057, 1.418 and 14.180, and 1.971 and 14.221 for **1·ClO₄·H₂O**, **1·BPh₄**, and **1·PF₆·H₂O**, respectively. Both ideal geometries are connected through the minimal distortion pathway, and the value that determines how the experimental geometries deviate from it are 24.6, 19.9, and 25.2, for **1·ClO₄·H₂O**, **1·BPh₄**, and **1·PF₆·H₂O**, respectively. In conclusion, all three complexes exhibit an octahedral geometry, being **1·ClO₄·H₂O** and **1·PF₆·H₂O** slightly more distorted than **1·BPh₄**.

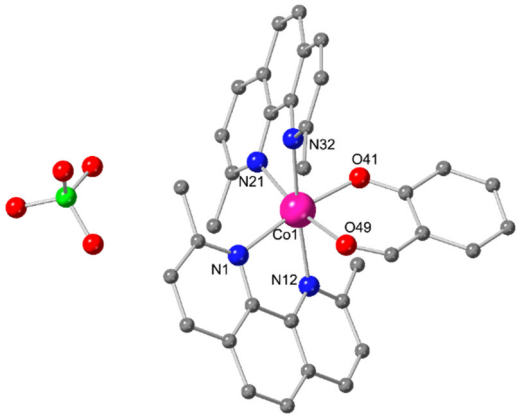

Figure II.1. Perspective view of **1·ClO₄·H₂O**. Hydrogen atoms are omitted for clarity. Colour code: magenta, cobalt; blue, nitrogen; red, oxygen; grey, carbon; green, chlorine.

Although the main change in these three compounds is the counterion, differences in bond lengths and angles occur in the coordination sphere. Selected bond lengths and angles are listed in Table II.1. The Co–N distances are in the range of 2.15–2.24 Å, 2.16–2.18 Å and 2.15–2.23 Å for **1·ClO₄·H₂O**, **1·BPh₄** and **1·PF₆·H₂O**, respectively. The chelating N–Co–N angles (75.10–78.16°) are in the range reported in the literature.[26–28] The larger number of carbon atoms linking the oxygen atoms in the Sal ligand, favours a O–Co–O angle (86.99, 84.96 and 87.40° for **1·ClO₄·H₂O**, **1·BPh₄** and **1·PF₆·H₂O**) greater than for a chelating carboxylate (~62°).[17,29,30] The angles between the two pyridyl rings of the Me₂phen are 10.64° and 11.50° for **1·ClO₄·H₂O**, 9.32° and 9.76° for **1·BPh₄** and 9.72° and 9.85° for **1·PF₆·H₂O**. Furthermore, the dihedral angle between the phenyl ring of the salicylaldehyde ligand and the O–Co–O plane is 22.84, 11.94 and 14.96° for **1·ClO₄·H₂O**, **1·BPh₄** and **1·PF₆·H₂O**, respectively.

Table II.1. Selected bond distances and angles for **1·X** (X = ClO₄·H₂O, BPh₄ and PF₆·H₂O).

Compound	1·ClO₄·H₂O	1·BPh₄	1·PF₆·H₂O
Bond distances [Å]			
Co1–N1	2.1461(8)	2.1802(10)	2.154(5)
Co1–N21	2.1487(8)	2.1624(10)	2.167(5)
Co1–N32	2.1732(8)	2.1804(11)	2.197(5)
Co1–N12	2.2396(8)	2.1748(11)	2.229(4)
Co1–O41	2.0000(7)	2.0422(13)	2.007(4)
Co1–O49	2.1120(7)	2.1371(13)	2.117(4)
Bond angles [°]			
O41–Co1–O49	86.99(3)	84.61(6)	87.40(16)
N1–Co1–N12	76.05(3)	77.63(4)	76.53(17)
N21–Co1–N32	77.04(3)	77.77(4)	77.02(18)
N12–Co1–N32	173.46(3)	179.45(4)	173.77(18)
N12–Co1–O41	96.23(3)	98.77(5)	97.70(16)
N12–Co1–N21	109.32(3)	102.33(4)	108.90(17)

Despite the significant similarity, at the molecular level, between the three compounds, each one shows a different crystal packing (Figures A.6–8). In **1·ClO$_4$·H$_2$O** and **1·PF$_6$·H$_2$O**, the crystallisation water molecule and the anion are involved in hydrogen bonding (Table A.2), whereas in **1·BPh$_4$** such types of interactions are absent. In all complexes, π–π interactions form a supramolecular chain developed along the *c*-axis in **1·ClO$_4$·H$_2$O** and **1·PF$_6$·H$_2$O** and between the *b*-axis and *c*-axis in **1·BPh$_4$** (Table A.3 and Figures II.2–4). Moreover, the counterion is involved in these interactions in **1·BPh$_4$**. Intermolecular Co1···Co1 distances along this chain take values of 9.599 and 9.992 Å, 9.881 and 10.413 Å, and 9.806 and 9.978 Å for **1·ClO$_4$·H$_2$O**, **1·BPh$_4$** and **1·PF$_6$·H$_2$O**, respectively. However, the shortest intermolecular Co···Co distances (7.540, 7.812 and 7.546 Å for **1·ClO$_4$·H$_2$O**, **1·BPh$_4$** and **1·PF$_6$·H$_2$O**, respectively) occur between neighbouring chains. In **1·ClO$_4$·H$_2$O**, the supramolecular chains are organised in layers built from a zig-zag arrangement of the cobalt(II) complexes along the *a*-axis. These layers ordered along *b*-axis are separated from each other by anions and water molecules (Figure A.6). The same organisation in the crystal structure of the metal complexes and the emerged supramolecular chain is also found in **1·PF$_6$·H$_2$O** (Figure A.8). However, in **1·BPh$_4$**, the counterion is also involved in the cobalt(II) supramolecular chain through its phenyl ring (Figure A.7).

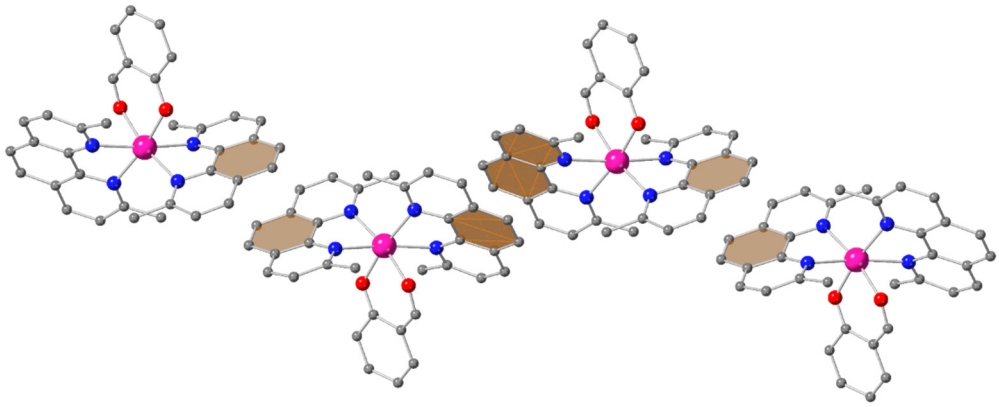

Figure II.2. Perspective view of the supramolecular chain of **1·ClO$_4$·H$_2$O** with π–π interactions involving phenanthroline coloured in orange. Perchlorate anions, hydrogen atoms and crystallisation solvent molecules are omitted for clarity. Colour code: magenta, cobalt; blue, nitrogen; red, oxygen; grey, carbon.

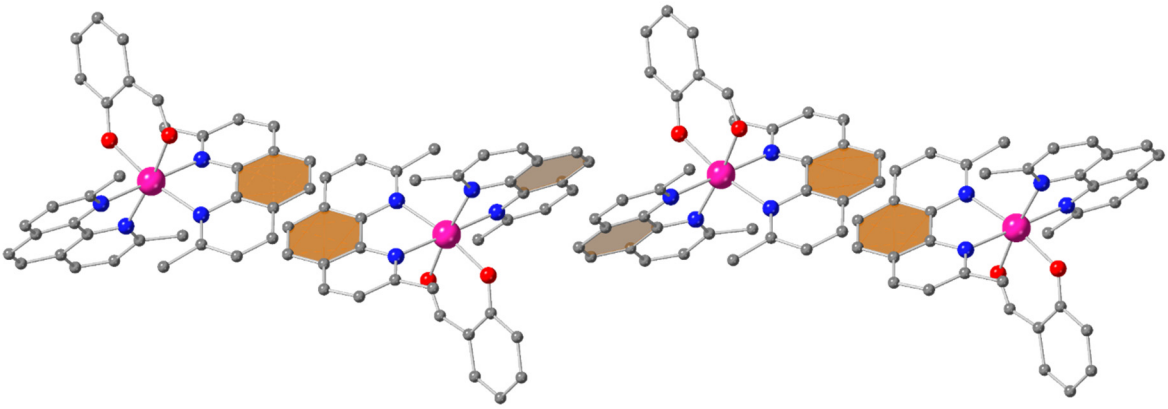

Figure II.3. Perspective view of the supramolecular chain of **1·BPh$_4$** with π−π interactions involving phenanthroline coloured in orange. Tetraphenylborate anions and hydrogen atoms are omitted for clarity. Colour code: magenta, cobalt; blue, nitrogen; red, oxygen; grey, carbon.

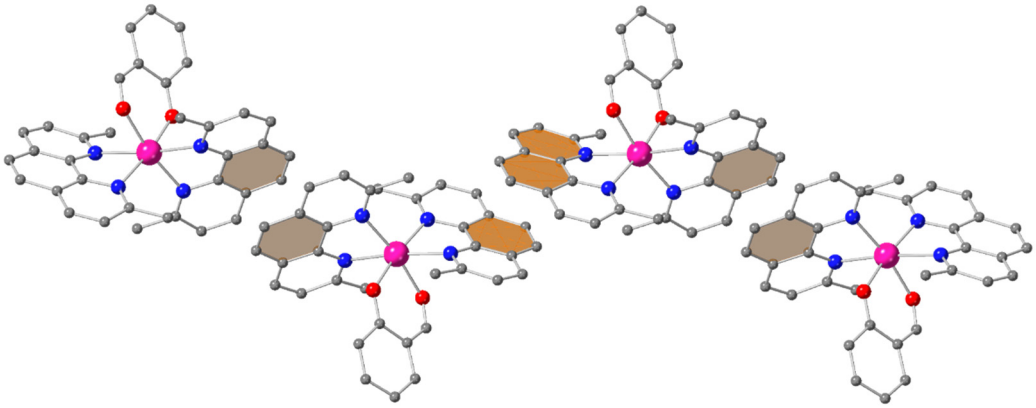

Figure II.4. Perspective view of the supramolecular chain of **1·PF$_6$·H$_2$O** with π−π interactions involving phenanthroline coloured in orange. Hexafluorophosphate anions, hydrogen atoms and crystallisation solvent molecules are omitted for clarity. Colour code: magenta, cobalt; blue, nitrogen; red, oxygen; grey, carbon.

II.3.2 Magnetic properties, FIRMS, HFEPR and theoretical calculations

The direct current (dc) magnetic properties of **1·X** (X = ClO$_4$·H$_2$O, BPh$_4$ and PF$_6$·H$_2$O) are shown as $\chi_M T$ *vs* T and M *vs* H/T curves (Figure II.5). In all of them, the $\chi_M T$ value at room temperature: 2.85 (**1·ClO$_4$·H$_2$O**), 3.17 (**1·BPh$_4$**) and 2.92 cm^3 K mol^{-1} (**1·PF$_6$·H$_2$O**) is higher than the expected spin-only value for a S = 3/2 with g = 2.0 (1.875 cm^3 K mol^{-1}) for **1·X** (X = ClO$_4$·H$_2$O, BPh$_4$ and PF$_6$·H$_2$O), respectively. These high values are typical for Co^{II} ions with significant spin-orbit coupling (SOC). When cooling, the $\chi_M T$ product decreases gradually until 100 K and then more abruptly until reaching values of 1.57, 1.90 and 1.62 at 2 K, suggesting the presence of a strong first-order spin-orbit coupling (SOC) only, as usually observed in octahedral cobalt(II) complexes. The drop of $\chi_M T$ below 5 K is simulated by the applied magnetic field (5.0 kOe) during the recording data. The absence of any

magnetic coupling is supported by the fact that the mononuclear cobalt(II) complexes are well crystallographically isolated between them (Co···Co distances > 7.54 Å).

The magnetisation values at 50 kOe and 2 K are 2.13, 2.32 and 2.20 Nβ for **1·X** (X = $ClO_4 \cdot H_2O$, BPh_4 and $PF_6 \cdot H_2O$), respectively. These values are significantly below the saturation limit of 3 Nβ for an S = 3/2 spin moment with a g = 2, suggesting the presence of a significant zero-field splitting (zfs). The isothermal magnetisation curves in the 2–10 K temperature range are close to superimposition, which suggests well separated excited and ground Kramers doublet states with the ground Kramers doublet populated only, due to a significant zfs.

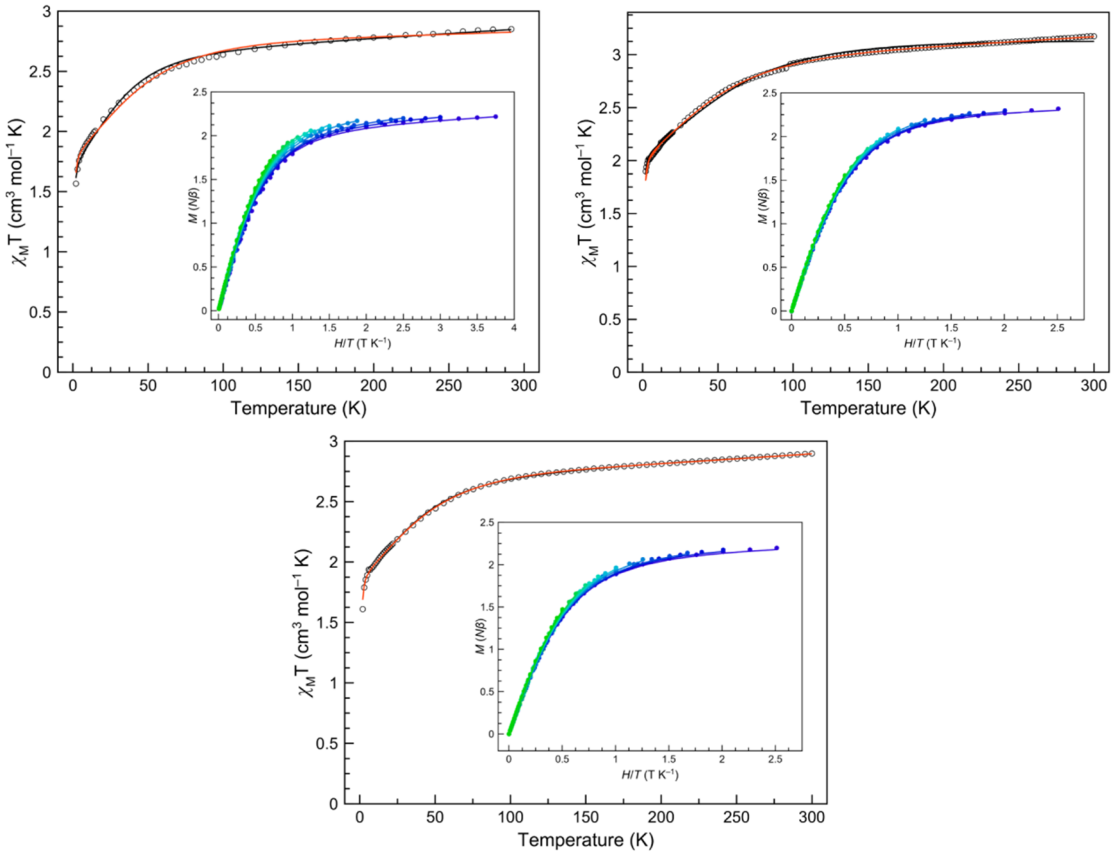

Figure II.5. Plots of $\chi_M T$ *vs* T in the range 2–300 K in 5.0 kOe applied field and M *vs* H/T (inset) for **1·ClO₄·H₂O** (top left) and **1·BPh₄** (top right) and **1·PF₆** (bottom) in the 2–10 K temperature range (2 K blue to 10 K green gradient). The solid lines are the best-fit curves (see text).

The experimental magnetic susceptibility and magnetisation data of **1·X** (X = $ClO_4 \cdot H_2O$, BPh_4 and $PF_6 \cdot H_2O$) were analysed in the whole temperature range through the T-P isomorphism formalism expressed with the following SOC Hamiltonian (Figure II.5, red line):

$$\hat{H}_{SOC+Zeeman} = -\alpha\lambda\hat{L}\hat{S} + \Delta\left[\hat{L}_z^2 - \frac{1}{3}L(L+1)\right] + \beta H\left[g_e\hat{S} - \alpha\hat{L}\right] \qquad (1)$$

where λ is the spin-orbit coupling parameter, and α the orbital reduction factor ($\alpha = A\kappa$). The κ parameter takes into account the reduction of the orbital momentum caused by the delocalisation of the unpaired electrons, while the *A* parameter represents the contribution of the upper $^4T_{1g}(^4P)$ state into the $^4T_{1g}(^4F)$ ground state. Therefore, *A* takes values ranging between 1.5 and 1 in the weak and strong crystal-field limits, respectively. Furthermore, under an axial distortion of the ideal O_h symmetry of the cobalt(II) coordination sphere, the triplet orbital $^4T_{1g}$ splits into the singlet $^4A_2$ and doublet ^4E levels, separated by an energy gap described by the Δ parameter. Both levels split by second-order spin-orbit coupling give rise to two and four Kramers doublets, respectively. The best fits of the parameters to the magnetic data using the PHI software[31] are shown in Table II.2. In the table, the parameter *F* is the agreement factor defined as $F = \sum[P_{exp} - P_{calcd}]^2/\sum[P_{exp}]^2$, being *P* the measured physical property. The values of the parameters are similar in the three compounds, which was expected, with the correspondence being larger for **1·ClO$_4$·H$_2$O** and **1·PF$_6$·H$_2$O** than for **1·BPh$_4$**, *i.e.*, for the compounds in which a water crystallisation molecule is present and whose geometries are close to each other. The obtained values fall within the range of those observed for other already reported six-coordinate high-spin cobalt(II) compounds.[28,32]

Independently, the magnetic susceptibility data were also analysed using a spin Hamiltonian corresponding to an isolated $S = 3/2$ state with significant SOC (Figure II.5, black line):

$$\widehat{H}_{zfs+Zeeman} = D\left[\hat{S}_z^2 - \frac{1}{3}S(S+1)\right] + E\left(\hat{S}_x^2 - \hat{S}_y^2\right) + \beta H\left[g_{\parallel}\hat{S}_z + g_{\perp}\left(\hat{S}_x + \hat{S}_y\right)\right] \quad (2)$$

where *S* is the spin ground state, *D* and *E* are the axial and transverse magnetic anisotropies respectively, β is the Bohr magneton and *H* is the applied magnetic field. This approach is possible because only the two ground state Kramers doublets are populated at low temperatures, but a TIP parameter should be considered to empirically account for the depopulation when lowering the temperature of the higher states coming from the first-order SOC approach. The best fit to the magnetic data using the PHI software[31] gave the values that are shown in Table II.3. An agreement between the experimental and calculated curves is obtained for all compounds, with a near-maximum rhombicity of the zfs tensor achieved in all cases. In such a situation, the obtained positive *D* sign for **1·ClO$_4$·H$_2$O** and **1·BPh$_4$** and the negative *D* sign for **1·PF$_6$·H$_2$O** through this model should be disregarded, *i.e.*, in such conditions no sign of *D* exists. The calculated energy gap between the lowest Kramers doublets connects both models, first-order SOC and zfs, validating both models (Table II.4). Nevertheless, the large differences in the magnitude of *D* in all systems were unexpected. The high value of the *E*/*D* ratio must be associated with a loss of symmetry of the ligand field, rather than a structural distortion, due to

different donor atoms (oxygen and nitrogen) and the different chemical character of these oxygen atoms in the Sal ligand.

Table II.2. Spin Hamiltonian parameters for **1·X** (X = $ClO_4·H_2O$, BPh_4 and $PF_6·H_2O$) obtained following the SOC model.

Compound	λ (cm^{-1})	Δ (cm^{-1})	α	TIP × 10^6 (cm^3 mol^{-1})	F^a × 10^6
1·ClO_4·H_2O	−113.6	−194.0	1.01	970	110.0
1·BPh_4	−109.8	−194.3	1.22	1494	23.3
1·PF_6 H_2O	−113.4	−283.0	1.02	1425	1.58

[a] F is the agreement factor defined as $F = \sum[P_{exp} - P_{calcd}]^2/\sum[P_{exp}]^2$

Table II.3. Spin Hamiltonian parameters for **1·X** (X = $ClO_4·H_2O$, BPh_4 and $PF_6·H_2O$) obtained following the zfs model.

Compound	D (cm^{-1})[a]	$\lvert E/D \rvert$	$g_\perp$	$g_{\lvert\lvert}$	g_{av}	TIP × 10^6 (cm^3 mol^{-1})	F^b × 10^5
1·ClO_4·H_2O	+38.69	0.299	2.49	2.00	2.33	856	9.70
1·BPh_4	+76.33	0.249	2.73	2.16	2.54	323	6.48
1·PF_6 H_2O	–47.36	0.321	2.23	2.64	2.37	798	2.15

[a] The sign is required to achieve a good simulation with the PHI software. However, the sign should be treated with care (see text). [b] F is the agreement factor defined as $F = \sum[P_{exp} - P_{calcd}]^2/\sum[P_{exp}]^2$

To better determine the sign and amplitude of zfs parameters of **1·X** (X = $ClO_4·H_2O$, BPh_4 and $PF_6·H_2O$), frequency and field-domain magnetic resonance experiments were also performed. Far-infrared magnetic spectroscopy (FIRMS) spectra were recorded at 5 K. FIRMS spectra (Figure II.6 and A.9) show a single magnetic zero-field absorption at 107, 130 and 115 cm^{-1} for **1·ClO_4·H_2O, 1·BPh_4** and **1·PF_6·H_2O**, respectively, corresponding to the inter-Kramers transition in each compound. This absorption is recognizable in the three cases despite the stronger coupling with vibrons/phonons in **1·BPh_4** than in the other compounds. Magnetic transitions differ from non-magnetic transitions by linear splitting caused by an increase in the applied magnetic field. The FIRMS spectra show a clear spin-phonon coupling in all cases (blue line Figure A.9), and the energy gap (Δ) between the two lowest Kramers doublets can be directly determined from that transition. Δ is related to D and E (the axial and transverse magnetic anisotropies, respectively) through the formula $\Delta = 2\sqrt{D^2 + 3E^2}$.

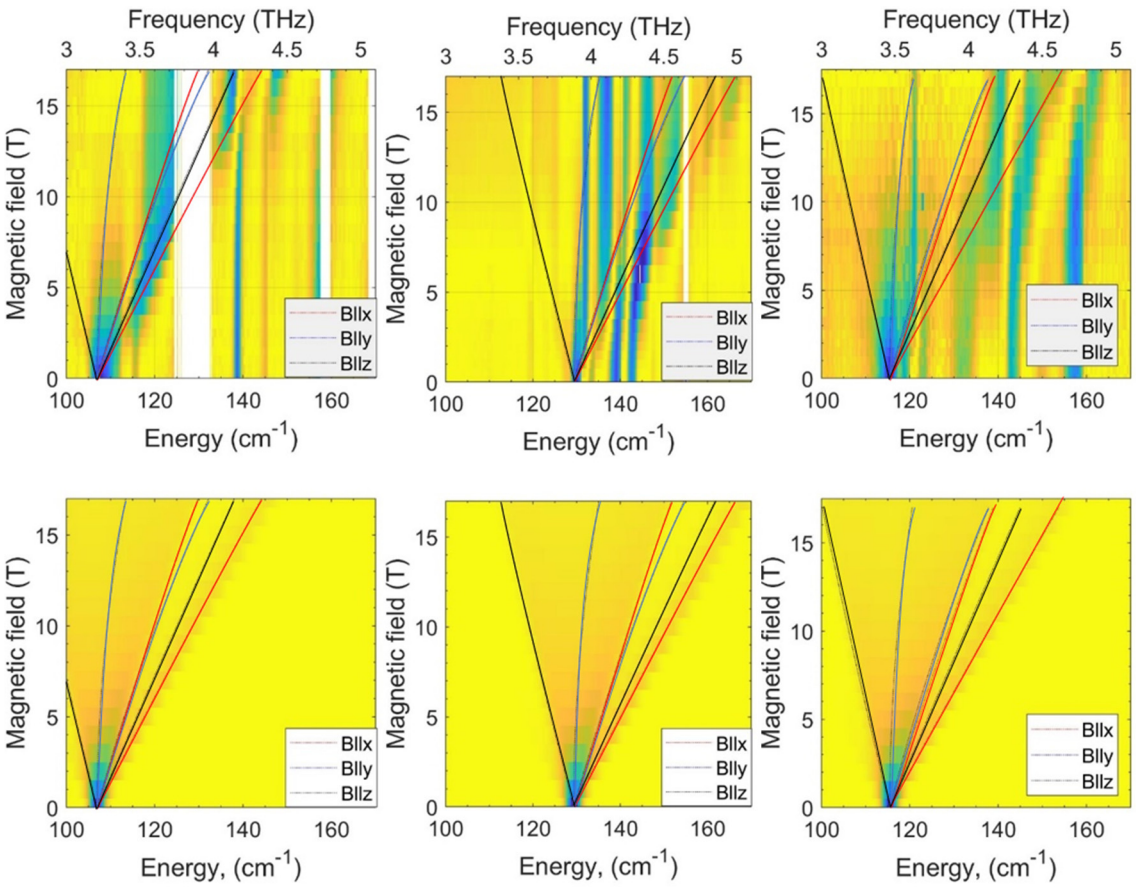

Figure II.6. A false-colour (contour) FIRMS map (upper row) and their magnetic resonance simulations (lower row) of **1·ClO₄·H₂O** (left column), **1·BPh₄** (middle column) and **1·PF₆·H₂O** (right column) at 5 K. The tendency towards the blue colour means the absorbance increases, whereas the yellow colour corresponds to the transparent regions.

Although FIRMS is the most direct and accurate technique to measure the energy gap between the two lowest Kramers doublets, it generally cannot bring information on the rhombicity of the zfs tensor, and the *g*-values. To obtain this information, HFEPR studies are required. HFEPR single-frequency spectra and multifrequency studies on *n*-eicosane pellets of **1·X** (X = $ClO_4·H_2O$, BPh_4 and $PF_6·H_2O$) are shown in (Figure II.7). As expected, three distinct turning points of the intra-Kramers transition within the lower doublet are found in each case (Figures II.7–8). In all three cases, simulating that pattern required the assumption of maximum rhombicity for the zfs tensor (E/D = 1/3) and significant rhombicity of the *g*-tensor as well, with the simulated values indicated in Table II.5. In short, the high rhombicity of the zfs tensor makes the sign of D undefined. This phenomenon explains the difficulty in establishing the sign from magnetometry. This difficulty is transferred to the CASSCF/NEVPT2 study (see below) due to the lower quality of the E/D evaluation of these calculations. The perpendicular components of the *g*-tensor are larger than the parallel one, which resembles other octahedral cobalt(II) complexes with an axial anisotropy.

The previous conclusions were confirmed through a theoretical study based on CASSCF/NEVPT2 calculations. Values found for the parameters of the spin Hamiltonian expressed in equation (2) are shown in Table II.5. Their values are similar to those obtained by experimental techniques. In all three cases, like in the rest of the cobalt(II) octahedral complexes, D is primarily determined by the contribution of the quadruplet states (D_Q and D_D equal to +46.6 and –1.5 (**1·ClO₄·H₂O**), +54.9 and +1.5 (**1·BPh₄**), –58.1 and –2.0 cm^{-1} (**1·PF₆·H₂O**), respectively), mainly from the first two excited states close to the ground state [D_{Q1}+D_{Q2} equal to +51.3 (**1·ClO₄·H₂O**), +57.3 (**1·BPh₄**), –58.1 cm^{-1} (**1·PF₆·H₂O**)], together with they make up the ground term $^4T_{1g}$ in an ideal geometry (Table A.4). Although **1·PF₆·H₂O** shows a negative D value, certain lack of accuracy in evaluating the E/D ratio from these calculations and its high value is the source of the discrepancy mentioned above.

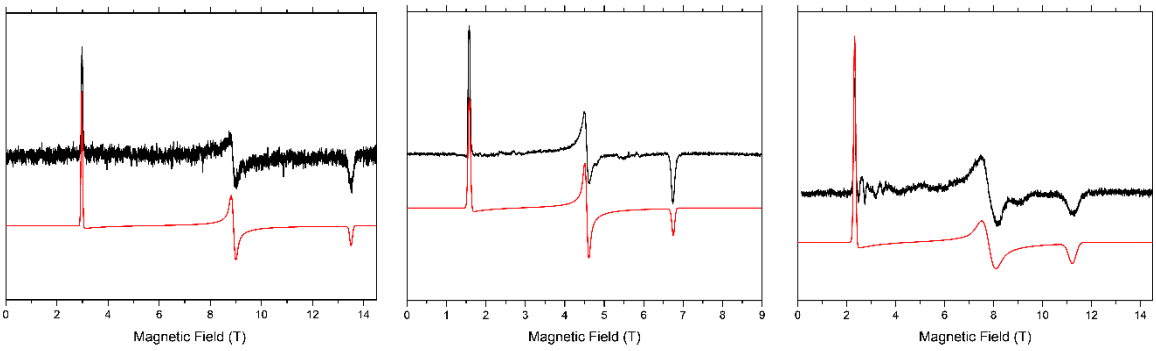

Figure II.7. HFEPR spectra of *n*-eicosane pellets made of **1·ClO₄·H₂O** (left) at ~5 K and 295.6 GHz, **1·BPh₄** (centre) at ~5 K and 157 GHz, and **1·PF₆·H₂O** (right) at ~10 K and 239 GHz accompanied by simulations using the values taken from FIRMS under the condition of E/D = 1/3 and indicated in Table II.5.

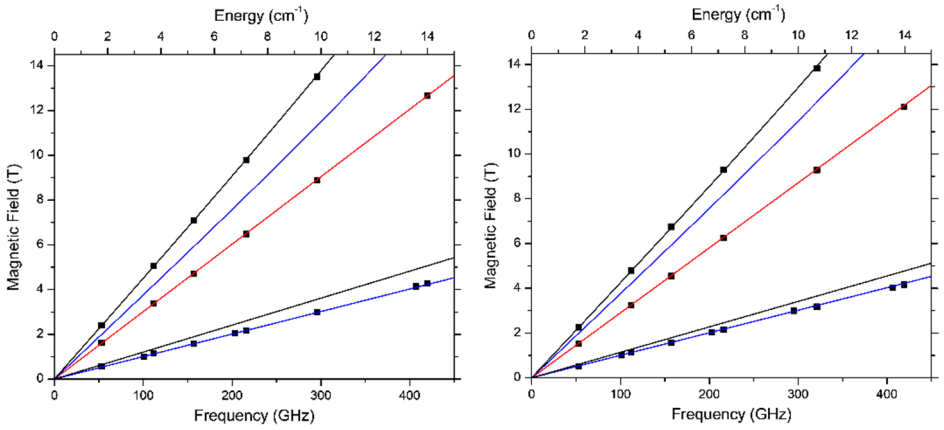

Figure II.8. Field *vs* frequency maps of turning points in the HFEPR spectra for **1·ClO₄·H₂O** (left) and **1·BPh₄** (right) at ~5 K. The squares are experimental points; lines were drawn using best-fitted parameters as in Table II.5. Red lines: turning points with magnetic field parallel to the x-axis of the zfs tensor; blue lines: B_0 || y; black lines: B_0 || z.

Table II.4. Energy gap (in cm^{-1}) between the ground and first excited Kramers doublets obtained from different experimental and theoretical techniques.[a]

Technique	Magnetometry: SOC model	Magnetometry: zfs model	FIRMS	CASSCF/NEVPT2
1·ClO_4·H_2O	117.7	87.2	107	120.6
1·BPh_4	135.1	166.3	130	141.9
1·PF_6·H_2O	115.4	108.4	115	136.8

[a] Except for magnetometry, where a first-order SOC approximation has also been used, a zfs model based on a second-order SOC coupling has been applied in the rest of the cases.

Table II.5. Spin Hamiltonian parameters for **1·X** (X = ClO_4·H_2O, **BPh_4** and **PF_6·H_2O**) obtained from different techniques.

Technique	D (cm^{-1})	E (cm^{-1})	E/D	g_x	g_y	g_z or $g_{\|\|}$	$g_\perp$[a]	g_{av}
1·ClO_4·H_2O								
CASSCF/NEVPT2	+52.81	17.22	0.326	2.36	2.72	2.02	2.55	2.42
FIRMS	46.33	15.44	0.333	–	–	–	–	–
HFEPR	–	–	–	2.37	2.60	2.18	2.49	2.38
1·BPh_4								
CASSCF/NEVPT2	+63.98	18.27	0.286	2.35	2.80	1.99	2.59	2.38
FIRMS	56.30	18.67	0.333	–	–	–	–	–
HFEPR	–	–	–	2.46	2.60	2.28	2.53	2.45
1·PF_6·H_2O								
CASSCF/NEVPT2	–60.03	19.51	0.325	2.35	2.00	2.80	2.19	2.37
FIRMS	51.12	17.04	0.333	–	–	–	–	–
HFEPR	–	–	–	2.16	2.64	2.07	2.41	2.29

[a] The perpendicular component of g is obtained by the formula $g_\perp = \sqrt{\frac{g_x^2+g_y^2}{2}}$.

II.3.3 Ac-magnetic properties

The relaxation properties of **1·X** (X = **ClO_4·H_2O**, **BPh_4** and **PF_6·H_2O**) were studied by recording the alternating current magnetic susceptibilities as a function of the applied magnetic field in the temperature range 2–10 K. In the absence of an external magnetic field no trace of out-of-phase (χ_M'') signals were found in such conditions. However, in the presence of an applied field, in-phase (χ_M') and χ_M'' show a frequency-dependent behaviour below ~6 K (Figures II.9–11). In the past, the emergence of slow magnetic relaxation was usually related with the presence of an energy barrier linked to an axial zfs tensor ($D < 0$) and a dc-magnetic field that hampers a faster quantum tunnelling relaxation. However, this behaviour is also usually observed in octahedral Co(II) complexes with $D > 0$, despite the absence of an energy barrier. Consequently, in these cases, the dc-magnetic

field slows down a fast intra-Kramers transition within the magnetic ground Kramers doublet, which may be responsible for the SIM behaviour (see below). **1·BPh4**, like **1·ClO4·H2O** and **1·PF6·H2O**, under static magnetic fields (H_{dc}) below 2.5 kOe, exhibits a single well-defined peak in the χ_M'' *vs* ν plots and, therefore, a unique relaxation process. Besides, the presence of one complete semicircle in the Cole-Cole plots (χ_M'' *vs* χ_M') supports this conclusion. In such situation, the generalised Debye model was used to analyse the experimental data as χ_M' and χ_M'' *vs* ν simultaneously with the DynVPMag program.[33,34] With this model, χ_M' and χ_M'' curves are described by the adiabatic (χ_S) and isothermal (χ_T) magnetic susceptibilities, the relaxation time (τ) and an exponential factor which defines the broadness of the spectra (α) through equations (3) and (4), being $\omega = 2\pi\nu$.

$$\chi'_{M_i} = \chi_S + (\chi_T - \chi_S)\frac{1+(\omega\tau)^{1-\alpha}Sin(\frac{\alpha\pi}{2})}{1+2(\omega\tau)^{1-\alpha}Sin(\frac{\alpha\pi}{2})+(\omega\tau)^{2(1-\alpha)}} \qquad (3)$$

$$\chi''_{M_i} = (\chi_T - \chi_S)\frac{(\omega\tau)^{1-\alpha}Cos(\frac{\alpha\pi}{2})}{1+2(\omega\tau)^{1-\alpha}Cos(\frac{\alpha\pi}{2})+(\omega\tau)^{2(1-\alpha)}} \qquad (4)$$

When $H_{dc} \geq 2.5$ kOe, χ_M'' *vs* ν plots of **1·ClO4·H2O** and **1·PF6·H2O** show a broad peak which evolves into the emergence of a shoulder at low temperatures ($T < 3.5$ K) and $H_{dc} = 5.0$ kOe. This particularity is better observed in the Cole-Cole plots, which clearly show two semicircles, suggesting the coexistence of multiple competing relaxation processes.[39] In such cases, χ_M' and χ_M'' must be described by equations (5) and (6) as the sum of two individual processes.

$$\chi'_M = \chi'_{M_1} + \chi'_{M_2} \qquad (5)$$

$$\chi''_M = \chi''_{M_1} + \chi''_{M_2} \qquad (6)$$

In all cases, the simulated data from the best-fit parameters fairly reproduce the experimental χ_M'' *vs* ν, χ_M'' *vs* ν and Cole-Cole plots (Figures II.9–11 and A.10–19). Under selected dc-magnetic fields (0.25–5.0 kOe) and for $T < 10$ K, the α values are below 0.3, discarding any spin glass behaviour. The inset figures within the ln(τ) *vs* 1/T curves, or Arrhenius plots, (Figures II.9–12 and A.10–19) display the thermal dependence of this parameter, showing, in general, a decrease for its value while increasing the temperature to, later, increase again above 7 K. The thermal dependences on relaxation times, at all magnetic fields, in the form of Arrhenius plots for the main relaxation process in **1·ClO4·H2O** and **1·PF6·H2O** and unique for **1·BPh4** are shown in Figure II.12.

At $H_{dc} \leq 1.0$ kOe, the Arrhenius plots of **1·BPh4** show two linear tendencies in different temperature regions, each of them being unambiguously associated with thermally activated (TA, $\frac{1}{\tau} = \tau_0^{-1}e^{\frac{Ea}{k_BT}}$) relaxation processes. The experimental data for the predominant relaxation at high temperatures are scarce at low magnetic fields, so the

values of the physical parameters are poorly determined. However, better data analyses at high temperature are obtained as H_{dc} increases, as this relaxation expands its relevance to a wider temperature range. At the lowest H_{dc} (0.25 kOe) and below 3 K, a curvature in the Arrhenius plot is observed, which evolves towards an almost utterly horizontal line when H_{dc} increases up to 5.0 kOe. This last behaviour can only correspond to a temperature-independent intra-Kramers relaxation (IK, $\tau = \tau_{0,IK}$) between the two components of the ground Kramers doublet. The evolution of the Arrhenius plots with the applied static magnetic field indicates that H_{dc} activates and prioritises some relaxation mechanisms (2 TA + IK, $\frac{1}{\tau} = \sum_{i=1}^{2} (\frac{1}{\tau_{0,i}} e^{-\frac{Ea_i}{k_B T}}) + \frac{1}{\tau_{0,IK}}$). At H_{dc} = 2.5 kOe (**1·BPh$_4$**), the predominant relaxation at high temperature (TA_{HT}) for the lower magnetic fields with the highest energy barrier ($H_{dc} \leq 1.0$ kOe, $E_a > 60.7$ cm^{-1}), undergoes a pronounced decrease of the E_a value (34.1 cm^{-1}). However, the previous magnitude is recovered by adding an extra TA relaxation (3 TA + IK, $\frac{1}{\tau} = \sum_{i=1}^{3} \frac{1}{\tau_{0,i}} e^{-\frac{Ea_i}{k_B T}} + \frac{1}{\tau_{0,IK}}$). This result indicates that the E_a value obtained at first (34.1 cm^{-1}) was an average between the values corresponding to TA_{HT} and a new intermediate TA_{MT} one (49.0 and 19.0 cm^{-1}). For this H_{dc} (2.5 kOe), the relaxation occurring at low temperature (TA_{LT}) decreases its range of influence until almost its disappearance and, therefore, the evaluation of the parameters that describe it worsens resulting in larger parameter errors.

The observed behaviour for **1·BPh$_4$** at H_{dc} = 2.5 kOe also occurs at H_{dc} = 5.0 kOe. However, the analysis at this magnetic field was carried out by removing experimental data (χ_M'' and χ_M' data) at low ν values and $T < 3$ K, corresponding the analyses to a general process. The inclusion of these data is only possible if the coexistence of two independent relaxation processes is considered (Figure A.20) that is making use of equations (5) and (6). From these new Arrhenius plots representing the individual relaxation processes, it is concluded that in the first process (RP_1) three relaxation mechanisms compete: two thermally assisted (TA_{HT} and TA_{MT}) together with one IK (Figure A.20 left). Meanwhile, the second process (RP_2) incorporates the previous third TA_{LT} relaxation (Figure A.20 right). In such a case, the τ and E_a values are better determined when considering two processes than one general process without the low frequency χ_M'' and χ_M' data. There is no certainty that TA_{MT} relaxation does not occur via a two-phonon Raman mechanism ($\tau^{-1} = C \cdot T^n$). A linear dependence of $\ln(\tau)$ *vs* $\ln(T)$ plot could indicate the presence of a Raman relaxation mechanism, $-\ln(C)$ and $-n$ being the ordinate at the origin and the slope. This feature exactly happens at H_{dc} = 2.5 kOe (also at 5.0 kOe, 3.5–7.0 K) in the temperature range between 4.5 and 9.0 K, providing values of 4.5 and 5.0 for C and n (Figure II.13 left). Instead, three linear regimes occur in these graphs for H_{dc} = 0.5 kOe (Figure II.13 right). However, there is no indication that a first-order direct mechanism ($\tau^{-1} = A \cdot T$) is following a linear dependence with a slope equal to –1. The sum of several competing TA relaxations

can give a single Raman's appearance in an Arrhenius plot, with parameters *C* and *n* being defined by τ and E_a of the former ones, as can be deduced from expansion series. However, these multiple regimes in ln(τ) *vs* ln(*T*) graphs cannot be reproduced by the combination of multiple Raman relaxations in a single fit, although it seemed so at a first glance. In short, since it is impossible to confirm any of the alternatives experimentally, and for coherence with the analysis of the data for low H_{dc}, we have operated exclusively with thermally assisted relaxation mechanisms. The thermal dependence for the secondary process of **1·ClO$_4$·H$_2$O** and **1·PF$_6$·H$_2$O** are shown in Figures A.21–22. Several approaches with different amount of thermally activated processes are included in Figures A.23–25.

Since **1·BPh$_4$** has allowed establishing TA relaxation mechanisms as the cause of its magnetic dynamics and, due to the similarities between the three compounds, the same procedure considering a model of multiple TA relaxations and discarding other options was applied for **1·ClO$_4$·H$_2$O** and **1·PF$_6$·H$_2$O**. The dynamic behaviour of **1·ClO$_4$·H$_2$O** is similar to that observed for **1·BPh$_4$**. However, in the latter, the correct analysis of the experimental data (high frequencies and low temperatures) when applying a static magnetic field of 0.5 kOe also requires a combination of two independent relaxation processes, RP$_1$ and RP$_2$. The former, is similar to the relaxations found for higher H_{dc}. Instead, RP$_2$ preferably correspond to a faster IK relaxation that must be considered a real interchange within the ground Kramers doublet (Table A.5). In any case, due to the difficulty of deconvolution into two processes and the limited data set that confirms it, this conclusion should be taken with caution.

Similar conclusions to those found in the preceding compounds are reached for **1·PF$_6$·H$_2$O**. However, their experimental data at H_{dc} = 5.0 kOe do not distinguish the three established TA relaxations (TA$_{LT}$, TA$_{MT}$ and TA$_{HT}$). This problem is linked to the scarcity of data in temperature regions where one of the relaxations predominates or should do it. However, it is possible to simulate the Arrhenius plot for this magnetic field using parameters similar to those found with other less intense H_{dc}. Furthermore, good results are obtained with a model composed of two competing TA and one IK relaxations for $T \leq 5$ K.

Briefly, the three compounds show a similar dynamic of magnetic properties since they contain the same cobalt (II) complex and only differ in the counterion, with the presence or absence of crystallisation water molecules. This last factor is the one that introduces subtle but significant differences. These differences are more linked to the conditions (H_{dc}) in that relaxations begins to manifest than to their nature. In other words, the differences lie in small or moderate changes in the parameters that define these processes that control the relaxation of magnetisation.

The fact that Co(II) complexes exhibit SIM behaviour regardless of the sign of *D* imply that these properties are not related to the existence of a spin-reversal barrier.[36] In such a case,

other relaxation mechanisms can compete or even become the most relevant at specific temperatures. As discussed before, several thermally activated and intra-Kramers mechanisms are responsible for the SIM behaviour in the three compounds, being each the predominant one in a certain temperature range. In all cases, the IK mechanism is occasionally observed and only at low temperatures. Several authors have opted for molecular or network vibrations, through a spin-phonon coupling, as those responsible for the relaxation that makes possible the spin-reversal. In this way, relaxation slows down considerably when these vibrations are not accessible.[28,37–39]

There are only a few Co(II) complexes with $D > 0$ exhibiting two relaxation processes.[35] The presence of a second process is usually attributed to intermolecular interactions enhanced by applying a magnetic field or one-phonon direct relaxation process.[40] On the one hand, in our case, a first-order direct mechanism was discarded from the experimental data. On the other hand, several competing relaxation mechanisms and different independent processes were observed in all three compounds. Hence, it is difficult to state a conclusion. Some subtle differences can be related to a crystallisation water molecule presents in two compounds (**1·ClO$_4$·H$_2$O** and **1·PF$_6$·ClO$_4$**) and to the hydrogen-bonding network built with the counterion and the cationic unit, as discussed above. However, α parameter can also provide some indirect information.

Sometimes understanding how α and temperature are related is not evident. However, we can point to some possible reasons for the behaviour observed in the compounds studied. At low temperature, there might be certain domains in the lattice. Therefore, each domain can exhibit slightly different phonons or each molecule vibrates slightly differently due to inhomogeneity in the environments created by neighbouring molecules (complexes, anions, solvent molecules, ...). The additional energy coming from an increase in temperature would homogenise the domains, leading to a decrease in α value. Above 7 K, access to other phonons in the lattice or overtones or new vibrational modes in the metal complex could be the source of the unexpected increase in α. The decrease in α when cooling below 3 K is, in principle, not usual and more difficult to explain. Although this phenomenon could be caused by a high correlation between some of the evaluated parameters in the fitting, it is only present in **1·BPh$_4$**, being the only one that do not have crystallisation water molecules. It is reasonable to think that weak hydrogen bonds could favour the formation of different domains, while their absence could promote a greater homogeneity of the network. However, these observations and their explanations are aspects that should be studied more deeply in the future.

All these complexes have the same first coordination sphere, being the main difference the counterion. However, the role of the counterion is, apparently, relevant enough to induce differences in the anisotropy and the dynamic properties. To design SIMs with better performance, it is still relevant to understand and establish magneto-structural

correlations. Researchers have suggested several reasons that are responsible for the *D* parameter tuning in tetrahedral complexes such as structural distortions, heavier atom substitution, meta-ligand covalence and changes in the second coordination sphere.[4,14,45,46] In octahedral complexes, not so many correlations exist. K. Dumbar *et al.* suggested a linear correlation of *D* with the axial-to equatorial metal-bond length ratio in octahedral Co(II) complexes.[12] We have also observed a similar correlation in the past. [43] However, the use of this correlation between the studied parameters are related to electronic factors rather than geometrical ones. These can be misleading when the coordination sphere is made up of different ligands and even different donor atoms.[17,44] In our case, CoN_2 and CoN_2O_2 forms the axial axis and the equatorial plane, respectively. In consequence, this explanation is not so straightforward since the linear magneto-structural trend found by other authors is not followed here. It must be noted that these simple correlations can be established in almost ideal geometries, but the use of chelating ligands can largely distort the ideal geometry of the coordination sphere by modifying the ligand field. These distortions split the ground term and, thus, the contributions of the first excited states that are the biggest contributors to the *D* parameter. Besides, this kind of the geometrical distortion directly influences the rhombicity of the zfs tensor, the *E*/*D* ratio, and particularly manifested in the large asymmetry of the equatorial Co–O bond length.[17]

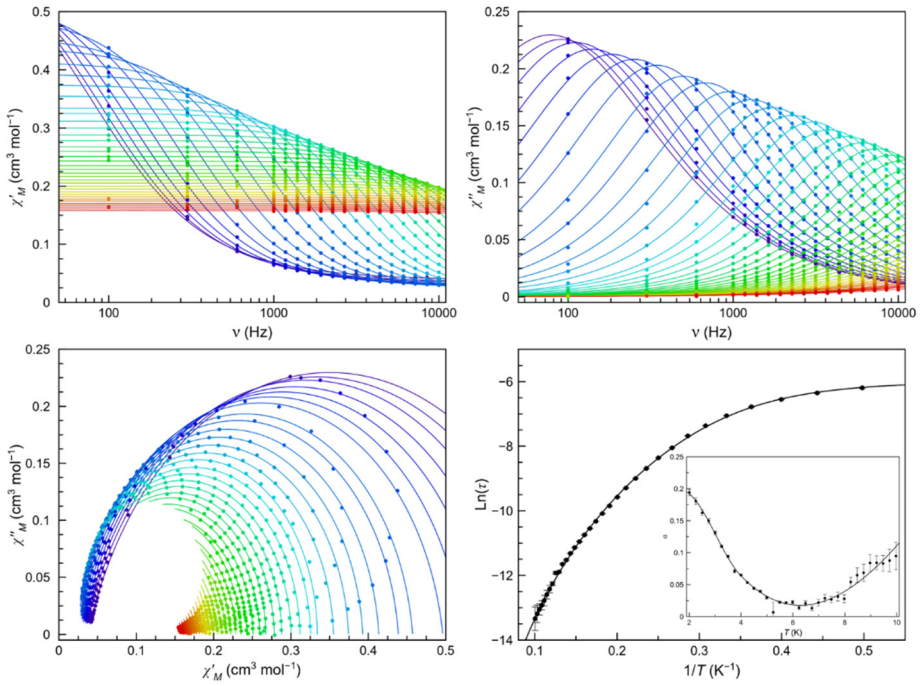

Figure II.9. Frequency dependence of χ_M' (top left) and χ_M'' (top right), Cole-Cole plots (bottom left) and Arrhenius plots of **1·ClO₄·H₂O** (bottom right) in a dc-applied static field of 2.5 kOe with ± 0.005 kOe oscillating field in the temperature range of 2.0–10.7 K (purple to red gradient). Thermal dependence of α is included on the bottom right figure as an inset, where the black line are eye-guides. Standard deviation appears as vertical error bars.

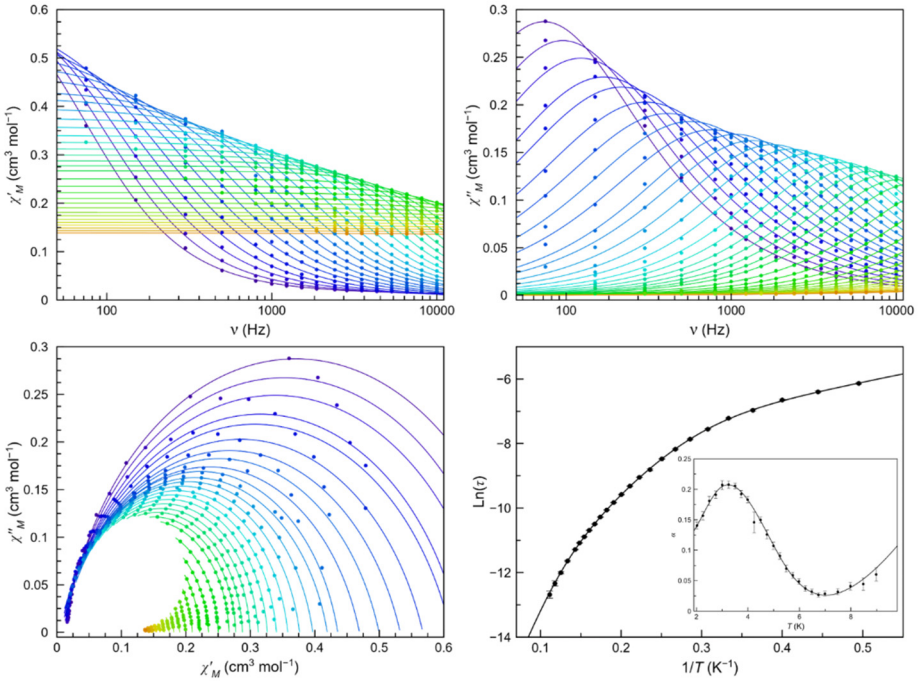

Figure II.10. Frequency dependence of χ_M' (top left) and χ_M'' (top right), Cole-Cole plots (bottom left) and Arrhenius plots of **1·BPh$_4$** (bottom right) in a dc-applied static field of 2.5 kOe with ± 0.005 kOe oscillating field in the temperature range of 2.0–9.0 K (purple to red gradient). Thermal dependence of α is included on the bottom right figure as an inset, where the black line are eye-guides. Standard deviation appears as vertical error bars.

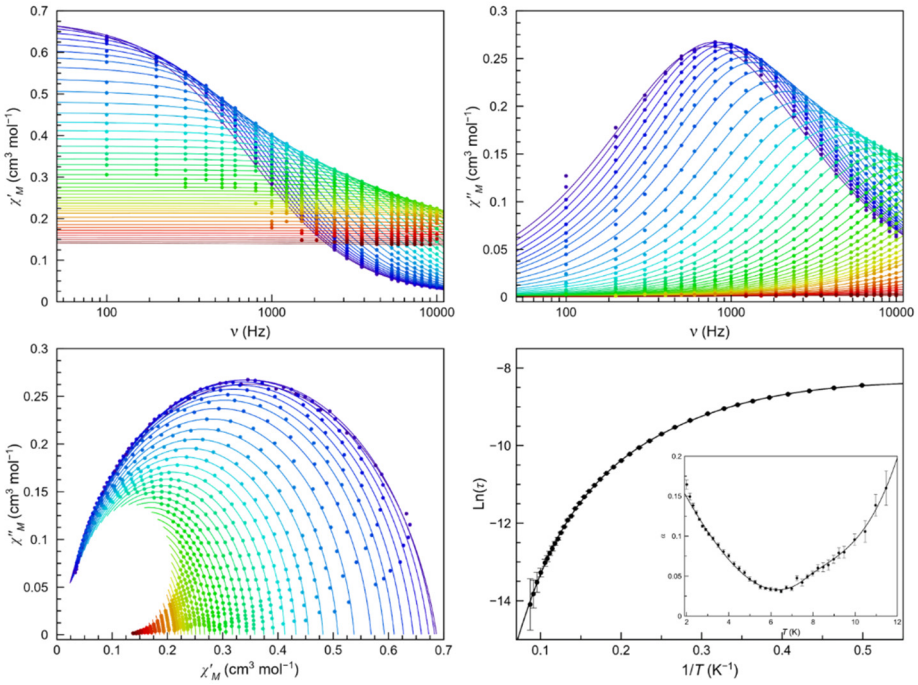

Figure II.11. Frequency dependence of χ_M' (top left) and χ_M'' (top right), Cole-Cole plots (bottom left) and Arrhenius plots of **1·PF$_6$·H$_2$O** (bottom right) in a dc-applied static field of 2.5 kOe with ± 0.005 kOe oscillating field in the temperature range of 2.0–11.5 K (purple to red gradient). Thermal dependence of α is included on the bottom right figure as an inset, where the black line are eye-guides. Standard deviation appears as vertical error bars.

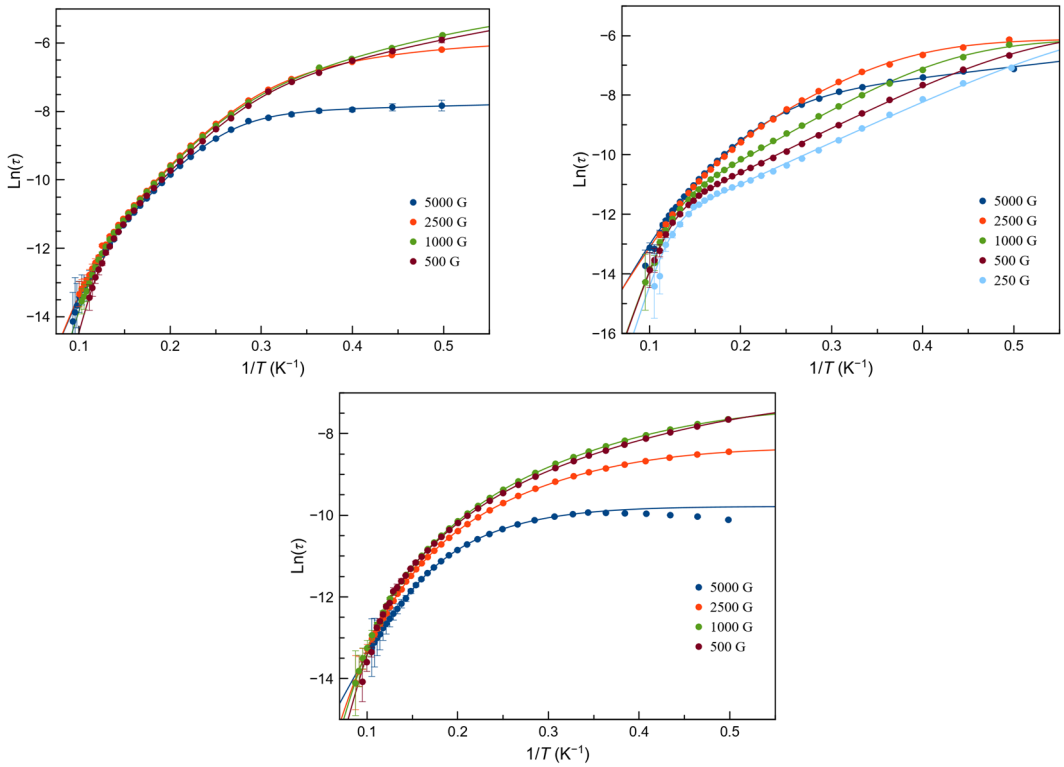

Figure II.12. Arrhenius plots for the main process of **1·ClO₄·H₂O** (left), **1·BPh₄** (right) and **1·PF₆·H₂O** (bottom) under 0.25–5.0 kOe applied static field. The solid lines are the best fit-curves (see text). Standard deviations appear as vertical error bars.

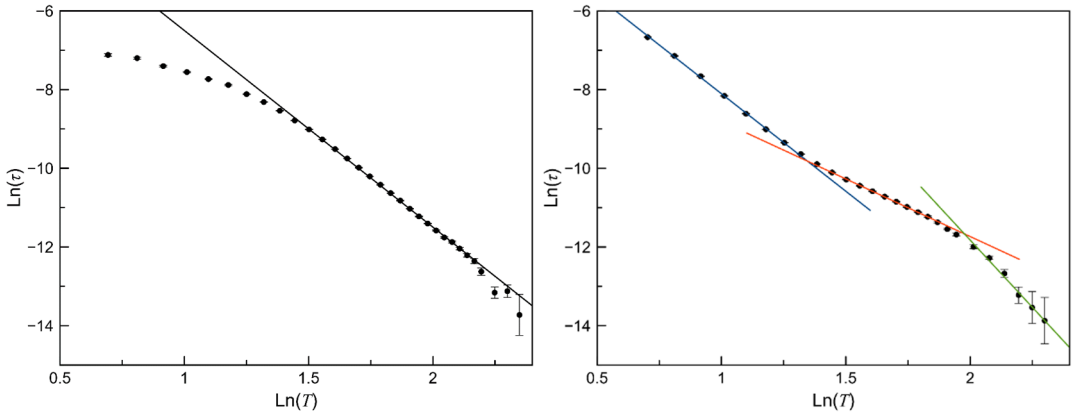

Figure II.13. Ln(τ) *vs* ln(T) graphs of **1·BPh₄** in a dc-static magnetic field of 2.5 (left) and 0.5 kOe (right) with a perpendicular ± 0.005 kOe oscillating field. The black line (left) represents the linear fitting for a Raman mechanism $\tau^{-1} = C \cdot T^{n}$. The coloured lines (right) are a guide to the eye to distinguish the different linear regions.

II.3.4 Conclusions

Mononuclear cobalt(II) complexes with a CoN_4O_2 octahedral environment have been reported with the counterion (ClO_4^-, BPh_4^-, and PF_6^-) as the main difference between them. Magnetisation and theoretical calculations reveal an easy-plane anisotropy for **1·ClO₄·H₂O** and **1·BPh₄** and easy-axis anisotropy for **1·PF₆·H₂O**, exhibiting in all of them strong rhombic distortions. To confirm the *D* magnitude and sign, field- and frequency-domain magnetic resonance techniques were performed. As a result, the high rhombicity observed for these compounds makes it not possible to establish a sign for *D*. Dynamic magnetic properties indicate field-induced slow magnetic relaxation for all compounds. However, the counterion induces a distortion in the first coordination sphere through supramolecular interactions that leads to a tuning of the *D* parameter and dynamic magnetic properties. Whereas in **1·ClO₄·H₂O** and **1·PF₆·H₂O** two processes are observed at H_{dc} 5.0 kOe, a single one is characteristic of **1·BPh₄**. Despite the fact that a combination of several TA relaxations can simulate a Raman curve, the Arrhenius plots for **1·BPh₄** could not be fitted with a combination of Raman mechanisms. The main processes in all compounds might be governed by the combination of multiple thermally activated mechanisms plus an intra-Kramers one, where each one is predominant in different temperature ranges. These differences might come from the absence of crystallisation water molecules that might change the vibrational domains in the lattice, resulting in slightly similar but different behaviour in their relaxation dynamics. The results highlight the importance of small distortions of the metal core, the influence of crystallisation molecules and the requirement of magneto-structural correlations.

II.4 References

1. Troiani, F. & Affronte, M. Molecular spins for quantum information technologies. *Chem. Soc. Rev.* **40**, 3119 (2011).

2. Cavallini, M. *et al.* Magnetic Information Storage on Polymers by Using Patterned Single-Molecule Magnets. *Angew. Chemie Int. Ed.* **44**, 888–892 (2005).

3. Bogani, L. & Wernsdorfer, W. Molecular spintronics using single-molecule magnets. in *Nanoscience and Technology* **99**, 194–201 (Co-Published with Macmillan Publishers Ltd, UK, 2009).

4. Meng, Y.-S., Jiang, S.-D., Wang, B.-W. & Gao, S. Understanding the Magnetic Anisotropy toward Single-Ion Magnets. *Acc. Chem. Res.* **49**, 2381–2389 (2016).

5. Frost, J. M., Harriman, K. L. M. & Murugesu, M. The rise of 3-d single-ion magnets in molecular magnetism: towards materials from molecules? *Chem. Sci.* **7**, 2470–2491 (2016).

6. Murrie, M. Cobalt(II) single-molecule magnets. *Chem. Soc. Rev.* **39**, 1986 (2010).

7. Sarkar, A., Dey, S. & Rajaraman, G. Role of Coordination Number and Geometry in Controlling the Magnetic Anisotropy in Fe^{II} , Co^{II} , and Ni^{II} Single-Ion Magnets. *Chem. – A Eur. J.* **26**, 14036–14058 (2020).

8. Duboc, C. Determination and prediction of the magnetic anisotropy of Mn ions. *Chem. Soc. Rev.* **45**, 5834–5847 (2016).

9. Acharya, J. *et al.* Influence of ligand field on magnetic anisotropy in a family of pentacoordinate Co^{II} complexes. *Dalt. Trans.* **49**, 4785–4796 (2020).

10. Kumar, P. *et al.* Probing the Magnetic Anisotropy of Co(II) Complexes Featuring Redox-Active Ligands. *Inorg. Chem.* **59**, 16178–16193 (2020).

11. Vaidya, S. *et al.* Substituted versus Naked Thiourea Ligand Containing Pseudotetrahedral Cobalt(II) Complexes: A Comparative Study on Its Magnetization Relaxation Dynamics Phenomenon. *Inorg. Chem.* **57**, 3371–3386 (2018).

12. Deng, Y.-F. *et al.* Probing the Axial Distortion Effect on the Magnetic Anisotropy of Octahedral Co(II) Complexes. *Inorg. Chem.* **59**, 7622–7630 (2020).

13. Saber, M. R. & Dunbar, K. R. Ligands effects on the magnetic anisotropy of tetrahedral cobalt complexes. *Chem. Commun.* **50**, 12266–12269 (2014).

14. Tripathi, S. *et al.* Influence of a Counteranion on the Zero-Field Splitting of Tetrahedral Cobalt(II) Thiourea Complexes. *Inorg. Chem.* **58**, 9085–9100 (2019).

15. Busschaert, N., Caltagirone, C., Van Rossom, W. & Gale, P. A. Applications of Supramolecular Anion Recognition. *Chem. Rev.* **115**, 8038–8155 (2015).

16. Gasa, T. B., Valente, C. & Stoddart, J. F. Solution-phase counterion effects in supramolecular and mechanostereochemical systems. *Chem. Soc. Rev.* **40**, 57–78 (2011).

17. Vallejo, J. *et al.* Coligand Effects on the Field-Induced Double Slow Magnetic Relaxation in Six-Coordinate Cobalt(II) Single-Ion Magnets (SIMs) with Positive Magnetic Anisotropy. *Inorg. Chem.* **58**, 15726–15740 (2019).

18. Sheldrick, G. M. SHELXS97 and SHELXL97. Program for Crystal Structure Solution and Refinement. (1997).

19. Sheldrick, G. M. SHELXT – Integrated space-group and crystal-structure determination. *Acta Crystallogr. Sect. A Found. Adv.* **71**, 3–8 (2015).

20. Sheldrick, G. M. A short history of SHELX. *Acta Crystallogr. Sect. A Found. Crystallogr.* **64**, 112–122

(2008).

21. Spek, A. L. Structure validation in chemical crystallography. *Acta Crystallogr. Sect. D Biol. Crystallogr.* **65**, 148–155 (2009).

22. Angeli, C., Cimiraglia, R., Evangelisti, S., Leininger, T. & Malrieu, J.-P. Introduction of n -electron valence states for multireference perturbation theory. *J. Chem. Phys.* **114**, 10252–10264 (2001).

23. Eichkorn, K., Weigend, F., Treutler, O. & Ahlrichs, R. Auxiliary basis sets for main row atoms and transition metals and their use to approximate Coulomb potentials. *Theor. Chem. Accounts Theory, Comput. Model. (Theoretica Chim. Acta)* **97**, 119–124 (1997).

24. Vancoillie, S. *et al.* Multireference Ab Initio Calculations of g tensors for Trinuclear Copper Clusters in Multicopper Oxidases. *J. Phys. Chem. B* **114**, 7692–7702 (2010).

25. Llunell, M., Casanova, D., Cirera, J., Alemany, P. & Alvarez, S. SHAPE v2.1. (2013).

26. Smolko, L. *et al.* Field-Induced Slow Magnetic Relaxation in Mononuclear Tetracoordinate Cobalt(II) Complexes Containing a Neocuproine Ligand. *Eur. J. Inorg. Chem.* **2017**, 3080–3086 (2017).

27. Eni, D. B., Yufanyi, D. M., Nono, J. H., Tabong, C. D. & Agwara, M. O. Synthesis, characterization and thermal properties of 1,10-phenanthroline mixed-ligand complexes of cobalt(II) and copper(II): metal-mediated transformations of the dicyanamide ion. *Chem. Pap.* **74**, 3003–3016 (2020).

28. Vallejo, J. *et al.* Field-Induced Slow Magnetic Relaxation in a Six-Coordinate Mononuclear Cobalt(II) Complex with a Positive Anisotropy. *J. Am. Chem. Soc.* **134**, 15704–15707 (2012).

29. Yang, Y., Zeng, M.-H., Zhang, S.-H. & Liang, H. catena -Poly[[diaquacobalt(II)]-μ 3 -5-aminoisophthalato-κ 4 O , O ′: O ″: N]. *Acta Crystallogr. Sect. E Struct. Reports Online* **63**, m2056–m2057 (2007).

30. Evangelio, E. Graphical Abstract: Eur. J. Inorg. Chem. 15/2005. *Eur. J. Inorg. Chem.* **2005**, 2945–2952 (2005).

31. Chilton, N. F., Anderson, R. P., Turner, L. D., Soncini, A. & Murray, K. S. PHI: A powerful new program for the analysis of anisotropic monomeric and exchange-coupled polynuclear d - and f -block complexes. *J. Comput. Chem.* **34**, 1164–1175 (2013).

32. Vallejo, J. *et al.* Coligand Effects on the Field-Induced Double Slow Magnetic Relaxation in Six-Coordinate Cobalt(II) Single-Ion Magnets (SIMs) with Positive Magnetic Anisotropy. *Inorg. Chem.* **58**, 15726–15740 (2019).

33. Cole, K. S. & Cole, R. H. Dispersion and Absorption in Dielectrics I. Alternating Current Characteristics. *J. Chem. Phys.* **9**, 341–351 (1941).

34. Carbonell-Vilar, J. M. & Cano, J. Dyn-VPMag. *University of Valencia* (2019).

35. Boča, R., Miklovič, J. & Titiš, J. Simple mononuclear cobalt(II) complex: A single-molecule magnet showing two slow relaxation processes. *Inorg. Chem.* **53**, 2367–2369 (2014).

36. Świtlicka, A. *et al.* Slow magnetic relaxation in hexacoordinated cobalt(II) field-induced single-ion magnets. *Inorg. Chem. Front.* **7**, 2637–2650 (2020).

37. Vallejo, J. *et al.* Reversible solvatomagnetic switching in a single-ion magnet from an entatic state. *Chem. Sci.* **8**, 3694–3702 (2017).

38. Viciano-Chumillas, M. *et al.* Single-Ion Magnetic Behaviour in an Iron(III) Porphyrin Complex: A Dichotomy Between High Spin and 5/2–3/2 Spin Admixture. *Chem. - A Eur. J.* **26**, 14242–14251 (2020).

39. Lucaccini, E., Sorace, L., Perfetti, M., Costes, J.-P. & Sessoli, R. Beyond the anisotropy barrier: slow relaxation of the magnetization in both easy-axis and easy-plane Ln(trensal) complexes. *Chem. Commun.* **50**, 1648–1651 (2014).

40. Lunghi, A. & Sanvito, S. Multiple spin-phonon relaxation pathways in a Kramer single-ion magnet. *J.*

Chem. Phys. **153**, (2020).

41. Ding, Y.-S., Deng, Y.-F. & Zheng, Y.-Z. The Rise of Single-Ion Magnets as Spin Qubits. *Magnetochemistry* **2**, 40 (2016).

42. Vaidya, S. *et al.* What Controls the Sign and Magnitude of Magnetic Anisotropy in Tetrahedral Cobalt(II) Single-Ion Magnets? *Inorg. Chem.* **55**, 9564–9578 (2016).

43. Vallejo, J. Estudio de Imanes Moleculares de Co(II): desde sistemas aislados hasta sistemas organizados y multifuncionales. (University of Valencia, 2016).

44. Switlicka, A. *et al.* Magneto-structural diversity of Co(II) compounds with 1–benzylimidazole induced by linear pseudohalide coligands. *Inorg. Chem. Front.* **6**, 33 (2020).

Chapter III

Assembling cobalt(II) SIMs as potential qu-gates

Dinuclear compounds with the general formula of {[Co(Me$_2$phen)$_2$]$_2$(L)]X (X = ClO_4 or BPh_4) were synthesised. The bridging ligand L is linear and asymmetrical, with salicylaldehyde and carboxylate groups on each side. All Co^{II} ions within the compounds show a positive anisotropy. The zfs parameters for the asymmetric dinuclear cobalt(II) compounds are different and their electronic transitions are distinguishable. Thus, it might be a good candidate for building qu-gates, where each Co^{II} ion could be selected. Moreover these compounds present field-induced slow relaxation of magnetisation, with similar behaviour as for the mononuclear cobalt(II) compounds in Chapter II.

III.1 Introduction

Quantum information science is an emerging field to improve computing and information processing by relying on quantum properties. Qubits exhibit two-level quantum systems and constitute the basic units for quantum computation, but they should fulfil DiVincenzo criteria.[1,2] Different particles have been proposed for this purpose, but the use of molecules with a spin moment is not too exploited. These entities or spin qubits can be in a superposition state, whose lifetime is determined by T_2 that is the spin-spin relaxation or coherence time. Finding molecules that meet these requirements, and that can be synthesised and studied, is challenging. Magnetic molecules have emerged as an alternative to solid-state systems such as diluted defects in bulk materials, like N vacancies in diamonds, or vacancies in Si and SiC_2. They are promising candidates due to countless design possibilities offered by the tuning of the coordination sphere, its geometry, and the nature of the bonds.[3] Despite this advantage, these molecular systems still display shorter T_2, or the usually estimated phase-memory time, T_m.[4] However, improvements have been achieved by reducing the number of donor atoms with nuclear spins and bound to the metal ion, by removing them with the appropriate choice of ligands, or by engineering qubit states undisturbed by magnetic field fluctuations.[5] Most of these systems are based on metal ions as Cu^{II}, V^{IV} or lanthanides(III) ions showing ground $S = 1/2$ or m_j doublets.[6]

Quantum computation requires multiqubit systems for gate operations and the integration of qubits into diverse device architectures. The richness of coordination and supramolecular chemistry can be very useful for such implementation. The entanglement of two spin momenta, that is the weak communication between them via superexchange or dipolar interactions, is a requirement in the operation of a quantum gate and the main experimental challenge. Nevertheless, the two qubits must be electronically distinguishable to be manipulated with an electromagnetic external radiation. Some examples have been reported incorporating two inequivalent metal ions.[7,8] Another strategies for getting a two-qubit quantum gate consist of design asymmetrical ligands that induce asymmetry in dinuclear complexes,[12] or metal-based pairs of qubits with a switchable interaction[9–11].

Although high-spin Co^{II} ion is not the most straightforward ion for qubit implementation (the SOC increases decoherence), at low temperatures only one of the two Kramers doublets become populated, and it behaves as an effective $S = ½$ system. Hence, in suitable conditions, these ions might be seen as potential qubits.[13]

In Chapter II, mononuclear octahedral cobalt(II) complexes with a CoN_4O_2 surrounding were described, where one deprotonated salicylaldehyde and two Me_2phen (2,9-dimethyl-1,10-phenanthroline) ligands constitute their coordination sphere. These complexes with

a large axial zero-field splitting (zfs), and therefore behaving as an effective S = 1/2 spin momentum, are potential qubits. In fact, preliminary studies show a Hahn echo signal for **1·BPh$_4$** in X-band at 4.3 K (see below).[14] In the past, our research group have shown that the cationic $[Co(Me_2phen)_2]^{2+}$ unit is an excellent building block able to incorporate a carboxylate group to make a single-ion magnet (SIM) and a possible qubit.[15] In this chapter, two units of this building block were connected by both several asymmetric and symmetric ligands to build dinuclear cobalt(II) complexes as potential qu-gates (Scheme III.1). These ligands incorporate one coordinating carboxylate group on one side and either other carboxylate or aldehyde group in the other side. The different coordination sphere induced by these ligands undoubtedly influences the zfs, and their lengths and substituents alters their electronic nature and, therefore, the entanglement. Therefore, in this chapter we report the synthesis, X-ray structures, EPR and magnetic studies of a family of dinuclear cobalt(II) complexes.

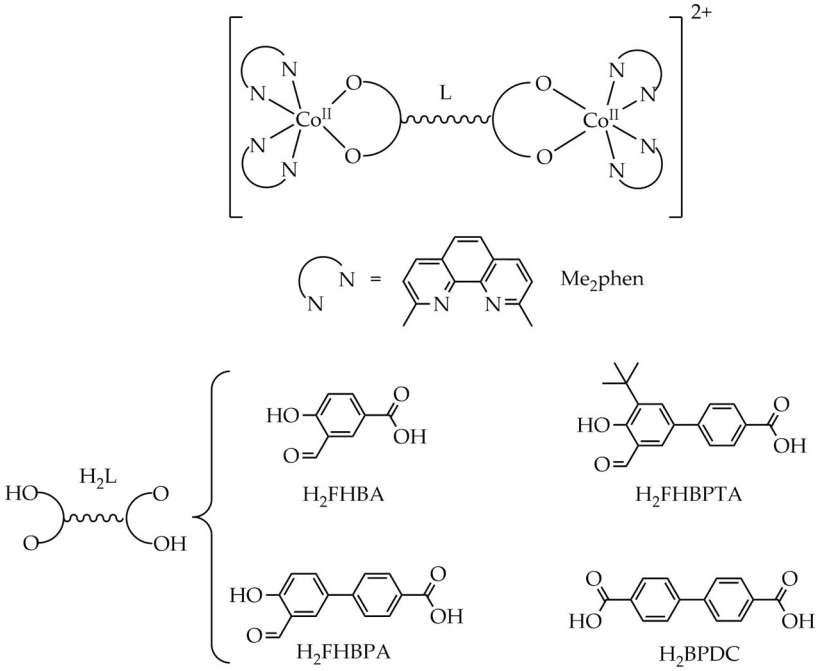

Scheme III.1. Representation showing the dinuclear cobalt(II) cationic unit $\{[Co(Me_2phen)_2]_2L\}^{2+}$ and the ligands connecting them.

III.2 Experimental section

III.2.1 Materials

All chemicals, including the H_2L ligands 3-formyl-4-hydroxybenzoic acid (H_2FHBA) and biphenyl-4,4′-dicarboxylic acid (H_2BPDC) were obtained from commercial sources and used as received. The ligands 3'-formyl-4'-hydroxy-1,1'-biphenyl-4-carboxylic (H_2FHBPA) and 3'-(*tert*-butyl)-5'-formyl-4'-hydroxy-1,1'-biphenyl-4-carboxylic acids (H_2FHBPTA) were synthesised following the reported procedures.[16]

Caution! Perchlorate salts are potentially explosive. They should be used in small quantities and should be treated with the utmost care at all times.

III.2.2 Syntheses

General synthetic procedures of {[Co(Me$_2$phen)$_2$]$_2$(L)}(ClO$_4$)$_2$: $Co(ClO_4)_2{\cdot}6H_2O$ (160 mg, 0.44 mmol, 2 eq) and 2,9-dimethyl-1,10-phenanthroline (191 mg, 0.88 mmol, 4 eq) were dissolved in methanol (20 mL). Then, a methanol solution of the corresponding bridging ligand (0.22 mmol, 1 eq) and NaH (60% in oil) (18 mg, 0.44 mmol, 2 eq) was added affording yellow to red suspensions, which were dissolved by adding acetonitrile (2-5 mL).

General synthetic procedures of {[Co(Me$_2$phen)$_2$]$_2$(L)}(BPh$_4$)$_2$: The tetraphenylborate-containing compounds were synthesised with the subsequent addition of $NaBPh_4$ (228 mg, 0.66 mmol, 3 eq) to the previous final solutions of $\{[Co(Me_2phen)_2]_2(L)\}(ClO_4)_2$.

{[Co(Me$_2$phen)$_2$]$_2$(FHBA)}(ClO$_4$)$_2$·4MeOH (2). Orange-yellowish single crystals suitable for X-ray were obtained by slow diffusion of toluene into the solution. Yield: 170 mg, 57%. IR (ν_{max}/cm^{-1}): 3440(w), 3058(vw), 3021(vw), 2974(vw), 2919(vw), 2851(vw), 1627(s), 1594(s), 1550(m), 1511(m), 1500(m), 1412(m), 1356(w), 1292(vw), 1223(vw), 1153(m), 1120(vs), 1088(vs), 860(m), 812(vw), 793(w), 770(w), 733(w), 718(w), 696(vw), 686(vw), 652(vw), 637(vw), 623(m), 551(w), 490(w), 465(w). Elemental Analysis Calculated for **2** ($C_{68}H_{68}Cl_2Co_2N_8O_{16}$): C, 56.64; H, 4.75; N, 7.77. Found: C, 56.17; H, 4.46; N, 8.00.

{[Co(Me$_2$phen)$_2$]$_2$(FHBA)}(BPh$_4$)$_2$·1MeOH (2′). Red single crystals suitable for X-ray were obtained by slow diffusion of diethyl ether into the solution. Yield: 125 mg, 33%. IR (ν_{max}/cm^{-1}): 3422(w), 3054(m), 3000(w), 2983(w), 2924(vw), 2852(vw), 1629(vs), 1593(s), 1561(m), 1547(w), 1510(m), 1499(m), 1476(w), 1425(s), 1408(s), 1384(s), 1356(m), 1292(w), 1267(vw), 1233(vw), 1211(vw), 1175(w), 1154(w), 1132(w), 1118(w), 1101(w), 1031(w), 992(vw), 940(vw), 855(m), 812(vw), 794(w), 772(w), 746(w), 732(m), 704(m), 653(w), 613(w), 551(w), 485(w). Elemental Analysis Calculated for **2′** ($C_{113}H_{96}B_2Co_2N_8O_5$): C, 76.01; H, 5.42; N, 6.28. Found: C, 76.10; H, 4.63; N, 6.16.

{[Co(Me$_2$phen)$_2$]$_2$(FHBPA)}(ClO$_4$)$_2$·6H$_2$O (3). Yellow-orangish single crystals suitable for X-ray were obtained by slow diffusion of toluene into the solution. Yield: 131 mg, 40%. IR (ν_{max}/cm^{-1}): 3422(m), 3067(w), 3020(w), 2923(w), 2515(vw), 1626(vs), 1597(vs), 1561(m), 1510(s), 1500(s), 1420(vs), 1358(m), 1293(w), 1246(w), 1222(w), 1203(vw), 1155(m), 1090(vs), 857(s), 814(w), 788(w), 772(w), 758(w), 732(m), 713(vw), 682(w), 653(w), 623(m), 551(m), 474(w), 455(w). Elemental Analysis Calculated for **3** ($C_{70}H_{68}Cl_2Co_2N_8O_{18}$): C, 56.12; H, 4.58; N, 7.48. Found: C, 55.55; H, 3.94; N, 7.26.

{[Co(Me$_2$phen)$_2$]$_2$(FHBPA)}(BPh$_4$)$_2$·2MeOH (3'). Orange-reddish crystals were obtained by slow evaporation. Yield: 168 mg, 35%. IR (ν_{max}/cm^{-1}): 3429(w), 3053(m), 3033(m), 2998(m), 2983(m), 2922(w), 2516(w), 1943(vw), 1628(vs), 1598(vs), 1581(s), 1561(m), 1511(s), 1500(vs), 1479(m), 1457(m), 1424(vs), 1355(m), 1309(w), 1292(w), 1267(w), 1241(m), 1222(w), 1212(w), 1154(m), 1122(w), 1100(w), 1067(w), 1031(m), 853(s), 787(w), 772(w), 731(vs), 705(vs), 652(w), 625(w), 612(m), 551(w), 507(vw), 472(w), 456(w). Elemental Analysis Calculated for **3'** ($C_{120}H_{104}B_2Co_2N_8O_6$): C, 76.11; H, 5.54; N, 5.92. Found: C, 76.02; H, 5.22; N, 5.75.

{[Co(Me$_2$phen)$_2$]$_2$(FHBPTA)}(ClO$_4$)$_2$·2H$_2$O (4). Red single crystals were obtained by slow evaporation. Yield: 107 mg, 36%. IR (ν_{max}/cm^{-1}): 3433(w), 3065(w), 2953(w), 2924(m), 2854(w), 1621(s), 1598(s), 1510(m), 1501(s), 1412(s), 1382(m), 1358(m), 1293(w), 1278(w), 1255(vw), 1223(w), 1202(vw), 1154(m), 1092(vs), 856(m), 813(vw), 789(w), 772(w), 732(w), 682(vw), 653(vw), 623(m), 551(w), 477(w). Elemental Analysis Calculated for **4** ($C_{74}H_{68}Cl_2Co_2N_8O_{14}$): C, 59.97; H, 4.62; N, 7.56. Found: C, 59.88; H, 4.32; N, 7.50.

{[Co(Me$_2$phen)$_2$]$_2$(BPDC)}(ClO$_4$)$_2$·2H$_2$O·2MeOH (5). Garnet-pinkish single crystals suitable for X-ray were obtained by slow evaporation. Yield: 107 mg, 35%. IR (ν_{max}/cm^{-1}): 3429(w), 3068(w), 3020(w), 2924(w), 2854(w), 2014(vw), 1626(m), 1594(s), 1568(m), 1510(s), 1500(s), 1414(vs), 1358(m), 1316(w), 1294(w), 1271(w), 1248(w), 1222(vw), 1177(vw), 1155(w), 1088(vs), 1063(w), 980(w), 963(w), 926(w), 855(m), 767(vw), 774(m), 732(w), 683(w), 623(m), 551(w), 537(vw), 519(vw), 428(vw). Elemental Analysis Calculated for **5** ($C_{72}H_{68}Cl_2Co_2N_8O_{16}$): C, 58.03; H, 4.60; N, 7.52. Found: C, 58.61; H, 3.91; N, 7.69.

III.2.3 Physical measurements

Infrared spectra (4000–400 cm^{-1}) were recorded on a Nicolet 5700 spectrophotometer as KBr pellets. Elemental analyses (C, H, N) were performed at the Microanalytical Service of the Universitat de València.

X-ray powder diffraction (XRPD) patterns were recorded on a Panalytical Empyrean X-ray diffractometer by using Cu Kα radiation (λ = 1.5406 Å), in which the X-ray tube was operated at 45 kV and 40 mA ranging from 2 to 40°. The XRPD data was background corrected with the *HighScore Plus* software.

Static direct current (dc) measurements were carried out on all samples by powdering and restraining the samples with *n*-eicosane to prevent any displacement. Variable-temperature (2.0–300 K) dc-magnetic susceptibility under an applied field of 0.25 (T < 20 K) and 5.0 kOe (T ≥ 20 K), and variable-field (0–5.0 kOe) magnetisation in the temperature range from 2 to 10 K were recorded with a Quantum Design SQUID magnetometer. Variable-temperature (2.0–10 K) alternating current (ac) magnetic susceptibility measurements under ±0.005 kOe oscillating field at frequencies in the range of 0.1–10 kHz were carried out on crystalline samples under different applied static dc fields in the range 0.0–5.0 kOe with a Quantum Design Physical Property Measurement System (PPMS). The magnetic susceptibility data were corrected for the diamagnetism of the constituent atoms and the sample holder.

Powder continuous wave EPR measurements were carried out on all samples by powdering and restraining the samples with *n*-eicosane to prevent any alignment with the magnetic field due to the high magnetic anisotropy. The EPR measurements in X- and Q-band were performed in an EMX spectrophotometer and in an Elexsys E580 spectrophotometer, both with a 18 kOe electromagnet (EPSRC National Service for Electron Paramagnetic Resonance Spectroscopy, University of Manchester). The samples were cooled down with a liquid ^{4}He flow together with an external N_2 gas flow to prevent O_2 and water moisture inside the cavity. Frozen solution samples were performed in acetonitrile ~5 mM, and they were subjected to three freezing cycles with liquid N_2 and degassed with ^{4}He before their data collection. The collected EPR data was corrected with a previous strong pitch measurement with g = 2.0028. The EPR simulations were obtained by using the *EasySpin* software.[17]

III.2.4 X-ray Crystallography

Single-crystal X-ray diffraction data of **2**, **2'**, **3** and **5** were collected on a Bruker-AXS Kappa Mach3 APEX-II diffractometer equipped with an Incoatec Helios monochromator mirror (Mo-Kα λ = 0.71073 Å) and a nitrogen cold stream adjusted to 100 K. Data integration, data scaling and absorption correction were done using the SAINT and SADABS programs, respectively. The structures were solved with the SHELXS structure solution program, using the Patterson method.[18] The model was refined with version 2018/3 of SHELXL against F2 on all data by full-matrix least squares.[19,20] All non-hydrogen atoms were refined with anisotropic displacement parameters. Hydrogen atoms were placed at calculated positions. The final geometrical calculations and the graphical manipulations were carried out with the PLATON package.[21] Crystallographic data for compounds **2**, **2'**, **3** and **5** are given in Table A.8.

III.2.5 Computational details

Calculations based on a second-order *N*-electron valence state perturbation theory (CASSCF/NEVPT2) applied on the wave function, which was previously obtained from complete active space (CAS) calculation, were performed on the structurally characterised dinuclear complexes **2**–**5** (or **2**, **2'**, **3**, **3'**, **4** and **5**) aiming to evaluate the parameters that determine axial (*D*) and rhombic (*E*) zfs.[22] These mononuclear species keep the experimental dispositions of the ligands around the metal. The calculations were carried out with version 4.0.1 of the ORCA and the auxiliary TZV/C Coulomb fitting basis sets.[23] The spin−orbit coupling contributions to zfs from 10 quartet and 20 doublet excited states generated from an active space with seven electrons in five d-orbitals were included from an effective Hamiltonian. The *g*-tensors were calculated for the ground Kramers pair using Multireference Configuration Interaction (MRCI) wave functions with a first-order perturbation theory on the SOC matrix.[24] The RIJCOSX method was used combining resolution of the identity (RI) and "chain of spheres" COSX approximations for the Coulomb and exchange terms, respectively. [25,26]

III.3 Results and discussion

III.3.1 Syntheses and X-ray Structure description

The reaction of Me_2phen and $Co(ClO_4)_2{\cdot}6H_2O$ with the respective bridging H_2L ligands and NaH in methanol yielded the dinuclear cobalt(II) complexes **{[Co(Me$_2$phen)$_2$]$_2$(L)}(ClO$_4$)$_2$** (**2**, **3**, **4** and **5**). The addition of 3 equivalents of $NaBPh_4$ to solutions of **2** and **3** allowed the anion exchange affording **{[Co(Me$_2$phen)$_2$]$_2$(L)}(BPh$_4$)$_2$** compounds (**2'** and **3'**).

The infrared spectra of **2**–**5** suggest the coordination of the bridging ligand to the Co^{II} ions as indicated by the strong absorption peak at ~1626 cm^{-1}. This peak, assigned to the $\nu_{C=O}$ stretching vibration, is shifted to lower energies for the complexes than on the free ligand (~1686 and ~1655 cm^{-1}, for the carboxylic and aldehyde groups, respectively). Strong and medium absorption peaks at ~1595 and ~1500 cm^{-1} are assigned to aromatic C–C stretching bands. For all compounds, the medium peak at ~1561 cm^{-1} is assigned to ν_{as}(COO). Together with the ν_s(COO) strong peak in the ~1424–1414 cm^{-1} range ($\Delta\nu$ = ~137 to ~147 cm^{-1}) confirms the presence of a bidentate carboxylate group for all compounds.[27] The counterion presence was confirmed by the strong peaks at 1094 cm^{-1} (ν_{Cl-O}) in **2**, **3**, **4** and **5** and 704 cm^{-1} (δ_{BPh4}) in **2'** and **3'**.

XRPD studies reveal a good match between the patterns simulated from the single-crystal X-ray and the experimental data of compounds **2'**, **3** and **5**, confirming the phase purity of the polycrystalline samples (Figures A.26–31). The XRPD of **2** do not match precisely between the experimental and simulated patterns. This phenomenon can be related to the presence of other crystalline phase or to the higher symmetric of the crystal structure than the one imposed by the bridging ligand. No better refinements were obtained with a non-centrosymmetric space group, then, the experimental and simulated patterns might differ. Although compounds **3'** and **4** exhibit a good powder diffraction pattern, they did not afford suitable crystals for their X-ray structure determination. Nevertheless, mass spectroscopy studies reveal the presence of the cationic dinuclear cobalt(II) entities in **2**–**5** (data not shown).

All compounds crystallise in the monoclinic system; **2** and **3** in the $P2_1/c$ space group, and **2'** and **5** in the $P2_1/n$ and Cc space groups. All these compounds are dinuclear cobalt(II) complexes, formed by $[Co(Me_2phen)_2]^{2+}$ units linked by one doubly deprotonated bridging ligand. The presence of two counterions, ClO_4^- (**2**, **3**, and **5**) or BPh_4^- (**2'**), balances the charge of the resulting cationic dinuclear unities (Figures III.1–4). These complexes exhibit distorted octahedral coordination spheres (CoN_4O_2) with the equatorial plane constituted by two nitrogen atoms from two Me_2phen ligands and two oxygen atoms from one chelating group from the bridging ligand. One nitrogen atom from each phenanthroline

ligand occupies an axial position. The Co^{II} ions are almost in the N_2O_2 equatorial plane with distances of 0.002 (**2**), 0.029 (**2**) and 0.03 Å (**3**) from the plane with the salicylaldehyde (Sal) coordination group and 0.029 (**2**), 0.063 (**2'**), 0.03 (**3**), 0.029 and 0.063 Å (**5**) from the plane with the carboxylate group. The distortion degree for all compounds was calculated with the continuous shape measure theory with the SHAPE program.[28] In this analysis, the OC-6 and TPR-6 parameters measure the distortion from ideal octahedron and trigonal prisms, which deviates from zero as the coordination geometry moves away. The parameters OC-6 and TPR-6, respectively, takes values of 2.512 and 13.834 for Co1a (carboxylate group), 1.632 and 13.941 for Co1b (Sal group) in **2**; 1.616 and 13.625 for Co1, 3.422 and 13.466 for Co2 in **2'**; 3.021 and 15.158 for Co1, 1.972 and 13.835 for Co2 in **3**; 3.891 and 11.458 for Co1, 4.073 and 11.833 for Co2 in **5**. These values agree with those obtained for the equivalent mononuclear complexes previously discussed in Chapter II. The Co^{II} ion with the carboxylate group shows more considerable distortions than the one with the salicylaldehyde moiety.[29] While we have seen that an intermediate point on this path indicates a deviation from these ideal geometries, there may also be a deviation from it, indicating an additional distortion. As before, the geometric distortion is more significant as this value moves away from zero. The values for this distortion are 28.2 (Co1) and 21.2 (Co2), 19.9 (Co1) and 33.3 (Co2), 36.3 (Co1) and 23.9 (Co2), 29.0 (Co1) and 31.5 (Co2) for **2**, **2'**, **3** and **5**, respectively. In conclusion, all four complexes exhibit an octahedral geometry being those Co^{II} ions more distorted when coordinated to the carboxylate group than to the salicylaldehyde group, probably due to the lower bite angle of the first one in their coordination.

Selected bond lengths and angles are listed in Table III.1. The Co−N distances are in the range of 2.15−2.24 Å, 2.13−2.22 Å, 2.12−2.22 Å, and 2.11−2.18 Å for **2**, **2'**, **3** and **5**, respectively, whereas the Co−O distances are of 2.15−2.24 Å, 2.09−2.25 Å, 2.01−2.21 Å and 2.10−2.26 Å, for **2**, **2'**, **3** and **5**, respectively. The chelating N−Co−N angles are in the 77.05−79.69° range. The O−Co−O angles are 78.66° (Sal group) and 70.44° (acid group) (**2**), 87.28° and 60.08° (**2'**), 61.99° and 82.33° (**3**) and 60.54° and 60.85° (**5**) for Co1 and Co2, respectively. As expected, this deviation is larger for the bidentate carboxylate moiety than for the salicylaldehyde group. The distortion of the coordination sphere is somehow reflected in the deviation of the planarity of the two pyridyl rings of the Me_2phen with dihedral angles between 6.88−7.54° (**2**), 7.52−10.49° (**2'**), 7.61−9.81° (**3**) and 3.63−8.36° (**5**). Moreover, the two phenyl rings of the bridging ligand are not planar with dihedral angles of 33.12° (**3**) and 27.37° (**5**). Neither the phenyl groups of the bridging ligand with the donor atoms groups are. Therefore, the N_2O_2 equatorial planes of the Co^{II} ions form a dihedral angle of 3.08° (**2**), 18.96° (**2'**), 12.97° (**3**) and 29.69° (**5**).

The intramolecular Co···Co distances are 9.546 (**2**), 9.639 (**2'**), 13.947 (**3**) and 15.028 Å (**5**), while the shortest intermolecular Co···Co distances are 9.344 (**2**), 9.395 (**2'**), 8.356 (**3**) and

8.353 Å (**5**). The crystal packing of **2**, **2'**, **3** and **5** is shown in Figures A.32–35, respectively. There are no classical hydrogen bonds in these compounds. However, π–π interactions involving phenyl and pyridyl rings of Me_2phen ligand and the phenyl group of the bridging ligand occur (Table A.9), giving rise to a supramolecular arrangement (a layer-like structure parallel to the (1, 0, 0) plane for **2**, a chain along the *c*-axis for **3**, a layer-like structure parallel to the (0, 1, 0) plane for **4** and a layer-like structure parallel to the (0, 1, 0) lattice plane for **5**). Particularly, **3** and **5** show intermolecular π–π interactions between a phenanthroline ligand and the bridging ligand (3.925 and 3.589 Å, respectively).

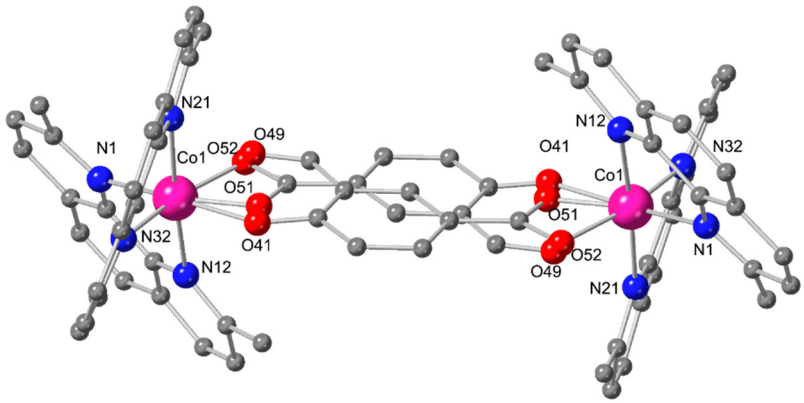

Figure III.1. Perspective view of the dinuclear cationic entity of **2**. The perchlorate anions and hydrogen atoms are omitted for clarity. Colour code: magenta, cobalt; blue, nitrogen; red, oxygen; grey, carbon.

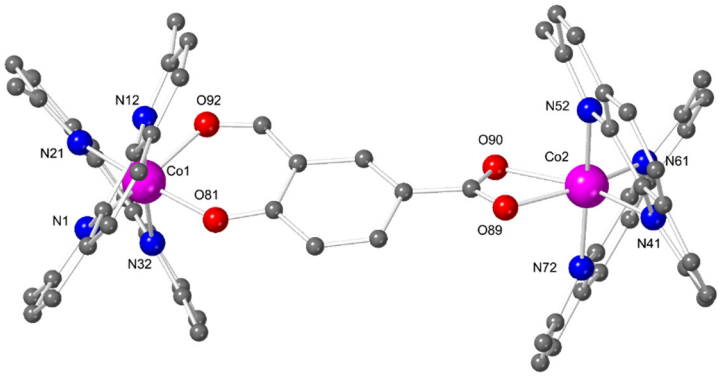

Figure III.2. Perspective view of the dinuclear cationic entity of **2'**. The tetraphenylborate anions and hydrogen atoms are omitted for clarity. Colour code: magenta, cobalt; blue, nitrogen; red, oxygen; grey, carbon.

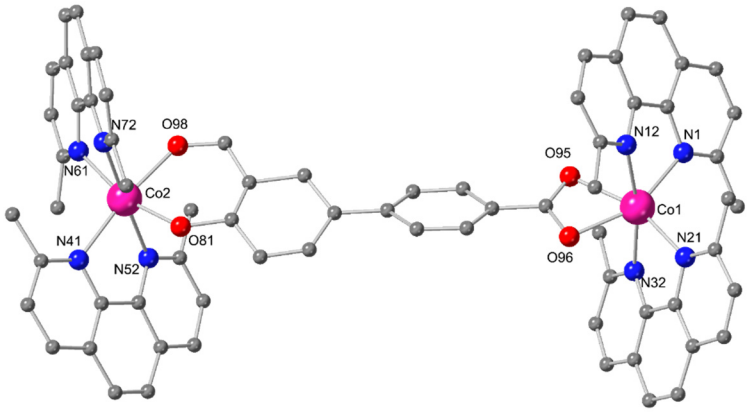

Figure III.3. Perspective view of the dinuclear cationic entity of **3**. The perchlorate anions and hydrogen atoms are omitted for clarity. Colour code: magenta, cobalt; blue, nitrogen; red, oxygen; grey, carbon.

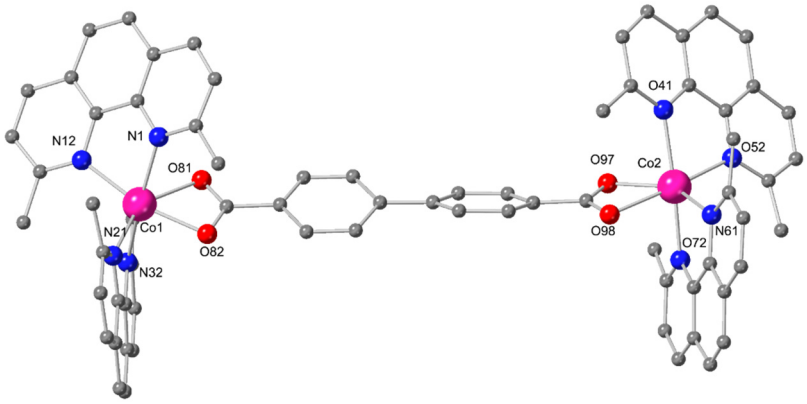

Figure III.4. Perspective view of the dinuclear cationic entity of **5**. The perchlorate anions and hydrogen atoms are omitted for clarity. Colour code: magenta, cobalt; blue, nitrogen; red, oxygen; grey, carbon.

Table III.1. Selected bond distances and angles for **2**, **2′**, **3** and **5**.

Compound	2	2′	3	5
Bond distances [Å]				
Co1–N1	2.123(7)	2.129(4)	2.1258(1)	2.167(3)
Co1–N12	2.189(7)	2.184(5)	2.1742(1)	2.108(3)
Co1–N21	2.181(7)	2.128(5)	2.1186(1)	2.106(3)
Co1–N32	2.123(6)	2.177(4)	2.1853(1)	2.121(3)
Co1–Oa	2.14(2)	1.985(11)	2.2088(1)	2.259(3)
Co1–Ob	2.20(5)	2.103(6)	2.1118(1)	2.097(3)
Co2–N41	–	2.224(9)	2.1551(1)	2.184(3)
Co2–N52	–	2.176(10)	2.2208(1)	2.137(3)
Co2–N61	–	2.134(4)	2.1507(1)	2.109(3)
Co2–N72	–	2.168(4)	2.1759(1)	2.138(3)
Co2–Oc	1.96(3)	2.091(7)	2.0133(1)	2.118(3)
Co2–Od	2.07(5)	2.250(9)	2.1018(1)	2.232(3)

Bond angles [°]				
Oa–Co1–Ob	78.7(14)	87.3(4)	61.99(1)	60.54(11)
N1–Co1–N12	77.5(3)	78.39(16)	78.33(1)	78.23(13)
N12–Co1–N32	105.2(3)	174.43(15)	169.44(1)	166.54(13)
N21–Co1–N32	78.5(2)	78.23(17)	78.61(1)	79.45(12)
N12–Co1–Oa	95.9(6)	84.2(3)	80.73(1)	77.96(11)
N12–Co1–N21	176.0(2)	104.80(17)	107.34(1)	113.97(12)
Oc–Co2–Od	70.4(15)	60.1(3)	82.33(1)	60.85(11)
N41–Co2–N52	–	76.2(4)	77.05(1)	77.91(12)
N52–Co2–N72	–	173.9(3)	176.52(1)	169.17(13)
N61–Co2–N72	–	78.22(15)	77.99(1)	79.69(13)
N52–Co2–Oc	97.8(6)	83.1(3)	80.36(1)	83.05(11)
N52–Co2–N61	–	107.3(3)	105.49(1)	111.00(13)

Due to different atomic labelling among the structures, the oxygen atoms have been renamed as Oa, Ob, Oc and Od for comparison purposes. For **2**: Oa = O41, Ob = O49, Oc = O51a, Od = O52a. For **2'**: Oa = O81, Ob = O92, Oc = O89, Od = O90. For **3**: Oa = O95, Ob = O96, Oc = O81, Od = O98. For **5**: Oa = O81, Ob = O83, Oc = O97, Od = O98.

III.3.2 Magnetic properties, EPR spectroscopy and theoretical calculations

The direct current (dc) magnetic properties of **2**–**5** are shown as $\chi_M T$ *vs* T and M *vs* H/T curves (Figure III.5). The $\chi_M T$ value at room temperature of **2**–**5** ranges from 5.77 to 6.29 $cm^3\ K\ mol^{-1}$ and they are higher than the expected for two non-interacting Co^{II} ions with spin-only value for $S = 3/2$ with $g = 2.0$ (3.75 $cm^3\ K\ mol^{-1}$). These high values are typical for Co^{II} ions with significant spin-orbit coupling (SOC). Upon cooling, the $\chi_M T$ product decreases gradually until 100 K and then more rapidly until reaching values of around 3.31–3.74 at 2 K, suggesting the presence of a strong first-order SOC. In addition, neither intramolecular nor intermolecular magnetic exchange coupling between Co^{II} ions is detected from the $\chi_M T$ and M *vs* H/T curves, which is confirmed by DFT calculations ($|J|_{intra} < 0.02\ cm^{-1}$ and $|J|_{inter} < 0.01\ cm^{-1}$). This fact is also supported by the long intramolecular distances between the Co^{II} ions ($Co\cdots Co_{intra} > 9.55$ Å for **2**, $Co\cdots Co_{intra} > 13.95$ Å for **3**–**5** and $Co\cdots Co_{inter} > 8.28$ Å for **2**–**5**). Moreover, a twist angle greater than 27° between the biphenyl rings is present for **3** and **5**, which should weaken any exchange coupling based on a spin polarization through the π pathway provided by the bridging ligand. The drop of $\chi_M T$ values below ~5 K is well simulated considering the applied magnetic field (5.0 kOe) during the recording data.

The magnetisation values at 50 kOe and 2 K are in between 4.25 and 4.70 for **2**–**5**. These values are significantly below the saturation limit of 6 Nβ for two $S = 3/2$ spin moment with $g = 2$, suggesting the presence of a significant zfs. The isothermal magnetisation curves in the 2–10 K temperature range almost superimpose for all compounds, which suggests a significant zfs with large D values, with big separation between the excited and ground Kramers doublet states. Then, only the ground Kramers doublet is populated.

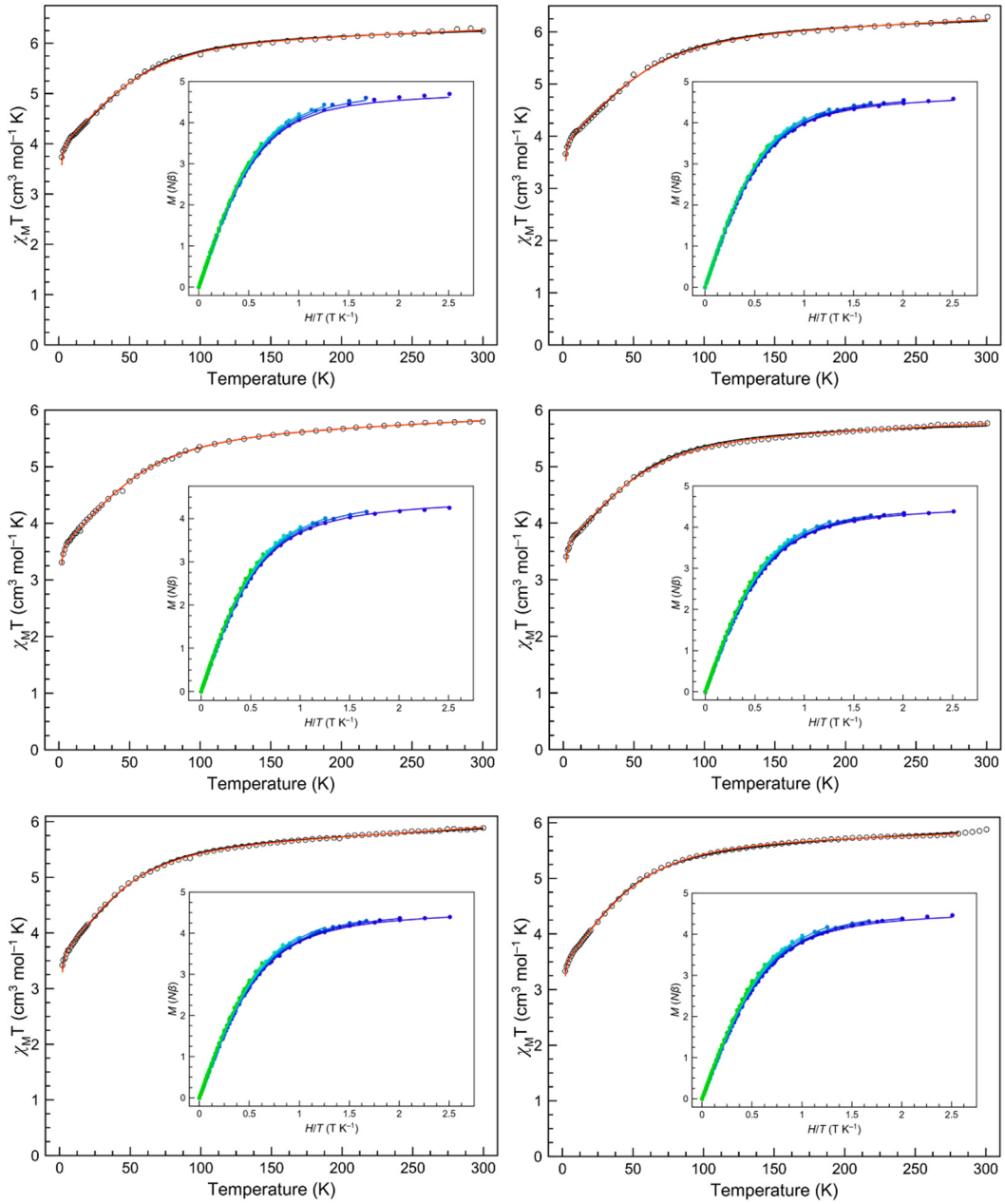

Figure III.5. Plots of $\chi_M T$ *vs* T in the range 2–300 K in 5.0 kOe applied field and M *vs* H/T (inset) for **2** (top left), **2′** (top right), **3** (middle left), **3′** (middle right), **4** (bottom left) and **5** (bottom right) in the 2–10 K temperature range (2 K blue to 10 K green gradient). The solid lines are the best-fit curves (see text).

The experimental magnetic susceptibility and magnetisation data of **2**–**5** were analysed in the whole temperature range through the T-P isomorphism formalism expressed with the SOC Hamiltonian (equation 1) shown in Chapter II (Figure III.5, red line). The best fit of the magnetic data using the PHI software,[30] and considering two identical Co^{II} ions are shown in Table III.2. In compounds with two crystallographically independent Co^{II} ions, they have been considered equivalent during the fitting of the spin Hamiltonian expressed in the equation (1) to avoid overparametrization. The obtained values of the parameters are similar in the six compounds, not being able to distinguish the different coordination

spheres. Then, the obtained values are an average from the two crystallographic Co^{II} ions. Besides, they are within the range of those observed for the mononuclear high-spin cobalt(II) building-blocks described in Chapter II and similar compounds.[15,31]

Additionally, the magnetic susceptibility data were also analysed with a spin Hamiltonian corresponding to an isolated $S = 3/2$ with significant zfs (Equation (2) from Chapter II; and Figure III.5, black line). This approach is also possible because only the two most stable Kramers doublets are populated at low temperatures. A TIP parameter is considered to empirically account the depopulation of the higher states coming from the first-order order SOC approach when cooling down. The experimental magnetic data analysis was carried out once again considering two identical Co^{II} ions through the spin Hamiltonian expressed by equation (2) from Chapter II. The best fitting of this model to the experimental data using the PHI software[30] provided the following parameter values shown in Table III.3. A good agreement between the experimental and calculated curves is obtained for all six compounds, but only when positive D values were considered, being the usual case in cobalt(II) octahedral complexes with similar coordination spheres. The calculated energy gap between the lowest Kramers doublets connects both models, first-order SOC and zfs. Once again, these values obtained by SOC and zfs models are very similar, verified with CASSCF/NEVPT2 calculations as well (see below), validating them (Table III.4). As a result, the D and g values, and the gap between the ground and first excited doublets of **2**–**5** are similar. However, the rhombicity expressed as the E/D ratio varies depending on the compounds. These values are around 0.185, except for **3** and **5**, which is almost half the 0.333 value obtained for **1·X** (X = $ClO_4 \cdot H_2O$, BPh_4 and $PF_6 \cdot H_2O$) from Chapter II. When looking at the values of **5**, these reveal the lowest rhombicity for these complexes, being attributed to the carboxylate coordination site.[29] Therefore, the values obtained from magnetometry do not distinguish the distinct cobalt(II) geometries of the complexes, but these point towards the presence averaged zfs parameters from low and high rhombic Co^{II} ions (E/D ~0.09 and 0.33, avg = 0.21) in **2**–**4**. As a reminder, the $|E/D|$ values of zero and 1/3 correspond to ideal geometries with high rhombic distortion. Therefore, the rhombicity of the ligand field should be moderate in these complexes.

Table III.2. Spin Hamiltonian parameters for **2–5** obtained following the SOC model.

Compound	λ (cm^{-1})	Δ (cm^{-1})	α	TIP $\times 10^6$ ($cm^3\ mol^{-1}$)	$F \times 10^6$
2	−103.3	−147.1	1.21	2530	34.10
2′	−111.7	−166.7	1.18	2640	36.03
3	−126.6	−209.9	1.01	2350	5.75
3′	−123.4	−232.9	1.00	2350	13.74
4	−109.3	−188.8	1.01	2825	16.38
5	−107.4	−144.3	1.01	2340	9.16

F is the agreement factor defined as $F = \sum[P_{exp} - P_{calcd}]^2/\sum[P_{exp}]^2$

Table III.3. Spin Hamiltonian parameters for **2–5** obtained following the zfs model.

Compound	D (cm^{-1})	$\lvert E/D \rvert$	$g_{\perp}$	$g_{\parallel}$	g_{av}	TIP × 10^6 (cm^3 mol^{-1})	$F \times 10^5$
2	+66.2	0.123	2.69	2.00	2.46	1080	8.28
2′	+67.8	0.181	2.66	2.07	2.46	1080	2.42
3	+58.2	0.301	2.54	2.06	2.38	1260	1.46
3′	+61.8	0.197	2.56	2.01	2.38	840	2.31
4	+56.4	0.189	2.56	2.00	2.37	1430	1.88
5	+52.6	0.099	2.51	2.16	2.39	1390	1.59

F is the agreement factor defined as $F = \sum[P_{exp} - P_{calcd}]^2/\sum[P_{exp}]^2$

To gain more information, Q and X-band EPR studies were performed. High-spin Co^{II} ion exhibits larger D values than the excitation energy (frequency band), therefore the D value cannot be determined by neither Q and X-band EPR. However, this technique allows estimating the components of the g-tensor and the $\lvert E/D \rvert$ ratio. The spectra for polycrystalline powdered samples of **2–5** at ~5 K were measured as *n*-eicosane pellets as shown in Figure III.6 and A.36. The Q and X-band EPR spectra of **2–5** exhibit patterns typical for an S = 3/2 spin state with large zfs, this being the reason that only the fundamental Kramers doublet is populated at low temperature. Then their EPR spectra at these temperatures corresponds to only $\Delta M_S = \pm 1$ transitions between this Kramers doublet. To make a proper estimation of the g tensor and the $\lvert E/D \rvert$ ratio, X and Q-band EPR spectra were simulated as two isolated S = 3/2 spin systems with large zfs (D >> 20 cm^{-1}) and the obtained parameters were double-checked by simulating the X-band spectra too. As a result, the values for the best-fit parameters considering two set of parameters for **2–4′**, each one corresponding to each ion of the asymmetric dinuclear complex are shown in Table III.4. However, only one set of parameters is used in symmetrical compound **5**, also shown in Table III.4. For comparison purposes with the magnetometry results, $g_{\perp}$ component is extracted from g_x and g_y following the equation (7):

$$g_{\perp} = \sqrt{\frac{g_x{}^2 + g_y{}^2}{2}} \qquad (7)$$

In tune with positive D values, the perpendicular components of the g-tensor are larger than the parallel one.

After confirming by mass spectroscopy that these compounds are stable in solution, which is the dinuclear entity is preserved, X-band EPR spectra at ~5 K on frozen acetonitrile solutions (~5 mM) of **2–5** were also recorded (Figure III.7 left). The best simulations for **2–3′** were obtained with identical parameters (g_{x1} = 2.41, g_{y1} = 2.75, g_{z1} = 2.16, $\lvert E/D \rvert_1$ = 0.038 and g_{x2} = 2.35, g_{y2} = 2.66, g_{z2} = 2.13, $\lvert E/D \rvert_2$ = 0.320), being them close to those found in solid state. Good simulations for **4** and **5** were found with the following values: g_{x1} = 2.41, g_{y1} = 2.75, g_{z1} = 2.16, $\lvert E/D \rvert_1$ = 0.038 and g_{x2} = 2.46, g_{y2} = 2.60, g_{z2} = 2.13, $\lvert E/D \rvert_2$ = 0.303 for **4**, and

$g_x = 2.41$, $g_y = 2.75$, $g_z = 2.16$, $|E/D| = 0.038$ for **5**. Only solutions of **2′** and **3** gave good spectra in Q-band EPR, which validated previous results (Figure A.37). The values for the best-fit parameters are shown in Table III.4.

Table III.4. Spin Hamiltonian parameters for **2–5** obtained by CASSCF/NEVPT2 and EPR.

Technique	D (cm^{-1})	E/D	g_x	g_y	g_z or $g_{\|\|}$	$g_\perp$[b]	g_{av}
2							
CASSCF/NEVPT2[a]	+46.87/+60.19	0.162/0.213	2.42/2.42	2.58/2.71	2.03/2.01	2.50/2.57	2.34/2.38
Solid EPR[a]	>> +20	0.076/0.266	2.49/2.40	2.63/2.71	2.19/2.09	2.34/2.56	2.44/2.40
Solution EPR[a]	>> +20	0.038/0.320	2.41/2.35	2.75/2.66	2.16/2.13	2.59/2.51	2.44/2.38
2′							
CASSCF/NEVPT2[a]	–93.86/+57.98	0.286/0.174	2.23/2.45	1.84/2.68	3.00/2.04	2.05/2.57	2.37/2.39
Solid EPR[a]	>> +20	0.068/0.327	2.40/2.35	2.52/2.86	2.00/2.16	2.46/2.62	2.31/2.46
Solution EPR[a]	>> +20	0.038/0.320	2.41/2.35	2.75/2.66	2.16/2.13	2.59/2.51	2.44/2.38
3							
CASSCF/NEVPT2[a]	+65.03/–85.62	0.200/0.252	2.43/2.26	2.72/2.96	2.00/2.96	2.58/2.09	2.38/2.37
Solid EPR[a]	>> +20	0.058/0.254	2.44/2.46	2.70/2.85	2.04/2.00	2.57/2.66	2.39/2.44
Solution EPR[a]	>> +20	0.038/0.320	2.41/2.35	2.75/2.66	2.16/2.13	2.59/2.51	2.44/2.38
3′							
CASSCF/NEVPT2[a]	–	–	–	–	–	–	–
Solid EPR[a]	>> +20	0.077/0.161	2.67/2.51	2.94/2.95	2.07/2.09	2.81/2.74	2.56/2.52
Solution EPR[a]	>> +20	0.038/0.320	2.41/2.35	2.75/2.66	2.16/2.13	2.59/2.51	2.44/2.38
4							
CASSCF/NEVPT2[a]	–	–	–	–	–	–	–
Solid EPR[a]	>> +20	0.058/0.284	2.36/2.41	2.62/2.58	2.12/2.18	2.49/2.50	2.37/2.39
Solution EPR[a]	>> +20	0.038/0.303	2.41/2.46	2.75/2.60	2.16/2.13	2.59/2.53	2.44/2.40
5							
CASSCF/NEVPT2[a]	+53.21/+52.96	0.123/0.198	2.48/2.39	2.60/2.63	2.16/2.03	2.54/2.52	2.39/2.37
Solid EPR[a]	>> +20	0.007	2.40	2.57	2.21	2.49	2.39
Solution EPR[a]	>> +20	0.038	2.41	2.75	2.16	2.59	2.44

[a] Each pair of values refer to the values for Co1 and Co2, respectively. [b] The perpendicular component of g is obtained by the formula $g_\perp = \sqrt{\frac{g_x^2+g_y^2}{2}}$.

X- and Q-band EPR spectra (in solid and frozen solution) established a positive sign of D for all complexes, as observed in the mononuclear building-blocks cobalt(II) complexes (see Chapter II and ref.[29]). The similar but different coordination sphere of the Co^{II} ions caused by the asymmetry of the bridging ligands results in identifiable different EPR signals for each ion in **2**–**4**. This is in agreement with the two different crystallographically Co^{II} ions. For **2**–**4**, the major differences between these parameters of metal ions with the ones found in solid state is attributed to weak distortions in the coordination spheres imposed by the crystal packing.

As stated before, the zfs parameters are in agreement with the two crystallographic Co^{II} ions. In fact, the zfs values correspond with the values obtained for the mononuclear complexes. On the one hand, the Co^{II} ion with the coordinated carboxylate group exhibits low rhombicity in all compounds ($|E/D| < 0.1$) in agreement with the already reported mononuclear $[Co(Me_2phen)_2(benzoate)](ClO_4)_2$ compound.[29] On the other hand, the Co^{II} ion coordinated to the salicylaldehyde group exhibits high rhombicity ($|E/D| \sim 1/3$) as seen in Chapter II. Moreover, the absorption band assignment is also confirmed by comparing the X-band EPR spectra of the asymmetrical complexes **2**–**4** with the symmetrical **5**. In fact, the absorption band at ~4 kOe is absent in **5** (Figure III.7 right). Therefore, this absorption is attributed to the cobalt(II)–salicylaldehyde coordination sphere. In Figure III.8, the individual simulation of the zfs parameters is plotted with the frozen solution sample EPR of **3**. The differences between these two curves support the presence of two zfs parameter sets in the complexes with asymmetric ligands.

The previous statements were confirmed through a theoretical study based on CASSCF/NEVPT2 calculations. Values found for the parameters of the spin Hamiltonian expressed in equation (2), from Chapter II, are shown in Table III.4. Their values confirm the distinct coordination spheres for the Co^{II} ions, which are similar to those obtained by experimental techniques. In all these cases, D is primarily determined by the contribution of the quadruplet and doublet states (D_Q and D_D). They are equal to +41.8 and –1.08 cm^{-1} for Co1 with the carboxylate group, +51.4 and +0.7 cm^{-1} for Co1 with the salicylaldehyde group (**2**); –91.265 and –1.8 cm^{-1} for Co1, +48.7 and –0.1 cm^{-1} for Co2 (**2'**); +55.5 and +3.0 cm^{-1} for Co1, –83.8 and –1.3 cm^{-1} for Co2 (**3**); +46.1 and –1.6 cm^{-1} for Co1, +45.0 and +4.5 cm^{-1} for Co2 (**5**) for D_Q and D_D, respectively. Mainly, these contributions arise from the first two excited states close to the ground state [D_{Q1}+D_{Q2} equal to +46.9 for Co1 with the carboxylate group, +54.5 for Co1 with the salicylaldehyde group (**2**); –91.6 for Co1, +54.6 for Co2 (**2'**); +56.4 for Co1, –85.2 for Co2 (**3**); +50.6 for Co1, +43.7 cm^{-1} for Co2 (**5**)], together with they make up the ground term $^4T_{1g}$ in an ideal geometry (Table A.10). These D contributions show that Co1 from **2'** and Co2 from **3** should exhibit a negative D value, but these values are in contrast to what observed experimentally. Then, the lack of accuracy in the evaluation of the E/D ratio in CASSCF/NEVPT2 calculations together with its high value (0.286 and 0.252, respectively) must be considered as the source of the discrepancy in the sign of D between theoretical and experimental values.

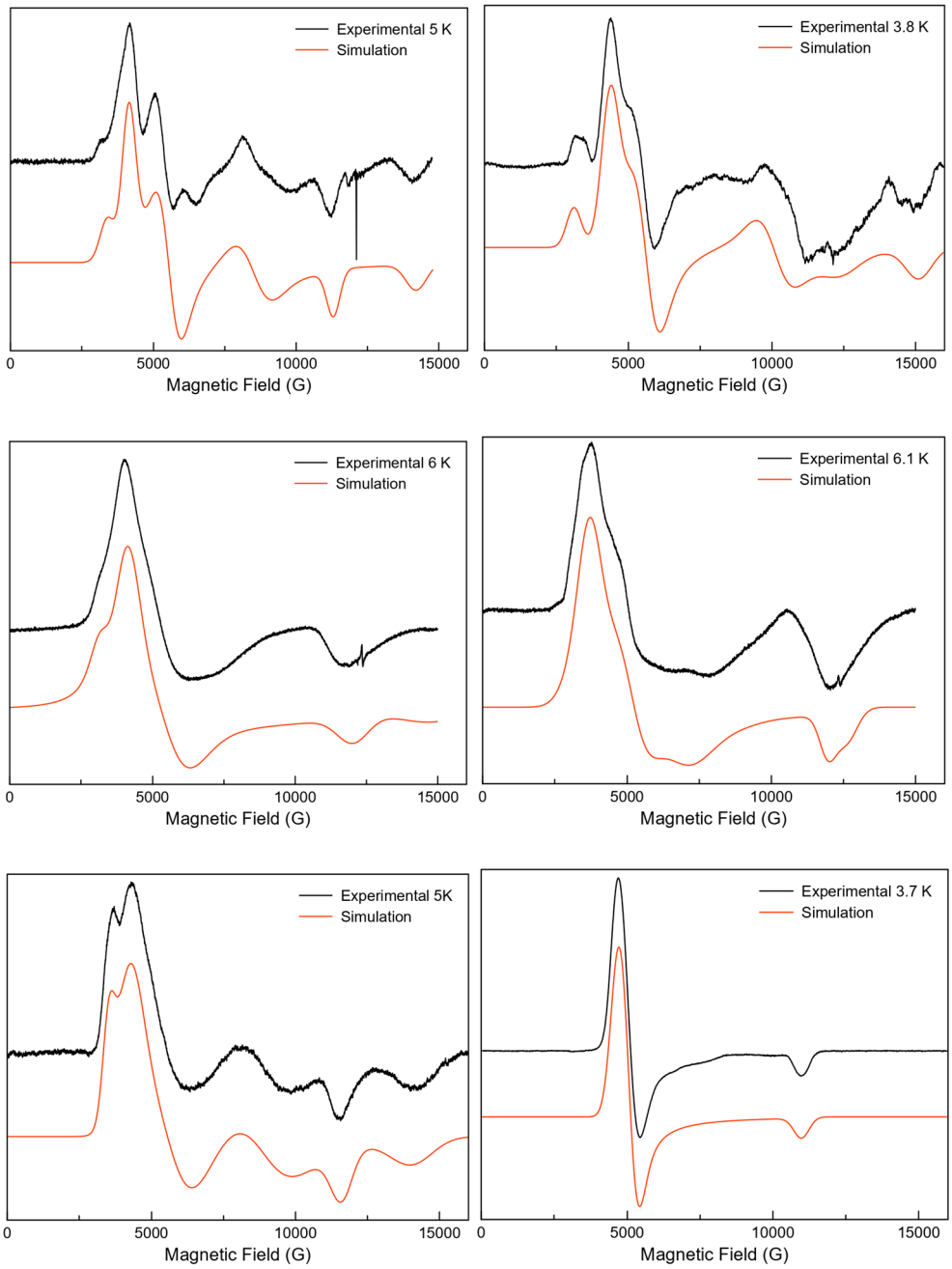

Figure III.6. Q-band EPR in the 0–16 kOe range for polycrystalline powdered samples of **2** (top left), **2'** (top right), **3** (middle left), **3'** (middle right), **4** (bottom left) and **5** (bottom right) at ~5 K. The simulated red curves were obtained by using the parameters of Table III.4.

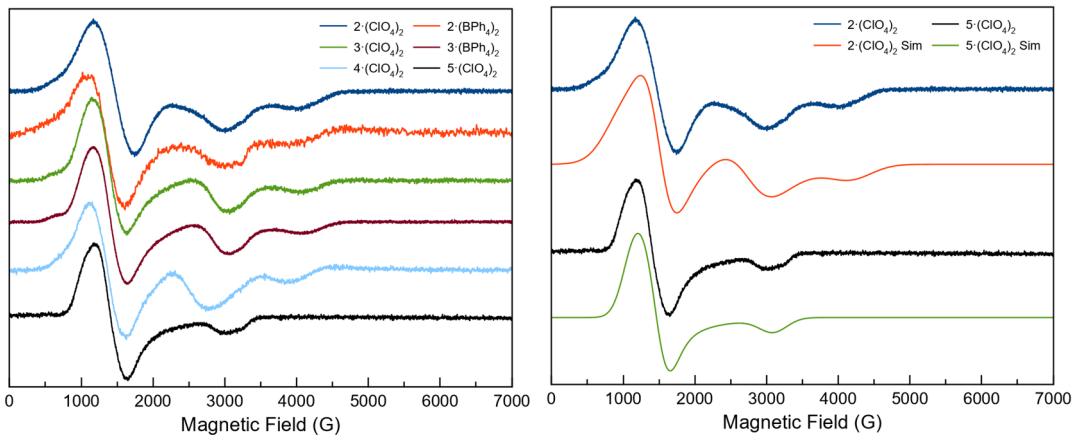

Figure III.7. X-band EPR in the 0–7 kOe range for frozen solution samples in AcN ~5 mM of **2**·(blue), **2′** (orange), **3** (green), **3′** (red), **4** (light blue) and **5** (black) at ~6 K (left). X-band EPR simulations for **2** and **5** in the 0–7 kOe range in red and green, respectively (right). The simulations were performed using the parameters of Table III.4.

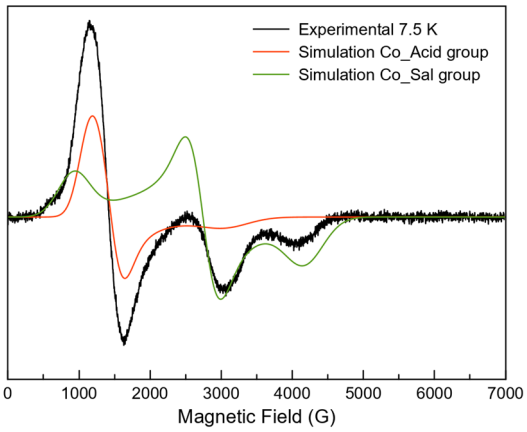

Figure III.8. X-band EPR in the 0–7 kOe range for a frozen solution sample of **3** in AcN ~5 mM at ~7.5 K (black). The red and green curves correspond to the individual simulation for each set of the fit parameters for the frozen solution of **3**. The simulations were performed using the parameters of Table III.4.

Table III.5. Energy gap (in cm^{-1}) between the ground and first excited Kramers doublets from experimental magnetometry according to SOC and zfs models, and theoretical CASSCF/NEVPT2 calculations.

Compound	Magnetometry: SOC model	Magnetometry: zfs model	CASSCF/NEVPT2
2	128.9	135.4	97.4/128.3
2′	135.5	142.1	121.1/209.5
3	131.1	131.2	137.7/189.1
3′	125.7	130.5	–
4	112.6	118.8	–
5	114.4	106.7	108.8/112.0

III.3.3 Ac-magnetic properties

For all six compounds, the dynamic properties were evaluated by measuring alternating current (ac) magnetic susceptibilities as a function of the applied dc-magnetic field (0.5–5.0 kOe) and the frequency (0.1–10.0 kHz) of the oscillating field (±0.005 kOe) in the temperature range 2.0–12.0 K. In zero dc-magnetic field, no χ_M'' signals were observed for **2–5**, but a frequency-dependent behaviour appears in χ_M' and χ_M'' below ~4 K in the presence of an H_{dc} magnetic field (Figure III.9–14 and A.38–59). The emergence of magnetic relaxation was usually related to an energy barrier linked to a negative zfs tensor ($D < 0$). In these complexes, this assumption is not valid due to the absence of an energy barrier ($D > 0$), as seen in Chapter II and previously reported cobalt(II) complexes. The χ_M' and χ_M'' *vs* ν data were analysed together with the DynVPMag program resulting in a unique set of values following the generalised Debye model.[36,37] With this model, the χ_M' and χ_M'' are described by the adiabatic (χ_S) and isothermal (χ_T) magnetic susceptibilities, the relaxation time (τ) and the exponential factor which defines the broadness of the spectra (α) through equations (3) and (4) from Chapter II. In some cases, the χ_M' and χ_M'' *vs* ν curves are only described correctly by the addition of a second individual relaxation process through equations (5) and (6) from Chapter II.

As a result, the simulated curves with the best-fit parameters reproduce the experimental data rightly and, therefore, the Cole-Cole plots as shown in (Figure III.9–14 and A.38–59). Simulation of different methods to the Arrhenius plots of **2–5** are shown in Figures A.60–65. The best-fit values are shown in Tables A.11–A.16. The α values are below 0.4, rejecting any spin-glass behaviour. Usually, as for what is seen in Chapter II, α exhibits a thermal dependence for both primary and incipient relaxations and that are, which is similar in all cases.

At $H_{dc} > 2.5$ kOe and below 3.5 K, **2–3'** show a broad peak in χ_M'' *vs* ν due to the emergence at lower frequencies of a second incipient relaxation, which leads to an asymmetric or double Cole-Cole plot. Similar behaviour is found for **3** and **4** at $H_{dc} > 1.5$ kOe, while **5** shows a shoulder in the Cole-Cole at all fields. The presence of several peaks in the Cole-Cole plots suggests multiple and independent relaxation processes. To get more insights into such mechanisms, the thermal dependences on relaxation times in the form of Arrhenius plots for the main and incipient relaxation processes in **2–5** are shown in Figure III.15.

For **2**, these graphs for the primary relaxation process show two linear dependencies that can only be associated to relaxations governed by a thermally activated (TA) mechanism, that is, to a relaxation whose rate is directly linked to an energy barrier. This type of Arrhenius plots rules out any Raman or direct mechanism. At 5.0 kOe, τ tends to be constant at low temperature, *i.e.*, they are not temperature dependent, associating it to a

relaxation of a different nature. It cannot be a usual quantum tunnelling since the positive value of *D* disables the existence of an energy barrier caused by a zfs. In this case, there are only two alternatives: i) quantum tunnelling of a different nature, or ii) a slowed passage between the two components of the ground Kramers doublet without the intervention of any other state. The latter case refers to an intra-Kramers (IK) mechanism, which was the choice to justify these properties in compounds in the previous chapter. In summary, these dynamic behaviours were analysed through a model with two TA and one IK processes competing in the whole temperature region (2 TA + IK, $\frac{1}{\tau} = \sum_{i=1}^{2} (\frac{1}{\tau_i} e^{-\frac{Ea_i}{k_B T}}) + \frac{1}{\tau_{0,IK}}$). The results are shown in Tables A.11–16.

The rest of the compounds show similar behaviour in their Arrhenius plots, but some of them do not exhibit the two linear regimes clearly. However, when their data are analysed in the same way as for **2**, similar E_a and τ_0 values are found, supporting the chosen model. In a similar way as in the previous chapter, **4** and **5** show, particularly at 5.0 kOe, a third high-temperature TA process (TA_{HT}). Only the inclusion of this third mechanism with a large E_a allows reproducing E_a and τ_0 values of the TA processes found for lower H_{dc}, but with higher standard deviations. The similarity between the results obtained for all the compounds in this chapter and the previous chapter is remarkable. On the one hand, this fact highlights that these cobalt(II) complexes, with the same or similar coordination environments, show similar dynamic behaviours. On the other hand, these dynamics confirms the validity of the proposed physical model. As already seen in the previous chapter, E_a values are connected to the energies required to achieve low-lying vibrational states favouring or accelerating the spin-reversal. E_a values and vibrational frequencies almost coincide in these compounds, which is linked to the similarity in their coordination spheres.

The implication of a Raman mechanism in the relaxation of the magnetisation was questioned in the previous chapter, but this possibility has been considered here also. For this purpose, the analysis was done through a model that includes Raman and IK mechanisms, since the presence of the IK mechanism is beyond doubt. In some cases, this model cannot adequately reproduce the data when linear dependences appear in the Arrhenius plots. However, it does so in the rest of the cases, but in a limited temperature range ($T < 5$ K). Indeed, this result is worse than the one studied with a 2TA + IK model ($T < 12$ K). Whereas the exponential *n* factor oscillates in the range 5.5–6.5 in **5** for the Raman + IK model, it moves between 2.3 and 3.9 in the rest of compounds. Therefore, it seems than in **5** the Raman process occurs via an acoustic phonon, while in the rest optical phonons seems to be involved. The disparity of the results, a high thermal restriction and the low fidelity when reproducing the experimental data leads to discarding this model.

The experimental data of χ_M' and χ_M'', mainly when used in Cole-Cole plots, clearly show two independent relaxation processes under certain conditions. The deconvolution of them in the way described above has allowed having more precise data for the primary process. However, the quality of data for the incipient process is not fair to carry out analyses that allow drawing reliable conclusions. Nevertheless, this process seems to correspond to an IK mechanism with τ_0 values of the order of 10^{-2}–10^{-3} s.

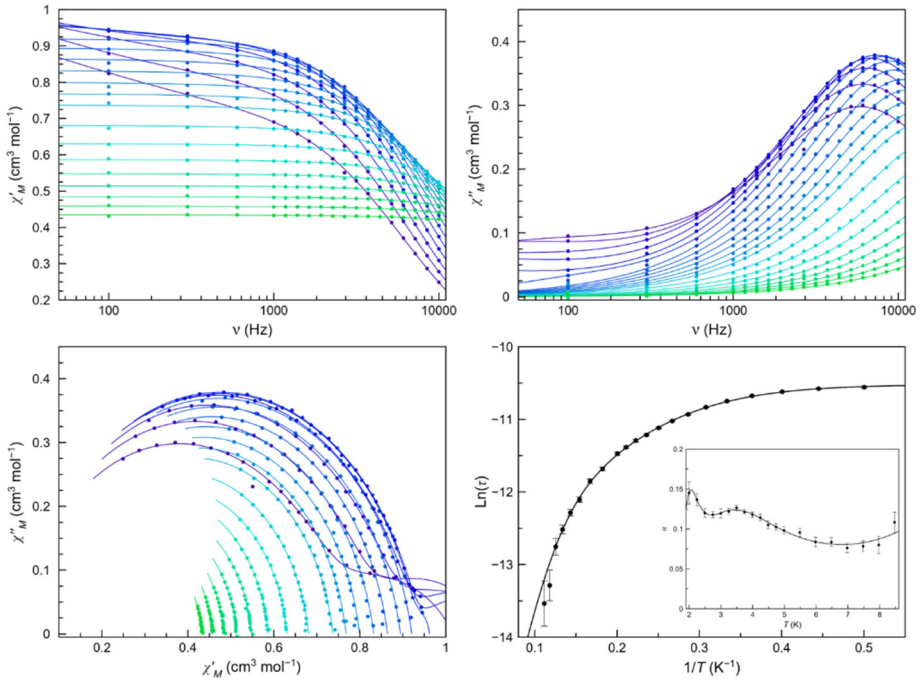

Figure III.9. Frequency dependence of χ_M' (top left) and χ_M'' (top right), Cole-Cole plots (bottom left) and Arrhenius plots of **2** (bottom right) in a dc-applied static field of 5.0 kOe with ± 0.005 kOe oscillating field in the temperature range of 2.0–9.0 K (purple to green gradient). Thermal dependence of α is included on the bottom right figure as an inset, where the black line are eye-guides. Standard deviation appears as vertical error bars.

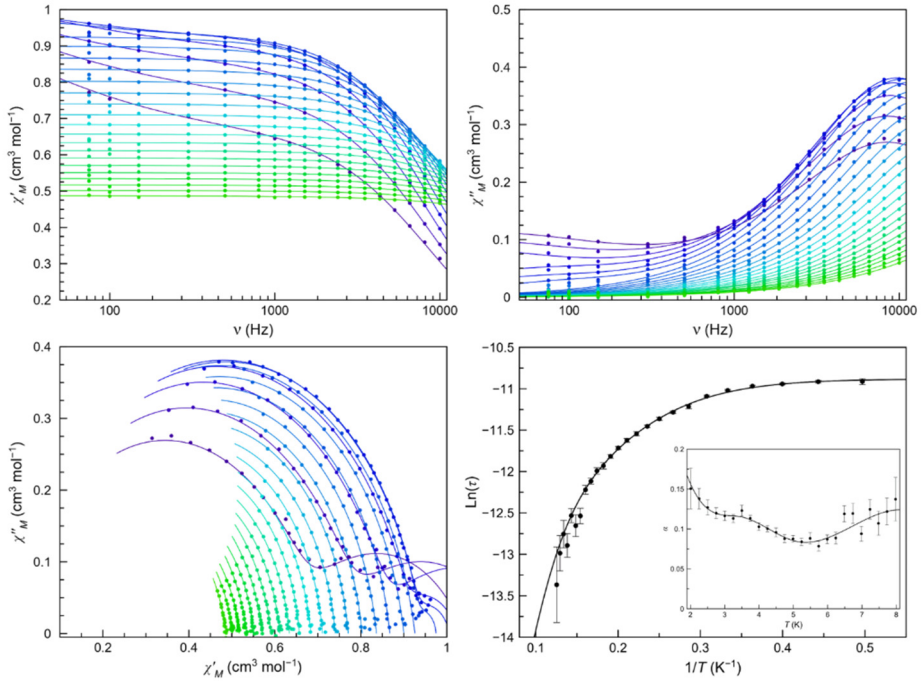

Figure III.10. Frequency dependence of χ_M' (top left) and χ_M'' (top right), Cole-Cole plots (bottom left) and Arrhenius plots of **2′** (bottom right) in a dc-applied static field of 5.0 kOe with ± 0.005 kOe oscillating field in the temperature range of 2.0–8.0 K (purple to green gradient). Thermal dependence of α is included on the bottom right figure as an inset, where the black line are eye-guides. Standard deviation appears as vertical error bars.

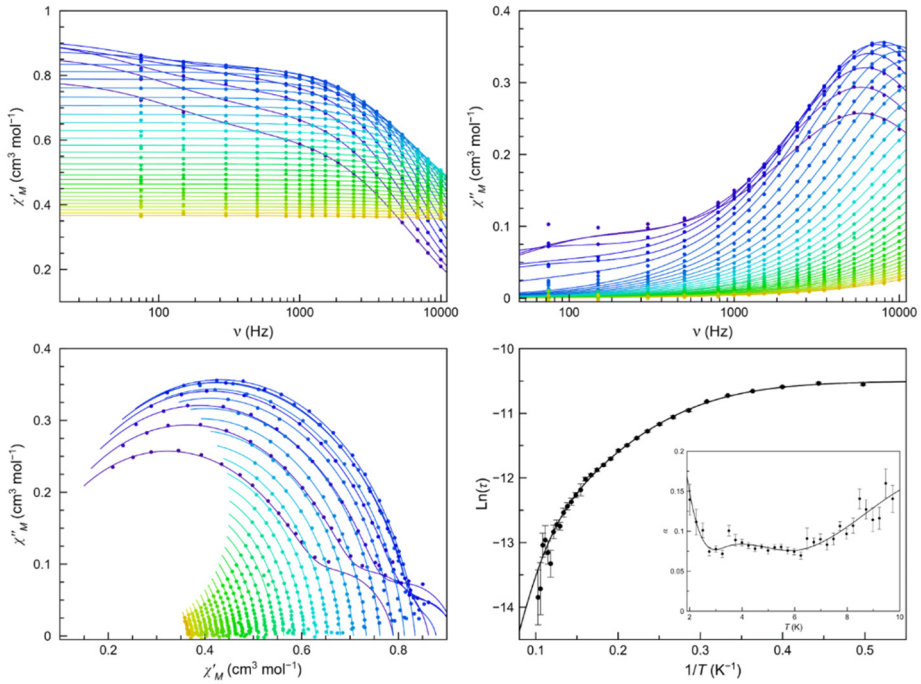

Figure III.11. Frequency dependence of χ_M' (top left) and χ_M'' (top right), Cole-Cole plots (bottom left) and Arrhenius plots of **3** (bottom right) in a dc-applied static field of 5.0 kOe with ± 0.005 kOe oscillating field in the temperature range of 2.0–10.0 K (purple to red gradient). Thermal dependence of α is included on the bottom right figure as an inset, where the black line are eye-guides. Standard deviation appears as vertical error bars.

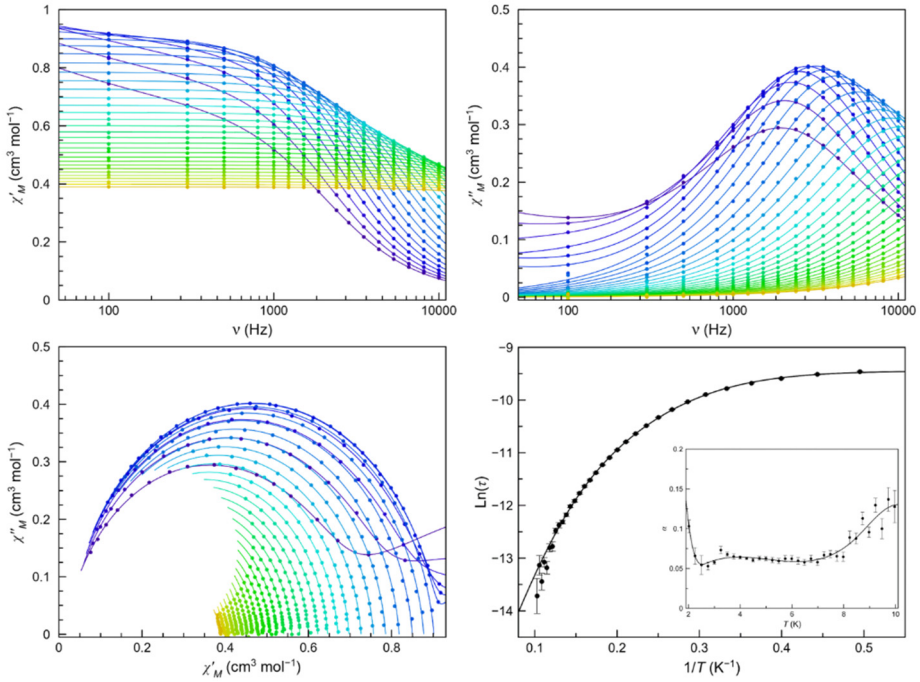

Figure III.12. Frequency dependence of χ_M' (top left) and χ_M'' (top right), Cole-Cole plots (bottom left) and Arrhenius plots of **3'** (bottom right) in a dc-applied static field of 5.0 kOe with ± 0.005 kOe oscillating field in the temperature range of 2.0–10.0 K (purple to red gradient). Thermal dependence of α is included on the bottom right figure as an inset, where the black line are eye-guides. Standard deviation appears as vertical error bars.

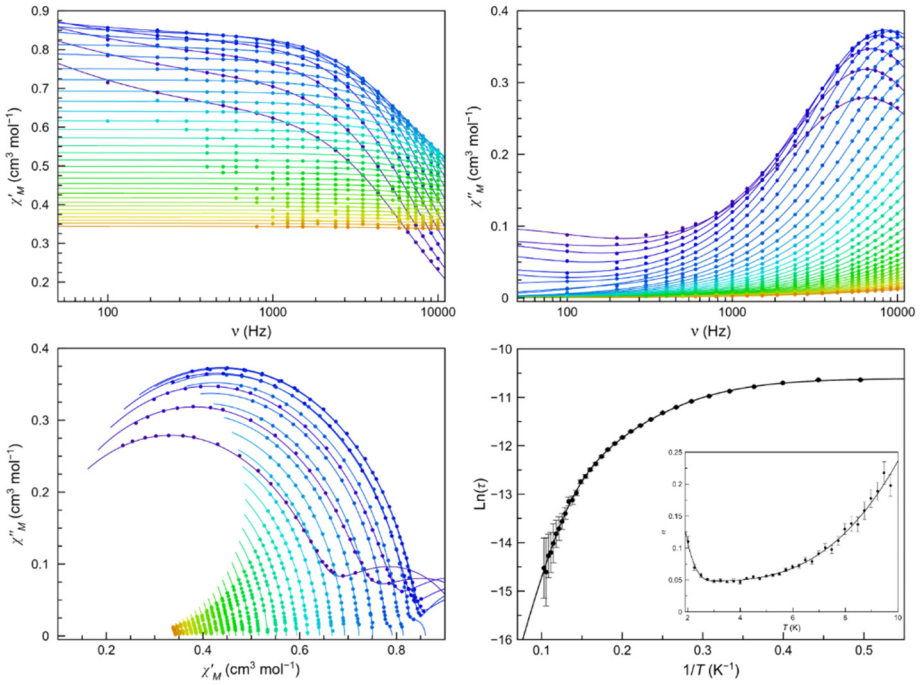

Figure III.13. Frequency dependence of χ_M' (top left) and χ_M'' (top right), Cole-Cole plots (bottom left) and Arrhenius plots of **4** (bottom right) in a dc-applied static field of 5.0 kOe with ± 0.005 kOe oscillating field in the temperature range of 2.0–10.5 K (purple to red gradient). Thermal dependence of α is included on the bottom right figure as an inset, where the black line are eye-guides. Standard deviation appears as vertical error bars.

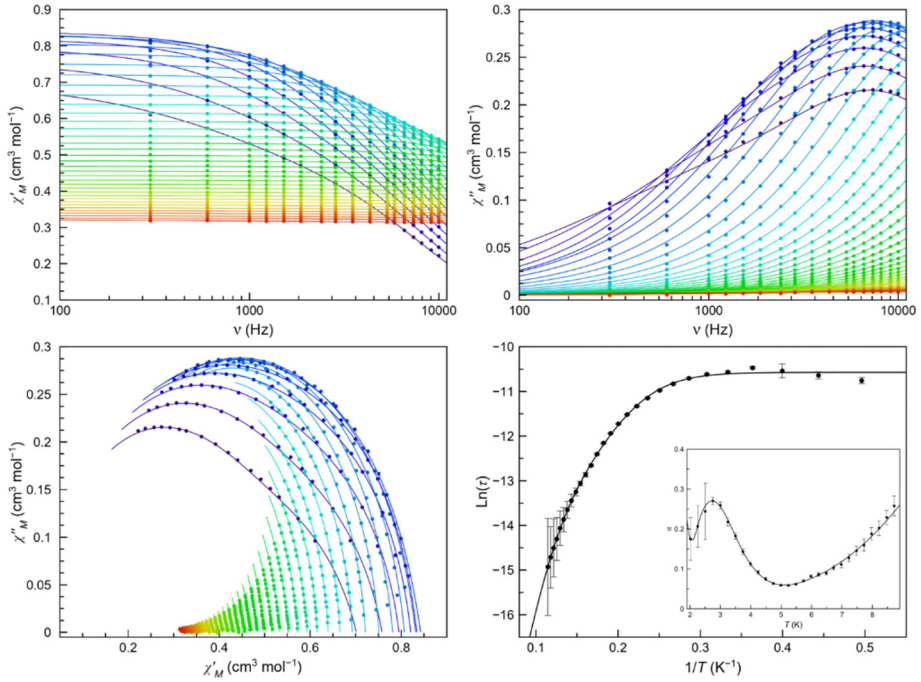

Figure III.14. Frequency dependence of χ_M' (top left) and χ_M'' (top right), Cole-Cole plots (bottom left) and Arrhenius plots of **5** (bottom right) in a dc-applied static field of 5.0 kOe with ± 0.005 kOe oscillating field in the temperature range of 2.0–11.5 K (purple to red gradient). Thermal dependence of α is included on the bottom right figure as an inset, where the black line are eye-guides. Standard deviation appears as vertical error bars.

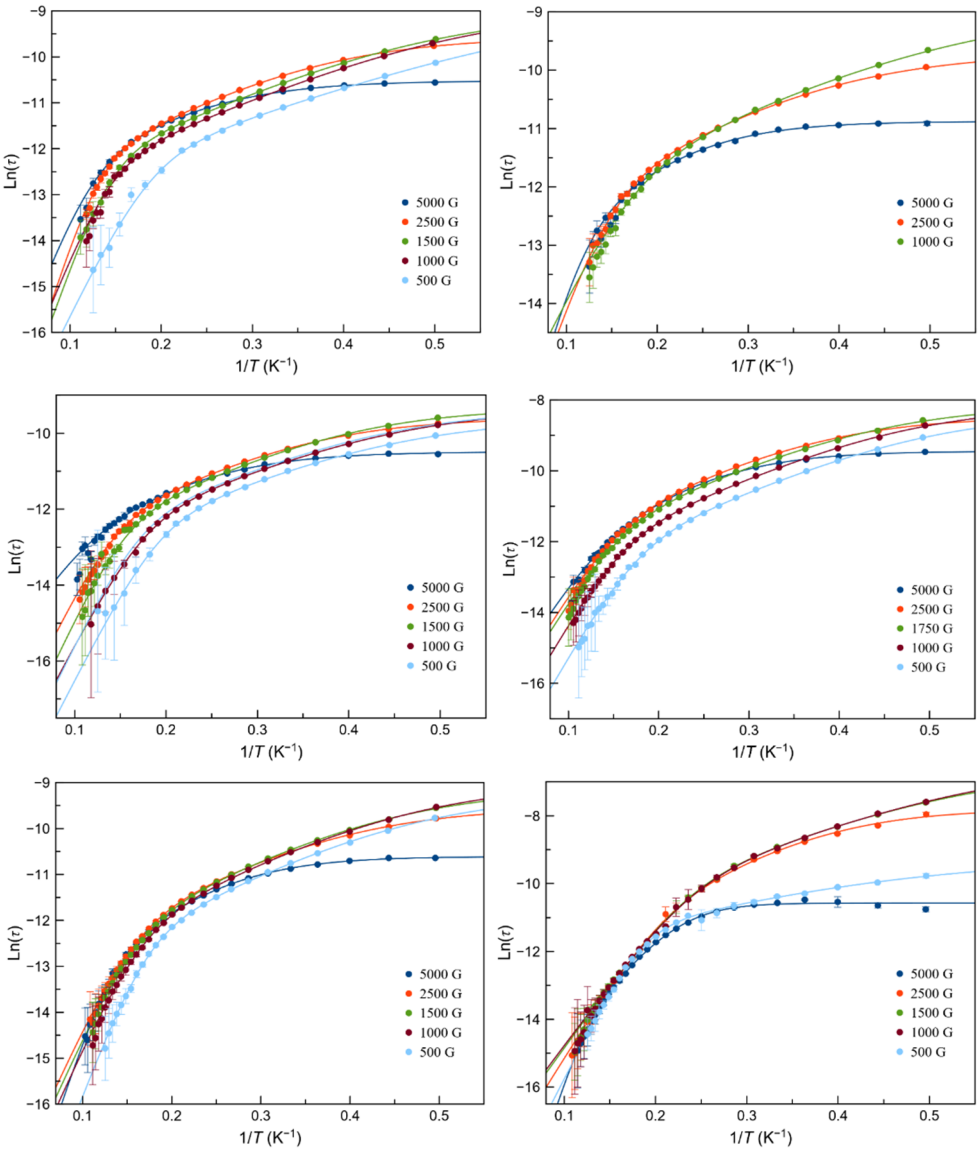

Figure III.15. Arrhenius plots for the main process of **2** (top left), **2′** (top right), **3** (middle left), **3′** (middle right), **4** (bottom left) and **5** (bottom right) under 0.5–5.0 kOe applied static field. The solid lines are the best fit-curves (see text). Standard deviations appear as vertical error bars.

III.3.4 Preliminary Pulsed EPR spectra

EPR spectroscopy on asymmetrical dinuclear compounds, shown in this chapter, present different electronic transitions for each of the distinct Co^{II} ions. This allows to distinguish them and, therefore, to study them individually. A quantum gate is composed of two qubits; therefore, the first stage consists on studying the performance as a qubit of a mononuclear complex with the same coordination environment shown by one of the Co^{II} ions in the dinuclear complex. Then, the mononuclear **1·BPh$_4$**, which exhibits a Hahn echo signal at ~4.3 K, is the chosen candidate.

First, an Echo Detection Field-Sweep (EDFS) was done for a ~2 mM frozen solution in acetonitrile of **1·BPh$_4$** (Figure III.16). These measurements made it possible to distinguish the meaningful resonance points with two π/2-τ-π-τ-*echo* sequence pulses, t_π = 12 ns with τ = 150 ns and t_π = 32 ns with τ = 234 ns; where t_π and τ are the duration of the pulse and the time elapsed between two consecutive pulses. **1·BPh$_4$** evinces three distinct resonant signals at 2.073, 2.687 and 3.573 kOe, which were selected to collect their spin-echo decay data. Only the phase memory time (T_M) has been studied through the pulsed EPR spectroscopy. The collected spectra were analysed with the stretched exponential function for strongly modulated spectra (8).

$$Y(2\tau) = B + Y(0) \cdot e^{-\left(\frac{2\tau}{T_m}\right)^X} (1 + k \cdot Sin(2\omega\tau + \varphi)) \qquad (8)$$

Where 2τ is the sequence time, Y(2τ) the echo integral for the pulse separation τ, Y(0) the intensity at t = 0, B the baseline correction, X is the exponential stretch parameter ranging from 0 to 1 (up to 2 in rigid samples)[34], k is the modulation depth, ω the Larmor angular frequency of a nuclear spin (I) coupled to the electron spin and φ the phase correction.[42]

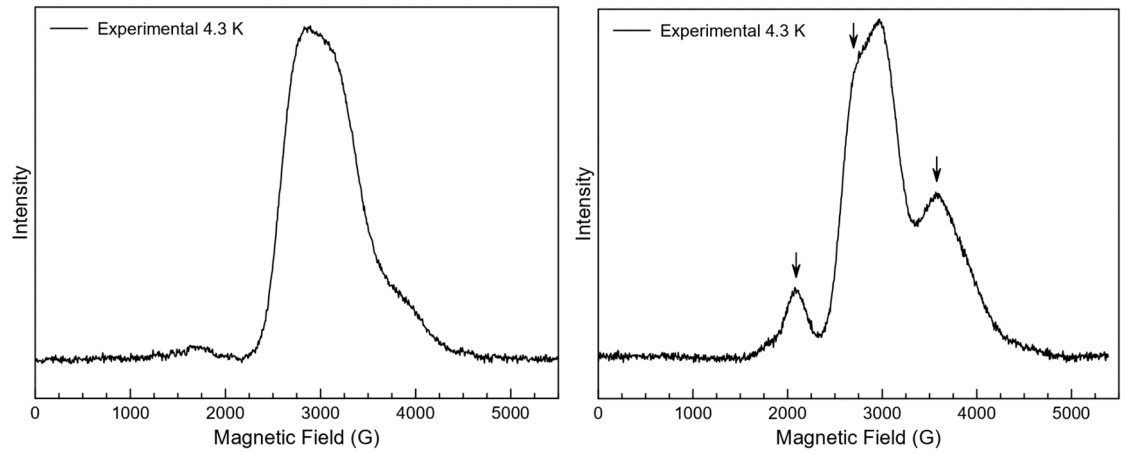

Figure III.16. EDFS spectra in X-band for a frozen solution sample of **1·BPh$_4$**, recorded with a primary echo sequence π/2-τ-π-τ-*echo* with π = 12 and 32 ns and τ = 150 and 234 ns (left and right, respectively).

The fitting of the equation (8) to the collected data for the two-pulse electron spin-echo decay gave the best-fit parameters shown in Table III.6. The electron spin-echo decay shows a wave-shaped spectrum, typical for a modulated electron-spin decay, caused by interaction of the electron spin interacting with a nuclear spin (^{14}N) through hyperfine coupling. A compromise was achieved between the pulse length and the intensity, where the more prolonged the pulses, the more selective to the cobalt(II) transitions (less interaction with other nuclei), but the weaker the echo signal. **1·BPh$_4$** shows T_m shorter than the best complexes based on other metal ions but, at least, at 3.573 kOe it is comparable to other reported molecular cobalt(II) qubits,[36] which are a bit longer than 1 μs.[13] The best-fit T_m values obtained from the spin-echo decays at 2.073 and 2.687 kOe fields are shorter than the shortest experimental measurement (180 ns), which cannot be possible. The low quality spectra for these fields difficult the treatment the data and tiny considerations in the fitting can raise the T_m values up to ~500 ns. Thus, the fit values for the spectra recorded at 2.073 and 2.687 kOe should not be considered.

Mainly and as seen in the cw-EPR discussion (section 3.2), a signal attributed to salicylaldehyde-Co(Me$_2$phen) coordination sphere appears in the region of the magnetic field around 3.573 kOe, as occurs for dinuclear cobalt(II) complexes **2**–**4**. However, carboxylate-Co(Me$_2$phen) coordination sphere shows a signal at a different magnetic field (1.5 kOe) that previous coordination environment or similar (2.7 kOe) but with longer T_m (see Table III.6). These preliminary results then allow us to postulate **2**–**4** as possible qu-gates since each of the two different Co^{II} ions could be "activated" individually and independently. To improve the Hahn echo signal both distinct Co^{II} ions in these dinuclear complexes, the pulsed EPR should be performed at lower temperatures, such 1.8 K, so the population of the excited Kramers doublets (m_s = ±3/2) would decrease even more, avoiding additional relaxation paths and leading to greater coherence and thus, longer T_m. Finally, to use these compounds as possible qu-gates, the application of a three-pulse sequence would be required. The latter constitutes the continuation of this project.

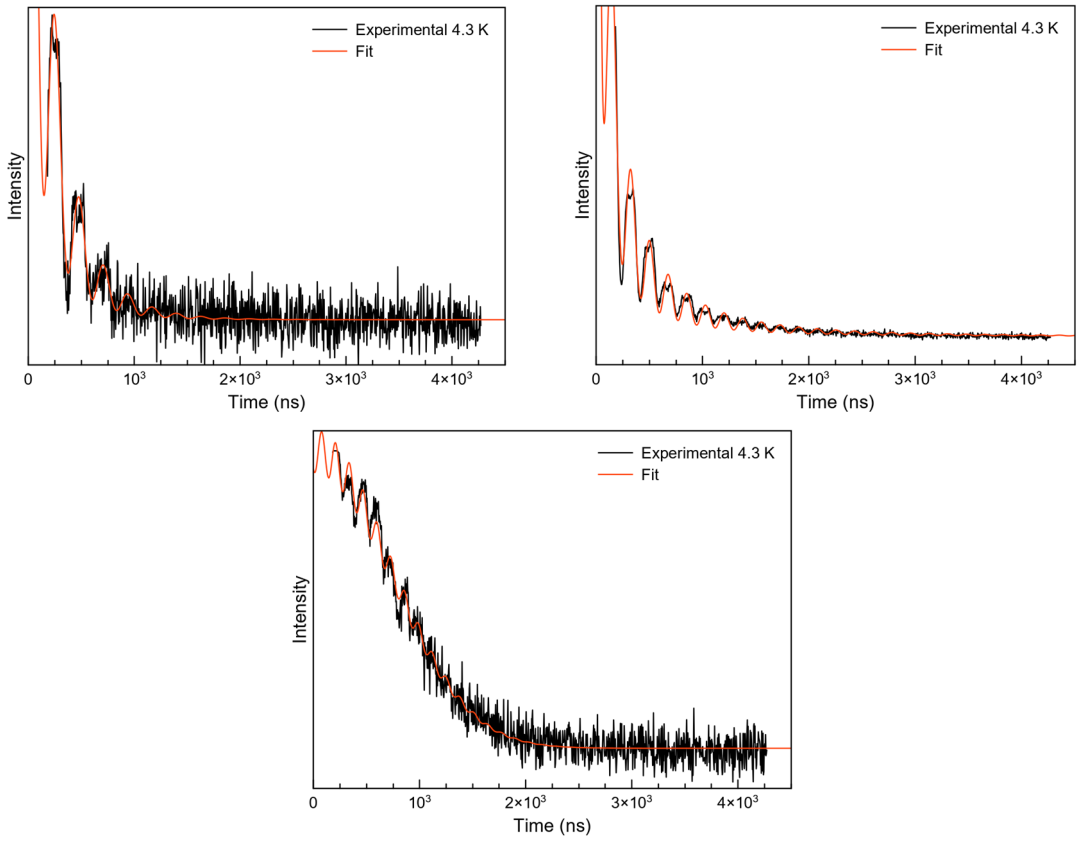

Figure III.17. Two-pulse electron spin-echo decays at X-band on a ~2 mM frozen solution in AcN of **1·BPh$_4$** at 4.3 K for the representative resonance fields 2.073 (top left), 2.687 (top right) and 3.573 (bottom) kOe. Recorded with t_π = 16 ns with τ = 150 ns pulses. The red lines represent the best-fit curves with the equation (8).

Table III.6. Selected X-band pulsed EPR data for **1·BPh$_4$**.[a]

	T_m **(ns)**	**X**
2.073 kOe	160 ± 50	0.77 ± 0.11
2.687 kOe	9 ± 5	0.35 ± 0.03
3.573 kOe	1022 ± 8	2.00 ± 0.04

[a] Measurement performed on a Bruker ElexSys E580 spectrometer operating at X-band frequency (~9.7 GHz) and 5 K.

III.3.5 Conclusions

In this chapter, cationic [Co(Me$_2$phen)$_2$]$^{2+}$ complex has been proven as suitable building block for their assembly by O-donor atoms bridging ligands to form dinuclear complexes. The ligands were designed to tune their length and to study the influence of their steric effects. Furthermore, coordinating groups (carboxylate and salicylaldehyde) were carefully selected to form symmetrical and asymmetrical bridging ligands.

All complexes display large and positive magnetic *D* anisotropy. Furthermore, in the asymmetric complexes, the two Co^{II} ions are differentiable among others by the low and large rhombicity when the Co^{II} ions are coordinated to the carboxylate and the salicylaldehyde groups, respectively. Magnetic and EPR studies, and theoretical calculations, confirms these results. Moreover, all complexes exhibit SIM behaviour under dc-magnetic field with two relaxation processes at high H_{dc}, but only **5** exhibits it at any applied H_{dc}. A detailed analysis of the main process reveal that two thermally activated mechanisms together with an intra-Kramers mechanism are responsible of the slow magnetic relaxation behaviour, which is comparable to what observed in the mononuclear cobalt(II) complexes presented in Chapter II.

In all these complexes, the barrier energies of the thermally activated relaxations are similar suggesting that, despite exhibiting different zfs parameters and environments, the relaxation mechanisms occur probably via phonons. Low-frequency lattice phonons, molecular vibrational modes, overtones, and higher energy vibrational modes might be responsible for the range of energy barriers.

III.4 References

1. DiVincenzo, D. P. The Physical Implementation of Quantum Computation. *Fortschritte der Phys.* **48**, 771–783 (2000).

2. DiVincenzo, D. P. Two-bit gates are universal for quantum computation. *Phys. Rev. A* **51**, 1015–1022 (1995).

3. Aromí, G., Aguilà, D., Gamez, P., Luis, F. & Roubeau, O. Design of magnetic coordination complexes for quantum computing. *Chem. Soc. Rev.* **41**, 537–546 (2012).

4. Ardavan, A. *et al.* Will Spin-Relaxation Times in Molecular Magnets Permit Quantum Information Processing? *Phys. Rev. Lett.* **98**, 057201 (2007).

5. Luis, F. *et al.* A dissymmetric [Gd2] coordination molecular dimer hosting six addressable spin qubits. *Commun. Chem.* **3**, 176 (2020).

6. Lenz, S. *et al.* Chromium(iii)-based potential molecular quantum bits with long coherence times. *Phys. Chem. Chem. Phys.* **21**, 6976–6983 (2019).

7. Luis, F. *et al.* Molecular Prototypes for Spin-Based CNOT and SWAP Quantum Gates. *Phys. Rev. Lett.* **107**, 117203 (2011).

8. Aguilà, D. *et al.* Heterodimetallic [LnLn'] lanthanide complexes: Toward a chemical design of two-qubit molecular spin quantum gates. *J. Am. Chem. Soc.* **136**, 14215–14222 (2014).

9. Ferrando-Soria, J. *et al.* Switchable Interaction in Molecular Double Qubits. *Chem* **1**, 727–752 (2016).

10. Ferrando-Soria, J. *et al.* A modular design of molecular qubits to implement universal quantum gates. *Nat. Commun.* **7**, 11377 (2016).

11. Uber, J. S. *et al.* Molecules Designed to Contain Two Weakly Coupled Spins with a Photoswitchable Spacer. *Chem. - A Eur. J.* **23**, 13648–13659 (2017).

12. Aguilà, D. *et al.* Lanthanide Contraction within a Series of Asymmetric Dinuclear [Ln 2] Complexes. *Chem. - A Eur. J.* **19**, 5881–5891 (2013).

13. Vallejo, J. *et al.* Molecular Cobalt(II)-based SIM/qubits: Unvealing the Spin Dynam-ics and the Decoherence Mechanism. [Unpublished manuscript].

14. Viciano-Chumillas, M., Carbonell-Vilar, J. M., Tuna, F., Weyhermüller, T. & Cano, J. [Unpublished manuscript].

15. Vallejo, J. *et al.* Coligand Effects on the Field-Induced Double Slow Magnetic Relaxation in Six-Coordinate Cobalt(II) Single-Ion Magnets (SIMs) with Positive Magnetic Anisotropy. *Inorg. Chem.* **58**, 15726–15740 (2019).

16. Patterson, J. bruce & Lonergan, D. G. IRE-1A INHIBITORS. **2008**, 213 (2008).

17. Stoll, S. & Schweiger, A. EasySpin, a comprehensive software package for spectral simulation and analysis in EPR. *J. Magn. Reson.* **178**, 42–55 (2006).

18. Sheldrick, G. M. SHELXS97 and SHELXL97. Program for Crystal Structure Solution and Refinement. (1997).

19. Sheldrick, G. M. SHELXT – Integrated space-group and crystal-structure determination. *Acta Crystallogr. Sect. A Found. Adv.* **71**, 3–8 (2015).

20. Sheldrick, G. M. A short history of SHELX. *Acta Crystallogr. Sect. A Found. Crystallogr.* **64**, 112–122 (2008).

21. Spek, A. L. Structure validation in chemical crystallography. *Acta Crystallogr. Sect. D Biol. Crystallogr.* **65**, 148–155 (2009).

22. Angeli, C., Cimiraglia, R., Evangelisti, S., Leininger, T. & Malrieu, J.-P. Introduction of n-electron valence states for multireference perturbation theory. *J. Chem. Phys.* **114**, 10252–10264 (2001).

23. Eichkorn, K., Weigend, F., Treutler, O. & Ahlrichs, R. Auxiliary basis sets for main row atoms and transition metals and their use to approximate Coulomb potentials. *Theor. Chem. Accounts Theory, Comput. Model. (Theoretica Chim. Acta)* **97**, 119–124 (1997).

24. Vancoillie, S. *et al.* Multireference Ab Initio Calculations of g tensors for Trinuclear Copper Clusters in Multicopper Oxidases. *J. Phys. Chem. B* **114**, 7692–7702 (2010).

25. Kossmann, S. & Neese, F. Efficient Structure Optimization with Second-Order Many-Body Perturbation Theory: The RIJCOSX-MP2 Method. *J. Chem. Theory Comput.* **6**, 2325–2338 (2010).

26. Kossmann, S. & Neese, F. Comparison of two efficient approximate Hartee–Fock approaches. *Chem. Phys. Lett.* **481**, 240–243 (2009).

27. Nakamoto, K. Applications in Coordination Chemistry. in *Infrared and Raman Spectra of Inorganic and Coordination Compounds* 1–273 (John Wiley & Sons, Inc., 2008).

28. Llunell, M., Casanova, D., Cirera, J., Alemany, P. & Alvarez, S. SHAPE v2.1. (2013).

29. Vallejo, J. *et al.* Coligand Effects on the Field-Induced Double Slow Magnetic Relaxation in Six-Coordinate Cobalt(II) Single-Ion Magnets (SIMs) with Positive Magnetic Anisotropy. *Inorg. Chem.* **58**, 15726–15740 (2019).

30. Chilton, N. F., Anderson, R. P., Turner, L. D., Soncini, A. & Murray, K. S. PHI: A powerful new program for the analysis of anisotropic monomeric and exchange-coupled polynuclear d - and f -block complexes. *J. Comput. Chem.* **34**, 1164–1175 (2013).

31. Vallejo, J. *et al.* Field-Induced Slow Magnetic Relaxation in a Six-Coordinate Mononuclear Cobalt(II) Complex with a Positive Anisotropy. *J. Am. Chem. Soc.* **134**, 15704–15707 (2012).

32. Cole, K. S. & Cole, R. H. Dispersion and Absorption in Dielectrics I. Alternating Current Characteristics. *J. Chem. Phys.* **9**, 341–351 (1941).

33. Carbonell-Vilar, J. M. & Cano, J. Dyn-VPMag. *University of Valencia* (2019).

34. Kveder, M., Merunka, D., Jokić, M. & Rakvin, B. Low-temperature electron-spin relaxation in the crystalline and glassy states of solid ethanol. *Phys. Rev. B* **77**, 094202 (2008).

35. Wedge, C. J. *et al.* Chemical Engineering of Molecular Qubits. *Phys. Rev. Lett.* **108**, 107204 (2012).

36. Ferrando-Soria, J. *et al.* Molecular magnetism, quo vadis? A historical perspective from a coordination chemist viewpoint, *Coord. Chem. Rev.* **339**, 17–103 (2017).

Chapter IV

Self-assembly of cobalt(II) complexes with tricarboxylate ligands and structural transformations

Two trinuclear cobalt(II) compounds and a molecular cobalt(II) chain were synthesised. The bridging ligand has a threefold symmetry with carboxylic acid groups as anchoring groups. The trinuclear cobalt(II) complex bearing the short ligand exhibits a small magnetic exchange coupling, whereas the one with the long ligand does not. The molecular chain exhibits magnetic exchange coupling also, through hydrogen bonds. The interaction vanishes when the compound is dehydrated, changing its colour from rose to blue. These changes are reversible upon rehydration. All the compounds exhibit SIM behaviour assigned to a combination of competing optical and acoustic Raman mechanisms. However, it can also be explained considering the same relaxation mechanisms as in previous chapters that is several thermally activated and intra-Kramers mechanisms.

IV.1 Introduction

Polycarboxylic acid ligands containing two or more carboxylic groups are versatile ligands due to the multiple coordination modes and the numerous backbones available.[1] Furthermore, they act as hydrogen bond acceptors and donors depending on the deprotonation degree. Therefore, these ligands have often been investigated to construct porous coordination polymers with diverse topology and properties.[2–4] Among these properties, magnetism has attracted the attention of researchers. The wide range of binding modes of the carboxylates affords numerous super-exchange magnetic pathways between paramagnetic metal centres, and they have been the object of magnetostructural correlation studies useful to design molecular magnetic materials.[5–7]

In Chapter III, dinuclear complexes with carboxylic acid ligand derivatives were presented as potential qu-gates. To increase the nuclearity and complexity of the previous systems, in this chapter, two tricarboxylic acid ligands are explored (Scheme IV.1), namely benzene-1,3,5-tricarboxylic acid (H_3BTC) and 1,3,5-tris(4-carboxyphenyl)benzene (H_3BTB). They, exhibiting threefold symmetry, are widely used to design coordination polymers,[8,9] but not so exploited for building isolated systems. Although the bridging ligands used in this chapter have the same symmetry, the extra phenyl rings in H_3BTB break backbone's planarity and induce effects on the crystal structure. Furthermore, these spacer modifications allow tuning the magnitude of the magnetic exchange coupling.

Herein, in this chapter, two triangular trinuclear cobalt(II) complexes are presented with the general formula $\{[Co(Me_2phen)_2]_3L\}(ClO_4)_3$ where L^{3-} = BTC (**6**) and BTB (**7**) and Me_2phen = 2,9-dimethyl-1, 10-phenanthroline. The ligand influence on the structure and magnetic properties is discussed. Additionally, other typologies are explored as a chain with the formula $\{[Co(Me_2phen)][Co(H_2O)_2(Me_2phen)BTB]\}_n(ClO_4)_n \cdot xH_2O$ (**8**), which exhibits reversible phase transformation upon dehydration and rehydration with water molecules.

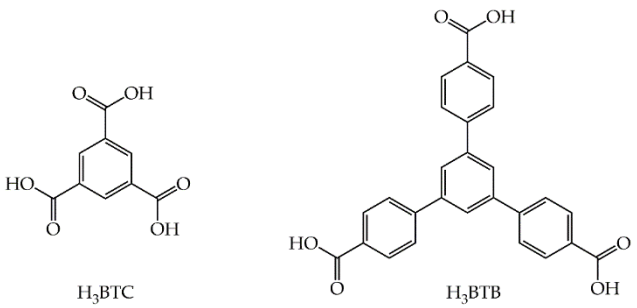

Scheme IV.1. Bridging ligands used in this chapter.

IV.2 Experimental section

IV.2.1 Materials

All chemicals were obtained from commercial sources and used as received.

Caution! Perchlorate salts are potentially explosive. They should be used in small quantities and should be treated with the utmost care at all times.

IV.2.2 Syntheses

{[Co(Me$_2$phen)$_2$]$_3$BTC}(ClO$_4$)$_3$·4H$_2$O (6). Co(ClO$_4$)$_2$·6H$_2$O (128 mg, 0.35 mmol, 3.5 eq) and Me$_2$phen (152 mg, 0.7 mmol, 7 eq) were dissolved in warm methanol (12 mL). Then, a warm methanolic solution of H$_3$BTC (21 mg, 0.10 mmol, 1 eq) and NaH (60% in oil) (12 mg, 0.30 mmol, 3 eq) was added affording a pink precipitate that was filtered off. Suitable pink crystals were obtained by cooling crystallisation after dissolving the pink precipitate in boiling methanol. Yield: 101 mg, 50%. IR (ν_{max}/cm^{-1}): 3436(m), 3054(vw), 2922(vw), 1618(s), 1594(m), 1559(m), 1510(m), 1500(s), 1446(m), 1380(s), 1359(m), 1294(w), 1146(s), 1120(vs), 1086(vs), 862(m), 773(w), 732(m), 636(m), 625(m), 551(w), 502(w), 471(w). Elemental Analysis calculated for **6** (C$_{93}$H$_{83}$Cl$_3$Co$_3$N$_{12}$O$_{22}$): C, 55.74; H, 4.18; N, 8.39. Found: C, 55.27; H, 3.75; N, 8.13.

{[Co(Me$_2$phen)$_2$]$_3$BTB}(ClO$_4$)$_3$·4.5tol (7). Co(ClO$_4$)$_2$·6H$_2$O (90 mg, 0.35 mmol, 3.5 eq) and Me$_2$phen ligand (152 mg, 0.7 mmol, 7 eq) were dissolved in a mixture of methanol/acetonitrile (1:1, 4 mL). Then, H$_3$BTB (44 mg, 0.10 mmol, 1 eq) in methanol/acetonitrile (1:1) with NaH (60% in oil) (12 mg, 0.30 mmol, 3 eq) were added affording a pink-reddish solution. Pink single crystals suitable for X-ray were obtained by slow diffusion of toluene into the solution. Yield: 113 mg, 44%. IR (ν_{max}/cm^{-1}): 3549(w), 3470(m), 3414(m), 3236(w), 3063(w), 3023(w), 2922(vw), 1617(m), 1594(s), 1565(w), 1532(m), 1510(m), 1501(m), 1417(s), 1384(m), 1358(m), 1294(w), 1221(vw), 1154(w), 1091(vs), 857(m), 813(w), 783(w), 731(w), 672(vw), 623(m), 551(w), 479(w). Elemental Analysis calculated for **7** (C$_{285}$H$_{246}$Cl$_6$Co$_6$N$_{24}$O$_{36}$): C, 66.47; H, 4.82; N, 6.53. Found: C, 58.67; H, 3.32; N, 7.22. The discrepancy between calculated and obtained percentages arises from the incomplete combustion of the sample during the analytical processing. The purity of the sample was checked by XRPD.

{[Co(Me$_2$phen)][Co(H$_2$O)$_2$(Me$_2$phen)BTB]}$_n$(ClO$_4$)$_n$·xH$_2$O (8). Co(ClO$_4$)$_2$·6H$_2$O (77 mg, 0.30 mmol, 3 eq) and the corresponding phenanthroline ligand (131 mg, 0.6 mmol, 6 eq) were dissolved in methanol (20 mL). Then, H$_3$BTB (44 mg, 0.10 mmol, 1 eq) in methanol (20 mL) with NaH (60% in oil) (12 mg, 0.30 mmol, 3 eq) were added and stirred for 10 minutes affording a thin suspension. The pink suspension was filtered off with a 0.22 μm pore filter affording an orange solution. Orange-purplish single crystals were obtained by layer

diffusion of toluene during 2 months, at least. Yield: 128 mg, 79%. IR (ν_{max}/cm^{-1}): 3419(m), 3072(vw), 2930(vw), 1606(m), 1593(s), 1534(m), 1507(m), 1411(vs), 1385(vs), 1153(w), 1121(m), 1108(m), 1085(m), 859(m), 815(w), 781(m), 731(w), 706(w), 625(w), 485(w).

{[Co(Me$_2$phen)][Co(Me$_2$phen)BTB]}$_n$(ClO$_4$)$_n$ (8-dh). A powdered pink-purplish sample of **8** was placed in an oven at 80 °C during one hour. After, a dark blue powder was recovered and it was quickly characterised. IR (ν_{max}/cm^{-1}): 3419(w), 3072(vw), 2957(w), 2924(m), 2854(w), 1606(m), 1593(s), 1534(m), 1507(m), 1411(vs), 1385(vs), 1153(w), 1121(m), 1108(m), 1085(m), 859(m), 815(w), 781(m), 731(w), 706(w), 625(vw), 485(w). Elemental Analysis calculated for **8-dh** ($C_{55}H_{39}ClCo_2N_4O_{10}$): C, 61.78; H, 3.68; N, 5.24. Found: C, 62.41; H, 3.81; N, 5.05.

IV.2.3 Physical measurements

Infrared spectra (4000–400 cm^{-1}) were recorded on a Nicolet 5700 spectrophotometer as KBr pellets. Elemental analyses (C, H, N) were performed at the Microanalytical Service of the Universitat de València.

X-ray powder diffraction (XRPD) patterns were collected on a Panalytical Empyrean X-ray diffractometer by using Cu Kα radiation (λ = 1.5406 Å), in which the X-ray tube was operated at 45 kV and 40 mA ranging from 2 to 40°. The XRPD data was background corrected with the *HighScore Plus* software.

Static direct current (dc) measurements were carried out on all samples by powdering and restraining the samples with *n*-eicosane to prevent any displacement. Variable-temperature (2.0–300 K) dc-magnetic susceptibility under an applied field of 0.25 (T < 20 K) and 5.0 kOe (T ≥ 20 K), and variable-field (0–5.0 kOe) magnetisation in the temperature range from 2 to 10 K were recorded with a Quantum Design SQUID magnetometer. Variable-temperature (2.0–10 K) alternating current (ac) magnetic susceptibility measurements under ±0.005 kOe oscillating field at frequencies in the range of 0.1–10 kHz were carried out on crystalline samples under different applied static dc fields in the range 0.0–5.0 kOe with a Quantum Design Physical Property Measurement System (PPMS). The magnetic susceptibility data were corrected for the diamagnetism of the constituent atoms and the sample holder.

IV.2.4 X-ray Crystallography

Single-crystal X-ray diffraction data of **6** and **8** were collected on a Bruker-Nonius X8APEXII CCD area detector diffractometer using graphite-monochromated Mo-Kα radiation (λ = 0.7173 Å) at T = 296 K. The single-crystal X-ray diffraction data of **7** were

collected at 100 K and room pressure at the Diamond Light Source (Synchrotron) in United Kingdom. All calculations for data reduction, structure solution, and refinement were done through the SAINT[10] and SADABS[11] programs. The structure was solved with the SHELXS structure solution program, using the Patterson method.[12] The model was refined with version 2018/3 of SHELXL against F2 on all data by full-matrix least squares.[13,14] Non-hydrogen atoms were refined with anisotropic displacement parameters. The hydrogen atoms were included at geometrically calculated positions and refined using a riding model. Crystallisation water molecules were found in **6** while toluene molecules are present in the crystal structure of **7**. The perchlorate ions in **6** are disordered over two positions. No residual electronic density could be linked to perchlorate ions in **8**. All attempts to increase the quality of data of **8** was unsuccessful. The final geometrical calculations and the graphical manipulations were carried out with the PLATON[15] package and CrystalMaker[10] software. Crystallographic data for compounds are given in Table A.17.

IV.2.5 Computational details

Aiming to evaluate the parameters that determine the axial (D) and rhombic (E) zfs in **6**–**8**, calculations based on a second-order N-electron valence state perturbation theory (CASSCF/NEVPT2) applied on wave functions obtained from complete active space (CAS) calculations on experimental geometries.[16] Since these complexes exhibit negligible magnetic exchange coupling, the trinuclear entities were split into mononuclear species keeping the experimental dispositions of the ligands around the metal. The calculations were carried out with version 4.0.1 of the ORCA and the auxiliary TZV/C Coulomb fitting basis sets.[17] The spin−orbit coupling contributions to zfs from 10 quartet and 20 doublet excited states generated from an active space with seven electrons in five d-orbitals were included from an effective Hamiltonian. The g-tensors were calculated for the ground Kramers pair using Multireference Configuration Interaction (MRCI) wave functions with a first-order perturbation theory on the SOC matrix.[18]

IV.3 Results and discussion

IV.3.1 Syntheses and X-ray Structure description

Mononuclear $[Co(Me_2phen)_2]^{2+}$ complex proves to be an excellent starting material for compounds of higher nuclearity, as it was shown in previous chapters. The reaction mixture of $Co(ClO_4)_2{\cdot}6H_2O$ and the phenanthroline ligand in methanol, methanol/acetonitrile or water/methanol, followed by a non-stoichiometric ratio of H_3BTC or H_3BTB and NaH afforded trinuclear complexes (**6** and **7**) and a molecular chain compound (**8**). In these syntheses, a little excess of $[Co(Me_2phen)_2]^{2+}$ cationic complex from the stoichiometric ratio metal to polycarboxylate ligand is required to achieve pure isolated trinuclear compounds. Otherwise, trinuclear and chain mixtures are formed. In these mixtures, the crystalline samples of the trinuclear compound are converted into a chain structure, **8** by long-time exposition in the mother solution, where water molecules displace one phenanthroline ligand of each Co^{II} centre.

The polycrystalline XRPD studies reveal a good agreement between the simulated patterns of the single-crystal X-ray structures and the experimental data of **6** and **7**, confirming their purity and bulk phase (Figure A.66–68). For **8**, some discrepancies are observed, but these are attributed to the low quality crystal resolution, as stated before, where no counterions with huge electronic density neither water molecules could be unambiguously assigned (Figure A.68).

Infrared spectra of **6**–**8** and the dehydrated **8** (**8-dh**) show a shift of the band at 1680 cm^{-1} of the acid groups of the tricarboxylic acid H_3BTC and H_3BTB ligands to 1618–1605 cm^{-1}, suggesting the coordination to the Co^{II} ion. Medium and strong peaks at ~1560 (**6**) or ~1534 cm^{-1} (**7**–**8-dh**), and ~1450 (**6**) or 1411 cm^{-1} (**7**–**8-dh**) are assigned to $\nu_{as}(COO)$ and $\nu_s(COO)$ stretching, respectively. The $\Delta\nu$ values between ~110 and ~123 cm^{-1} confirm the presence of a bidentate carboxylate group for all compounds.[19] The band at ~1090 cm^{-1} confirm the presence of the perchlorate counterion,[20] while the band at ~640 cm^{-1} is assigned to non-coordinated perchlorate anions.[21]

Compounds **6** and **7** crystallise in trigonal *R*−*3* and monoclinic *P2₁/c* space groups, respectively. Both form trinuclear triangular cobalt(II) clusters formed by $[Co(Me_2phen)_2]^{2+}$ units linked by one central triply deprotonated bridging ligand, being benzene-1,3,5-tricarboxylate (BTC^{3-}) for **6** and 1,3,5-tris(4-carboxylatephenyl)benzene (BTB^{3-}) for **7** (Figures IV.1 and IV.2, respectively). While all cobalt centres are crystallographically equivalent in **6**, two crystallographically independent asymmetric trinuclear complexes are found in **7**, so there are six different cobalt centres in this compound. Three ClO_4^- counterions are present in **6** and **7** to balance the charge of each trinuclear entity, but water (**6**) and toluene (**7**) solvent molecules are also present. Instead,

compound **8** that crystallises in the orthorhombic *Pbca* space group, does not form trinuclear species. However, these unities, after releasing phenanthroline molecules, evolve into a cationic molecular chain along the *b*-axis (Figure IV.3). Even though a counterion is necessary to achieve neutrality and Energy-Dispersive X-ray spectroscopy (EDX) analyses reveal chlorine atoms, the presence of perchlorate anions by single-crystal X-ray diffraction could not be established.

The Co^{II} ions are hexacoordinated in all compounds. In **6** and **7**, the equatorial plane is formed by two oxygen atoms from the deprotonated tricarboxylate ligand and two nitrogen atoms of two different Me_2phen ligands. The two remaining nitrogen atoms from these two Me_2phen ligands occupy axial positions. The cobalt(II) chain in **8** exhibits two different crystallographic metal centres, Co1 and Co2. One of them (Co2) is part of a zig-zag chain, while the other (Co1) hangs from it. Although the CoN_2O_4 environment is the same for both cobalt centres, they are not equivalent. The equatorial plane for Co1 is formed by two oxygen and two nitrogen atoms from a chelating carboxylate and a Me_2phen ligand. However, three oxygen atoms from two chelating carboxylate ligands and one nitrogen atom from the chelating Me_2phen ligand forms the equatorial plane for Co2. Whereas oxygen atoms from two water molecules cover the axial positions in Co1, the remaining oxygen and nitrogen atoms of the chelating carboxylate group and Me_2phen ligand do so in Co2. Selected bond lengths and angles are shown in Tables IV.1–2.

In all compounds, Co^{II} ions are almost in N_2O_2 equatorial plane, but them slightly move away from it: 0.018 Å for **6**; 0.003–0.140 (Co1–Co3) and 0.052–0.069 Å (Co4–Co6) Å for **7**; 0.012 (Co1) and 0.042 Å Co(2) for **8**. The Co−N distances are in the range of 2.11−2.19 (**6**), 2.07−2.21 (**7**) and 2.10−2.14 Å (**8**). The bidentate coordination of carboxylate groups induces asymmetrical Co−O distances with values in the 2.16−2.25 (**6**), 2.11−2.21 (**7**), and 2.11−2.23 Å (**8**). Due to the chelating character of two of the coordinated ligands, their bite angle are lesser than the ideal for an octahedral geometry (90°). O−Co−O: 60.26° (**6**), 60.40−62.46° (**7**) and 60.19−60.83° (**8**); and N−Co−N: 79.26−79.39° (**6**), 78.30−81.20° (**7**) and 78.30−80.09° (**8**). In **7** and **8**, phenyl rings of the bridging ligand are not coplanar, being the dihedral angle between them 10.69−44.17° (**7**) and 32.76−36.09° (**8**).

The distortion of cobalt coordination sphere from the octahedral (OC-6) and trigonal ideal (TPR-6) prisms has been evaluated with the SHAPE program.[26] A continuous shape measure (CShM) deviates from zero as the coordination polyhedron diverges from the ideal geometry. CShM values for **6** and **7** [OC-6: 3.334 (**6**) and 2.895–4.378 (**7**), and TPR-6: 13.446 (**6**) and 11.449–14.614 (**7**)] confirms the distorted octahedral CoN_4O_2 coordination sphere in all cases. Co1 in **8** shows a similar, but lesser, distortion as that found in **6** and **7** (OC-6: 2.640 and TPR-6: 14.518) with two water molecules, one carboxylate group and one phenanthroline forming a CoN_2O_4 coordination sphere. The Co2 centre, in **8**, presents an octahedral CoN_2O_4 coordination environment too, but it is formed by a phenanthroline

ligand and two carboxylate groups with a smaller bite angle than the phenanthroline ligand. Consequently, the CoN_2O_4 polyhedron with two carboxylate ligands, in Co2, exhibits a more pronounced distortion than the previous ones (OC-6: 6.646 and TPR-6: 11.824).

Intramolecular Co···Co distances are 9.308 Å in **6** with the BTC^{3-} bridging ligand. However, in **7** and **8**, bearing the BTB^{3-} bridging ligand, the metal ions are further apart exhibiting similar intermetallic distances. These are 16.793, 16.462 and 16.890 Å for Co(1)···Co(2), Co(1)···Co(3) and Co(2)···Co(3) and 16.393, 16.768 and 16.792 Å for Co(4)···Co(5), Co(5)···Co(6) and Co(5)···Co(6) in **7**; and 16.046 for Co(1)···Co(2), 17.128 for Co(1)···Co(2′) and 16.967 Å for Co(2)···Co(2′) in **8**. The shortest intermolecular Co···Co distances are 9.053 (**6**), 7.815 (**7**) 5.632 Å (**8**). Hydrogen bonds interactions are present in **8**, where water molecules coordinate to Co1 interact with other water molecules from a neighbouring chain (Figure IV.4 and A.71, Table A.18). Intermolecular π−π interactions are present in all compounds, exhibiting a complex arrangement. Centroid-centroid distances are shown in Table A.19. In **6**, a supramolecular layer parallel to the (0, 1, 0) lattice plane is present, while for **7** and **8** these interactions are extended through the whole lattice (Figures A.69–70). Particularly, supramolecular interactions in **8** arrange the molecular chains in a Metal-Organic Framework (MOF)-like structure, where rectangular voids along the *b*-axis are present.

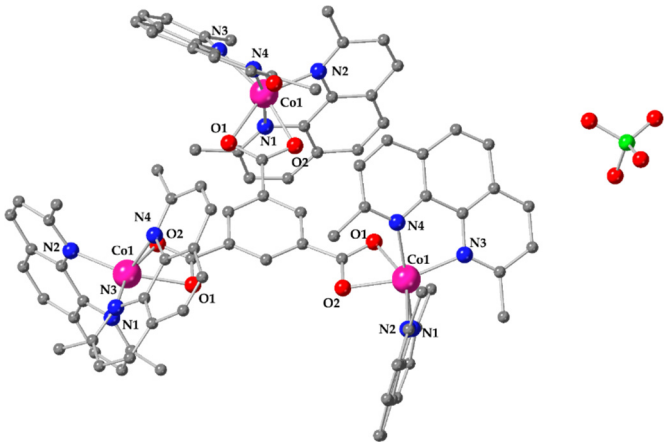

Figure IV.1. Perspective view for the unit cell of **6**. Hydrogen atoms are omitted for clarity. Colour code: magenta, cobalt; blue, nitrogen; red, oxygen; grey, carbon; green, chlorine.

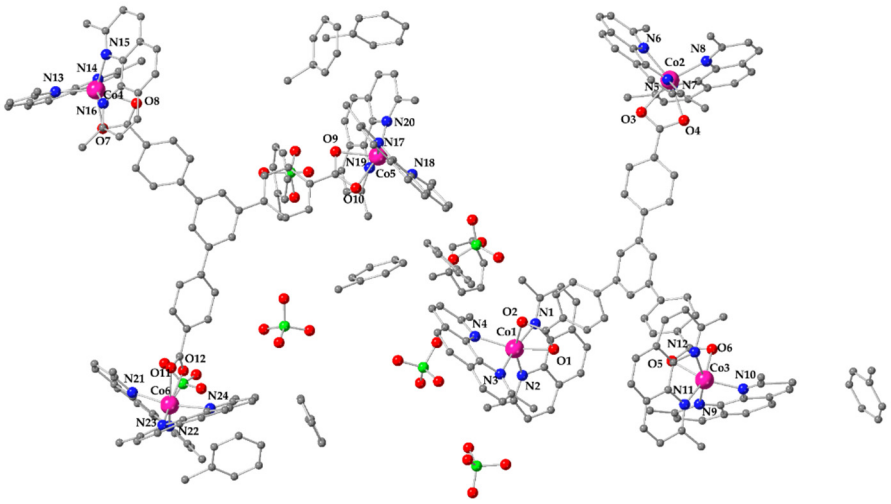

Figure IV.2. Perspective view for the unit cell of **7**. Hydrogen atoms are omitted for clarity. Colour code: magenta, cobalt; blue, nitrogen; red, oxygen; grey, carbon; green, chlorine.

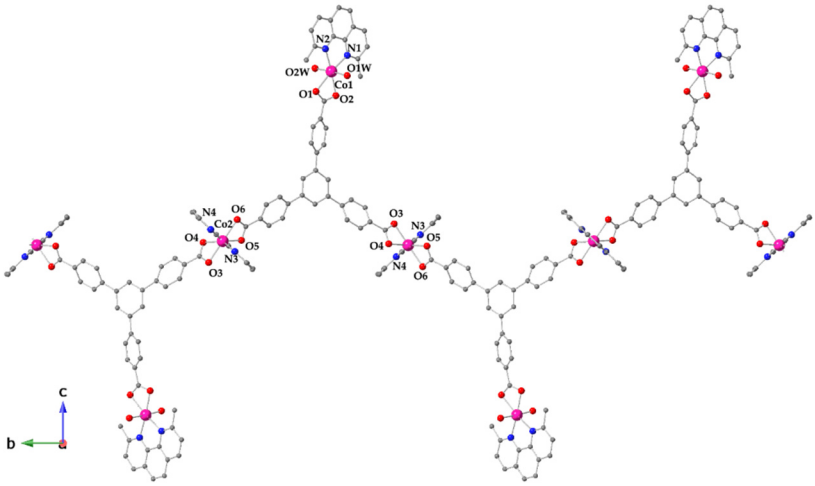

Figure IV.3. Perspective view along the *a*-axis for the molecular chain of **8**. Hydrogen atoms are omitted for clarity. Colour code: magenta, cobalt; blue, nitrogen; red, oxygen; grey, carbon.

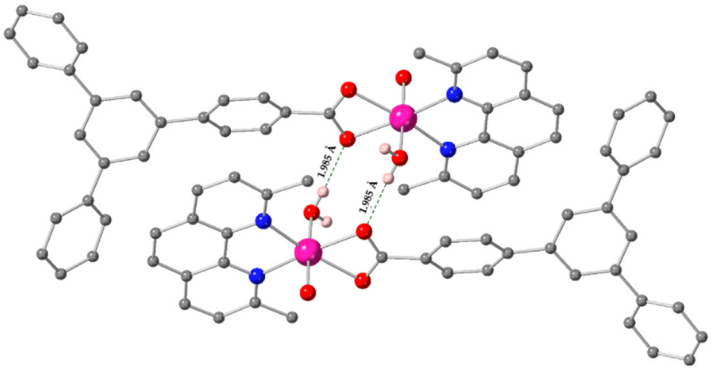

Figure IV.4. Perspective view for the hydrogen bonding interaction in **8**. Non-interacting hydrogen atoms in the hydrogen bonding are omitted for clarity. Colour code: magenta, cobalt; blue, nitrogen; red, oxygen; grey, carbon.

Table IV.1. Selected bond distances and angles for **6** and **7**.

Compound	6		7			
Bond distances [Å]						
Co1–N1	2.171(5)	2.151(5)	Co3–N9	2.143(7)	Co5–N17	2.189(5)
Co1–N2	2.134(4)	2.102(5)	Co3–N10	2.048(5)	Co5–N18	2.067(5)
Co1–N3	2.122(4)	2.154(5)	Co3–N11	2.098(4)	Co5–N19	2.162(5)
Co1–N4	2.193(5)	2.110(4)	Co3–N12	2.143(5)	Co5–N20	2.073(5)
Co1–O1	2.158(4)	2.210(3)	Co3–O5	2.143(4)	Co5–O9	2.167(5)
Co1–O2	2.246(4)	2.123(4)	Co3–O6	2.180(4)	Co5–O10	2.138(4)
Co2–N5	–	2.160(5)	Co4–N13	2.160(5)	Co6–N21	2.153(5)
Co2–N6	–	2.124(6)	Co4–N14	2.124(6)	Co6–N22	2.099(5)
Co2–N7	–	2.176(5)	Co4–N15	2.176(5)	Co6–N23	2.076(7)
Co2–N8	–	2.123(5)	Co4–N16	2.123(5)	Co6–N24	2.209(5)
Co2–O3	–	2.179(4)	Co4–O7	2.179(4)	Co6–O11	2.150(4)
Co2–O4	–	2.162(3)	Co4–O8	2.162(3)	Co6–O12	2.140(4)
Bond angles [°]						
N1–Co1–N2	79.39(18)	78.67(18)	N9–Co3–N10	81.2(2)	N17–Co5–N18	78.8(2)
N3–Co1–N4	79.26(18)	114.10(16)	N11–Co3–N12	79.02(17)	N19–Co5–N20	79.3(2)
O1–Co1–O2	60.26(13)	60.77(14)	O5–Co3–O6	60.40(17)	O9–Co5–O10	62.46(17)
N1–Co1–N3	169.06(18)	170.22(16)	N9–Co3–N11	97.3(2)	N17–Co5–N19	168.9(2)
N2–Co1–N4	111.14(18)	114.10(16)	N10–Co3–N12	119.49(18)	N18–Co5–N20	111.2(2)
N2–Co1–O2	150.54(15)	159.09(16)	N10–Co3–O5	139.3(2)	N18–Co5–O9	148.7(2)
N5–Co2–N6	–	174.24(17)	N13–Co4–N14	79.1(2)	N21–Co6–N22	79.2(2)
N7–Co2–N8	–	78.62(19)	N15–Co4–N16	78.54(17)	N23–Co6–N24	79.1(2)
O3–Co2–O4	–	61.12(16)	O7–Co4–O8	61.86(14)	O11–Co6–O12	62.27(17)
N5–Co2–N7	–	78.3(2)	N13–Co4–N15	113.0(2)	N21–Co6–N23	108.5(2)
N6–Co2–N8	–	103.5(2)	N14–Co4–N16	167.0(2)	N22–Co6–N24	106.1(2)
N6–Co2–O4	–	158.6(2)	N13–Co4–O8	151.7(2)	N22–Co6–O22	149.95(18)

Table IV.2. Selected bond distances and angles for **8**.

Compound	8		
Bond distances [Å]			
Co1–N1	2.141(6)	Co2–N3	2.104(5)
Co1–N2	2.123(5)	Co2–N4	2.100(5)
Co1–O1W	2.089(5)	Co2–O5_a	2.152(4)
Co1–O2W	2.063(5)	Co2–O6_a	2.158(4)
Co1–O1	2.230(4)	Co2–O3	2.114(4)
Co1–O2	2.133(4)	Co2–O4	2.203(4)
Bond angles [°]			
O1W–Co1–O2W	176.93(17)	N4–Co2–O5_a	147.74(16)
N1–Co1–N2	78.3(2)	O3–Co2–O4	60.83(15)
O1–Co1–O2	60.19(17)	N3–Co2–O6_a	97.60(17)
O2–Co1–N1	109.25(19)	N3–Co2–N4	80.09(18)
N1–Co1–O1W	95.0(2)	N3–Co2–O3	88.50(16)
N1–Co1–O1	168.7(2)	O5_a–Co2–O6_a	60.76(16)

IV.3.2 Structural transformations by dehydration and rehydration processes

Compound **8** is very sensitive to mother liquor removal, which is understood by the large number of crystallisation and coordination water molecules present in the structure. The dehydration of **8** begins immediately once the crystals are separated from the mother liquor. The progressive disappearance of the peaks from the original XRPD pattern reveals a crystal-to-amorphous transformation from **8** to **8-dh** (Figure IV.5). This transformation is also accompanied by a gradual substantial colour change from pink (hydrated) via pink-purplish to dark blue (dehydrated) shown in Figure IV.6. This is a consequence of the progressive evolution in the cobalt coordination geometry, from octahedral to tetrahedral, by the removal of two coordinated water molecules. This solvatochromic equilibrium of the Co^{II} ion is well-known.[23,24] The thermal stability of **8** was checked by TGA analysis in the temperature range 30–200 °C (Figure IV.7). An abrupt mass drop of mass was observed in the 30−80 °C range for freshly prepared **8**. The weight loss of **8** after 1-hour exposure to air is not so pronounced. In the first case, the weight loss corresponds to ~9 water molecules while in the second case, to ~1 water molecule. As observed, **8** is very susceptible to fast water molecules removal. In addition, the dehydrated form (**8-dh**) was also characterised by EA and IR. FTIR spectra of **8-dh** only show a decrease in intensity for the wide O−H band at ~3420 cm^{-1} compared to **8**, and the bands in the ~2960−2850 cm^{-1} range more visible.

The dehydrated compound (**8-dh**) exposed to a vaporous water environment, or suspended in water, recovers the original crystalline phase (Figure IV.5). The freshly prepared sample (**8**) loses crystallinity after a brief exposure to air, being its XRPD pattern not compatible with the theoretical one, but with those of **8-dh** and **8** exposed to air.

The reversibility of the dehydration-hydration process and recovery of the original crystal structure up to two cycles, at least, are confirmed by the agreement between XRPD patterns of the rehydrated **8-dh** and **8**.

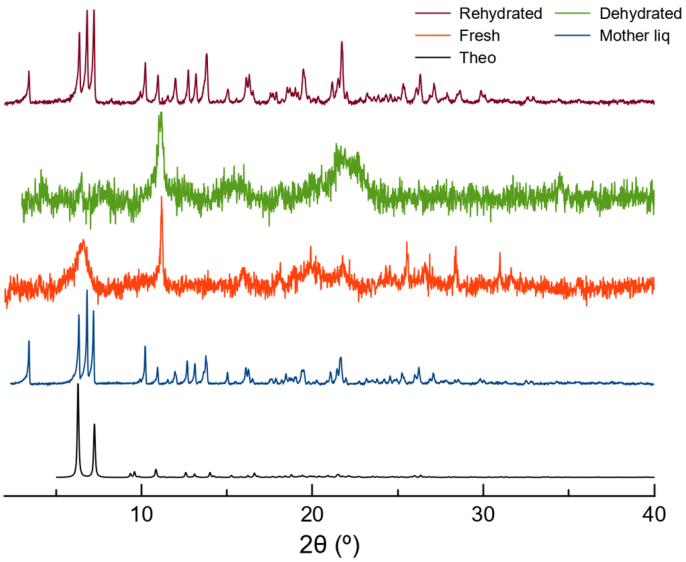

Figure IV.5. XRPD patterns of **8** in different states: simulated from single-crystal X-ray diffraction data (black), with mother liquor (blue), fresh (red), dehydrated air or 1 h oven 80 °C (**8-dh**, green), rehydrated by water suspension (garnet).

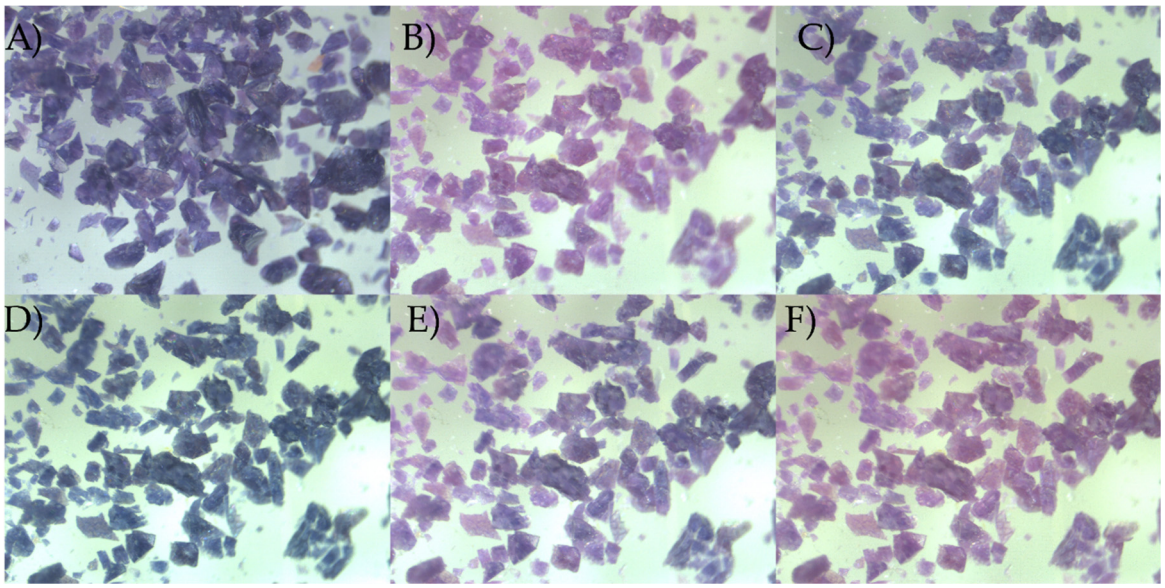

Figure IV.6. Crystal to crystal transformations of **8** to **8-dh**: A) **8** exposed +1 h in air, B) exposed to vaporous water environment, C) exposed to air, D) heated at 80 °C 1 h, E) exposed to a vaporous water environment for short times, F) exposed to vaporous water environment for longer times.

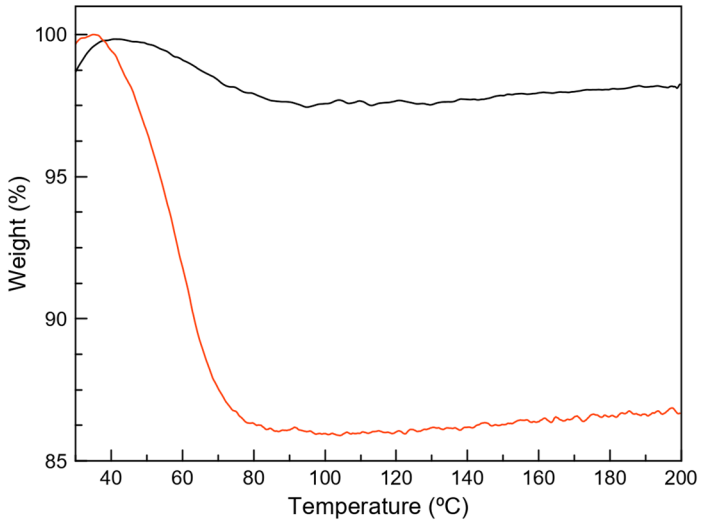

Figure IV.7. TGA plots for rehydrated **8** (red) and **8** exposed to the air for 1 hour (black).

IV.3.3 Magnetic properties, EPR and theoretical calculations

The variable-temperature magnetic properties for polycrystalline samples of **6**–**8** and **8-dh** were measured in the 2–300 K range under an applied direct-current (dc) field of 5.0 kOe as $\chi_M T$ *vs* T and M *vs* H/T curves (Figure IV.8). The $\chi_M T$ values at room temperature are 8.91 (**6**), 8.85 (**7**); and 5.72 (**8**) and 5.68 (**8-dh**) cm^3 K mol^{-1}. These values are below the expected spin-only values (S = 3/2 with g = 2.0) for three and two isolated Co^{II} ions, which are 5.63 and 3.75 cm^3 K mol^{-1}, respectively, indicating the presence of a significant spin-orbit coupling (SOC). The $\chi_M T$ values remain almost constant down to 100 K and then, decrease with a larger slope until 5.23 (**6**), 5.06 (**7**), 2.54 (**8**) and 2.90 cm^3 K mol^{-1} (**8-dh**) at 2 K. The decrease of $\chi_M T$ can be due to SOC effects and/or antiferromagnetic interactions. The $\chi_M T$ value of **6** and **7** at 2 K is approximately equal or higher than the one expected (4.50–5.10 cm^3 K mol^{-1}) at 0 K for trinuclear cobalt(II) complexes with octahedral geometry,[25] confirming only the presence of SOC and the absence of significant magnetic exchange interactions. For **8**, the $\chi_M T$ value at 2 K is lower than the one expected (3.00–3.40 cm^3 K mol^{-1}), then the existence of an antiferromagnetic exchange coupling (J) between the Co^{II} ions must be considered. As discussed earlier, one octahedral and one tetrahedral Co^{II} ions are expected to be present in **8-dh**, explaining the low, but not excessive, $\chi_M T$ value at 2 K. However, this is not that obvious from the shape of the $\chi_M T$ curve.

The field-dependent magnetisation studies at low temperatures for **6** and **7** are included as inset figures in Figure IV.8. The magnetisation values at 50 kOe and 2 K are 6.63 (**6**) and 6.67 Nβ (**7**). These values are below the saturation limit of 9 Nβ for three Co^{II} ions (S = 3/2 with g = 2), suggesting the presence of significant axial anisotropy for both compounds. The isothermal magnetisation curves in the 2–10 K temperature range superimpose in all

H/*T* range. As seen in previous chapters, these behaviours are typical for Co^{II} ions with large *D* values.

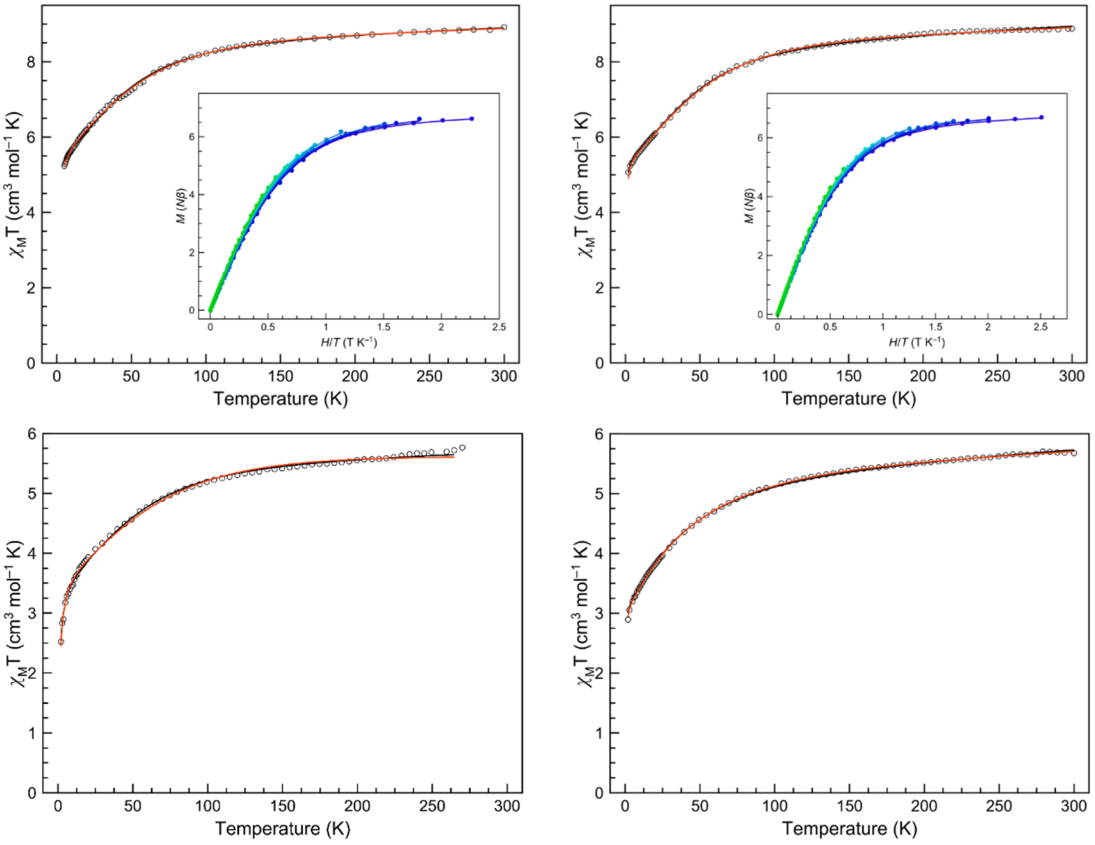

Figure IV.8. Plots of $\chi_M T$ *vs T* in the range 2–300 K in 5.0 kOe applied field and *M vs H*/*T* (inset) for **6** (top left), **7** (top right), **8** (bottom left), **8-dh** (bottom right) in the 2–10 K temperature range (2 K blue to 10 K green gradient). The solid lines are the best-fit curves (see text).

The experimental magnetic susceptibility and magnetisation data of **6**–**8** and **8-dh** were analysed with the spin Hamiltonian following the previous two approaches with a T-P isomorphism formalism (SOC model), equation (1) and considering zfs with equation (2). Based on the possible exchange paths in the molecular structures in **6** and **8**, isotropic exchange Hamiltonian was added to the previous equations (1 and 2) of the two models. Then, the spin Hamiltonian equations for three and two spin *S* = 3/2 are the following:

$$\hat{H}_{total1} = \hat{H}_{eq\ 1\ or\ 2} - J(\hat{S}_1\hat{S}_2 + \hat{S}_1\hat{S}_3 + \hat{S}_2\hat{S}_3) \qquad (9)$$

$$\hat{H}_{total2} = \hat{H}_{eq\ 1\ or\ 2} - J\hat{S}_1\hat{S}_2 \qquad (10)$$

where *J* represents the spin exchange coupling strength between the Co^{II} ions. In **8-dh**, the tetrahedral Co^{II} ion can only be analysed with the corresponding spin Hamiltonian for a zfs approach (equation 2 in Chapter II), which was included in the fitting with the SOC model (corresponding to the remaining octahedral Co^{II} ion).

The best fit values of the magnetic data with the two models were obtained using the PHI software[26], and they are shown in Figure IV.8 as red (T-P isomorphism formalism model) and black (zfs model) lines and in Tables IV.3–4. The obtained values fall within the range typical for other already reported octahedral high-spin cobalt(II) compounds (Chapter II and III).

In **6**, with both approaches, the small drop of $\chi_M T$ at low temperatures cannot be very well-reproduced by means of the magnetisation blockage simulation under the strong applied magnetic field. Then, the inclusion of a magnetic exchange coupling J in this system is required. A very tiny J is detected despite the relatively long intramolecular Co···Co distances (~9.308 Å). This is a common phenomenon since other similar complexes exhibit weak exchange magnetic coupling based on spin polarization mechanism, that goes through the π pathway of the aromatic bridging ligand.[2,27–30] The mentioned interaction occurs since the dihedral angle between the carboxylate group and the phenyl ring is low (~6°). Such pathway interaction is not considered in **7** and **8** given the long intramolecular Co···Co distances (Co···Co >16.393 Å) and the large dihedral angle present between the phenyl rings in the bridging ligand (~30°). The best fits for **6** and **7** were obtained considering D positive values.

The lack of field-dependent magnetisation studies for **8** and **8-dh** complicates the correct estimation of the D and $|E/D|$ values considerably. These studies mainly establish the sign of D. Nevertheless, as reported in previous chapters, the sign of the Co^{II} ion with this coordination geometry might be positive. Despite the absence of crystal structure of **8-dh**, the requirement of a J in **8**, but not in **8-dh**, suggests the existence of a magnetic pathway between different Co1 atoms that goes through the hydrogen bonds of their coordinated water molecules. However, the values for **8** and **8-dh** must be taken with caution, since adding two different centres for a $\chi_M T$ curve only can end in overparametrization.

Besides the difficulties in determining the best parameters values, the energy gap values obtained with the SOC and zfs models are in fair agreement in all compounds, except for **6**, validating both models. The discrepancies in **6** might arise from the different obtained J values.

The values obtained by theoretical CASSCF/NEVPT2 calculations are somehow in agreement with the parameters except for $g_{//}$, which is underestimated, as shown in Table IV.6. In these complexes, the contribution to the D values is mainly determined by the two first quartet excited states, as observed for the previous compounds shown in Chapters II-III. Their values are shown in Table A.20.

Table IV.3. Spin Hamiltonian parameters for **6–8** obtained from the first-order SOC model.

Compound	λ (cm^{-1})	Δ (cm^{-1})	α	TIP × 10^6 ($cm^3\ mol^{-1}$)	$F \times 10^6$	J (cm^{-1})	D (cm^{-1})	$g_\perp$	$g_{\parallel}$	$\lvert E/D \rvert$
6	−119.4	−188.1	1.09	3239	10.6	−0.09	–	–	–	–
7	−110.7	−135.8	1.09	1181	16.1	–	–	–	–	–
8	−145.4	−192.0	1.10	1115	83.8	−0.48	–	–	–	–
8-dh	−131.7	−131.1	1.11	1929	5.61	–	+22.03	2.09	2.60	0.000

F is the agreement factor defined as $F = \sum[P_{exp} - P_{calcd}]^2/\sum[P_{exp}]^2$

Table IV.4. Spin Hamiltonian parameters for **6–8** obtained from the zfs model.

Compound	D (cm^{-1})	$\lvert E/D \rvert$	$g_\perp$	$g_{\parallel}$	TIP × 10^6 ($cm^3\ mol^{-1}$)	$F \times 10^5$	J (cm^{-1})
6	+56.13	0.115	2.53	2.25	1631	3.73	−0.03
7	+62.19	0.008	2.57	2.15	709	2.30	–
8	+58.38	0.325	2.51	2.16	1667	4.73	−0.49
8-dh[a]	+21.61/+74.23	0.085/0.104	2.08/2.54	2.65/2.25	547	3.70	–

[a] Co1/Co2 atoms. F is the agreement factor defined as $F = \sum[P_{exp} - P_{calcd}]^2/\sum[P_{exp}]^2$

Table IV.5. Values for the energy gap between the ground and first excited Kramers doublets in cm^{-1} for SOC, zfs and CASSCF/NEVPT2.

Technique	Magnetometry: SOC model	Magnetometry: zfs model	CASSCF/NEVPT2[a]
6	158.0	118.1	114.0
7[a]	127.2	124.4	135.6/120.1/100.2/ 145.4/128.0/157.6
8	157.4	134.0	105.2/211.9
8-dh[b]	157.6/44.1	150.9/43.7	–

[a] Co1/Co2/ up to /Co6 atoms.[b] The second value for the SOC model is obtained through a zfs model.

Table IV.6. Spin Hamiltonian parameters for **6–8** obtained from CASSCF/NEVPT2 calculations.

Compound	D (cm^{-1})	E/D	$g_\perp$	$g_{\parallel}$
6	+55.35	0.141	2.55	2.03
7[a]	+63.68/+59.22/+43.43/ +69.78/+61.70/71.42	0.211/0.097/0.332/ 0.169/0.159/0.270	2.57/2.57/2.49/ 2.61/2.56/2.59	1.99/2.02/2.08/ 1.97/1.99/1.93
8[a]	+51.24/+92.59	0.134/0.321	2.57/2.56	1.99/2.02

[a] Co1/Co2/…/Co6 atoms.

IV.3.4 Ac-magnetic properties

Ac-magnetic susceptibility studies of **6**–**8** were performed to study their relaxation properties. A frequency (ν = 0.1–10.0 kHz) dependent component appears for **6** and **7** in χ_M' (in-phase) and χ_M'' (out-of-phase) signals below ~3 and 4.5 K under a dc-applied field (H_{dc} = 0.25–5.0 kOe). This behaviour indicates a slow magnetic relaxation, not though traditional relaxation mechanisms due to the positive *D* values. However, in the case of **8**, the frequency-dependent in χ_M'' signals with a maximum below 3 K is not so straightforward. When plotting the data in the χ_M'' *vs T* form, the χ_M'' signals are not frequency-dependent (Figure IV.9 left), being this behaviour reminiscent of a spin-glass transition[31,32] Signals emerge at 2.5 and 5.0 kOe, but intensely weaken at lower magnetic fields. Given the crystal structure of **8**, this behaviour might be attributed to the presence of small magnetic domains, caused by an exchange coupling interaction between the Co1 atoms, that is overcome when applying a strong external magnetic field. The weak signals at low magnetic fields might come from the remaining isolated Co2 atom. Comparing **8** with **8-dh**, we can conclude that spin-glass behaviour does not occur in the latter (Figure IV.9 right), suggesting the annihilation of the exchange coupling after removal of water molecules. In such a case, the collapse of the MOF-like crystal structure or the disappearance of the hydrogen bond network would cause the magnetic isolation of the Co^{II} ions. Moreover, **8-dh** exhibits more intense χ_M'' signals than **8**, confirming that the magnetic interaction in **8** weakens the SIM behaviour.

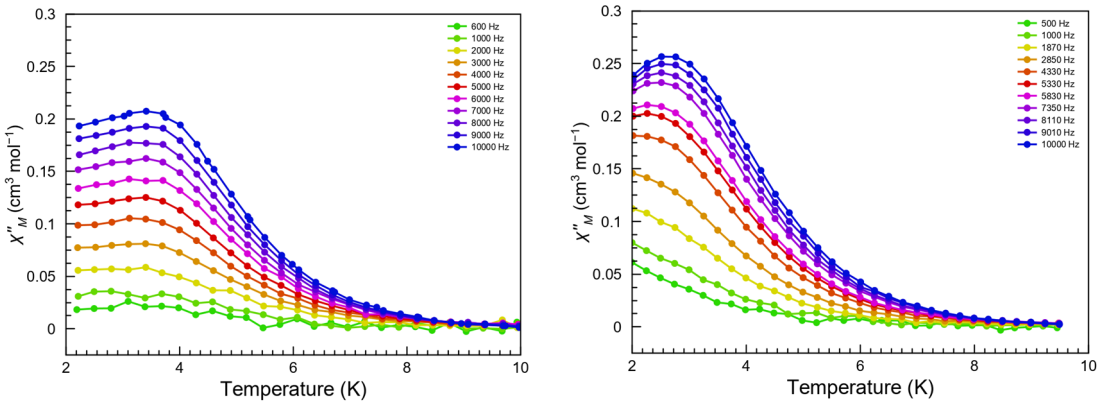

Figure IV.9. Temperature dependence of χ_M'' under a 5.0 kOe applied static field of **8** (left) and **8-dh** (right) at different frequencies (0.5–10.0 kHz). The solid lines are not a fit.

A generalised Debye model with equations (3–6, Chapter II) was applied to the χ_M' and χ_M'' *vs* ν data with the DynVPMag program.[33,34]

As a result, the simulated data using the best-fit values reproduce the experimental Cole-Cole plots, as shown in Figures IV.10–13 and A.72-83. Whereas one process is observed in **6**, **8** and **8-dh**, a secondary relaxation emerges in compound **7** at low temperatures in all magnetic fields. For the 1.0 kOe field of **7**, two processes are present, but they overlap,

being mathematically impossible to distinguish them both and, thus, to obtain trustful parameters from the fittings. The thermal relaxation values for the incipient process are between ~10^{-2} and 10^{-3} s, but the plots are not shown.

Occasionally, for some applied H_{dc} fields, the analysis of these Arrhenius data may lead to several sets of values for the parameters determining the relaxation mechanisms. This fact makes it difficult to find a similarity or correlation between the results obtained. Therefore, to avoid this issue, data at different H_{dc} are analysed together. This procedure requires introducing a dependency with the H_{dc} field already known for an IK or a quantum-tunnelling relaxation and, according to a Zeeman effect on a spin momentum, a linear one for the activation energies from TA mechanism. In this way, the model is summarised with the following equation:

$$\frac{1}{\tau} = \frac{1}{\tau_{LT}} e^{-\frac{Ea_{LT}}{k_B T}} + \frac{1}{\tau_{MT}} e^{-\frac{Ea_{MT}}{k_B T}} + \frac{1}{\tau_{HT}} e^{-\frac{Ea_{HT}}{k_B T}} + \frac{B_1}{1+B_2 H^2} \qquad (11)$$

where H is the external applied magnetic field, B_1 and B_2 are constants. The simulations obtained agree with the experimental data (Figure IV.14), and the values of the parameters involved in the IK and TA mechanisms are reasonable and similar to those found in other chapters of this report (Table IV.7). It is important to remember that these activation energies do not correspond to the energy barriers of an Orbach model arising from the presence of a zfs on the Co^{II} ion, but rather correspond to the energy necessary to trigger vibrational modes that, in their molecular motion, facilitates or speeds up the spin-reversal.

Undoubtedly, this relationship between E_a and H_{dc} forces the relaxing excited state to be modified by the applied magnetic field. Regarding this fact, a couple of clarifications must be made: i) the results show that the change induced by H_{dc} in E_a is not very significant, and ii) the spin density from the paramagnetic ion is shared on the whole molecule by spin delocalisation and polarisation mechanisms. This arrangement is modifiable by the applied magnetic field, which implies a change in the electronic distribution and the vibrational modes.

It has already been seen that the best way to find and analyse direct or Raman relaxations is to use $\ln(\tau)$ *vs* $\ln(T)$ plots, which will show straight lines with slopes –1 or $-n$, respectively (Figure IV.15 and A.84–87). These graphs for **6**–**8** and **8-dh** show two regimes with two different Raman mechanisms (acoustic and optical) governing the magnetic relaxation, but discarding any contribution from a direct process. At specific fields and low temperatures, a straight line with a zero slope is sensed, caused by the participation of an IK mechanism. Sometimes the regimes in which each mechanism is predominant are not well defined, causing difficulties in obtaining a set of unique values for their parameters. As in the previous model, it is advisable to analyse the data to all H_{dc} fields

simultaneously, imposing certain relationships, already known or with logical criteria, of the parameters to be determined with H_{dc}. This model is finally expressed as follows:

$$\frac{1}{\tau} = A_{LT}T^{n_{LT}} + A_{HT}T^{n_{HT}} + \frac{B_1}{1+B_2H^2} \qquad (12)$$

Results obtained from this analysis are summarised in Table IV.8, and the simulated curves with these values match with the experimental ones (Figure IV.14). Shortly, the two Raman processes activating a fast spin-reversal are assisted by optical (n ~ 2, T < 4 K) and acoustic (n ~ 6–8, T > 5 K) phonons. The IK process results are similar to those found by the previous model combining two TA and one IK mechanisms.

Moreover, all Arrhenius and ln(τ) *vs* ln(T) plots were also fitted independently following the equations for several TA + IK ($\frac{1}{\tau} = \frac{1}{\tau_{LT}}e^{-\frac{Ea_{LT}}{k_BT}} + \frac{1}{\tau_{MT}}e^{-\frac{Ea_{MT}}{k_BT}} + \frac{1}{\tau_{HT}}e^{-\frac{Ea_{HT}}{k_BT}} + \frac{1}{\tau_{IK}}$) and several Raman + IK ($\frac{1}{\tau} = A_{LT}T^{n_{LT}} + A_{HT}T^{n_{HT}} + \frac{1}{\tau_{IK}}$) mechanisms, respectively. These simulations are shown in Figures A.72-87 and the best-fit values are shown in Tables A.21–28.

The α values are below 0.4 in all cases, discarding any signs of spin-glass behaviour. For the case of **8**, this feature is quite odd since a frequency-independent behaviour occurs in the χ_M'' *vs* T plots,[35] as shown above. This fact might arise from the presence of the isolated Co2 atom in **8** which, probably, exhibits a different relaxation mechanism that is not discerned due to the insufficient quality data. For **6**, **7** and **8-dh**, the dependency of α with the temperature follows the same trend found in Chapter II, where the α values diminish while warming from 2.0 to ~5.0 K, but, then, it increases again until ~8.0–9.0 K. There are few exceptions of this tendency found at low H_{dc} for **7**, which is attributed to the uncertainties and high deviation errors obtained when applying the two generalised Debye models in the analyses.

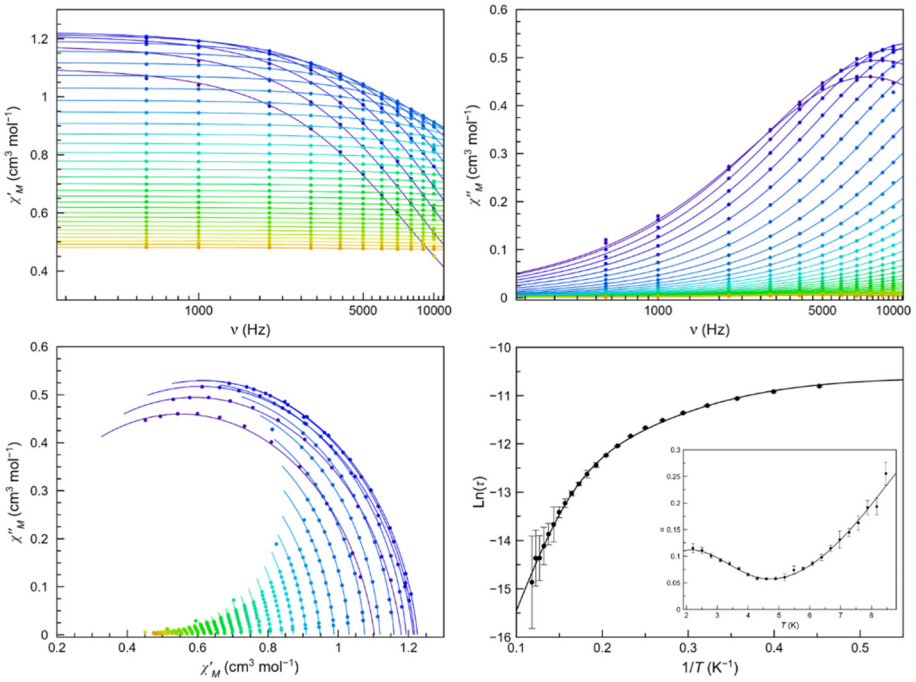

Figure IV.10. Frequency dependence of χ_M' (top left) and χ_M'' (top right), Cole-Cole plots (bottom left) and Arrhenius plots of **6** (bottom right) in a dc-applied static field of 5.0 kOe with ± 0.005 kOe oscillating field in the temperature range of 2.0–12.0 K (purple to green gradient). Thermal dependence of α is included on the bottom right figure as an inset, where the black line are eye-guides. Standard deviation appears as vertical error bars.

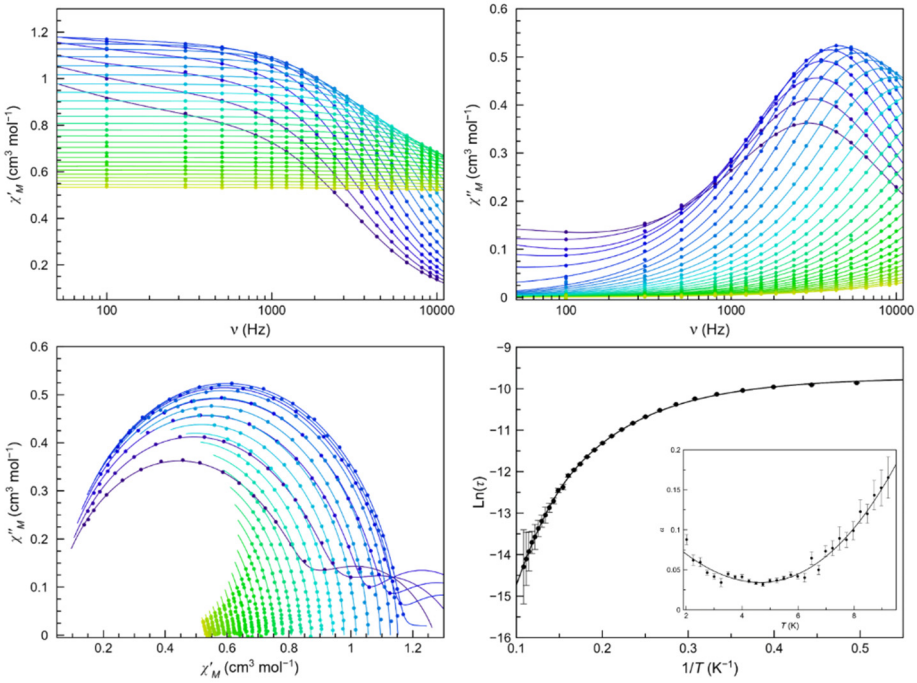

Figure IV.11. Frequency dependence of χ_M' (top left) and χ_M'' (top right), Cole-Cole plots (bottom left) and Arrhenius plots of **7** (bottom right) in a dc-applied static field of 5.0 kOe with ± 0.005 kOe oscillating field in the temperature range of 2.0–9.0 K (purple to green gradient). Thermal dependence of α is included on the bottom right figure as an inset, where the black line are eye-guides. Standard deviation appears as vertical error bars.

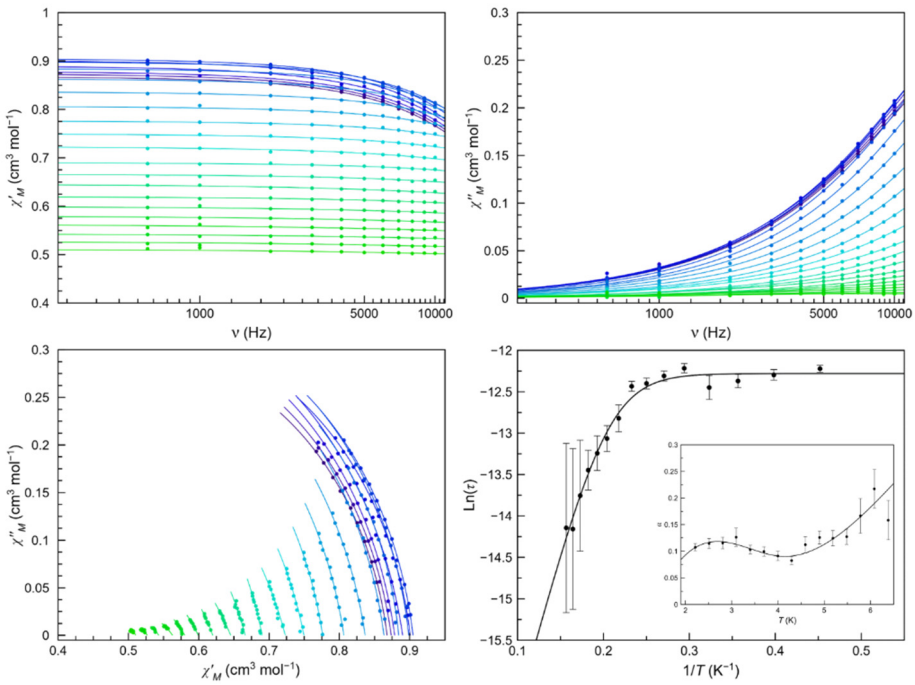

Figure IV.12. Frequency dependence of χ_M' (top left) and χ_M'' (top right), Cole-Cole plots (bottom left) and Arrhenius plots of **8** (bottom right) in a dc-applied static field of 5.0 kOe with ± 0.005 kOe oscillating field in the temperature range of 2.0–9.5 K (purple to red gradient). Thermal dependence of α is included on the bottom right figure as an inset, where the black line are eye-guides. Standard deviation appears as vertical error bars.

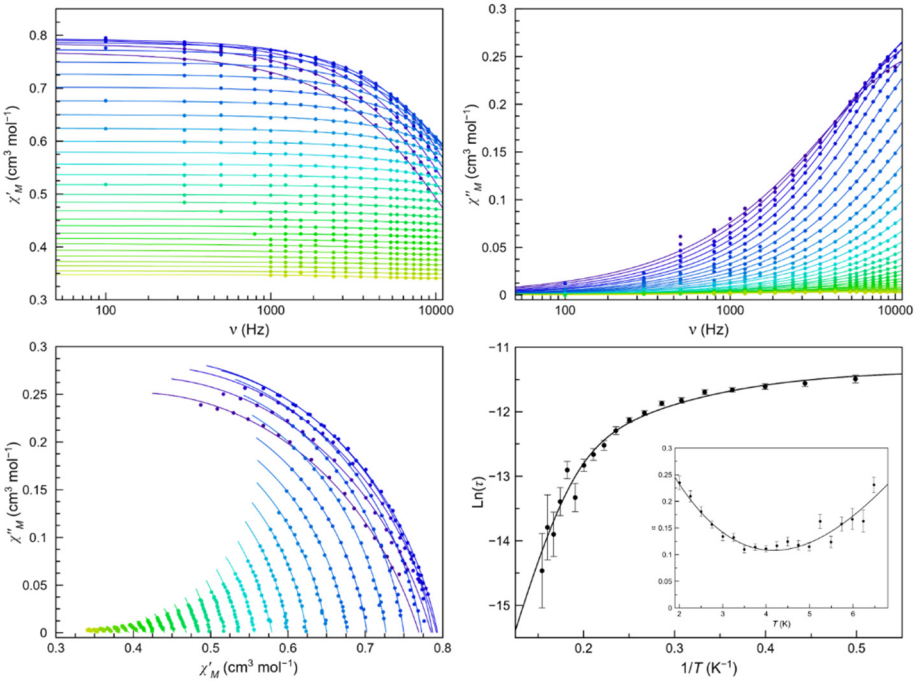

Figure IV.13. Frequency dependence of χ_M' (top left) and χ_M'' (top right), Cole-Cole plots (bottom left) and Arrhenius plots of **8-dh** (bottom right) in a dc-applied static field of 5.0 kOe with ± 0.005 kOe oscillating field in the temperature range of 2.0–9.5 K (purple to red gradient). Thermal dependence of α is included on the bottom right figure as an inset, where the black line are eye-guides. Standard deviation appears as vertical error bars.

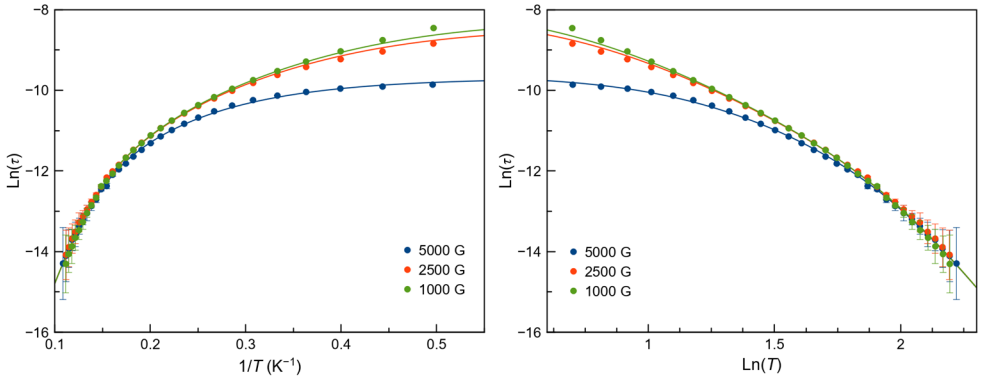

Figure IV.14. Arrhenius plots (left) and ln(τ) *vs* ln(T) plots (right) for the main process of **7** under 1.0–5.0 kOe applied static field. The solid lines are the best fit-curves by using the field-dependent equations. Standard deviations appear as vertical error bars.

Table IV.7. Best-fit parameters for the altogether H_{dc} analyses of **7** following the equation (11).

B_1 (s^{-1})	B_2 (kOe^{-1})	Ea_{LT} (cm^{-1})	$\tau_{LT} \times 10^6$ (s)	Ea_{MT} (cm^{-1})	$\tau_{MT} \times 10^7$ (s)	Ea_{HT} (cm^{-1})	$\tau_{HT} \times 10^{10}$ (s)
3769.79	–0.03	7.05	3.75	18.89	1.62	47.56	5.04

Table IV.8. Best-fit parameters for the altogether H_{dc} analyses of **7** following the equation (12).

B_1 (s^{-1})	B_2 (kOe^{-1})	A_{LT} (s^{-1} K^{-nLT})	n_{LT}	A_{HT} (s^{-1} K^{-nLT})	n_{HT}
2740.28	–0.03	292.28	3.28	0.02	8.22

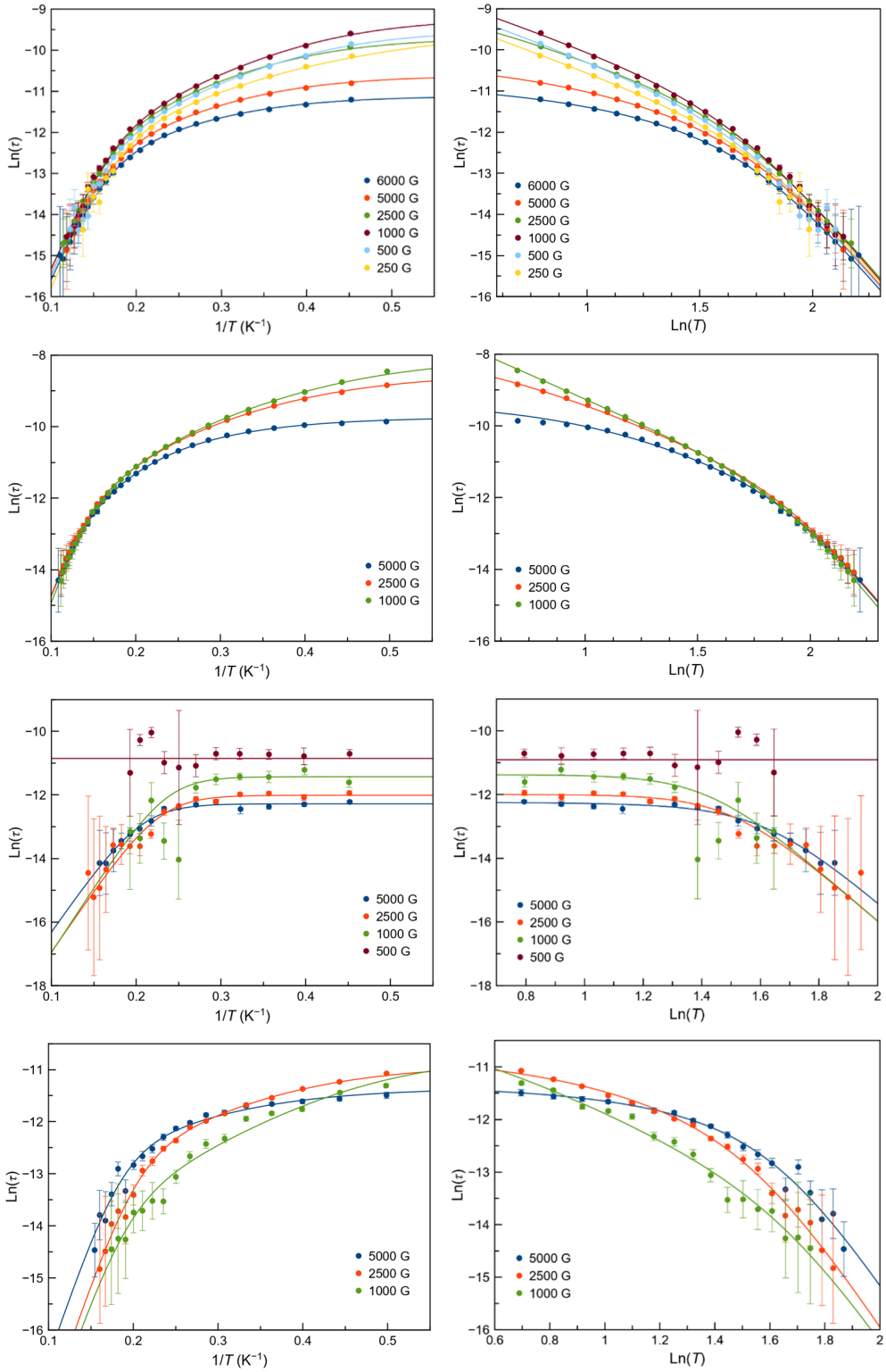

Figure IV.15. Arrhenius plots (left column) and ln(τ) *vs* ln(T) plots (right column) for the main process of **6** (first row), **7** (second row), **8** (third row) and **8-dh** (fourth row) under 0.25–6.0 kOe applied static field. The solid lines are the best fit-curves (see text). Standard deviations appear as vertical error bars.

IV.3.5 Conclusions

One chain and two trinuclear cobalt(II) complexes have been synthesised with tricarboxylic derivatives with threefold symmetry where the Co^{II} ions possess distorted octahedral geometry. Ligands were carefully selected to tune intramolecular cobalt-cobalt distances and to study their effects on the magnetic properties. Longer spacers and loss of coplanarity between their phenyl rings cause intramolecular magnetic interactions only occur in **6**. Magnetic studies reveal that both complexes display positive large *D* values. All compounds exhibit slow magnetic of the relaxation under dc-magnetic field, which can arise from either thermally activated mechanism assisted by affordable vibrational modes or Raman assisted by acoustic and optical phonons. In both models, intra-Kramers relaxations into the ground Kramers doublet are always competing. Each of the mechanisms prevails in a particular temperature region. One-dimensional **8** exhibits weak intermolecular magnetic interactions between two Co^{II} ions of two adjacent chains connected by hydrogen bonds, which are established between coordinated water molecules. Removal of solvent molecules leads to the loss of these weak bonds and magnetic interaction.

Slightly variations of the reactions conditions afforded a cobalt(II) chain, which is also achieved by structural transformations of the trinuclear complex under prolonged times in mother solution. The cobalt(II) chain shows a water reversible crystal-to-amorphous transformation. These transformations modify the coordination environment of one Co^{II} ion, changing from tetrahedral to octahedral spheres. The SIM behaviour is slightly enhanced upon removal of water molecules.

IV.4 References

1. Desiraju, G. R. Crystal Engineering: From Molecule to Crystal. *J. Am. Chem. Soc.* **135**, 9952–9967 (2013).

2. Livage, C., Guillou, N., Marrot, J. & Férey, G. Construction of Two- and Three-Dimensional Coordination Polymers from Cobalt Trimesate. *Chem. Mater.* **13**, 4387–4392 (2001).

3. Custelcean, R. & Gorbunova, M. G. A metal-organic framework functionalized with free carboxylic acid sites and its selective binding of a $Cl(H_2O)^{4-}$ cluster. *J. Am. Chem. Soc.* **127**, 16362–16363 (2005).

4. Castells-Gil, J. *et al.* Surface Functionalization of Metal-Organic Frameworks for Improved Moisture Resistance. *J. Vis. Exp.* **2018**, 1–6 (2018).

5. Patra, R., Titi, H. M. & Goldberg, I. Coordination polymers of flexible polycarboxylic acids with metal ions. V. polymeric frameworks of 5-(3,5-dicarboxybenzyloxy)-3-pyridine carboxylic acid with Cd(ii), Cu(II), Co(II), Mn(II) and Ni(II) ions; synthesis, structure, and magnetic properties. *CrystEngComm* **15**, 2863 (2013).

6. Kurmoo, M. Magnetic metal–organic frameworks. *Chem. Soc. Rev.* **38**, 1353 (2009).

7. Zheng, Y.-Z., Zheng, Z. & Chen, X.-M. A symbol approach for classification of molecule-based magnetic materials exemplified by coordination polymers of metal carboxylates. *Coord. Chem. Rev.* **258–259**, 1–15 (2014).

8. Dong, B.-X. *et al.* The first tritopic bridging ligand 1,3,5-tris(4-carboxyphenyl)-benzene (H_3BTB) functionalized porous polyoxometalate-based metal–organic framework (POMOF): from design, synthesis to electrocatalytic properties. *Dalt. Trans.* **44**, 1435–1440 (2015).

9. Zhang, W.-X. *et al.* Metal cluster-based functional porous coordination polymers. *Coord. Chem. Rev.* **293–294**, 263–278 (2015).

10. SAINT, Version 6.45, Bruker Analytical X-ray Systems, M. SAINT. (2012).

11. Sheldrick, G. M. *SADABS Program for absorption correction, version 2.10, Analytical X-ray Systems; Madison,WI,*. (2003).

12. Sheldrick, G. M. SHELXS97 and SHELXL97. Program for Crystal Structure Solution and Refinement. (1997).

13. Sheldrick, G. M. SHELXT – Integrated space-group and crystal-structure determination. *Acta Crystallogr. Sect. A Found. Adv.* **71**, 3–8 (2015).

14. Sheldrick, G. M. A short history of SHELX. *Acta Crystallogr. Sect. A Found. Crystallogr.* **64**, 112–122 (2008).

15. Spek, A. L. Structure validation in chemical crystallography. *Acta Crystallogr. Sect. D Biol. Crystallogr.* **65**, 148–155 (2009).

16. Angeli, C., Cimiraglia, R., Evangelisti, S., Leininger, T. & Malrieu, J.-P. Introduction of n -electron valence states for multireference perturbation theory. *J. Chem. Phys.* **114**, 10252–10264 (2001).

17. Eichkorn, K., Weigend, F., Treutler, O. & Ahlrichs, R. Auxiliary basis sets for main row atoms and transition metals and their use to approximate Coulomb potentials. *Theor. Chem. Accounts Theory, Comput. Model. (Theoretica Chim. Acta)* **97**, 119–124 (1997).

18. Vancoillie, S. *et al.* Multireference Ab Initio Calculations of g tensors for Trinuclear Copper Clusters in Multicopper Oxidases. *J. Phys. Chem. B* **114**, 7692–7702 (2010).

19. Nakamoto, K. Applications in Coordination Chemistry. in *Infrared and Raman Spectra of Inorganic and Coordination Compounds* 1–273 (John Wiley & Sons, Inc., 2008).

20. Hathaway, B. J. & Underhill, A. E. 592. The infrared spectra of some transition-metal perchlorates. *J.*

Chem. Soc. 3091 (1961).

21. Lewis, D. L., Estes, E. D. & Hodgson, D. J. The infrared spectra of coordinated perchlorates. *J. Cryst. Mol. Struct.* **5**, 67–74 (1975).

22. Llunell, M., Casanova, D., Cirera, J., Alemany, P. & Alvarez, S. SHAPE v2.1. (2013).

23. Craig, P. J. Book review: Chemistry of the elements, 2nd edn N.N. Greenwood and A. Earnshaw Butterworth -Heinemann, Oxford, 1997. 340 pages, ISBN 0-7506-3365-4. *Appl. Organomet. Chem.* **12**, 880–880 (1998).

24. Vallejo, J. *et al.* Reversible solvatomagnetic switching in a single-ion magnet from an entatic state. *Chem. Sci.* **8**, 3694–3702 (2017).

25. Lloret, F., Julve, M., Cano, J., Ruiz-García, R. & Pardo, E. Magnetic properties of six-coordinated high-spin cobalt(II) complexes: Theoretical background and its application. *Inorganica Chim. Acta* **361**, 3432–3445 (2008).

26. Chilton, N. F., Anderson, R. P., Turner, L. D., Soncini, A. & Murray, K. S. PHI: A powerful new program for the analysis of anisotropic monomeric and exchange-coupled polynuclear d - and f -block complexes. *J. Comput. Chem.* **34**, 1164–1175 (2013).

27. Oshio, H. & Ichida, H. Control of Intramolecular Magnetic Interaction by the Spin Polarization of d.pi. Spin to p.pi. Orbital of an Organic Bridging Ligand. *J. Phys. Chem.* **99**, 3294–3302 (1995).

28. Dul, M.-C. *et al.* Ferromagnetic Coupling by Spin Polarization in a Trinuclear Copper(II) Metallacyclophane with a Triangular Cage-Like Structure. *Inorg. Chem.* **48**, 5244–5249 (2009).

29. Pascu, M., Lloret, F., Avarvari, N., Julve, M. & Andruh, M. Ferromagnetic Coupling through Spin Polarization in the Hexanuclear [Mn II 3 Cu II 3] Complex. *Inorg. Chem.* **43**, 5189–5191 (2004).

30. Klingele, J. *et al.* Tetranuclear Nickel(II) Complexes Composed of Pairs of Dinuclear LNi2 Fragments Linked by Acetylenedicarboxylate, Terephthalate, and Isophthalate Dianions: Synthesis, Structures and Magnetic Properties. *Eur. J. Inorg. Chem.* **2007**, 5277–5285 (2007).

31. Trachenko, K. Understanding the spin glass transition as a dynamic phenomenon. *J. Phys. Condens. Matter* **23**, 366003 (2011).

32. Mydosh, J. A. *Spin Glasses: An Experimental Introduction*. (CRC Press, 2014).

33. Cole, K. S. & Cole, R. H. Dispersion and Absorption in Dielectrics I. Alternating Current Characteristics. *J. Chem. Phys.* **9**, 341–351 (1941).

34. Carbonell-Vilar, J. M. & Cano, J. Dyn-VPMag. *University of Valencia* (2019).

35. Bałanda, M. AC Susceptibility Studies of Phase Transitions and Magnetic Relaxation: Conventional, Molecular and Low-Dimensional Magnets. *Acta Phys. Pol. A* **124**, 964–976 (2013).

Chapter V

Dithienylethene-based dinuclear cobalt(II) photoswitches

Dinuclear compounds with general formula {[Co(Me_xphen)$_2$]$_2$(Sw-CO_2)](ClO_4)$_2$ (x = 1 or 2) were synthesised. The bridging ligand is a well-known photochromic molecule, a dithienylethene derivative, which undergoes reversible switching behaviour under UV and visible light irradiation. Under these conditions, the bridging ligand exhibits 1,2-dyotopic rearrangement between its open-ring and the closed-ring isomers. All Co^{II} ions within the compounds exhibit an octahedral geometry and $D > 0$ values. No magnetic interactions are detected with the applied techniques. The different phenanthroline derivative causes small variations in the slow magnetic relaxation properties, but all complexes seem to adjust to several Raman relaxation mechanisms or a combination of thermally activated mechanisms with an intra-Kramers.

V.1 Introduction

Single-ion magnets (SIMs) are molecules with only a paramagnetic centre that present slow relaxation of the magnetisation.[1] They are based mainly in lanthanides[2–4] and 3d-transition-metal mononuclear complexes, mostly cobalt(II) complexes.[5–7] These molecules have been proposed as qubits, the basic unit of quantum computers.[8,9] The main requirement is a well-defined $m_s = \pm 1/2$ ground state (either isolated or magnetic ground state) that can be manipulated into a superposition state with pulsed microwaves. At present, the main challenge resides on the formation of quantum gates based on two or more qubits with long coherence times. Some examples based on dinuclear lanthanides complexes,[10] heterometallic Cr_7Ni rings[11] and dinuclear vanadyl[12,13] complexes have been reported in the literature.

Photoswitchable magnetic materials are a valuable class of materials. External stimuli as light radiation can control their magnetic properties. Among these materials, diarylethenes (DAEs) are a type of photoswitchable molecules that undergo reversible ring-opening or closing reactions by irradiation with ultraviolet or visible light (Scheme V.1).[14] The photochromic behaviour results from the extension of the π conjugation in the closed isomer.[15] Furthermore, they are thermally irreversible and fatigue-resistant. This type of ligands has been proved as good candidates to tune the magnetic interactions between paramagnetic centres.[16,17]

In previous work, we reported $[Co(Me_2phen)_2(benzoate)]ClO_4 \cdot 0.5H_2O \cdot 0.5CH_3OH$ that behaves as SIMs under an applied magnetic field.[18] This complex is envisaged as an excellent building block to form more complex architectures, as proved in Chapter III and IV. Whereas in Chapter III, the aim was to use asymmetrical ligands to form dimers of inequivalent entangled metal ions as possible qu-gates with this building block, in this Chapter our approach consists in the design of metal-based pairs of qubits with switchable interactions. Then, the mononuclear cobalt(II) complex and a photoswitch ligand (Scheme V.1) have been employed to form dinuclear cobalt(II) complexes to explore such complexes as candidates for possible photoswitchable qu-gates.[19] Here, we report dinuclear cobalt(II) complexes with the formula $\{[Co(Me_xphen)_2]_2(Sw\text{-}CO_2)\}(ClO_4)_2$ [x = 1 (2-methyl-1, 10-phenanthroline), 2 (2,9-dimethyl-1, 10-phenanthroline)]; $H_2Sw\text{-}CO_2$ = 1,2-bis(5-carboxy-2-methylthien-3-yl)-cyclopentene). The synthesis, X-ray structures, magnetic properties and UV/Vis studies are presented here. Furthermore, the influence of symmetric and asymmetric phenanthroline ligands at the terminal positions are studied.

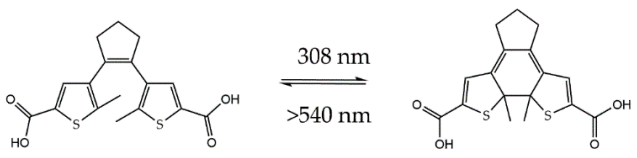

Scheme V.1. Photoreactivity of the ligand of this study.

V.2 Experimental section

V.2.1 Materials

All chemicals were obtained from commercial sources and used as received. 1,2-Bis(5-carboxy-2-methylthien-3-yl)cyclopentene (H_2Sw-CO_2-o) was synthesised according to the literature.[20] All syntheses were performed in the dark. The closed 1,2-bis(5-carboxy-2-methylthien-3-yl)cyclopentene ligand (H_2Sw-CO_2**-**c) is obtained by irradiation of a methanol solution of the open-ring isomer with 308 nm lamp tubes in a photoreactor.

Caution! Perchlorate salts are potentially explosive. They should be used in small quantities and should be manipulated with the utmost care at all times.

V.2.2 Syntheses

General synthetic procedures of cobalt(II) complexes: $Co(ClO_4)_2{\cdot}6H_2O$ (146 mg, 0.4 mmol, 2 eq) and the corresponding phenanthroline ligand (0.8 mmol, 4 eq) were dissolved in hot methanol (25 mL) in the dark, followed by the addition of H_2Sw-CO_2 (70 mg, 0.2 mmol, 1 eq) and KOH (19 mg, 0.3 mmol, 1.5 eq) in methanol. The solution mixture resulted in the formation of a white precipitate, which was filtered off and discarded. Pinkish-orange (open-form) and violet (closed-form) single crystals suitable for X-ray diffraction were grown by slow diffusion of toluene into the methanolic solution with some drops of acetonitrile.

{[Co(Me$_2$phen)$_2$]$_2$(Sw-CO_2)}$(ClO_4)_2$·2tol (9-o). Yield: 107 mg, 36%. IR (ν_{max}/cm^{-1}): 3417(w), 3066(w), 3023(w), 2921(w), 2844(w), 2015(w), 1623(m), 1594(m), 1563(m), 1540(m), 1511(m), 1500(s), 1465(m), 1437(m), 1406(m), 1384(m), 1358(m), 1294(m), 1205(w), 1154(m), 1091(s), 938(w), 857(m), 814(w), 778(m), 732(m), 682(w), 654(w), 623(m), 551(w). Elemental Analysis calculated for **9-o** ($C_{87}H_{78}Cl_2Co_2N_8O_{12}S_2$): C, 62.18; H, 4.68; N, 6.67; S, 3.95. Found: C, 62.45; H, 4.58; N, 6.70; S, 4.01.

{[Co(Me$_2$phen)$_2$]$_2$(Sw-CO_2)}$(ClO_4)_2$·2tol (9-c). Yield: 70 mg, 35%. IR (ν_{max}/cm^{-1}): 3414(w), 3069(w), 2921(w), 2514(w), 1623(w), 1594(m), 1560(w), 1528(m), 1511(m), 1501(m), 1396(m), 1384(m), 1359(m), 1295(w), 1204(w), 1154(m), 1093(s), 860(m), 813(w), 774(w), 732(w), 655(w), 623(m), 551(w). Elemental Analysis calculated for **9-c** ($C_{87}H_{78}Cl_2Co_2N_8O_{12}S_2$): C, 62.18; H, 4.68; N, 6.67; S, 3.95. Found: C, 62.45; H, 4.38; N, 6.30; S, 4.02.

{[Co(Mephen)$_2$]$_2$(Sw-CO_2)}$(ClO_4)_2$·2.5tol (10-o). Yield: 144 mg, 72%. IR (ν_{max}/cm^{-1}): 3419(w), 3066(w), 3021(w), 2947(w), 2915(w), 2841(w), 1625(m), 1592(m), 1574(m), 1557(m), 1539(m), 1513(m), 1499(m), 1466(m), 1439(m), 1406(m), 1389(m), 1253(w), 1225(w), 1147(m), 1090(s), 908(w), 856(m), 779(m), 730(m), 694(w), 650(w), 623(m), 575(w), 465(w),

419(w). Elemental Analysis calculated for **10-o** ($C_{86.5}H_{74}Cl_2Co_2N_8O_{12}S_2$): C, 62.20; H, 4.47. N, 6.71; S, 3.84. Found: C, 63.12; H, 4.42; N, 6.77; S, 3.72.

{[Co(Mephen)$_2$]$_2$(Sw-CO$_2$)}(ClO$_4$)$_2$·2tol (10-c). Yield: 79 mg, 46%. IR (ν_{max}/cm^{-1}): 3422(w), 3066(w), 3023(w), 2949(w), 2919(w), 2844(w), 1626(m), 1592(m), 1574(m), 1558(m), 1513(m), 1499(m), 1465(m), 1439(m), 1388(m), 1253(w), 1224(w), 1147(m), 1091(s), 908(w), 855(m), 779(m), 731(m), 650(w), 623(m), 558(w), 420(w). Elemental Analysis calculated for **10-c** ($C_{83}H_{70}Cl_2Co_2N_8O_{12}S_2$): C, 61.37; H, 4.34. N, 6.90; S, 3.95. Found: C, 61.45; H, 4.32; N, 6.97; S. 3.98.

V.2.3 Physical measurements

Infrared spectra (4000–400 cm^{-1}) were recorded on a Nicolet 5700 spectrophotometer as KBr pellets. Elemental analyses (C, H, N, S) were performed at the Microanalytical Service of the Universitat de València. UV/Vis absorption spectra were recorded with a Jasco V-670 spectrometer. Irradiation experiments were conducted within a Luzchem LZC4-4V photoreactor, equipped with seven LZC-UVA FL8BL-B 350 nm or seven visible Sylvania Cool White F8T5 lamps with orange LuzChem filters (> 540 nm) under an argon atmosphere.

X-ray powder diffraction (XRPD) measurements were performed on a Panalytical Empyrean X-ray diffractometer by using Cu Kα radiation (λ = 1.5406 Å), in which the X-ray tube was operated at 45 kV and 40 mA ranging from 2 to 40°. The XRPD data was background corrected with the *HighScore Plus* software.

Static direct current (dc) measurements were carried out on all samples by powdering and restraining the samples with *n*-eicosane to prevent any displacement due to the magnetic anisotropy. Variable-temperature (2.0–300 K) dc-magnetic susceptibility under an applied field of 0.25 (T < 20 K) and 5.0 kOe (T ≥ 20 K), and variable-field (0–5.0 kOe) magnetisation in the temperature range from 2 to 10 K were recorded with a Quantum Design SQUID magnetometer. Variable-temperature (2.0–12 K) alternating current (ac) magnetic susceptibility measurements under ±0.005 kOe oscillating field at frequencies in the range of 0.1–10 kHz were carried out on crystalline samples under different applied static dc fields in the range 0.0–5.0 kOe with a Quantum Design Physical Property Measurement System (PPMS). The magnetic susceptibility data were corrected for the diamagnetism of the constituent atoms and the sample holder.

Powder continuous wave EPR measurements were carried out on all samples by powdering and restraining the samples with *n*-eicosane to prevent any alignment with the magnetic field due to the high magnetic anisotropy. EPR measurements in X-band and Q-band were performed with an EMX spectrophotometer with an 18 kOe electromagnet and

an Elexsys E580 spectrophotometer with a 18 kOe electromagnet, respectively (EPSRC National Service for Electron Paramagnetic Resonance Spectroscopy, University of Manchester). The samples were cooled down with a liquid ^{4}He flow together with an external N_2 gas flow to prevent O_2 and water moisture inside the cavity. Frozen solution samples were performed in acetonitrile ~5 mM, and they were subjected to three freezing cycles with liquid N_2 and degassed with ^{4}He before their data collection. The collected EPR data was corrected with a previous strong pitch measurement with g = 2.0028. The EPR simulations were obtained by using *EasySpin* software.[21]

V.2.4 X-ray Crystallography

Single-crystal X-ray diffraction data of **9-o/c** and **10-o/c** (open and closed forms) were collected on a Bruker-AXS Kappa Mach3 APEX-II diffractometer equipped with an Incoatec Helios mirror monochromator (Mo-Kα λ = 0.71073 Å) and a nitrogen cold stream adjusted to 100 K. Data integration, data scaling and absorption correction were done using programs SAINT[22] and SADABS[23], respectively. The structures were solved with the SHELXS structure solution program, using the Patterson method.[24] The model was refined with version 2018/3 of SHELXL against F2 on all data by full-matrix least squares.[25,26] All non-hydrogen atoms were refined with anisotropic displacement parameters. Hydrogen atoms were placed at calculated positions. In **9-o**, the coordination sphere of Co2 is disordered over two positions (Co2 and Co2'). In **10-o**, the phenanthroline ligand coordinated to Co2 is disordered. In **9-o** and **9-c**, toluene molecules are also disordered. In **10-o**, toluene molecules are also present, but they were removed due to poor quality refinements. The final geometrical calculations and the graphical manipulations were carried out with the PLATON package.[27] Crystallographic data for compounds **9-o/c** are given in Table A.29.

V.2.5 Computational details

Calculations based on a second-order *N*-electron valence state perturbation theory (CASSCF/NEVPT2) applied on the wave function, previously obtained from complete active space (CAS) calculation, were performed on the structurally characterised dinuclear complexes **9**–**10** (or **9-o**, **9-c**, **10-o** and **10-c**) aiming to evaluate the parameters that determine the axial (*D*) and rhombic (*E*) components of the zero-field splitting (zfs).[28] The dinuclear species were split into mononuclear unities, keeping the experimental dispositions of the ligands around the metal. The calculations were carried out with version 4.0.1 of the ORCA and the auxiliary TZV/C Coulomb fitting basis sets.[29] The spin–orbit coupling contributions to zfs from 10 quartet and 20 doublet excited states generated from an active space with seven electrons in five d-orbitals were included from

an effective Hamiltonian. The *g*-tensors were calculated for the ground Kramers pair using Multireference Configuration Interaction (MRCI) wave functions with a first-order perturbation theory on the SOC matrix.[34]

V.3 Results and discussion

V.3.1 Syntheses and X-ray Structure description

The reaction between $Co(ClO_4)_2{\cdot}6H_2O$ and the corresponding phenanthroline derivative ligand in methanol, followed by the addition of $H_2Sw\text{-}CO_2$ and KOH, affords compounds **9-o/c** and **10-o/c**. Other bases as NaOMe and NaH can also be employed. Although the reaction is performed in stoichiometric ratio metal to ligand, a defect of the base is preferred to avoid cobalt(III) impurities. To obtain the closed forms of **9-o** and **10-o** the photochromic ligand ($H_2Sw\text{-}CO_2$) was first irradiated in MeOH (~0.7 mM) during 1 hour at 308 nm, and subsequent syntheses of complexes were performed in the absence of light. Except for **10-c**, single crystals suitable for X-ray diffraction were obtained by slow diffusion of toluene into methanol solutions of all compounds.

Infrared spectra of open and closed-ring isomers of **9** and **10** show a shift of the band at 1680 cm^{-1} corresponding to carboxylic groups of the photochromic ligand ($H_2Sw\text{-}CO_2$), suggesting the coordination to the Co^{II} ion. Medium size absorption peaks at ~1595 and ~1560 cm^{-1} are assigned to aromatic C–C stretching bands. The bands at 1091, 930 and 623 cm^{-1} confirm the presence of perchlorate counterions.[31] No apparent differences between the IR spectra for the open and closed forms of compounds **9-o/c** and **10-o/c** are visible.

Compounds **9-o**, **9-c** and **10-o** crystallise in the triclinic P−1 space group. Their crystal structures, shown in Figures V.1–2, consist of two $[Co(Me_xphen)_2]^{2+}$ [x = 1 (**9-o/c**) and 2 (**10-o**)] units linked by the deprotonated photochromic $H_2Sw\text{-}CO_2$ ligand, and two perchlorate anions to balance the charge. Disordered crystallisation toluene molecules are also present in **9-o** and **9-c**. The low quality of the crystal structure of **9-o** can be noticed in the Co2 atom and its environment, which are disordered over two positions (Co2a and Co2b). In **10-o**, the disorder not only concerns the coordination sphere, but one phenanthroline molecule coordinated to Co2 atom is also disordered. All compounds show distorted CoN_4O_2 coordination sphere. Two oxygen atoms from the carboxylate anchoring point of the $Sw\text{-}CO_2$ ligand and one nitrogen atom from each phenanthroline ligand constitute the equatorial plane. Meanwhile, the two remaining nitrogen atoms from each phenanthroline ligand occupy the axial positions. The distortion degree from the ideal octahedral or trigonal prisms was calculated with the continuous shape measure theory and the SHAPE software.[32] An ideal polyhedron exhibits a zero value for the parameter that defines the

distortion, and the values are larger the more distorted it is. The parameter was evaluated with this software for octahedral (OC-6) and trigonal (TPR-6) prisms. The found values for a OC-6 geometry were 3.380 (Co1), 3.116 (Co2a) and 3.069 (Co2b); 3.235 (Co1) and 3.533 (Co2); 3.817 (Co1) and 3.003 (Co2) for **9-o**, **9-c** and **10-o**, respectively; and for a TPR-6 geometry, 13.267 (Co1), 14.155 (Co2a) and 14.048 (Co2b); 14.208 (Co1) and 14.046 (Co2); 9.577 (Co1) and 13.145 (Co2) (TPR-6) for **9-o**, **9-c** and **10-o**. Consequently, Co^{II} ions in isomers of **9-o/c** and **10-o/c** show an octahedral geometry with a degree of distortion similar to that found for the compounds of Chapters III and IV, bearing the same coordinated functional groups.

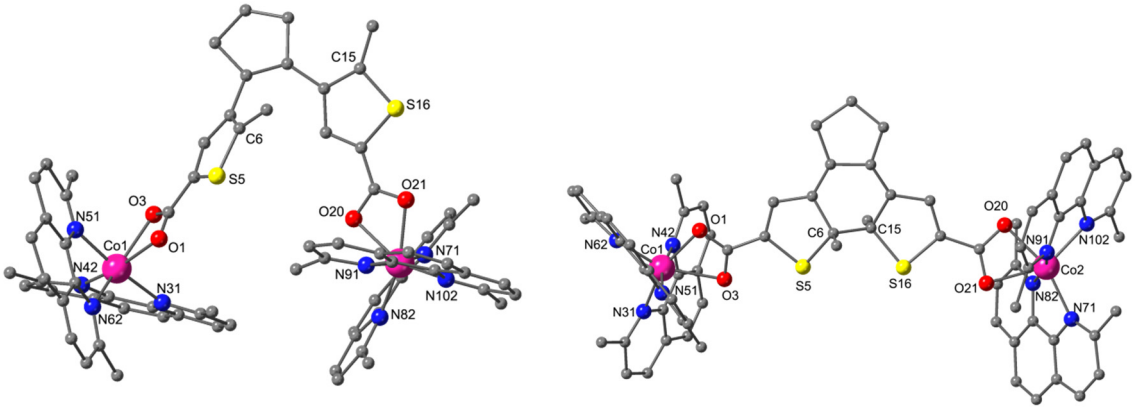

Figure V.1. Perspective view of the dinuclear cation $[Co_2(Me_2phen)_4(Sw\text{-}CO_2)]^{2+}$ of **9-o** (left) and **9-c** (right). Hydrogen atoms and the disordered Me_2phen molecule are omitted for clarity. Colour code: magenta, cobalt; yellow, sulphur; red, oxygen; blue, nitrogen; grey, carbon.

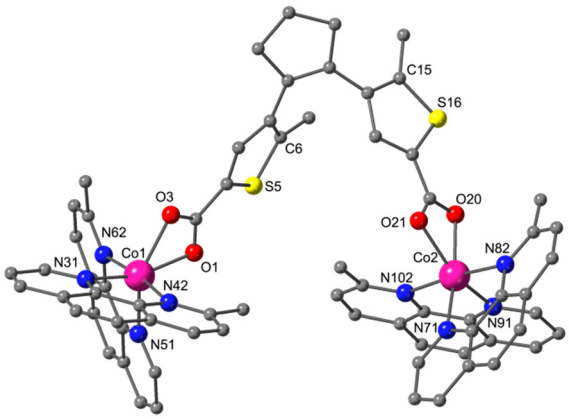

Figure V.2. Perspective view of the dinuclear cation $[Co_2(Mephen)_4(Sw\text{-}CO_2)]^{2+}$ of **10-o**. Hydrogen atoms and the disordered Me_2phen molecule are omitted for clarity. Colour code: magenta, cobalt; yellow, sulphur; red, oxygen; blue, nitrogen; grey, carbon.

Selected bond distances and angles of **9-o**, **9-c** and **10-o** are in Table II.1. Co–O distances are in the range of 2.10–2.28 Å (**9-o**), 2.11–2.28 (**9-c**) and 2.11–2.20 (**10-o**), whereas Co–N lie

in the range of 2.07−2.17 Å (**9-o**), 2.09−2.17 (**9-c**) and 2.05−2.21 (**10-o**). The Co^{II} ions are slightly moved from the N_2O_2 equatorial plane with distances to this plane of 0.036, 0.053 and 0.008 Å (**9-o**), 0.032 and 0.046 Å (**9-c**), and 0.015 and 0.001 Å (**10-o**). The chelating angles are similar in all compounds, with N−Co−N angle values between 77.09 and 79.94° and O−Co−O angles between 59.79−62.90°. These O−Co−O angles values are in agreement with those chelating carboxylate ligands reported on the literature.[33,34]

Table V.1. Selected bond distances and angles for **9-o**, **9-c** and **10-o**.

Compound	9-o	10-o	9-c
Bond distances [Å]			
Co1−N51	2.0956(11)	2.0990(21)	2.137(3)
Co1−N62	2.1388(11)	2.1553(23)	2.087(3)
Co1−N42	2.1683(11)	2.1766(22)	2.133(3)
Co1−N31	2.1399(11)	2.0883(18)	2.103(3)
Co1−O3	2.2030(12)	2.1766(22)	2.284(3)
Co1−O1	2.1392(11)	2.1942(17)	2.125(3)
Co2−N82	2.1478(11)	2.2134(49)	2.155(3)
Co2−N102	2.0922(11)	2.1564(21)	2.112(3)
Co2−N91	2.1638(11)	2.0791(19)	2.174(3)
Co2−N71	2.1325(11)	2.0587(47)	2.093(3)
Co2−O21	2.1789(12)	2.1968(17)	2.255(3)
Co2−O20	2.1179(11)	2.1140(17)	2.113(3)
Bond angles [°]			
N51−Co1−N62	79.24(1)	79.18(09)	79.94(12)
N31−Co1−N42	77.76(1)	78.23(07)	78.77(13)
O1−Co1−O3	60.68(1)	60.82(06)	59.79(10)
N71−Co2−N82	77.74(1)	78.76(14)	78.58(12)
N91−Co2−N102	78.45(1)	79.99(08)	78.56(61)
O20−Co2−O21	62.90(1)	61.16(06)	60.39(10)

Intramolecular C6···C15 distances are 4.465 and 4.111 Å for **9-o** and **10-o**, being slightly longer than the value required to undergo a cyclisation reaction, 4.000 Å. The thiophene rings present a distorted parallel configuration in the crystalline structures which, in theory, is unlikely to undergo a cyclisation reaction in solid state. Ethylene torsion angle in the cyclopentene unit is 0.73 and 7.13° for **9-o** and **10-o**, and the dihedral angle between thiophene rings takes values of 52.78 (55.83° for the disordered ring), 6.70 and 57.39° for **9-o**, **9-c** and **10-o**, respectively. The shortest intramolecular Co···Co distances are 9.359 and 9.681 Å, for **9-o** and **10-o**, being longer for the closed forms, *i.e.*, 13.864 Å (**9-c**). The shortest intermolecular Co···Co distances are 9.028 Å, 8.403 Å and 8.261 Å for **9-o**, **9-c** and **10-o**.

Intermolecular π−π interactions in the open forms of **9** and **10** involve phenanthroline ligands coordinated to both cobalt atoms (Table A.30 and Figures A.88–90). However, in **9-c**, these interactions occur only between phenanthroline ligands coming from Co2 atom. This last compound also shows π−π interactions between the phenanthroline ligand and toluene molecules. As a result, a supramolecular packing is achieved in all cases. A supramolecular chain is present in **9-o** and **9-c**, which in the case of **9-o** the chain is along the *a*-axis and along a no clear direction for **9-c**. However, **10-o** shows a supramolecular layer-like (2D) arrangement parallel to the (−1, 0, 1) lattice plane.

V.3.2 Spectroscopic Studies

The UV/Vis absorption spectra for the $H_2Sw\text{-}CO_2$ ligand is detailed in the literature,[15] but the photoswitching behaviour is not reported in acetonitrile (the same solvent used as for the complexes, see below). Figure V.3 shows the electronic spectrum after irradiation at 308 nm of an acetonitrile solution of $H_2Sw\text{-}CO_2$ at different time steps. A broad band of the closed-ring form emerges at ~532 nm; but, after several irradiation hours, this absorption band and the isosbestic point at 308 nm vanish as a consequence of the ligand degradation.[35] These changes are visible by the naked eye since the solution goes from brownish (open) to dark purple colour (closed).

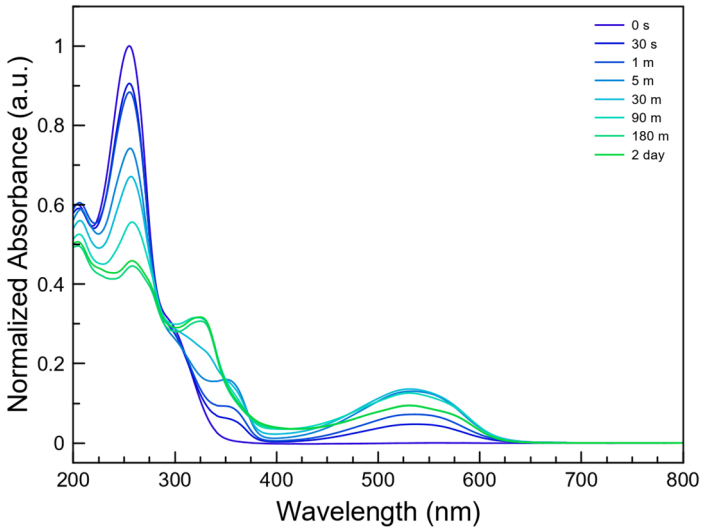

Figure V.3. UV/Vis absorption spectra for $H_2Sw\text{-}CO_2$ in AcN at 308 nm.

The UV/Vis absorption spectra for ~0.007 mM solutions of **9-o** and **10-o** in AcN are shown in Figure V.4. The absorption spectra display two bands at 230 and 270 nm that, after irradiation at 308 nm, the intensity of these two bands decrease and two new bands appear at 350 and 540 nm, suggesting the cyclisation of the ligand as observed for the free ligand.[36] This process is accompanied by a colour change from light orange (**9-o** and **10-o**) to pink (**9-c** and **10-c**), as Figure V.5 shows. At 533 nm, the molar attenuation coefficient at 533 nm

for **10-o** is larger than in **9-o** (8414 and 5428 cm M^{-1}, respectively), indicating greater yield in the cyclisation of **10-o**.

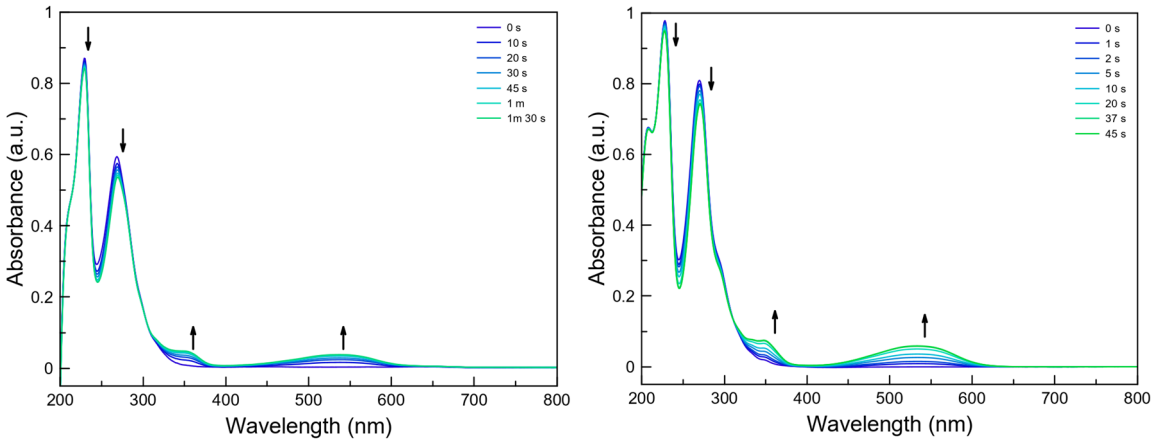

Figure V.4. Electronic absorption spectra of **9-o** (left) and **10-o** (right) in acetonitrile ~0.007 mM subjected to irradiation with UV light (308 nm) at different times.

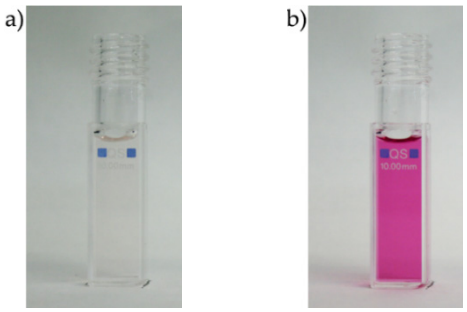

Figure V.5. Picture of 0.26 mg/mL solutions of **9-o** or **10-o** (a) and **9-c** or **10-c** (b).

Cyclisation can be reverted by irradiating the resultant solution at wavelengths within the ~450–600 nm range. However, the ring-aperture is much slower than the ring-closure, as Figure V.6 shows.[37] For long periods of exposure, photochromic ligand undergoes degradation (Figure A.91), leading to the formation of a third species no longer photoswitchable.[35] The formation of this species can be registered by monitoring the absorbance at 533 nm over time (Figure A.92). A linear dependence is observed with short irradiation times until reaching a maximum at ~90 (**9-o**) and 45 s (**10-o**): Later, a drastic decrease is recorded.

Reversibility and fatigue of the systems were evaluated with consecutive closing-opening cycles. In the region outside the linear dependence ligand degradation begins, in fact, fatigue becomes noticeable (Figure A.93) for closure irradiation times of 40 (**9-o**) and 45 s (**10-o**). Irradiation times of 10 s allow overcoming this inconvenient (Figure A.94).

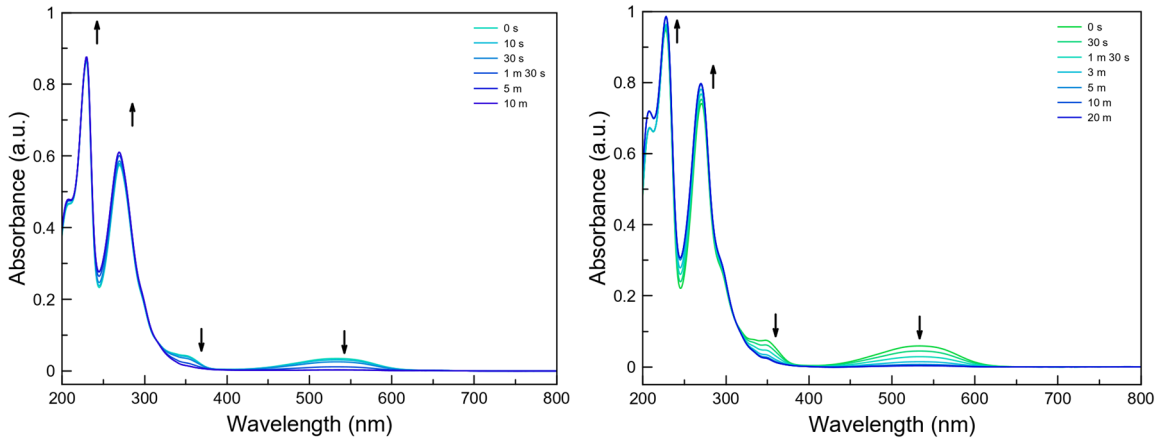

Figure V.6. Electronic absorption spectra for the reversal irradiation of **9-c** (left) and **10-c** (right) samples in acetonitrile ~0.007 mM subjected to visible (>540 nm) light at different times.

V.3.3 Magnetic properties, EPR and theoretical calculations

The direct current (dc) magnetic properties of **9-o/c** and **10-o/c** were measured as $\chi_M T$ *vs* T and M *vs* H/T curves, as shown in FigureV.7. The $\chi_M T$ values at room temperature are 6.12 (**9-o**), 6.03 (**10-o**), 6.18 (**9-c**) and 6.17 (**10-c**) $cm^3\ K\ mol^{-1}$, which are higher than the spin-only value for two S = 3/2 with g = 2.0 (3.75 $cm^3\ K\ mol^{-1}$). The $\chi_M T$ values decrease gradually until 100 K and then more abruptly until values of 3.31 (**9-o**), 3.46 (**10-o**), 3.32 (**9-c**) and 3.38 (**10-c**) $cm^3\ K\ mol^{-1}$ at 2 K. The high values of $\chi_M T$ at room temperature and the form of the curve suggest the presence of strong spin-orbit coupling (SOC), as observed for the isolated dinuclear cobalt(II) compounds **2**–**5** (Chapter III). There is a drop of $\chi_M T$ below 5 K that is not caused by an exchange coupling due to the long intramolecular Co···Co distance (> 9.36 Å). However, the effect of the applied magnetic field simulates well this drop of $\chi_M T$. Therefore, as foreseen, the long photoswitchable ligand does not mediate any significant magnetic exchange coupling between cobalt(II) centres.

The field-dependent magnetisation studies at low temperatures for **9-o/c** and **10-o/c** are included as inset figures in Figure V.7. The magnetisation values at 50 kOe and 2 K are 4.40 (**9-o**), 4.50 (**10-o**), 4.41 (**9-c**) and 4.43 Nβ (**10-c**). These values are below the saturation limit of 6 Nβ for two S = 3/2 with g = 2, suggesting significant axial zfs for the four compounds. The isothermal magnetisation curves in the temperature range 2–10 K almost superimpose. As seen in previous chapters, these behaviours are typical for Co^{II} ions with large D values.

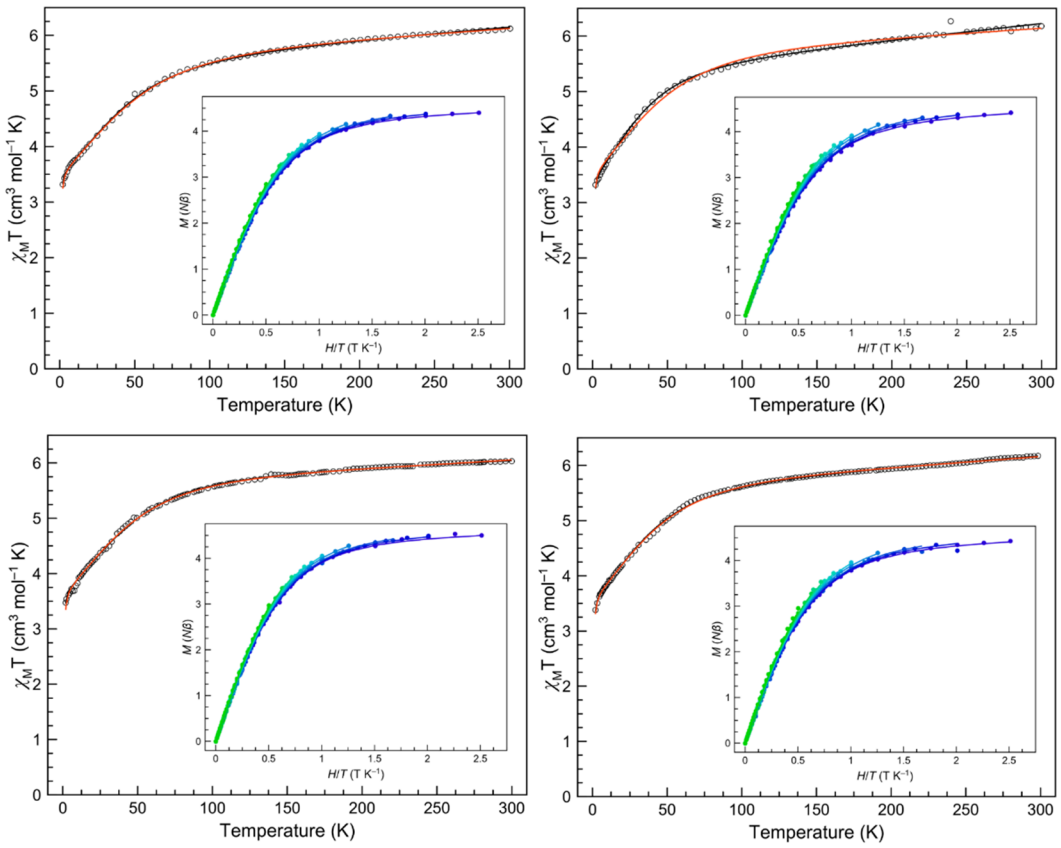

Figure V.7. Plots of $\chi_M T$ *vs* T in the range 2–300 K in 5.0 kOe applied field and M *vs* H/T (inset) for **9-o** (top left), **9-c** (top right), **10-o** (bottom left), **10-c** (bottom right) in the 2–10 K temperature range (2 K blue to 10 K green gradient). The solid lines are the best-fit curves (see text).

Experimental magnetic susceptibility and magnetisation data of **9-o/c** and **10-o/c** were analysed in the whole temperature range using the T-P isomorphism formalism expressed following the SOC Hamiltonian mentioned in previous chapters (Figure V.7, red line). The best fit of the magnetic data using the PHI software,[38] and considering two identical Co^{II} ions are listed in Table V.2.

Magnetic susceptibility data were also analysed with a more limited zfs approach through the equation (4) (Figure V.7, black line). The best fit of the magnetic data using the PHI software,[42] and considering two identical Co^{II} ions are in Table V.3. A good agreement between experimental and calculated curves was obtained with both approaches for all compounds. The values of the energy gap between the ground and first excited Kramers doublets found with first-order SOC and zfs models are very similar, validating both models (Table V.4). Furthermore, the obtained values are within the range of those observed for other six-coordinate high-spin cobalt(II) compounds (see previous chapters).

X-Band EPR spectra for powdered crystalline samples with *n*-eicosane and ~5 mM frozen-acetonitrile solution samples of **9-c** and **10-o/c** at ~5 K were measured, as shown in Figures V.9 and A.95. As in Chapter III, these spectra only show +1/2 → −1/2 transitions, typical

for high-spin Co^{II} ions with large *D* positive values, which cannot be determined with the X-band energy. However, *g* tensors and the $|E/D|$ ratio can be estimated. Since these dinuclear cobalt(II) complexes show almost identical coordination spheres, CoN_4O_2, both metal ions were considered equivalents (Table V.5). However, the analysis of the EPR spectrum for **10-o** required to consider two different Co^{II} ions.

EPR analyses established a positive sign of *D* and a larger perpendicular component of the *g*-tensor than the parallel one for all complexes. All of them exhibit low rhombicity, as observed in the complexes bearing carboxylate groups in Chapter III and other works,[18] except **10-o** which exhibited high rhombicity as a polycrystalline solid sample, but no so high in the frozen solution spectra. Extended π−π interactions in the structure might cause a high distortion, being the origin of this experimental feature. Indeed, previous continuous shape measures proved that this compound has the most distorted coordination polyhedron. Small differences between the *E*/*D* ratio and *g*-tensor are found between the open and closed isomers in solid state **10-o** *vs* **10-c**, although these differences are not appreciable in the frozen solution. Therefore, the expected increase in the magnetic interaction through the conjugated π ligand (for the closed-ring isomer) after the cyclisation reaction is negligible or almost negligible, not being detected with this technique.

Theoretical values of *g* components, *D* and *E*/*D* ratio obtained from CASSCF/NEVPT2 calculations agree with those found from experimental data (magnetometry and EPR spectroscopy), as shown in Table V.5. Like the other cobalt(II) complexes studied in this dissertation, *D* value is primarily determined by the first two excited quartet states (Table A.31). CASSCF/NEVPT2 results for the Co2 atom in **9-o** are not shown, due to the uncommon atomic disposition of the disordered carboxylate group.

Table V.2. Spin Hamiltonian parameters for **9–10** obtained from the first-order SOC model.

Compound	λ (cm^{-1})	Δ (cm^{-1})	α	TIP × 10^6 ($cm^3\ mol^{-1}$)	$F \times 10^6$
9-o	−115.4	−154.5	1.02	3208	7.99
9-c	−104.2	−153.5	1.07	2900	15.9
10-o	−106.1	−133.4	1.05	3130	99.6
10-c	−100.0	−141.0	1.05	3400	11.3

F is the agreement factor defined as $F = \sum[P_{exp} - P_{calcd}]^2/\sum[P_{exp}]^2$

Table V.3. Spin Hamiltonian parameters for **9–10** obtained from the zfs model.

Compound	D (cm^{-1})	$\lvert E/D \rvert$	$g_{\perp}$	$g_{\parallel}$	g_{av}	TIP × 10^6 (cm^3 mol^{-1})	$F \times 10^5$
9-o	+56.53	0.122	2.51	2.16	2.39	2290	1.11
9-c	+59.50	0.080	2.59	2.04	2.41	1530	1.78
10-o	+42.01	0.148	2.48	2.13	2.36	3050	3.38
10-c	+48.34	0.216	2.54	2.16	2.41	2120	3.70

F is the agreement factor defined as $F = \sum[P_{exp} - P_{calcd}]^2/\sum[P_{exp}]^2$

Table V.4. Values for the energy gap between the ground and first excited Kramers doublets in cm^{-1} from magnetometry (SOC and zfs approaches) and CASSCF/NEVPT2 calculations.

Technique	Magnetometry: SOC model	Magnetometry: zfs model	CASSCF/NEVPT2[a]
9-o	123.7	115.6	115.9/130.3
9-c	117.3	86.8	142.1/124.6
10-o	115.3	120.2	117.3/130.4
10-c	109.0	103.3	–

[a] Co1/Co2 atoms.

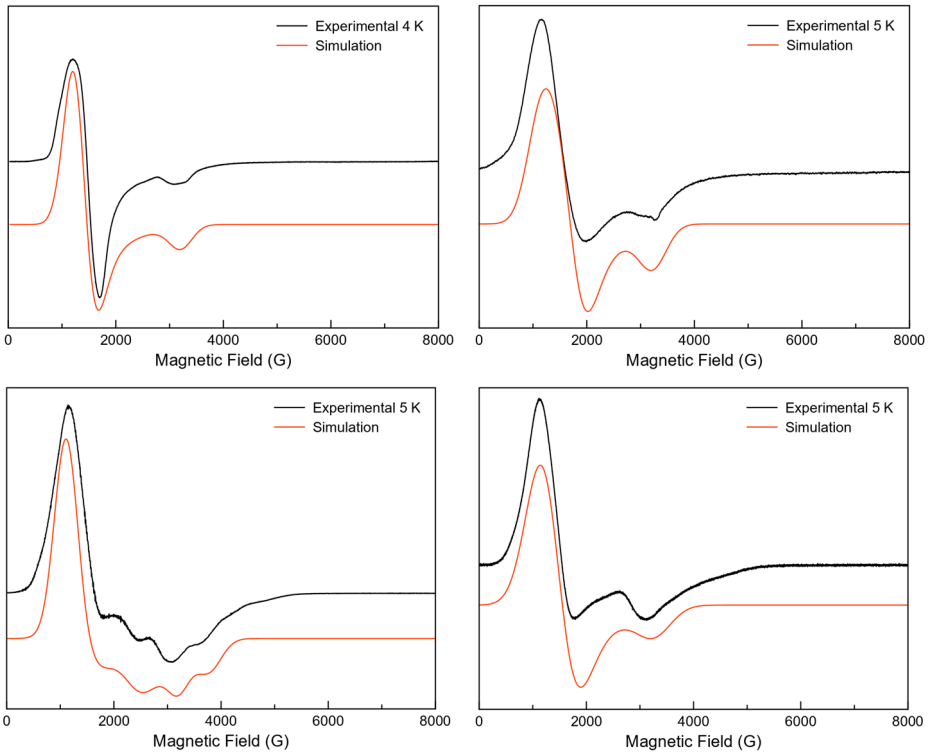

Figure V.8. X-band EPR in the 0–8 kOe range for polycrystalline powdered samples of **9-o** (top left), **9-c** (bottom left) and **10-c** (bottom right) at ~5 K. The simulated red curves were obtained by using the parameters on text and Table II.5.

Table V.5. Spin Hamiltonian parameters for **9–10** obtained from different techniques.

Technique	D (cm^{-1})	E/D	g_x	g_y	g_z or $g_{\|\|}$	$g_\perp$[b]	g_{av}
9-o							
CASSCF/NEVPT2[a]	+58.09/+63.71	0.060/0.122	2.51/2.49	2.59/2.66	2.02/2.00	2.55/2.58	2.37/2.38
Solid EPR	>> +20	0.002	2.53	2.58	2.11	2.56	2.41
Solution EPR	–	–	–	–	–	–	–
9-c							
CASSCF/NEVPT2[a]	+65.19/+58.84	0.260/0.223	2.38/2.41	2.75/2.69	2.00/2.01	2.57/2.56	2.38/2.37
Solid EPR	>> +20	0.129	2.46	2.50	2.18	2.48	2.38
Solution EPR	>> +20	0.070	2.48	2.53	2.17	2.51	2.40
10-o							
CASSCF/NEVPT2[a]	+54.40/+59.93/ 63.47	0.250/0.131/ 0.160	2.35/2.48/ 2.46	2.68/2.64/ 2.68	2.02/2.04/ 2.00	2.52/2.56/ 2.57	2.35/2.39/ 2.38
Solid EPR	>> +20	0.027/0.266	2.32/2.52	2.69/2.58	2.09/2.17	2.51/2.55	2.37/2.43
Solution EPR	>> +20	0.145	2.40	2.62	2.08	2.52	2.37
10-c							
CASSCF/NEVPT2[a]	–	–	–	–	–	–	–
Solid EPR	>> +20	0.061	2.51	2.56	2.07	2.53	2.38
Solution EPR	>> +20	0.145	2.40	2.62	2.08	2.52	2.37

[a] Co1/ Co2a/Co2b atoms.[b] The perpendicular component of g is obtained by the formula $g_\perp = \sqrt{\frac{g_x^2+g_y^2}{2}}$.

V.3.4 Ac-magnetic properties

Ac-magnetic susceptibilities were recorded in 2−10 K temperature range as a function of the applied magnetic field (H_{dc}, 0.5−5.0 kOe) and frequency (0.1−10.0 kHz) for the open and closed-ring isomers of **9-o/c** and **10-o/c**. No χ_M'' signals were observed for **9**–**10** in the absence of a magnetic field. However, χ_M' and χ_M'' signals emerge at $H_{dc} > 0$ with a χ_M'' maximum below ~3 and 3.5 K. The χ_M' and χ_M'' *vs* ν data were analysed together, following the generalised Debye model with the DynVPMag program, resulting in a set of values for the already described τ, E_a, and α parameters.[39,40] With this model, the χ_M' and χ_M'' curves are analysed through equations (3−6) from Chapter II. The obtained theoretical curves have a good match with the experimental χ_M' and χ_M'' *vs* ν data and the Cole-Cole plots (Figures V.9–12 and A.96–111). All complexes show a secondary incipient process at low frequencies and temperatures for $H_{dc} \geq 2.5$ kOe (**9-c** only at $H_{dc} = 5.0$ kOe), which is manifested in the rise of a second semicircle in Cole-Cole plots. Figure V.13 show the thermal dependences of the relaxation times, Arrhenius plots, for the primary process for each compound.

Figures A.112-115 show that the incipient process is ruled by an intra-Kramers mechanism, except for **10-o**, which requires an additional thermally assisted relaxation competing with the IK one (see Tables A33–36).

For the primary relaxation, Arrhenius plots were analysed with several combinations of possible mechanisms governing the slow magnetisation relaxation, but trying to find a

unique and suitable model that covers the whole range of temperatures and fields. A model combining Raman plus direct mechanisms (Raman + D, $\frac{1}{\tau} = CT^n + AT$) gave inconsistent results at different magnetic fields for all compounds. This model can only reproduce data at low or high temperature, but not both at the same time. In such cases, n ranges from 2 to 8, which points to a domain of Raman relaxations governed by acoustic and optical phonons depending on temperature. Therefore, the combination of competing direct, acoustic and optic Raman mechanisms is an alternative option that has not been investigated so far. Then, this study has been applied for these compounds.

Sometimes the multiple Raman analysis from Arrhenius data carries certain difficulties (Table A.32). A more efficient way of operating is based on working on ln(τ) *vs* ln(T) data and plots. If the Raman mechanism is predominant, these graphs will show a linear dependence whose slope is $-n$. This treatment also reports the operability of a direct mechanism if n is 1. These graphs for the two isomers of **9** and **10** allow to immediately conclude that a direct mechanism must be discarded, of the presence of two competing Raman relaxations ($\frac{1}{\tau} = C_{LT}T^{n_{LT}} + C_{HT}T^{n_{HT}}$) and the operability of an IK mechanism on a few occasions (Figures V.14 and A.116–119, Tables A.37–40). Unfortunately, the moderate quality of the data, and the limited operating ranges of each mechanism, lead to high standard deviations in the estimations of the parameters that govern each relaxation mechanism. Therefore, or it is not possible to distinguish between Raman processes operating at high and low temperatures, obtaining unrealistic intermediate results. In the cases where these inconvenient do not appear, it could be established that while the relaxation assisted by optical photons predominates at lower temperatures (n_{LT} ~2), acoustic photons play a relevant role at higher temperatures (n_{HT} ~8).

Some Arrhenius plots, mainly at high H_{dc}, show the presence of an IK relaxation although in the past it has been described as quantum tunnelling arising from the zfs of the metal ion, which is not feasible for $D > 0$. Attempts to simulate Arrhenius plots combining an IK relaxation with other Raman or direct ones have failed, and they are only successful when the data is limited to the low-temperature region and moderate or high H_{dc}. In such cases, the found values of n range between 2 and 3 corresponding to optical phonon-assisted relaxations, which are more atypical than the acoustic ones. In previous chapters, we have argued that these relaxations could be governed by thermally assisted processes (TA, $\frac{1}{\tau} = \frac{1}{\tau_0} e^{-\frac{E_a}{k_B T}}$) in, at least, some temperature regions. These assisted processes are linked to molecular (or even network) vibrational modes, since an Orbach mechanism is ruled out in systems with $D > 0$. Also, the presence of several of these competing processes has already been discussed, *i.e.*, an increase in temperature allows to populate other more energetic vibrational modes or some overtones of the first mode. Therefore, the results of this applied strategy are discussed below.

The Arrhenius plots of the two isomers of **9-o/c** and **10-o/c** can be simulated below 5 K with a model that combines IK and TA relaxations (TA_{LT} + IK, $\frac{1}{\tau} = \frac{1}{\tau_0} e^{-\frac{Ea}{k_B T}} + \frac{1}{\tau_{0,IK}}$). However, an additional TA process is required to reproduce the data in the whole temperature regime (2TA + IK, $\frac{1}{\tau} = \frac{1}{\tau_{0,LT}} e^{-\frac{Ea_{LT}}{k_B T}} + \frac{1}{\tau_{0,HT}} e^{-\frac{Ea_{HT}}{k_B T}} + \frac{1}{\tau_{0,IK}}$). This last model provides the most coherent results, with smaller standard deviations than the multiple Raman relaxations model, despite the fact that sometimes little amounts of data is available in that region with good quality. The performed analyses by combining two TA and an IK mechanisms afford similar energy barriers between the isomers for the primary process, being E_{a1} ~6–11 cm^{-1}. In general, E_{a2} values are between 28–36 cm^{-1}, but in some cases and for particular H_{dc}, an increase of the activation energy to 46–51 cm^{-1} occurs. In such cases and as seen in Chapter II, the TA processes at high and low temperatures cannot be distinguished or another additional process begins to be operational. However, these cannot be discerned from the previous ones leading to average of the intermediate and high E_a values.

The incipient process found by deconvolution of the experimental data using a model with two generalised Debye relaxations provides insufficient quality data. Then, it can only be concluded that it corresponds to an IK mechanism with τ values around 10^{-2}–10^{-3} s.

Even though there is a thermal dependence on α values, these ones are below 0.3 in the 2 to 10 K temperature range for the primary process of **9-o/c** and **10-o/c**, discarding any signs of spin glass behaviour (see Figures V.9–12 and A.96–115). These plots show some cycles in which, as expected, α decreases with increasing temperature in a region where a mechanism is predominant. When another competing relaxation mechanism appears, α increases until reaching the temperature region in which the latter becomes the main one, and the cycle begins again. These complexes exhibit similar coordination spheres, deviation from octahedral polyhedron, and crystallisation molecules with two toluene molecules each. Then, the main differences might arise from the different phenanthroline derivative ligand used in **9-o/c** and **10-o/c**. These probably cause small differences in the mechanisms involved at low temperatures, but these differences increase at higher temperatures, being related to lattice phonon relaxations.

Dithienylethene ligands induce modifications on the coordination geometry of the metal ions and intramolecular metal ions distances.[41] In **9** and **10**, with large positive zfs, since the relaxation mechanisms are not based in QTM, the photoswitching ligand induces slight changes in E_a. However, these small changes are not enough for a switch on/off of the magnetic properties of the complex. Probably, measurements in solution can be of especial help to avoid the packing effects or magnetic dipolar to unravel the dynamics of these magnetic properties.[41]

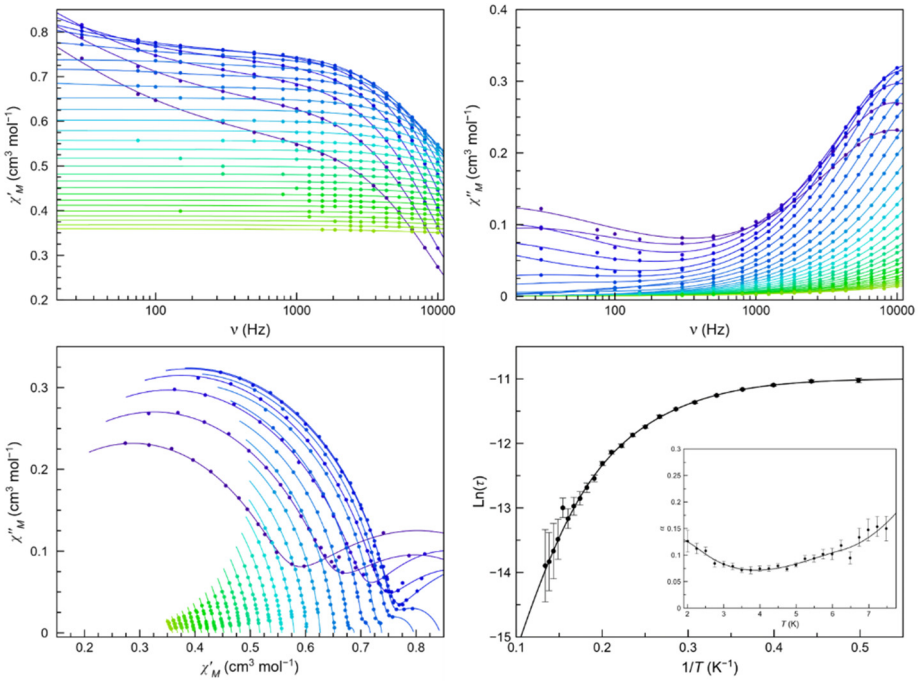

Figure V.9. Frequency dependence of χ_M' (top left) and χ_M'' (top right), Cole-Cole plots (bottom left) and Arrhenius plots of **9-o** (bottom right) in a dc-applied static field of 5.0 kOe with ± 0.005 kOe oscillating field in the temperature range of 2.0–9.0 K (purple to green gradient). Thermal dependence of α is included on the bottom right figure as an inset, where the black line are eye-guides. Standard deviation appears as vertical error bars.

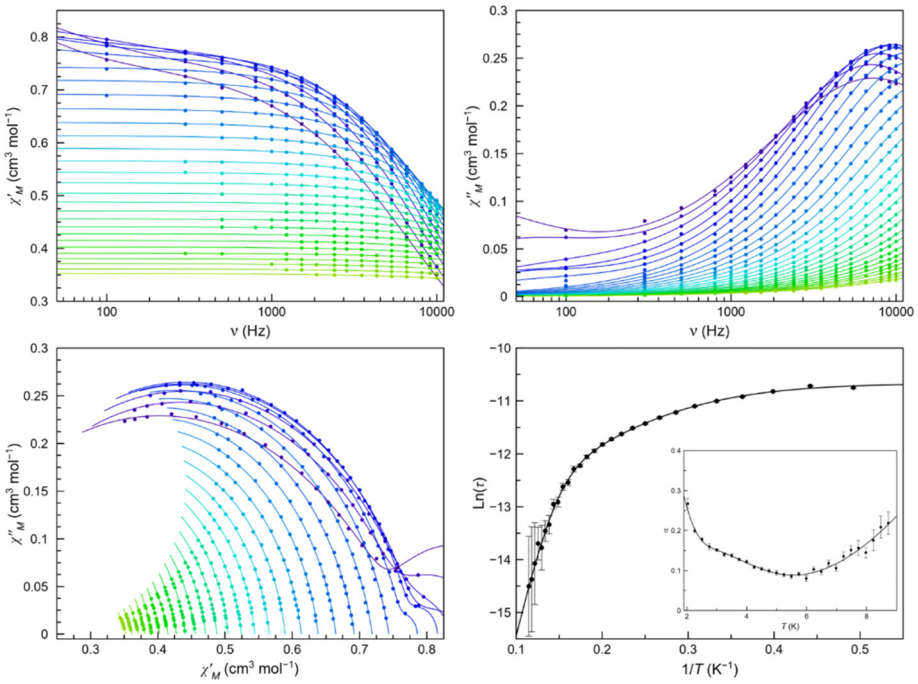

Figure V.10. Frequency dependence of χ_M' (top left) and χ_M'' (top right), Cole-Cole plots (bottom left) and Arrhenius plots of **9-c** (bottom right) in a dc-applied static field of 5.0 kOe with ± 0.005 kOe oscillating field in the temperature range of 2.0–9.0 K (purple to green gradient). Thermal dependence of α is included on the bottom right figure as an inset, where the black line are eye-guides. Standard deviation appears as vertical error bars.

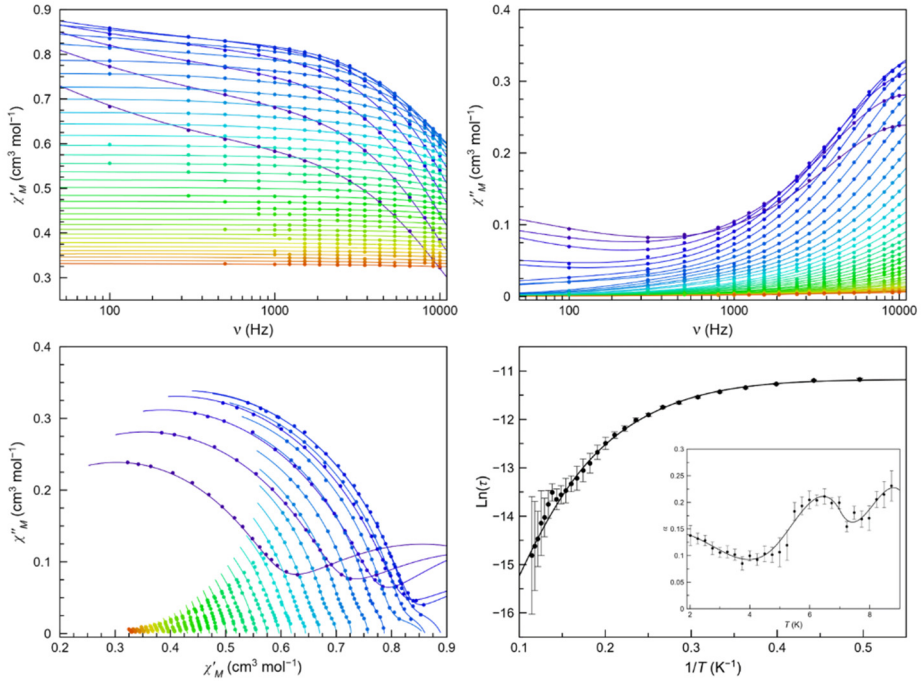

Figure V.11. Frequency dependence of χ_M' (top left) and χ_M'' (top right), Cole-Cole plots (bottom left) and Arrhenius plots of **10-o** (bottom right) in a dc-applied static field of 5.0 kOe with ± 0.005 kOe oscillating field in the temperature range of 2.0–11.0 K (purple to red gradient). Thermal dependence of α is included on the bottom right figure as an inset, where the black line are eye-guides. Standard deviation appears as vertical error bars.

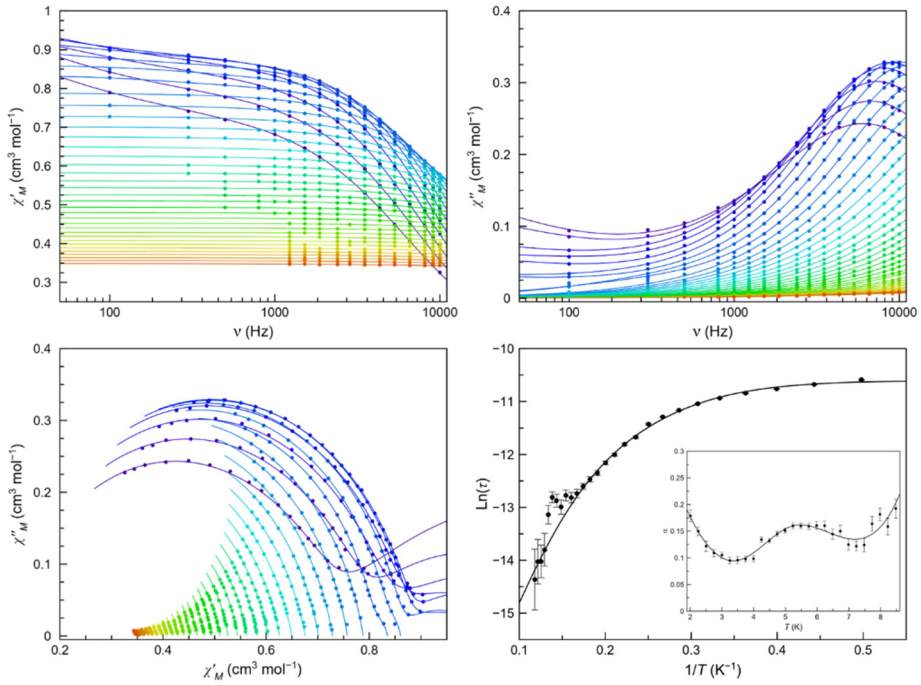

Figure V.12. Frequency dependence of χ_M' (top left) and χ_M'' (top right), Cole-Cole plots (bottom left) and Arrhenius plots of **10-c** (bottom right) in a dc-applied static field of 5.0 kOe with ± 0.005 kOe oscillating field in the temperature range of 2.0–11.0 K (purple to red gradient). Thermal dependence of α is included on the bottom right figure as an inset, where the black line are eye-guides. Standard deviation appears as vertical error bars.

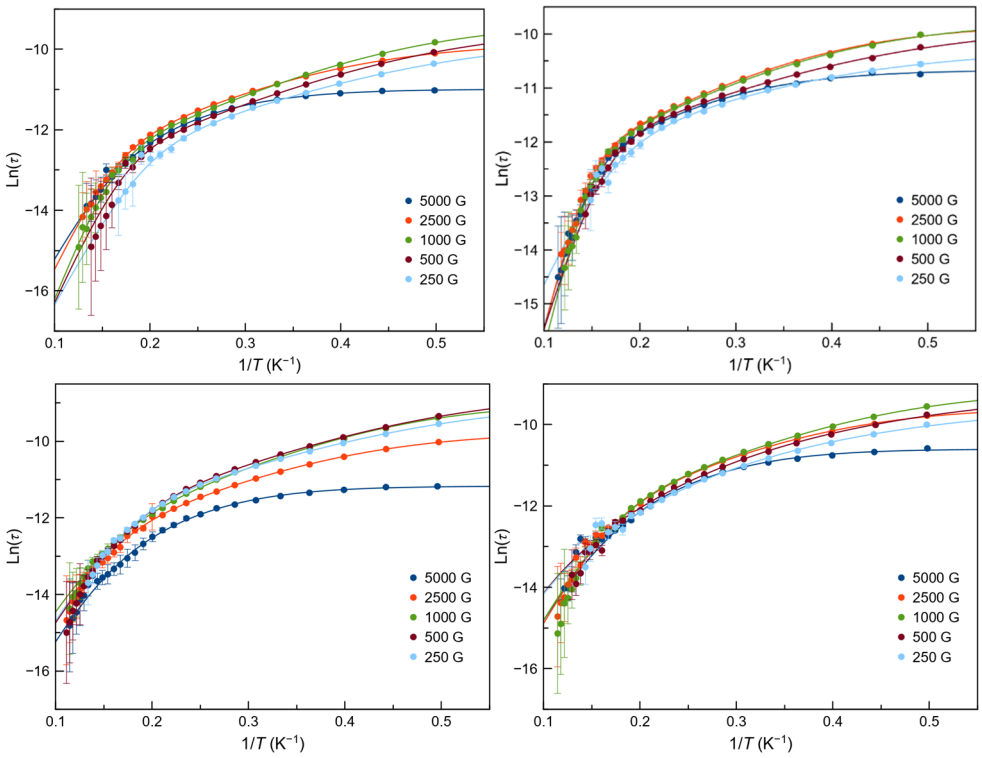

Figure V.13. Arrhenius plots for the main process of **9-o** (top left), **9-c** (top right), **10-o** (bottom left) and **9-c** (bottom right) under 0.25–5.0 kOe applied static field. The solid lines are the best fit-curves with two thermally activated plus one intra-Kramers mechanisms. Standard deviations appear as vertical error bars.

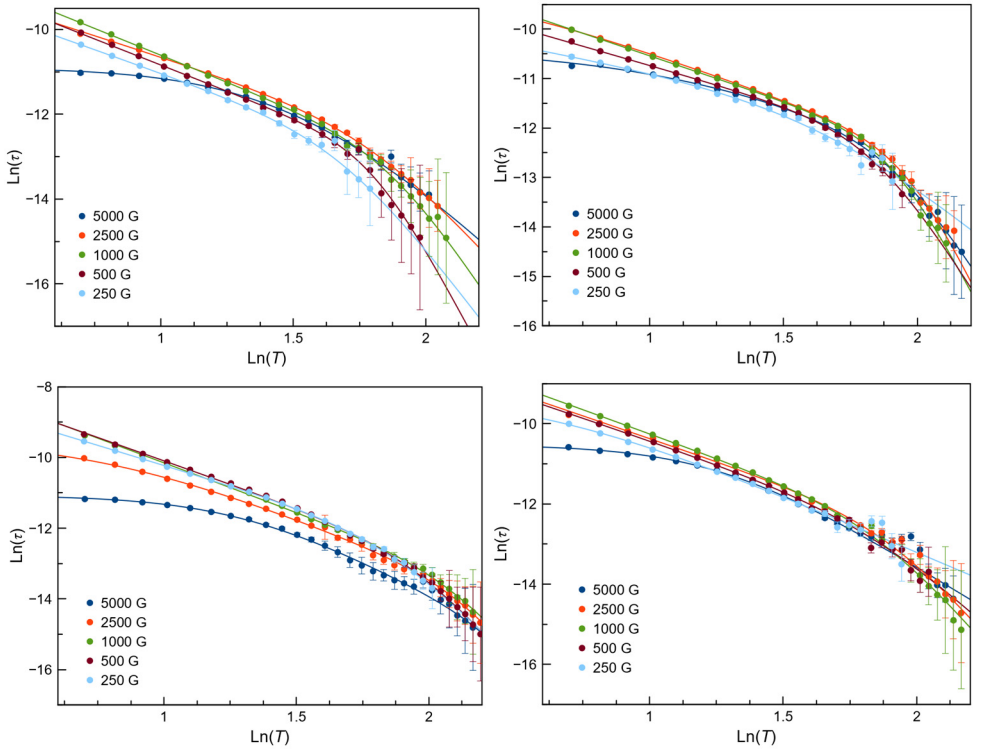

Figure V.14. Ln(τ) *vs* ln(T) plots for the main process of **9-o** (top left), **9-c** (top right), **10-o** (bottom left) and **9-c** (bottom right) under 0.25–5.0 kOe applied static field. The solid lines are the best fit-curves with a combination of Raman and intra-Kramers mechanisms. Standard deviations appear as vertical error bars.

V.3.5 Conclusions

In this Chapter, dinuclear cobalt(II) complexes, $\{[Co(Me_xphen)_2]_2(Sw\text{-}CO_2)\}(ClO_4)_2$ (x = 1, 2) bearing a photoswitchable ligand have been synthesised. These have been proved to exhibit photoswitchable properties in solution, with almost no fatigue upon light irradiation after finding their proper conditions, but these changes are not present in solid state experiments.

All complexes display large and positive magnetic *D* anisotropy. Both Co^{II} ions behave as one unique cobalt(II) centre in solid state, except for **10-o**, despite the crystal structures show two distinct cobalt(II) environments. The capability of discerning the two Co^{II} ions in **10-o**, only in solid state, might arise from its crystalline structure that displays the shortest π−π interaction bond, causing small distortions on the zfs. Magnetic and EPR studies, and theoretical calculations, confirms these results. Moreover, all complexes exhibit single-ion magnet (SIM) behaviour under dc-magnetic field with two relaxation processes at high H_{dc}. A detailed analysis of the main process reveal that two thermally activated mechanisms together with an intra-Kramers mechanism are responsible of their relaxation dynamics. The values of the parameters describing this model are comparable to those observed for the dinuclear cobalt(II) complexes presented in Chapter III. However, satisfactory results are also achieved with a model that describes the dynamic magnetic behaviour in these compounds through acoustic and optical phonons as in Chapter IV.

Future work regarding the multifunctional magnetic properties for these compounds will evaluated as potential photoswitchable qu-gates with pulsed EPR spectroscopy.

V.4 References

1. Gatteschi, D., Sessoli, R. & Villain, J. *Molecular Nanomagnets*. (Oxford University Press, 2006).
2. Rinehart, J. D. & Long, J. R. Exploiting single-ion anisotropy in the design of f-element single-molecule magnets. *Chem. Sci.* **2**, 2078 (2011).
3. Woodruff, D. N., Winpenny, R. E. P. & Layfield, R. A. Lanthanide Single-Molecule Magnets. *Chem. Rev.* **113**, 5110–5148 (2013).
4. Dey, A., Kalita, P. & Chandrasekhar, V. Lanthanide(III)-Based Single-Ion Magnets. *ACS Omega* **3**, 9462–9475 (2018).
5. Craig, G. A. & Murrie, M. 3D Single-Ion Magnets. *Chem. Soc. Rev.* **44**, 2135–2147 (2015).
6. Feng, M. & Tong, M.-L. Single Ion Magnets from 3d to 5f: Developments and Strategies. *Chem. - A Eur. J.* **24**, 7574–7594 (2018).
7. Xu, M.-X. *et al.* Single-Crystal Study of a Low Spin Co(II) Molecular Qubit: Observation of Anisotropic Rabi Cycles. *Inorg. Chem.* **58**, 2330–2335 (2019).
8. Shiddiq, M. *et al.* Enhancing coherence in molecular spin qubits via atomic clock transitions. *Nature* **531**, 348–351 (2016).
9. Troiani, F. & Affronte, M. Molecular spins for quantum information technologies. *Chem. Soc. Rev.* **40**, 3119 (2011).
10. Aguilà, D. *et al.* Heterodimetallic [LnLn'] lanthanide complexes: Toward a chemical design of two-qubit molecular spin quantum gates. *J. Am. Chem. Soc.* **136**, 14215–14222 (2014).
11. Ferrando-Soria, J. *et al.* A modular design of molecular qubits to implement universal quantum gates. *Nat. Commun.* **7**, 11377 (2016).
12. Graham, M. J., Zadrozny, J. M., Fataftah, M. S. & Freedman, D. E. Forging Solid-State Qubit Design Principles in a Molecular Furnace. *Chem. Mater.* **29**, 1885–1897 (2017).
13. Moreno-Pineda, E., Godfrin, C., Balestro, F., Wernsdorfer, W. & Ruben, M. Molecular spin qudits for quantum algorithms. *Chem. Soc. Rev.* **47**, 501–513 (2018).
14. Nakamura, S. *et al.* Theoretical investigation on photochromic diarylethene: A short review. *J. Photochem. Photobiol. A Chem.* **200**, 10–18 (2008).
15. Massaad, J. *et al.* Gated Photochromism and Acidity Photomodulation of a Diacid Dithienylethene Dye. *Chem. - A Eur. J.* **18**, 6568–6575 (2012).
16. Uber, J. S. *et al.* Molecules Designed to Contain Two Weakly Coupled Spins with a Photoswitchable Spacer. *Chem. - A Eur. J.* **23**, 13648–13659 (2017).
17. Wang, J., Hou, L., Browne, W. R. & Feringa, B. L. Photoswitchable intramolecular through-space magnetic interaction. *J. Am. Chem. Soc.* **133**, 8162–8164 (2011).
18. Vallejo, J. *et al.* Coligand Effects on the Field-Induced Double Slow Magnetic Relaxation in Six-Coordinate Cobalt(II) Single-Ion Magnets (SIMs) with Positive Magnetic Anisotropy. *Inorg. Chem.* **58**, 15726–15740 (2019).
19. Zhang, J.-H. *et al.* Coordinative-to-covalent transformation, isomerization dynamics, and logic gate application of dithienylethene based photochromic cages. *Chem. Sci.* **11**, 8885–8894 (2020).
20. Lucas, L. N., Jong, J. J. D. de, Esch, J. H. van, Kellogg, R. M. & Feringa, B. L. Syntheses of Dithienylcyclopentene Optical Molecular Switches. *European J. Org. Chem.* **2003**, 155–166 (2003).
21. Stoll, S. & Schweiger, A. EasySpin, a comprehensive software package for spectral simulation and analysis in EPR. *J. Magn. Reson.* **178**, 42–55 (2006).

22. SAINT, Version 6.45, Bruker Analytical X-ray Systems, M. SAINT. (2012).

23. Sheldrick, G. M. *SADABS Program for absorption correction, version 2.10, Analytical X-ray Systems; Madison,WI,*. (2003).

24. Sheldrick, G. M. SHELXS97 and SHELXL97. Program for Crystal Structure Solution and Refinement. (1997).

25. Sheldrick, G. M. SHELXT – Integrated space-group and crystal-structure determination. *Acta Crystallogr. Sect. A Found. Adv.* **71**, 3–8 (2015).

26. Sheldrick, G. M. A short history of SHELX. *Acta Crystallogr. Sect. A Found. Crystallogr.* **64**, 112–122 (2008).

27. Spek, A. L. Structure validation in chemical crystallography. *Acta Crystallogr. Sect. D Biol. Crystallogr.* **65**, 148–155 (2009).

28. Angeli, C., Cimiraglia, R., Evangelisti, S., Leininger, T. & Malrieu, J.-P. Introduction of n -electron valence states for multireference perturbation theory. *J. Chem. Phys.* **114**, 10252–10264 (2001).

29. Eichkorn, K., Weigend, F., Treutler, O. & Ahlrichs, R. Auxiliary basis sets for main row atoms and transition metals and their use to approximate Coulomb potentials. *Theor. Chem. Accounts Theory, Comput. Model. (Theoretica Chim. Acta)* **97**, 119–124 (1997).

30. Vancoillie, S. *et al.* Multireference Ab Initio Calculations of g tensors for Trinuclear Copper Clusters in Multicopper Oxidases. *J. Phys. Chem. B* **114**, 7692–7702 (2010).

31. Hathaway, B. J. & Underhill, A. E. 592. The infrared spectra of some transition-metal perchlorates. *J. Chem. Soc.* 3091 (1961). doi:10.1039/jr9610003091

32. Llunell, M., Casanova, D., Cirera, J., Alemany, P. & Alvarez, S. SHAPE v2.1. (2013).

33. Baca, S. G. *et al.* From Mono- and Dinuclear to Polynuclear Cobalt(II) and Cobalt(III) Coordination Compounds Based ono-Phthalic Acid and 2,2′-Bipyridine: Synthesis, Crystal Structures, and Properties. *Eur. J. Inorg. Chem.* **2005**, 3118–3130 (2005).

34. Cano, J. *et al.* Ability of terephthalate (ta) to mediate exchange coupling in ta-bridged copper(II), nickel(II), cobalt(II) and manganese(II) dinuclear complexes. *J. Chem. Soc. Dalt. Trans.* 1915–1924 (1997). doi:10.1039/A700323D

35. Herder, M. *et al.* Improving the Fatigue Resistance of Diarylethene Switches. *J. Am. Chem. Soc.* **137**, 2738–2747 (2015).

36. Lucas, L. N., Jong, J. J., Esch, J. H., Kellogg, R. M. & Feringa, B. L. Syntheses of Dithienylcyclopentene Optical Molecular Switches. *Eur. J. Org. Chem.* **2003**, 155–166 (2003).

37. Ern, J. *et al.* Ring-Opening and -Closure Reaction Dynamics of a Photochromic Dithienylethene Derivative. *J. Phys. Chem. A* **106**, 1654–1660 (2002).

38. Chilton, N. F., Anderson, R. P., Turner, L. D., Soncini, A. & Murray, K. S. PHI: A powerful new program for the analysis of anisotropic monomeric and exchange-coupled polynuclear d - and f -block complexes. *J. Comput. Chem.* **34**, 1164–1175 (2013).

39. Cole, K. S. & Cole, R. H. Dispersion and Absorption in Dielectrics I. Alternating Current Characteristics. *J. Chem. Phys.* **9**, 341–351 (1941).

40. Carbonell-Vilar, J. M. & Cano, J. Dyn-VPMag. *University of Valencia* (2019).

41. Fetoh, A. *et al.* Photo-activation of Single Molecule Magnet Behavior in a Manganese-based Complex. *Sci. Rep.* **6**, 23785 (2016).

Chapter VI

Ferrocene-based cobalt(II) redox switches

Two ferrocene-based cobalt(II) complexes were synthesised. These, are composed by a ferrocenecarboxylate derivatives forming dinuclear and trinuclear compounds presenting slow-magnetic relaxation of the magnetisation. The ferrocene moiety exhibits reversible redox behaviour in both compounds and the dinuclear $Co^{II}Fe^{II}$ complex can be oxidised to a new $Co^{II}Fe^{III}$ dinuclear complex by using the magic blue oxidiser. The magnetic properties of the oxidised compound are studied and a magnetic exchange coupling between the $Co^{II}Fe^{III}$ ions is detected, which cancel the SIM behaviour for the complex. Thus, these complexes can be used to switch on/off the slow-magnetic relaxation of the magnetisation of the Co^{II} ion through magnetic exchange interactions. The non-oxidised compounds exhibits slow-magnetic relaxation of the magnetisation, assigned to a combination of competing optical and acoustic Raman mechanisms or to several thermally activated and intra-Kramers mechanisms.

VI.1 Introduction

The discovery of single-molecule magnets (SMMs) in the 90's was a considerable achievement in the field of molecular magnetism,[1] because of their potential applications in molecular spintronics, data storage devices and quantum computing.[2–4] These molecules exhibit slow magnetic relaxation from a purely molecular origin. It was believed that their performance depended on the magnetic anisotropy and the total spin of the molecule. In recent years, new strategies have emerged to control the magnetic anisotropy efficiently with the synthesis of mononuclear transition metal or lanthanide complexes, the so-called single-ion magnets (SIMs).[5–8] In this way, as there is only one paramagnetic centre, the sum of local magnetic anisotropies are not cancelled as it often occurs in polynuclear SMMs complexes.[9]

The next step would be to obtain switchable SMMs. In these, the magnetic behaviour can be reversibly switched on/off with a controlled external stimulus, such an electrical current, an electrical voltage or an electrochemical potential.[10] Hence, the archetypical terbium(III)- and dysprosium(III)-bis(phthalocyaninato) complexes, and their polyalkoxy-substituted derivatives, afford unique examples of electro-switchable mononuclear lanthanide SMMs because of the redox-active nature of the phthalocyanine ligands.[11–13] In their mono- and di-radical ligand-containing terbium(III) species obtained after consecutive oxidation, a progressively decrease of the magnetic relaxation rate occurs upon the subsequent incorporation of the π-radical ligands (S_{rad} = 1/2). Moreover, the singly oxidised π-radical ligand form of the parent mononuclear terbium SMM exhibits a resonance Kondo peak in the electrical conductance at zero-bias voltage typical of a spin transistor-like behaviour when adsorbed on a gold surface.[14]

Until now, however, only a few electroactive SMMs based on transition-metal complexes have been reported.[15–20] One strategy to achieve this goal can be related with the employment of redox-active ligands[19–21] or metalloligands.[15–18] Ferrocene is a very well-known redox-active organometallic compound with a diamagnetic low-spin (S = 0) Fe^{II} ion, which can be easily reversibly oxidised to the paramagnetic low-spin (S = 1/2) Fe^{III} ion. Besides, it can easily be functionalised with diverse coordinating donor groups to build more complex structures.[22–24]

Recently, a family of mononuclear octahedral cobalt(II) SMMs has been synthesised and studied in our group with N_2 donor ligands such as 2,9-dimethyl-1,10-phenanthroline (Me_2phen) or 6,6'-dimethyl-2,2'-bipyridine (Me_2bpy) and diverse coligands like water, thiocyanate, or benzoate.[25–27] We observed how slight differences in the coordination sphere of the Co^{II} ion could tune the zero-field splitting magnitude and sign (zfs). In this work, it is shown the use of the ferrocenecarboxylic acid (Fc-CO_2H) and 1,1'-

ferrocenedicarboxylic acid (Fc-$(CO_2H)_2$) as redox-active metalloligands with such cobalt(II) SIMs (Scheme VI.1). Herein, we report a dinuclear $Fe^{II}Co^{II}$ and a trinuclear $Fe^{II}Co^{II}_2$ compounds with formulas $[Co(Me_2phen)_2Fc\text{-}CO_2](ClO_4)\cdot Et_2O$ (**11**) and $\{[Co(Me_2phen)_2]_2Fc\text{-}(CO_2)_2\}(ClO_4)_2\cdot 2Et_2O\cdot 2AcN$ (**12**). Their synthesis and the molecular structures, together with electrochemical, magnetic and HFEPR studies are described in detail.

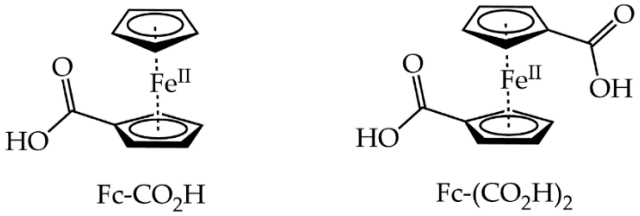

Scheme VI.1. Ferrocene-carboxylic derivative ligands used in this chapter.

VI.2 Experimental section

VI.2.1 Materials

All chemicals were obtained from commercial sources and used as received.

Caution! Perchlorate salts are potentially explosive. They should be used in small quantities and should be treated with the utmost care at all times.

VI.2.2 Syntheses

Pip[Fc-(CO_2)] and (Pip)$_2$[Fc-(CO_2)$_2$]. To a solution of ferrocene-carboxylic acid (Fc-CO_2H) or 1,1'-ferrocenedicarboxylic acid (Fc-(CO_2H)$_2$) (2 mmol, 1 eq) in methanol, piperidine (4 mmol and 8 mmol, respectively) was added.

[Co(Me$_2$phen)$_2$(Fc-CO_2)](ClO_4)·Et$_2$O (11). To a solution of Co(ClO_4)$_2$·6H_2O (183 mg, 0.5 mmol, 1 eq) and Me$_2$phen (217 mg, 1 mmol, 2 eq) in AcN was added a solution of Pip[Fc-CO_2] (0.5 mmol) in AcN/MeOH (1:1). The reaction mixture was stirred for 5 minutes and filtered. Orange rectangular-shaped single crystals suitable for X-ray were obtained by slow diffusion of diethyl ether into the solution. Yield: 346 mg (81%). IR (ν_{max}/cm^{-1}): 3483(br, s), 3065(vw), 3025(vw), 2971(vw), 2926(vw), 2853(vw), 1637(m), 1623(m), 1592(s), 1565(w), 1526(m), 1510(m), 1497(s), 1392(m), 1360(m), 1296(m), 1225(m), 1205(w), 1088(s), 940(w), 862(s), 814(w), 772(w), 734(w), 681(vw), 654(vw), 623(m), 551(m), 507(w).

{[Co(Me$_2$phen)$_2$]$_2$[Fc-(CO_2)$_2$]}(ClO_4)$_2$·2Et$_2$O·2AcN (12). A solution of (Pip)$_2$[Fc-(CO_2)$_2$] (225 mg, 0.5 mmol) in AcN with some ml of methanol was added to a solution of Co(ClO_4)$_2$·6H_2O (368 mg, 1 mmol) and Me$_2$phen (434 mg, 2 mmol) in AcN. Orange single crystals suitable for X-ray were obtained by slow diffusion of diethyl ether into the solution. Yield: 506 mg (87%). IR (ν_{max}/cm^{-1}): 3435(br, w), 3068(vw), 3025(vw), 2973(vw), 2925(vw), 2855(vw), 1624(w), 1593(s), 1565(m), 1534(s), 1498(vs), 1422(m), 1392(s), 1358(s), 1294(w), 1205(vw), 1155(m), 1093(vs), 1029(w), 996(vw), 938(vw), 861(m), 801(m), 772(w), 733(m), 662(w), 655(w), 623(m), 552(w), 505(w), 456(vw), 437(vw).

[Co(Me$_2$phen)$_2$(Fc-CO_2)]$_2$(ClO_4)·$SbCl_6$ (11-ox). To a solution of **11** (439 mg, 0.5 mmol, 1eq) in DCM was added tris(4-bromophenyl)ammoniumyl hexachloroantimonate (408 mg, 0.5 mmol, 1 eq). The reaction mixture was stirred for 10 minutes under an argon atmosphere. After addition of diethyl ether, the green-bluish solid was collected by filtration. Yield: 346 mg (81%). IR (ν_{max}/cm^{-1}): 3389(br, m), 3055(w), 2916(vw), 2865(vw), 1638(m), 1625(s), 1062(m), 1568(vw), 1533(w), 1500(w), 1465(w), 1384(w), 1361(m), 1282(w), 1224(w), 1156(m), 1110(s), 1086(vs), 1031(vw), 875(m), 785(vw), 728(vw), 636(w), 546(w). EDX analysis: Co/Fe 1:1; Cl/Sb 7:1.

VI.2.3 Physical measurements

Infrared spectra (4000–400 cm^{-1}) were recorded on a Nicolet 5700 spectrophotometer as KBr pellets. Elemental analyses (C, H, N) were performed at the Microanalytical Service of the Universitat de València. Energy Dispersive X-ray (EDX) analyses were performed without metallisation on an XLS-30 microscope operating at a voltage of 20 kV in SCSIE, Universitat de València.

X-ray powder diffraction (XRPD) patterns were recorded on a Panalytical Empyrean X-ray diffractometer by using Cu Kα radiation (λ = 1.5406 Å), in which the X-ray tube was operated at 45 kV and 40 mA ranging from 2 to 40°. The XRPD data was background corrected with the *HighScore Plus* software.

Cyclic voltammetry measurements were carried out at 25 °C using an AUTOLAB PGSTAT 204 potentiostat. A three-electrode system was used, consisting of a static glassy carbon working electrode, a platinum wire auxiliary electrode and an Ag/AgCl reference electrode. Acetonitrile solutions of compounds **11** and **12** (~1.0×10^{-3} M) with 0.10 M of [*n*-Bu_4N]PF_6 as supporting electrolyte and cobaltocenium hexafluorophosphate, $[Cp_2Co]PF_6$ as internal standard were measured. The values of the measured formal potential are $E[CoCp_2^+/CoCp_2]$ = –0.91V *vs* Ag/AgCl.

Static direct current (dc) measurements were carried out on all samples by powdering and restraining the samples **11**, **11-ox** and **12** with *n*-eicosane to prevent any displacement due to the magnetic anisotropy. Variable-temperature (2.0–300 K) dc magnetic susceptibility under an applied field of 0.25 (T < 20 K) and 5.0 kOe (T ≥ 20 K), and variable-field (0–5.0 kOe) magnetisation in the temperature range from 2 to 10 K were recorded with a Quantum Design SQUID magnetometer. Variable-temperature (2–12 K) alternating current (ac) magnetic susceptibility measurements under ±0.005 kOe oscillating field at frequencies in the range of 0.1–10 kHz were carried out on crystalline samples under different applied static dc fields in the range 0.0–5.0 kOe with a Quantum Design Physical Property Measurement System (PPMS). The magnetic susceptibility data were corrected for the diamagnetism of the constituent atoms and the sample holder.

HFEPR spectra of **11** and **12** were recorded at 4.5 K on polycrystalline samples (20–25 mg) using a homodyne spectrometer associated with a 150/170 kOe superconducting magnet and a frequency range from 52 to 610 GHz. Detection was provided with an InSb hot electron bolometer (QMC Ltd., Cardiff, UK). The magnetic field was modulated at 50 kHz for detection purposes. A Stanford Research Systems SR830 lock-in amplifier converted the modulated signal to dc voltage. The single-frequency spectra were simulated with the *SPIN* software.

VI.2.4 X-ray Crystallography

Single-crystal X-ray diffraction data of **11** and **12** were collected on a Bruker-Nonius X8APEXII CCD area detector diffractometer using graphite-monochromated Mo-Kα radiation at T = 293 K. All calculations for data reduction, structure solution, and refinement were done through the SAINT[29] and SADABS[30] programs. The structures were solved with the ShelXS structure solution program, using the Patterson method. The models were refined with version 2013/4 of ShelXL against F2 on all data by full-matrix least squares.[31] All non-hydrogen atoms were refined with anisotropic displacement parameters. All hydrogen atoms were included at geometrically calculated positions and refined using a riding model. The final geometrical calculations and the graphical manipulations were carried out with the PLATON package.[32] Crystallographic data for compounds **11** and **12** are given in Table A.41.

VI.3 Results and discussion

Syntheses and X-ray Structure description

The reaction of the corresponding ferrocene-based ligand with a solution of cobalt(II) perchlorate and phenanthroline in a mixture of acetonitrile and methanol (1:1) affords compounds **11** and **12**. The ferrocene-based ligand can be employed in form of acids, Fc-(CO_2H) and Fc-($CO_2H)_2$, or piperidine (Pip) salts, Pip[Fc-(CO_2)] and $(Pip)_2$[Fc-$(CO_2)_2$], improving the yield of the reactions in the latter due to the better ligand solubility.

In the infrared spectra of **11** and **12**, the lack of a peak at 1680 cm^{-1} suggests the deprotonation of the acid groups of the ferrocene derivative ligands, Fc-(CO_2H) and Fc-($CO_2H)_2$, and the coordination to the Co^{II} ion. The peaks around 1592 and 1500 cm^{-1} are assigned to aromatic C–C stretches. The strong peaks at ~1530 and 1392 cm^{-1} are assigned to ν_{as}(COO) and ν_s(COO) ($\Delta\nu$ = ~138 cm^{-1}), which confirm the presence of a bidentate carboxylate group for all compounds.[33] Bands at 1091, 930 and 623 cm^{-1} confirms the presence of the perchlorate counterion.[34]

The crystal structure of **11** reveals a dinuclear $Co^{II}Fe^{II}$ compound formed by a cationic unit, $[Co(Me_2phen)_2(Fc\text{-}CO_2)]^+$, one perchlorate anion and one molecule of diethyl ether at the unit cell (Figure VI.1). The Co^{II} ion displays a very distorted octahedral geometry with a CoN_4O_2 environment formed by four nitrogen atoms from two chelating Me_2phen ligands and two oxygen atoms from the deprotonated ferrocene-carboxylic acid ligand. Compound **12** comprises two $[Co^{II}(Me_2phen)_2]^{2+}$ units linked by a ferrocene-dicarboxylate ligand, with two perchlorate anions to balance the charges and two acetonitrile and two

diethyl ether molecules in the molecular unit (Figure VI.2). Continuous Shape and Symmetry measures (CShM) through SHAPE software show that the cobalt octahedral environment is distorted in both compounds.[35] This software calculates the distortions by providing the octahedral (OC-6) and trigonal (TPR-6) prims parameters that deviate from zero when the deviation is larger from the ideal geometry. The values for these parameters are 13.671 (**11**) and 14.637 (**12**) for TPR-6 and 3.333 (**11**) and 3.298 (**12**) for OC-6, confirming a distorted octahedral geometry of the Co^{II} ions. Selected bond distances and angles for **11** and **12** are listed in Table VI.1. The O–Co–O angles are 60.9° (**11**) and 61.6° (**12**) which are smaller than the N–Co–N angles with values that range between 77.9–78.4° (**11**) and 78.2–78.5° (**12**) as observed in previous chapters and in the literature.[36,37] In **11**, the cyclopentadienyl rings are almost parallel forming an angle of 1.76° and these adopt a staggered conformation, with Fe-centroid Cp (cyclopentadienyl) distances of 1.649 and 1.653 Å. In **12**, the cyclopentadienyl rings are parallel, and these adopt an antiperiplanar staggered configuration with the torsion angle of 180°. The intramolecular Co···Fe distances are 5.510 and 5.474 Å for **11** and **12**, respectively. The intramolecular Co···Co distance in **12** is 10.948 Å and the shortest intermolecular Co···Co distance are 8.639 and 9.214 Å for **11** and **12**. No supramolecular π–π interactions nor classical hydrogen bonds are present.

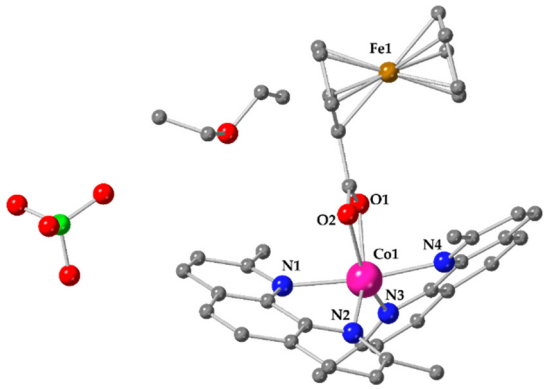

Figure VI.1. Perspective view of the molecular unit of **11**. Hydrogen atoms are omitted for clarity. Colour code: magenta, cobalt; red, oxygen; blue, nitrogen; grey, carbon; green, chlorine; brown, iron.

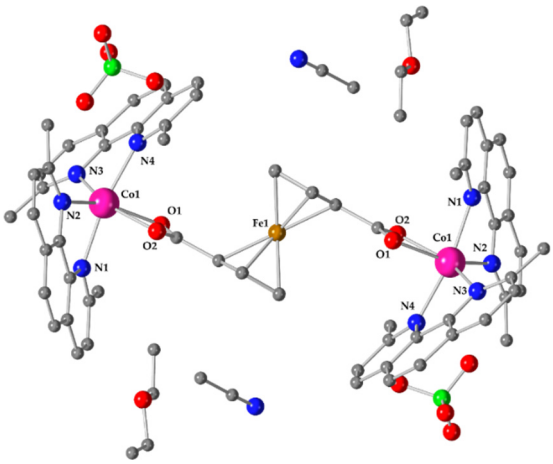

Figure VI.2. Perspective view of the molecular unit of **12**. Hydrogen atoms are omitted for clarity. Colour code: magenta, cobalt; red, oxygen; blue, nitrogen; grey, carbon; green, chlorine; brown, iron.

Table VI.1. Selected bond distances and angles for **11** and **12**.

Compound	11	12
Bond distances [Å]		
Co1–O1	2.188(5)	2.195(9)
Co1–O2	2.156(5)	2.167(9)
Co1–N1	2.164(6)	2.143(12)
Co1–N2	2.151(6)	2.132(11)
Co1–N3	2.116(6)	2.119(11)
Co1–N4	2.149(6)	2.162(10)
Fe–C_{avg}	2.043	2.036
Bond angles [°]		
O1–Co1–O2	60.85(17)	60.6(3)
O1–Co1–N1	90.8(2)	89.0(4)
O1–Co1–N2	153.66(19)	153.4(4)
N1–Co1–N2	77.9(2)	78.5(4)
N3–Co1–N4	78.4(2)	78.2(4)

VI.3.1 Electrochemical studies

Cyclic voltammetry studies of compounds **11** and **12** were performed in acetonitrile (Figure VI.3). The compounds are sparingly soluble in acetonitrile. However, more polar solvents as methanol were discarded because they are not suitable for working with magic blue (see below). Compounds **11** and **12** show one clear reversible oxidation wave at ~0.59 and 0.75 V *vs* Ag/AgCl couple, corresponding to one single-electron oxidation of ferrocene-carboxylate (**11**) and 1,1'-ferrocene-dicarboxylate (**12**) ligands, respectively. Similar redox behaviour has been observed for the free ligands.[38] The half-wave potentials of the ligand are shifted to lower potentials by coordinating to the Co^{II} ion, removing

electron density from the ligand. However, no oxidation of Co^{II} ion is observed up to 2 V. The electrochemical behaviour of **11** and **12** points that they are chemically accessible to be oxidised.

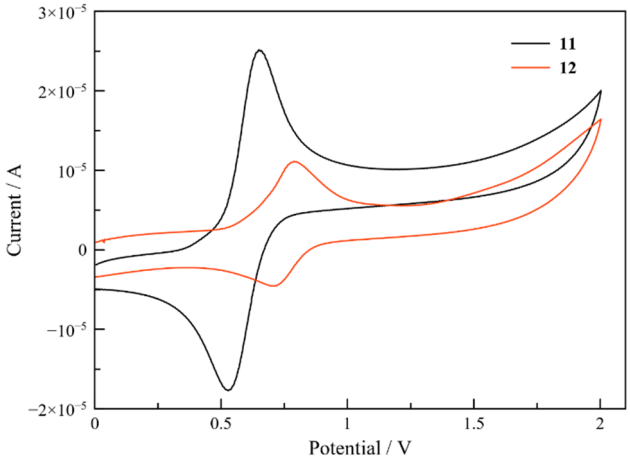

Figure VI.3. Cyclic voltammograms of compounds **11** and **12** in acetonitrile. Potentials are referenced to internal $CoCp_2/CoCp_2^+$ (defined as 0). Scan rate is 100 mVs^{-1}.

Magic blue, $[N(p\text{-}C_6H_4Br)_3]SbCl_6$, is a well-known aromatic oxidant for one-electron oxidation of organic and inorganic compounds.[39,40] Besides, it has high stability and good oxidising power with potentials higher than ferrocene (E_{red} = 0.70 V *vs* Fc/Fc^+). Therefore, compounds **11** and **12** were chemically oxidised by magic blue and derivatives ($[N(p\text{-}C_6H_3\text{-}2,4\text{-}Br)_3]SbCl_6$) affording air stable green-bluish solids. Attempts to obtain single crystals at room temperature were unsuccessful, and $[Co(Me_2phen)Cl_2]$ (ref.[41]) was isolated instead. The powders were analysed by infrared spectroscopy, EDX analysis, XRPD (Figure VI.4) and magnetic studies (see below). The infrared spectrum of **11-ox** is very similar to **11**, as expected. The XRPD of **11-ox** is different from the starting materials and $[Co(Me_2phen)Cl_2]$. The EDX analysis reveals the presence of Sb, Cl, Co and Fe elements with the expected ratios (Co/Fe = 1, Cl/Sb = 7). All these analyses suggest the formation of the oxidised $Fe^{III}Co^{II}$ species.

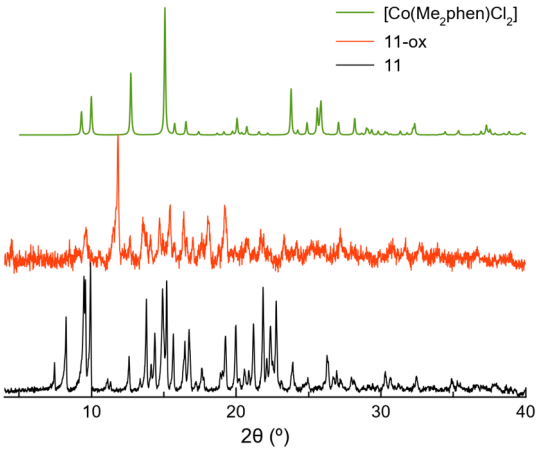

Figure VI.4. Experimental powder X-ray diffraction patterns of **11** (black), **11-ox** (red) and simulated diffraction pattern of [Co(Me2phen)Cl2] (green).

VI.3.2 Magnetic properties, EPR and theoretical calculations

Direct current (dc) magnetic properties of **11**, **11-ox** and **12** were measured and plotted in the form of $\chi_M T$ *vs* T and M *vs* H/T curves, as shown in Figure VI.5. At room temperature, the $\chi_M T$ values of **11** and **12** are 2.80 and 5.80 cm^3 K mol^{-1}, which are higher than the spin-only values expected for mononuclear (1.88 cm^3 K mol^{-1}) and dinuclear (3.75 cm^3 K mol^{-1}) cobalt(II) complexes with a significant spin-orbit coupling (SOC), typical of the Co^{II} ions. The $\chi_M T$ values decrease gradually with the temperature until 100 K and more abruptly until 2 K to reach values of 1.52 (**11**) and 3.32 cm^3 K mol^{-1} (**12**). In contrast, the $\chi_M T$ plot of **11-ox** is different, with $\chi_M T$ values of 3.60 and 1.28 cm^3 K mol^{-1} at room temperature and 2 K. These changes suggest the oxidation of low-spin Fe^{II} (S = 0) into low-spin Fe^{III} (S = 1/2) exhibiting a strong SOC,[42–45] and the existence of a strong antiferromagnetic exchange coupling (J) between the Co^{II} and Fe^{III} ions. The values for **11-ox** differ from the crystallised impurity [Co(Me2phen)Cl2].[41] The magnetisation values at 70 kOe and 2 K for **11** and **12** are 2.13 and 4.61 Nβ (inset Figure VI.5). These values are below the saturation limit of 3 and 6 Nβ for one and two S = 3/2 with g = 2.0. For **11-ox** the magnetisation value at 50 kOe and 2 K is 2.94 Nβ (Figure VI.5). The isothermal magnetisation curves in the form M *vs* H/T in the 2−10 K temperature range for **11** and **12** almost superimpose, suggesting a large zfs (inset Figure VI.5).

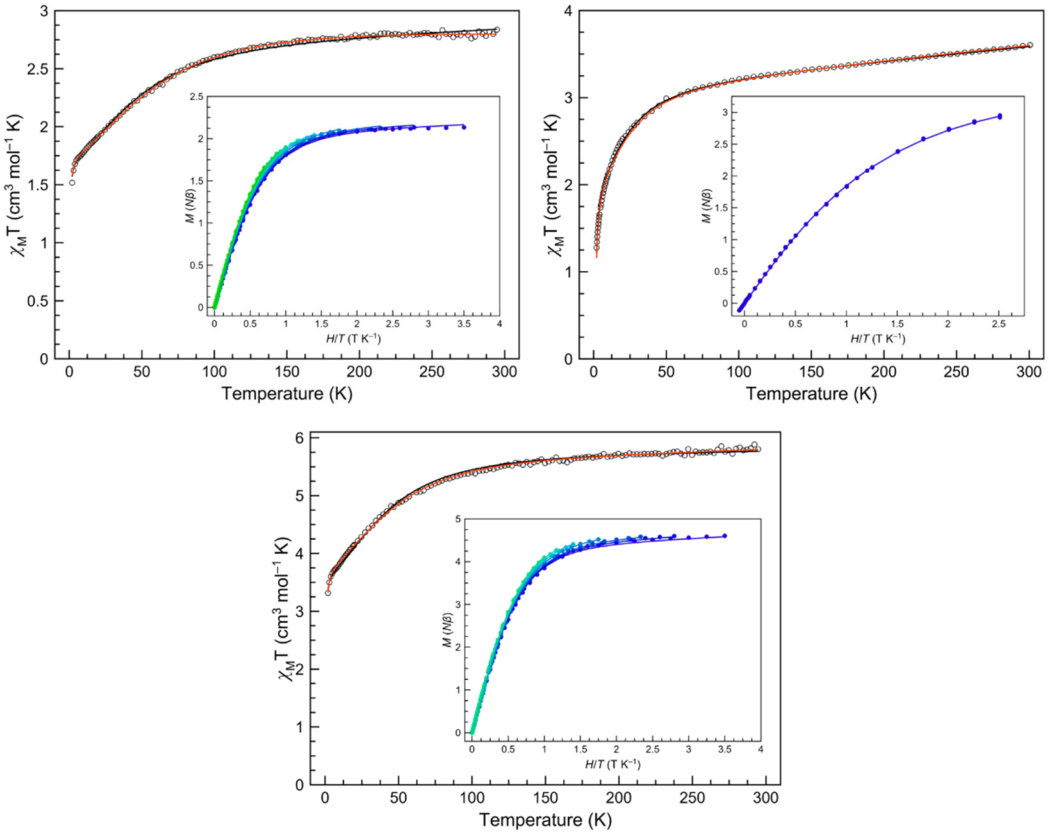

Figure VI.5. Plots of $\chi_M T$ *vs* T in the range 2–300 K in 5.0 kOe applied field and M *vs* H/T (inset) for **11** (top left), **11-ox** (top right) and **12** (bottom) in the 2–10 K temperature range (2 K blue to 10 K green gradient). The solid lines are the best-fit curves (see text).

Magnetic data of **11** and **12** were analysed in the whole temperature range through the T-P isomorphism approach summarised in the SOC Hamiltonian described in equation (1) from Chapter II (red lines in Figure VI.5). However, for **11-ox**, a spin exchange term should be included into the spin Hamiltonian, resulting in the modified equation (10) from Chapter IV. The best fits of the magnetic data using the PHI software[46] for **11**, **11-ox** and **12**, are shown in Table VI.2. Furthermore, the analyses of the magnetic properties of **11**, **11-ox** and **12**, where the Hamiltonian SOC for the Co^{II} ion was replaced by one considering a zfs, equation (2) from Chapter II, returns the best-fit values shown in Table VI.3.

Values found for SOC and zfs parameters in **11** and **12** fall within the usual range for non-coupled mononuclear and dinuclear cobalt(II) systems. In the case of **11-ox**, both models support the existence of moderate antiferromagnetic coupling between Co^{II} and Fe^{III} ions in **11-ox** as the shape of the curve indicated. The parameter α (or orbital reduction parameter), is usually related quantifying the covalence between the Co^{II} T_{2g} orbitals with the π orbitals of the ligand.[47] The best-fit parameter values for the Fe^{III} ion fall within the range reported for ferrocenium complexes, being the averaged g-factor a bit low.[42–45,48] The differences found in **11-ox** regarding the Δ, D and energy gap values should be taken with

care, since these might arise from the need of many parameters in the fitting, causing overparametrization.

Table VI.2. Spin Hamiltonian parameters for **11**, **11-ox** and **12** obtained from the first-order SOC model.

Compound	λ (cm^{-1})	Δ (cm^{-1})	α	TIP × 10^6 (cm^3 mol^{-1})	$F \times 10^5$	J (cm^{-1})	Gap[b] (cm^{-1})
11	−139.1	−142.0	1.03	498	2.44	–	155.2
11-ox[a]	−105.0/−350.6	+123.2/−196.7	1.46/−0.72	1204	9.34	−1.926	71.0/–
12	−114.8	−184.0	1.04	1330	2.15	–	122.8

[a] SOC parameter values for the Co/Fe atoms.[b] Energy gap between the ground and first excited Kramers doublets. F is the agreement factor defined as $F = \sum[P_{exp} - P_{calcd}]^2/\sum[P_{exp}]^2$

Table VI.3. Spin Hamiltonian parameters for **11**, **11-ox** and **12** obtained from the zfs model.

Compound	D (cm^{-1})	$\lvert E/D \rvert$	$g_\perp$	$g_{\lvert\lvert}$	TIP × 10^6 (cm^3 mol^{-1})	$F \times 10^5$	J (cm^{-1})	Gap[b] (cm^{-1})
11	+55.7	0.228	2.44	2.30	567	6.57	–	119.7
11-ox[a]	+25.7/–	0.000/–	2.43/1.69	2.43/2.06	1619	2.25	−1.416	55.0/–
12	+54.4	0.008	2.52	2.33	380	4.31	–	108.6

[a] zfs parameter values for the Co/Fe atoms.[b] Energy gap between the ground and first excited Kramers doublets. F is the agreement factor defined as $F = \sum[P_{exp} - P_{calcd}]^2/\sum[P_{exp}]^2$

High-Field EPR spectra of compounds **11** and **12** were measured at ~10 K and 203.2–238.6 GHz. (Figure VI.6). The simulations of these spectra established a positive D sign in both compounds, according to magnetometry. However, it is not possible to obtain a D value, because the energy gap between the two Kramers doublets ($m_s = \pm 1/2$) from the $S = 3/2$ ground state is larger than the microwave source of the HFEPR. Instead, the $\Delta m_s = \pm 1$ allowed transition between the $|-1/2> \rightarrow |+1/2>$ levels of the $M_S = |\pm 1/2>$ manifold is observed. These spectra were interpreted with a $S = 3/2$ spin Hamiltonian assuming an arbitrary large value of D ($D = +100$ cm^{-1}), which afford the following parameters: $g_\perp = 2.63$, $g_{\lvert\lvert} = 2.27$ and $E/D = 0.150$ for **11** and $g_\perp = 2.53$, $g_{\lvert\lvert} = 2.26$ and $E/D = 0.16$ for **12**. Moreover, the HFEPR spectrum of **12** indicates a negligible magnetic exchange coupling between the Co^{II} ions. HFEPR spectra were uninformative with a single $g = 2.00$ line through all the frequency range. The g-factor values obtained from HFEPR are similar to those obtained by magnetometry, validating them. However, the E/D ratio is apparently underestimated in the magnetometry for **12**, although this fact is quite common.

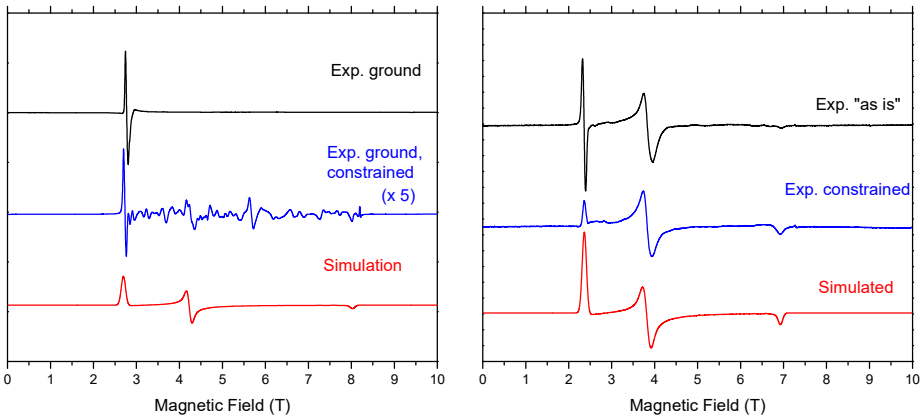

Figure VI.6. HFEPR spectra of **11** and **12** at ~10 K and 238.6 and 203.2 GHz (black trace) and as *n*-eicosane pellets (blue trace). The simulations are shown as red lines.

VI.3.3 Ac-magnetic properties

Alternating current (ac) magnetic susceptibility measures were performed on **11**, **11-ox** and **12** as a function of an external dc magnetic field (1.0–5.0 kOe), with a perpendicular oscillating field (±0.005 kOe), in the temperature range of 2.0–13.0 K, and frequencies in the 0.1–10.0 kHz range. In absence of a dc magnetic field, no χ_M'' signals were observed for all three compounds. However, when a dc-field is applied, frequency-dependent behaviour in χ_M'' emerged below ~8 and ~6 K for **11** and **12** (Figures VI.7–8 and A.124–127), but no signals appeared for **11-ox**. Here, the presence an exchange coupling between the Fe^{III} and Co^{II} ions, established by the magnetometry studies, annihilate the SIM behaviour, as other researchers reported for other redox switchable compounds.[49,50] **11** and **12** exhibit field-induced SIM behaviour as the other reported cobalt(II) compounds discussed in the previous chapters.

The χ_M' and χ_M'' *vs* ν data were analysed in unison with the DynVPMag program resulting in a unique set of values following the generalised Debye model.[51,52] With this model, the χ_M' and χ_M'' are described by the adiabatic (χ_S) and isothermal (χ_T) magnetic susceptibilities, the relaxation time (τ) and the exponential factor which defines the broadness of the spectra (α), through equations (3) and (4) from Chapter II. However, χ_M' and χ_M'' *vs* ν curves at H_{dc} = 1.0 kOe for **11** are only described correctly with the addition of a second individual relaxation process through equations (5-6) from Chapter II, where the second process is ruled by an IK mechanism with $\tau_{0,IK}$ in the ~10^{-5} s order.

The simulated curves with the best-fit parameters reproduce the experimental data rightly and, therefore, the Cole-Cole plots (Figures VI.7–8 and A.124–127). The α values are below 0.3 (**11**) and 0.2 (**12**), rejecting any spin-glass behaviour. These values are greater as the applied magnetic field increases, probably because the fast direct spin-reversal in the ground Kramers doublet (intra-Kramer, IK, $\tau^{-1} = \tau_{0,IK}^{-1}$) is prevented. As observed in other compounds studied in this dissertation, α parameter exhibits a broadly similar thermal

dependence (Figures VI.7–8 and A.124–127). As the temperature increases, α decreases due to a homogenisation of the domains created at low temperature. However, at $T > 6$ K the α values increase again, *i.e.*, the dominant relaxation process at $T < 6$ K is no longer so. Then, other relaxation process prevails with its corresponding α value, different from the previous process, which will be reached after the increase (T > 13 K). At higher temperatures (T > 13 K) it is expected that, as observed in other compounds, α decreases again due to a thermal homogenisation of the process: the different domains disappear. However, this last trend is not observed in **11** and **12**.

As in Chapter IV, the study of the dynamic properties of magnetisation and the mechanisms that control them has been carried out through the analysis of the ln(τ) *vs* 1/T (Arrhenius plots) and ln(τ) *vs* ln(T) plots (Figures VI.9 and A.128–129). While the first one is optimal for studying thermally assisted relaxations (TA, $\tau^{-1} = \tau_0^{-1} e^{-\frac{E_a}{k_B T}}$), the second is useful for Raman ($\tau^{-1} = A \cdot T^n$) and direct types ($\tau^{-1} = C \cdot T$). The aforementioned experimental curves have been simulated using two different models, as we have seen in previous chapters. Each of them involves the combination of several competing relaxations. While in the ln(τ) *vs* 1/T plots only TA mechanisms are considered, in the ln(τ) *vs* ln(T) plots only the Raman type. Ln(τ) *vs* ln(T) plots rule out the participation of a direct mechanism since no straight line with slope equal to –1 is observed in any case. An IK relaxation can always be operative and, for that reason, it is included in both models.

The values that best simulate the experimental data for both models are listed in Tables A.42-45. While **11** required a combination of three TA relaxations, **12** only used two. However, this fact may be the consequence of two overlapping TA relaxations in the experimental temperature range that cannot be distinguished, obtaining averaged E_a values [(E_{aMT}+E_{aHT})/2], which seems to be the case (Table A.44). The results found for the multi Raman model point towards relaxations that occur via phonons of different nature: optical at low temperature (n ~ 2) and acoustic at higher temperatures (n ~ 6–8). The parameters of this model are invariant with H_{dc}, behaviour of which is expected in a Raman relaxation (Tables A.43 and A.45). In a TA relaxation, we believe that the activation energy is linked to the energy of a vibrational mode or one overtone and, therefore, it will not depend on the applied dc-magnetic field either, as shown by the results in Tables A.42 and A.44. As expected in a process where magnetic states (m_s = ±1/2 ground Kramers doublet) are involved, it is influenced by the applied H_{dc} magnetic field. However, as discussed in the past, $\tau_{0,IK}$ decreases with an increasing H_{dc}, contrary to what might be foreseen. This unexpected result should be the subject of future study.

The oxidation of the diamagnetic and redox-active ferrocene group gives a paramagnetic ferrocenium ion, enabling a magnetic interaction between the ferrocenium and the Co^{II} ion of the complex in **11-ox**. This magnetic coupling modifies the electronic and magnetic

nature of the system, in which the Co^{II} ion can no longer be considered isolated. All this leads to the suppression of the slow relaxation of the magnetisation of **11-ox**. The subsequent reduction of **11-ox** should lead to the original electronic and magnetic form, again enabling SIM behaviour. This particularity makes **11** a molecular switch that modifies its magnetic dynamics, controlled by a redox process. Although an SMM can store information at the nanoscopic scale, this design that requires an active redox centre, should allow the erasing of information by an external stimulus.[53]

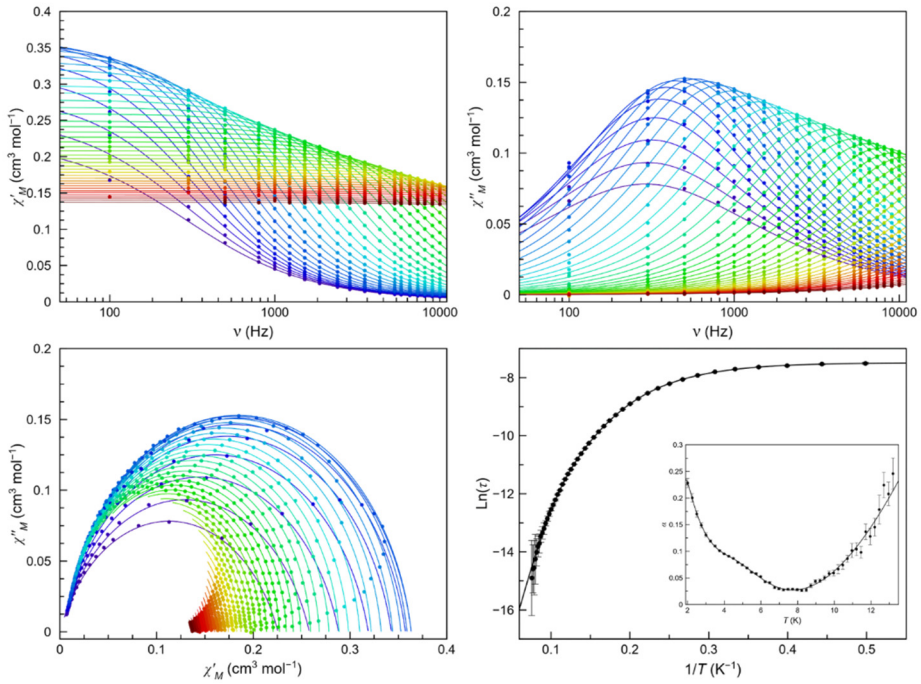

Figure VI.7. Frequency dependence of χ_M' (top left) and χ_M'' (top right), Cole-Cole plots (bottom left) and Arrhenius plots of **11** (bottom right) in a dc-applied static field of 5.0 kOe with ± 0.005 kOe oscillating field in the temperature range of 2.0–13.0 K (purple to green gradient). Thermal dependence of α is included on the bottom right figure as an inset, where the black line are eye-guides. Standard deviation appears as vertical error bars.

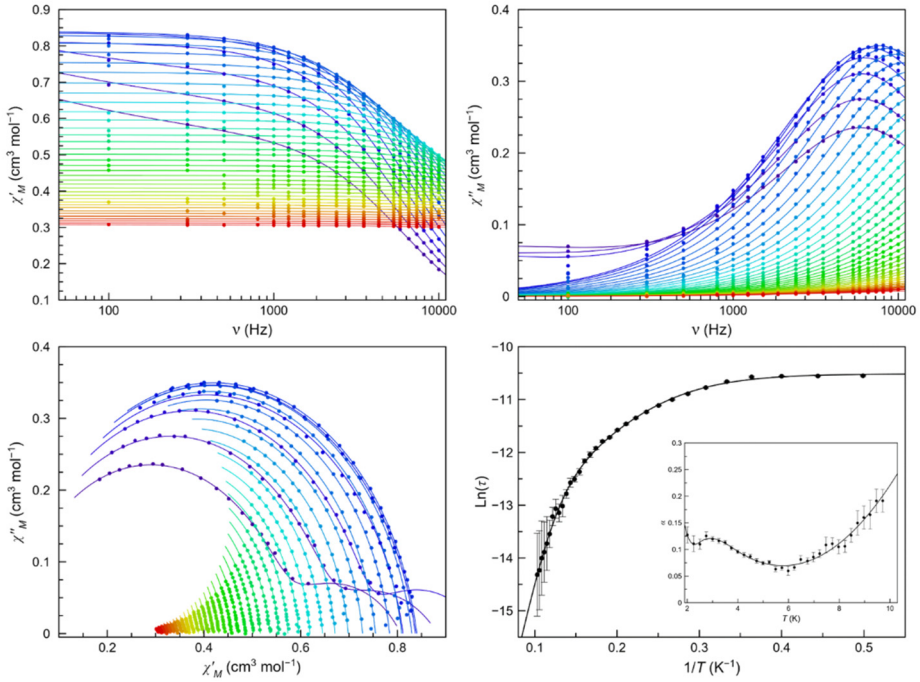

Figure VI.8. Frequency dependence of χ_M' (top left) and χ_M'' (top right), Cole-Cole plots (bottom left) and Arrhenius plots of **12** (bottom right) in a dc-applied static field of 5.0 kOe with ± 0.005 kOe oscillating field in the temperature range of 2.0–12.0 K (purple to green gradient). Thermal dependence of α is included on the bottom right figure as an inset, where the black line are eye-guides. Standard deviation appears as vertical error bars.

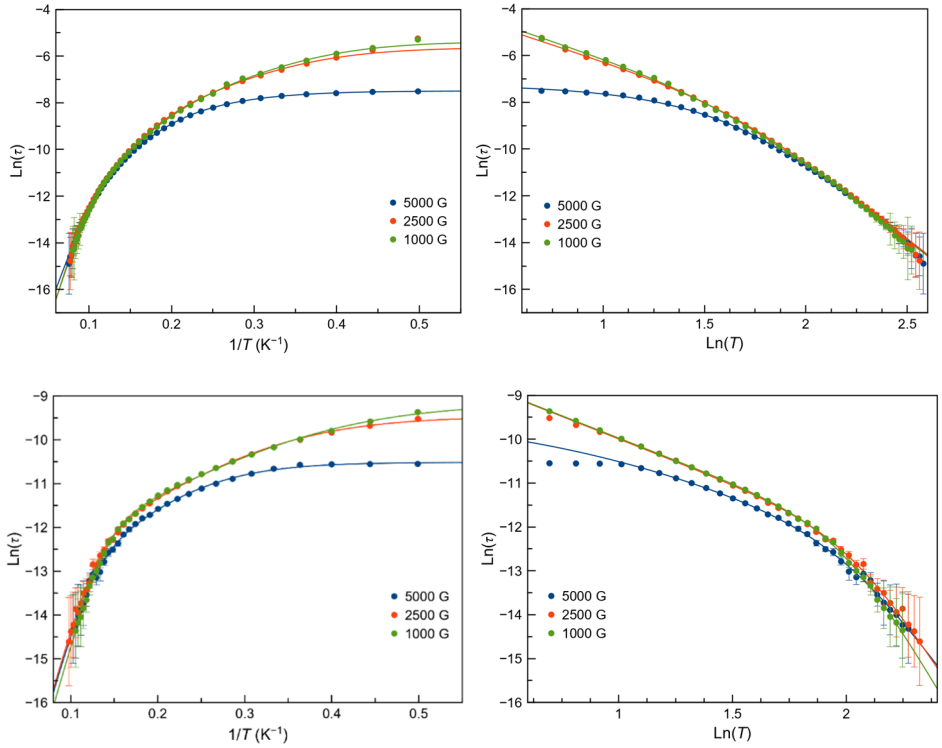

Figure VI.9. Arrhenius plots (left column) and ln(τ) *vs* ln(T) plots (right column) for the main process of **11** (first row) and **12** (second row) under 1.0–5.0 kOe applied static field. The solid lines are the best fit-curves by using the field-dependent equations. Standard deviations appear as vertical error bars.

VI.3.4 Conclusions

Mononuclear and dinuclear cobalt(II) complexes have been synthesised bearing redox-active ligands such as ferrocene derivatives (Fc-CO_2H and Fc-$(CO_2H)_2$). They present strong axial magnetic anisotropy ($D > 0$) and non-negligible rhombic component. Both compounds (**11** and **12**) exhibit slow magnetic relaxation under applied dc-magnetic fields. By oxidising the ferrocene moiety to the paramagnetic ferrocenium moiety (**11-ox**), previous isolated Co^{II} ions become antiferromagnetically coupled with the low-spin S =1/2 Fe^{III} ion. This operation deactivates SIM behaviour by chemical oxidation, proving that this approach works to design switchable SMMs by switching off this dynamic magnetic behaviour.

As observed for previous complexes, the slow magnetic relaxation of the magnetisation for **11** and **12** is ruled by both optical and acoustic phonons or by thermally activated processes which are assigned to different vibrational modes and overtones.

VI.4 References

1. Gatteschi, D., Sessoli, R. & Villain, J. *Molecular Nanomagnets*. (Oxford University Press, 2006).
2. Troiani, F. & Affronte, M. Molecular spins for quantum information technologies. *Chem. Soc. Rev.* **40**, 3119 (2011).
3. Leuenberger, M. N. & Loss, D. Quantum computing in molecular magnets. *Nature* **410**, 789–793 (2001).
4. Sanvito. Molecular spintronics. *Chem. Soc. Rev.* **40**, 3336–3355 (2011).
5. Feng, M. & Tong, M. L. Single ion magnets from 3d to 5f: Developments and strategies. *Chem. Eur. J.* **24**, 7574–7594 (2018).
6. Craig, G. A. & Murrie, M. 3d single-ion magnets. *Chem. Soc. Rev.* **44**, 2135–2147 (2015).
7. Frost, J. M., Harriman, K. L. M. & Murugesu, M. The rise of 3-d single-ion magnets in molecular magnetism: towards materials from molecules? *Chem. Sci.* 2470–2491 (2016).
8. Gómez-Coca, S., Aravena, D., Morales, R. & Ruiz, E. Large magnetic anisotropy in mononuclear metal complexes. *Coord. Chem. Rev.* **289–290**, 379–392 (2015).
9. Ruiz, E. *et al.* Can large magnetic anisotropy and high spin really coexist? *Chem. Commun.* **2**, 52–54 (2008).
10. Ferrando-Soria, J. *et al.* Molecular magnetism, quo vadis? A historical perspective from a coordination chemist viewpoint☆. *Coord. Chem. Rev.* **339**, 17–103 (2017).
11. Damjanović, M., Morita, T., Katoh, K., Yamashita, M. & Enders, M. Ligand π-Radical Interaction with f-Shell Unpaired Electrons in Phthalocyaninato-Lanthanoid Single-Molecule Magnets: A Solution NMR Spectroscopic and DFT Study. *Chem. - A Eur. J.* **21**, 14421–14432 (2015).
12. Takamatsu, S., Ishikawa, T., Koshihara, S. & Ishikawa, N. Significant Increase of the Barrier Energy for Magnetization Reversal of a Single-4f-Ionic Single-Molecule Magnet by a Longitudinal Contraction of the Coordination Space. *Inorg. Chem.* **46**, 7250–7252 (2007).
13. Ishikawa, N. *et al.* Upward Temperature Shift of the Intrinsic Phase Lag of the Magnetization of Bis(phthalocyaninato)terbium by Ligand Oxidation Creating an $S = 1/2$ Spin. *Inorg. Chem.* **43**, 5498–5500 (2004).
14. Komeda, T. *et al.* Observation and electric current control of a local spin in a single-molecule magnet. *Nat. Commun.* **2**, 217 (2011).
15. Nava, A. *et al.* Redox-Controlled Exchange Bias in a Supramolecular Chain of Fe_4 Single-Molecule Magnets. *Angew. Chemie - Int. Ed.* **54**, 8777–8782 (2015).
16. Zhu, X. *et al.* Redox effects of low-spin Ru(II/III) on slow magnetic relaxation of Ru-Mn(III) 1D cyanide-bridged complexes. *Dalt. Trans.* **46**, 7267–7272 (2017).
17. Tong, J., Demeshko, S., John, M., Dechert, S. & Meyer, F. Redox-Induced Single-Molecule Magnetism in Mixed-Valent [2 × 2] Co4Grid Complexes. *Inorg. Chem.* **55**, 4362–4372 (2016).
18. Freedman, D. E., Jenkins, D. M., Iavarone, A. T. & Long, J. R. A Redox-Switchable Single-Molecule Magnet Incorporating $[Re(CN)_7]^{3-}$. *J. Am. Chem. Soc.* **130**, 2884–2885 (2008).
19. Gaudette, A. I. *et al.* Electron Hopping through Double-Exchange Coupling in a Mixed-Valence Diiminobenzoquinone-Bridged Fe2 Complex. *J. Am. Chem. Soc.* **137**, 12617–12626 (2015).
20. Fortier, S. *et al.* A dinuclear cobalt complex featuring unprecedented anodic and cathodic redox switches for single-molecule magnet activity. *J. Am. Chem. Soc.* **135**, 14670–14678 (2013).
21. Jeon, I. R., Park, J. G., Xiao, D. J. & Harris, T. D. An azophenine radical-bridged Fe2 single-molecule magnet with record magnetic exchange coupling. *J. Am. Chem. Soc.* **135**, 16845–16848 (2013).

22. Beer, P. D. & Hayes, E. J. Transition metal and organometallic anion complexation agents. *Coord. Chem. Rev.* **240**, 167–189 (2003).

23. Metzler-Nolte, N. & Salmain, M. The Bioorganometallic Chemistry of Ferrocene. in *Ferrocenes: Ligands, Materials and Biomolecules* 499–639 (2008).

24. Astruc, D. Why is Ferrocene so Exceptional? *European Journal of Inorganic Chemistry* **2017**, 6–29 (2017).

25. Vallejo, J. *et al.* Field-induced slow magnetic relaxation in a six-coordinate mononuclear cobalt(II) complex with a positive anisotropy. *J. Am. Chem. Soc.* **134**, 15704–15707 (2012).

26. Vallejo, J. Estudio de Imanes Moleculares de Co(II): desde sistemas aislados hasta sistemas organizados y multifuncionales. (University of Valencia, 2016).

27. Vallejo, J. *et al.* Reversible solvatomagnetic switching in a single-ion magnet from an entatic state. *Chem. Sci.* **8**, 3694–3702 (2017).

28. Matthews, S. L. & Heinekey, D. M. An oxidised active site model for the FeFe hydrogenase: Reduction with hydrogen gas. *Inorg. Chem.* **50**, 7925–7927 (2011).

29. *SAINT, Computer Program*. (Bruker Analytical X-ray Systems, 2003).

30. Sheldrick, G. M. SADABS. *SADABS,Empiracal Absorption corrections program, University of Göttingen* based on the methods of Blessing. (1995).

31. Sheldrick, G. M. A short history of SHELX. *Acta Crystallogr. Sect. A Found. Crystallogr.* **64**, 112–122 (2008).

32. Spek, A. L. Platon a multipurpose crystallographic tool. (2003).

33. Nakamoto, K. Applications in Coordination Chemistry. in *Infrared and Raman Spectra of Inorganic and Coordination Compounds* 1–273 (John Wiley & Sons, Inc., 2008).

34. Hathaway, B. J. & Underhill, A. E. 592. The infrared spectra of some transition-metal perchlorates. *J. Chem. Soc.* 3091 (1961).

35. Llunell, M., Casanova, D., Cirera, J., Alemany, P. & Alvarez, S. *SHAPE v2.1.* (2013).

36. Baca, S. G. *et al.* From Mono- and Dinuclear to Polynuclear Cobalt(II) and Cobalt(III) Coordination Compounds Based ono-Phthalic Acid and 2,2′-Bipyridine: Synthesis, Crystal Structures, and Properties. *Eur. J. Inorg. Chem.* **2005**, 3118–3130 (2005).

37. Cano, J. *et al.* Ability of terephthalate (ta) to mediate exchange coupling in ta-bridged copper(II), nickel(II), cobalt(II) and manganese(II) dinuclear complexes. *J. Chem. Soc. Dalt. Trans.* 1915–1924 (1997).

38. Cassidy, J. Note on the voltammetry of ferrocene carboxylate in aqueous solution. *Electrochem. commun.* **1**, 69–71 (1999).

39. Zhang, S. *et al.* Controllable, Wide-Ranging n-Doping and p-Doping of Monolayer Group 6 Transition-Metal Disulfides and Diselenides. *Adv. Mater.* **30**, 1802991 (2018).

40. Hofmann, A. I. *et al.* Chemical Doping of Conjugated Polymers with the Strong Oxidant Magic Blue. *Adv. Electron. Mater.* **6**, 2000249 (2020).

41. Smolko, L. *et al.* Field-Induced Slow Magnetic Relaxation in Mononuclear Tetracoordinate Cobalt(II) Complexes Containing a Neocuproine Ligand. *Eur. J. Inorg. Chem.* **2017**, 3080–3086 (2017).

42. Hendrickson, D. N., Sohn, Y. S. & Gray, H. B. Magnetic Susceptibility Study of Various Ferricenium and Iron(III) Dicarbollide Compounds. *Inorg. Chem.* **10**, 1559–1563 (1971).

43. Ding, M. *et al.* Magnetization Slow Dynamics in Ferrocenium Complexes. *Chem. - A Eur. J.* **25**, 10625–10632 (2019).

44. Sohn, Y. S., Hendrickson, D. N. & Gray, H. B. Electronic Structure of Ferricenium Ion. *J. Am. Chem.*

Soc. **92**, 3233–3234 (1970).

45. Maki, A. H. & Berry, T. E. Paramagnetic Resonance of Some Carborane Analogs of Ferricenium Cation. *J. Am. Chem. Soc.* **87**, 4437–4441 (1965).

46. Chilton, N. F., Anderson, R. P., Turner, L. D., Soncini, A. & Murray, K. S. PHI: A powerful new program for the analysis of anisotropic monomeric and exchange-coupled polynuclear d - and f -block complexes. *J. Comput. Chem.* **34**, 1164–1175 (2013).

47. Gerloch, M. & Miller, J. R. Covalence and the Orbital Reduction Factor, k , in Magnetochemistry. in **10**, 1–47 (2007).

48. Appel, M., Frick, B., Elbert, J., Gallei, M. & Stühn, B. Direct observation of electronic and nuclear ground state splitting in external magnetic field by inelastic neutron scattering on oxidised ferrocene and ferrocene containing polymers. *EPJ Web Conf.* **83**, 02001 (2015).

49. Meng, Y.-S. *et al.* Weak exchange coupling effects leading to fast magnetic relaxations in a trinuclear dysprosium single-molecule magnet. *Inorg. Chem. Front.* **7**, 447–454 (2020).

50. Dickie, C. M., Laughlin, A. L., Wofford, J. D., Bhuvanesh, N. S. & Nippe, M. Transition metal redox switches for reversible on/off and slow/fast single-molecule magnet behaviour in dysprosium and erbium bis-diamidoferrocene complexes. *Chem. Sci.* **8**, 8039–8049 (2017).

51. Cole, K. S. & Cole, R. H. Dispersion and Absorption in Dielectrics I. Alternating Current Characteristics. *J. Chem. Phys.* **9**, 341–351 (1941).

52. Carbonell-Vilar, J. M. & Cano, J. Dyn-VPMag. *University of Valencia* (2019).

53. Geerlings, K. *et al.* Demonstrating a Driven Reset Protocol for a Superconducting Qubit. *Phys. Rev. Lett.* **110**, 120501 (2013).

Chapter VII

Molecular functionalisation of 2D-MoS_2‡

Chemically exfoliated MoS_2 flakes are functionalised with a photochromic molecule, a dithienylethene derivative. The functionalisation syntheses were performed following electrostatically and covalent approaches, where the molecule is attached through charge compensation or by the formation of new C–S bonds, respectively. The compounds retain some of the photoswitching behaviour and this property is evaluated through different techniques.

‡ The work of this whole chapter has been done in collaboration with Dr. Marc Morant-Giner under the supervision of Dr. Alicia Forment-Aliaga, in the Maria de Maeztu framework.

VII.1 Introduction

Among 2D materials, layered transition metal dichalcogenides (TMDs), and particularly MoS_2, have attracted much attention in the last decades, because of their applications in electronics,[1] optoelectronics,[2,3] sensing,[4,5] energy storage,[6] photovoltaic devices[5] and catalysis.[7,8] The properties of MoS_2 can be tailored by chemical and physical modifications, expanding the possible applications for these 2D materials.[9–12] Hence, the study of molecular functionalisation is a crucial topic for 2D materials research. MoS_2 functionalisation can be carried out by physisorption as well as chemisorption of molecules.[13,14]

Charge transfer and Van der Waals interactions usually dominate the physisorption of molecules in MoS_2. The type of doping by charge transfer depends on the redox potential of molecules respect to the Fermi level of MoS_2.[15] Van der Waals approaches exploit the generated molecular electric field to modulate the local charge carrier density of MoS_2.[12] Some examples are the physisorption of fullerenes,[16] tetracyanoquinodimethane (TCNQ)[17] derivatives or tetrathiafulvalene (TTF) derivatives.[18]

Chemisorption of molecules in edge and basal MoS_2 plane has been carried out with different approaches: i) coordinative functionalisation via coordination of S-atoms of MoS_2 to metal centres using metal salts;[19] ii) covalent functionalisation with the formation of S–Mo bond at S-vacancies or iii) covalent functionalization with the formation of C–S bond on the basal plane.[20] Thiol derivatives, which fill S vacancies in MoS_2 generated during the exfoliation process or by electrochemistry, are the most commonly employed molecules.[21,22] Electrophiles as alkyl halides and diazonium salts are also alternatives exploited due to the reactivity of the negatively charged 1T-MoS_2s.[23–25] Click chemistry is an alternative to functionalise covalently other typical phases, as 2H-MoS_2.[26]

The semiconducting nature of 2D MoS_2 has motivated its potential application in optoelectronics.[27] Thus, some researchers have focused on the use of photochromic molecules, mainly with molecules bearing azobenzene groups, to induce optical changes into MoS_2.[14,28,29] However, so far, other interesting photochromic molecules like dithienylethene derivatives remain unexplored as optical MoS_2 modulators.[30]

In this scenario, the aim of this chapter is to functionalise exfoliated MoS_2 (ce-MoS_2) flakes with a photoswitchable molecule, Sw-$PhNH_2$, via covalent and electrostatic approaches (Scheme VII.1). In the first case, using a dithienylethene derivative bearing two terminal amino groups leads us to consider the possibility of performing MoS_2 cross-linking (extended networks of flakes physically and electronically interconnected through molecular linkers) by a diazotisation reaction. In the second case, the previous mentioned dithienylethene derivative is protonated (positively charged) and mixed with 1T MoS_2

flakes (negatively charged) resulting in an electrostatic functionalisation.[31] Finally, a physical mixture of ce-MoS_2 flakes with the photoswitchable molecule was prepared to understand better the photoswitching capacity of the functionalised MoS_2 materials studied in this Chapter.

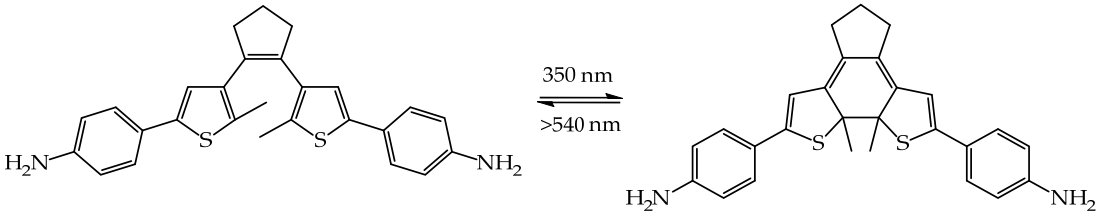

Scheme VII.1. Photoswitching behaviour of **Sw-PhNH$_2$-o** (left) and **Sw-PhNH$_2$-c** (right).

VII.2 Experimental section

VII.2.1 Materials

All chemicals were obtained from commercial sources and used as received. 1,2-bis(5-chloro-2-methylthien-3-yl)cyclopentene (**Sw-Cl-o**) and 1,2-bis(2-methyl-5-phenylthien-3-yl)cyclopentene (**Sw-PhH-o**) have been synthesised following the reported procedures.[32]

VII.2.2 Syntheses

5,6,9a,9b-Tetrahydro-9a,9b-dimethyl-2,8-diphenyl-4H-indeno[5,4-b:6,7-b']dithiophene (Sw-PhH-c). Sw-PhH-o (0.20 g) was dissolved in hexane (100 mL) and then subjected to UV irradiation (by means of UVB lamps centred at 308 nm) in a photoreactor for 1 h and 15 minutes giving a dark purple solution. The compound was crystallized by slow evaporation in acetonitrile yielding a mixture of dark purple and colourless crystals as minor impurities, which were manually removed. ^{1}H-NMR (300 MHz, $CDCl_3$) δ = 7.52 (t, *J* = 7.76 Hz, 4H, phenyl), 7.36 (t, *J* = 7.06 Hz, 4H, phenyl), 7.32 (t, *J* = 6.60 Hz, 2H, phenyl), 6.42 (s, 2H, thiophene), 2.50 (t, *J* = 7.34 Hz, 4H, cyclopentene), 2.03 (s, 6H, CH_3), 1.92 (qt, *J* = 7.29 Hz, 2H, cyclopentene).

1,2-Bis[2-methyl-5-(4-*N*-(*tert*-butoxycarbonylamino)-phenyl)thien-3-yl]cyclopentene (Sw-PhNHBoc-o). Sw-Cl-o (0.58 g, 1.76 mmol, 1 eq) and 13 mL of dry THF were added in a two-necked flask under an argon atmosphere. Then, *n*-butyllithium (2.30 mL, 3.69 mmol, 1.6 M in hexane, 2.1 eq) was very slowly added, giving a black solution. Next, tributyl borate (1.42 mL, 5.26 mmol, 3 eq) was quickly added affording a reddish-orange solution, which was stirred for 1 h at room temperature. Then, *N*-(tert-butoxycarbonyl)-4-bromoaniline (1.43 mg, 5.27 mmol, 3 eq), $Pd(PPh_3)_4$ (203 mg, 0.176 mmol, 0.1 eq), sodium carbonate (11.40 mL, 22.83 mmol, 2 M in H_2O, 13 eq) and few drops of ethylene glycol were added sequentially to the reaction mixture, which was refluxed overnight. The reaction mixture was led cool down to room temperature and, then, H_2O (120 mL) was added. Liquid-liquid extraction was performed by adding ethyl acetate (2 x 55 mL). The organic phase was washed with brine, dried over magnesium sulphate, and the solvent was removed in a rotary evaporator giving a reddish-brown oil. The product was purified by column chromatography on silica gel (8.5 hexane: 1.5 ethyl acetate) affording a brown solid (0.64 g, 60%). ^{1}H-NMR (300 MHz, $CDCl_3$) δ = 7.43 (d, *J* = 8.62 Hz, 4H, phenyl), 7.34 (d, *J* = 8.80 Hz, 4H, phenyl), 6.97 (s, 2H, thiophene), 6.60 (s, 2H, NH), 2.85 (t, *J* = 7.52 Hz, 4H, cyclopentene), 2.08 (qt, *J* = 7.52 Hz, 2H, cyclopentene), 1.99 (s, 6H, CH_3), 1.54 (s, 18H, CH_3).

1,2-Bis[2-methyl-5-(4-aminophenyl)thien-3-yl]cyclopentene (Sw-PhNH$_2$-o). Sw-PhNHBoc-o (0.64 g, 1 mmol, 1 eq) was dissolved in dichloromethane (25 mL). Next,

trifluoroacetic acid (2.48 mL, 53.08 mmol, 53 eq) was added and stirred vigorously overnight and, later, the solvent was removed with a rotary evaporator. Sodium bicarbonate (33 mL, saturated in H_2O) was added and extracted with dichloromethane (6 x 20 mL). The organic phase was collected, dried over magnesium sulphate and filtered under vacuum, giving a red solution. A grey solid was obtained after the solvent was evaporated with a rotary evaporator, washed with diethyl ether, and filtered off. Again, the red solution was evaporated with a rotary evaporator giving a brown powder used without further purification (0.38 g, 85%). ^{1}H-NMR (300 MHz, $CDCl_3$) δ = 7.31 (d, *J* = 8.62 Hz, 4H, phenyl), 6.88 (s, 2H, thiophene), 6.66 (d, *J* = 8.62 Hz, 4H, phenyl), 2.83 (t, *J* = 7.43 Hz, 4H, cyclopentene), 2.06 (qt, *J* = 7.38 Hz, 2H, cyclopentene), 1.97 (s, 6H, CH_3). HRMS *m*/*z* 443.1590 ($[M + H]^+$, calculated for $C_{27}H_{27}N_2S_2$, 443.1616).

4,4'-(9a,9b-dimethyl-5,6,9a,9b-tetrahydro-4H-indeno[5,4-b:6,7-b']dithiophene-2,8-diyl)dianiline (Sw-PhNH$_2$-c). The molecule was prepared in-situ and not isolated. **Sw-PhNH$_2$-o** (0.7 mM) in MeOH was placed in a beaker with stirring and then subjected to UV irradiation (350 nm) in a photoreactor for approximately 15 min. A dark purple solution was obtained, which was rotary evaporated to afford a dark purple solid, and it was used without any purification.

1,2-Bis[2-methyl-5-(4-aminophenyl)thien-3-yl]cyclopentene hydrochloride (Sw-PhNH$_3$Cl-o). Sw-PhNH$_2$-o (12.30 mg, 0.028 mmol,1 eq) was dissolved in EtOH/H_2O (2:1, 68 mL) and HCl 6M (18 μL, 0.108 mmol, 3.9 eq) was added. A grey-yellowish solution was obtained and it was precipitated with diethyl ether. A grey solid was obtained which was used without any other purification. IR (ν_{max}/cm^{-1}): 3442(vs, br), 2911(s), 2839(s), 2583(m), 1616(m), 1540(m), 1509(s), 1473(vw), 1437(w), 1311(vw), 1288(vw), 1210(w), 1117(w), 1016(vw), 948(vw), 820(m), 755(vw), 678(vw), 659(vw), 634(w), 558(vw), 487(m), 473(w), 429(w).

4,4'-(9a,9b-dimethyl-5,6,9a,9b-tetrahydro-4H-indeno[5,4-b:6,7-b']dithiophene-2,8-diyl)dibenzenaminium chloride (Sw-PhNH$_3$Cl-c). Sw-PhNH$_2$-o (12.30 mg, 0.028 mmol, 1 eq) was dissolved in EtOH/H_2O (2:1, 68 mL) and HCl 6M (18 μL, 0.108 mmol, 3.9 eq) was added. Then, the solution was placed in a beaker with stirring and then subjected to UV irradiation (350 nm) in a photoreactor for approximately 10 min. A dark violet solution was obtained and it was used without any purification nor isolation. A few amount was dried giving a purple solid for FTIR measurements. IR (ν_{max}/cm^{-1}): 3399(m, br), 3178(m), 2920(vs), 2851(vs), 2567(s), 1604(s), 1560(m), 1509(s), 1471(s), 1425(s), 1349(m), 1315(s), 1269(s), 1177(vs), 1163(vs), 1076(m), 1059(m), 1019(w), 997(s), 921(w), 894(m), 821(m), 743(vw), 669(vw), 632(vw), 542(w), 487(w).

ce-MoS$_2$. This material was provided by Dr Marc Morant-Giner (under the supervision of Dr Alicia Forment-Aliaga) and was used for the following reactions.[6,33]

ce-MoS_2+Sw-PhH-o. The physical mixture of ce-MoS_2 with **Sw-PhH-o** was prepared by grinding 7.2 mg of ce-MoS_2 flakes and 2.3 mg of **Sw-PhH-o** in a mortar (**Sw-PhH-o**/MoS_2 molar ratio of ≈0.1).

ce-MoS_2+Sw-PhH-c. The physical mixture of ce-MoS_2 with **Sw-PhH-c** was prepared by grinding 7.4 mg of ce-MoS_2 flakes and 2.2 mg of **Sw-PhH-c** in a mortar (**Sw-PhH-c**/MoS_2 molar ratio of ≈0.1).

ce-MoS_2-Sw-Ph-o. Sw-PhNH_2-o (12.30 mg, 0.028 mmol, 1 eq) was introduced in a round-bottom flask under an argon atmosphere. Subsequently, sodium nitrite (5.77 mg, 0.084 mmol, 3 eq) and HCl 6 M (511 μL, 110 eq) were poured into the reaction system at 0 °C (ice bath), under a constant flow of argon and the resultant mixture was kept under stirring for 1 h. A suspension of ce-MoS_2 flakes (0.28 mmol) was added and led react at room temperature for 24 h. After, the obtained mixture was filtered by using a nylon membrane. The resultant solid collected on the filter was washed with ultrapure (Milli-Q) water, DMSO, and MeOH. Finally, the purified solid was vacuum-dried for 14 h in the darkness, at least. IR (ν_{max}/cm^{-1}): 3411(s), 2920(w), 2854(w), 2518(vw), 1685(w), 1635(m), 1420(w), 1199(s), 1162(s), 1055(s), 949(m), 910(w), 833(w), 754(w), 664(w), 593(w), 480(w).

ce-MoS_2-Sw-Ph-c. Sw-PhNH_2-c was synthesised in-situ by dissolving **Sw-PhNH_2-o** (12.30 mg, 0.028 mmol) in 40 mL of MeOH and then subjected to UV irradiation (350 nm) in a photoreactor during 15 min under vigorous magnetic stirring. The resulting dark purple solution was rotary evaporated to yield a purple solid (**Sw-PhNH_2-c**). Finally, the protocol described for the synthesis of **ce-MoS_2-Sw-Ph-o** was followed. IR (ν_{max}/cm^{-1}): 3394(s), 2920(w), 2854(w), 2512(vw), 1695(w), 1617(m), 1419(w), 1204(s), 1156(s), 1054(s), 1035(s), 946(m), 909(m), 833(vw), 754(w), 662(w), 593(w), 503(w).

ce-MoS_2-Sw-PhNH_3-o. Sw-PhNH_3Cl-o (43.97 mg, 0.1 mmol, 1 eq) was dissolved in EtOH/H_2O (2:1, 180 mL). Then, HCl 6M (64.4 μL, 3.9 eq) was added to the mixture giving a change in colour for the solution from salmon to grey-yellowish (pH_{theo} = 2.6). An aqueous solution of ce-MoS_2 (0.1 mmol, 1 eq) was added dropwise in an inert atmosphere (Ar). The reaction mixture was stirred for 30 minutes yielding a black suspension. The suspension was centrifuged, and the supernatant was discarded. The remaining solid was washed thrice with a mixture of EtOH/H_2O (2:1), then dried on a desiccator under vacuum. Finally, a black powder was collected. IR (ν_{max}/cm^{-1}): 3431(m), 2918(w), 2851(w), 2515(vw), 1600(w), 1559(w), 1540(vw), 1506(w), 1385(m), 1257(vw), 1174(s), 1108(vw), 1071(w), 895(w), 816(m), 479(vw).

ce-MoS_2-Sw-PhNH_3-c. Sw-PhNH_3Cl-o (43.97 mg, 0.1 mmol, 1 eq) was dissolved in EtOH/H_2O (1:1, 244 mL). Then, HCl 6M (64.4 μL, 3.9 eq) was added to the mixture giving a change in colour for the solution from salmon to grey-yellowish (pH_{theo} = 2.8). Next, the reaction mixture was subjected to UV irradiation (350 nm) in a photoreactor for 10 min.

An aqueous solution of ce-MoS_2 (0.1 mmol, 1 eq) was added dropwise in an inert atmosphere (Ar). The reaction mixture was stirred for 30 minutes yielding a black suspension. The suspension was centrifuged, and the supernatant was discarded. The remaining solid was washed thrice with a mixture of EtOH/H_2O (2:1), then dried on a desiccator under vacuum. Finally, a black powder was collected (25.97 mg). IR (ν_{max}/cm^{-1}): 3430(m), 2918(w), 2851(w), 2518(vw), 1599(w), 1559(w), 1541(vw), 1506(w), 1419(m), 1396(m), 1254(vw), 1167(s), 1107(vw), 1093(vw), 1072(w), 895(m), 817(m), 515(w), 479(vw).

VII.2.3 Physical measurements

Photoirradiation experiments were performed inside a commercial photoreactor (LuzChem LZC-4V). Along with the experiments, 14 UVB (308 nm) lamps, 14 UVA FL8BL-B (350 nm) lamps and 12 Sylvania Cool White F8T5 (visible) lamps with LuzChem orange filters (> 540 nm) were used. Liquid UV/Vis spectra were recorded using Heillma quartz cuvettes and on a Jasco V-670 and powder UV/Vis spectra were recorded using PIN-757 adaptor. ^{1}H-RMN data were collected with a Bruker DPX300 spectrophotometer. Chemical displacements are given in ppm, and they are referenced to their respective chemical deuterated solvents. Infrared spectra (4000–400 cm^{-1}) were recorded on a Nicolet 5700 spectrophotometer as KBr pellets. All samples were measured as KBr pellets, and transmittance intensities were scaled for comparison purposes. High-resolution electrospray mass spectra (ESI-MS) in methanol solution were obtained on an AB SCIEX TripleTOF™ 5600 LC/MS/MS System.

Raman spectra were recorded with a Raman Horiba-LabRam HR Evolution Spectrometer in ambient conditions onto a clean SiO_2 (285 nm)/Si substrate. The Raman measurements were performed with 8 mW (532 nm), 17 mW (633 nm) and 26 mW (785 nm) excitation power, on the same spot area (~2 μm diameter). The spectrophotometer is equipped with laser filters that allow to diminish the laser beam power by selecting 0.1, 0.5, 1, 5, 10, 25, 50 and 100% laser power. Laser intensity powers of 1% and 5% where used for measuring and irradiating the sample, respectively. Lower intensity laser powers lead to very noisy measurements; higher intensity powers lead to MoS_2 oxidation and sample burnings.

X-ray powder diffraction (XRPD) measurements were recorded on a Panalytical Empyrean X-ray diffractometer by using Cu Kα radiation (λ = 1.5406 Å), in which the X-ray tube was operated at 45 kV and 40 mA ranging from 2 to 90°. The XRPD data was background corrected with the *HighScore Plus* software.

TGA was conducted using TA TGA550 in the 25–850 °C range under a 10 °C min^{-1} scan rate and N_2 flow of 100 mL min^{-1}.

XPS measurements were analysed using a Thermo Scientific K-alpha X-ray photoelectron spectrometer, using a monochromatic Al Kα radiation (1486.6 eV) at a pressure of 4×10^{-9} mBar. XPS data were analysed with Avantage software, where the carbon tape was used as reference (C 1s = 284.8 eV).

FESEM studies were performed without metallization on a Hitachi S-4800 microscope operating at a voltage of 20 kV. HRTEM studies were carried out on a Tecnai G2 F20 microscope operating at 200 kV. Samples were prepared by dropping suspensions on lacey formvar/carbon copper grids (300 mesh).

VII.3 Results and discussion

VII.3.1 Organic syntheses and photoconversion

All the synthetic procedures are described in Figures VII.1–3.

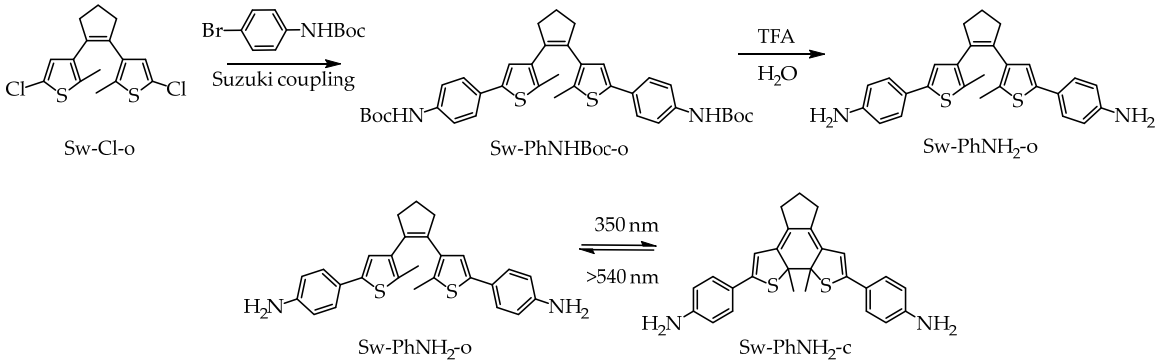

Figure VII.1. Synthetic procedures for obtaining **Sw-PhNH$_2$-o** and **Sw-PhNH$_2$-c**.

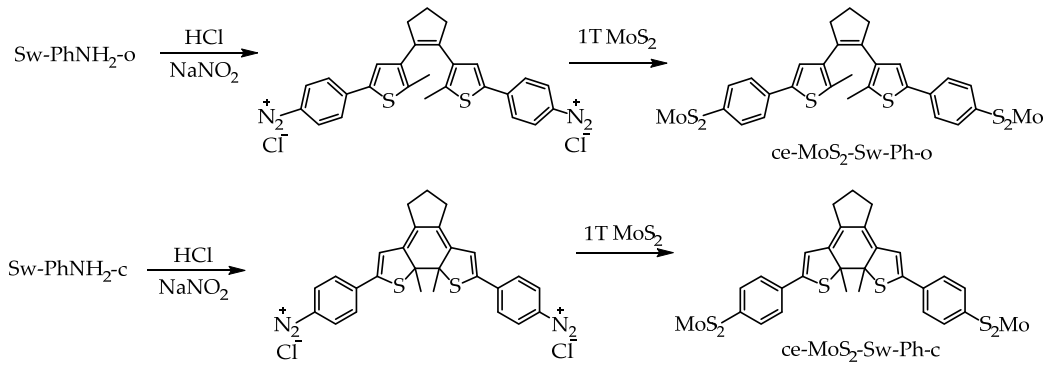

Figure VII.2. Covalent functionalisation of ce-MoS_2 with the photochromic molecule.

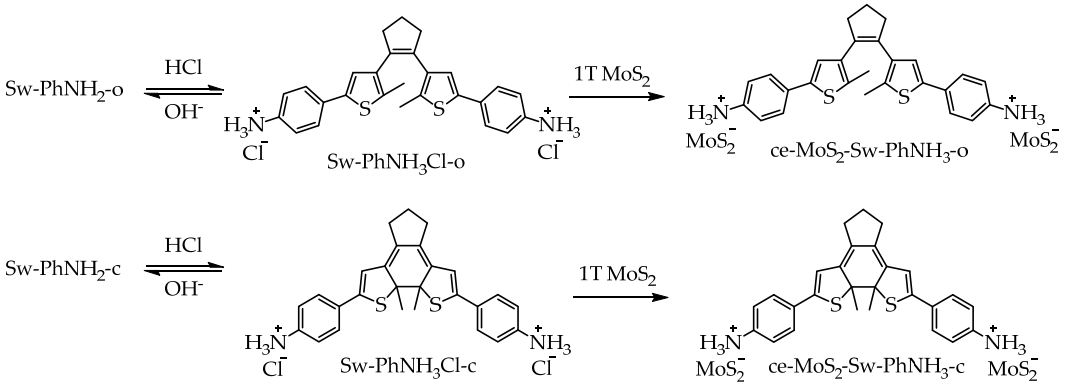

Figure VII.3. Electrostatic functionalisation of ce-MoS_2 with the photochromic molecule.

Sw-PhNH$_2$-o was synthesised via Suzuki coupling reaction of **Sw-Cl** with *N*-(*tert*-butoxycarbonyl)-4-bromoaniline, as the general method described by B. Feringa,[34] to afford **Sw-PhNHBoc-o** and subsequent removal of the protective Boc (*tert*-butyloxycarbonyl) group by using trifluoroacetic acid. The **Sw-PhNH$_3$Cl-o** salt was obtained by the addition of ~4 equivalents of HCl to **Sw-PhNH$_2$-o**.

All closed-ring isomers were obtained by subjecting the open-ring isomers solutions to UV irradiation. The closure reactions were followed by UV/Vis spectroscopy, which helped to establish the best conditions for the cyclization reaction. The isolation of **Sw-PhH-c** as dark violet crystals was performed by slow evaporation in acetonitrile of **Sw-PhH-o** after UV irradiation. The purity of **Sw-PhH-c** was determined by ^{1}H-NMR since the photocyclization of **Sw-PhH-o** yields a significant change in the chemical displacements for the -CH_2- protons of the cyclopentene ring from 2.86 and 2.10 ppm to 2.50 and 1.92 ppm, and for the aromatic –CH- protons of the thiophene ring from 7.06 to 6.42 ppm, for **Sw-PhH-o** and **Sw-PhH-c**, respectively.

Photoswitchable properties (interconversion reactions) of the organic molecules can be studied by UV/Vis spectroscopy since the differences in the conjugation of the two structures result in a different colour and absorption spectrum for each form, *i.e.*, open and closed forms. For the interconversion between the open and closed forms of dithienylethene molecules, the thiophene rings must remain antiparallel to each other so they can undergo the photocyclisation reaction.[35] Additionally, the required irradiation wavelengths and the fatigue resistance depend on the substituents on the thiophene units.[36] Typically, the cyclization reaction (closing process) requires from UV light meanwhile reversing the reaction (the ring-opening) requires from visible light. An excess of UV light irradiation time can lead to the photodegradation of the closed-ring isomer giving other by-products that are not reversible, *i.e.*, annulated isomers formed as a result of a 1,2-dyotropic rearrangement,[37] as observed by the loss of the isosbestic point in the absorption spectra, in this case. Therefore, UV/Vis experiments at different concentrations and irradiation times were performed to determine the optimum irradiation conditions of the synthesised compounds.

The photoswitchable properties of **Sw-PhH-o** and **Sw-PhH-c** molecules (**Sw-PhH**)[§] have already been described.[34] The UV/Vis spectra of **Sw-PhNH$_2$**, **Sw-PhNH$_3$Cl** are shown in Figure VII.4–5. The UV spectra for an **Sw-PhNH$_2$-o** solution in MeOH or EtOH/H_2O (2:1) present an absorption band at ~310 nm, which is almost solvent-independent. After irradiation, there is a shift of the ~309 nm band to ~319 nm and the emergence of two absorption bands, one very intense at ~529 nm, with a shoulder at ~560 nm, and another less intense at 836 nm (Figure VII.4). The optimum pH for a quantitative protonation of **Sw-PhNH$_2$-o** into **Sw-PhNH$_3$Cl-o** is 2.8 (Figure VII.5a), which was determined by monitoring the absorbance decreasing for the band at ~309 nm, attributed to the conjugation loss after the protonation.[31,38] The irradiation of **Sw-PhNH$_3$Cl-o** shows in its

[§] The "-o" and "-c" suffixes refer to the open and closed-ring isomers (or forms) of the photoswitchable molecule. Without those suffixes, open and closed-ring isomers are considered indistinctly.

UV/Vis spectrum a shift of the ~280 nm band to ~268 nm and the emergence of absorption bands at 353, 418, 463, 526, 554, 606 and 660 nm (Figure VII.5b).

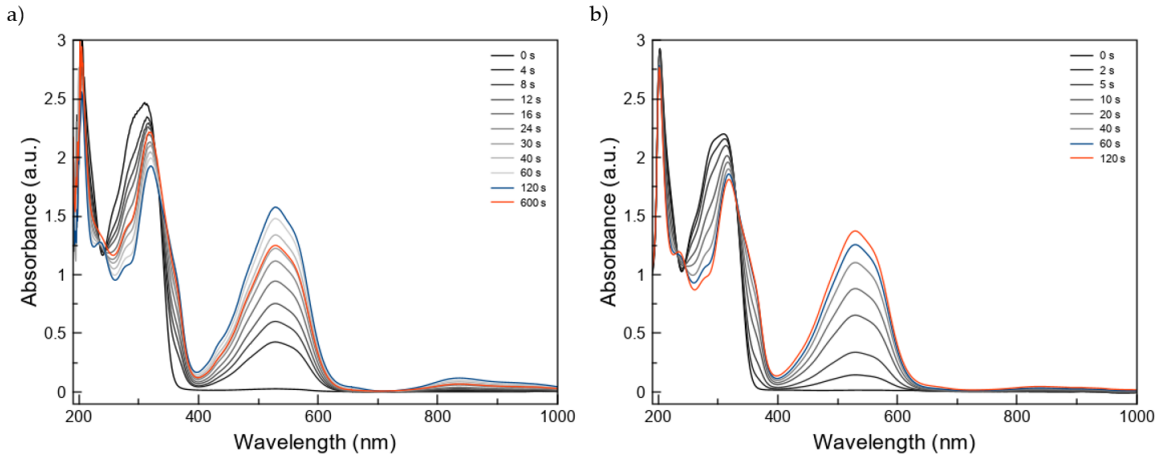

Figure VII.4. UV/Vis absorption spectra of **Sw-PhNH$_2$-o** 0.07 mM in a) MeOH and b) EtOH/H$_2$O 2:1 at different irradiation times with 350 nm lamps. The blue line represents the maximum time prior to degradation. The red line represents the time in which the isosbestic point at ~240 nm is lost.

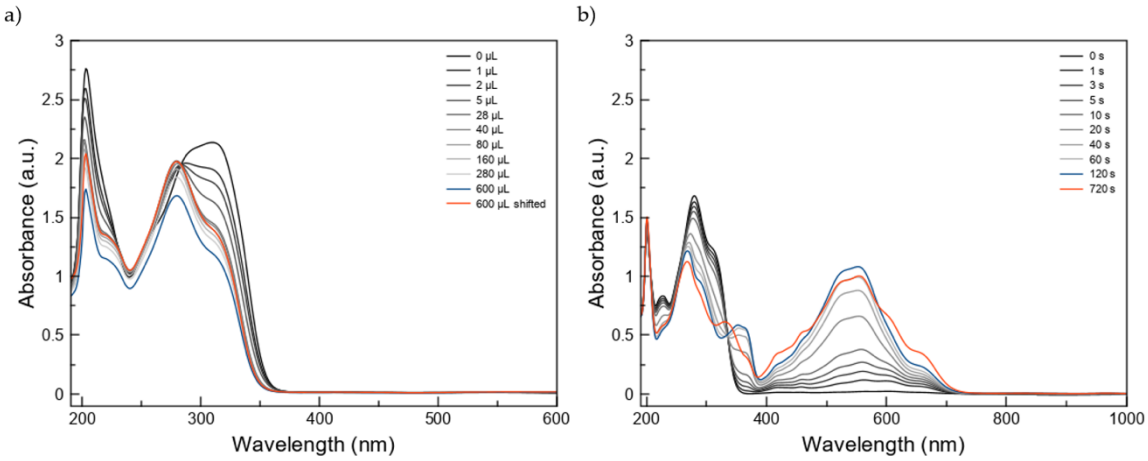

Figure VII.5. UV/Vis absorption spectra of a) **Sw-PhNH$_2$-o** (3 mL, 0.07 mM in EtOH/H$_2$O 2:1) upon addition of HCl 1M, where the red line is the blue one adjusted to match the isosbestic point; and b) **Sw-PhNH$_3$Cl-o** (0.06 mM in EtOH/H$_2$O (3:5)) photoconversion at different irradiation times with 350 nm lamps, where the blue line represents the maximum time prior to degradation and the red line represents the time in which the isosbestic point at ~335 nm is lost.

The obtained irradiation times for the maximum conversion into the closed-ring isomers for both **Sw-PhNH$_2$-o** and **Sw-PhNH$_3$Cl-o** were 120, 720 and 1020 seconds for 0.07, 0.41 and 0.70 mM solutions, respectively. These times were roughly estimated by following the time in which the isosbestic point is lost due to degradation processes for the corresponding **Sw-PhNH$_2$-o** and **Sw-PhNH$_3$Cl-o** solutions (blue line in Figure VII.4b and Figure VII.5b, respectively). The syntheses of closed-ring isomers were performed by irradiating 0.41 and 0.70 mM solutions of **Sw-PhNH$_3$Cl-o** and **Sw-PhNH$_2$-o**, respectively.

The optimal irradiation times were shortened to 600 and 900 seconds for **Sw-PhNH$_3$Cl-o** and **Sw-PhNH$_2$-o**, to prevent the generation of by-products,[36] because the closed-ring species can easily undergo degradation.[39] Unfortunately, this approach does not interconvert all photoswitching molecules into the closed form, then, some of these open form molecules remain as an impurity for the closed syntheses.

VII.3.2 Functionalisation of ce-MoS_2 by using Sw-PhNH$_2$

Functionalisation of ce-MoS_2 with the organic molecules was performed following two main approaches, covalent and electrostatic methods. The only difference is the para-substituent of the phenyl ring on the molecule (**Sw-PhNH$_2$** and **Sw-PhNH$_3$Cl** for covalent and electrostatic methods). Moreover, physical mixtures of **Sw-PhH** with **ce-MoS_2** are studied to understand the role of the type of interactions that drive the functionalisation.

The covalent functionalisation approach was carried out by means of diazonium derivatives. The diazonium salts were formed in-situ without isolation by mixing **Sw-PhNH$_2$** with sodium nitrite in a hydrochloric medium at 0 °C (ice bath, required for preventing azo couplings[40]), under magnetic stirring and argon atmosphere. Whereas the diazotisation reaction yielded an orangish colour, visible for **Sw-PhNH$_2$-o**, no visible changes were observed for **Sw-PhNH$_2$-c** due to its original intense purple colour. After an hour, a freshly prepared aqueous suspension of ce-MoS_2 flakes was added dropwise into the reaction, and it was allowed to react for 24 h at room temperature. The nucleophilic attack of the negatively charged ce-MoS_2 to the aryl cation (formed by the displacement of the diazonium salt) forms a new C–S bond, affording **ce-MoS_2-Sw-Ph**. Several washing cycles with different solvents (H_2O, DMSO and MeOH) were performed to eliminate impurities in the **ce-MoS_2-Sw-Ph-o** and **ce-MoS_2-Sw-Ph-c** (**ce-MoS_2-Sw-Ph**) materials until recording a flat UV/Vis spectrum.

The electrostatic approach was performed by mixing **Sw-PhNH$_2$** with MoS_2 in an EtOH/H_2O solution with an approximate pH of 2.8. Three washing cycles with EtOH/H_2O (2:1) were performed to remove impurities in the resulting **ce-MoS_2-Sw-PhNH$_3$** materials.

In addition, physical mixtures of **Sw-PhH** (-o and -c) with ce-MoS_2, named as **ce-MoS_2+Sw-PhH-o** and **ce-MoS_2+Sw-PhH-c**, were carried out in a mortar. Covalent bonds are not expected to form, but these mixtures are used as an approach or blank to **ce-MoS_2-Sw-Ph** and **ce-MoS_2-Sw-PhNH$_3$** products.

Fourier-Transform Infrared spectroscopy (FTIR)

The diazotisation of Sw-PhNH$_2$ and ulterior covalent functionalisation from MoS$_2$ removes the diazo group leading to a new C–S bond. Therefore, the band at ~2290 cm^{-1} typical of the diazo group disappears. Since **Sw-PhH-o/c** resembles the resultant covalent functionalisation with photochromic molecules, FTIR spectra of **ce-MoS$_2$-Sw-Ph**, **Sw-PhH-o**[40] and **Sw-PhH-c** were compared to get some insights about this functionalisation (Figure VII.6). However, it is known that the substituents of the thiophene ring alter the properties of the organic molecule.[41]

The most intense vibration peaks in the FTIR spectrum of **Sw-PhH-o** appear at ~2197 and 2851 cm^{-1} (CH$_2$ and CH$_3$ stretching), 1650–1450 cm^{-1} (C–C aromatic stretching) and 900–650 cm^{-1} (out-of-plane C–H bending of aromatic rings). Overtone peaks of benzene rings are also visible (1990–1650 cm^{-1}). The vibrations coming from the cyclopentene unit can be spotted in the 1620–1450 cm^{-1} range.[42]

The FTIR spectra of **Sw-PhH-c** and **Sw-PhH-o** are very similar.[42] The main differences are the disappearance of peaks at 1635, 1532, 1465, 1292, 1173 and 950 cm^{-1}, and a shift of 1383 and 849 cm^{-1} peaks to 1362 cm^{-1} and 827 cm^{-1} for **Sw-PhH-c**. The changes in the vibrational modes in the 1650–900 cm^{-1} region are due to the perturbation of peripheral aromatic rings. In particular, the red-shift is owed to the increase in communication between the thiophene and phenyl ring systems breathing vibration at ~1600 cm^{-1}.[42]

Both **ce-MoS$_2$-Sw-Ph** FTIR spectra present O–H stretching modes at ~3420 cm^{-1}, from H$_2$O molecules, and C–H stretching modes at ~2920 and ~2850 cm^{-1} coming from the photochromic molecule. Mo–S stretching at ~470 cm^{-1} is present,[43] but merged as a shoulder with a peak at ~480 cm^{-1} coming from the organic moiety. The weak C–S stretching expected for the covalent functionalisation is visible in the 667 cm^{-1}.[44] Additionally, the lack of peaks associated with aryl diazo groups[45] between 2309 and 2136 cm^{-1} is consistent with the covalent functionalisation to MoS$_2$ flakes instead of polymerisation.[46] The aromatic C–S stretching peak expected for the thiophene is shown at ~1071 cm^{-1}.[47] Moreover, the vibration peak at ~830 cm^{-1} is assigned to the out-of-plane C–H bending in 1,4-disubstituted benzenes,[48] which provides additional evidence of covalent functionalisation in the para position. No evidence that helps to distinguish between both structures was found with this technique (Figure VII.6). The low spectral resolution does not discern the red-shift of the closed-ring isomer from those coming from the open form.

For the case of **Sw-PhNH$_3$Cl** (Figure VII.7 left), both O–H and C–H stretching modes are also present. Both of them display a broad band between 3100–2700 cm^{-1}, which can be attributed to the N–H stretching bands. The new band at ~2570 cm^{-1} is attributed to the protonated amino salt stretching band.[49] In contrast to **Sw-PhH** spectra, **Sw-PhNH$_3$Cl-c**

has significantly more bands than **Sw-PhNH$_3$Cl-o** in the 1650–900 cm^{-1} region. Nevertheless, the compounds still share some peaks at 1509, 1473, 1313, 1117, 820, 633 and 487 cm^{-1}.

Composites **ce-MoS$_2$-Sw-PhNH$_3$** (Figure VII.7 right) present the O–H and C–H stretching modes as in the covalent composites. The peaks around 1620–1590 cm^{-1} are assigned to either C=C aromatic bonds or N–H deformation vibrations.[49] These peaks together with the ~817 cm^{-1} peak, assigned to the out-of-plane C–H bending, confirm the presence of the organic molecule. In contrast to the covalent functionalisation, the C–S peak at ~670 cm^{-1} is not found, as expected for an electrostatic composite. The small differences in peak intensities cannot be directly related to any band present in the **Sw-PhNH$_3$**.

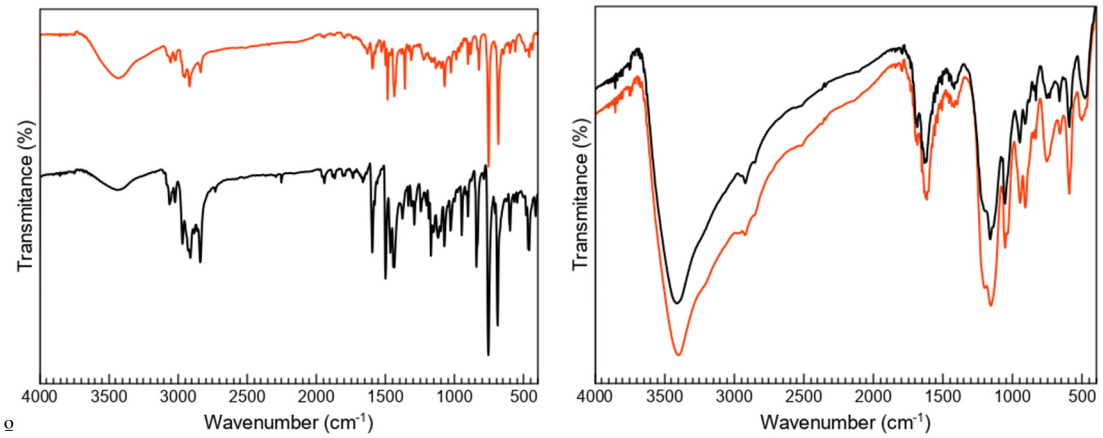

Figure VII.6. FTIR spectra for the open (black) and closed (red) forms of **Sw-PhH** (left) and **ce-MoS$_2$-Sw-Ph** (right).

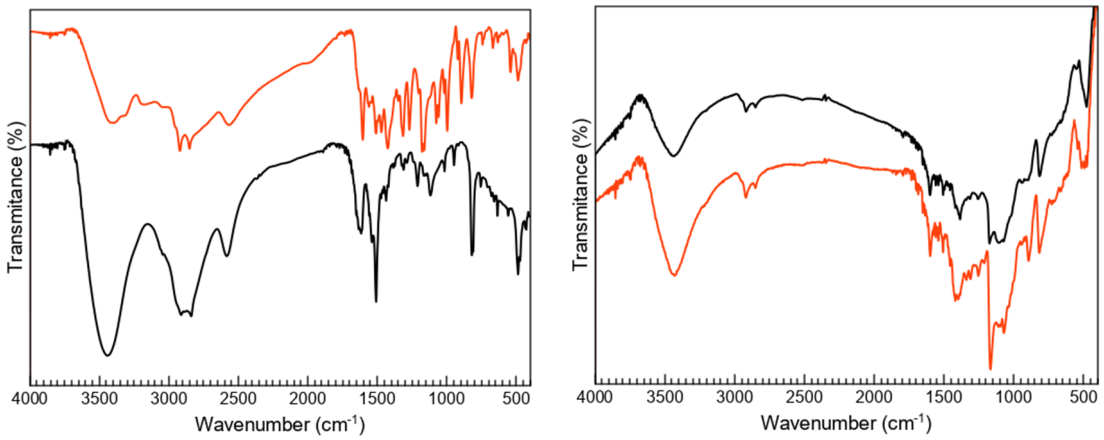

Figure VII.7. FTIR spectra for the open (black) and closed (red) forms of **Sw-PhNH$_3$Cl** (left) and **ce-MoS$_2$-Sw-PhNH$_3$** (right).

X-Ray Photoelectron Spectroscopy (XPS)

XPS, which gives essential details about the binding energies of the electrons for an atom and its oxidation state, has been used to get information about the molecular composition as well as the 1T/2H ratio in functionalised ce-MoS_2-Sw composites. Table VII.1 shows the peak values and the assignments of Mo, S and N elements for **Sw-PhNH$_2$-o, ce-MoS$_2$-Sw-Ph-o** and **ce-MoS$_2$-Sw-Ph-c** (Figure VII.8).[50–54]

The XPS spectra of **ce-MoS$_2$-Sw-Ph-o** and **ce-MoS$_2$-Sw-Ph-c** overlap perfectly. In both **ce-MoS$_2$-Sw-Ph**, C–S contributions include the C–S bonds coming from MoS_2 functionalisation and those present in the thiophene rings. Consistently, the peaks ascribed to C–S bonds are broader (Full Width at Half Maximum, FWHM, of ~1.5 eV) than those assigned to aromatic C–S from the thiophene in **Sw-PhNH$_2$-o** (FWHM ~1.1 eV). Both **ce-MoS$_2$-Sw-Ph** do not reveal clear N signals in the N 1s region but Mo $3p_{3/2}$ peaks. The absence of N 1s peaks in the region suggests that no nitrogen-containing by-products (like azo derivatives) or starting materials are present, confirming the purity of the sample. Furthermore, the absence of N peaks and the detection of broader C–S signals prove the efficacy of diazo moieties as leaving groups and the attachment of the Sw backbone into ce-MoS_2 flakes. The XPS spectrum suggests that the 1T MoS_2 polytype, obtained by the chemical exfoliation with *n*-BuLi in H_2O, have transformed into the 2H polytype, thermodynamically stable.[54] The results contrast with those obtained by C. Backes *et al.* and C. Rao *et al.*,[20,55] which showed covalently functionalised ce-MoS_2, by means of pure diazonium salts, maintain the 1T polytype but with unusual semiconducting properties, more typical for the 2H polytype. Respect to the total Mo(IV) amount, ~73.6 and ~71.4% is present as 2H MoS_2 in **ce-MoS$_2$-Sw-Ph-o** and **ce-MoS$_2$-Sw-Ph-c**, respectively. In both cases, the remaining percentage corresponds to MoO_2 and oxidized Mo(V). The MoS_2/molecule ratios were calculated from the S peak areas ($S_{MoS2}/S_{C–S}$), and these are ~3.09 (45.3% mass) and 2.89 (47.0% mass) for open and closed forms, respectively. No peaks corresponding to the Li^+ ion were detected.

Overall, both **ce-MoS$_2$-Sw-PhNH$_3$-o** and **ce-MoS$_2$-Sw-PhNH$_3$-c**, show the same XPS spectra. The Mo and S region, in these spectra, are dominated by 1T/2H MoS_2 and Mo^{IV} peaks with a small contribution of S 2s, and six peaks from 1T MoS_2 and 2H MoS_2 polytypes with a small contribution from the C–S bonds of the thiophene rings, respectively. Sulphur atom in thiophene rings shows FWHM (~1.1 eV) comparable to those observed in **Sw-PhNH$_2$**. 1T/2H MoS_2 (S_{1T}/S_{2H} = ~0.37 and 0.48 for open and closed forms, respectively) and MoS_2/molecule ratios [$S_{MoS2}/S_{C–S}$ = ~3.31 (45.6% mass) and 2.30 (54.7% mass) for open and closed forms, respectively] were calculated from the S peak areas. In contrast to the spectra of **ce-MoS$_2$-Sw-Ph**, there is a peak corresponding to the amino group, which is slightly shifted from the expected protonated amine.[56–58] The absence of Cl in the XPS survey also support the non-covalent functionalisation between

negative-charged MoS_2 flakes and the protonated amino groups. Li^+ peaks were not detected.

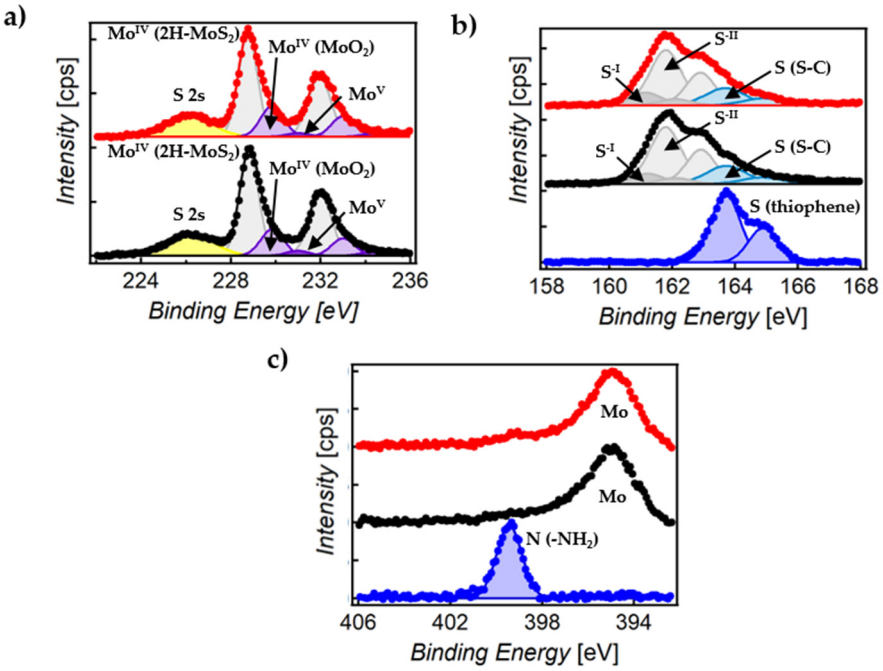

Figure VII.8. a) Normalised Mo 3d spectra of **ce-MoS_2-Sw-Ph-o** (black) and **ce-MoS_2-Sw-Ph-c** (red); b) Normalised S 2p spectra of **Sw-$PhNH_2$-o** (blue), **ce-MoS_2-Sw-Ph-o** (black), and **ce-MoS_2-Sw-Ph-c** (red); c) Normalised N 1s spectra of **Sw-$PhNH_2$-o** (blue), **ce-MoS_2-Sw-Ph-o** (black), **ce-MoS_2-Sw-Ph-c** (red). Each XPS spectrum is normalised respect to the highest value registered in its envelope. The figures were provided by Dr Marc Morant-Giner.

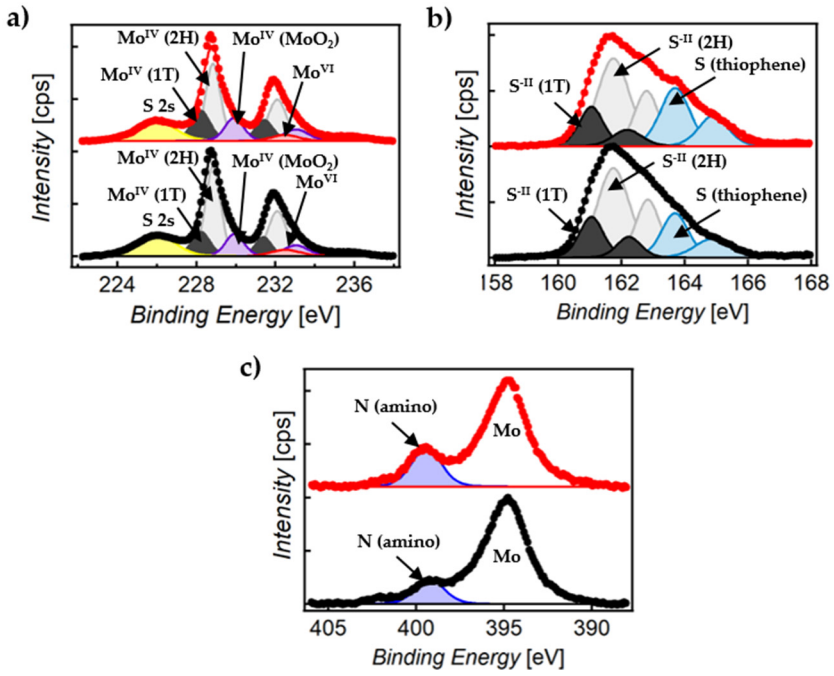

Figure VII.9. Normalised Mo 3d (a), S 2p (b) N 1s (c) spectra of **ce-MoS_2-Sw-$PhNH_3$-o** (black) and **ce-MoS_2-Sw-$PhNH_3$-c** (red). Each XPS spectrum is normalised respect to the highest value registered in its envelope. The figures were provided by Dr Marc Morant-Giner.

Table VII.1. XPS values observed in **ce-MoS_2-Sw-Ph**, **ce-MoS_2-Sw-$PhNH_3$**, and **Sw-$PhNH_2$-o**.

Composite	Mo peaks (eV)	S peaks (eV)	N Peaks (eV)
ce-MoS_2-Sw-Ph-o & ce-MoS_2-Sw-Ph-c	~228.8 Mo^{IV} $3d_{5/2}$ (2H MoS_2)	~161.2 S^{-I} $2p_{3/2}$	–
	~232.0 Mo^{IV} $3d_{3/2}$ (2H MoS_2)	~162.1 S^{-I} $2p_{1/2}$	
	~229.9 Mo^{IV} $3d_{5/2}$ (2H MoO_2)	~161.8 S^{-II} $2p_{3/2}$ (2H MoS_2)	
	~233.0 Mo^{IV} $3d_{3/2}$ (2H MoO_2)	~162.9 S^{-II} $2p_{1/2}$ (2H MoS_2)	
	~231.0 Mo^{V} $3d_{5/2}$	~163.7 S^{-II} $2p_{3/2}$ (S–C)	
	~234.3 Mo^{V} $3d_{3/2}$	~164.9 S^{-II} $2p_{1/2}$ (S–C)	
	–	~226.2 S^{-II} 2s	
ce-MoS_2-Sw-$PhNH_3$-o & ce-MoS_2-Sw-$PhNH_3$-c	~228.2 Mo^{IV} $3d_{5/2}$ (1T MoS_2)	~161.1 S^{-II} $2p_{3/2}$ (1T MoS_2)	~399.4 N 1s (NH_2)
	~228.9 Mo^{IV} $3d_{5/2}$ (2H MoS_2)	~161.8 S^{-II} $2p_{3/2}$ (2H MoS_2)	
	~229.9 Mo^{IV} $3d_{5/2}$ (MoO_2)	~162.2 S^{-II} $2p_{1/2}$ (1T MoS_2)	
	~231.4 Mo^{IV} $3d_{3/2}$ (1T MoS_2)	~162.9 S^{-II} $2p_{1/2}$ (2H MoS_2)	
	~232.1 Mo^{IV} $3d_{3/2}$ (2H MoS_2)	~163.7 S^{-II} $2p_{3/2}$ (S-C)	
	~232.5 Mo^{VI} $3d_{5/2}$	~164.9 S^{-II} $2p_{1/2}$ (S-C)	
	~233.0 Mo^{IV} $3d_{3/2}$ (MoO_2)	~226.1 S^{-II} 2s	
	~235.7 Mo^{VI} $3d_{3/2}$	–	
Sw-$PhNH_2$-o	–	~163.7 S^{-II} $2p_{3/2}$ (S–C)	~399.4 N 1s (NH_2)
		~164.9 S^{-II} $2p_{1/2}$ (S–C)	

X-Ray Powder Diffraction (XRPD)

The XRPD patterns of **ce-MoS_2-Sw-Ph** are similar to that simulated for 2H MoS_2 (Figure VII.10). The most intense peak at ~14.3° (6.2 Å) is present in both composites and corresponds to the (002) plane of MoS_2. The absence of a shift of the (002) peak at lower 2θ values indicates that the interlayer distance along the *c*-axis remains unaffected after the functionalisation. However, the broadened (00*l*) and (10*l*) peaks indicate a low number of layers along the *c*-axis and small particle sizes.[59,60]This statement is supported by the XRPD pattern of restacked ce-MoS_2 flakes in water, where a water bilayer between the MoS_2 monolayer is form,[37] showing a peak at 2θ ~7.2° (12.2 Å) caused by the presence these intercalated cations (Figure VII.10, green line).[61] A similar situation also occurs in **ce-MoS_2-Sw-$PhNH_3$-c**, where Sw-$PhNH_3$-c molecules seem to be located between MoS_2 layers, causing the development of a new reflection peak at 2θ ~6.4° (13.8 Å).

The question arises where the molecule attach on the covalent functionalisation. Three main possibilities are considered: i) in the basal plane of the MoS_2 flakes (*c*-axis), ii) in the edges of the MoS_2 flakes, iii) cross-linking different MoS_2 flakes through the edges or the *c*-axis. The arrival of new broad reflections at low 2θ values should support the functionalisation of the basal plane or a cross-linking along the *c*-axis. In this sense, Rao *et al.* achieved a cross-linking of MoS_2 flakes by using rigid linking molecules, where the (002) peak shifted to 2θ ~4°. However, H. Lee *et al.*, observe no shift of (002) peak, as in our

samples, which they relate to a cross-linking functionalisation through the edges and not through the *c*-axis. Therefore, the hypotheses related a basal plane functionalisation are ruled out because the length/volume of the organic molecule is enough to space out adjacent MoS_2 flakes, as seen for the electrostatic functionalisation. Then, the second and third hypotheses seem plausible for **ce-MoS_2-Sw-Ph**.

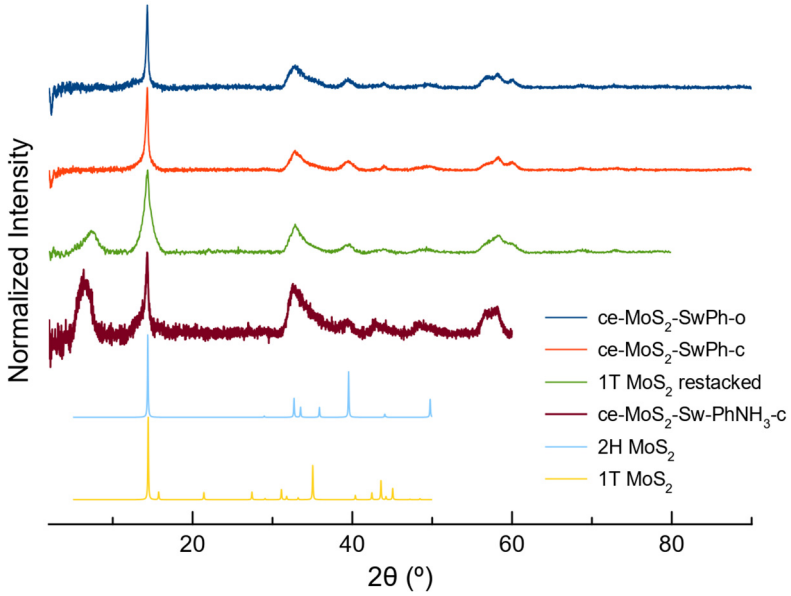

Figure VII.10. Normalised XRPD patterns of **ce-MoS_2-Sw-Ph-o** (blue), **ce-MoS_2-Sw-Ph-c** (red), restacked ce-MoS_2 flakes (green), **ce-MoS_2-Sw-$PhNH_3$-c** (garnet), simulated 2H MoS_2 structure (cyan) and simulated 1T MoS_2 structure (yellow). Pauling ID's are SD1415863 and SD0453841 for 1T MoS_2 and 2H MoS_2 structures, respectively.

UV/Vis spectroscopy

The UV/Vis spectra of ce-MoS_2 flakes in DMSO shows only a plasmon band at ~311 nm, since the other band appears below the cut-off of the DMSO band. These results suggest the presence of 1T MoS_2 polytype, in agreement with previously reported works.[63]

The UV/Vis spectra of **ce-MoS_2-Sw-Ph-o** and **ce-MoS_2-Sw-Ph-c** resuspended in DMSO are shown in Figure VII.11. No unambiguous absorption bands can be ascribed to plasmon bands (~257/257 and 308/311 nm 1T MoS_2 polytype in H_2O/DMSO, respectively) nor excitonic transitions (390–520 nm and 600–700 nm, 2H MoS_2 polytype in H_2O or DMSO).[27,64,65] Then, it is hard to assign the functionalised MoS_2 to any of the known polytypes with this technique. Unfortunately, no bands can be assigned to the molecule with certainty.

Composites **ce-MoS_2-Sw-$PhNH_3$** were resuspended in H_2O and measured with UV/Vis spectroscopy (Figure VII.12 left). The spectrum of **ce-MoS_2-Sw-$PhNH_3$-c** shows a broad absorption band from 520 to 980 nm, with a maximum at 720 nm, while a band from 550

to 830 nm, with a maximum at 685 nm, appears for **ce-MoS$_2$-Sw-PhNH$_3$-o**. Despite the small differences, their absorption spectra share bands at ~206, 332 and 450 nm. The electronic spectra of **ce-MoS$_2$-Sw-PhNH$_3$-o** and **Sw-PhNH$_3$Cl-c** are similar (Figure VII.12), but the composite evidences a red-shift larger than 80 nm after being electrostatically functionalisation in ce-MoS$_2$ flakes. None of these bands can be related with the MoS$_2$ polytypes, but they can be assigned to the Sw-PhNH$_3$ moiety. Then, these spectra show that **Sw-PhNH$_3$Cl-o** might undergo a partial ring-closure reaction after the functionalisation (Figure VII.12 right).

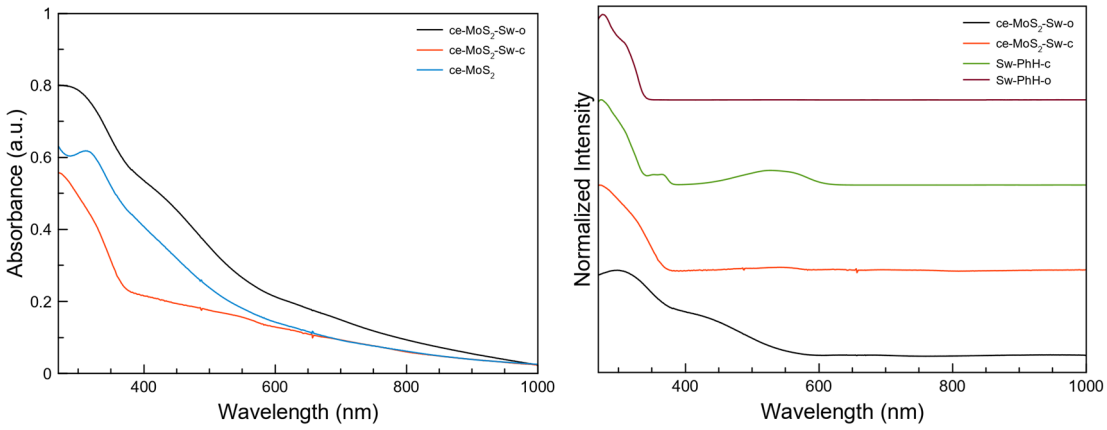

Figure VII.11. UV/Vis absorption spectra of **ce-MoS$_2$-Sw-Ph-o** (black), **ce-MoS$_2$-Sw-Ph-c** (red), and ce-MoS$_2$ (blue) in DMSO (left). Normalised and baseline corrected spectra via a parabolic function for both **ce-MoS$_2$-Sw-Ph** composites, together with **Sw-PhH-o** (garnet) and **Sw-PhH-c** (green) for comparison purposes (right).

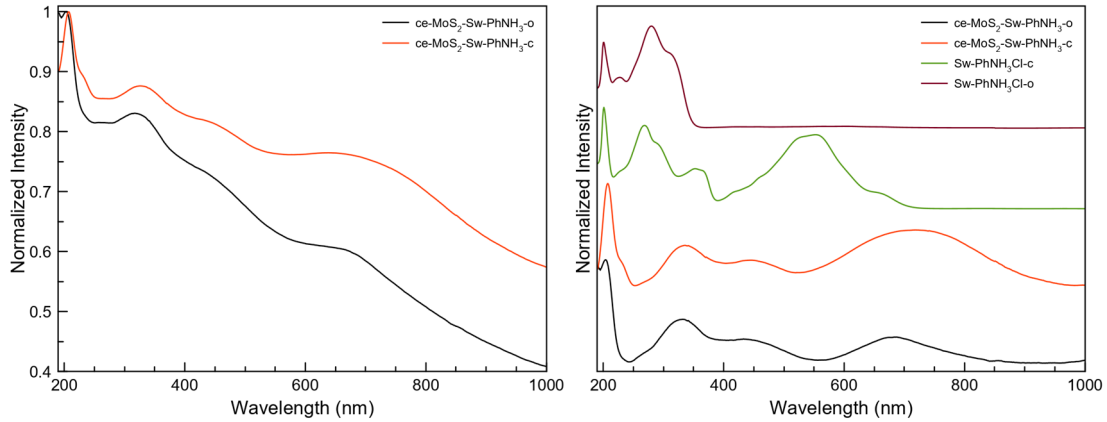

Figure VII.12. Normalised UV/Vis absorption spectra of **ce-MoS$_2$-Sw-PhNH$_3$-c** (black), **Sw-PhNH$_3$Cl-c** (red) in H$_2$O (left). Normalised and baseline corrected spectra via a parabolic function for both **ce-MoS$_2$-Sw-PhNH$_3$** composites, together with **Sw-PhNH$_3$Cl-o** (garnet) and **Sw-PhNH$_3$Cl-c** (green) for comparison purposes (right).

Raman spectroscopy

Raman spectroscopy was performed as second vibrational-related spectroscopy to determine the MoS_2 polytype and distinguish between the open- and closed-ring isomers of the photochromic molecule.

First, **Sw-PhH-o** and **Sw-PhH-c** were measured through Raman spectroscopy using the 785 nm near-infrared (NIR) laser (Figure VII.13) and are comparable to those reported in the literature.[42] Clear differences in the Raman spectra are observed between the open and close configuration in contrast to the similar IR spectra.

Due to the rigid shape of the closed structure (lower number of degrees of freedom), **Sw-PhH-c** displays less vibrational modes than **Sw-PhH-o**. For more energetic wavelengths (638 and 532 nm), PL is observed in both molecules, being more accentuated for **Sw-PhH-c**.

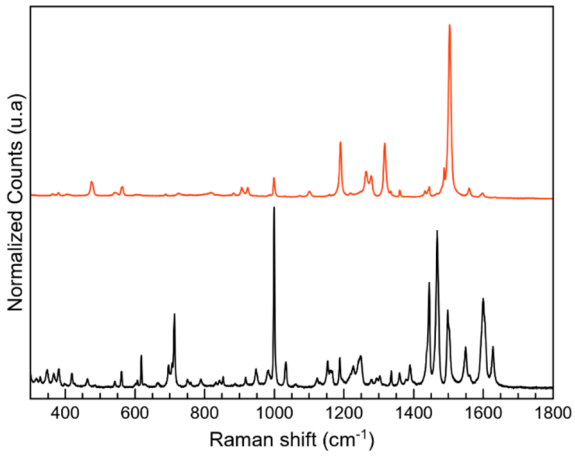

Figure VII.13. Normalised Raman spectra of **Sw-PhH-o** (black) and **Sw-PhH-c** (red) at 785 nm wavelength.

In contrast to the observed characteristics for **Sw-PhH** molecules, the Raman spectra for **ce-MoS_2-Sw-Ph** composites were not well resolved with the 785 nm laser. The most evident differences between both Raman spectra were registered when using the 532 nm laser. For the 638 nm excitation wavelength, low contrast between both Raman spectra was appreciated.

As expected, the Raman spectra for both systems (Figure VII.14a) show the coexistence of MoS_2 and Sw signals. While the peaks at ~382 and 407 cm^{-1} correspond to MoS_2 (E^1_{2g} and A_{1g} modes, respectively), the peaks located in the 1100–1700 cm^{-1} range are assigned to the organic molecule.[42] No *J* peaks (characteristic of 1T MoS_2) were detected,[66] confirming the 2H MoS_2 phase already determined by XPS. The signals observed in the 1100–1700 cm^{-1} range are very different from those in pure **Sw-PhH** molecules. These changes can be attributed to the covalent functionalisation since the vibrations are very sensitive to the

substitution of the aromatic rings.[42] Furthermore, the covalent bond is most likely to diminish the degrees of freedom of the organic backbone, decreasing the number of available vibration modes. The Raman spectra of the open and closed form composites are very similar, being the main differences related to the relative peak intensities.

The Raman peaks assigned to the organic molecule are ~1141, 1196, 1403, 1439, 1520 and 1597 cm^{-1} for **ce-MoS_2-Sw-Ph-o** and ~1144, 1191, 1403, 1521 and 1593 cm^{-1} for **ce-MoS_2-Sw-Ph-c**. Peaks at ~1141 and 1403 cm^{-1} are only attributed to the open configuration, but they are also present in **ce-MoS_2-Sw-Ph-c** (1144 and 1403 cm^{-1}). This fact is attributed to the syntheses protocol, where the cyclization reaction is stopped before reaching the maximum conversion, then, some **ce-MoS_2-Sw-Ph-o** can be present as a small impurity. Using the 532 nm laser, the PL of **ce-MoS_2-Sw-Ph** exhibits two bands related to the A_1 and B_1 excitonic transitions typical for 2H MoS_2 polytype (Figure VII.14b). Overall, the presence of PL together with the no detection of *J* peaks agree with the semiconducting 2H nature of **ce-MoS_2-Sw-Ph**.

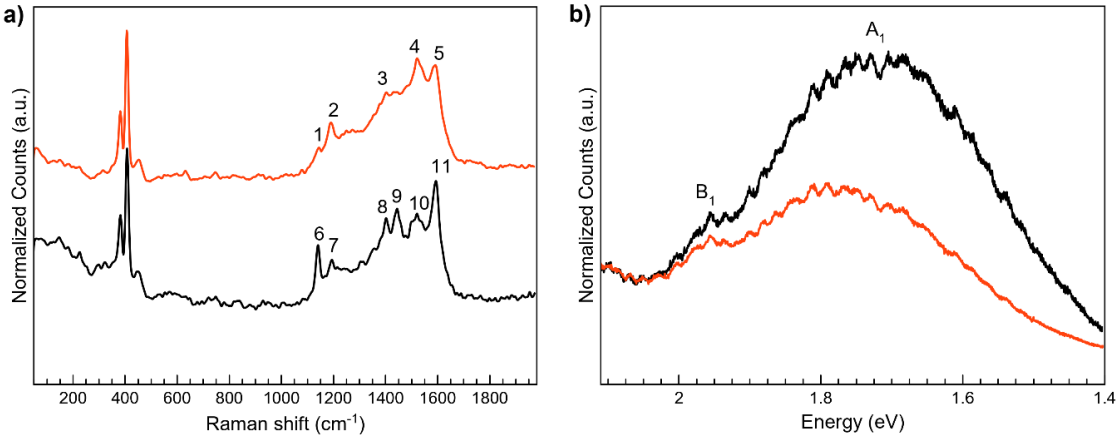

Figure VII.14. Normalised Raman (a) and PL (b) spectra and for **ce-MoS_2-Sw-Ph-o** (black) and **ce-MoS_2-Sw-Ph-c** (red) at 532 nm wavelength. In a), vibration bands for **ce-MoS_2-Sw-Ph-o** appears at ~1141 (*6*), 1196 (*7*), 1403 (*8*), 1439 (*9*), 1520 (*10*), 1597 (*11*) cm^{-1} whereas for **ce-MoS_2-Sw-Ph-c** are at ~1144 (*1*), 1191 (*2*), 1403 (*3*), 1521 (*4*), 1593 (*5*) cm^{-1}.

The Raman spectra for **Sw-$PhNH_3Cl$** shows PL at any wavelength laser (473, 532, 633, 785 nm) as shown in Figure VII.15 left. Nevertheless, using the NIR laser (785 nm) some signals coming from the organic molecule are hardly spotted together with the PL. A parabolic background correction has been applied to reveal the masked peaks in the 1000–1750 cm^{-1} range (Figure VII.15 right). Negligible peaks are found for **Sw-$PhNH_3Cl$-o** by using the NIR laser, but very weak peaks at ~1192, 1430, 1538 cm^{-1} are found for **Sw-$PhNH_3Cl$-c**.

Composites **ce-MoS_2-Sw-$PhNH_3$** share a similar Raman spectrum when the 532, 633 and 785 nm lasers (Figure VII.15 right). Then, the functionalisation of **Sw-$PhNH_3Cl$** molecules in ce-MoS_2 seems to quench their photoluminescence. Both composites present the characteristic peaks for the 2H and 1T polytypes located at ~382 and 407 cm^{-1}, and ~152

(J_1) and 328 cm^{-1} (J_3), respectively. Both composites exhibit the same spectrum, showing peaks at ~1137, 1190, 1249, 1413, 1535 and 1600 cm^{-1}. The most intense peaks somehow match with the ones registered for **Sw-PhNH$_3$Cl-c**, which suggests the presence of the closed-ring isomer in both composites. This fact agrees with what observed in their UV/Vis spectra and FTIR. The electrostatic functionalised composites (**ce-MoS$_2$-Sw-PhNH$_3$**) are similar to the covalently functionalised composites (**ce-MoS$_2$-Sw-Ph**), but the peaks are slightly shifted.

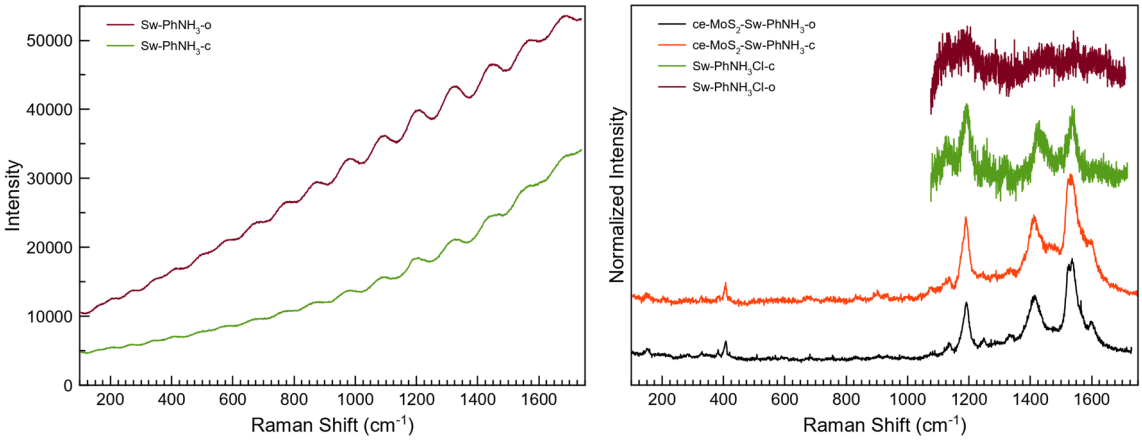

Figure VII.15. Photoluminescence spectra for **Sw-PhNH$_3$Cl-o** (garnet) and **Sw-PhNH$_3$Cl-c** (green) when using the 532 nm laser (left). Normalised Raman for **ce-MoS$_2$-Sw-PhNH$_3$-o** (black, 532 nm), **ce-MoS$_2$-Sw-PhNH$_3$-c** (red, 532 nm), **Sw-PhNH$_3$Cl-o** (garnet, 785 nm) and **Sw-PhNH$_3$Cl-c** (green, 785 nm) are shown together for comparison purposes (right).

Thermal Gravimetric Analysis (TGA)

TGA analysis were performed for ce-MoS_2, **Sw-PhH**, **ce-MoS$_2$-Sw-Ph** and **ce-MoS$_2$-Sw-PhNH$_3$**. At ~350 °C, both **Sw-PhH** undergo a significant mass loss (Figure VII.16). In addition, **Sw-PhH-o** displays an initial mass loss at 81 °C, which corresponds to removing acetonitrile crystallisation molecules.

For **ce-MoS$_2$-Sw-Ph-o** (Figure VII.16a), a mass drop of ~2.8% was detected between 25 °C and 140 °C, which would correspond to the loss of physisorbed solvent molecules. Then, two mass drops of ~6.1% and ~21.3% were registered in 140–325 °C and 325–700 °C ranges. The second mass drop is assigned to physisorbed photochromic molecules; meanwhile, the third is attributed to covalently attached molecules. The functionalisation degree was determined by assuming that the second and third mass losses arise from the organic molecule covalently attached to the MoS_2, except for a small contribution (~3.1%) corresponding to the S loss coming from MoS_2. With those considerations, a functionalisation percentage of ~24.3% (molar) is calculated.

For **ce-MoS_2-Sw-Ph-c** (Figure VII.16b), a mass drop of ~5.0% attributed to the loss of physisorbed solvent molecules was detected between 25 °C and 140 °C. Next, two mass drops of ~7.4% and ~14.5% were found in the 140–325 °C and 325–700 °C ranges. In this case, and following the same reasoning as for **ce-MoS_2-Sw-Ph-o**, the obtained functionalisation rate was ~18.8% (molar). As a result, both functionalisation rate degrees are comparable.

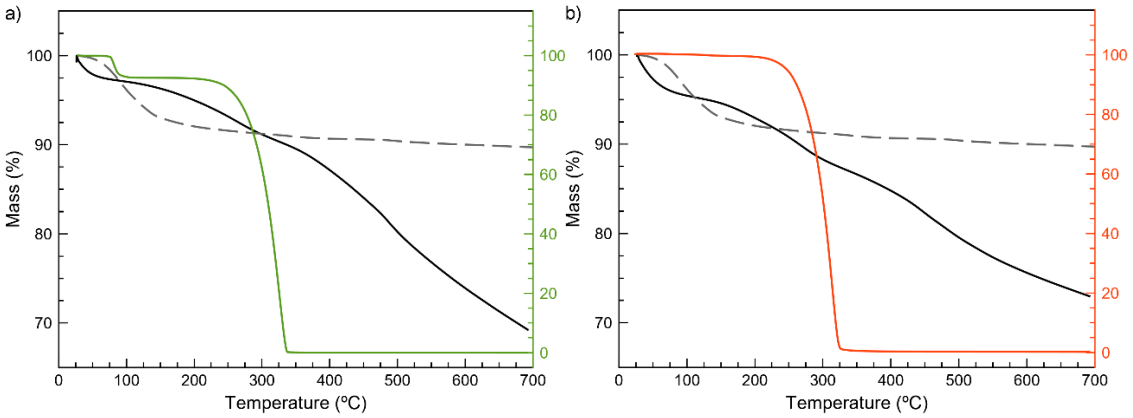

Figure VII.16. a) TGA plots for **Sw-PhH-o** (green line and y-axis), **ce-MoS_2-Sw-Ph-o** (black), and ce-MoS_2 flakes (dashed grey). b) TGA plots for **Sw-PhH-c** (red line and *y*-axis), **ce-MoS_2-Sw-Ph-c** (black), and ce-MoS_2 flakes (dashed grey).

For **ce-MoS_2-Sw-PhNH$_3$-o** (Figure VII.17), a mass drop of ~1.9% was detected in the 25–140 °C range, attributed to the loss of physisorbed solvent molecules. Next, two mass drops of ~1.5% and ~21.6% were found in the 140–275 °C and 275–700 °C ranges, respectively. The second mass drop is assigned to VdW interacting photochromic molecules and, the third one is attributed to electrostatically attached molecules. For **ce-MoS_2-Sw-PhNH$_3$-c**, the same drop temperatures and conclusions are found, but the mass losses are 2.5, 2.7 and 9.8% for 25–140 °C, 140–275 °C and 275–700 °C, respectively. The mass drops occur at slightly lower temperatures than for the covalent functionalisation, but with a lesser functionalisation yield. Considering a small contribution (~3.1%) corresponding to the S loss coming from MoS_2, the degree of functionalisation is 8.3 and 2.7% (molar) for **ce-MoS_2-Sw-PhNH$_3$-o** and **ce-MoS_2-Sw-PhNH$_3$-c**. These results disagree with the obtained ones from XPS

In the four cases, the degree of functionalisation does not match the ones calculated from the XPS analyses. However, the TGA analyses are require less user-considerations than XPS analyses, then, the former should be considered sample-representative. In fact, the expected mass drop of ~23% was found in the 140–700 °C region for the TGA analysis of **ce-MoS_2+Sw-Ph-o**.

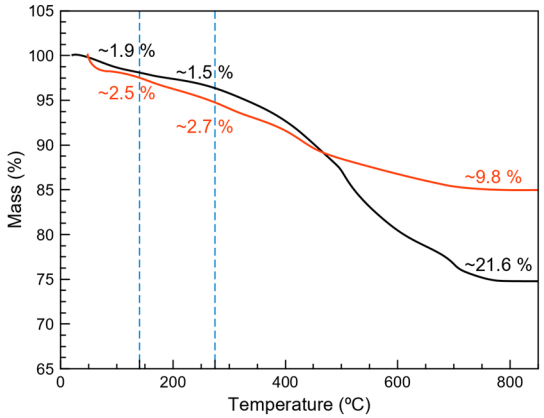

Figure VII.17. TGA plots for **ce-MoS_2-Sw-$PhNH_3$-o** (black), **ce-MoS_2-Sw-$PhNH_3$-c** (red). The mass drop ranges are shown as dashed blue lines.

VII.3.3 Photoswitching behaviour study for ce-MoS_2-Sw-Ph composites.

Photoswitchable studies were performed on **ce-MoS_2-Sw-Ph**, and also on the physical mixtures of ce-MoS_2 and **Sw-Ph**, namely **ce-MoS_2+Sw-Ph**, for comparative purposes. Therefore, a solution of the selected material was deposited onto clean SiO_2 (285nm)/Si substrates by drop-casting, giving white (**Sw-PhH-o**) and purple (**Sw-PhH-c**) crystals after the solvent removal. They were irradiated at 308 nm and >540 nm energies at different times with the photoreactor (see the experimental section for details) and were studied by Raman spectroscopy. Although UV/vis spectroscopy is a useful technique for colour changes (open and closed forms), this is not the case here, since the strong absorption of MoS_2 hinders the absorption bands from organic molecules in these materials.

Raman spectroscopic results (λ_{em} = 785 nm) highlight that 10 minutes of irradiation at 308 nm is enough to induce a qualitative photoinduced ring-closure **Sw-PhH-o** → **Sw-PhH-c** transformation (Figure VII.18a). Besides, the irradiation process can be extended until 1 hour without the appearance of other signals or loss in intensity bands. Unexpectedly, the peak intensity for **Sw-PhH-o** diminishes when dropcasted on the SiO_2 substrate, which did not happen when measuring its bulk nor for **Sw-PhH-c** (Figure VII.13). In the same way as for **Sw-PhH-o**, the characteristic Raman bands for the closed-ring isomer, **Sw-PhH-c**, disappeared under irradiation during 1 day at >540 nm, followed by the emergence of very weak intensity bands corresponding to the open-ring isomer (**Sw-PhH-o**) (Figure VII.18b). The weak signals registered after the irradiation can be attributed to a partial degradation upon the closed-ring aperture.[67] The required time for triggering the cycloreversion reaction (closed → open) are longer than the photocyclization reaction (open → closed), in agreement with the literature.[68] These results suggest that the molecule exhibit photoswitching behaviour in solid state in these conditions.

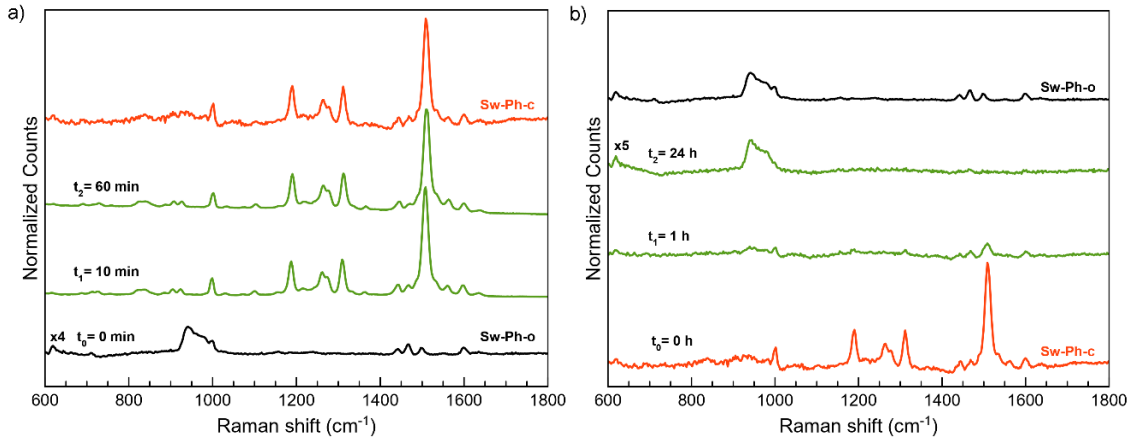

Figure VII.18. Raman spectra in the 600–1800 cm^{-1} region of a) **Sw-PhH-o** and b) **Sw-PhH-c** deposited onto a SiO_2/Si substrate and measured at 785 nm excitation wavelength before and after irradiation experiments. The spectra were baseline corrected and some spectra were magnified for comparison purposes.

The interconversion extent of the physical mixtures (~0.1 Sw-Ph/MoS_2 molar ratio) was analysed by Raman spectroscopy at 532 nm (Figure VII.19) since this is the most suitable λ_{ex} for **ce-MoS_2-Sw-Ph** materials. However, in this case, the photoluminescence of the organic moiety is pronounced, as for **Sw-PhH** (Figure VII.14), which impeded the recognition of bands corresponding to the molecule. Thus, when comparing the spectra of the physical mixtures with the ones for **ce-MoS_2-Sw-Ph**, it seems that the covalent functionalisation quench the photoluminescence of the molecule at any laser wavelength. The photoluminescence bands for **ce-MoS_2+Sw-PhH-o** were centred at ~1.81 and 2.13 eV, in contrast to what observed in **Sw-PhH-o** (~1.72 and 1.98 eV). However, the energy for these peaks is hard to determine with accuracy. No changes were appreciated after the irradiation using the 532 nm laser.

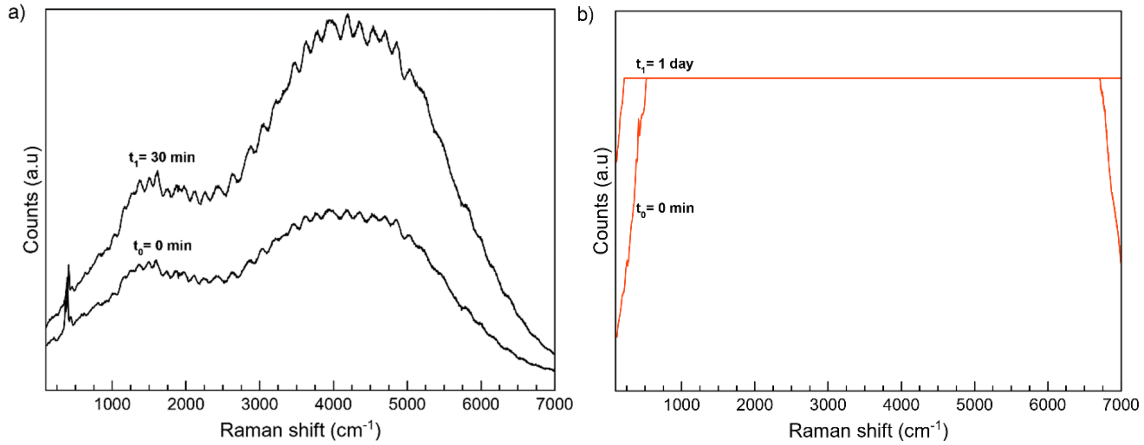

Figure VII.19. Raman spectra of the physical mixtures of a) **ce-MoS_2+Sw-PhH-o** and b) **ce-MoS_2+Sw-PhH-c** measured with 532 nm excitation laser before and after irradiation experiments. The plateaus registered for **ce-MoS_2+Sw-PhH-c** indicates saturation of PL signal.

Previous attempts to follow the interconversion with a photoreactor failed. Then, **ce-MoS_2-Sw-Ph** were irradiated and measured in-situ on the same spot area with the Raman spectrophotometer (Figure VII.20). The laser intensity powers used were 1% and 5% for measuring and irradiating the sample. Lower intensity laser powers led to very noisy measurements, and higher intensity laser powers resulted in MoS_2 oxidation and sample burnings.

The Raman spectra of the deposited **ce-MoS_2-Sw-Ph** samples (Figure VII.20) show small peak shifts and better peak resolution than the Raman spectra for their bulk samples (Figure VII.14a). The Raman peaks coming from the organic molecule are ~1140, 1195, 1316, 1403, 1439, 1533 and 1596 cm^{-1} for **ce-MoS_2-Sw-Ph-o** and ~1191, 1333, 1440, 1540 and 1593 cm^{-1} for **ce-MoS_2-Sw-Ph-c**.

When deposited **ce-MoS_2-Sw-Ph-o** was irradiated at 532 nm for 15 minutes, the peaks at ~1140, 1403 and 1439 cm^{-1} decreased in half their intensities. Meanwhile, the ~1195 and 1593 cm^{-1} peaks, characteristic for the closed-ring isomer, remained still after the first irradiation (ring closure). After irradiation at 633 nm during 90 minutes, the peaks reverted their intensity to the original ones and, after another irradiation of 15 minutes at 532 nm the peak intensities decreased again. These results suggest that the open-closed photoconversion might be occurring in some way (approximately 55%, considering that no peak is present for **Sw-PhH-c** at ~1140 cm^{-1}). However, when **ce-MoS_2-Sw-Ph-c** was irradiated at 633 nm (Figure VII.20b), no changes were observed at the 600–1800 cm^{-1} region, even increasing the power intensity laser or the irradiation times.

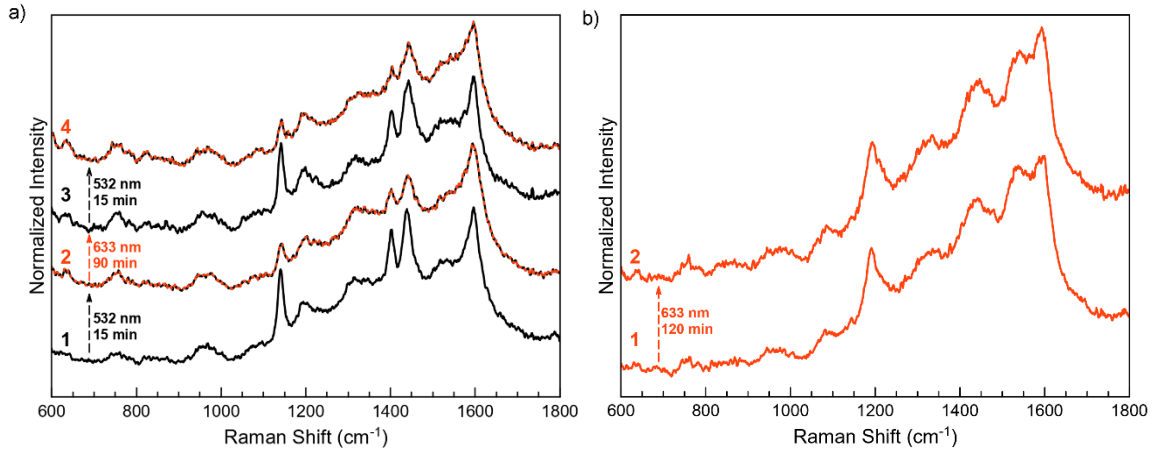

Figure VII.20. Raman spectra for the irradiated samples deposited on SiO_2 a) **ce-MoS_2-Sw-Ph-o** (3 irradiation steps) and b) **ce-MoS_2-Sw-Ph-c** (1 irradiation step) measured with a 532 nm excitation laser at 1% power. The open-ring isomer, the closed-ring isomer and a mixture of open-ring and closed-ring isomers are represented as black, red and black-red lines, respectively. The spectra were normalised for comparison purposes. In addition, Raman spectra were zoomed in the 600–1800 cm^{-1} region for clarity purposes.

The differences between irradiation experiments are assigned to a reduction of the freedom degrees of the molecule once covalently attached to MoS_2. Whereas the closed-ring ligand exhibits a rigid and linear disposition, the open-ring ligand can freely rotate the thiophene rings. While the open-form of the ligand displays numerous possibilities to attach the flakes, the closed form should be positioned in a straight manner to attach the flakes. As seen in Chapter V, the closed-ring ligand presents the shortest distance between the thiophene substituents. Thus, it might not undergo the ring-opening reaction since it involves a certain push from the functionalised edges (high energy barrier) to become further as in the open-ring isomers. Another possible explanation is a diastereoselective cyclization of the dithienylethene moiety by the reduction of its freedom degrees, where only one of the resulting diasteroisomers can undergo the reversible switching reactions.[69]

Raman irradiation experiments for the electrostatic functionalised **ce-MoS_2-Sw-$PhNH_3$** composites into SiO_2 substrates were also performed. Both of them behaved identically under light irradiation, then, only the irradiation experiments for **ce-MoS_2-Sw-$PhNH_3$-c** are shown in Figure VII.21. The composites were irradiated with 473, 532, 633 and 785 nm lasers and the ~1137, 1190, 1249, 1413 and 1535 cm^{-1} peaks underwent attenuation while the 2H MoS_2 peaks (~383 and 408 cm^{-1}) emerged and the 1600 cm^{-1} peak remained. None of the available lasers in Raman could revert these changes.

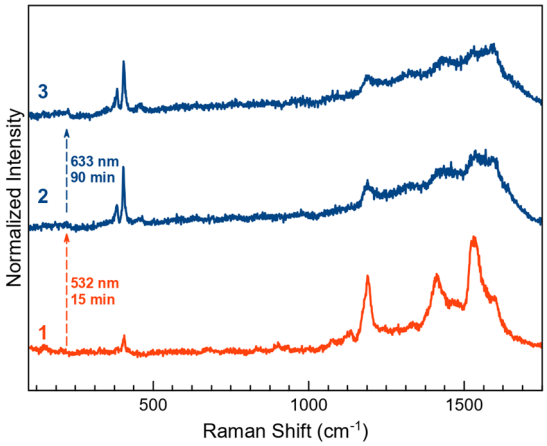

Figure VII.21. Raman spectra at 532 nm for **ce-MoS_2-Sw-$PhNH_3$-c** deposited into SiO_2 substrates (red) and the resulting irradiations with 532 and 633 nm lasers (blue).

As seen in Figure VII.12 and VII.16, it is difficult to distinguish between the open and closed-ring isomers of the electrostatic functionalised composites, **ce-MoS_2-Sw-$PhNH_3$**, with the Raman and UV/Vis spectroscopies. Unexpectedly, both present a band, in their UV/Vis spectra, which is compatible with the available set of lasers for Raman spectroscopy (520 to 980 nm), though apparently, it is broader and more intense for **ce-MoS_2-Sw-$PhNH_3$-c**. As pointed before, possible coexistence of the open and closed forms exits in **ce-MoS_2-Sw-$PhNH_3$-o**. Thus, the interconversion studies become very difficult to interpret. However, whereas weak bands are present in **Sw-$PhNH_3$Cl-c**, **Sw-$PhNH_3$Cl-o**

does not present any signal at Raman spectroscopy. Then, the signal attenuation of **ce-MoS_2-Sw-$PhNH_3$** might be ascribed to the ring-aperture reaction. UV/Vis experiments in solid state were also performed to elucidate the photoirradiation studies (Figure VII.22, left). A 2.5% mixture of **ce-MoS_2-Sw-$PhNH_3$-o** with KBr was irradiated in a photoreactor at 350 nm during 10 and 30 minutes. A small increase in absorbance in the 450–800 nm range is seen, which might be related to the switching of the few remaining open species. Additionally, a 4.2 % mixture of **ce-MoS_2-Sw-$PhNH_3$-c** with KBr was irradiated with visible lamps with orange filters (> 540 nm) in a photoreactor during 30, 120 and 180 minutes and measured by UV/Vis spectroscopy in solid (Figure VII.22, right These spectra show a decrease in absorbance in the 450–800 nm range, related to the ring-aperture of the photoswitchable molecule. Then, the molecule exhibits changes in **ce-MoS_2-Sw-$PhNH_3$** upon light irradiation, but no reversibility behaviour for the same sample is still achieved. Further experiments should be done to confirm these studies.

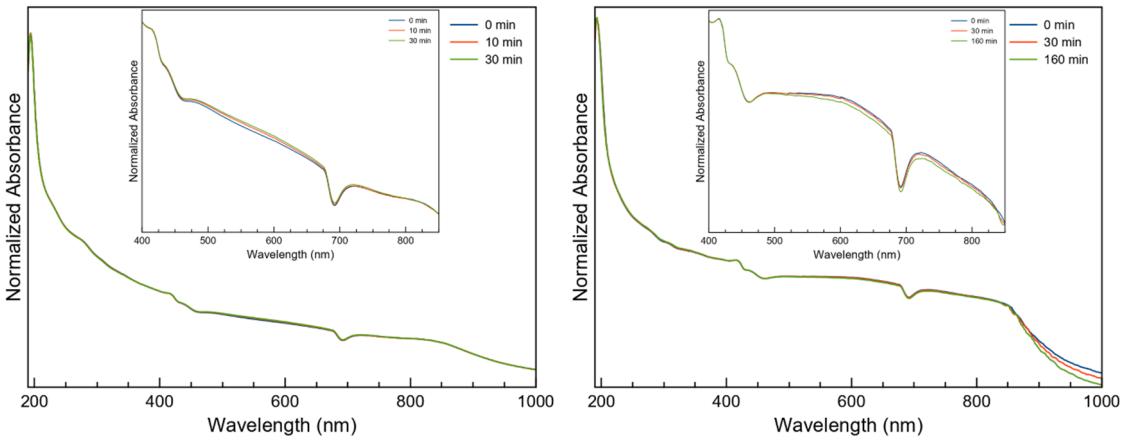

Figure VII.22. UV/Vis spectra for a 2.5% mixture of **ce-MoS_2-Sw-$PhNH_3$-o** with KBr and the resulting irradiations at 350 nm and different times with zoomed spectra as inset (left). UV/Vis spectra for a 4.2% mixture of **ce-MoS_2-Sw-$PhNH_3$-c** with KBr and the resulting irradiations at >540 nm and different times with zoomed spectra as inset (right)

VII.3.4 Conclusions

In this chapter, two photochromic dithienylethene derivatives, namely **Sw-$PhNH_2$** and **Sw-$PhNH_3Cl$,** are prepared under their open-ring and closed-ring isomers for ce-MoS_2 covalent and electrostatic functionalisation. Covalent functionalisation on ce-MoS_2 flakes by means of a diazotisation reaction of two photochromic molecules is achieved. The electrostatic approach resulted from the interactions between the positive-charged photochromic molecules and the negative-charged MoS_2 flakes.

Covalent and electrostatic functionalised **ce-MoS_2-Sw-Ph** were characterised by FTIR, XPS, Raman and TGA analyses. With the covalent strategy, the expected 1T-MoS_2 is wholly transformed into the 2H polytype, whereas some 1T polytype is still preserved in

the electrostatic functionalisation, as proven by Raman spectroscopy and XPS. This polytype stability is probably required for compensating the positive charges coming from the protonated photochromic molecule. In general, the averaged functionalisation degree was ~13% (molar) for both covalent and electrostatic approaches.

In both approaches, the composites with both isomers, as bulk and deposited into SiO_2 substrates, and the physical mixtures were prepared to gain more details about the functionalisation and possible photoswitching capacity by Raman spectroscopy (and UV/Vis spectroscopy).

Although the open and closed forms for the bare molecules display two different Raman spectra, these differences are not so straightforward in the functionalised MoS_2 materials. Then, a meticulous examination is necessary. First of all, the photoluminescence at 532 nm of the bare photochromic molecules is quenched after MoS_2 functionalisation for both covalent and electrostatic approaches. Irradiations experiments reveal that the open form of the covalent material undergoes partially and reversible close-open reactions. However, going from the closed to open material is not possible under the established experimental conditions. We believe that the reason behind this phenomenon is related to the freedom degree of the molecule once covalently bonded to the ce-MoS_2 flakes. In fact, the materials resultant from the electrostatic approach can be switched and registered by UV/Vis in solid state.

Further work dealing with electric transport measurements of molecular functionalised MoS_2 is envisaged to stablish the influence of the switchable conducting properties on the material.

VII.4 References

1. Lembke, D. & Kis, A. Breakdown of High-Performance Monolayer MoS_2 Transistors. *ACS Nano* **6**, 10070–10075 (2012).
2. Wang, H., Li, C., Fang, P., Zhang, Z. & Zhang, J. Z. Synthesis, properties, and optoelectronic applications of two-dimensional MoS_2 and MoS_2 -based heterostructures. *Chem. Soc. Rev.* **47**, 6101–6127 (2018).
3. Eda, G. & Maier, S. A. Two-Dimensional Crystals: Managing Light for Optoelectronics. *ACS Nano* **7**, 5660–5665 (2013).
4. Donarelli, M. & Ottaviano, L. 2D Materials for Gas Sensing Applications: A Review on Graphene Oxide, MoS_2, WS_2 and Phosphorene. *Sensors* **18**, 3638 (2018).
5. Nalwa, H. S. A review of molybdenum disulfide (MoS_2) based photodetectors: from ultra-broadband, self-powered to flexible devices. *RSC Adv.* **10**, 30529–30602 (2020).
6. Morant-Giner, M. *et al.* Prussian Blue@MoS2 Layer Composites as Highly Efficient Cathodes for Sodium- and Potassium-Ion Batteries. *Adv. Funct. Mater.* **28**, 1706125 (2018).
7. Wang, Y. *et al.* Catalysis with Two-Dimensional Materials Confining Single Atoms: Concept, Design, and Applications. *Chem. Rev.* **119**, 1806–1854 (2019).
8. Toh, R. J., Sofer, Z., Luxa, J., Sedmidubský, D. & Pumera, M. 3R phase of MoS_2 and WS_2 outperforms the corresponding 2H phase for hydrogen evolution. *Chem. Commun.* **53**, 3054–3057 (2017).
9. Nan, H. *et al.* Strong Photoluminescence Enhancement of MoS_2 through Defect Engineering and Oxygen Bonding. *ACS Nano* **8**, 5738–5745 (2014).
10. Kibsgaard, J., Chen, Z., Reinecke, B. N. & Jaramillo, T. F. Engineering the surface structure of MoS_2 to preferentially expose active edge sites for electrocatalysis. *Nat. Mater.* **11**, 963–969 (2012).
11. Stergiou, A. & Tagmatarchis, N. Molecular Functionalization of Two-Dimensional MoS_2 Nanosheets. *Chem. – A Eur. J.* **24**, 18246–18257 (2018).
12. Bertolazzi, S., Gobbi, M., Zhao, Y., Backes, C. & Samorì, P. Molecular chemistry approaches for tuning the properties of two-dimensional transition metal dichalcogenides. *Chem. Soc. Rev.* **47**, 6845–6888 (2018).
13. Zhao, Y. *et al.* Doping, Contact and Interface Engineering of Two-Dimensional Layered Transition Metal Dichalcogenides Transistors. *Adv. Funct. Mater.* **27**, 1603484 (2017).
14. Li, J. *et al.* Tuning the optical emission of MoS_2 nanosheets using proximal photoswitchable azobenzene molecules. *Appl. Phys. Lett.* **105**, 241116 (2014).
15. Daukiya, L., Seibel, J. & De Feyter, S. Chemical modification of 2D materials using molecules and assemblies of molecules. *Adv. Phys. X* **4**, 1625723 (2019).
16. Chen, M., Guan, R. & Yang, S. Hybrids of Fullerenes and 2D Nanomaterials. *Adv. Sci.* **6**, 1800941 (2019).
17. Jing, Y., Tan, X., Zhou, Z. & Shen, P. Tuning electronic and optical properties of MoS_2 monolayer via molecular charge transfer. *J. Mater. Chem. A* **2**, 16892–16897 (2014).
18. Selhorst, R. C. *et al.* Tetrathiafulvalene-containing polymers for simultaneous non-covalent modification and electronic modulation of MoS_2 nanomaterials. *Chem. Sci.* **7**, 4698–4705 (2016).
19. Lei, S. *et al.* Surface functionalization of two-dimensional metal chalcogenides by Lewis acid–base chemistry. *Nat. Nanotechnol.* **11**, 465–471 (2016).
20. Vishnoi, P., Sampath, A., Waghmare, U. V. & Rao, C. N. R. Covalent Functionalization of Nanosheets of MoS_2 and $MoSe_2$ by Substituted Benzenes and Other Organic Molecules. *Chem. - A Eur. J.* **23**, 886–

895 (2017).

21. Makarova, M., Okawa, Y. & Aono, M. Selective Adsorption of Thiol Molecules at Sulfur Vacancies on MoS2 (0001), Followed by Vacancy Repair via S–C Dissociation. *J. Phys. Chem. C* **116**, 22411–22416 (2012).

22. Sim, D. M. *et al.* Controlled Doping of Vacancy-Containing Few-Layer MoS_2 via Highly Stable Thiol-Based Molecular Chemisorption. *ACS Nano* **9**, 12115–12123 (2015).

23. Lee, H. *et al.* Highly Efficient Thin-Film Transistor via Cross-Linking of 1T Edge Functional 2H Molybdenum Disulfides. *ACS Nano* **11**, 12832–12839 (2017).

24. Pramoda, K., Gupta, U., Ahmad, I., Kumar, R. & Rao, C. N. R. Assemblies of covalently cross-linked nanosheets of MoS_2 and of MoS_2 –RGO: synthesis and novel properties. *J. Mater. Chem. A* **4**, 8989–8994 (2016).

25. Knirsch, K. C. *et al.* Basal-Plane Functionalization of Chemically Exfoliated Molybdenum Disulfide by Diazonium Salts. *ACS Nano* **9**, 6018–6030 (2015).

26. Vera-Hidalgo, M., Giovanelli, E., Navío, C. & Pérez, E. M. Mild Covalent Functionalization of Transition Metal Dichalcogenides with Maleimides: A "Click" Reaction for 2H-MoS_2 and WS_2. *J. Am. Chem. Soc.* **141**, 3767–3771 (2019).

27. Eda, G. *et al.* Photoluminescence from Chemically Exfoliated MoS_2. *Nano Lett.* **11**, 5111–5116 (2011).

28. Cabral, L. *et al.* Azobenzene Adsorption on the MoS_2 (0001) Surface: A Density Functional Investigation within van der Waals Corrections. *J. Phys. Chem. C* **122**, 18895–18901 (2018).

29. Zhao, Y., Bertolazzi, S. & Samorì, P. A Universal Approach toward Light-Responsive Two-Dimensional Electronics: Chemically Tailored Hybrid van der Waals Heterostructures. *ACS Nano* **13**, 4814–4825 (2019).

30. Pu, S.-Z., Sun, Q., Fan, C.-B., Wang, R.-J. & Liu, G. Recent advances in diarylethene-based multi-responsive molecular switches. *J. Mater. Chem. C* **4**, 3075–3093 (2016).

31. Iglesias, D., Ippolito, S., Ciesielski, A. & Samorì, P. Simultaneous non-covalent bi-functionalization of 1T-MoS_2 ruled by electrostatic interactions: towards multi-responsive materials. *Chem. Commun.* **56**, 6878–6881 (2020).

32. Lucas, L. N., De Jong, J. J. D., Van Esch, J. H., Kellogg, R. M. & Feringa, B. L. Syntheses of dithienylcyclopentene optical molecular switches. *European J. Org. Chem.* 155–166 (2003).

33. Sun, J. *et al.* Synthesis Methods of Two-Dimensional MoS_2: A Brief Review. *Crystals* **7**, 198 (2017).

34. Browne, W. R. *et al.* Oxidative Electrochemical Switching in Dithienylcyclopentenes, Part 1: Effect of Electronic Perturbation on the Efficiency and Direction of Molecular Switching. *Chem. - A Eur. J.* **11**, 6414–6429 (2005).

35. Yokojima, S. *et al.* Theoretical investigation on photochromic diarylethene: A short review. *J. Photochem. Photobiol. A Chem.* **200**, 10–18 (2008).

36. Herder, M. *et al.* Improving the Fatigue Resistance of Diarylethene Switches. *J. Am. Chem. Soc.* **137**, 2738–2747 (2015).

37. Mahmood, T., Arshad, M., Gilani, M. A., Iqbal, Z. & Ayub, K. Dyotropic rearrangement of bridgehead substituents in closed dithienylethenes; conjugated verses non-conjugated analogues. *J. Mol. Model.* **21**, 321 (2015).

38. Leal, J. M. & Garcia, B. Effects of Substituents on UV Spectra of Aniline and Anilinium Ion Derivatives. Hammett Correlations. *Zeitschrift für Phys. Chemie* **269O**, 26–32 (1988).

39. Matis, J. R., Schönborn, J. B. & Saalfrank, P. A multi-reference study of the byproduct formation for a ring-closed dithienylethene photoswitch. *Phys. Chem. Chem. Phys.* **17**, 14088–14095 (2015).

40. Yu, S. *et al.* An azo-coupling reaction-based surface enhanced resonance Raman scattering approach for ultrasensitive detection of salbutamol. *RSC Adv.* **8**, 5536–5541 (2018).

41. Browne, W. R. *et al.* Oxidative Electrochemical Switching in Dithienylcyclopentenes, Part 2: Effect of Substitution and Asymmetry on the Efficiency and Direction of Molecular Switching and Redox Stability. *Chem. - A Eur. J.* **11**, 6430–6441 (2005).

42. de Jong, J. J. D. *et al.* Raman scattering and FT-IR spectroscopic studies on dithienylethene switches—towards non-destructive optical readout. *Org. Biomol. Chem.* **4**, 2387–2392 (2006).

43. Maugé, F., Lamotte, J., Nesterenko, N. S., Manoilova, O. & Tsyganenko, A. A. FT-IR study of surface properties of unsupported MoS2. *Catal. Today* **70**, 271–284 (2001).

44. Coates, J. Interpretation of Infrared Spectra, A Practical Approach. in *Encyclopedia of Analytical Chemistry* (John Wiley & Sons, Ltd, 2006). doi:10.1002/9780470027318.a5606

45. Nakamoto, K. Applications in Coordination Chemistry. in *Infrared and Raman Spectra of Inorganic and Coordination Compounds* 1–273 (John Wiley & Sons, Inc., 2008). doi:10.1002/9780470405888.ch1

46. Mahouche-Chergui, S., Gam-Derouich, S., Mangeney, C. & Chehimi, M. M. Aryl diazonium salts: A new class of coupling agents for bonding polymers, biomacromolecules and nanoparticles to surfaces. *Chem. Soc. Rev.* **40**, 4143–4166 (2011).

47. Magdaline, J. D. & Chithambarathanu, T. Vibrational Spectra (FT-IR, FT-Raman), NBO and HOMO, LUMO Studies of 2-Thiophene Carboxylic Acid Based On Density Functional Method. *IOSR J. Appl. Chem. Ver. I* **8**, 6–14 (2015).

48. Katritzky, A. R. A Guide to the Complete Interpretation of Infrared Spectra of Organic Structures By Noel P. G. Roeges (Katholieke Industriele Hogeschool O-VI). Wiley: New York. 1994. x + 340 pp. $69.95. ISBN 0-471-93998-6. *J. Am. Chem. Soc.* **118**, 3543–3543 (1996).

49. Heacock, R. A. & Marion, L. THE INFRARED SPECTRA OF SECONDARY AMINES AND THEIR SALTS. *Can. J. Chem.* **34**, 1782–1795 (1956).

50. Li, O. L., Shi, Z., Lee, H. & Ishizaki, T. Enhanced Electrocatalytic Stability of Platinum Nanoparticles Supported on Sulfur-Doped Carbon using in-situ Solution Plasma. *Sci. Rep.* **9**, 12704 (2019).

51. Baltrusaitis, J., Jayaweera, P. M. & Grassian, V. H. XPS study of nitrogen dioxide adsorption on metal oxide particle surfaces under different environmental conditions. *Phys. Chem. Chem. Phys.* **11**, 8295 (2009).

52. Sun, Y., Hu, X., Luo, W. & Huang, Y. Ultrafine MoO_2 nanoparticles embedded in a carbon matrix as a high-capacity and long-life anode for lithium-ion batteries. *J. Mater. Chem.* **22**, 425–431 (2012).

53. Choi, J.-G. & Thompson, L. T. XPS study of as-prepared and reduced molybdenum oxides. *Appl. Surf. Sci.* **93**, 143–149 (1996).

54. Geng, X. *et al.* Pure and stable metallic phase molybdenum disulfide nanosheets for hydrogen evolution reaction. *Nat. Commun.* **7**, 10672 (2016).

55. Knirsch, K. C. *et al.* Basal-Plane Functionalization of Chemically Exfoliated Molybdenum Disulfide by Diazonium Salts. *ACS Nano* **9**, 6018–6030 (2015).

56. Liu, Q. *et al.* Gram-Scale Aqueous Synthesis of Stable Few-Layered 1T-MoS_2 : Applications for Visible-Light-Driven Photocatalytic Hydrogen Evolution. *Small* **11**, 5556–5564 (2015).

57. Wang, F. Z. *et al.* Ammonia intercalated flower-like MoS_2 nanosheet film as electrocatalyst for high efficient and stable hydrogen evolution. *Sci. Rep.* **6**, 31092 (2016).

58. Kehrer, M. *et al.* XPS investigation on the reactivity of surface imine groups with TFAA. *Plasma Process. Polym.* **16**, 1800160 (2019).

59. Jensen, H. *et al.* Determination of size distributions in nanosized powders by TEM, XRD, and SAXS. *J.*

Exp. Nanosci. **1**, 355–373 (2006).

60. Du, G. *et al.* Superior stability and high capacity of restacked molybdenum disulfide as anode material for lithium ion batteries. *Chem. Commun.* **46**, 1106–1108 (2010).

61. Acerce, M., Voiry, D. & Chhowalla, M. Metallic 1T phase MoS_2 nanosheets as supercapacitor electrode materials. *Nat. Nanotechnol.* **10**, 313–318 (2015).

62. Lee, H. *et al.* Highly Efficient Thin-Film Transistor via Cross-Linking of 1T Edge Functional 2H Molybdenum Disulfides. *ACS Nano* **11**, 12832–12839 (2017).

63. Paredes, J. I. *et al.* Impact of Covalent Functionalization on the Aqueous Processability, Catalytic Activity, and Biocompatibility of Chemically Exfoliated MoS_2 Nanosheets. *ACS Appl. Mater. Interfaces* **8**, 27974–27986 (2016).

64. Wilson, J. A. & Yoffe, A. D. The transition metal dichalcogenides discussion and interpretation of the observed optical, electrical and structural properties. *Adv. Phys.* **18**, 193–335 (1969).

65. Sim, D. M. *et al.* Long-Term Stable 2H-MoS_2 Dispersion: Critical Role of Solvent for Simultaneous Phase Restoration and Surface Functionalization of Liquid-Exfoliated MoS_2. *ACS Omega* **2**, 4678–4687 (2017).

66. Attanayake, N. H. *et al.* Effect of Intercalated Metals on the Electrocatalytic Activity of 1T-MoS_2 for the Hydrogen Evolution Reaction. *ACS Energy Lett.* **3**, 7–13 (2018).

67. Mendive-Tapia, D. *et al.* New insights into the by-product fatigue mechanism of the photo-induced ring-opening in diarylethenes. *Phys. Chem. Chem. Phys.* **16**, 18463–18471 (2014).

68. Ern, J. *et al.* Ring-Opening and -Closure Reaction Dynamics of a Photochromic Dithienylethene Derivative. *J. Phys. Chem. A* **106**, 1654–1660 (2002).

69. Uchida, K. *et al.* Diastereoselective cyclization of a dithienylethene switch through single crystal confinement. *Org. Biomol. Chem.* **4**, 1002 (2006).

Chapter VIII

General conclusions and future work

In the last decades, numerous efforts have been undertaken to develop SIMs as an alternative to SMMs to achieve a better control of the magnetic anisotropy. They are mononuclear coordination complexes based on lanthanides or transition metal ions, mainly Co^{II} ions. The interest of SIMs and SMMs resides on their magnetic bistability, necessary for quantum storage applications. In SMM, the slow relaxation of the magnetisation is related to an energy barrier imposed by a $D < 0$. However, this requirement has been recently questioned by the observation of slow relaxation in some SIMs, as in some Co^{II} complexes with $D > 0$ under an external magnetic field. Therefore, deep knowledge in the relaxation processes and mechanisms involved are still of essential interest.

In this dissertation, various cobalt(II)-based compounds have been synthesised to unravel the relaxation processes and mechanisms behind the SIM behaviour. All these compounds have been obtained by using a mononuclear cobalt(II) complex, as building block, with formula $[Co(Me_xphen)_2](ClO_4)_2$ (x = 1 or 2). These mononuclear complexes have been coordinated to ligands, which allowed the formation of mononuclear or polynuclear cobalt(II) species connected through different bridging ligands. Almost every Co^{II} ion exhibits the same octahedral coordination sphere (CoN_4O_2) displaying axial anisotropy ($D > 0$) with field-induced SIM behaviour.

In all these cases, the χ_M' and χ_M'' *vs* ν data analyses with the DynVPMag program (following one or two generalised Debye models) allow the representation of $\ln(\tau)$ *vs* $1/T$ (Arrhenius plot) and $\ln(\tau)$ *vs* $\ln(T)$ plots with small standard deviation errors in the range of 2.0 to 12.0 K. Different models were fit for these data plots and, as a result, the slow magnetic relaxation has been associated with several thermally activated, intra-Kramers or Raman mechanisms. The intra-Kramers mechanism is usually present at low temperature ($T \leq$ ~3.5 K) and its relevance increases while increasing the static dc-magnetic field. At intermediate (~3.5 < $T \leq$ ~7 K) and high temperatures (~7 < $T \leq$ ~12 K), several thermally activated mechanisms competing in the different temperature regimes are related to the existence of molecular and net vibrations with different energy barriers. Moreover, these results could also, in some chapters, be comprehended as several competing Raman relaxation mechanisms via two optic phonons and one acoustic phonon. These considerations must be taken with care, since the deviations in the experimental data affect these considerably. In fact, other researchers have pointed out the limitations on the experimental conditions.

In Chapter II, the study of the influence of the counterion on the zfs parameters is presented. The counterion induces a distortion in the first coordination sphere through supramolecular interactions. In fact, a careful investigation revealed that the crystallisation water molecules are responsible for the differences in the relaxation dynamics. The main process of each compound is studied as a combination of multiple

thermally activated plus an intra-Kramers mechanisms. A future study on magnetically diluted samples, with a diamagnetic complex, or on dried samples removing the water molecules might reveal new ways to understand these mechanisms.

In Chapter III, preliminary pulsed-EPR studies in solution of one mononuclear cobalt(II) compound (from Chapter II) indicated that it can be considered as an effective $S = 1/2$ spin momenta and a potential qubit. Therefore, this mononuclear entity was used as building blocks for synthetizing dinuclear cobalt(II) complexes, bearing asymmetric and symmetric bridging ligands. Particularly, the Co^{II} ions within the asymmetric dinuclear cobalt(II) compounds exhibit different zfs parameters and different EPR signals. Therefore, these compounds should be further studied with the pulsed-EPR technique, to evaluate their potential as qu-gates.

In Chapter IV, large and complex structures by using a short and long triscarboxylate ligands are obtained. With the short ligand, a small exchange coupling interaction is present between the Co^{II} ions, which does not longer exist in the long ligand. Furthermore, a chain is also reported. The molecular cobalt(II) chain does also display magnetic coupling between the Co^{II} ions from different chains, giving rise to a spin glass magnetic behaviour. Interestingly, the spin glass behaviour is tuned by the reversible removal of coordination water molecules by dehydration, accompanied with a change in colour.

Chapters V and VI deal with the idea of switchable SMMs. The possibility to tune the "on" and "off" the magnetic behaviour was studied by the synthesis of mono and dinuclear complexes with switchable ligands. In Chapter V, a photoswitchable diarylethene derivative is chosen for this purpose, while a redox ferrocene-based ligand is employed in Chapter VI. Photoswitchable dinuclear cobalt compounds are only distinguishable by their UV spectra but not that clearly by their magnetic properties. Then, other photoswitchable diarylethene ligand derivatives can be explored, as well, as different metal ions to achieve switchable SMMs. In contrast, the oxidation of the ferrocene centre into ferrocenium enables a magnetic exchange coupling that vanishes the cobalt(II) SIM properties.

In a different study area, molecular approaches are extremely appealing for functionalisation of 2D materials, to tune their physical properties. Then, in Chapter VII, chemically exfoliated MoS_2 flakes have been successfully functionalised through covalent and electrostatic approaches with a photochromic molecule. These composites have been proved to present partial and reversible photoswitching behaviour. As future work, the functionalisation of MoS_2 flakes with SIMs has not be studied. With this aim, the cobalt(I) complexes presented in this thesis can be a suitable choice to study the relaxation dynamics influenced by new environments.

Appendix A

Supporting Information

SI Chapter II

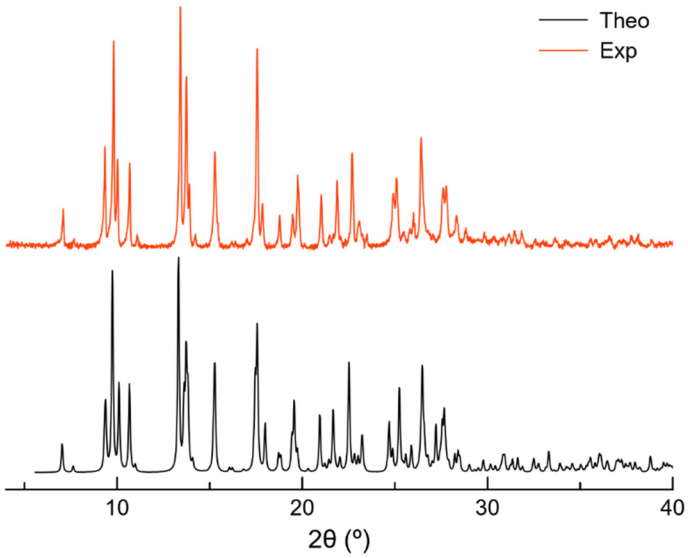

Figure A.1. Experimental and simulated powder X-ray diffraction patterns of **1·ClO$_4$·H$_2$O**.

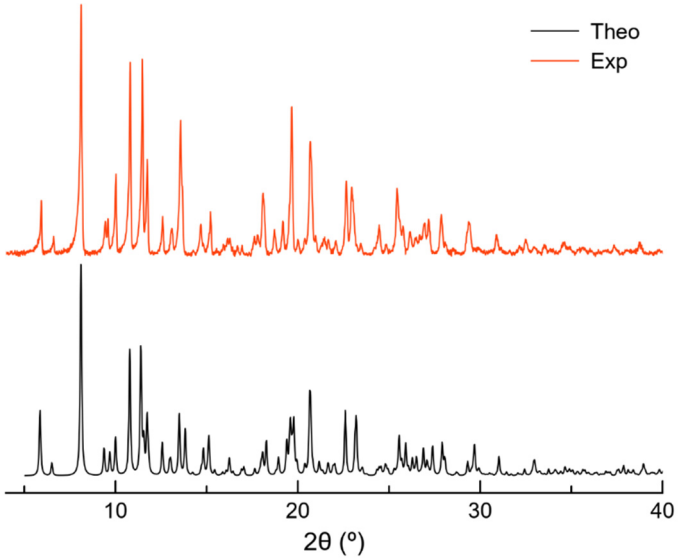

Figure A.2. Experimental and simulated powder X-ray diffraction patterns of **1·BPh$_4$**.

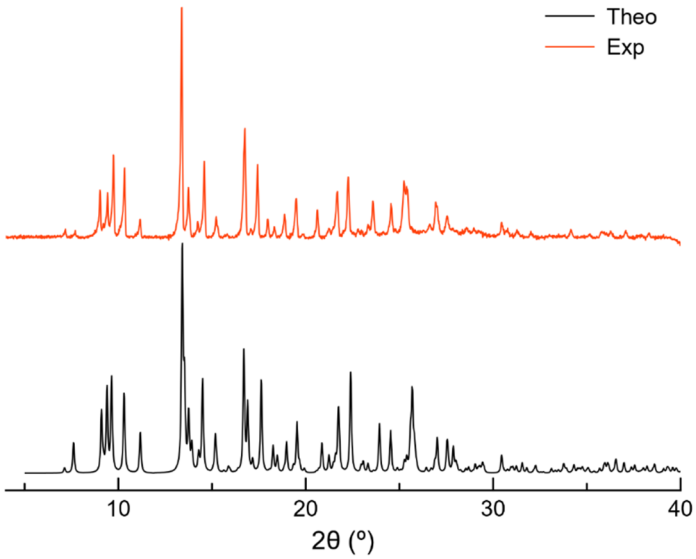

Figure A.3. Experimental and simulated powder X-ray diffraction patterns of **1·PF$_6$·H$_2$O**.

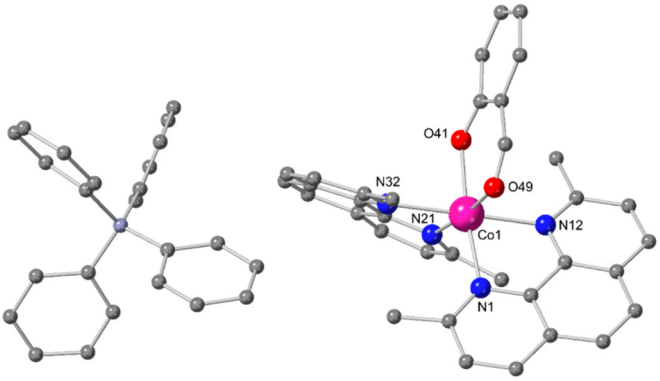

Figure A.4. Perspective view of **1·BPh$_4$**. Hydrogen atoms are omitted for clarity. Colour code: magenta, cobalt; blue, nitrogen; red, oxygen; grey, carbon; sky blue, boron.

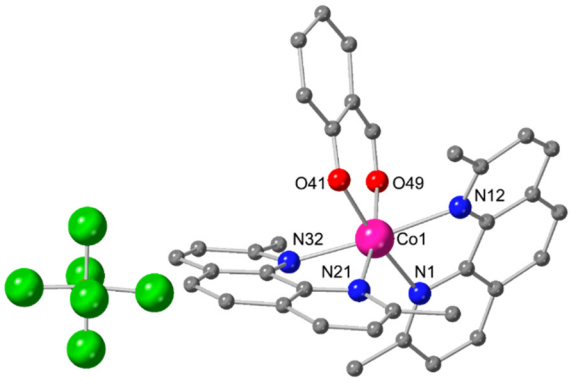

Figure A.5. Perspective view of **1·PF$_6$·H$_2$O**. Hydrogen atoms are omitted for clarity. Colour code: magenta, cobalt; blue, nitrogen; red, oxygen; grey, carbon; brown, phosphorus; green, fluorine.

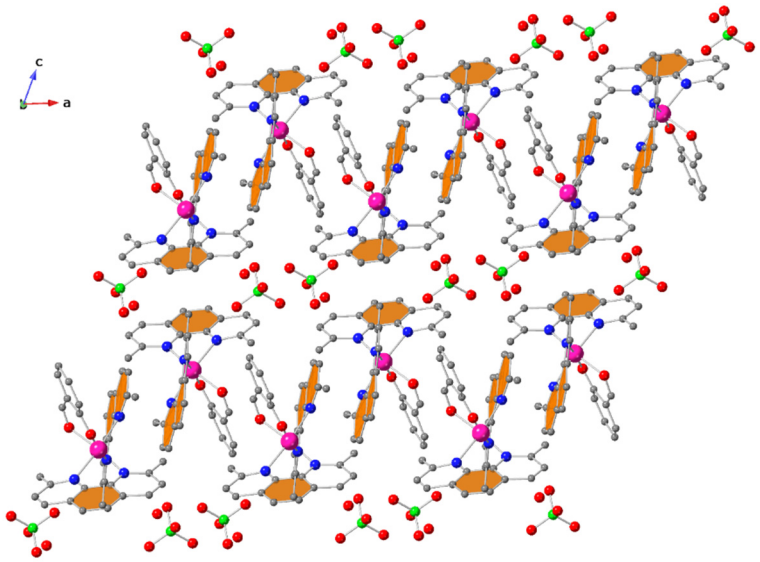

Figure A.6. Perspective view along the *b*-axis of the crystal packing of **1·ClO$_4$·H$_2$O** with π–π interactions involving phenanthroline coloured in orange. Hydrogen atoms are omitted for clarity. Colour code: magenta, cobalt; blue, nitrogen; red, oxygen; grey, carbon; green, chlorine; orange.

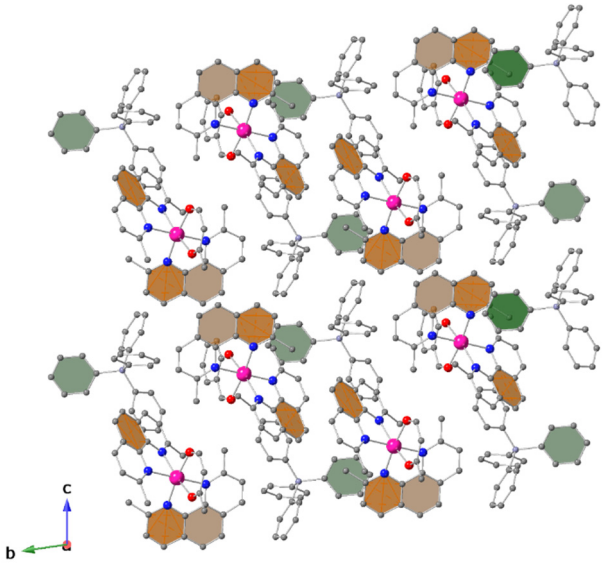

Figure A.7. Perspective view along the *a*-axis of the crystal packing of **1·BPh$_4$**. Rings involved in π–π interactions are coloured in orange (phenanthroline) and green (BPh$_4$). Hydrogen atoms are omitted for clarity. Colour code: magenta, cobalt; blue, nitrogen; red, oxygen; grey, carbon; sky blue, boron.

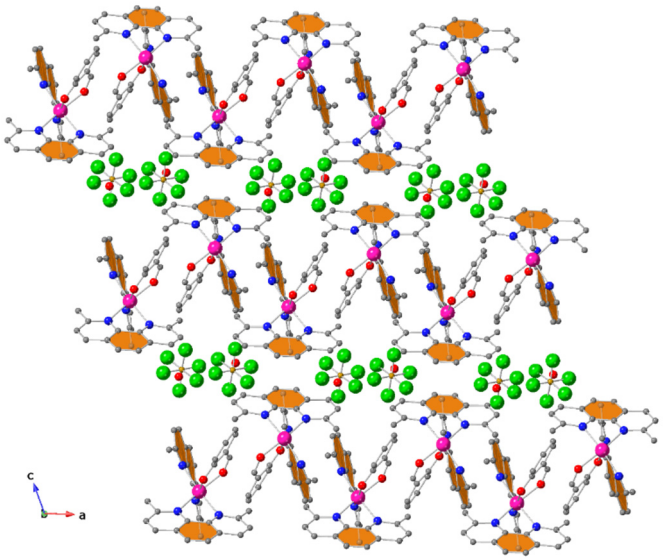

Figure A.8. Perspective view along the *b*-axis of the crystal packing of **1·PF$_6$·H$_2$O** with π–π interactions involving phenanthroline coloured in orange. Hydrogen atoms are omitted for clarity. Colour code: magenta, cobalt; blue, nitrogen; red, oxygen; grey, carbon; brown, phosphorus; green, fluorine.

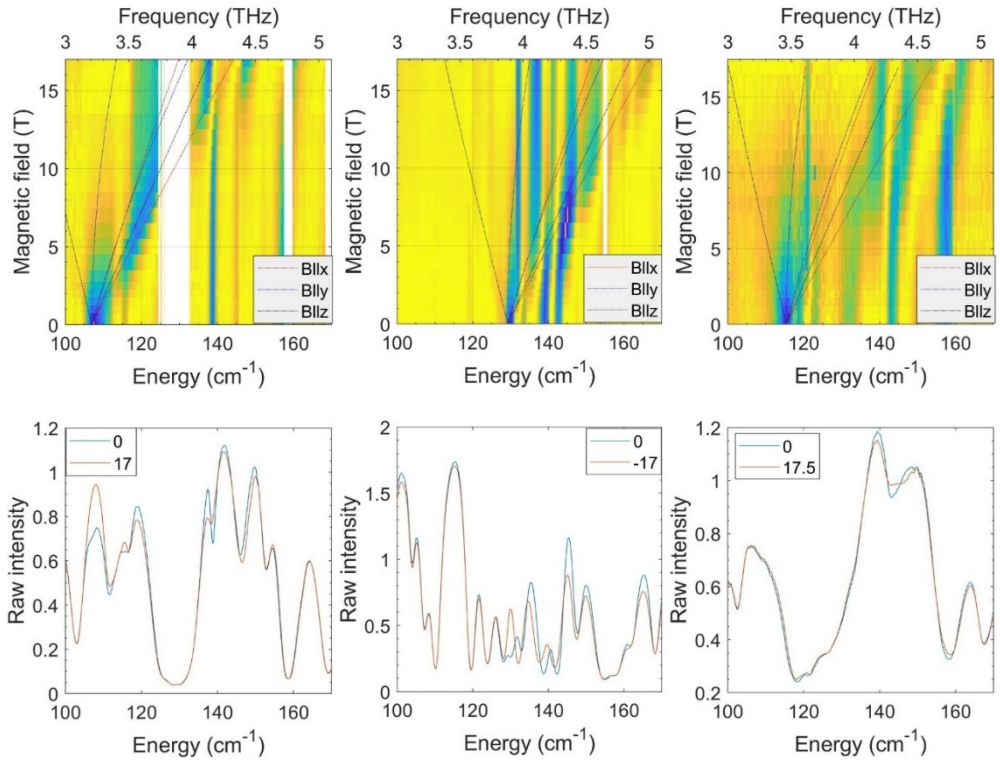

Figure A.9. A false-colour (contour) FIRMS map (upper row) and transmission spectrum (lower row) of **1·ClO$_4$·H$_2$O** (left), **1·BPh$_4$** (middle) and **1·PF$_6$·H$_2$O** (right) at 5 K. The straight line in the false-colour map is a guide to the eye and indicates the development of a high-field powder pattern magnetic absorption originating from the zero-field resonance, which value is equal to 2|Δ|. The other two strong zero-field resonances appear to be vibrons/phonons that couple to the magnon. The tendency towards the blue colour means that the absorbance increases, whereas the yellow colour corresponds to the transparent regions.

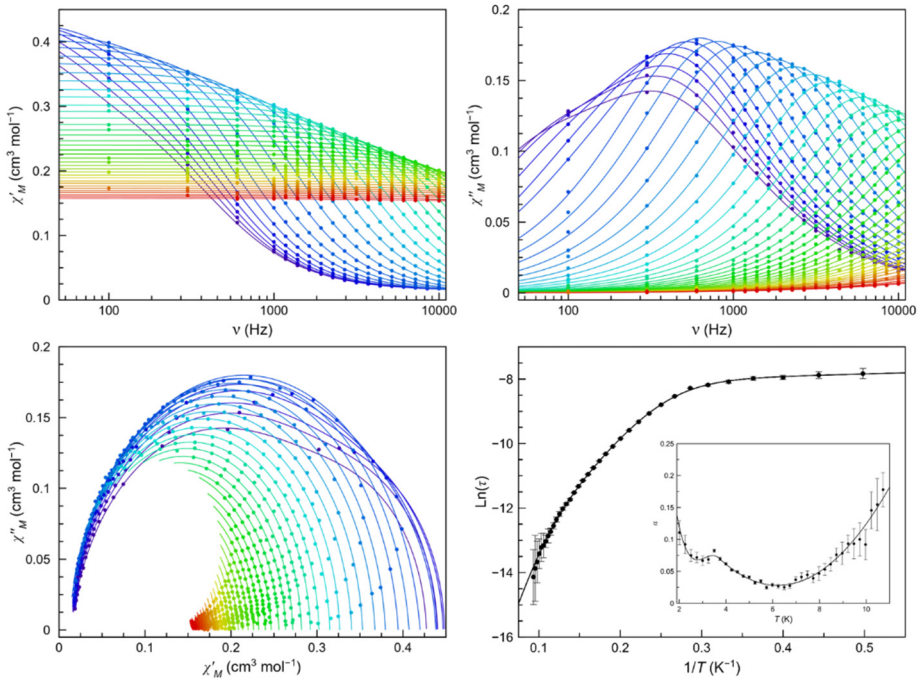

Figure A.10. Frequency dependence of χ_M' (top left) and χ_M'' (top right), Cole-Cole plots (bottom left) and Arrhenius plots of **1·ClO₄·H₂O** (bottom right) in a dc-applied static field of 5.0 kOe with ± 0.005 kOe oscillating field in the temperature range of 2.0–10.0 K (purple to red gradient). Thermal dependence of α is included on the bottom right figure as an inset, where the black line are eye-guides. Standard deviation appears as vertical error bars.

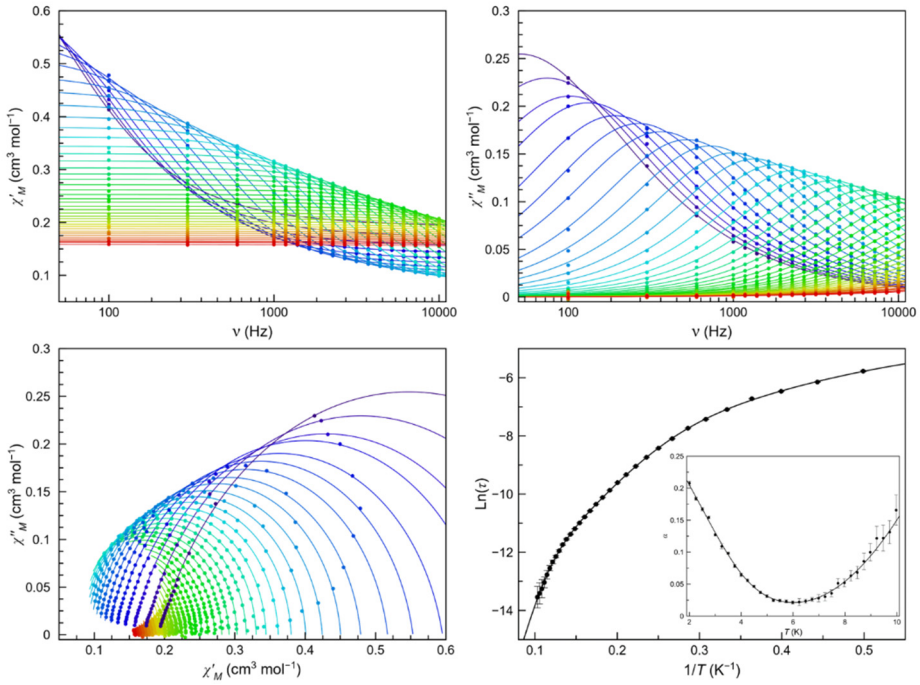

Figure A.11. Frequency dependence of χ_M' (top left) and χ_M'' (top right), Cole-Cole plots (bottom left) and Arrhenius plots of **1·ClO₄·H₂O** (bottom right) in a dc-applied static field of 1.0 kOe with ± 0.005 kOe oscillating field in the temperature range of 2.0–9.7 K (purple to red gradient). Thermal dependence of α is included on the bottom right figure as an inset, where the black line are eye-guides. Standard deviation appears as vertical error bars.

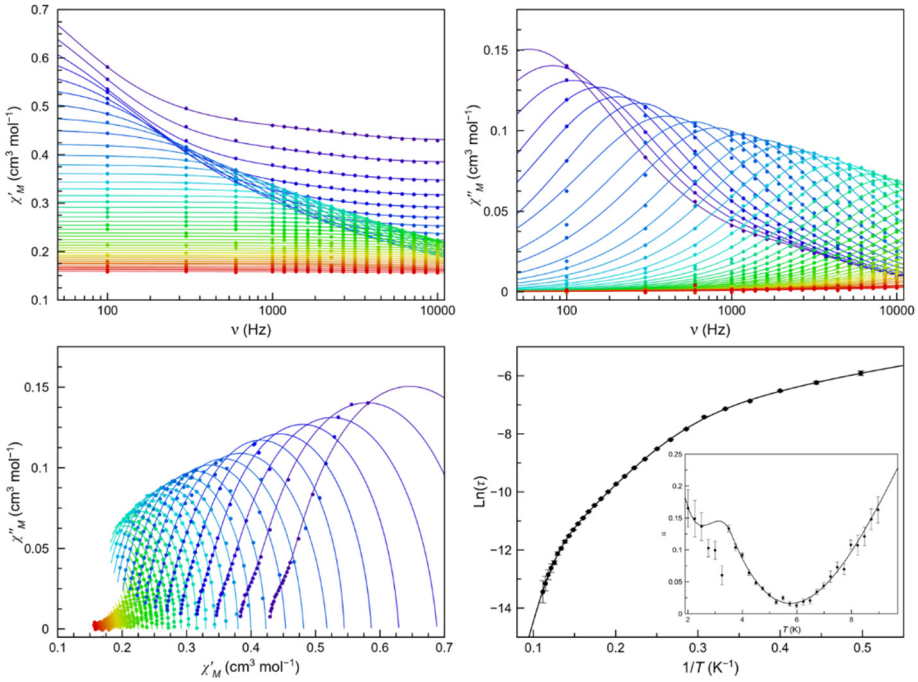

Figure A.12. Frequency dependence of χ_M' (top left) and χ_M'' (top right), Cole-Cole plots (bottom left) and Arrhenius plots of **1·ClO₄·H₂O** (bottom right) in a dc-applied static field of 0.5 kOe with ± 0.005 kOe oscillating field in the temperature range of 2.0–9.0 K (purple to red gradient). Thermal dependence of α is included on the bottom right figure as an inset, where the black line are eye-guides. Standard deviation appears as vertical error bars.

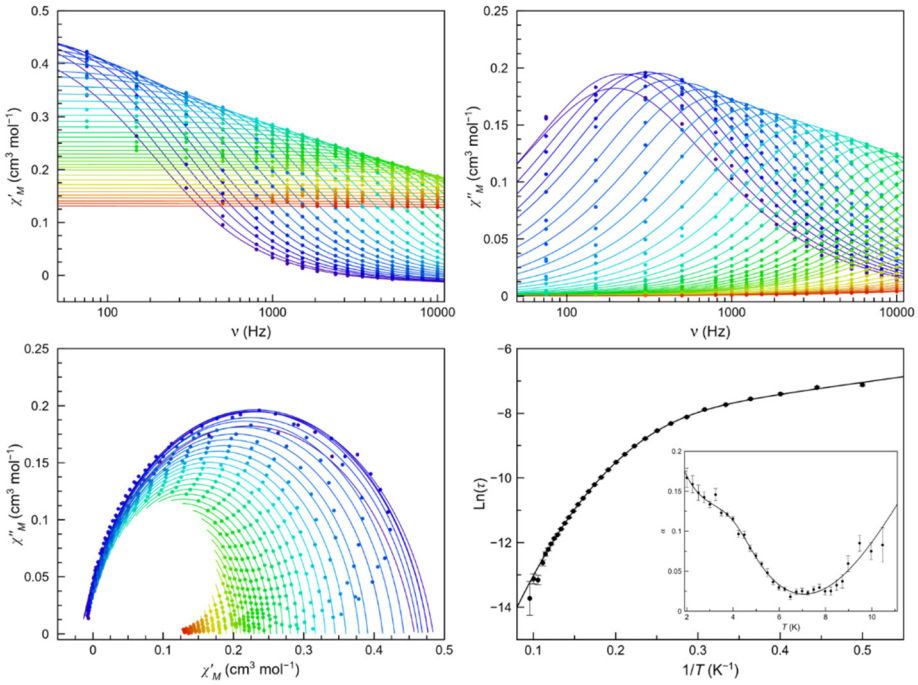

Figure A.13. Frequency dependence of χ_M' (top left) and χ_M'' (top right), Cole-Cole plots (bottom left) and Arrhenius plots of **1·BPh₄** (bottom right) in a dc-applied static field of 5.0 kOe with ± 0.005 kOe oscillating field in the temperature range of 2.0–10.5 K (purple to red gradient). Thermal dependence of α is included on the bottom right figure as an inset, where the black line are eye-guides. Standard deviation appears as vertical error bars.

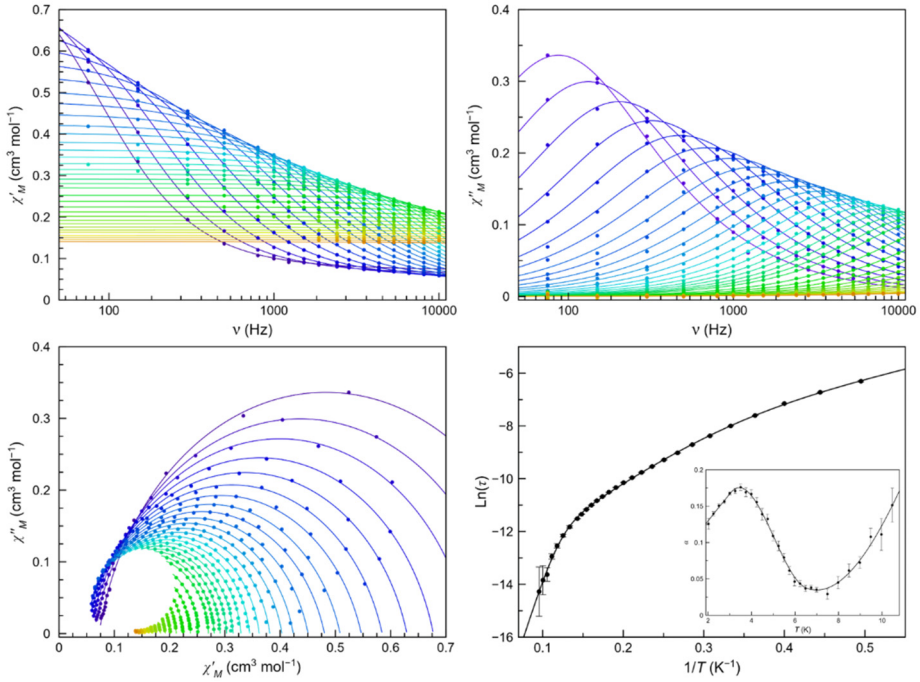

Figure A.14. Frequency dependence of χ_M' (top left) and χ_M'' (top right), Cole-Cole plots (bottom left) and Arrhenius plots of **1·BPh$_4$** (bottom right) in a dc-applied static field of 1.0 kOe with ± 0.005 kOe oscillating field in the temperature range of 2.0–10.5 K (purple to red gradient). Thermal dependence of α is included on the bottom right figure as an inset, where the black line are eye-guides. Standard deviation appears as vertical error bars.

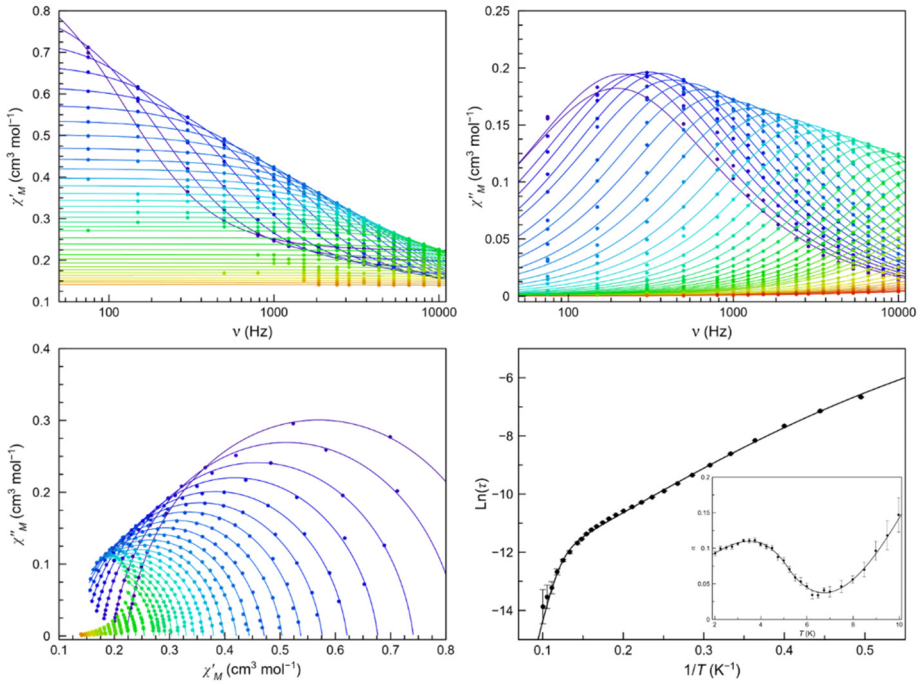

Figure A.15. Frequency dependence of χ_M' (top left) and χ_M'' (top right), Cole-Cole plots (bottom left) and Arrhenius plots of **1·BPh$_4$** (bottom right) in a dc-applied static field of 0.5 kOe with ± 0.005 kOe oscillating field in the temperature range of 2.0–10.0 K (purple to red gradient). Thermal dependence of α is included on the bottom right figure as an inset, where the black line are eye-guides. Standard deviation appears as vertical error bars.

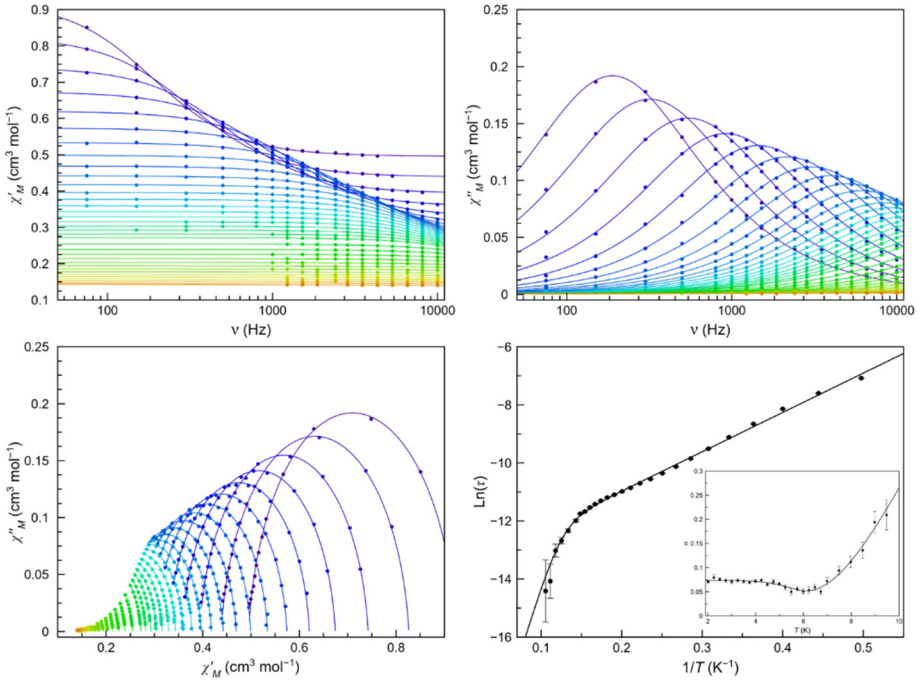

Figure A.16. Frequency dependence of χ_M' (top left) and χ_M'' (top right), Cole-Cole plots (bottom left) and Arrhenius plots of **1·BPh₄** (bottom right) in a dc-applied static field of 0.25 kOe with ± 0.005 kOe oscillating field in the temperature range of 2.0–9.5 K (purple to red gradient). Thermal dependence of α is included on the bottom right figure as an inset, where the black line are eye-guides. Standard deviation appears as vertical error bars.

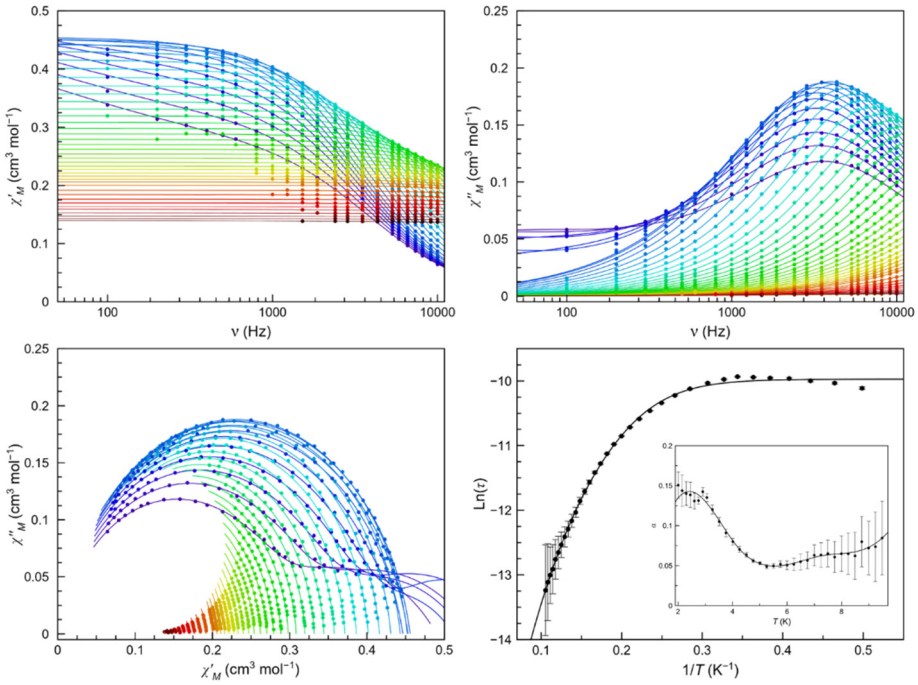

Figure A.17. Frequency dependence of χ_M' (top left) and χ_M'' (top right), Cole-Cole plots (bottom left) and Arrhenius plots of **1·PF₆·H₂O** (bottom right) in a dc-applied static field of 5.0 kOe with ± 0.005 kOe oscillating field in the temperature range of 2.0–9.5 K (purple to red gradient). Thermal dependence of α is included on the bottom right figure as an inset, where the black line are eye-guides. Standard deviation appears as vertical error bars.

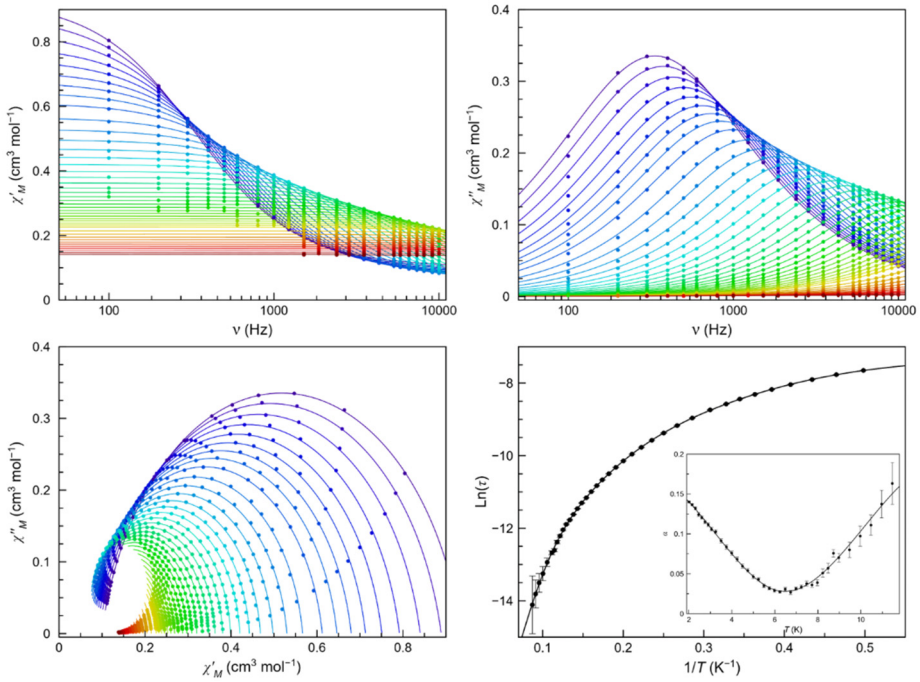

Figure A.18. Frequency dependence of χ_M' (top left) and χ_M'' (top right), Cole-Cole plots (bottom left) and Arrhenius plots of **1·PF$_6$·H$_2$O** (bottom right) in a dc-applied static field of 1.0 kOe with ± 0.005 kOe oscillating field in the temperature range of 2.0–11.5 K (purple to red gradient). Thermal dependence of α is included on the bottom right figure as an inset, where the black line are eye-guides. Standard deviation appears as vertical error bars.

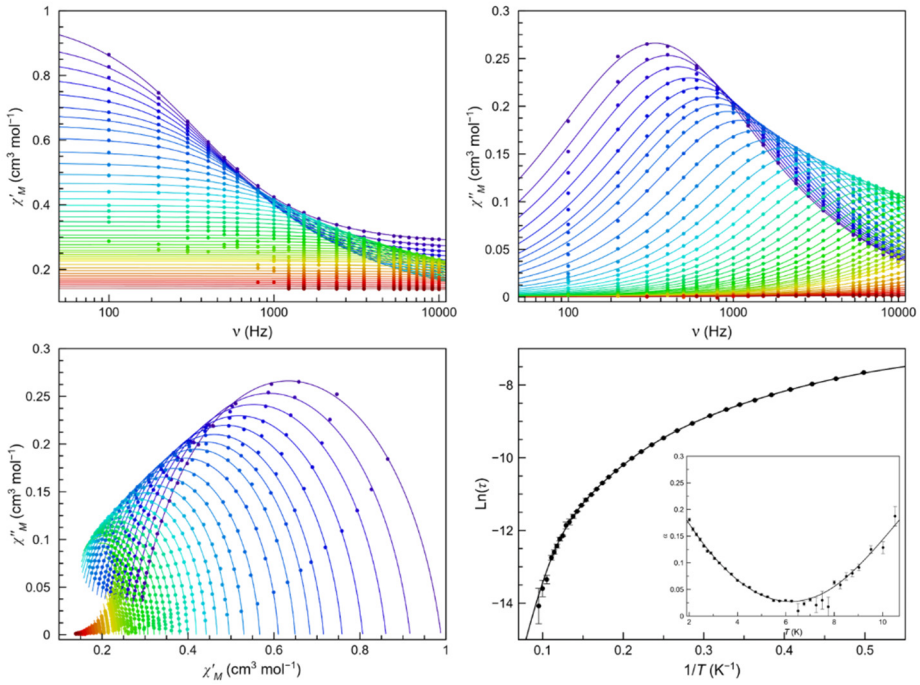

Figure A.19. Frequency dependence of χ_M' (top left) and χ_M'' (top right), Cole-Cole plots (bottom left) and Arrhenius plots of **1·PF$_6$·H$_2$O** (bottom right) in a dc-applied static field of 0.5 kOe with ± 0.005 kOe oscillating field in the temperature range of 2.0–10.5 K (purple to red gradient). Thermal dependence of α is included on the bottom right figure as an inset, where the black line are eye-guides. Standard deviation appears as vertical error bars.

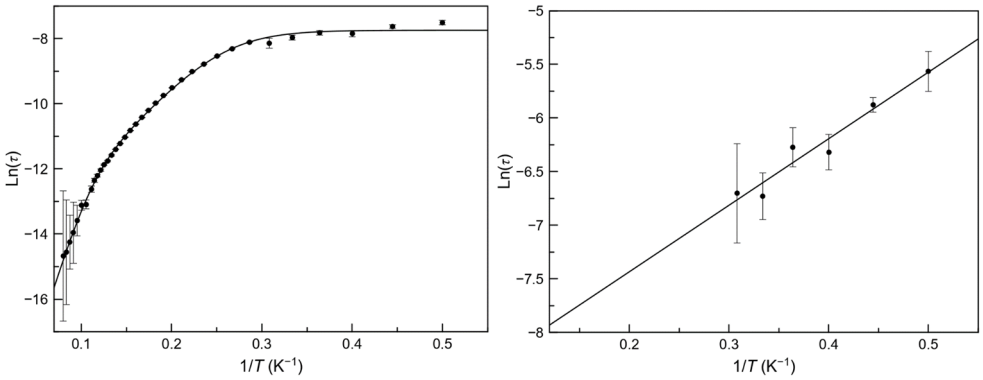

Figure A.20. Arrhenius plots for the main (left) and the second (right) process of **1·BPh₄** at 5.0 kOe dc-applied static fields with ± 0.005 kOe oscillating field when considering two processes in the analyses.

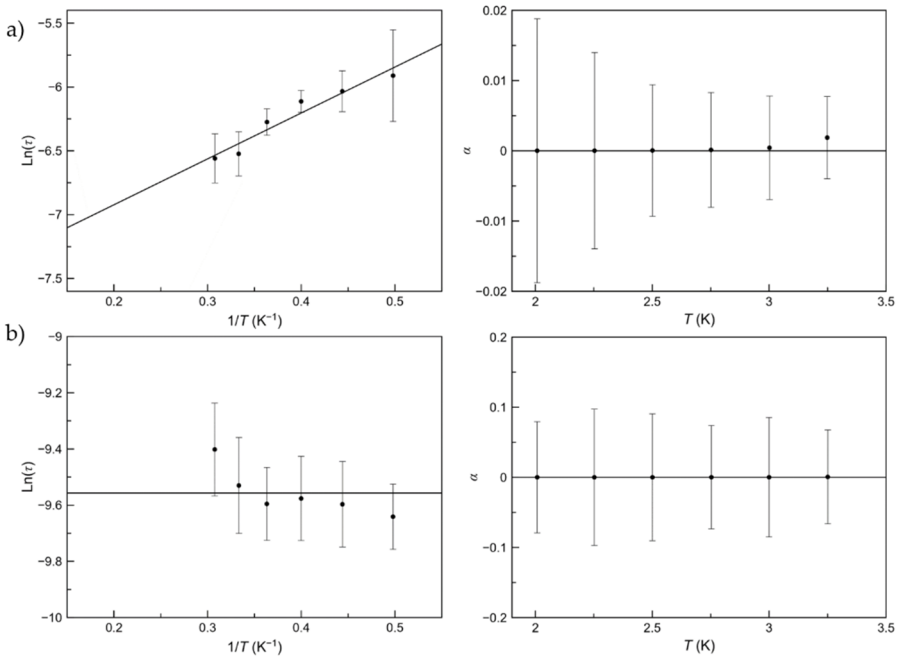

Figure A.21. Arrhenius plots (left) and thermal dependence of α (right) for the second process found in **1·ClO₄·H₂O** at 5.0 kOe (a) and 0.5 kOe (b) dc-applied static fields with ± 0.005 kOe oscillating field in the temperature range of 2.0–3.25 K. Standard deviation appears as vertical error bars.

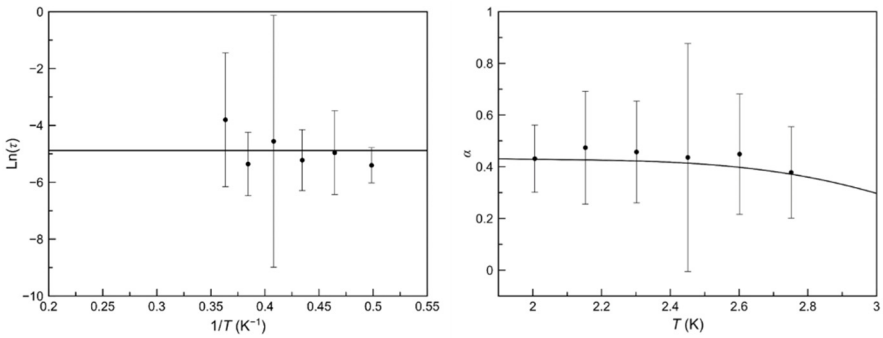

Figure A.22. Arrhenius plot (left) and thermal dependence of α (right) for the second process found in **1·PF₆·H₂O** at 5.0 kOe dc-applied static field with ± 0.005 kOe oscillating field in the temperature range of 2.0–2.75 K. Standard deviation appears as vertical error bars.

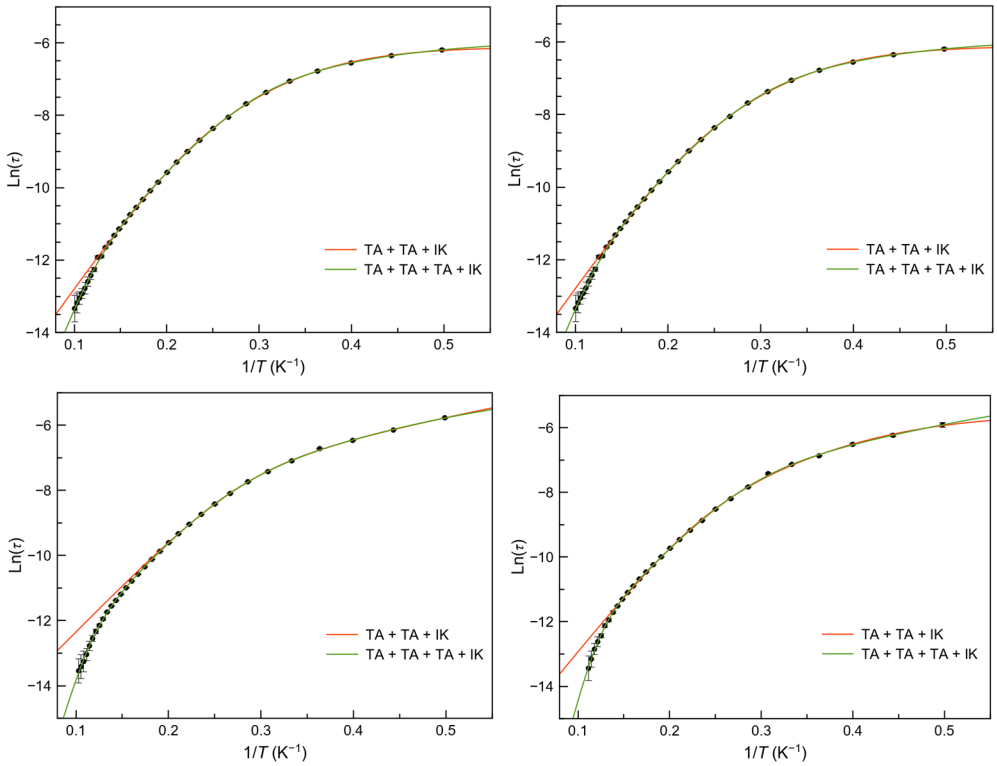

Figure A.23. Arrhenius plots for the main process of **1·ClO₄·H₂O** under 5.0 (top left), 2.5 (top right), 1.0 (bottom left) and 0.5 kOe (bottom right) applied static fields. The solid lines are the best fit-curves using the three applied relaxation mechanisms. Standard deviations appear as vertical error bars.

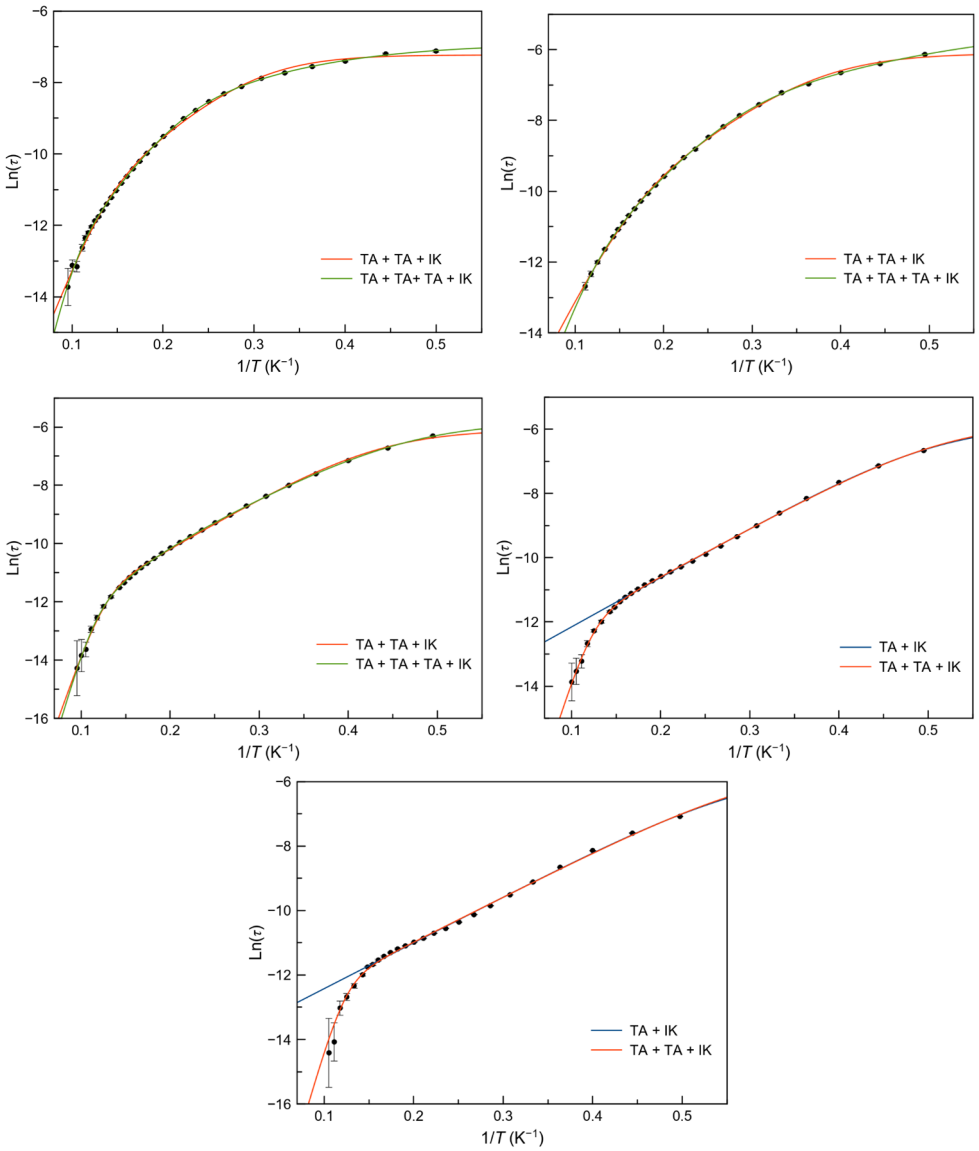

Figure A.24. Arrhenius plots for the unique process of **1·BPh$_4$** under 5.0 (top left), 2.5 (top right), 1.0 (middle left) and 0.5 (middle right) and 0.25 kOe (bottom) applied static fields. The solid lines are the best fit-curves using the three applied relaxation mechanisms. Standard deviations appear as vertical error bars.

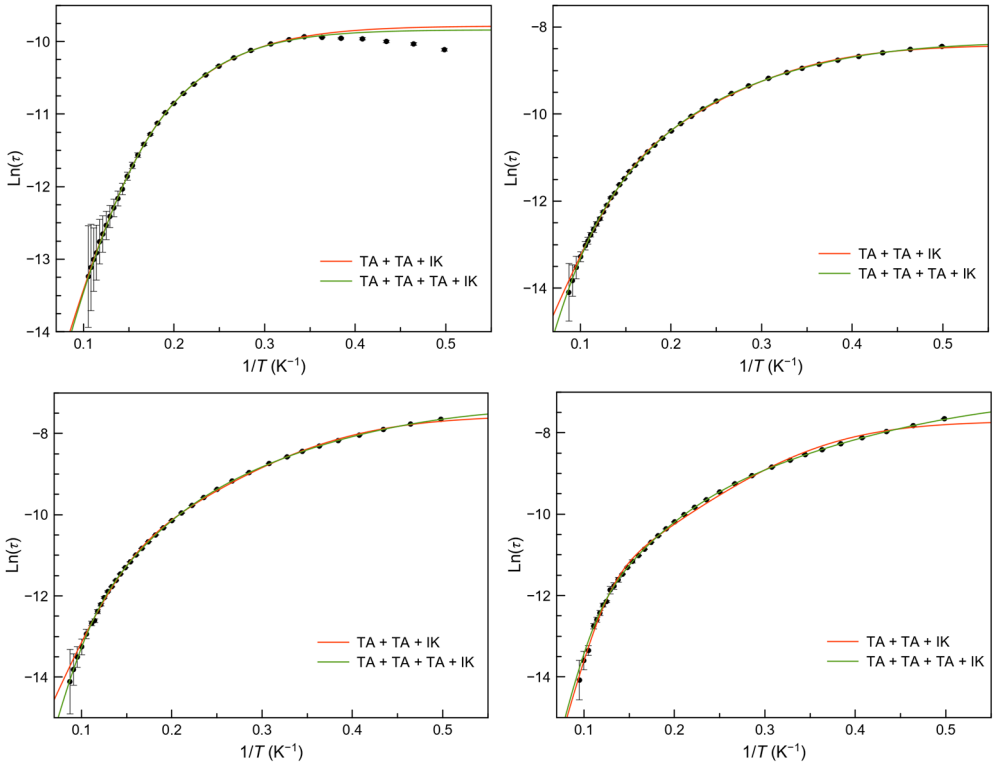

Figure A.25. Arrhenius plots for the main process of **1·PF$_6$·H$_2$O** under 5.0 (top left), 2.5 (top right), 1.0 (bottom left) and 0.5 kOe (bottom right) applied static fields. The solid lines are the best fit-curves using the three applied relaxation mechanisms. Standard deviations appear as vertical error bars.

Table A.1. Crystal data of compounds **1·ClO$_4$·H$_2$O**, **1·BPh$_4$** and **1·PF$_6$·H$_2$O**.

Compound	**1·ClO$_4$·H$_2$O**	**1·BPh$_4$**	**1·PF$_6$·H$_2$O**
Formula	$C_{35}H_{31}ClCoN_4O_7$	$C_{59}H_{49}BCoN_4O_2$	$C_{35}H_{31}CoF_6N_4O_3P$
Formula weight [g mol^{-1}]	714.02	915.76	759.54
Crystal system	Triclinic	Triclinic	Triclinic
Space group	P–1	P–1	P–1
a [Å]	10.6406(8)	10.9536(13)	11.202(4)
b [Å]	12.1790(9)	13.757(2)	12.546(4)
c [Å]	13.6038(10)	15.2602(2)	13.373(5)
α [°]	89.998(6)	98.086(2)	90.248(13)
β [°]	68.518(7)	93.181(2)	110.521(13)
γ [°]	73.272(2)	93.869(2)	110.703(13)
V [Å^3]	1560.0(2)	2266.5(5)	1628.7(8)
Z	2	2	2
D_{calc} [g cm^{-3}]	1.520	1.342	1.549
Temperature [K]	100	100	150
μ [mm^{-1}]	0.520	0.430	0.654
R (int)	0.0271	0.0262	0.075
Reflections collected	58613	66645	23306
Independent reflections	14619	14457	6874
Number of observed reflections ($I_o > 2\sigma(I_o)$)	-	-	-
Number of parameters	443	636	570
Goodness-of-fit *S* on F^2	1.056	1.030	1.12
R_1[a] [$I > 2.0\sigma(I)$]	0.0339	0.0391	0.0796
R_1[a] [all data]	0.0411	0.0487	0.0886
wR_2[b] [$I > 2.0\sigma(I)$]	0.0872	0.1033	0.2588
wR_2[b] [all data]	0.0913	0.1103	0.2765

[a] $R_1 = \sum||F_o| - |F_c|| / \sum|F_o|$. [b] $wR_2 = \{\sum[w(F_o^2 - F_c^2)^2]/\sum w(F_o^2)^2\}^{1/2}$.

Table A.2. Hydrogen bond details (distances [Å] and angles [°]) for **1·ClO$_4$·H$_2$O**.

Donor–H···Acceptor	D–H	H···A	D···A	D–H···A
O60–H61···O52	0.854(18)	2.160(19)	2.9211(19)	148(2)
O60–H62···O54	0.850(14)	2.095(12)	2.9374(14)	171(3)

Table A.3. π−π interactions in **1·X** (X = **ClO_4·H_2O**, **BPh_4** and **PF_6·H_2O**).

Compound	Cg···Cg[a]	Cg···Cg [Å]	α[b] [°]
1·ClO_4·H_2O			
	Cg5···Cg8	3.7265 (7)	4.94(5)
	Cg8···Cg8	3.7761(7)	0.00(6)
	Cg9···Cg9	3.5322(6)	0.00(4)
1·BPh_4			
	Cg4···Cg11	3.9836(10)	13.09(6)
	Cg5···Cg5	3.9607(10)	0.00(6)
	Cg6···Cg6	3.7511(9)	0.00(6)
1·PF_6·H_2O			
	Cg5···Cg8	3.895(4)	4.8(3)
	Cg8···Cg8	3.758(4)	0.0(3)
	Cg9···Cg9	3.616(3)	0.0(3)

[a] Cg are the six-membered rings: **1·ClO_4·H_2O**: Cg5: N12, C8-C11, C13; Cg8: C5-C8, C13, C14; Cg9: C25-C28, C33, C34;. **1·BPh_4**: Cg4; N21, C22-C25, C34; Cg5: C5-C8, C13, C14; Cg6: C25-C28, C33, C34; Cg11:C71-C76; **1·PF_6·H_2O**: Cg5: N12, C8-C11, C13; Cg8: C5-C8, C13, C14; Cg9: C25-C28, C33, C34.[b] dihedral angle between each pair ring planes.

Table A.4. Energy of the calculated quartet (D_Q) and doublet (D_D) excited states and their contributions to the *D* value for **1·ClO_4·H_2O**, **1·BPh_4** and **1·PF_6·H_2O** obtained from CASSCF/NEVPT2 calculations.

Compound	*D*	|*E*/*D*|	D_Q[a]	D_D[a]	D_{Q1}	D_{Q2}	D_{Q1} + D_{Q2}
1·ClO_4·H_2O							
Co1	+52.807	0.326	+46.629	–1.451	+33.466	+17.856	+51.322
1·BPh_4							
Co1	+63.979	0.286	+54.873	+1.456	+38.259	+18.997	+57.256
1·PF_6·H_2O							
Co1	–60.036	0.322	–58.103	–2.022	–72.995	+14.902	–58.093

[a] D_Q and D_D are the sum of spin-orbit contributions coming from quartet and doublet excited states.

Table A.5. Selected ac-magnetic data at different dc-applied field for **1·ClO$_4$·H$_2$O** obtained from the ln(τ) *vs* 1/*T* plots.

H_{dc} (kOe)\Model[a]	$\tau_{0,IK} \times 10^3$ (s)	$\tau_{0,IK} \times 10^5$ (s)	$\tau_{0,LT} \times 10^5$ (s)	E_{aLT} (cm^{-1})	$\tau_{0,MT} \times 10^7$ (s)	E_{aMT} (cm^{-1})	$\tau_{0,HT} \times 10^{11}$ (s)	E_{aHT} (cm^{-1})
500								
Global	–	–	–	–	–	–	–	–
Process 1	11 ± 12		10 ± 5	5.9 ± 1.1	1.68 ± 0.23	20.8 ± 0.6	1.1 ± 0.6	76 ± 3
Process 2	–	7.07 ± 0.24	–	–	–	–	–	–
1000								
Global	8 ± 4	–	6 ± 3	6.2 ± 1.1	1.6 ± 0.3	21.7 ± 0.8	7 ± 3	68 ± 3
Process 1	–	–	–	–	–	–	–	–
Process 2	–	–	–	–	–	–	–	–
2500								
Global	2.8 ± 0.5	–	10 ± 8	6.2 ± 1.9	2.4 ± 0.5	20.3 ± 0.9	150 ± 40	51.4 ± 2.2
Process 1	–	–	–	–	–	–	–	–
Process 2	–	–	–	–	–	–	–	–
5000								
Global	–	46.1 ± 0.6	–	–	3.4 ± 0.4	18.1 ± 0.3	330 ± 80	45.2 ± 1.7
Process 1	–	36.6 ± 0.8	–	–	1.61 ± 0.19	20.6 ± 0.4	19 ± 10	65 ± 4
Process 2	3.1 ± 0.6	–	8 ± 9	8 ± 3	–	–	–	–

[a] Global is the analysis considering only one general Debye model, and Processes 1 + 2 are the analyses with the sum of two individual Debye models (equations 5 and 6). All data were analysed by a combination of several TA relaxations plus one IK mechanism.

Table A.6. Selected ac-magnetic data at different dc-applied field for **1·BPh4** obtained from the ln(τ) *vs* 1/*T* plots.

H_{dc} (kOe)\Model[a]	$\tau_{0,IK} \times 10^4$ (s)	$\tau_{0,IK} \times 10^6$ (s)	$\tau_{0,LT} \times 10^6$ (s)	E_{aLT} (cm^{-1})	$\tau_{0,MT} \times 10^8$ (s)	E_{aMT} (cm^{-1})	$\tau_{0,HT} \times 10^{11}$ (s)	E_{aHT} (cm^{-1})
250								
Global	44 ± 22	–	1.03 ± 0.08	9.77 ± 0.21	–	–	4 ± 6	67 ± 8
Process 1	–	–	–	–	–	–	–	–
Process 2	–	–	–	–	–	–	–	–
500								
Global	32 ± 4	–	1.20 ± 0.06	10.56 ± 0.14	–	–	16 ± 5	61.3 ± 2.1
Process 1	–	–	–	–	–	–	–	–
Process 2	–	–	–	–	–	–	–	–
1000								
Global	22.7 ± 1.9	–	1.13 ± 0.09	12.22 ± 0.23	–	–	17 ± 6	60.7 ± 2.3
Process 1	–	–	–	–	–	–	–	–
Process 2	–	–	–	–	–	–	–	–
2500								
Global	22.3 ± 1.1	–	2.6 ± 0.5	12.6 ± 0.5	–	–	1701 ± 384	34.1 ± 1.4
	50 ± 22	–	89 ± 53	5.3 ± 1.3	36 ± 8	19.0 ± 0.9	215 ± 81	49 ± 3
Process 1	–	–	–	–	–	–	–	–
Process 2	–	–	–	–	–	–	–	–
5000								
Global	7.3 ± 0.4	–	1.1 ± 0.3	14.9 ± 0.9	–	–	304 ± 135	45 ± 3
	9.9 ± 1.9	–	25 ± 25	7.3 ± 2.3	9 ± 5	25.1 ± 2.5	5 ± 8	77 ± 12
Process 1	4.32 ± 0.17	–	–	–	27 ± 6	19.9 ± 0.7	34 ± 13	62 ± 3
Process 2	1.7 ± 0.5	–	–	–	–	–	–	–

[a] Global is the analysis considering only one general Debye model, and Processes 1 + 2 are the analyses with the sum of two individual Debye models (equations 5 and 6). All data were analysed by a combination of several TA relaxations plus one IK mechanism.

Table A.7. Selected ac-magnetic data at different dc-applied field for **1·PF$_6$·H$_2$O** obtained from the ln(τ) *vs* 1/*T* plots.

H_{dc} (kOe)\Model[a]	$\tau_{0,IK} \times 10^4$ (s)	$\tau_{0,IK} \times 10^5$ (s)	$\tau_{0,LT} \times 10^6$ (s)	E_{aLT} (cm^{-1})	$\tau_{0,MT} \times 10^8$ (s)	E_{aMT} (cm^{-1})	$\tau_{0,HT} \times 10^{11}$ (s)	E_{aHT} (cm^{-1})
500								
Global	4.5 ± 0.3	–	1.59 ± 0.21	11.1 ± 0.4	–	–	49 ± 20	56 ± 3
	9 ± 3	–	13 ± 7	6.1 ± 1.2	28 ± 12	19.8 ± 2.2	3 ± 3	62 ± 7
Process 1	–	–	–	–	–	–	–	–
Process 2	–	–	–	–	–	–	–	–
1000								
Global	4.78 ± 0.21	–	1.87 ± 0.21	11.0 ± 0.3	–	–	430 ± 80	42.9 ± 1.2
	6.7 ± 0.6	–	9 ± 3	7.2 ± 0.7	19 ± 6	21.6 ± 1.7	74 ± 24	58 ± 3
Process 1	–	–	–	–	–	–	–	–
Process 2	–	–	–	–	–	–	–	–
2500								
Global	2.13 ± 0.06	–	1.61 ± 0.18	10.9 ± 0.3	–	–	647 ± 91	40.0 ± 1.0
	2.4 ± 0.08	–	4.5 ± 1.1	8.4 ± 0.6	9 ± 5	25 ± 3	135 ± 86	56 ± 6
Process 1	–	–	–	–	–	–	–	–
Process 2	–	–	–	–	–	–	–	–
5000								
Global	–	–	–	–	–	–	–	–
Process 1	–	5.63 ± 0.18	1.6 ± 0.4	11.0 ± 0.9	2.3 ± 0.3	30.6 ± 1.0	–	–
Process 2	76 ± 19	–	–	–	–	–	–	–

[a] Global is the analysis considering only one general Debye model, and Processes 1 + 2 are the analyses with the sum of two individual Debye models (equations 5 and 6). All data were analysed by a combination of several TA relaxations plus one IK mechanism.

SI Chapter III

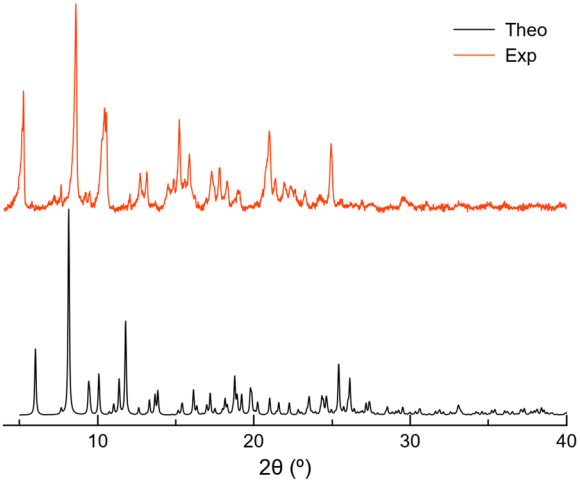

Figure A.26. Experimental and simulated powder X-ray diffraction patterns of **2**.

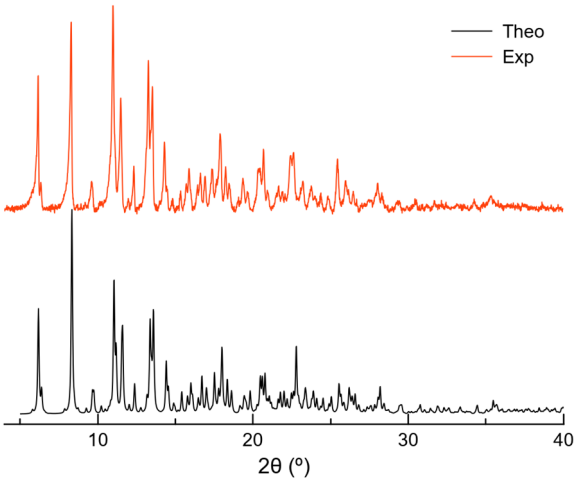

Figure A.27. Experimental and simulated powder X-ray diffraction patterns of **2'**.

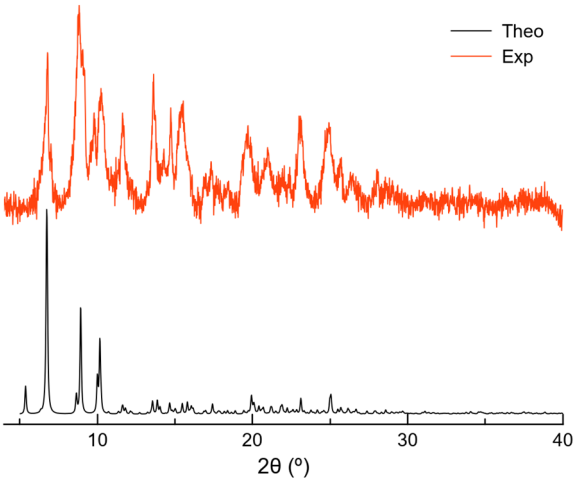

Figure A.28. Experimental and simulated powder X-ray diffraction patterns of **3**.

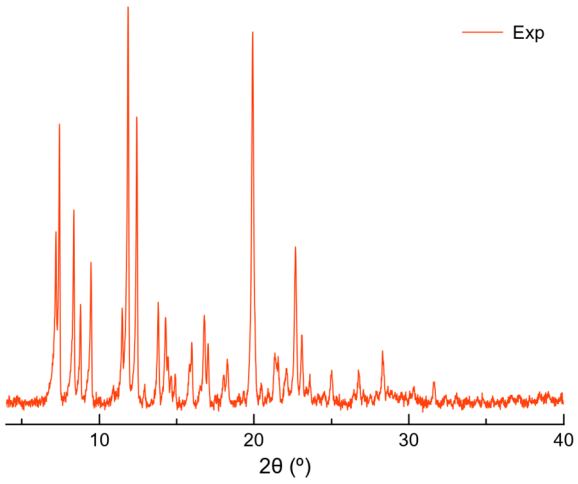

Figure A.29. Experimental powder X-ray diffraction pattern of **3′**.

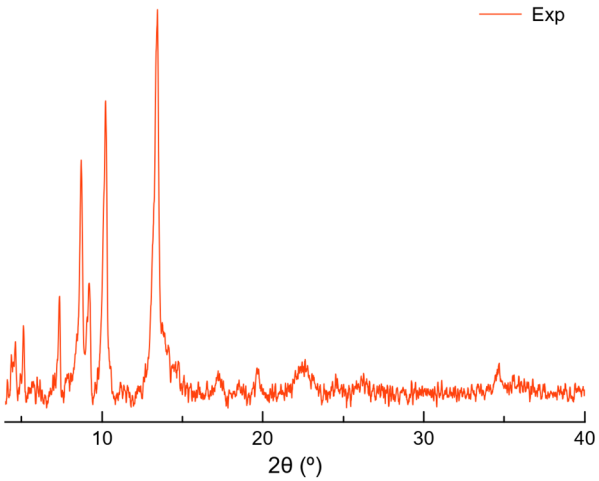

Figure A.30. Experimental powder X-ray diffraction pattern of **4**.

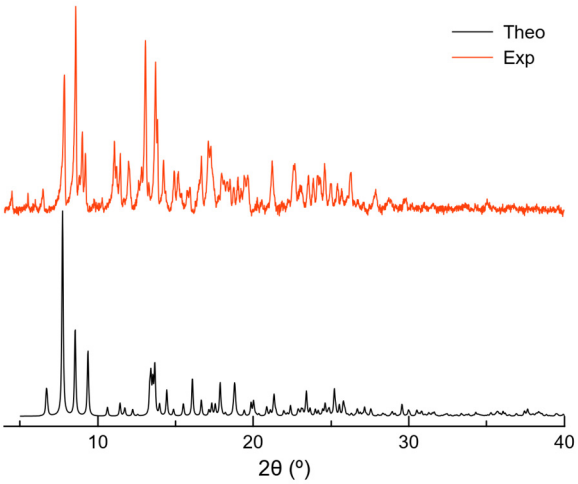

Figure A.31. Experimental and simulated powder X-ray diffraction patterns of **5**.

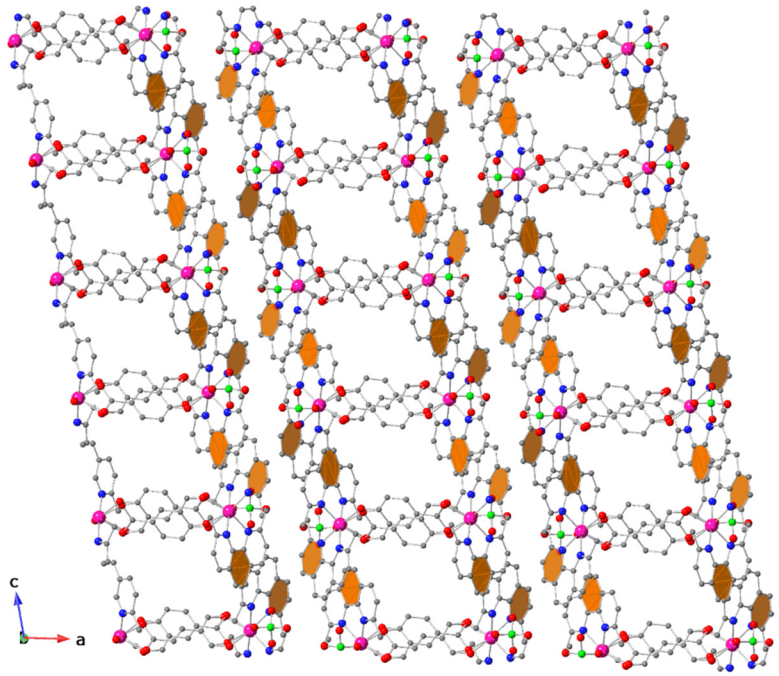

Figure A.32. Perspective view along the *b*-axis of the crystal packing of **2** with phenanthroline π–π interactions coloured in orange. Colour code: magenta, cobalt; blue, nitrogen; red, oxygen; grey, carbon; green, chlorine.

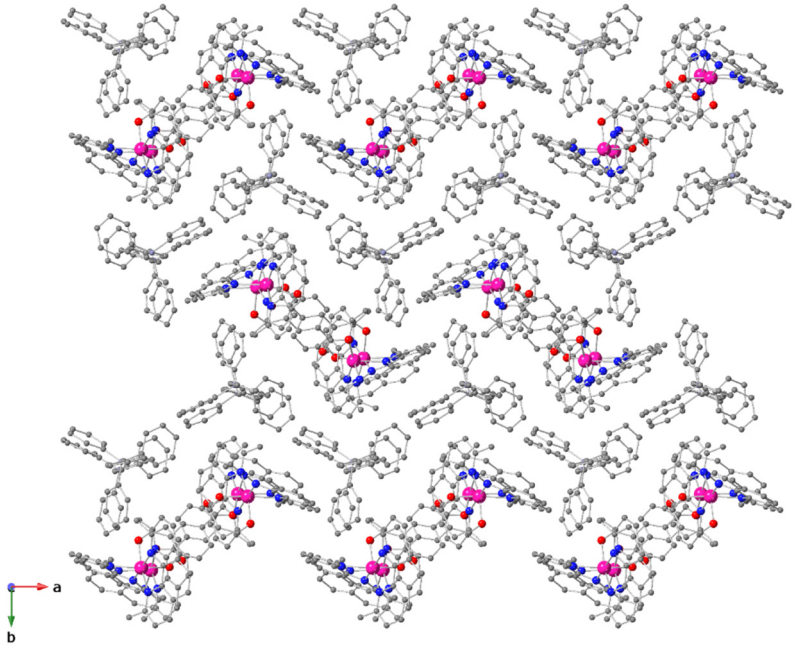

Figure A.33. Perspective view along the *c*-axis of the crystal packing of **2'**. Hydrogen atoms are omitted for clarity. Colour code: magenta, cobalt; blue, nitrogen; red, oxygen; grey, carbon; sky blue, boron.

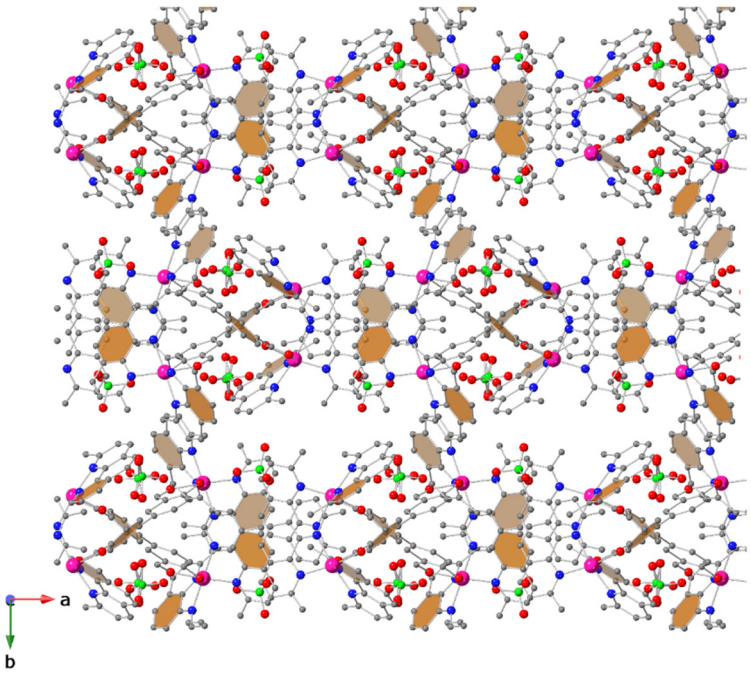

Figure A.34. Perspective view along the *c*-axis of the crystal packing of **3** with phenanthroline π–π interactions coloured in orange. Hydrogen atoms are omitted for clarity. Colour code: magenta, cobalt; blue, nitrogen; red, oxygen; grey, carbon; green, chlorine.

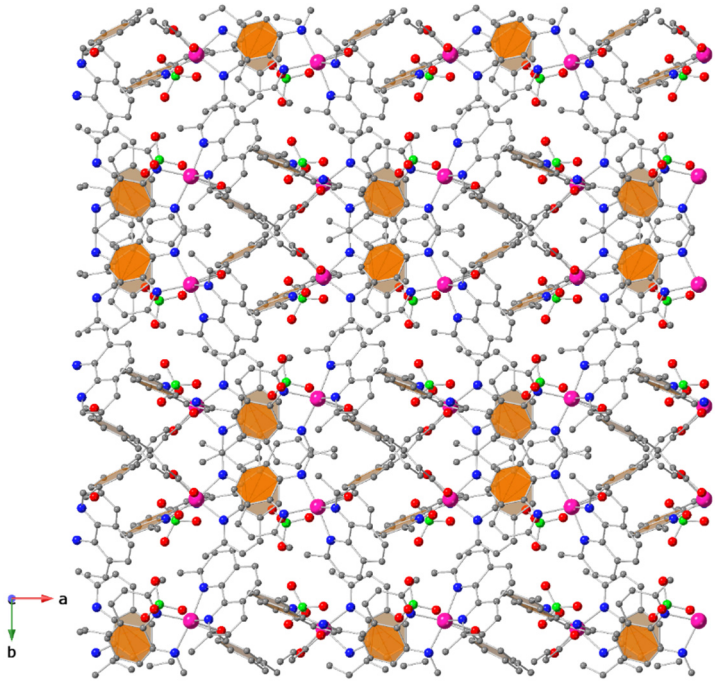

Figure A.35. Perspective view along the *c*-axis of the crystal packing of **5** with phenanthroline π–π interactions coloured in orange. Hydrogen atoms are omitted for clarity. Colour code: magenta, cobalt; blue, nitrogen; red, oxygen; grey, carbon; green, chlorine.

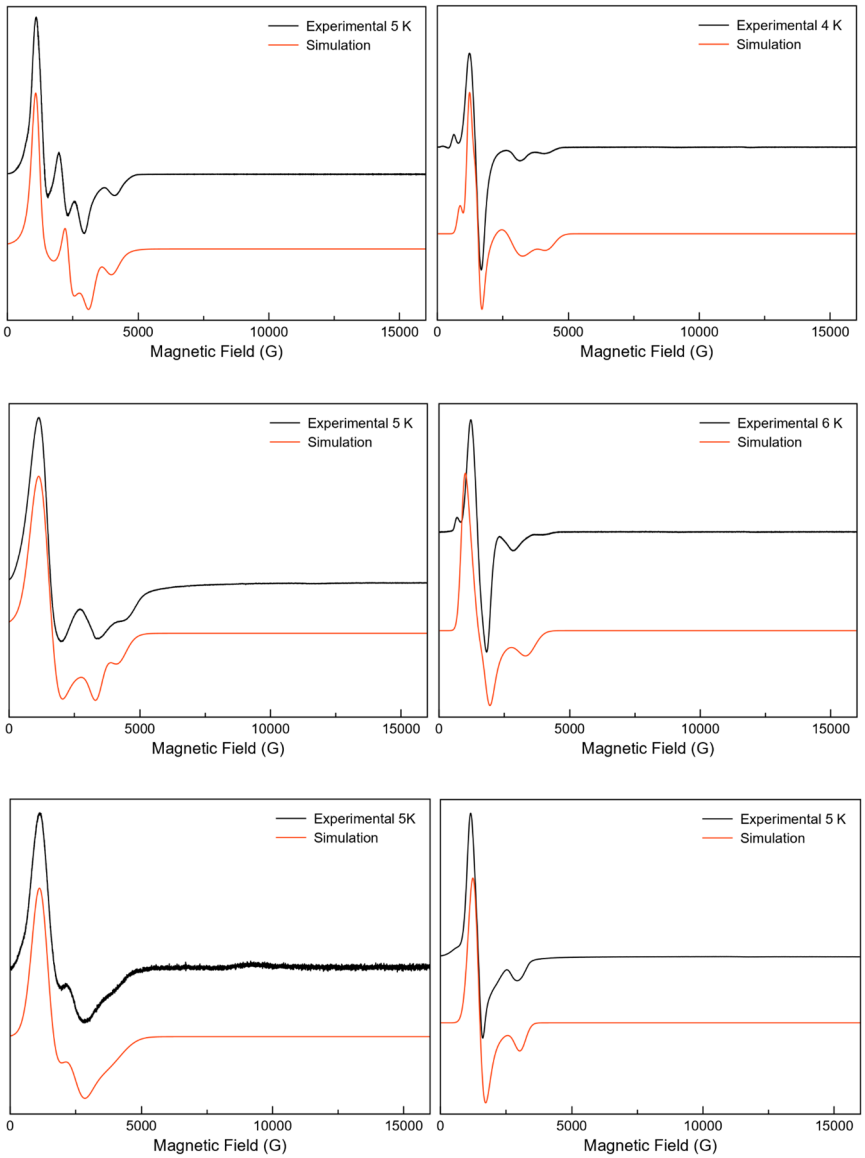

Figure A.36. X-band EPR in the 0−16 kOe range for polycrystalline powdered samples of **2** (top left), **2′** (top right), **3** (middle left), **3′** (middle right), **4** (bottom left) and **5** (bottom right) at ~5 K. The simulated red curves were obtained by using the parameters on Table III.4.

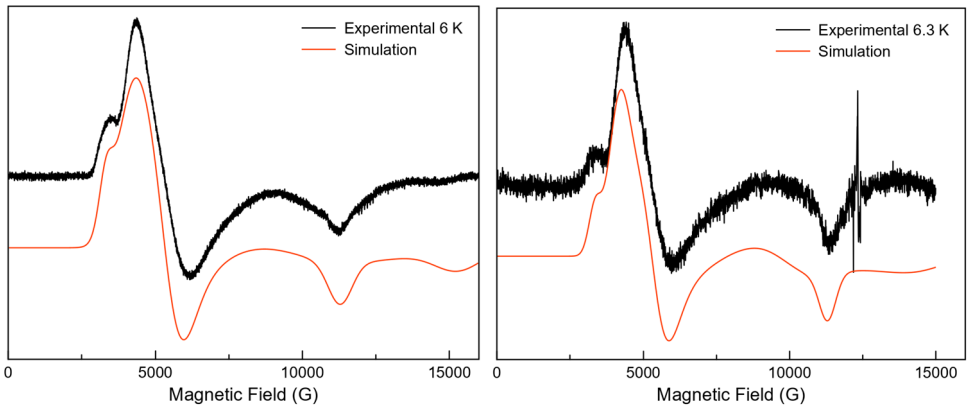

Figure A.37. Q-band EPR in the 0−16 kOe range for frozen solution samples in AcN ~5 mM of **2′** (left) and **3** (right). The simulated red curves were obtained by using the parameters on Table III.4.

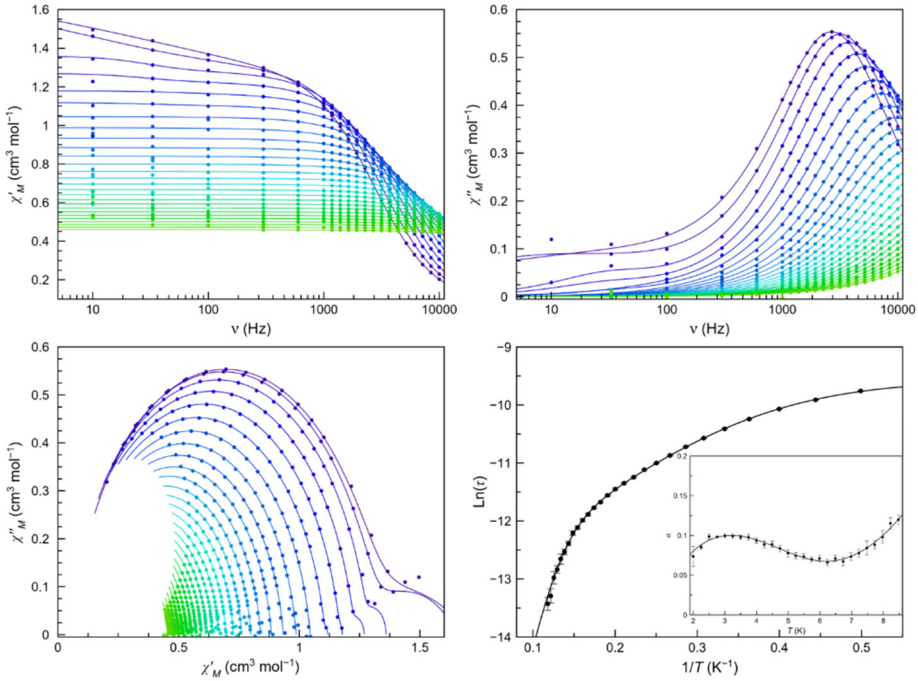

Figure A.38. Frequency dependence of χ_M' (top left) and χ_M'' (top right), Cole-Cole plots (bottom left) and Arrhenius plots of **2** (bottom right) in a dc-applied static field of 2.5 kOe with ± 0.005 kOe oscillating field in the temperature range of 2.0–8.5 K (purple to green gradient). Thermal dependence of α is included on the bottom right figure as an inset, where the black line are eye-guides. Standard deviation appears as vertical error bars.

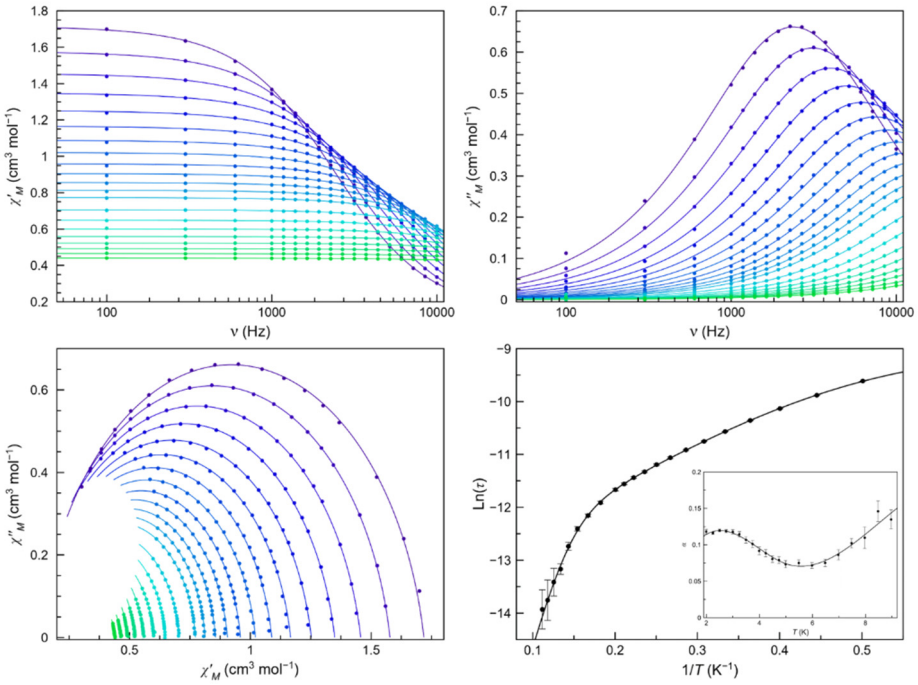

Figure A.39. Frequency dependence of χ_M' (top left) and χ_M'' (top right), Cole-Cole plots (bottom left) and Arrhenius plots of **2** (bottom right) in a dc-applied static field of 1.5 kOe with ± 0.005 kOe oscillating field in the temperature range of 2.0–9.0 K (purple to green gradient). Thermal dependence of α is included on the bottom right figure as an inset, where the black line are eye-guides. Standard deviation appears as vertical error bars.

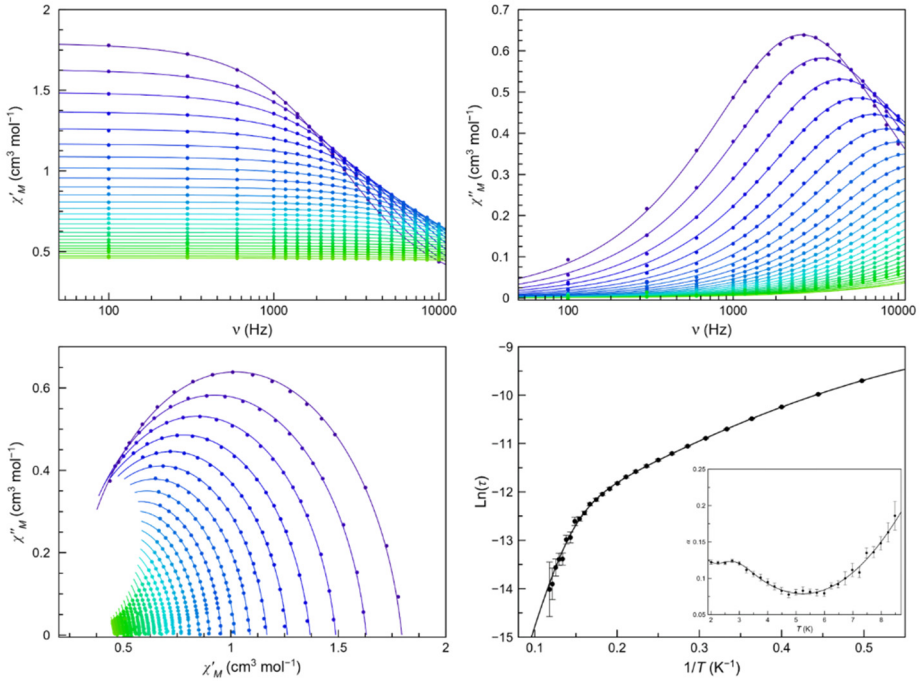

Figure A.40. Frequency dependence of χ_M' (top left) and χ_M'' (top right), Cole-Cole plots (bottom left) and Arrhenius plots of **2** (bottom right) in a dc-applied static field of 1.0 kOe with ± 0.005 kOe oscillating field in the temperature range of 2.0–8.5 K (purple to green gradient). Thermal dependence of α is included on the bottom right figure as an inset, where the black line are eye-guides. Standard deviation appears as vertical error bars.

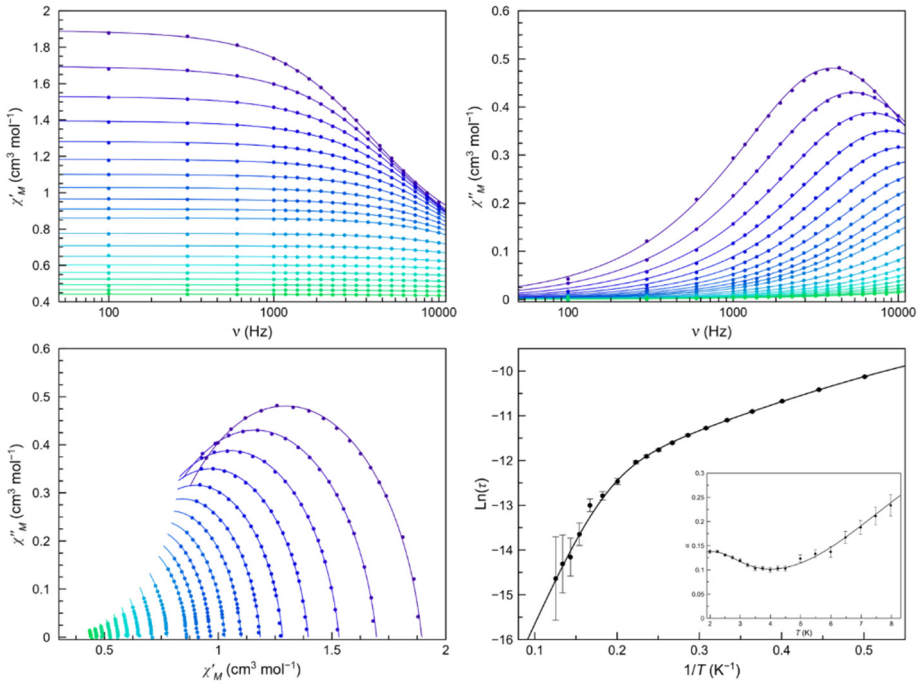

Figure A.41. Frequency dependence of χ_M' (top left) and χ_M'' (top right), Cole-Cole plots (bottom left) and Arrhenius plots of **2** (bottom right) in a dc-applied static field of 0.5 kOe with ± 0.005 kOe oscillating field in the temperature range of 2.0–9.0 K (purple to green gradient). Thermal dependence of α is included on the bottom right figure as an inset, where the black line are eye-guides. Standard deviation appears as vertical error bars.

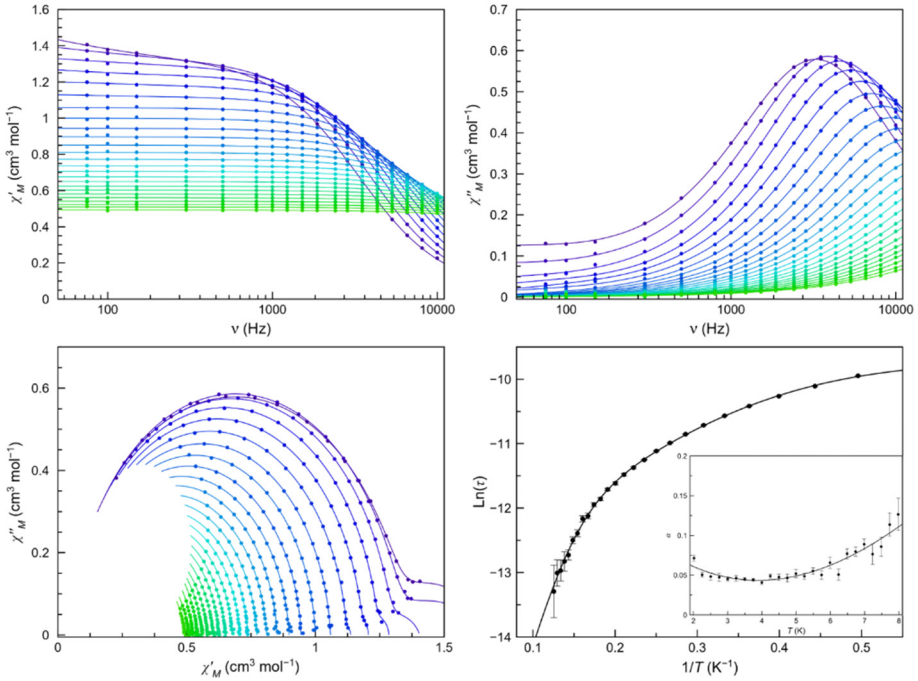

Figure A.42. Frequency dependence of χ_M' (top left) and χ_M'' (top right), Cole-Cole plots (bottom left) and Arrhenius plots of **2′** (bottom right) in a dc-applied static field of 2.5 kOe with ± 0.005 kOe oscillating field in the temperature range of 2.0–8.0 K (purple to red gradient). Thermal dependence of α is included on the bottom right figure as an inset, where the black line are eye-guides. Standard deviation appears as vertical error bars.

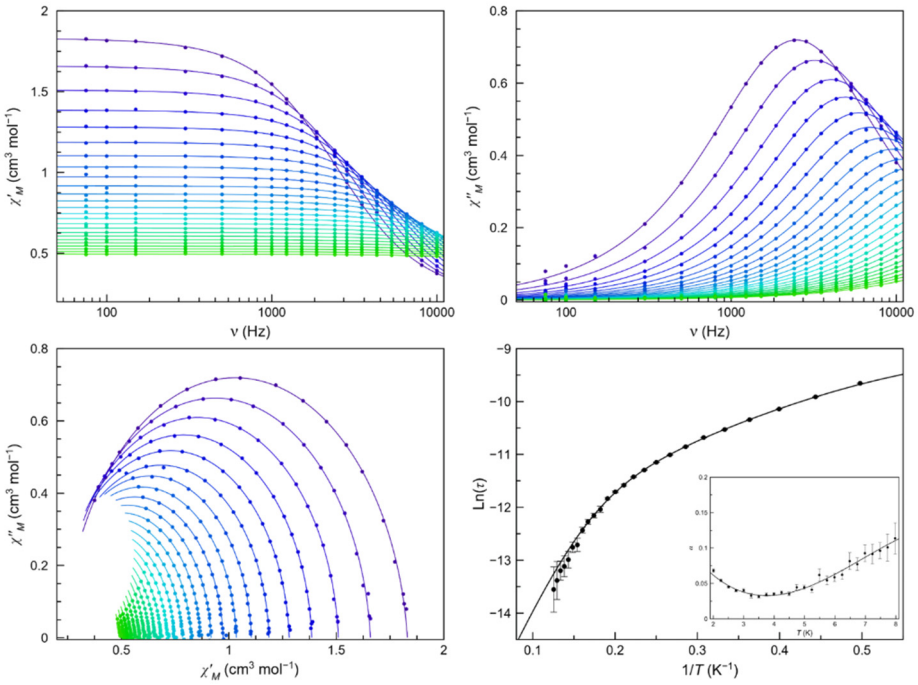

Figure A.43. Frequency dependence of χ_M' (top left) and χ_M'' (top right), Cole-Cole plots (bottom left) and Arrhenius plots of **2′** (bottom right) in a dc-applied static field of 1.0 kOe with ± 0.005 kOe oscillating field in the temperature range of 2.0–8.0 K (purple to red gradient). Thermal dependence of α is included on the bottom right figure as an inset, where the black line are eye-guides. Standard deviation appears as vertical error bars.

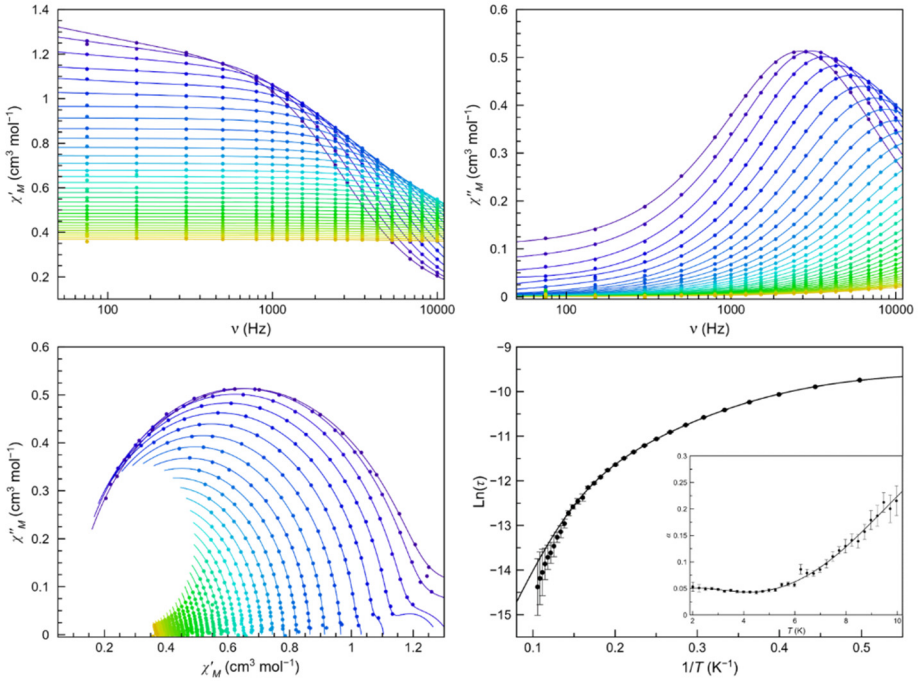

Figure A.44. Frequency dependence of χ_M' (top left) and χ_M'' (top right), Cole-Cole plots (bottom left) and Arrhenius plots of **3** (bottom right) in a dc-applied static field of 2.5 kOe with ± 0.005 kOe oscillating field in the temperature range of 2.0–10.0 K (purple to red gradient). Thermal dependence of α is included on the bottom right figure as an inset, where the black line are eye-guides. Standard deviation appears as vertical error bars.

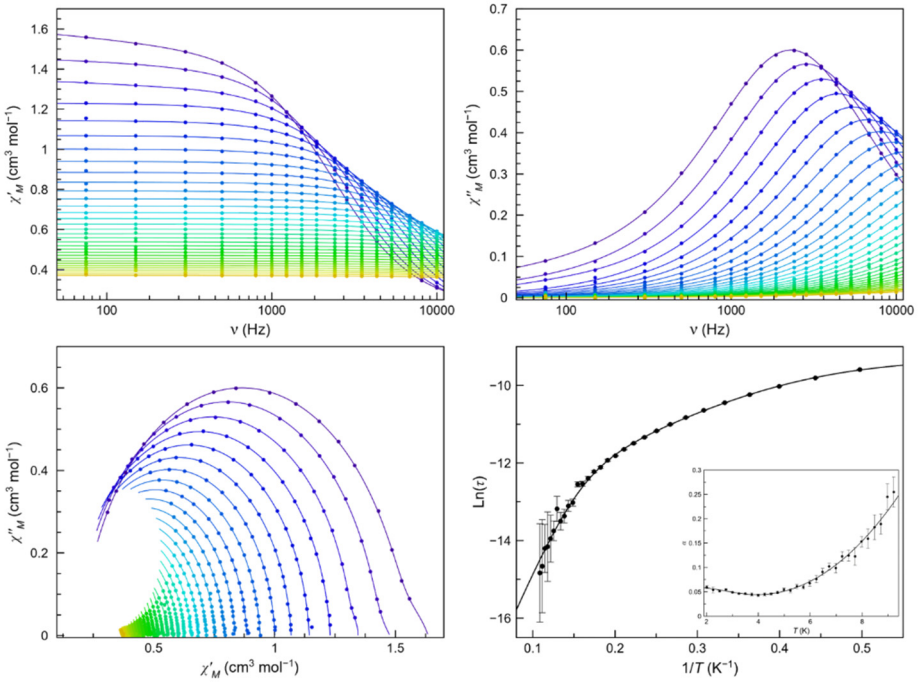

Figure A.45. Frequency dependence of χ_M' (top left) and χ_M'' (top right), Cole-Cole plots (bottom left) and Arrhenius plots of **3** (bottom right) in a dc-applied static field of 1.5 kOe with ± 0.005 kOe oscillating field in the temperature range of 2.0–10.0 K (purple to red gradient). Thermal dependence of α is included on the bottom right figure as an inset, where the black line are eye-guides. Standard deviation appears as vertical error bars.

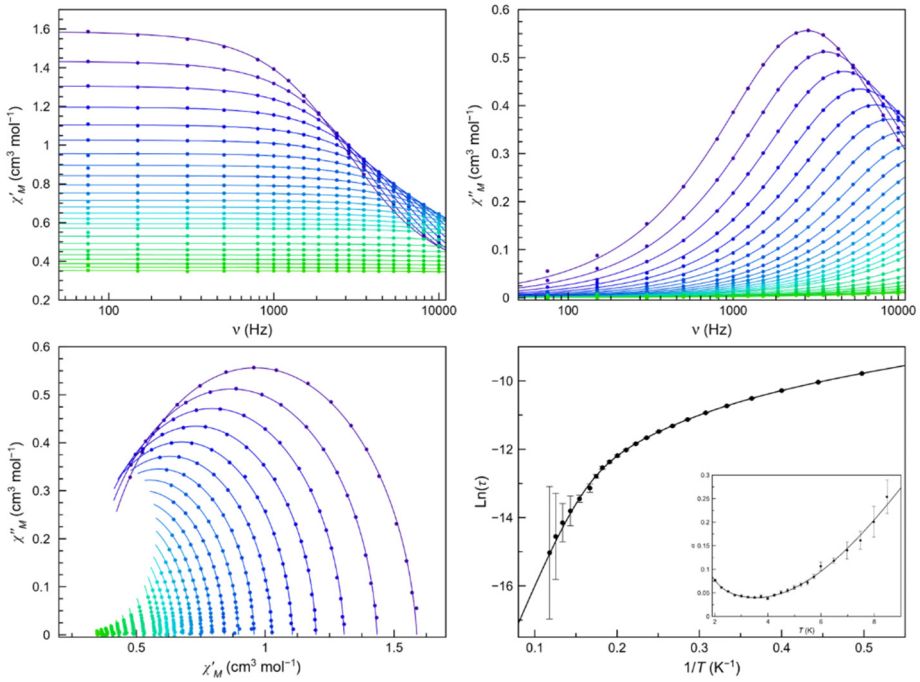

Figure A.46. Frequency dependence of χ_M' (top left) and χ_M'' (top right), Cole-Cole plots (bottom left) and Arrhenius plots of **3** (bottom right) in a dc-applied static field of 1.0 kOe with ± 0.005 kOe oscillating field in the temperature range of 2.0–10.0 K (purple to red gradient). Thermal dependence of α is included on the bottom right figure as an inset, where the black line are eye-guides. Standard deviation appears as vertical error bars.

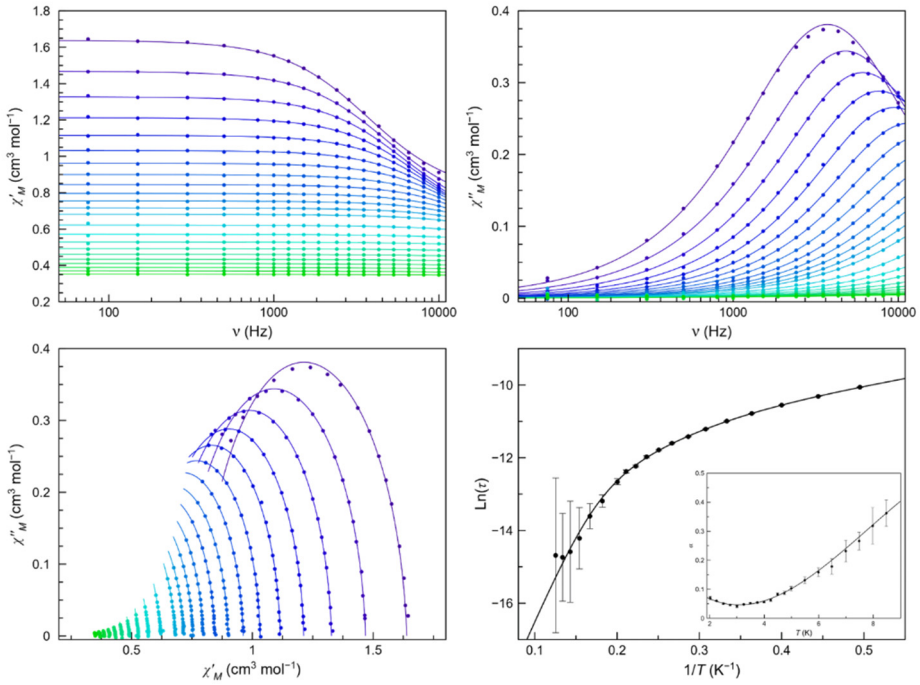

Figure A.47. Frequency dependence of χ_M' (top left) and χ_M'' (top right), Cole-Cole plots (bottom left) and Arrhenius plots of **3** (bottom right) in a dc-applied static field of 0.5 kOe with ± 0.005 kOe oscillating field in the temperature range of 2.0–10.0 K (purple to red gradient). Thermal dependence of α is included on the bottom right figure as an inset, where the black line are eye-guides. Standard deviation appears as vertical error bars.

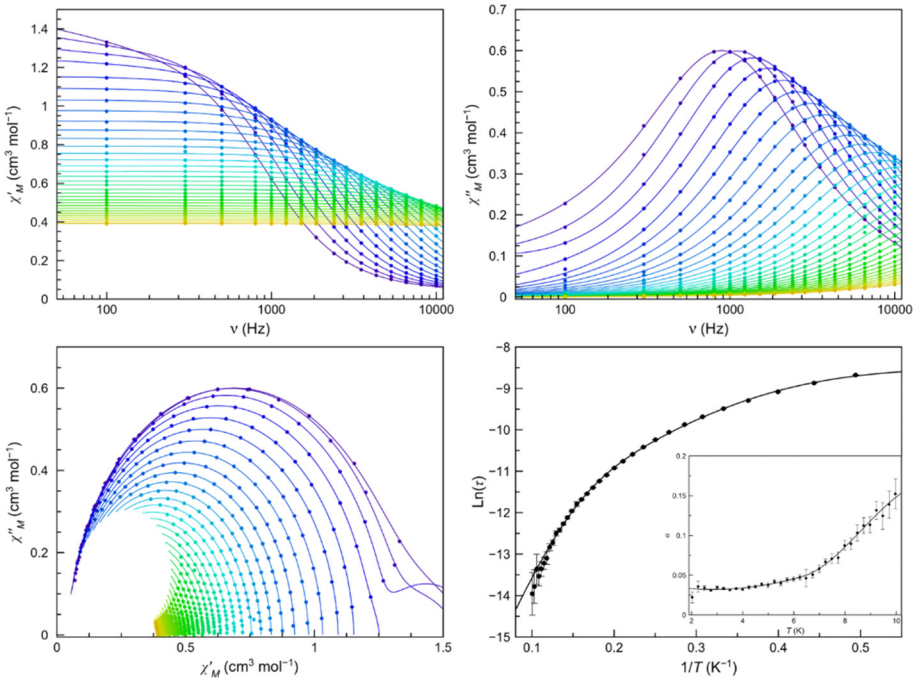

Figure A.48. Frequency dependence of χ_M' (top left) and χ_M'' (top right), Cole-Cole plots (bottom left) and Arrhenius plots of **3′** (bottom right) in a dc-applied static field of 2.5 kOe with ± 0.005 kOe oscillating field in the temperature range of 2.0–10.0 K (purple to red gradient). Thermal dependence of α is included on the bottom right figure as an inset, where the black line are eye-guides. Standard deviation appears as vertical error bars.

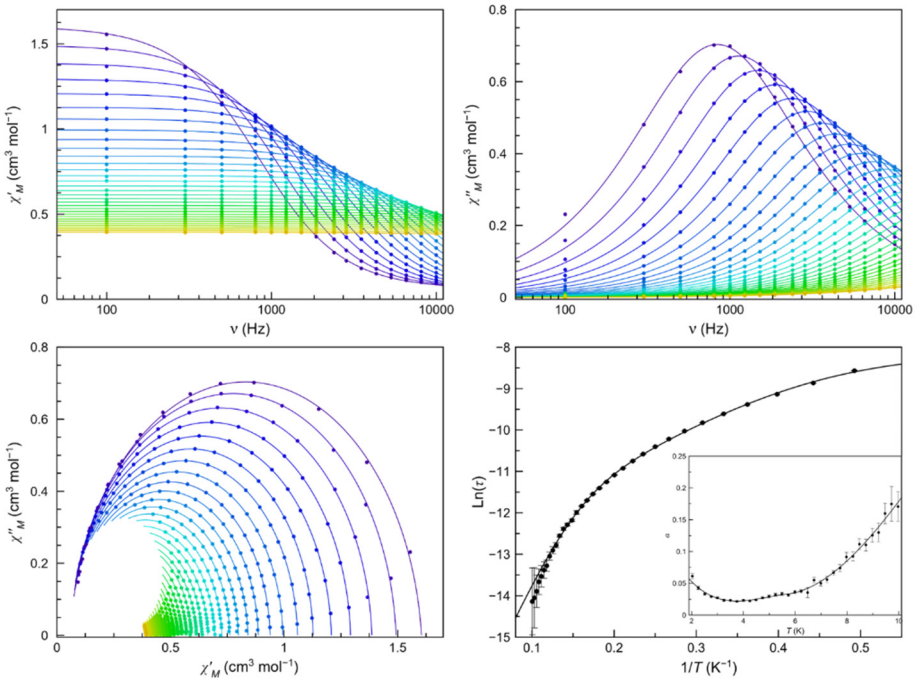

Figure A.49. Frequency dependence of χ_M' (top left) and χ_M'' (top right), Cole-Cole plots (bottom left) and Arrhenius plots of **3′** (bottom right) in a dc-applied static field of 1.75 kOe with ± 0.005 kOe oscillating field in the temperature range of 2.0–10.0 K (purple to red gradient). Thermal dependence of α is included on the bottom right figure as an inset, where the black line are eye-guides. Standard deviation appears as vertical error bars.

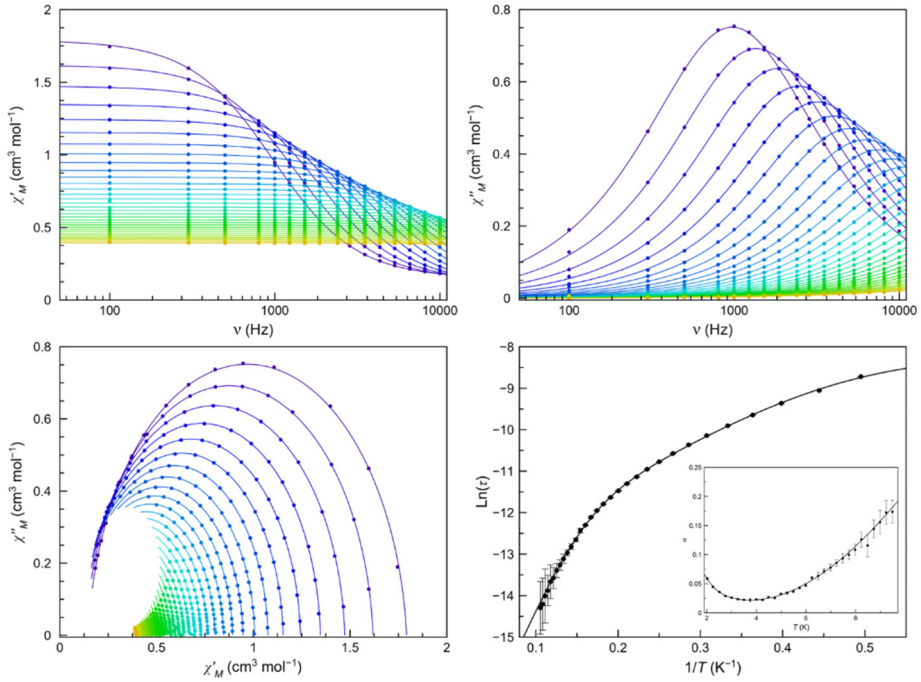

Figure A.50. Frequency dependence of χ_M' (top left) and χ_M'' (top right), Cole-Cole plots (bottom left) and Arrhenius plots of **3′** (bottom right) in a dc-applied static field of 1.0 kOe with ± 0.005 kOe oscillating field in the temperature range of 2.0–10.0 K (purple to red gradient). Thermal dependence of α is included on the bottom right figure as an inset, where the black line are eye-guides. Standard deviation appears as vertical error bars.

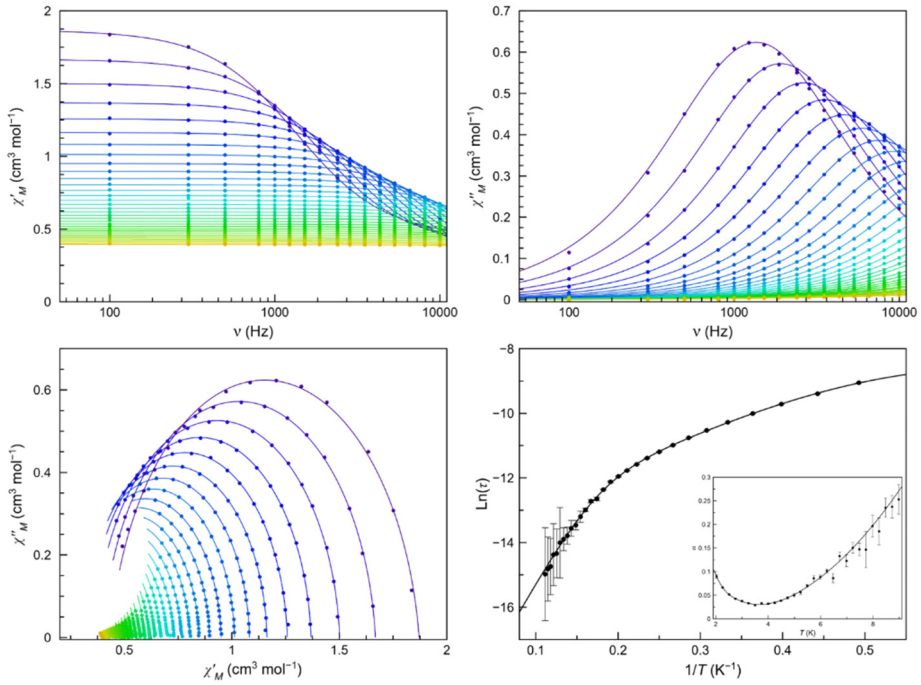

Figure A.51. Frequency dependence of χ_M' (top left) and χ_M'' (top right), Cole-Cole plots (bottom left) and Arrhenius plots of **3′** (bottom right) in a dc-applied static field of 0.5 kOe with ± 0.005 kOe oscillating field in the temperature range of 2.0–10.0 K (purple to red gradient). Thermal dependence of α is included on the bottom right figure as an inset, where the black line are eye-guides. Standard deviation appears as vertical error bars.

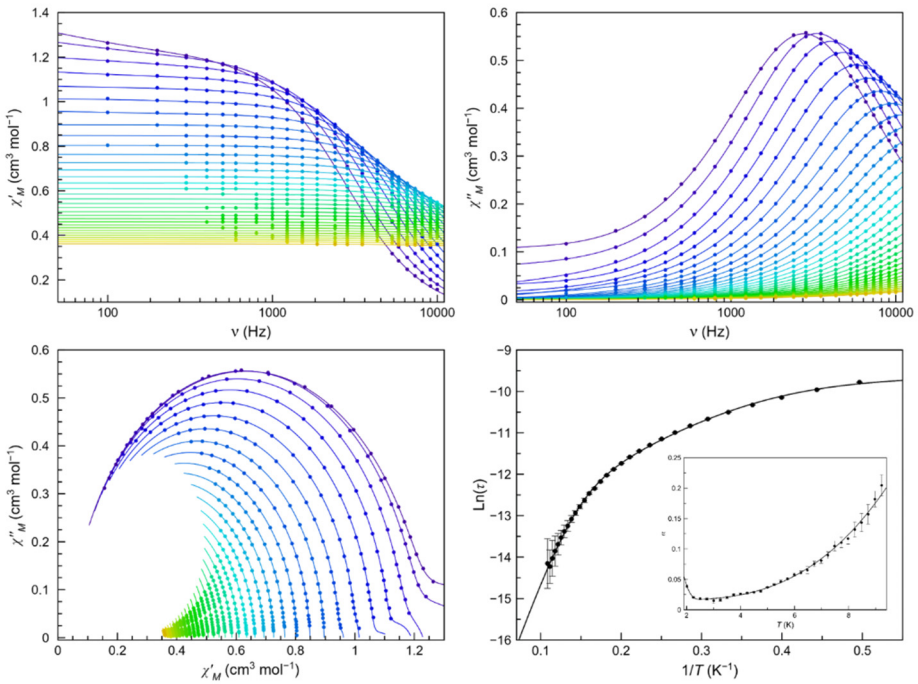

Figure A.52. Frequency dependence of χ_M' (top left) and χ_M'' (top right), Cole-Cole plots (bottom left) and Arrhenius plots of **4** (bottom right) in a dc-applied static field of 2.5 kOe with ± 0.005 kOe oscillating field in the temperature range of 2.0–10.0 K (purple to red gradient). Thermal dependence of α is included on the bottom right figure as an inset, where the black line are eye-guides. Standard deviation appears as vertical error bars.

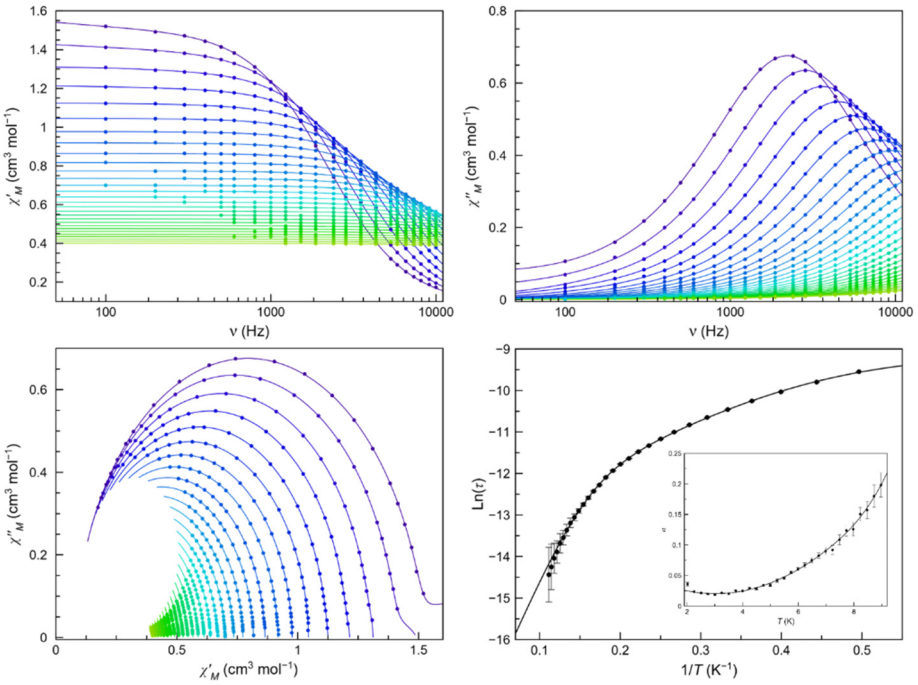

Figure A.53. Frequency dependence of χ_M' (top left) and χ_M'' (top right), Cole-Cole plots (bottom left) and Arrhenius plots of **4** (bottom right) in a dc-applied static field of 1.5 kOe with ± 0.005 kOe oscillating field in the temperature range of 2.0–9.0 K (purple to red gradient). Thermal dependence of α is included on the bottom right figure as an inset, where the black line are eye-guides. Standard deviation appears as vertical error bars.

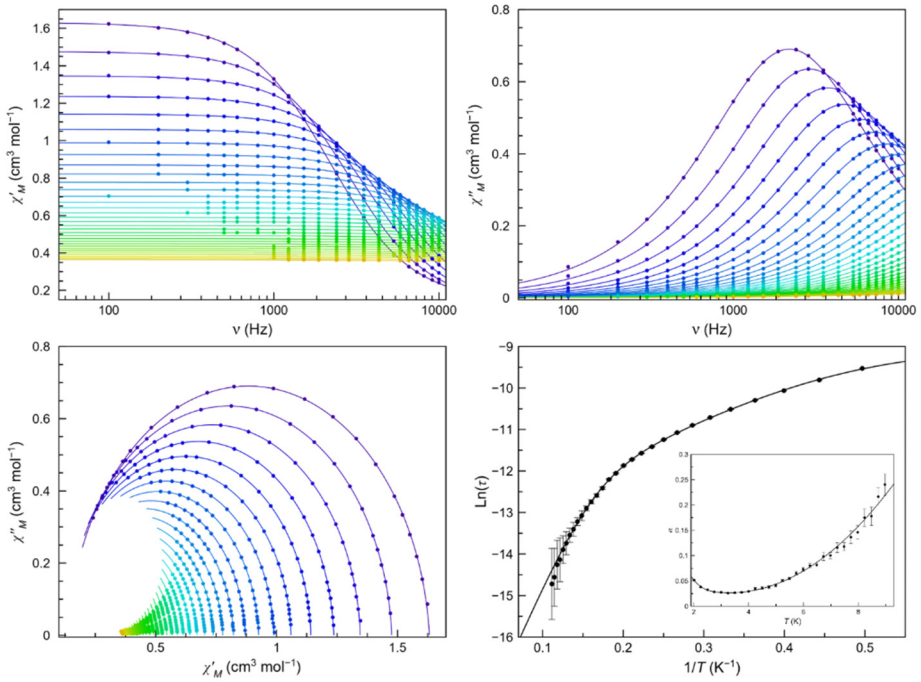

Figure A.54. Frequency dependence of χ_M' (top left) and χ_M'' (top right), Cole-Cole plots (bottom left) and Arrhenius plots of **4** (bottom right) in a dc-applied static field of 1.0 kOe with ± 0.005 kOe oscillating field in the temperature range of 2.0–10.0 K (purple to red gradient). Thermal dependence of α is included on the bottom right figure as an inset, where the black line are eye-guides. Standard deviation appears as vertical error bars.

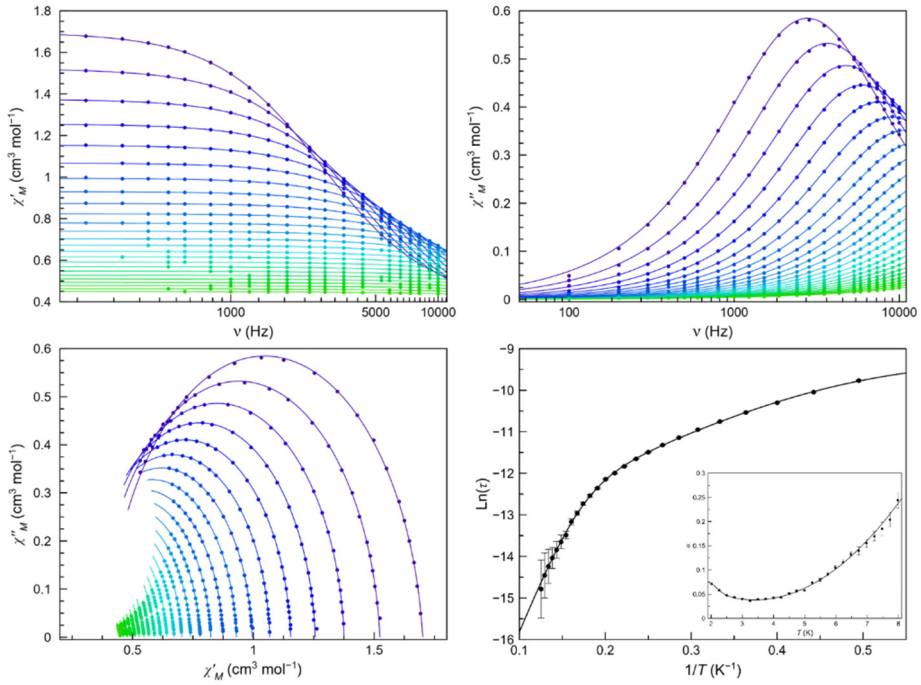

Figure A.55. Frequency dependence of χ_M' (top left) and χ_M'' (top right), Cole-Cole plots (bottom left) and Arrhenius plots of **4** (bottom right) in a dc-applied static field of 0.5 kOe with ± 0.005 kOe oscillating field in the temperature range of 2.0–8.0 K (purple to red gradient). Thermal dependence of α is included on the bottom right figure as an inset, where the black line are eye-guides. Standard deviation appears as vertical error bars.

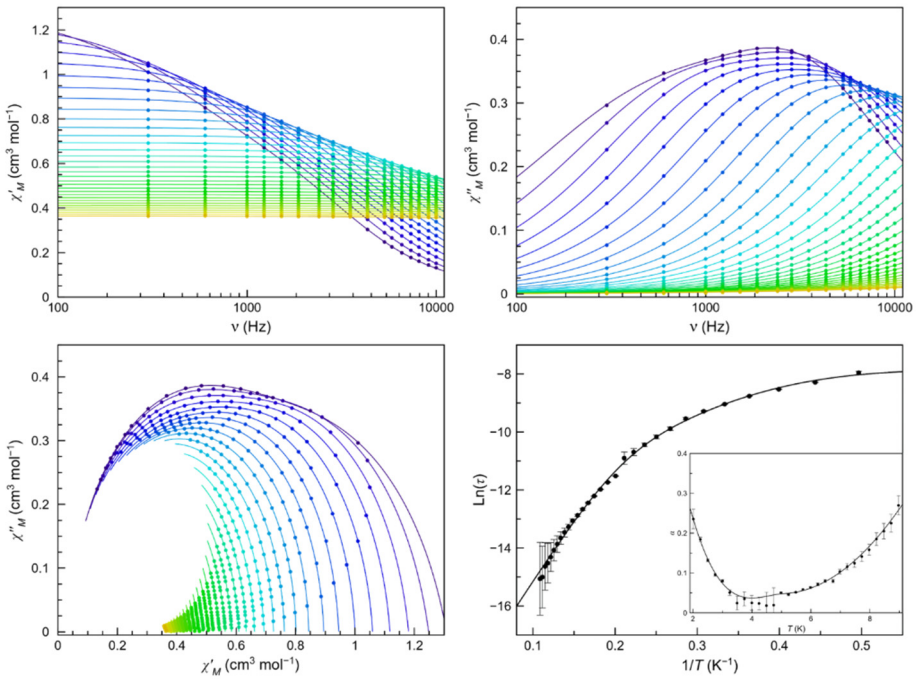

Figure A.56. Frequency dependence of χ_M' (top left) and χ_M'' (top right), Cole-Cole plots (bottom left) and Arrhenius plots of **5** (bottom right) in a dc-applied static field of 2.5 kOe with ± 0.005 kOe oscillating field in the temperature range of 2.0–10.0 K (purple to red gradient). Thermal dependence of α is included on the bottom right figure as an inset, where the black line are eye-guides. Standard deviation appears as vertical error bars.

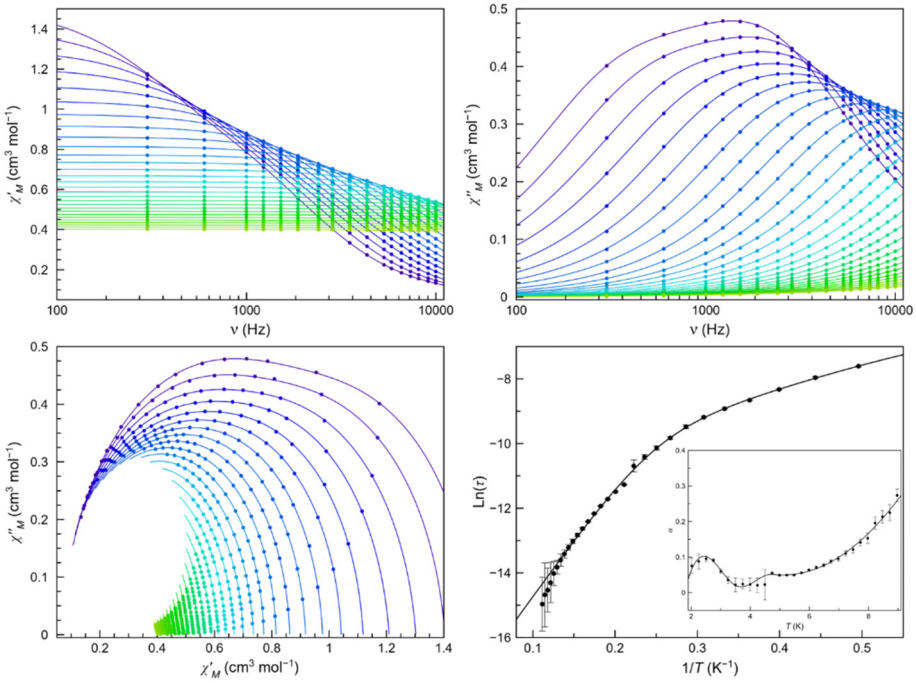

Figure A.57. Frequency dependence of χ_M' (top left) and χ_M'' (top right), Cole-Cole plots (bottom left) and Arrhenius plots of **5** (bottom right) in a dc-applied static field of 1.5 kOe with ± 0.005 kOe oscillating field in the temperature range of 2.0–9.0 K (purple to red gradient). Thermal dependence of α is included on the bottom right figure as an inset, where the black line are eye-guides. Standard deviation appears as vertical error bars.

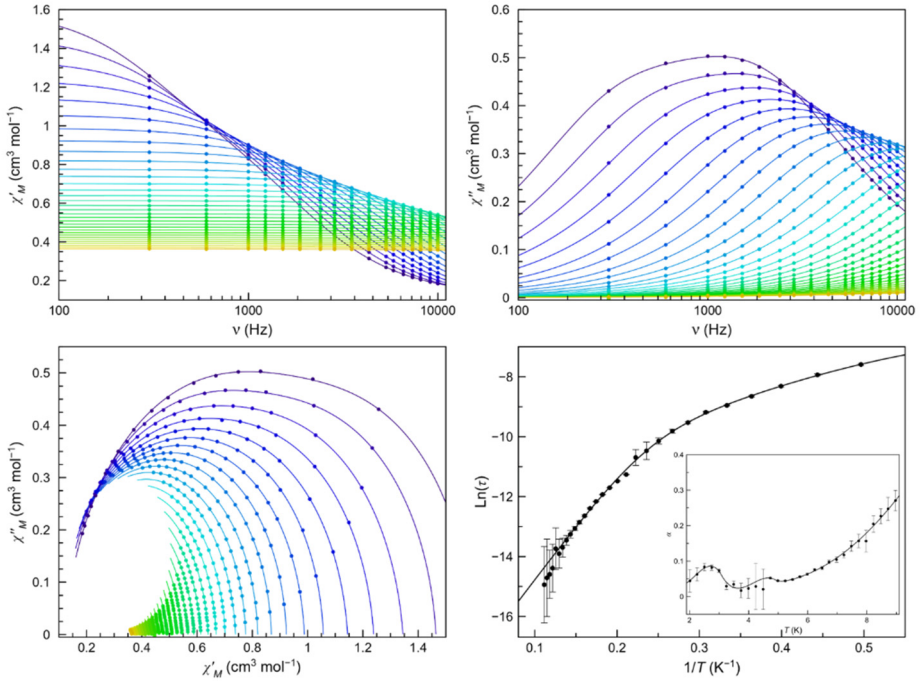

Figure A.58. Frequency dependence of χ_M' (top left) and χ_M'' (top right), Cole-Cole plots (bottom left) and Arrhenius plots of **5** (bottom right) in a dc-applied static field of 1.0 kOe with ± 0.005 kOe oscillating field in the temperature range of 2.0–10.0 K (purple to red gradient). Thermal dependence of α is included on the bottom right figure as an inset, where the black line are eye-guides. Standard deviation appears as vertical error bars.

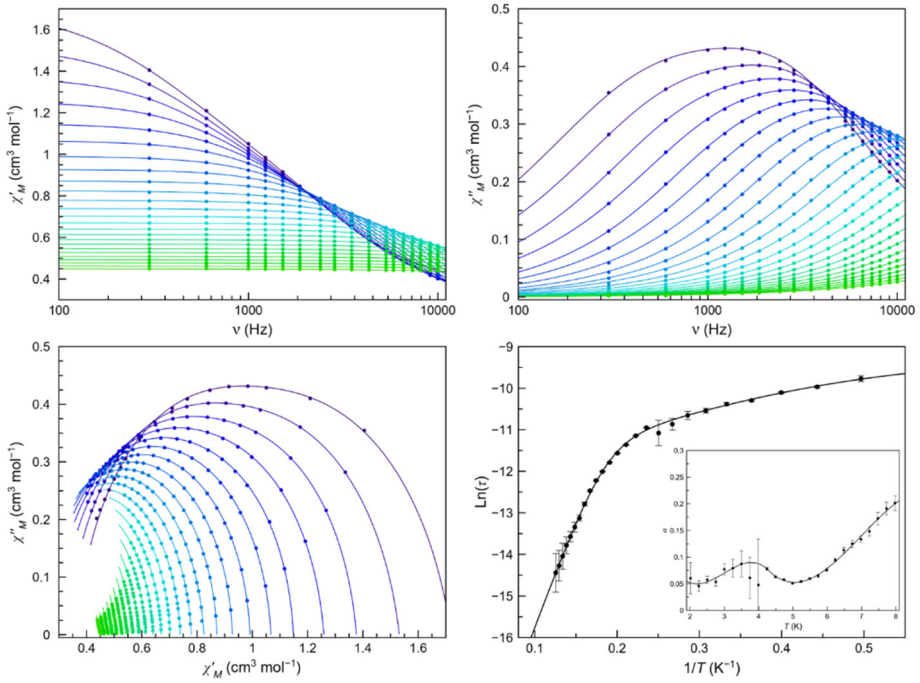

Figure A.59. Frequency dependence of χ_M' (top left) and χ_M'' (top right), Cole-Cole plots (bottom left) and Arrhenius plots of **5** (bottom right) in a dc-applied static field of 0.5 kOe with ± 0.005 kOe oscillating field in the temperature range of 2.0–8.0 K (purple to red gradient). Thermal dependence of α is included on the bottom right figure as an inset, where the black line are eye-guides. Standard deviation appears as vertical error bars.

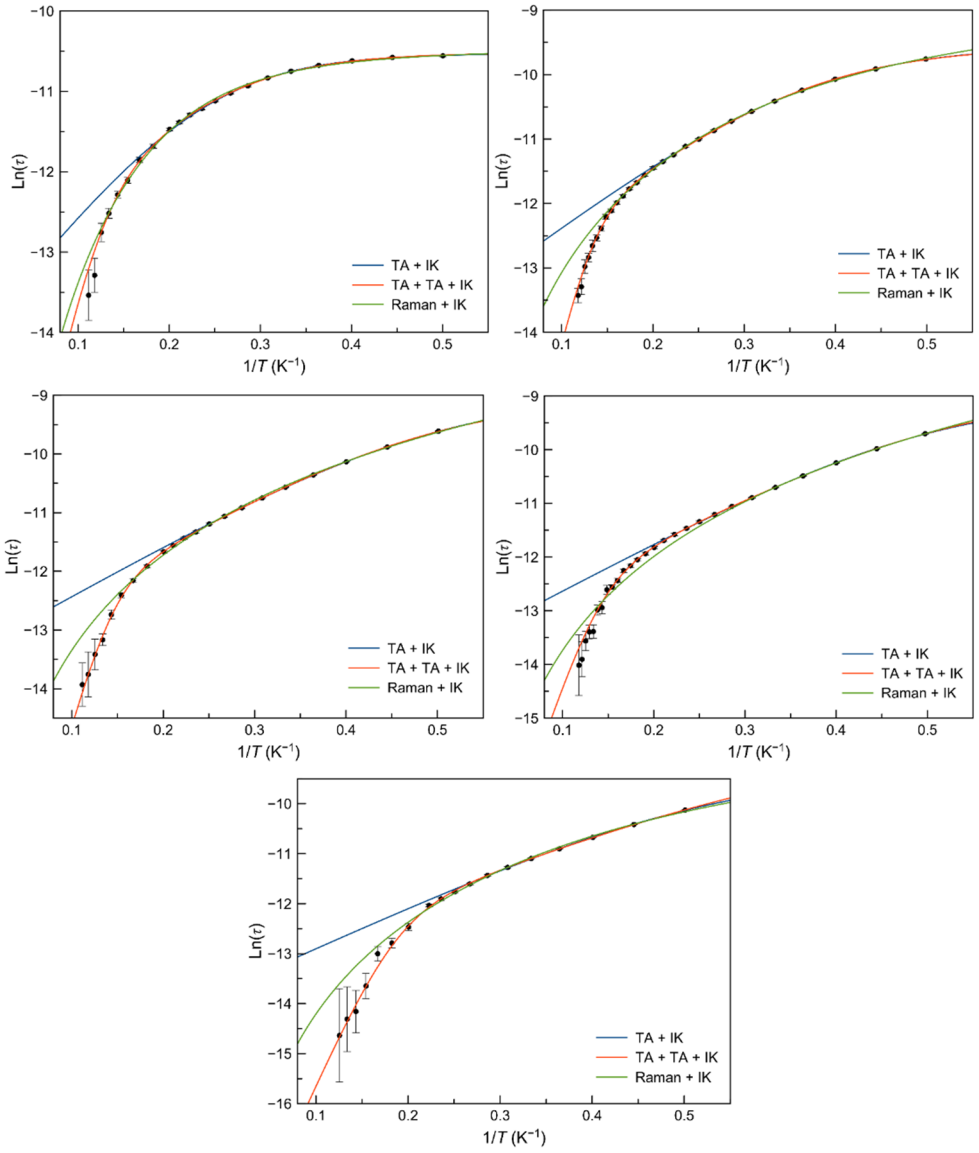

Figure A.60. Arrhenius plots for the main process of **2** under 5.0 (top left), 2.5 (top right), 1.5 (middle left), 1.0 (middle right) and 0.5 kOe (bottom) applied static fields. The solid lines are the best fit-curves using the three applied relaxation mechanisms. Standard deviations appear as vertical error bars.

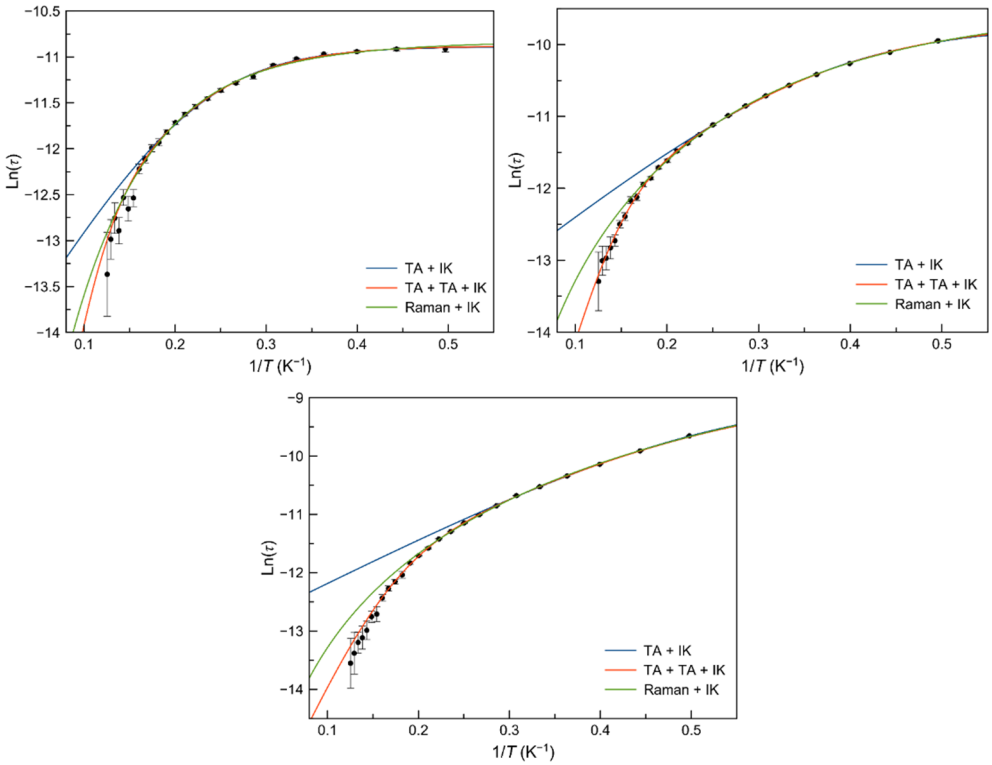

Figure A.61. Arrhenius plots for the main process of **2'** under 5.0 (top left), 2.5 (top right), 1.0 kOe (bottom) applied static fields. The solid lines are the best fit-curves using the three applied relaxation mechanisms. Standard deviations appear as vertical error bars.

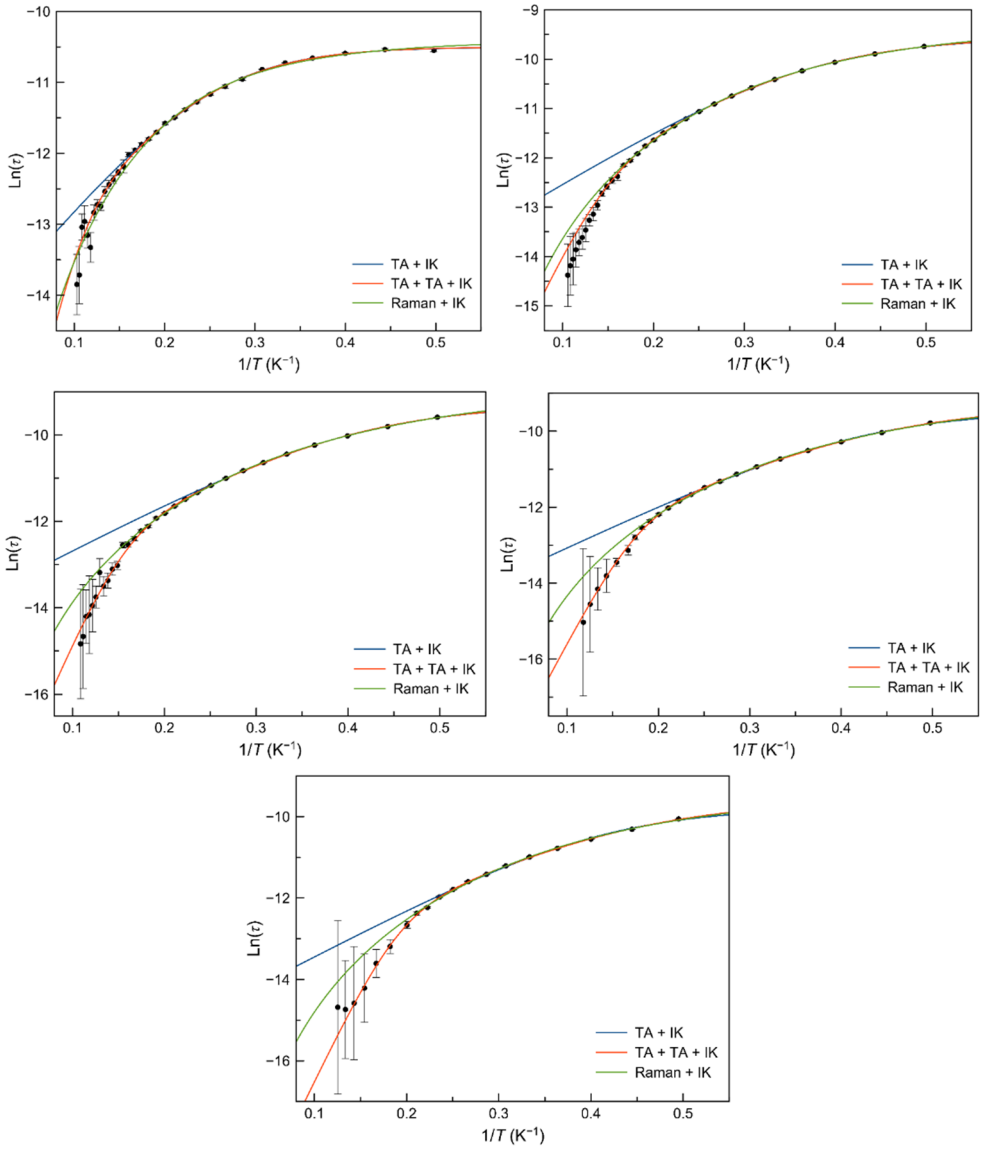

Figure A.62. Arrhenius plots for the main process of **3** under 5.0 (top left), 2.5 (top right), 1.5 (middle left), 1.0 (middle right) and 0.5 kOe (bottom) applied static fields. The solid lines are the best fit-curves using the three applied relaxation mechanisms. Standard deviations appear as vertical error bars.

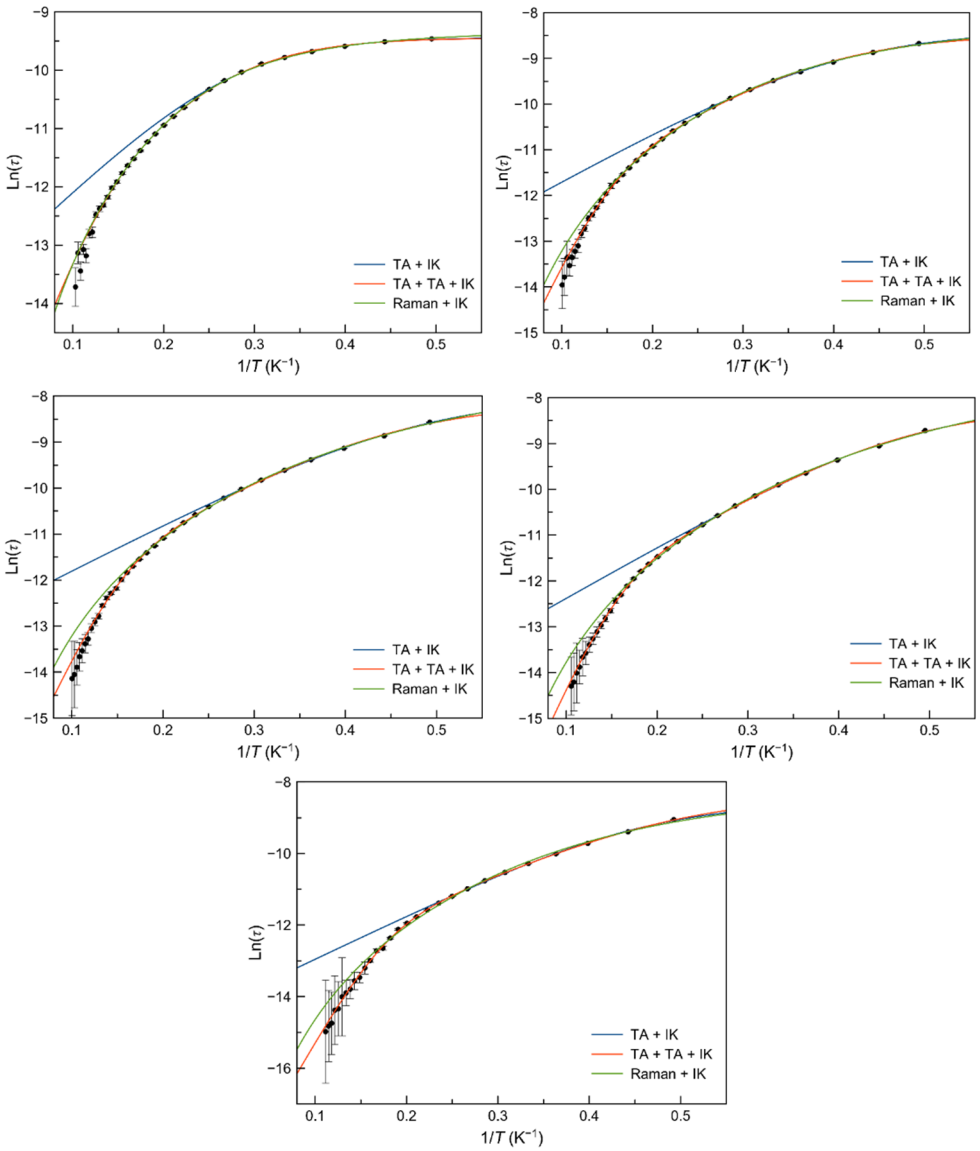

Figure A.63. Arrhenius plots for the main process of **3'** under 5.0 (top left), 2.5 (top right), 1.75 (middle left), 1.0 (middle right) and 0.5 kOe (bottom) applied static fields. The solid lines are the best fit-curves using the three applied relaxation mechanisms. Standard deviations appear as vertical error bars.

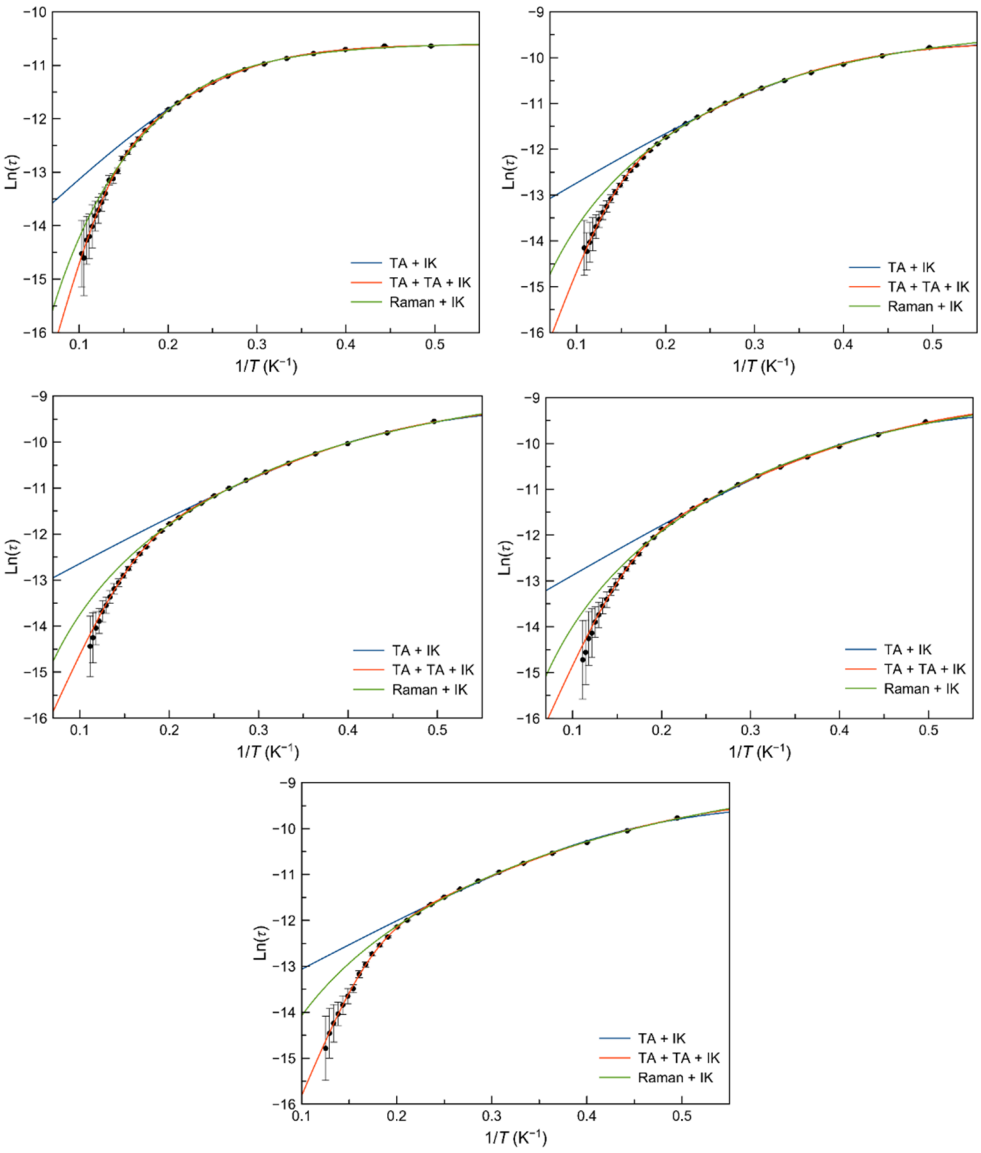

Figure A.64. Arrhenius plots for the main process of **4** under 5.0 (top left), 2.5 (top right), 1.5 (middle left), 1.0 (middle right) and 0.5 kOe (bottom) applied static fields. The solid lines are the best fit-curves using the three applied relaxation mechanisms. Standard deviations appear as vertical error bars.

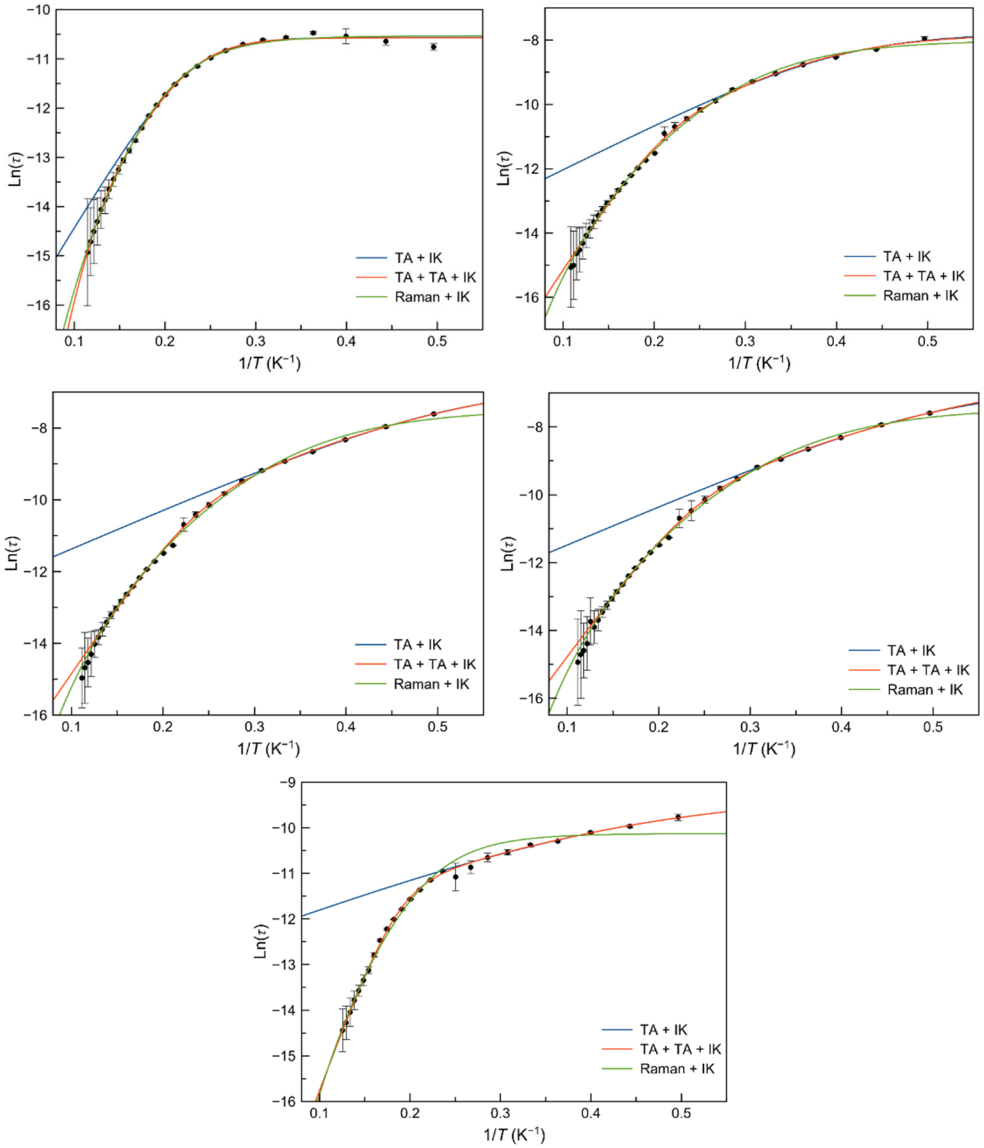

Figure A.65. Arrhenius plots for the main process of **5** under 5.0 (top left), 2.5 (top right), 1.5 (middle left), 1.0 (middle right) and 0.5 kOe (bottom) applied static fields. The solid lines are the best fit-curves using the three applied relaxation mechanisms. Standard deviations appear as vertical error bars.

Table A.8. Crystal data of compounds **2**, **2′**, **3** and **5**.

Compound	**2**	**2′**	**3**	**5**
Formula	$C_{64}H_{52}Cl_2Co_2N_8O_{12}$	$C_{112}H_{94}B_2Co_2N_8O_4$	$C_{70}H_{56}Cl_2Co_2N_8O_{12}$	$C_{70}H_{56}Cl_2Co_2N_8O_{12}$
Formula weight [g mol^{-1}]	1313.90	1753.41	1412.69	1389.98
Crystal system	Monoclinic	Monoclinic	Monoclinic	Monoclinic
Space group	$P2_1/c$	$P2_1/n$	$P2_1/c$	Cc
a [Å]	17.080(3)	17.168(2)	18.36250(8)	15.4464(14)
b [Å]	12.515(3)	28.579(3)	26.0919(1)	26.3668(10)
c [Å]	17.080(3)	19.690(2)	17.39470(2)	17.0683(13)
α [°]	90	90	90	90
β [°]	101.67(3)	112.990(9)	116.5922(2)	102.935(7)
γ [°]	90	90	90	90
V [Å^3]	3575.5(13)	8893.5(18)	7452.41(5)	6775.1(9)
Z	2	4	4	4
D_{calc} [g cm^{-3}]	1.220	1.310	1.259	1.363
Temperature [K]	100	100	100	100
μ [mm^{-1}]	0.598	0.435	0.572	0.635
R (int)	0.077	0.063	–	0.055
Reflections collected	21457	44015	–	52327
Independent reflections	3850	17205	–	18824
Number of observed reflections ($I_o > 2\sigma(I_o)$)	–	–	–	–
Number of parameters	431	1248	–	856
Goodness-of-fit *S* on F^2	1.54	1.12	–	1.05
R_1[a] [$I > 2.0\sigma(I)$]	0.1186	0.0853	–	0.0494
wR_2[b] [$I > 2.0\sigma(I)$]	0.3457	0.2114	–	0.1114

[a] $R_1 = \sum||F_o| - |F_c|| / \sum|F_o|$. [b] $wR_2 = \{\sum[w(F_o^2 - F_c^2)^2]/\sum w(F_o^2)^2\}^{1/2}$.

Table A.9. π–π interactions in **2**, **2′**, **3** and **5**.

Compound	Cg···Cg[a]	Cg···Cg [Å]	α[b][°]
2			
	Cg1···Cg6	3.975(5)	10.8(4)
2′			
	None	None	None
3			
	Cg6···Cg19	3.9247(1)	25
	Cg12···Cg15	3.7245(1)	5
	Cg16···Cg16	3.8039(1)	0
5			
	Cg5···Cg13	3.589(2)	5.46(19)
	Cg9···Cg12	3.870(3)	20.2(2)
	Cg11···Cg13	3.855(3)	6.4(2)

[a] Cg are the six-membered rings: **2**: Cg1: N1, C2-C5, C14; Cg6: C25-C28, C33, C34; **3**: Cg6; N21, C22-C25, C34; Cg12: C5-C8, C13, C14; Cg15: C45-C48, C53, C54; Cg16: C65-C68, C73, C74; Cg19: C84-C89; **5**: Cg5: N41, C42-C45, C54; Cg9: C5-C8, C13, C14; Cg11: C45-C48, C53, C54; Cg12: C65-C68, C73, C74; Cg13: C84-C89.[b] α is the dihedral angle between each pair of mean ring planes.

Table A.10. Energy of the calculated quartet (D_Q) and doublet (D_D) excited states and their contributions to the *D* value for **2**, **2′**, **3** and **5** obtained from CASSCF/NEVPT2 calculations.

Compound	*D*	|*E*/*D*|	D_Q[a]	D_D[a]	D_{Q1}	D_{Q2}	D_{Q1} + D_{Q2}
2							
Co1 (carboxylate)	+46.871	0.162	+41.841	–1.080	+26.998	+19.940	+46.938
Co1 (salicylaldehyde)	+60.190	0.213	+51.383	+0.683	+33.566	+20.948	+54.514
2′							
Co1	–93.860	0.286	–91.265	–1.819	–110.702	+19.078	–91.624
Co2	+57.977	0.174	+48.748	–0.105	+32.860	+21.695	+54.555
3							
Co1	+65.030	0.200	+55.527	+3.072	+35.387	+21.050	+56.437
Co2	–86.620	0.252	–83.7801	–1.335	–100.760	+15.539	–85.221
5							
Co1	+53.214	0.123	+46.081	–1.557	+26.627	+23.946	+50.573
Co2	+52.959	0.198	+44.991	+4.522	+27.833	+15.854	+43.687

[a] D_Q and D_D are the sum of spin-orbit contributions that comes from quartet and doublet excited states.

Table A.11. Selected ac-magnetic data at different dc-applied field for **2** obtained from the ln(τ) *vs* 1/*T* plots.

H_{dc} (kOe)\Model[a]	$\tau_{0,IK} \times 10^3$ (s)	$\tau_{0,IK} \times 10^4$ (s)	$\tau_{0,LT} \times 10^6$ (s)	E_{aLT} (cm^{-1})	$\tau_{0,HT} \times 10^9$ (s)	E_{aMT} (cm^{-1})
500						
Global	–	1.4 ± 1.1	1.6 ± 0.4	5.0 ± 0.8	2.7 ± 0.8	28.7 ± 1.6
Process 1	–		–	–	–	–
Process 2	–	–	–	–	–	–
1000						
Global	–	1.31 ± 0.09	1.48 ± 0.07	6.07 ± 0.13	3.9 ± 1.0	35.3 ± 1.3
Process 1	–	–	–	–	–	–
Process 2	–	–	–	–	–	–
1500						
Global	–	1.22 ± 0.12	1.63 ± 0.11	6.24 ± 0.21	1.6 ± 0.4	39.7 ± 1.3
Process 1	–	–	–	–	–	–
Process 2	–	–	–	–	–	–
2500						
Global	–	–	–	–	–	–
Process 1	–	0.703 ± 0.014	1.51 ± 0.06	7.41 ± 0.12	1.6 ± 0.3	43.6 ± 1.2
Process 2	6.5 ± 1.4	–	–	–	–	–
5000						
Global	–	–	–	–	–	–
Process 1	–	0.270 ± 0.003	1.24 ± 0.14	9.2 ± 0.4	9 ± 4	37 ± 3
Process 2	8 ± 4	–	–	–	–	–

[a] Global is the analysis considering only one general Debye model, and Processes 1 + 2 are the analyses with the sum of two individual Debye models (equations 5 and 6). All data were analysed by a combination of several TA relaxations plus one IK mechanism.

Table A.12. Selected ac-magnetic data at different dc-applied field for **2'** obtained from the ln(τ) *vs* 1/T plots.

H_{dc} (kOe)\Model[a]	$\tau_{0,IK} \times 10^3$ (s)	$\tau_{0,IK} \times 10^5$ (s)	$\tau_{0,LT} \times 10^6$ (s)	E_{aLT} (cm^{-1})	$\tau_{0,MT} \times 10^9$ (s)	E_{aMT} (cm^{-1})
1000						
Global	–	13 ± 6	2.7 ± 0.8	5.3 ± 0.8	36 ± 20	23 ± 3
Process 1	–	–	–	–	–	–
Process 2	–	–	–	–	–	–
2500						
Global	–	–	–	–	–	–
Process 1	–	6.1 ± 0.5	1.8 ± 0.3	6.6 ± 0.5	9 ± 4	31.7 ± 2.4
Process 2	2.3 ± 0.6	–	–	–	–	–
5000						
Global	–	–	–	–	–	–
Process 1	–	1.882 ± 0.024	0.72 ± 0.13	10.4 ± 0.5	4.3 ± 4.9	40 ± 6
Process 2	2.8 ± 0.5	–	–	–	–	–

[a] Global is the analysis considering only one general Debye model, and Processes 1 + 2 are the analyses with the sum of two individual Debye models (equations 5 and 6). All data were analysed by a combination of several TA relaxations plus one IK mechanism.

Table A.13. Selected ac-magnetic data at different dc-applied field for **3** obtained from the ln(τ) *vs* 1/*T* plots.

H_{dc} (kOe)\Model[a]	$\tau_{0,IK} \times 10^3$ (s)	$\tau_{0,IK} \times 10^4$ (s)	$\tau_{0,LT} \times 10^6$ (s)	E_{aLT} (cm^{-1})	$\tau_{0,MT} \times 10^9$ (s)	E_{aMT} (cm^{-1})
500						
Global	–	6.8 ± 1.0	0.76 ± 0.16	5.0 ± 0.8	0.061 ± 0.018	32.9 ± 1.4
Process 1	–		–	–	–	–
Process 2	–	–	–	–	–	–
1000						
Global	–	9.0 ± 1.3	1.00 ± 0.20	7.0 ± 0.5	0.18 ± 0.04	32.1 ± 1.3
Process 1	–	–	–	–	–	–
Process 2	–	–	–	–	–	–
1500						
Global	–	–	–	–	–	–
Process 1	–	8.9 ± 0.6	0.99 ± 0.13	7.9 ± 0.4	0.20 ± 0.10	36 ± 3
Process 2	1.93 ± 0.18	–	–	–	–	–
2500						
Global	–	–	–	–	–	–
Process 1	–	6.8 ± 0.3	1.08 ± 0.13	8.2 ± 0.3	0.48 ± 0.25	35 ± 3
Process 2	2.4 ± 0.4	–	–	–	–	–
5000						
Global	–	–	–	–	–	–
Process 1	–	2.78 ± 0.06	0.88 ± 0.23	9.8 ± 0.7	6 ± 4	28 ± 5
Process 2	1.81 ± 0.21	–	–	–	–	–

[a] Global is the analysis considering only one general Debye model, and Processes 1 + 2 are the analyses with the sum of two individual Debye models (equations 5 and 6). All data were analysed by a combination of several TA relaxations plus one IK mechanism.

Table A.14. Selected ac-magnetic data at different dc-applied field for **3′** obtained from the ln(τ) *vs* 1/T plots.

H_{dc} (kOe)\Model[a]	$\tau_{0,IK} \times 10^3$ (s)	$\tau_{0,IK} \times 10^4$ (s)	$\tau_{0,LT} \times 10^6$ (s)	E_{aLT} (cm^{-1})	$\tau_{0,MT} \times 10^9$ (s)	E_{aMT} (cm^{-1})
500						
Global	–	2.3 ± 0.5	1.00 ± 0.18	7.7 ± 0.5	0.27 ± 0.06	31.3 ± 1.2
Process 1	–		–	–	–	–
Process 2	–	–	–	–	–	–
1000						
Global	–	2.79 ± 0.20	1.40 ± 0.11	7.84 ± 0.20	0.72 ± 0.11	31.4 ± 0.8
Process 1	–	–	–	–	–	–
Process 2	–	–	–	–	–	–
1750						
Global	–	2.9 ± 0.3	2.2 ± 0.3	7.7 ± 0.4	1.7 ± 0.5	29.8 ± 1.6
Process 1	–	–	–	–	–	–
Process 2	–	–	–	–	–	–
2500						
Global	–	–	–	–	–	–
Process 1	–	2.09 ± 0.10	2.2 ± 0.3	8.3 ± 0.3	2.1 ± 0.5	30.0 ± 1.4
Process 2	3.3 ± 1.6	–	–	–	–	–
5000						
Global	–	–	–	–	–	–
Process 1	–	0.790 ± 0.010	1.23 ± 0.20	10.7 ± 0.4	3.4 ± 1.2	29.6 ± 2.2
Process 2	6.5 ± 0.6	–	–	–	–	–

[a] Global is the analysis considering only one general Debye model, and Processes 1 + 2 are the analyses with the sum of two individual Debye models (equations 5 and 6). All data were analysed by a combination of several TA relaxations plus one IK mechanism.

Table A.15. Selected ac-magnetic data at different dc-applied field for **4** obtained from the ln(τ) *vs* 1/*T* plots.

H_{dc} (kOe)\Model[a]	$\tau_{0,IK} \times 10^3$ (s)	$\tau_{0,IK} \times 10^4$ (s)	$\tau_{0,LT} \times 10^6$ (s)	E_{aLT} (cm^{-1})	$\tau_{0,MT} \times 10^9$ (s)	E_{aMT} (cm^{-1})	$\tau_{0,HT} \times 10^{10}$ (s)	E_{aHT} (cm^{-1})
500								
Global	–	0.97 ± 0.10	0.99 ± 0.11	6.9 ± 0.3	0.83 ± 0.18	35.6 ± 1.1	–	–
Process 1	–		–	–	–	–	–	–
Process 2	–	–	–	–	–	–	–	–
1000								
Global	–	1.22 ± 0.09	1.30 ± 0.10	6.86 ± 0.21	4.8 ± 0.6	30.7 ± 0.7	–	–
Process 1	–	–	–	–	–	–	–	–
Process 2	–	–	–	–	–	–	–	–
1500								
Global	–	–	–	–	–	–	–	–
Process 1	–	1.09 ± 0.06	1.38 ± 0.10	6.96 ± 0.20	6.2 ± 0.7	30.6 ± 0.7	–	–
Process 2	2.5 ± 1.7	–	–	–	–	–	–	–
2500								
Global	–	–	–	–	–	–	–	–
Process 1	–	0.730 ± 0.021	1.40 ± 0.09	7.19 ± 0.18	8.2 ± 1.0	30.2 ± 0.7	–	–
Process 2	3.9 ± 1.5	–	–	–	–	–	–	–
5000								
Global	–	–	–	–	–	–	–	–
Process 1	–	0.247 ± 0.005	0.47 ± 0.07	10.8 ± 0.5	–	–	12 ± 3	42.0 ± 1.8
Process 2	4.1 ± 2.0	–	–	–	–	–	–	–

[a] Global is the analysis considering only one general Debye model, and Processes 1 + 2 are the analyses with the sum of two individual Debye models (equations 5 and 6). All data were analysed by a combination of several TA relaxations plus one IK mechanism.

Table A.16. Selected ac-magnetic data at different dc-applied field for **5** obtained from the ln(τ) *vs* 1/T plots.

H_{dc} (kOe)\Model[a]	$\tau_{0,IK} \times 10^4$ (s)	$\tau_{0,LT} \times 10^6$ (s)	E_{aLT} (cm^{-1})	$\tau_{0,MT} \times 10^9$ (s)	E_{aMT} (cm^{-1})	$\tau_{0,HT} \times 10^{12}$ (s)	E_{aHT} (cm^{-1})
500							
Global	–	–	–	–	–	–	–
Process 1	0.94 ± 0.19	4.3 ± 0.8	4.9 ± 0.6	0.73 ± 0.11	36.9 ± 0.8	–	–
Process 2	–	9.5 ± 1.8	5.2 ± 0.3	–	–	–	–
1000							
Global	–	–	–	–	–	–	–
Process 1	15.1 ± 7.3	6.0 ± 2.0	6.8 ± 0.8	10.2 ± 1.4	25.4 ± 0.7	–	–
Process 2	–	3.7 ± 0.3	4.4 ± 0.15	–	–	–	–
1500							
Global	–	–	–	–	–	–	–
Process 1	13 ± 7	5.4 ± 2.3	7.0 ± 1.0	8.5 ± 1.3	26.2 ± 0.8	–	–
Process 2		3.5 ± 0.3	4.31 ± 0.17	–	–	–	–
2500							
Global	–	–	–	–	–	–	–
Process 1	4.1 ± 0.7	1.6 ± 0.9	9.7 ± 1.3	3.4 ± 0.8	30.4 ± 1.3	–	–
Process 2		4.2 ± 0.3	3.38 ± 0.12	–	–	–	–
5000							
Global	–	–	–	–	–	–	–
Process 1	0.256 ± 0.004	0.021 ± 0.004	21.88 ± 0.7	–	–	23 ± 17	61.6 ± 4.7
	0.281 ± 0.008	0.17 ± 0.23	16 ± 4	3 ± 4	33 ± 8	0.4 ± 1.5	90 ± 26
Process 2	–	114 ± 3	1.39 ± 0.04	–	–	–	–

[a] Global is the analysis considering only one general Debye model, and Processes 1 + 2 are the analyses with the sum of two individual Debye models (equations 5 and 6). All data were analysed by a combination of several TA relaxations plus one IK mechanism.

SI Chapter IV

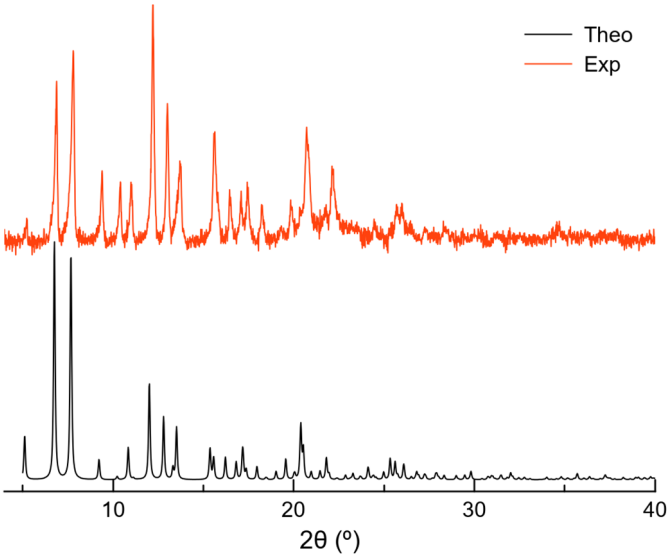

Figure A.66. Experimental and simulated powder X-ray diffraction patterns of **6**.

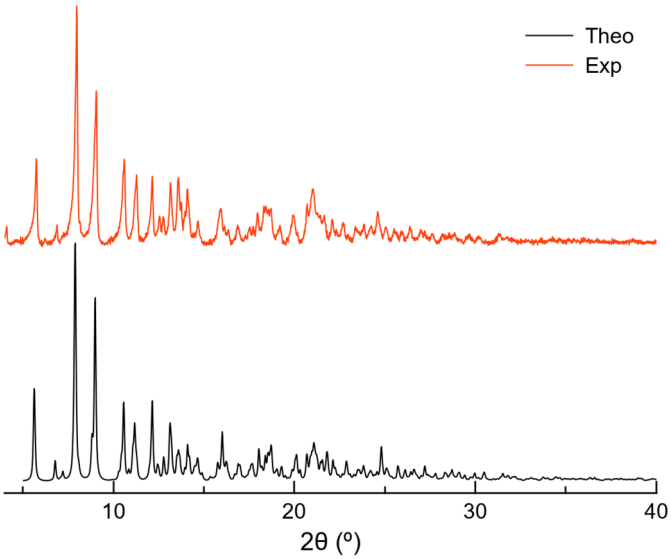

Figure A.67. Experimental and simulated powder X-ray diffraction patterns of **7**.

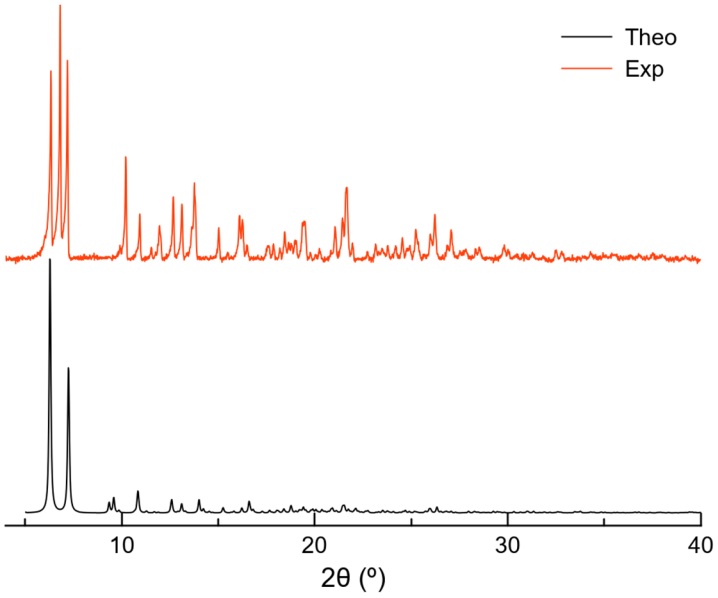

Figure A.68. XRPD patterns of **8** in different states: from single-crystal X-ray diffraction data (black) and fresh sample in mother liquor (red).

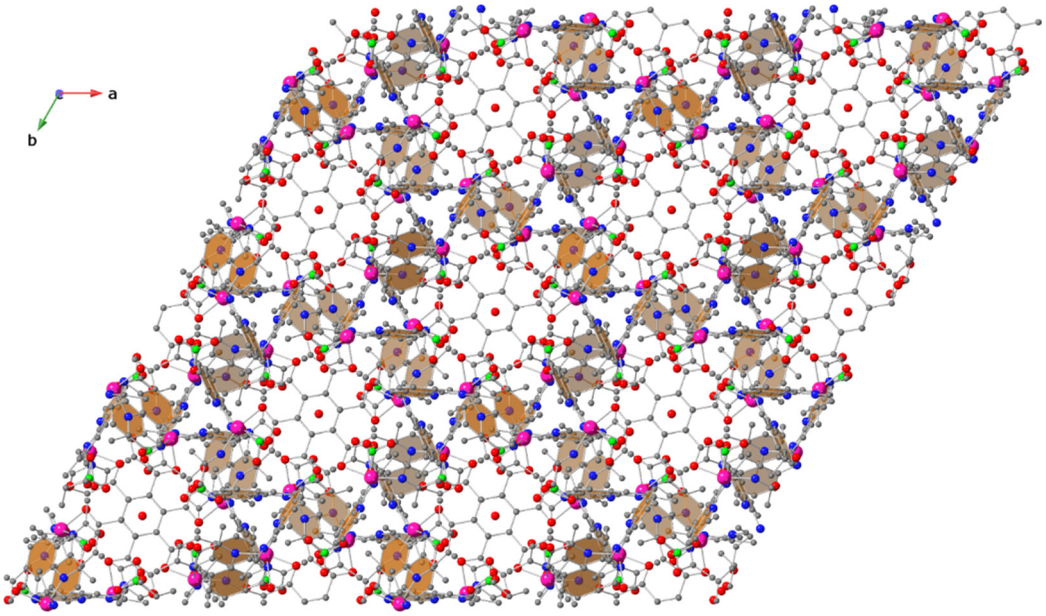

Figure A.69. Perspective view of the crystal along the *c*-axis of **6** with π−π interactions involving phenanthroline coloured in orange. Hydrogen atoms are omitted for clarity. Colour code: magenta, cobalt; blue, nitrogen; red, oxygen; grey, carbon; green, chlorine.

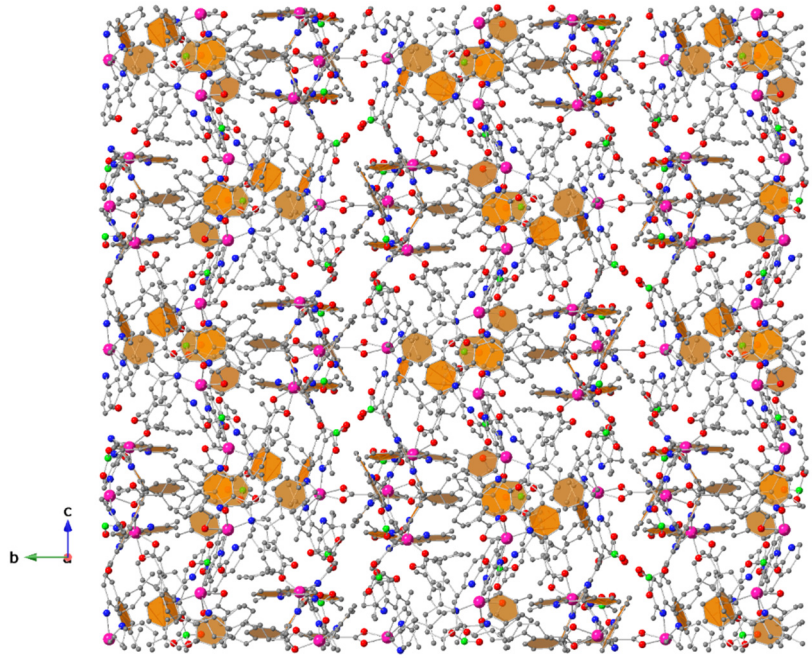

Figure A.70. Perspective view of the crystal along the *a*-axis of **7** with π–π interactions involving phenanthroline coloured in orange. Hydrogen atoms are omitted for clarity. Colour code: magenta, cobalt; blue, nitrogen; red, oxygen; grey, carbon; green, chlorine.

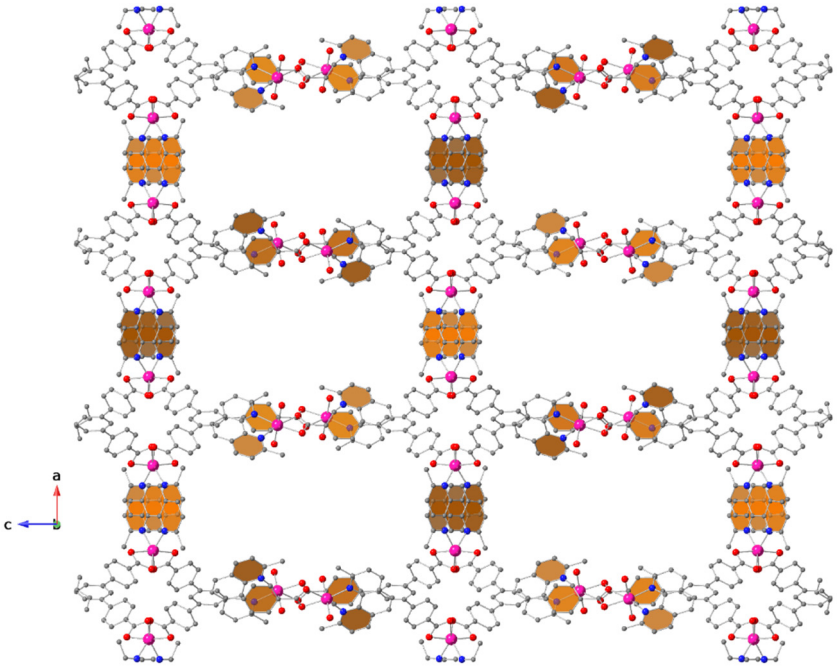

Figure A.71. Perspective view of the crystal along the *b*-axis of **8** with π–π interactions involving phenanthroline coloured in orange. Hydrogen atoms are omitted for clarity. Colour code: magenta, cobalt; blue, nitrogen; red, oxygen; grey, carbon; green, chlorine.

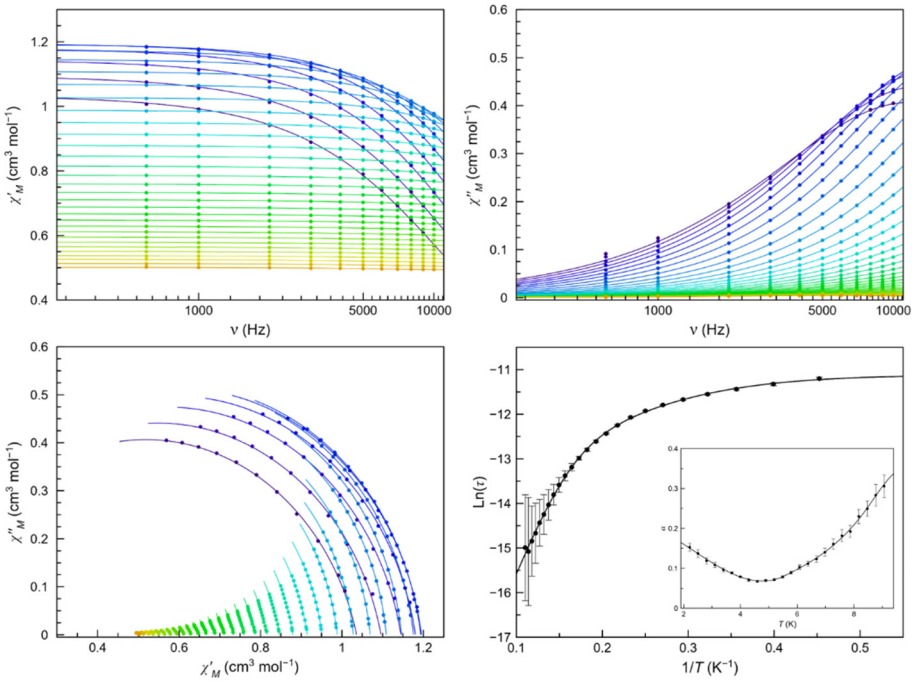

Figure A.72. Frequency dependence of χ_M' (top left) and χ_M'' (top right), Cole-Cole plots (bottom left) and Arrhenius plots of **6** (bottom right) in a dc-applied static field of 2.5 kOe with ± 0.005 kOe oscillating field in the temperature range of 2.0–12.0 K (purple to green gradient). Thermal dependence of α is included on the bottom right figure as an inset, where the black line are eye-guides. Standard deviation appears as vertical error bars.

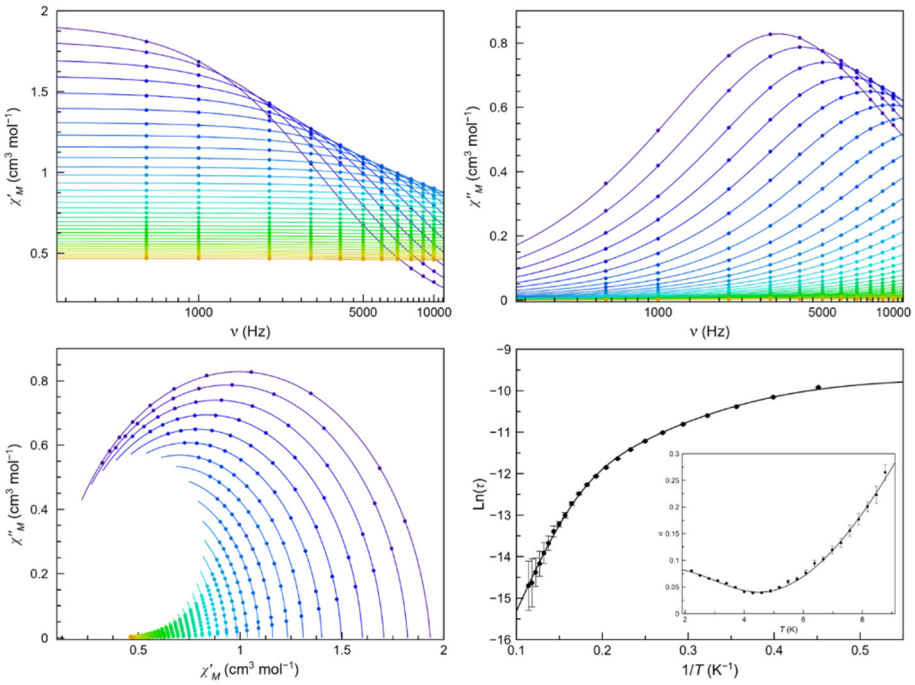

Figure A.73. Frequency dependence of χ_M' (top left) and χ_M'' (top right), Cole-Cole plots (bottom left) and Arrhenius plots of **6** (bottom right) in a dc-applied static field of 2.5 kOe with ± 0.005 kOe oscillating field in the temperature range of 2.0–12.0 K (purple to green gradient). Thermal dependence of α is included on the bottom right figure as an inset, where the black line are eye-guides. Standard deviation appears as vertical error bars.

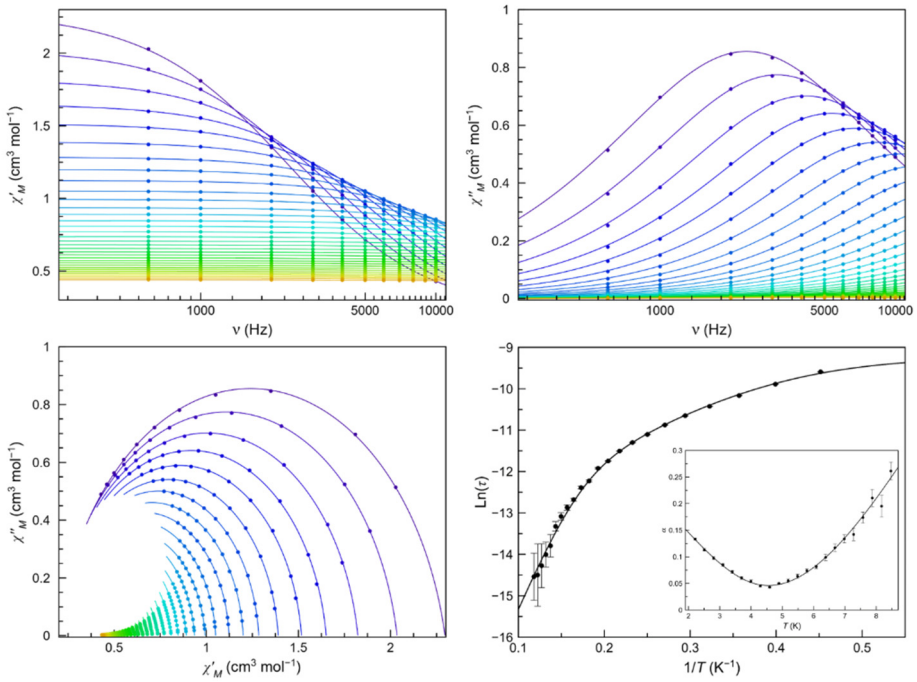

Figure A.74. Frequency dependence of χ_M' (top left) and χ_M'' (top right), Cole-Cole plots (bottom left) and Arrhenius plots of **6** (bottom right) in a dc-applied static field of 1.0 kOe with ± 0.005 kOe oscillating field in the temperature range of 2.0–12.0 K (purple to green gradient). Thermal dependence of α is included on the bottom right figure as an inset, where the black line are eye-guides. Standard deviation appears as vertical error bars.

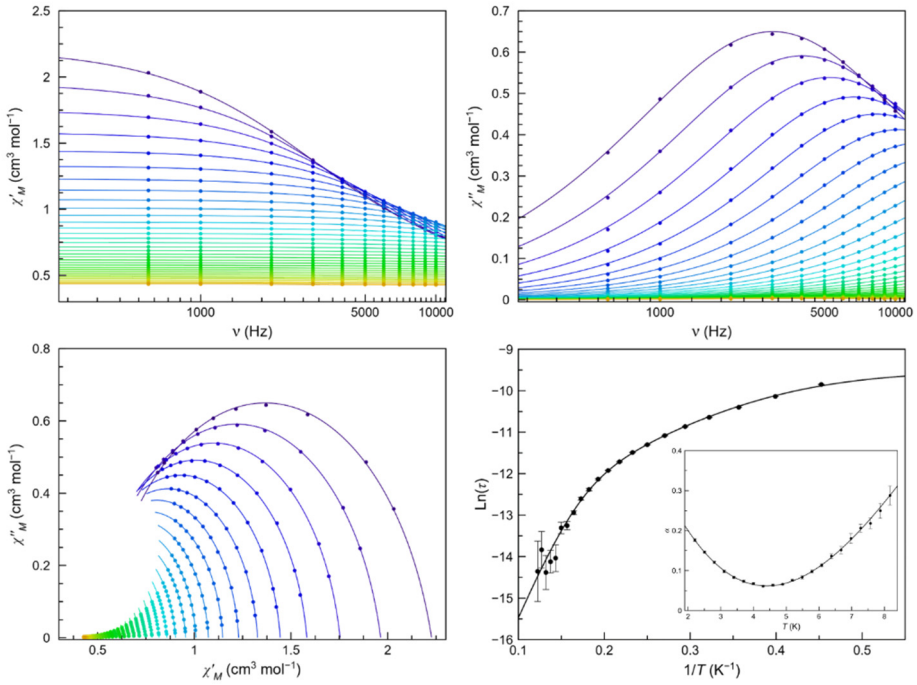

Figure A.75. Frequency dependence of χ_M' (top left) and χ_M'' (top right), Cole-Cole plots (bottom left) and Arrhenius plots of **6** (bottom right) in a dc-applied static field of 0.5 kOe with ± 0.005 kOe oscillating field in the temperature range of 2.0–12.0 K (purple to green gradient). Thermal dependence of α is included on the bottom right figure as an inset, where the black line are eye-guides. Standard deviation appears as vertical error bars.

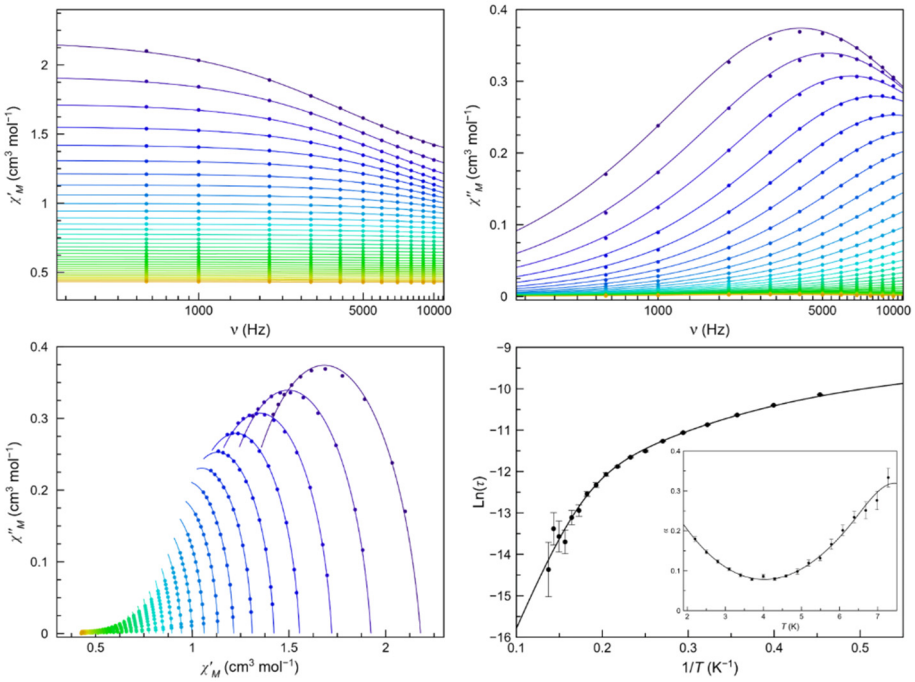

Figure A.76. Frequency dependence of χ_M' (top left) and χ_M'' (top right), Cole-Cole plots (bottom left) and Arrhenius plots of **6** (bottom right) in a dc-applied static field of 0.25 kOe with ± 0.005 kOe oscillating field in the temperature range of 2.0–12.0 K (purple to green gradient). Thermal dependence of α is included on the bottom right figure as an inset, where the black line are eye-guides. Standard deviation appears as vertical error bars.

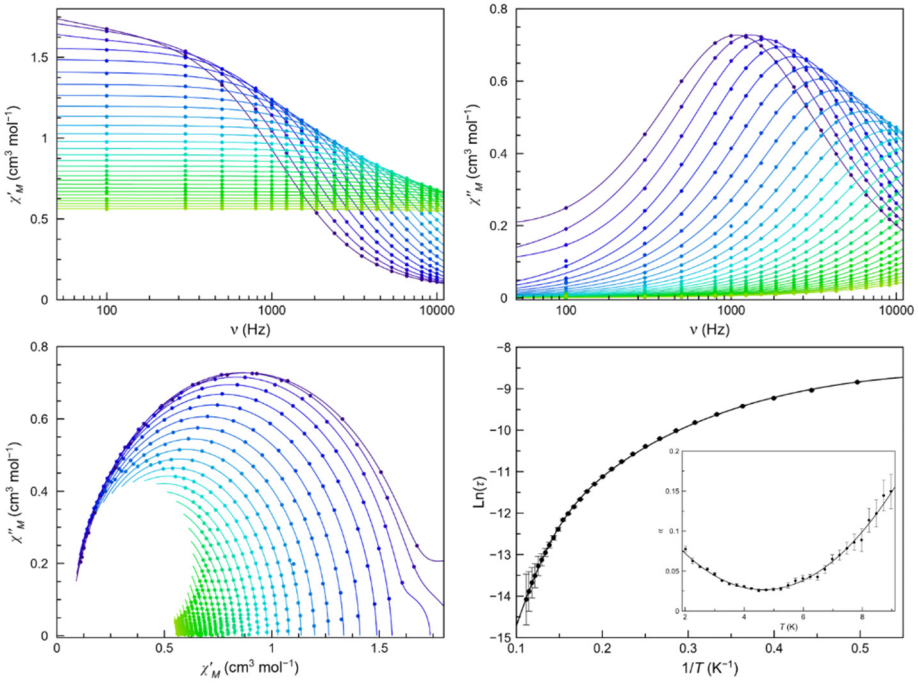

Figure A.77. Frequency dependence of χ_M' (top left) and χ_M'' (top right), Cole-Cole plots (bottom left) and Arrhenius plots of **7** (bottom right) in a dc-applied static field of 2.5 kOe with ± 0.005 kOe oscillating field in the temperature range of 2.0–9.0 K (purple to red gradient). Thermal dependence of α is included on the bottom right figure as an inset, where the black line are eye-guides. Standard deviation appears as vertical error bars.

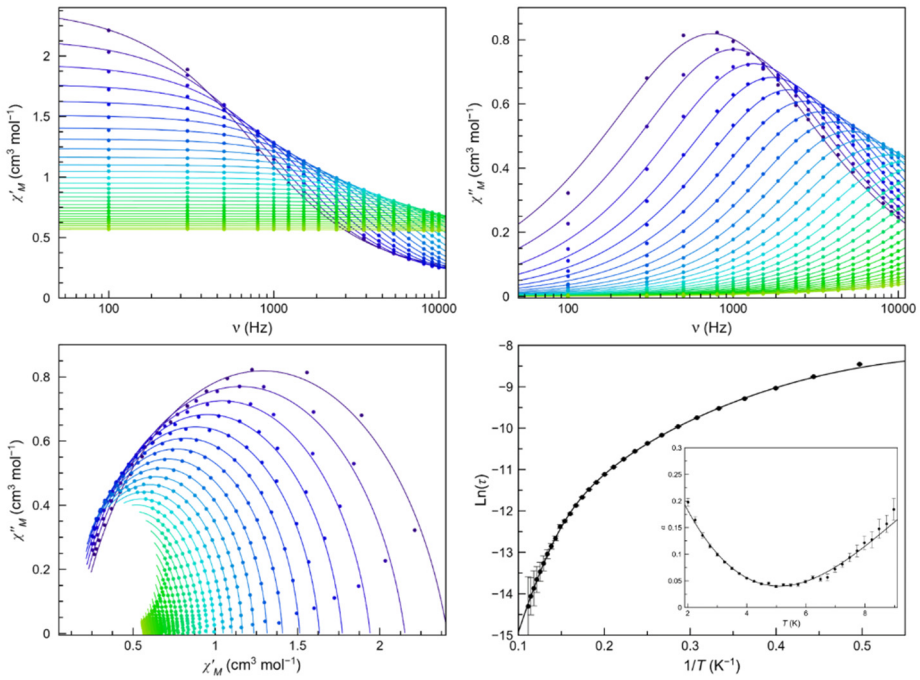

Figure A.78. Frequency dependence of χ_M' (top left) and χ_M'' (top right), Cole-Cole plots (bottom left) and Arrhenius plots of **7** (bottom right) in a dc-applied static field of 1.0 kOe with ± 0.005 kOe oscillating field in the temperature range of 2.0–9.0 K (purple to red gradient). Thermal dependence of α is included on the bottom right figure as an inset, where the black line are eye-guides. Standard deviation appears as vertical error bars.

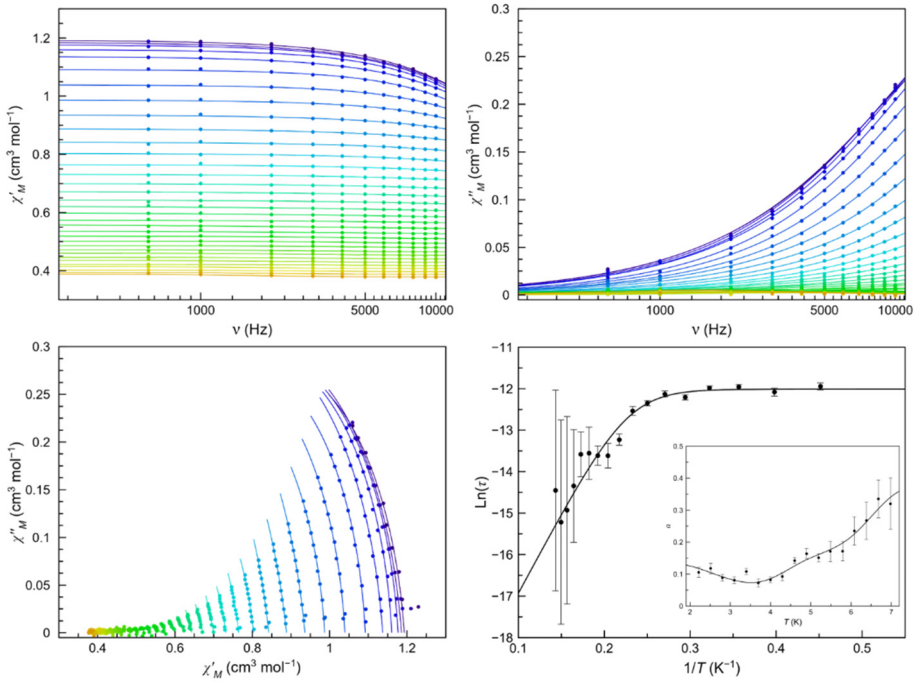

Figure A.79. Frequency dependence of χ_M' (top left) and χ_M'' (top right), Cole-Cole plots (bottom left) and Arrhenius plots of **8** (bottom right) in a dc-applied static field of 2.5 kOe with ± 0.005 kOe oscillating field in the temperature range of 2.0–9.0 K (purple to red gradient). Thermal dependence of α is included on the bottom right figure as an inset, where the black line are eye-guides. Standard deviation appears as vertical error bars.

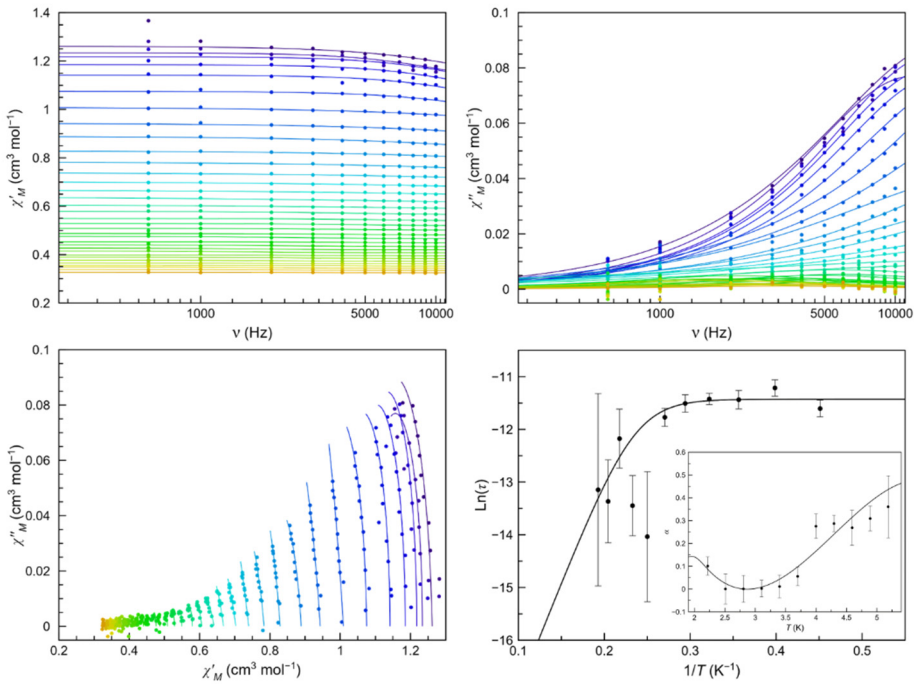

Figure A.80. Frequency dependence of χ_M' (top left) and χ_M'' (top right), Cole-Cole plots (bottom left) and Arrhenius plots of **8** (bottom right) in a dc-applied static field of 1.0 kOe with ± 0.005 kOe oscillating field in the temperature range of 2.0–9.0 K (purple to red gradient). Thermal dependence of α is included on the bottom right figure as an inset, where the black line are eye-guides. Standard deviation appears as vertical error bars.

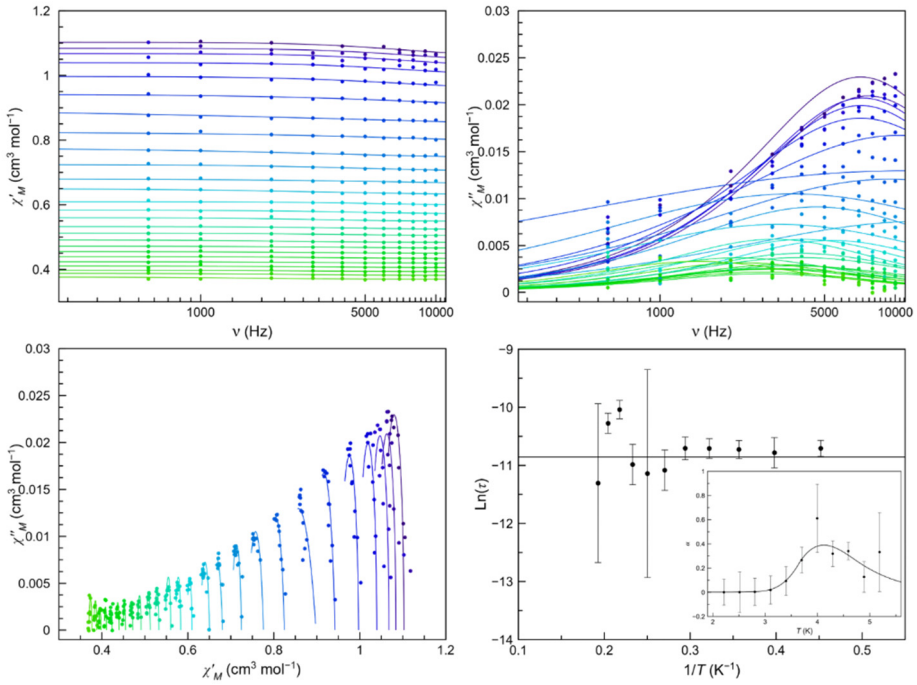

Figure A.81. Frequency dependence of χ_M' (top left) and χ_M'' (top right), Cole-Cole plots (bottom left) and Arrhenius plots of **8** (bottom right) in a dc-applied static field of 0.5 kOe with ± 0.005 kOe oscillating field in the temperature range of 2.0–9.0 K (purple to red gradient). Thermal dependence of α is included on the bottom right figure as an inset, where the black line are eye-guides. Standard deviation appears as vertical error bars.

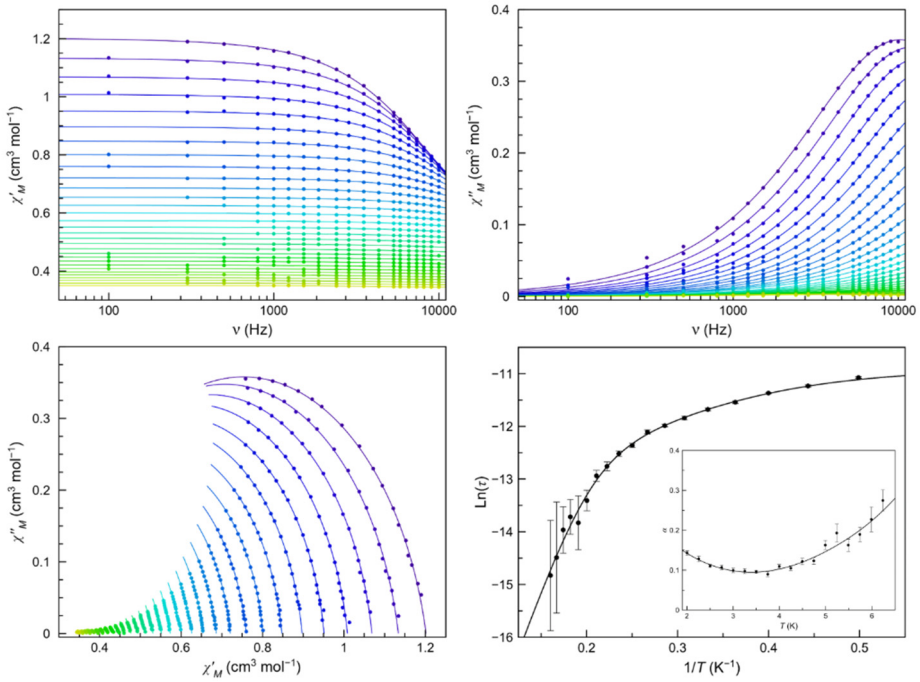

Figure A.82. Frequency dependence of χ_M' (top left) and χ_M'' (top right), Cole-Cole plots (bottom left) and Arrhenius plots of **8-dh** (bottom right) in a dc-applied static field of 2.5 kOe with ± 0.005 kOe oscillating field in the temperature range of 2.0–9.5 K (purple to red gradient). Thermal dependence of α is included on the bottom right figure as an inset, where the black line are eye-guides. Standard deviation appears as vertical error bars.

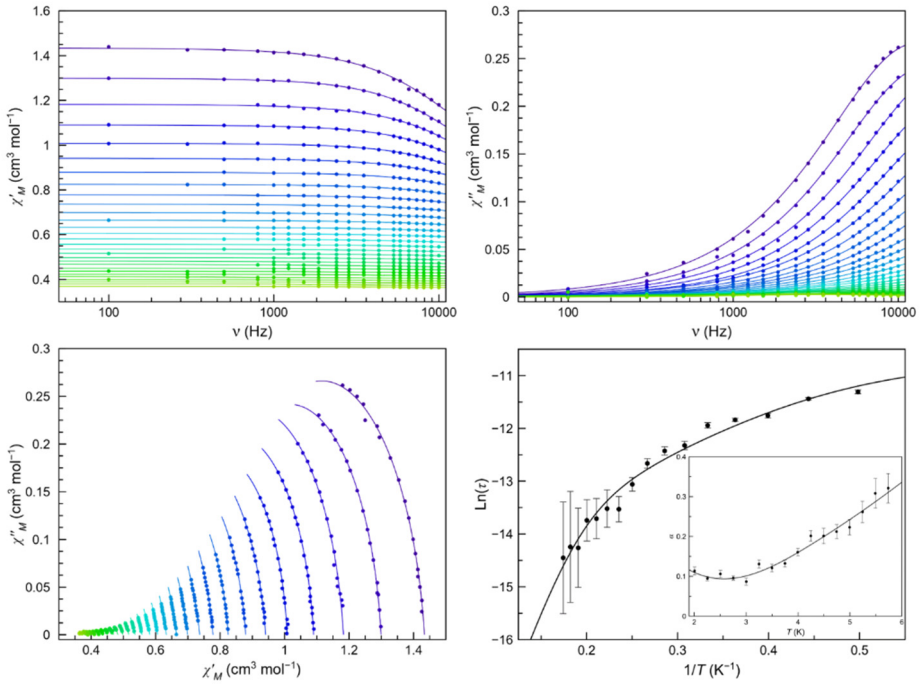

Figure A.83. Frequency dependence of χ_M' (top left) and χ_M'' (top right), Cole-Cole plots (bottom left) and Arrhenius plots of **8-dh** (bottom right) in a dc-applied static field of 1.0 kOe with ± 0.005 kOe oscillating field in the temperature range of 2.0–9.5 K (purple to red gradient). Thermal dependence of α is included on the bottom right figure as an inset, where the black line are eye-guides. Standard deviation appears as vertical error bars.

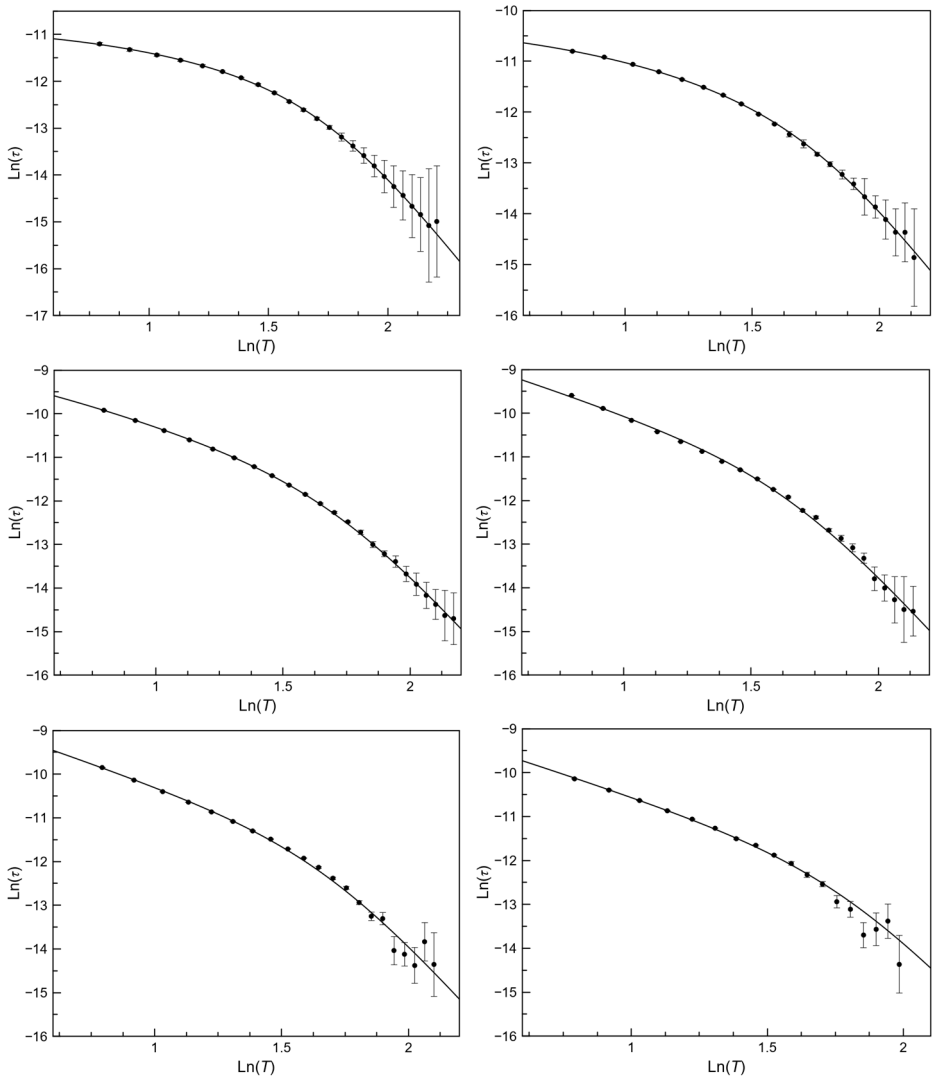

Figure A.84. Ln(τ) *vs* ln(T) plots for the main process of **6** under 6.0 (top left), 5.0 (top right), 2.5 (middle left), 1.0 (middle right), 0.5 (bottom left) and 0.25 kOe (bottom right) applied static fields. The solid lines are the best fit-curves using a combination of Raman plus intra-Kramers mechanisms. Standard deviations appear as vertical error bars.

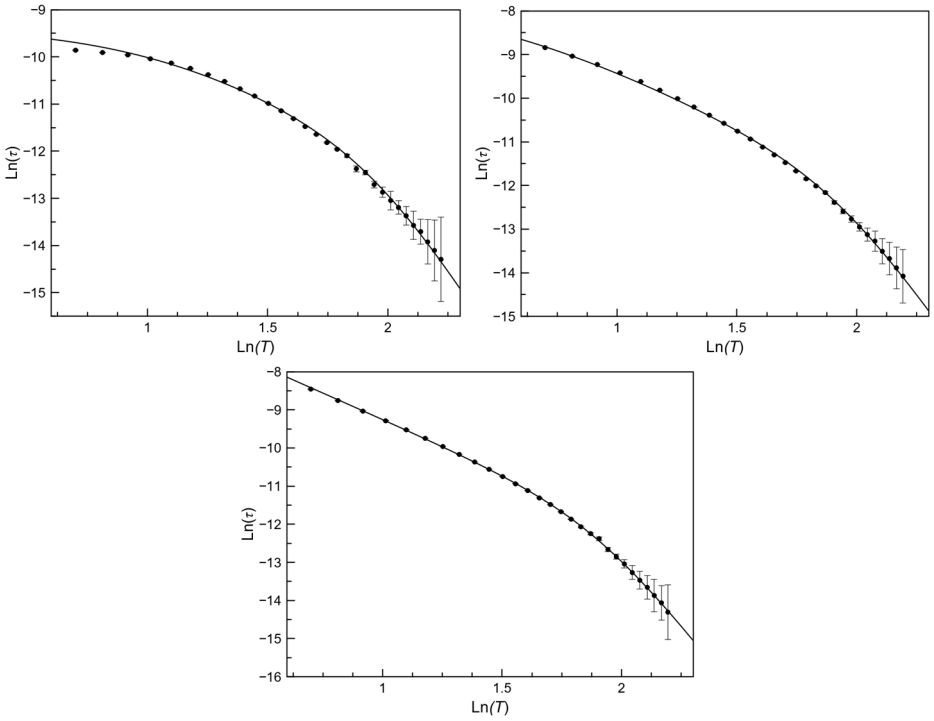

Figure A.85. Ln(τ) *vs* ln(T) plots for the main process of **7** under 5.0 (top left), 2.5 (top right) and 1.0 kOe (bottom) applied static fields. The solid lines are the best fit-curves using a combination of Raman plus intra-Kramers mechanisms. Standard deviations appear as vertical error bars.

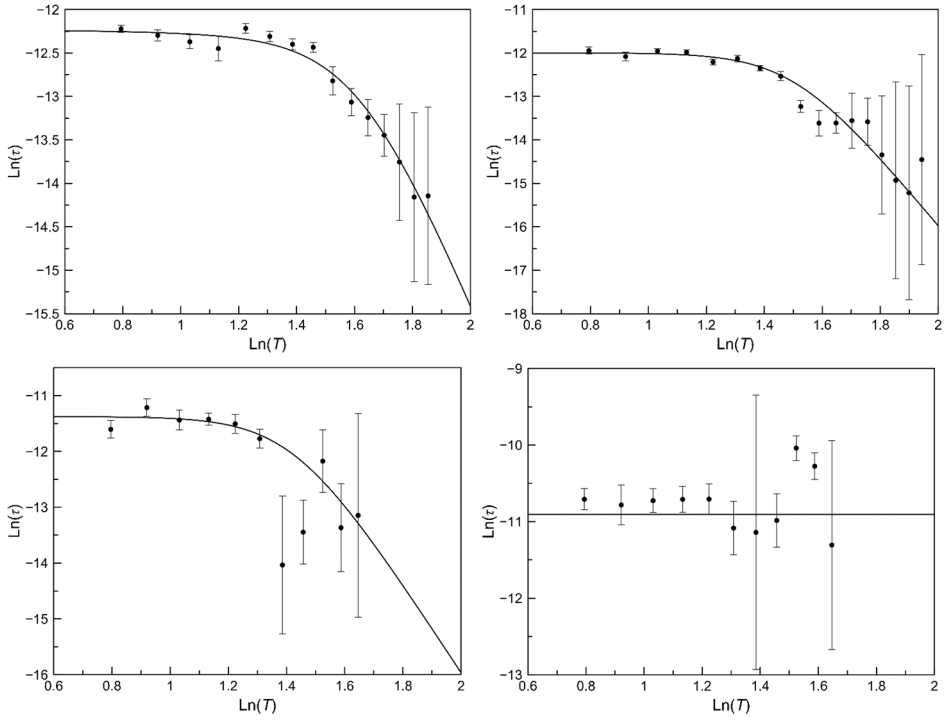

Figure A.86. Ln(τ) *vs* ln(T) plots for the main process of **8** under 5.0 (top left), 2.5 (top right), 1.0 (bottom left) and 0.5 kOe (bottom right) applied static fields. The solid lines are the best fit-curves using a combination of Raman plus intra-Kramers mechanisms. Standard deviations appear as vertical error bars.

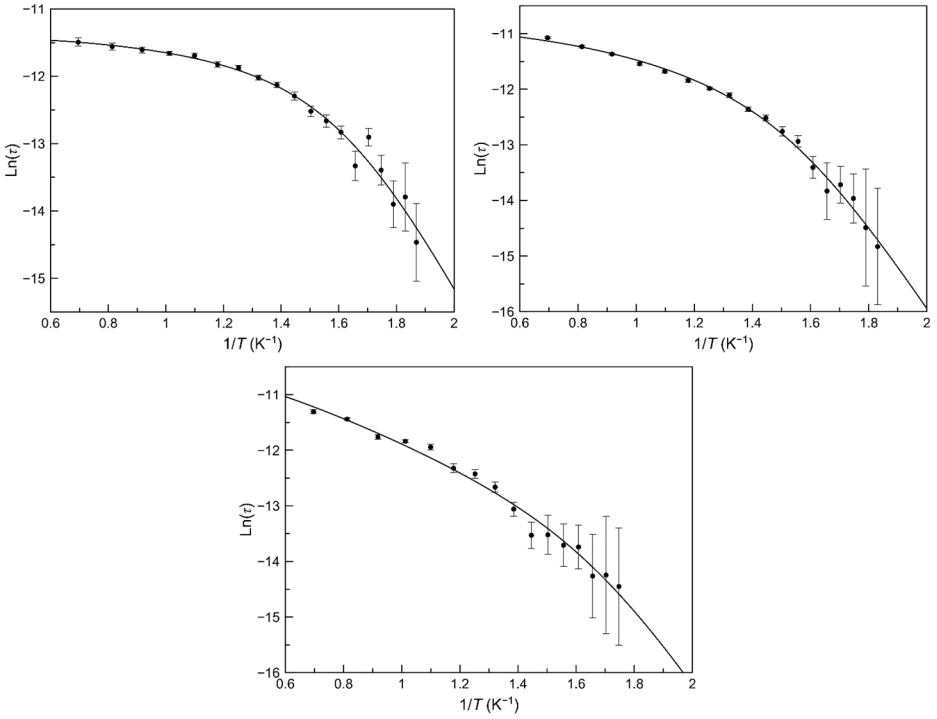

Figure A.87. Ln(τ) *vs* ln(T) plots for the main process of **8-dh** under 5.0 (top left), 2.5 (top right) and 1.0 kOe (bottom) applied static fields. The solid lines are the best fit-curves using a combination of Raman plus intra-Kramers mechanisms. Standard deviations appear as vertical error bars.

Table A.17. Crystal data of compounds **6**, **7** and **8**.

Compound	6	7	8
Formula	$C_{93}H_{80}Cl_3Co_3N_{12}O_{21}$	$C_{285}H_{246}Cl_6Co_6N_{24}O_{36}$	$C_{55}H_{43}Co_2N_4O_8$
Formula weight [g mol^{-1}]	1992.77	5149.35	1005.84
Crystal system	Trigonal	Monoclinic	Orthorhombic
Space group	*R*−3	*P*2$_1$/*c*	*Pbca*
a [Å]	23.016(3)	25.8869(3)	28.082(3)
b [Å]	23.016(3)	43.6615(4)	10.2520(6)
c [Å]	34.648(6)	26.0327(3)	48.833(5)
α [°]	90	90	90
β [°]	90	119.395(1)	90
γ [°]	120	90	90
V [Å^3]	15895(6)	25635.6(5)	14059(2)
Z	2	4	8
D_{calc} [g cm^{-3}]	1.249	1.334	0.947
Temperature [K]	296	100	296
μ [mm^{-1}]	0.609	0.473	0.513
R (int)	-	0.060	0.0715
Radiation [Å]	0.71073	0.68890	0.71073
Reflections collected	51602	375633	29131
Independent reflections	6200	61345	6377
Number of observed reflections (I_o > 2σ(I_o))	4248	26202	4303
Number of parameters	399	2857	627
Goodness-of-fit *S* on F^2	1.11	1.13	0.93
R_1[a] [*I*> 2.0σ(*I*)]	0.0955	0.1163	0.0589
wR_2[b] [*I*> 2.0σ(*I*)]	0.3028	0.3736	0.1567

[a] $R_1 = \sum||F_o| - |F_c|| / \sum|F_o|$. [b] $wR_2 = \{\sum[w(F_o^2 - F_c^2)^2]/\sum w(F_o^2)^2\}^{1/2}$.

Table A.18. Hydrogen bond details (distances [Å] and angles [°]) for **8**.

Donor–H···Acceptor	D–H	H···A	D···A	D–H···A
O(1W)···O2	0.850	1.985	2.786	162.72

Table A.19. π−π interactions in **6**, **7** and **8**.

Compound	Cg···Cg[a]	Cg···Cg [Å]	α[b][°]	Cg···Cg[a]	Cg···Cg [Å]	α[b][°]
6						
	Cg2···Cg6	3.978(4)	2.1(3)	Cg7···Cg7	3.891(5)	0.0(4)
7						
	Cg1···Cg38	3.725(3)	9.6(3)	Cg14···Cg20	3.776(3)	2.3(2)
	Cg2···Cg40	3.634(4)	5.6(3)	Cg16···Cg26	3.934(4)	4.5(3)
	Cg4···Cg20	3.663(3)	2.1(2)	Cg16···Cg29	3.989(4)	14.9(3)
	Cg6···Cg21	3.955(4)	3.3(3)	Cg19···Cg21	3.799(4)	3.7(3)
	Cg8···Cg14	3.847(3)	2.8(2)	Cg22···Cg40	3.754(3)	1.7(3)
	Cg10···Cg19	3.736(4)	5.4(3)	Cg29···Cg47	3.827(4)	19.7(4)
	Cg11···Cg40	3.677(4)	5.2(3)	Cg30···Cg51	3.994(11)	4
	Cg12···Cg38	3.646(3)	9.4(3)	Cg32···Cg46	3.768(3)	3.1(3)
	Cg13···Cg40	3.970(4)	1.4(3)			
8						
	Cg1···Cg6	3.887(4)	17.6(3)	Cg4···Cg10	3.882(4)	1.0(3)
	Cg3···Cg4	3.734(3)	0.7(3)			
	Cg3···Cg10	3.871(3)	0.9(3)			

[a] Cg are the six-membered rings: **6:** Cg2: N2, C10-C14; Cg6: C7-C10,C14, C15; Cg7: C21-C24, C28, C29; **7**: Cg1: N1, C1-C4, C12; Cg2: N2, C7-C11; Cg4: N4, C21-C25; Cg6: N6, C62-C66; Cg8: N8, C76-C79, C81; Cg10: N10, C90-C94; Cg11: N11, C98-C101, C108; Cg12: N12, C104-C107, C109; Cg13: C4-C7, C11, C12; Cg14: C18-C21, C25, C26; Cg16: C36-C41; Cg19: C59-C62, C66, C67; Cg20: C73-C76, C80, C81; Cg22: C101-C104, C108, C109; Cg26: N16, C132-C136; Cg29: N19, C181-C184, C192; Cg30: N20, C187-C191; Cg32: N22, C201-C205; Cg38: C147-C152; Cg40: C159-C164; Cg46: C8T-C13T; Cg47: C15T-C20T; Cg51: C43T-C48T; **8**: Cg1: N1, C1-C4, C12; Cg3: N3, C42-C45, C53; Cg4: N4, C48-C52; Cg6: C16-C21; Cg10: C45-C48, C52, C53.[b] α is the dihedral angle between each pair of mean ring planes.

Table A.20. Energy of the calculated quartet (D_Q) and doublet (D_D) excited states and their contributions to the *D* value for **6**, **7** and **8** obtained from CASSCF/NEVPT2 calculations.

Compound	*D*	|*E*/*D*|	D_Q[a]	D_D[a]	D_{Q1}	D_{Q2}	D_{Q1} + D_{Q2}
6							
Co1	+55.347	0.141	+47.679	+0.653	+28.813	+21.736	+50.549
7							
Co1	+63.682	0.211	+54.019	+4.288	+33.048	+18.836	+51.884
Co2	+59.218	0.097	+49.942	+1.466	+30.095	+22.620	+52.715
Co3	+43.431	0.332	+36.022	–1.781	+28.652	+14.794	+43.446
Co4	+69.780	0.169	+60.291	+5.551	+35.036	+22.642	+57.678
Co5	+61.702	0.159	+53.107	+5.229	+31.079	+20.036	+51.115
Co6	+71.417	0.270	+61.934	+10.842	+36.773	+15.950	+52.723
8							
Co1	+51.242	0.134	+43.871	–1.806	+31.978	+20.459	+52.437
Co2	+92.589	0.321	+74.970	+4.206	+52.133	+22.793	+74.926

[a] D_Q and D_D are the sum of spin-orbit contributions that comes from quartet and doublet excited states.

Table A.21. Selected fits of ac-magnetic data at different dc-applied field for **6** obtained from the ln(τ) *vs* 1/*T* plots.

H_{dc} (kOe)\Model[a]	$\tau_{0,IK} \times 10^5$ (s)	C (s^{-1} K^{-1})	$\tau_{0,LT} \times 10^6$ (s)	E_{aLT} (cm^{-1})	$\tau_{0,MT} \times 10^8$ (s)	E_{aMT} (cm^{-1})	$\tau_{0,HT} \times 10^{10}$ (s)	E_{aHT} (cm^{-1})
250								
Global	–	9800 ± 900	1.06 ± 0.12	8.2 ± 0.3	–	–	11.4 ± 1.2	33.8 ± 0.4
	5.2 ± 1.2	–	0.81 ± 0.15	7.9 ± 2.3	–	–	13 ± 16	33 ± 6
500								
Global	–	6400 ± 700	1.05 ± 0.10	8.11 ± 0.25	–	–	14.8 ± 1.3	33.7 ± 0.4
	7.4 ± 0.4	–	0.86 ± 0.03	8.08 ± 0.13	–	–	15.7 ± 0.7	33.85 ± 0.25
1000								
Global	9.9 ± 0.7	–	1.04 ± 0.04	8.08 ± 0.09	–	–	18.1 ± 0.7	33.28 ± 0.18
2500								
Global	6.15 ± 0.19	–	0.974 ± 0.020	8.17 ± 0.06	–	–	18.9 ± 0.4	33.67 ± 0.09
5000								
Global	2.45 ± 0.08	–	0.68 ± 0.22	8.18 ± 0.09	–	–	17.0 ± 0.6	33.61 ± 0.15
6000								
Global	1.49 ± 0.13	–	0.6 ± 0.3	8.2 ± 1.4	–	–	15 ± 4	33.5 ± 1.8

[a] Global is the analysis considering only one general Debye model. All data were analysed by a combination of several TA relaxations plus one IK or direct mechanisms.

Table A.22. Selected fits of ac-magnetic data at different dc-applied field for **7** obtained from the ln(τ) *vs* 1/*T* plots.

H_{dc} (kOe)\Model[a]	$\tau_{0,IK} \times 10^5$ (s)	C (s^{-1} K^{-1})	$\tau_{0,LT} \times 10^6$ (s)	E_{aLT} (cm^{-1})	$\tau_{0,MT} \times 10^7$ (s)	E_{aMT} (cm^{-1})	$\tau_{0,HT} \times 10^{10}$ (s)	E_{aHT} (cm^{-1})
1000								
Global	30.3 ± 0.8	–	3.41 ± 0.04	7.12 ± 0.03	1.74 ± 0.05	19.03 ± 0.10	3.78 ± 0.06	48.21 ± 0.08
2500								
Global	19.6 ± 0.4	–	3.57 ± 0.05	7.07 ± 0.03	1.64 ± 0.05	19.16 ± 0.09	4.98 ± 0.10	48.13 ± 0.10
5000								
Global	5.92 ± 0.07	–	4.19 ± 0.13	7.09 ± 0.08	1.29 ± 0.04	19.06 ± 0.11	5.10 ± 0.13	48.21 ± 0.13

[a] Global is the analysis considering only one general Debye model. All data were analysed by a combination of several TA relaxations plus one IK mechanism.

Table A.23. Selected fits of ac-magnetic data at different dc-applied field for **8** obtained from the ln(τ) *vs* 1/*T* plots.

H_{dc} (kOe)\Model[a]	$\tau_{0,IK} \times 10^5$ (s)	C (s^{-1} K^{-1})	$\tau_{0,LT} \times 10^6$ (s)	E_{aLT} (cm^{-1})	$\tau_{0,MT} \times 10^8$ (s)	E_{aMT} (cm^{-1})	$\tau_{0,HT} \times 10^{10}$ (s)	E_{aHT} (cm^{-1})
500								
Global	1.93 ± 0.13	–	–	–	–	–	–	–
1000								
Global	1.14 ± 0.20	–	–	–	–	–	11.3 ± 2.3	26.1 ± 0.7
2500								
Global	0.58 ± 0.05	–	–	–	–	–	11.8 ± 1.5	26.6 ± 0.5
5000								
Global	0.464 ± 0.020	–	–	–	–	–	18 ± 10	26.6 ± 2.1

[a] Global is the analysis considering only one general Debye model. All data were analysed by a combination of several TA relaxations plus one IK mechanism.

Table A.24. Selected fits of ac-magnetic data at different dc-applied field for **8-dh** obtained from the ln(τ) *vs* 1/*T* plots.

H_{dc} (kOe)\Model[a]	$\tau_{0,IK} \times 10^5$ (s)	C (s^{-1} K^{-1})	$\tau_{0,LT} \times 10^6$ (s)	E_{aLT} (cm^{-1})	$\tau_{0,MT} \times 10^8$ (s)	E_{aMT} (cm^{-1})	$\tau_{0,HT} \times 10^{10}$ (s)	E_{aHT} (cm^{-1})
1000								
Global	2.2 ± 0.6	–	0.23 ± 0.03	7.00 ± 0.16	–	–	1.8 ± 0.3	32.9 ± 0.5
2500								
Global	1.8 ± 1.1	–	0.6 ± 1.0	7 ± 5	–	–	2 ± 3	33 ± 6
5000								
Global	1.17 ± 0.12	–	0.88 ± 0.15	6.8 ± 0.3	–	–	5.4 ± 0.7	33.6 ± 0.4

[a] Global is the analysis considering only one general Debye model. All data were analysed by a combination of several TA relaxations plus one IK mechanism.

Table A.25. Selected fits of ac-magnetic data at different dc-applied field of **6** obtained from the ln(τ) *vs* ln(*T*) plots.

H_{dc} (kOe)\Model[a]	$\tau_{0,IK} \times 10^5$ (s)	C (s^{-1} K^{-1})	$A_{LT} \times 10^{-2}$ (s^{-1} K^{-nLT})	n_{LT}	A_{HT} (s^{-1} K^{-nHT})	n_{HT}
250						
Global	110 ± 50	–	44.6 ± 0.5	2.117 ± 0.011	1.40 ± 0.07	6.61 ± 0.03
500						
Global	150 ± 450	–	33.6 ± 2.4	2.12 ± 0.06	1.76 ± 0.15	6.58 ± 0.05
1000						
Global	120 ± 110	–	26.3 ± 0.8	2.12 ± 0.03	1.46 ± 0.05	6.592 ± 0.019
2500						
Global	27 ± 3	–	30.1 ± 0.4	2.133 ± 0.011	1.409 ± 0.021	6.580 ± 0.008
5000						
Global	3.59 ± 0.19	–	37.9 ± 1.1	2.150 ± 0.022	1.69 ± 0.05	6.571 ± 0.015
6000						
Global	2.02 ± 0.23	–	45 ± 1.9	2.1 ± 0.3	1.9 ± 0.8	6.57 ± 0.19

[a] Global is the analysis considering only one general Debye model. All data were analysed by a combination of several Raman relaxations and one IK mechanism.

Table A.26. Selected fits of ac-magnetic data at different dc-applied field of **7** obtained from the ln(τ) *vs* ln(T) plots.

H_{dc} (kOe)\Model[a]	$\tau_{0,IK} \times 10^5$ (s)	C (s^{-1} K^{-1})	A_{LT} (s^{-1} K^{-nLT})	n_{LT}	A_{HT} (s^{-1} K^{-nHT})	n_{HT}
1000						
Global	–	–	654 ± 25	2.77 ± 0.03	0.024 ± 0.007	8.12 ± 0.13
2500						
Global	42 ± 6	–	641 ± 7	2.755 ± 0.008	0.0241 ± 0.0004	8.026 ± 0.009
5000						
Global	8.5 ± 0.3	–	629 ± 13	2.819 ± 0.013	0.0200 ± 0.0005	8.118 ± 0.014

[a] Global is the analysis considering only one general Debye model. All data were analysed by a combination of several Raman relaxations and one IK mechanism.

Table A.27. Selected fits of ac-magnetic data at different dc-applied field of **8** obtained from the ln(τ) *vs* ln(T) plots.

H_{dc} (kOe)\Model[a]	$\tau_{0,IK} \times 10^5$ (s)	C (s^{-1} K^{-1})	A_{LT} (s^{-1} K^{-nLT})	n_{LT}	A_{HT} (s^{-1} K^{-nHT})	n_{HT}
500						
Global	2.20 ± 0.03	–	–	–	–	–
1000						
Global	1.17 ± 0.21	–	–	–	1.09 ± 0.22	8.01 ± 0.12
2500						
Global	0.57 ± 0.06	–	–	–	0.94 ± 0.10	8.01 ± 0.06
5000						
Global	0.46 ± 0.23	–	–	–	0.6 ± 0.8	8.0 ± 0.8

[a] Global is the analysis considering only one general Debye model. All data were analysed by a combination of several Raman relaxations and one IK mechanism.

Table A.28. Selected fits of ac-magnetic data at different dc-applied field of **8-dh** obtained from the ln(τ) *vs* ln(T) plots.

H_{dc} (kOe)\Model[a]	$\tau_{0,IK} \times 10^5$ (s)	C (s^{-1} K^{-1})	$A_{LT} \times 10^{-2}$ (s^{-1} K^{-nLT})	n_{LT}	A_{HT} (s^{-1} K^{-nHT})	n_{HT}
1000						
Global	5 ± 3	–	84± 10	2.68 ± 0.05	1.08 ± 0.23	7.99 ± 0.11
2500						
Global	2.1 ± 0.3	–	33 ± 5	2.64 ± 0.11	0.84 ± 0.07	8.01 ± 0.05
5000						
Global	1.17 ± 0.15	–	19 ± 5	2.68 ± 0.16	0.38 ± 0.05	8.0 ± 0.08

[a] Global is the analysis considering only one general Debye model. All data were analysed by a combination of several Raman relaxations and one IK mechanism.

SI Chapter V

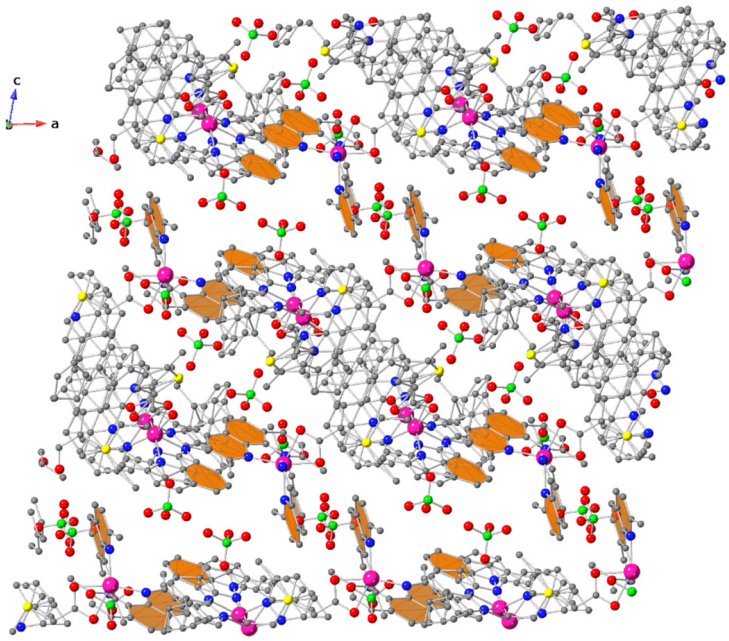

Figure A.88. Perspective view of the crystal along the *b*-axis of **9-o** with π−π interactions involving phenanthroline coloured in orange. Hydrogen atoms are omitted for clarity. Colour code: magenta, cobalt; blue, nitrogen; red, oxygen; grey, carbon; green, chlorine; yellow, sulphur.

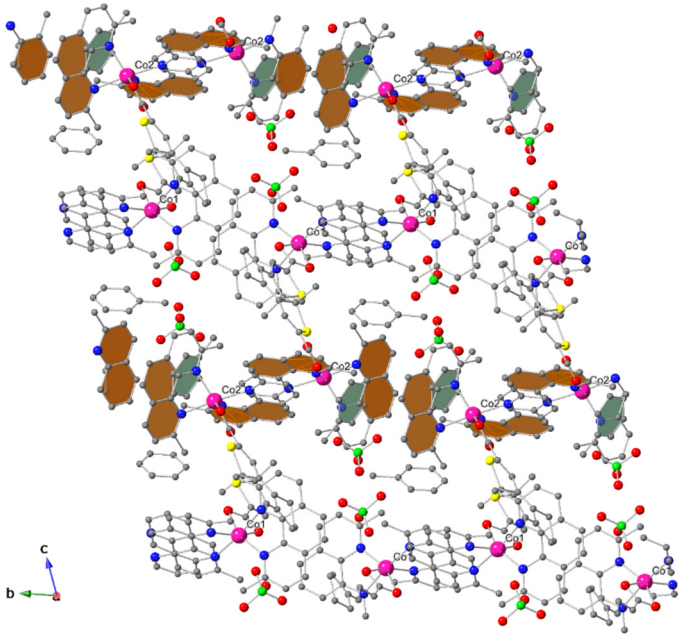

Figure A.89. Perspective view of the crystal along the *a*-axis of **9-c** Rings involved in π−π interactions are coloured in orange (phenanthroline) and green (toluene). Hydrogen atoms are omitted for clarity. Colour code: magenta, cobalt; blue, nitrogen; red, oxygen; grey, carbon; green, chlorine; yellow, sulphur.

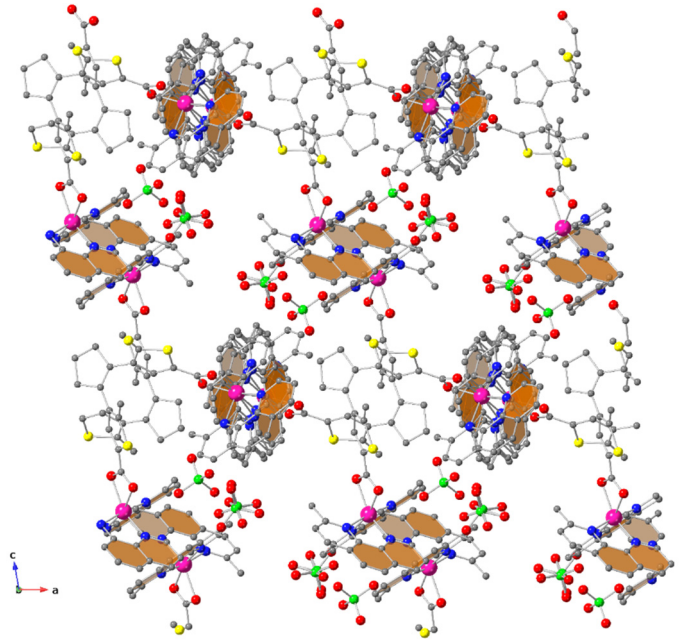

Figure A.90. Perspective view of the crystal along the *b*-axis of **10-o** with π−π interactions involving phenanthroline coloured in orange. Hydrogen atoms are omitted for clarity. Colour code: magenta, cobalt; blue, nitrogen; red, oxygen; grey, carbon; green, chlorine; yellow, sulphur.

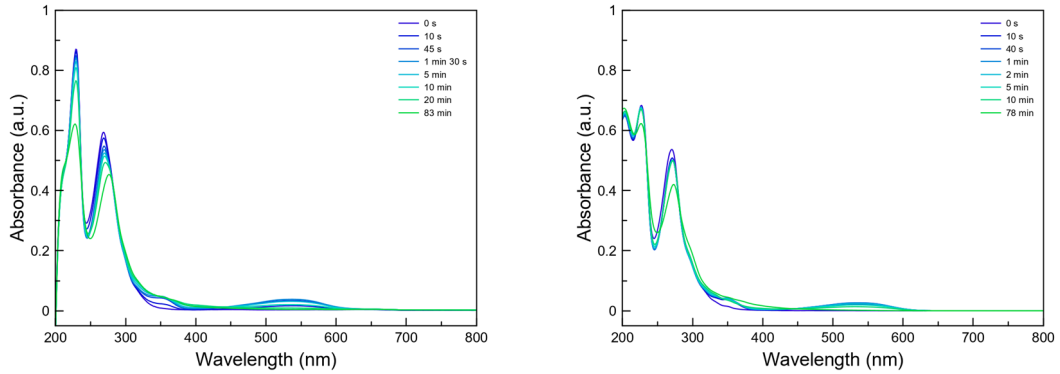

Figure A.91. Electronic absorption spectra of **9-o** (left) and **10-o** (right) in acetonitrile ~0.007 mM subjected to irradiation with UV light (308 nm) during long time, leading to degraded species.

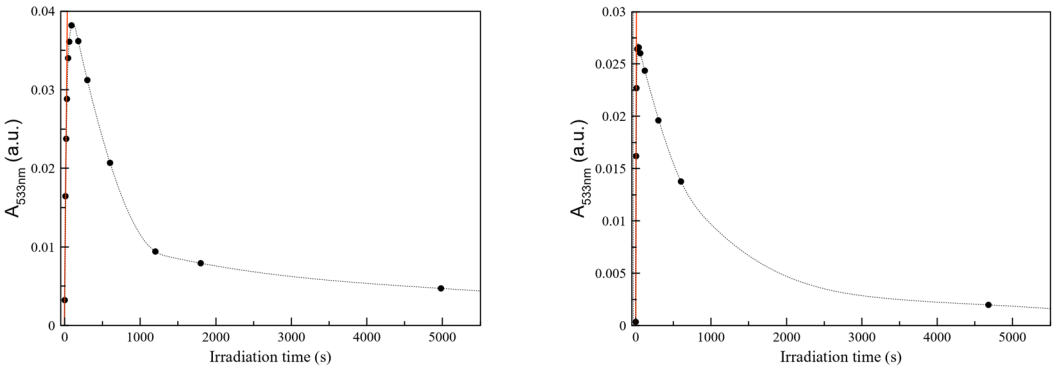

Figure A.92. Evolution of the absorbance at 533 nm over the time of **9-o** (left) and **10-o** (right) exposed to UV irradiation (308 nm). The red line shows the linear dependence of the absorbance with the time. The dashed black line is a trend guide to the eye.

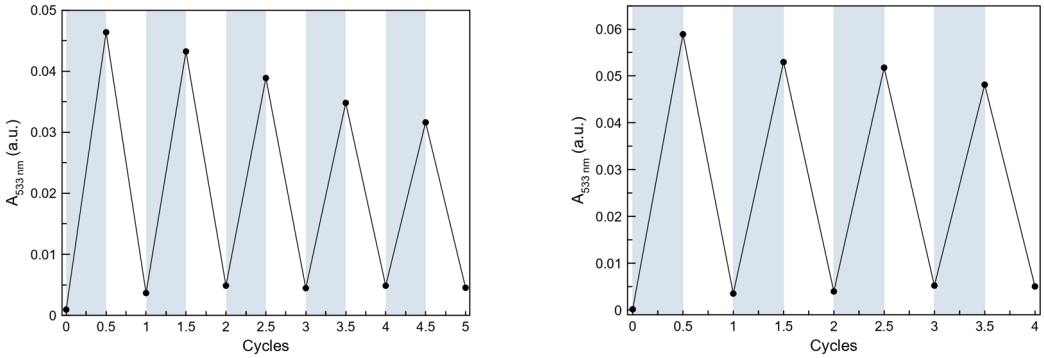

Figure A.93. Absorbance at 533 nm during repetitive switching cycles alternating UV (308 nm 40 and 45 s) and visible irradiation (> 540 nm, 1 h) for **9-o** and **10-o**.

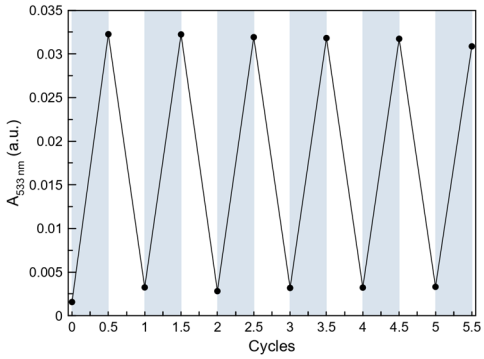

Figure A.94. Absorbance at 533 nm during repetitive switching cycles alternating UV (308 nm 10 s) and visible irradiation (> 540 nm, 1 h) for **9-o**.

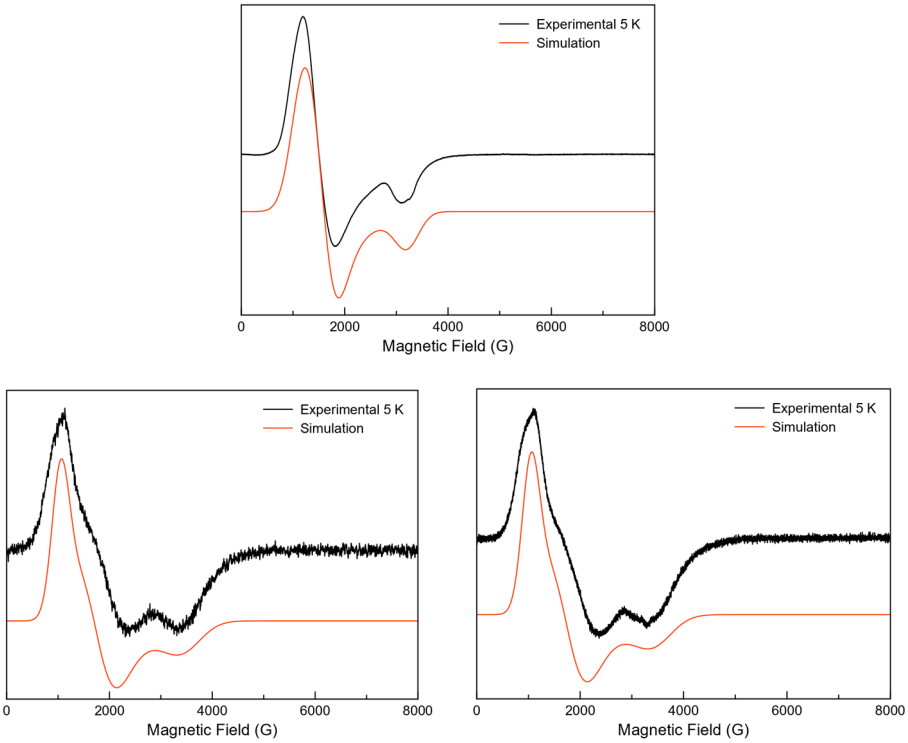

Figure A.95. X-band EPR in the 0–8 kOe range for ~5 mM in acetonitrile solutions of **9-c** (top), **10-o** (bottom left) and **10-c** (bottom right) at ~5 K. The simulated red curves were obtained by using the parameters on text and Table II.5.

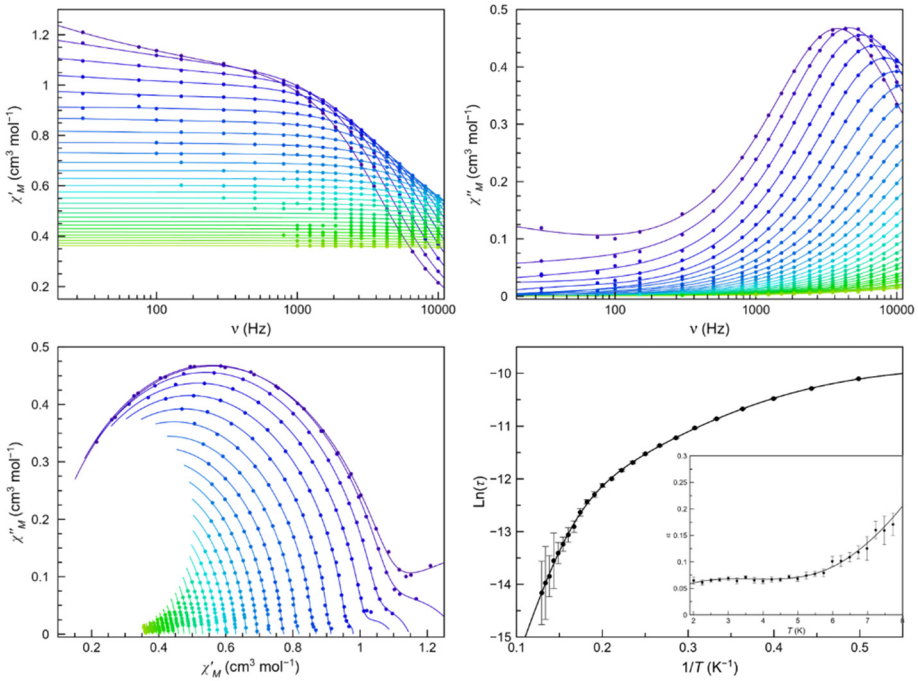

Figure A.96. Frequency dependence of χ_M' (top left) and χ_M'' (top right), Cole-Cole plots (bottom left) and Arrhenius plots of **9-o** (bottom right) in a dc-applied static field of 2.5 kOe with ± 0.005 kOe oscillating field in the temperature range of 2.0–9.0 K (purple to green gradient). Thermal dependence of α is included on the bottom right figure as an inset, where the black line are eye-guides. Standard deviation appears as vertical error bars.

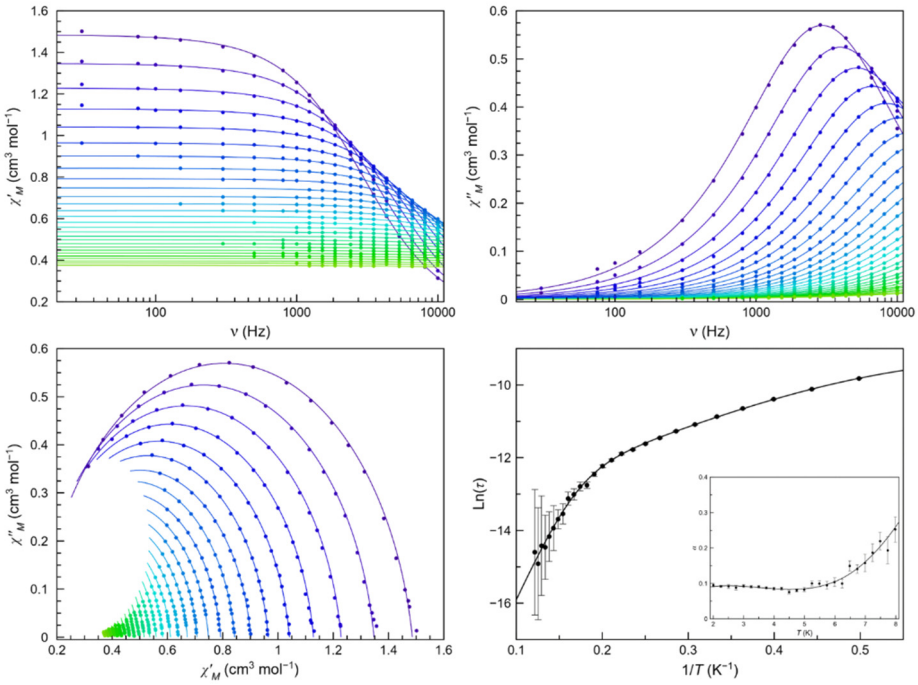

Figure A.97. Frequency dependence of χ_M' (top left) and χ_M'' (top right), Cole-Cole plots (bottom left) and Arrhenius plots of **9-o** (bottom right) in a dc-applied static field of 1.0 kOe with ± 0.005 kOe oscillating field in the temperature range of 2.0–8.75 K (purple to green gradient). Thermal dependence of α is included on the bottom right figure as an inset, where the black line are eye-guides. Standard deviation appears as vertical error bars.

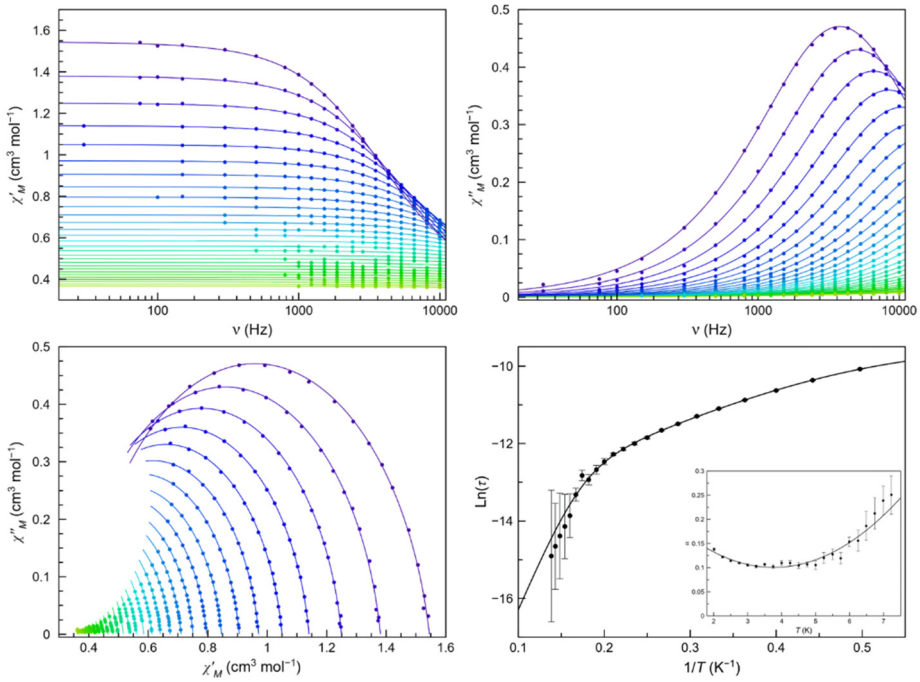

Figure A.98. Frequency dependence of χ_M' (top left) and χ_M'' (top right), Cole-Cole plots (bottom left) and Arrhenius plots of **9-o** (bottom right) in a dc-applied static field of 0.5 kOe with ± 0.005 kOe oscillating field in the temperature range of 2.0–9.0 K (purple to green gradient). Thermal dependence of α is included on the bottom right figure as an inset, where the black line are eye-guides. Standard deviation appears as vertical error bars.

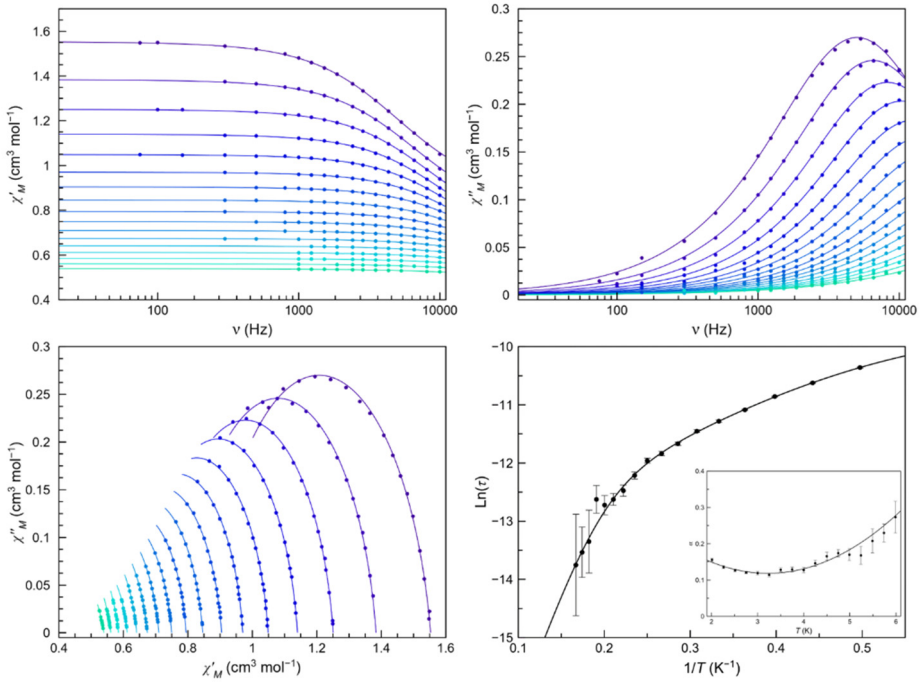

Figure A.99. Frequency dependence of χ_M' (top left) and χ_M'' (top right), Cole-Cole plots (bottom left) and Arrhenius plots of **9-o** (bottom right) in a dc-applied static field of 0.25 kOe with ± 0.005 kOe oscillating field in the temperature range of 2.0–6.0 K (purple to green gradient). Thermal dependence of α is included on the bottom right figure as an inset, where the black line are eye-guides. Standard deviation appears as vertical error bars.

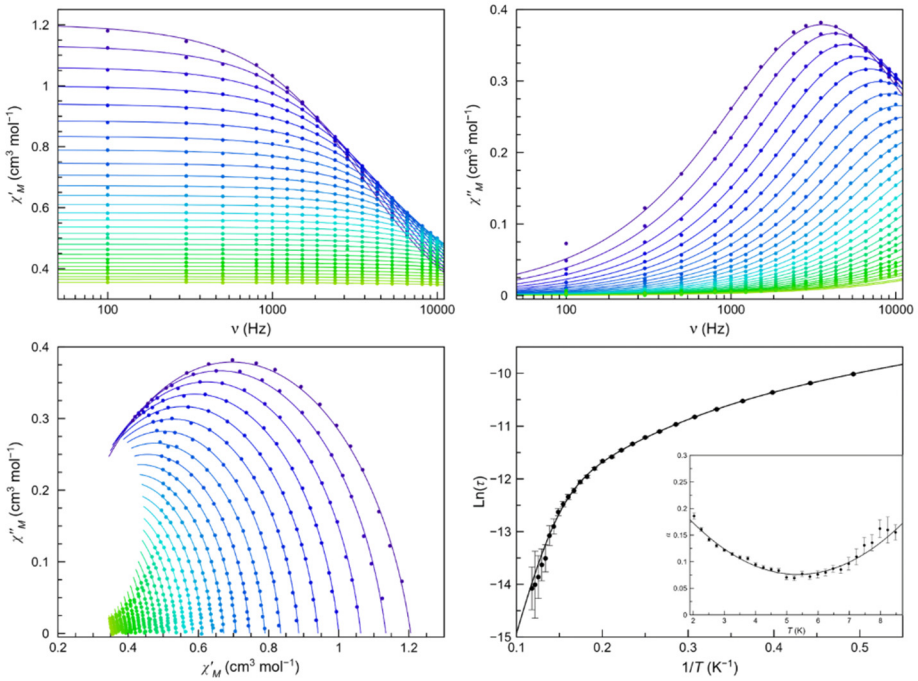

Figure A.100. Frequency dependence of χ_M' (top left) and χ_M'' (top right), Cole-Cole plots (bottom left) and Arrhenius plots of **9-c** (bottom right) in a dc-applied static field of 2.5 kOe with ± 0.005 kOe oscillating field in the temperature range of 2.0–9.0 K (purple to red gradient). Thermal dependence of α is included on the bottom right figure as an inset, where the black line are eye-guides. Standard deviation appears as vertical error bars.

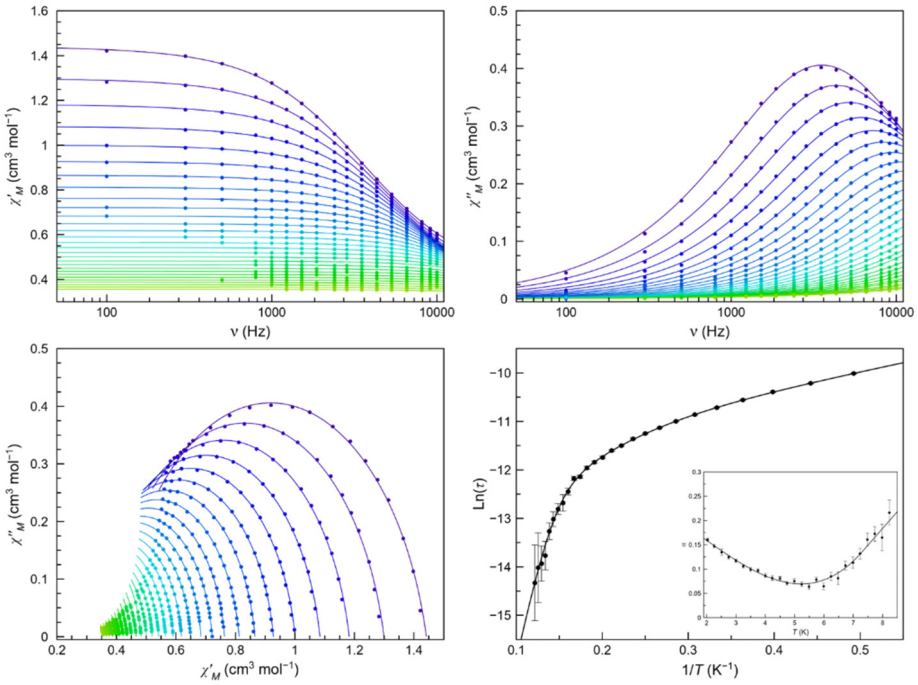

Figure A.101. Frequency dependence of χ_M' (top left) and χ_M'' (top right), Cole-Cole plots (bottom left) and Arrhenius plots of **9-c** (bottom right) in a dc-applied static field of 1.0 kOe with ± 0.005 kOe oscillating field in the temperature range of 2.0–9.0 K (purple to red gradient). Thermal dependence of α is included on the bottom right figure as an inset, where the black line are eye-guides. Standard deviation appears as vertical error bars.

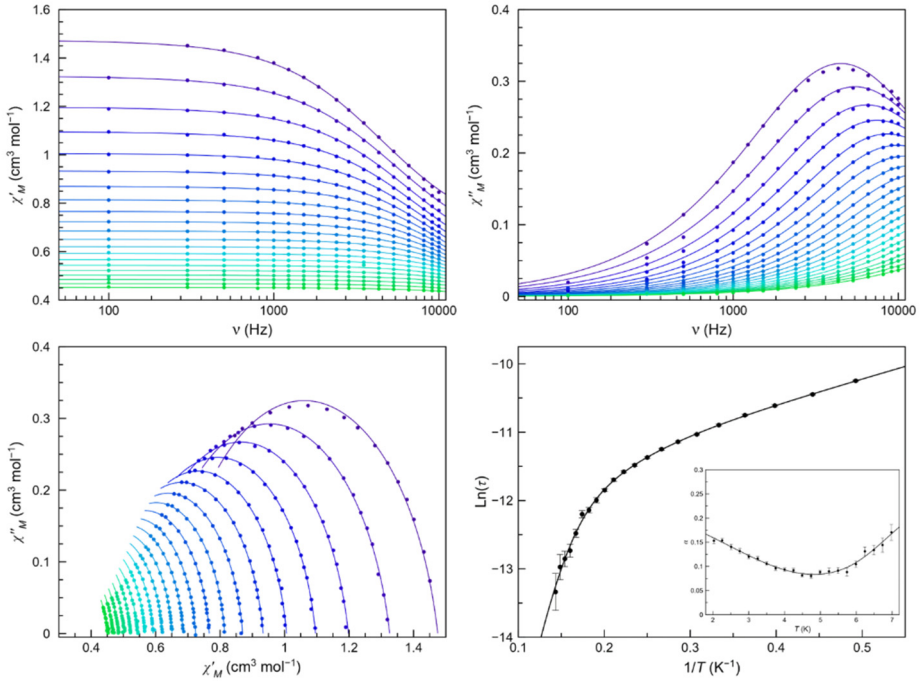

Figure A.102. Frequency dependence of χ_M' (top left) and χ_M'' (top right), Cole-Cole plots (bottom left) and Arrhenius plots of **9-c** (bottom right) in a dc-applied static field of 0.5 kOe with ± 0.005 kOe oscillating field in the temperature range of 2.0–7.0 K (purple to red gradient). Thermal dependence of α is included on the bottom right figure as an inset, where the black line are eye-guides. Standard deviation appears as vertical error bars.

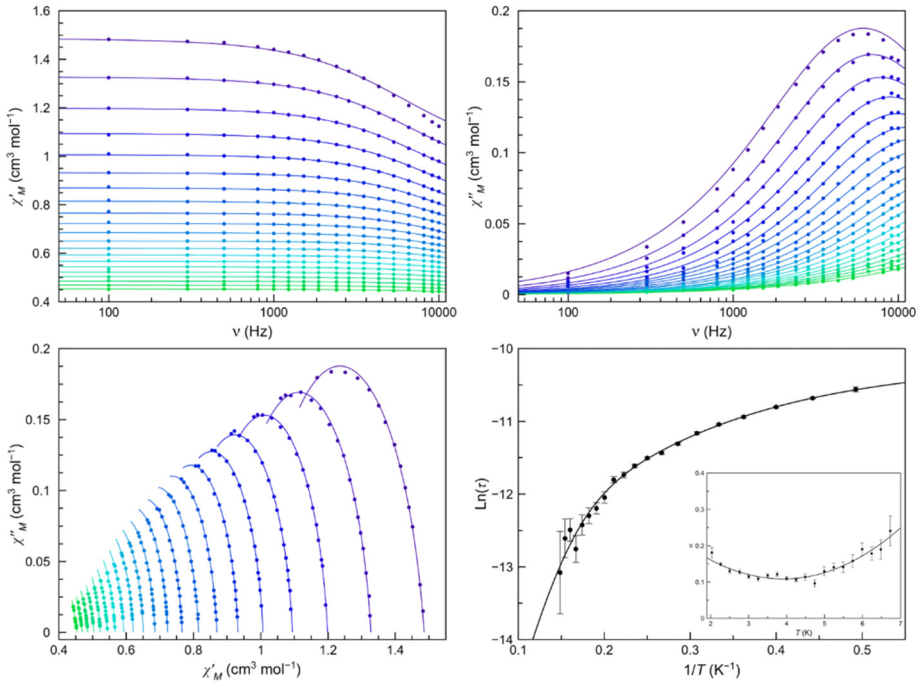

Figure A.103. Frequency dependence of χ_M' (top left) and χ_M'' (top right), Cole-Cole plots (bottom left) and Arrhenius plots of **9-c** (bottom right) in a dc-applied static field of 0.25 kOe with ± 0.005 kOe oscillating field in the temperature range of 2.0–7.0 K (purple to red gradient). Thermal dependence of α is included on the bottom right figure as an inset, where the black line are eye-guides. Standard deviation appears as vertical error bars.

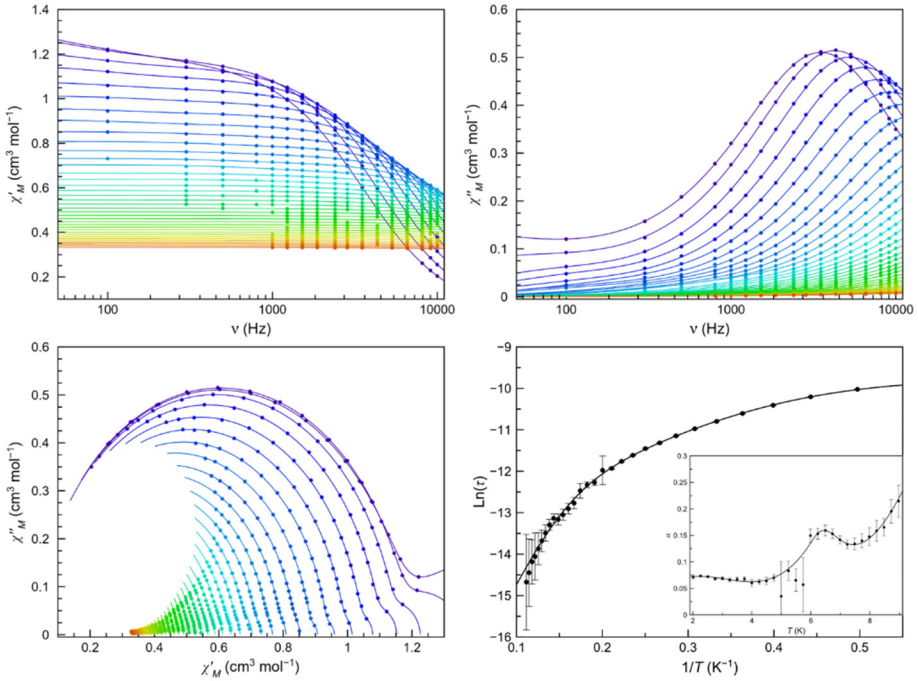

Figure A.104. Frequency dependence of χ_M' (top left) and χ_M'' (top right), Cole-Cole plots (bottom left) and Arrhenius plots of **10-o** (bottom right) in a dc-applied static field of 2.5 kOe with ± 0.005 kOe oscillating field in the temperature range of 2.0–11.0 K (purple to red gradient). Thermal dependence of α is included on the bottom right figure as an inset, where the black line are eye-guides. Standard deviation appears as vertical error bars.

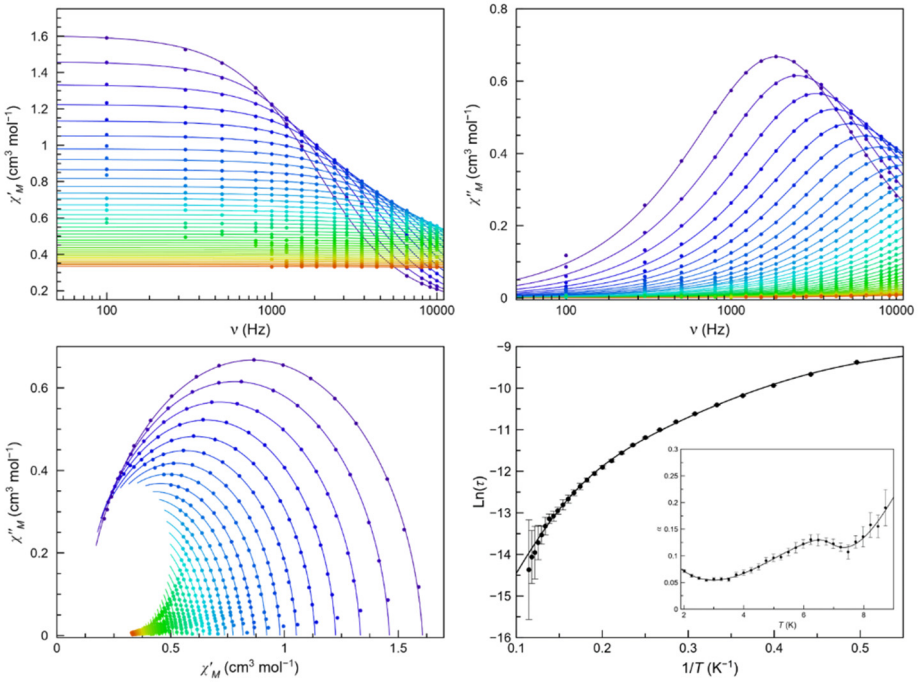

Figure A.105. Frequency dependence of χ_M' (top left) and χ_M'' (top right), Cole-Cole plots (bottom left) and Arrhenius plots of **10-o** (bottom right) in a dc-applied static field of 1.0 kOe with ± 0.005 kOe oscillating field in the temperature range of 2.0–11.0 K (purple to red gradient). Thermal dependence of α is included on the bottom right figure as an inset, where the black line are eye-guides. Standard deviation appears as vertical error bars.

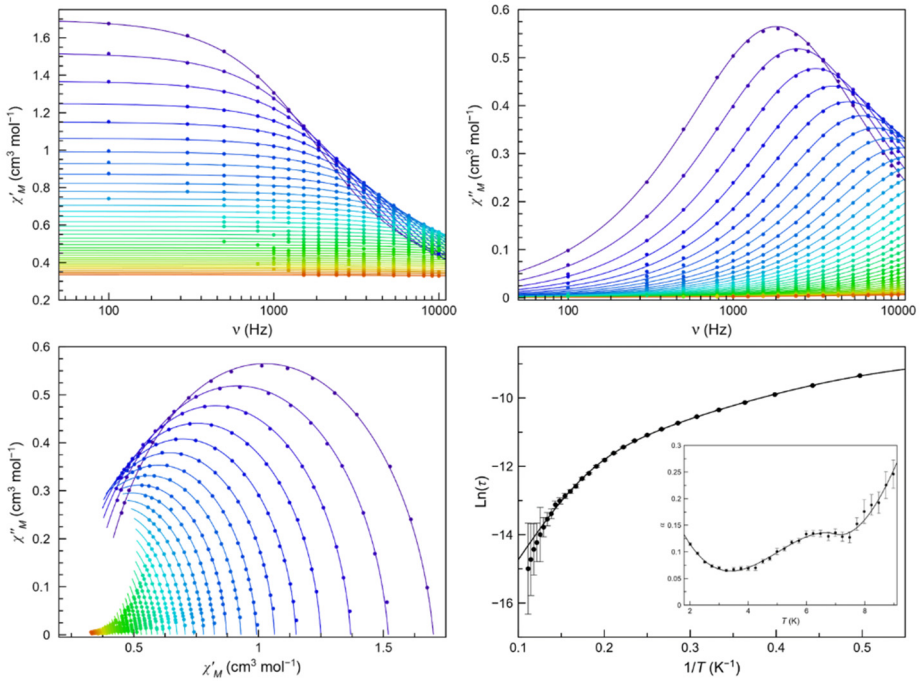

Figure A.106. Frequency dependence of χ_M' (top left) and χ_M'' (top right), Cole-Cole plots (bottom left) and Arrhenius plots of **10-o** (bottom right) in a dc-applied static field of 0.5 kOe with ± 0.005 kOe oscillating field in the temperature range of 2.0–11.0 K (purple to red gradient). Thermal dependence of α is included on the bottom right figure as an inset, where the black line are eye-guides. Standard deviation appears as vertical error bars.

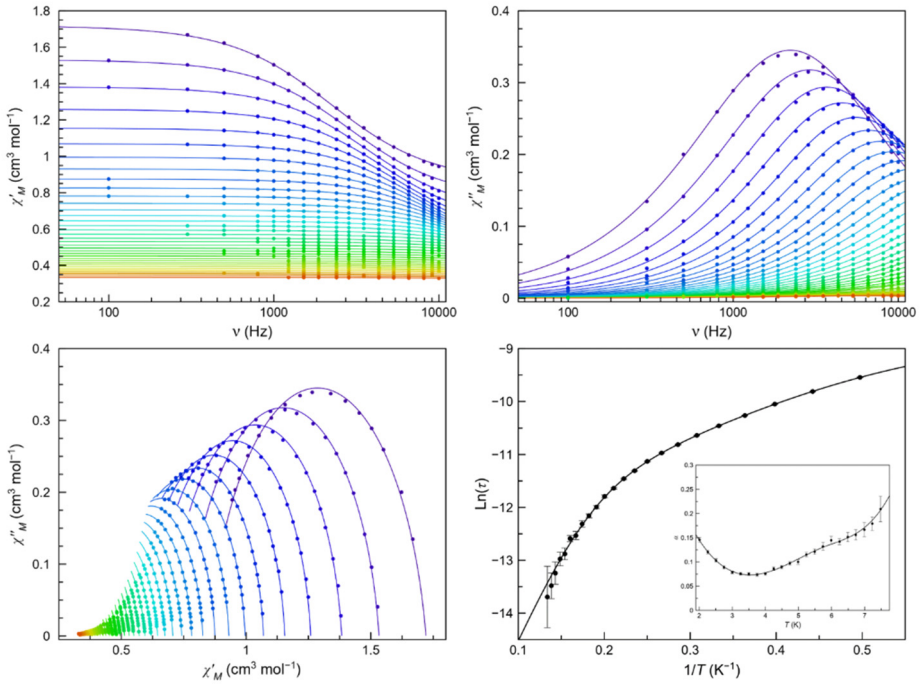

Figure A.107. Frequency dependence of χ_M' (top left) and χ_M'' (top right), Cole-Cole plots (bottom left) and Arrhenius plots of **10-o** (bottom right) in a dc-applied static field of 0.25 kOe with ± 0.005 kOe oscillating field in the temperature range of 2.0–11.0 K (purple to red gradient). Thermal dependence of α is included on the bottom right figure as an inset, where the black line are eye-guides. Standard deviation appears as vertical error bars.

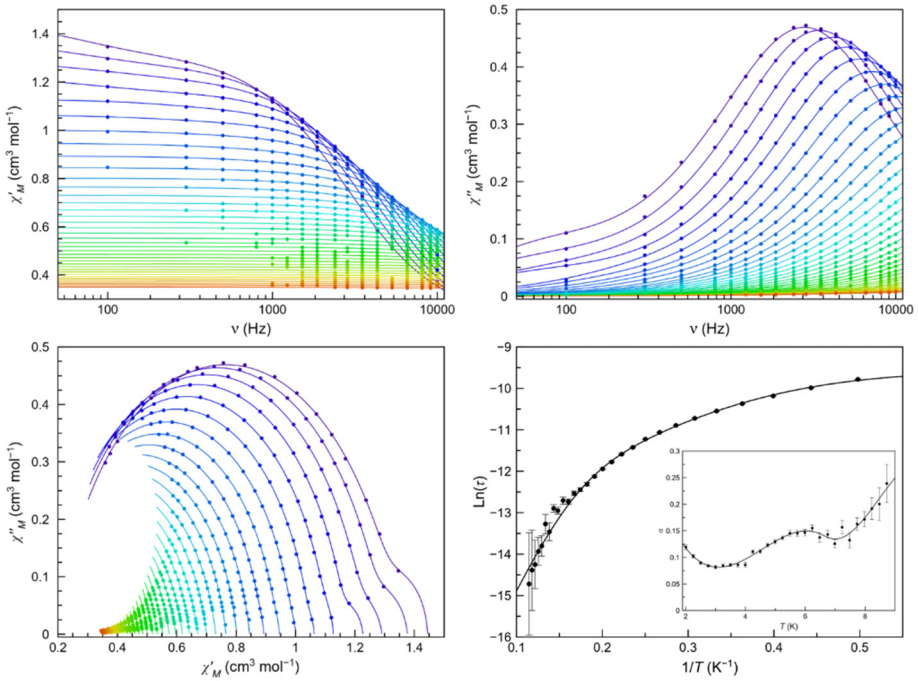

Figure A.108. Frequency dependence of χ_M' (top left) and χ_M'' (top right), Cole-Cole plots (bottom left) and Arrhenius plots of **10-c** (bottom right) in a dc-applied static field of 2.5 kOe with ± 0.005 kOe oscillating field in the temperature range of 2.0–11.0 K (purple to red gradient). Thermal dependence of α is included on the bottom right figure as an inset, where the black line are eye-guides. Standard deviation appears as vertical error bars.

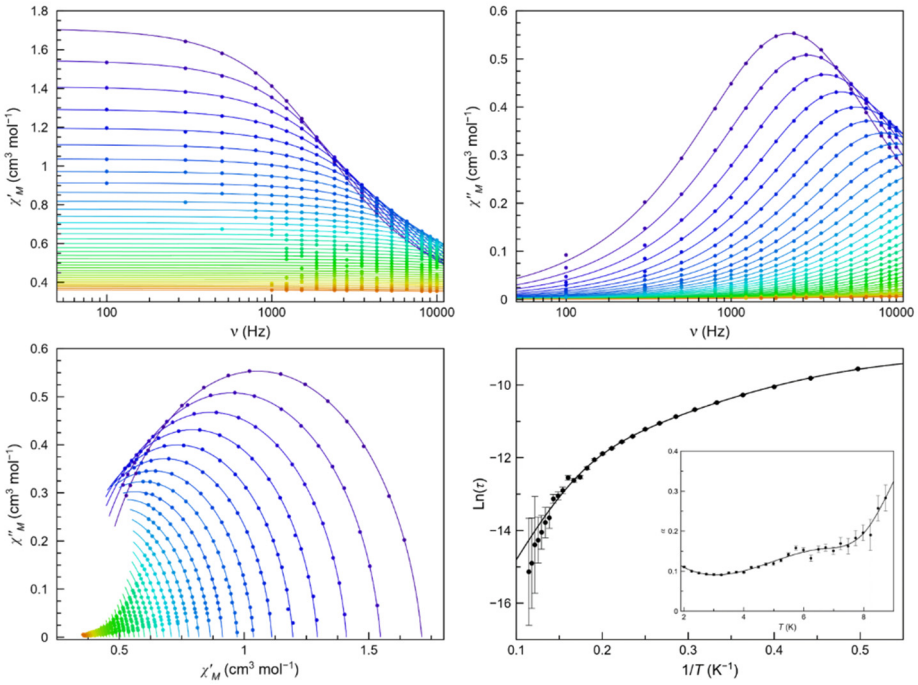

Figure A.109. Frequency dependence of χ_M' (top left) and χ_M'' (top right), Cole-Cole plots (bottom left) and Arrhenius plots of **10-c** (bottom right) in a dc-applied static field of 1.0 kOe with ± 0.005 kOe oscillating field in the temperature range of 2.0–10.75 K (purple to red gradient). Thermal dependence of α is included on the bottom right figure as an inset, where the black line are eye-guides. Standard deviation appears as vertical error bars.

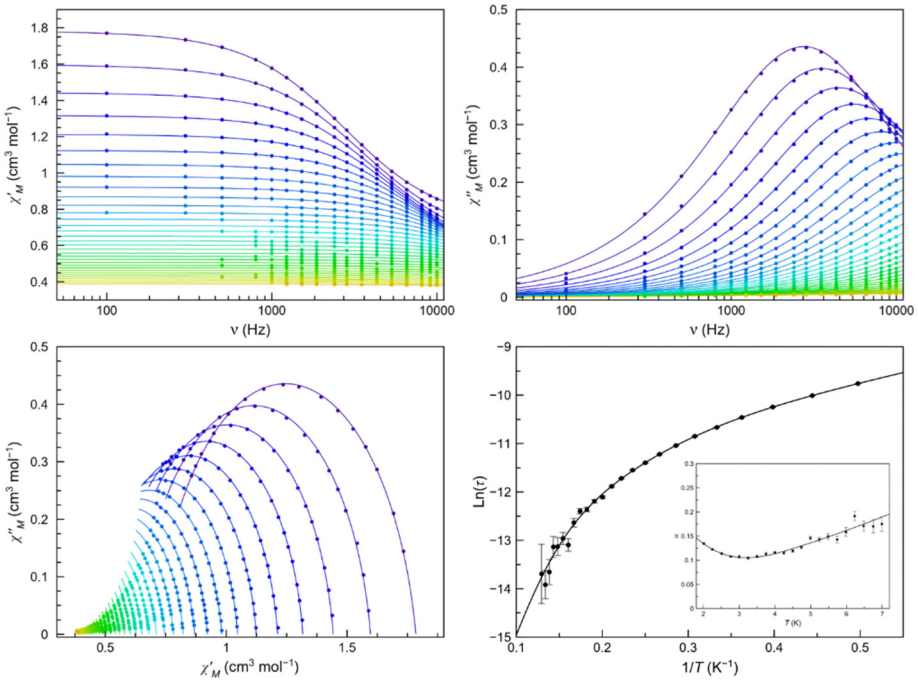

Figure A.110. Frequency dependence of χ_M' (top left) and χ_M'' (top right), Cole-Cole plots (bottom left) and Arrhenius plots of **10-c** (bottom right) in a dc-applied static field of 0.5 kOe with ± 0.005 kOe oscillating field in the temperature range of 2.0–10.0 K (purple to red gradient). Thermal dependence of α is included on the bottom right figure as an inset, where the black line are eye-guides. Standard deviation appears as vertical error bars.

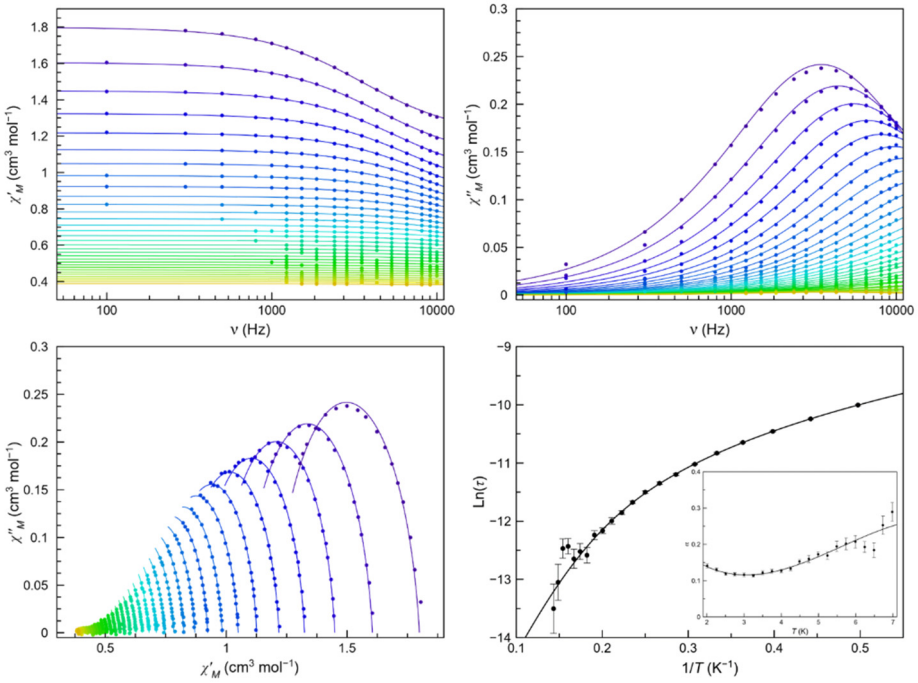

Figure A.111. Frequency dependence of χ_M' (top left) and χ_M'' (top right), Cole-Cole plots (bottom left) and Arrhenius plots of **10-c** (bottom right) in a dc-applied static field of 0.25 kOe with ± 0.005 kOe oscillating field in the temperature range of 2.0–10.0 K (purple to red gradient). Thermal dependence of α is included on the bottom right figure as an inset, where the black line are eye-guides. Standard deviation appears as vertical error bars.

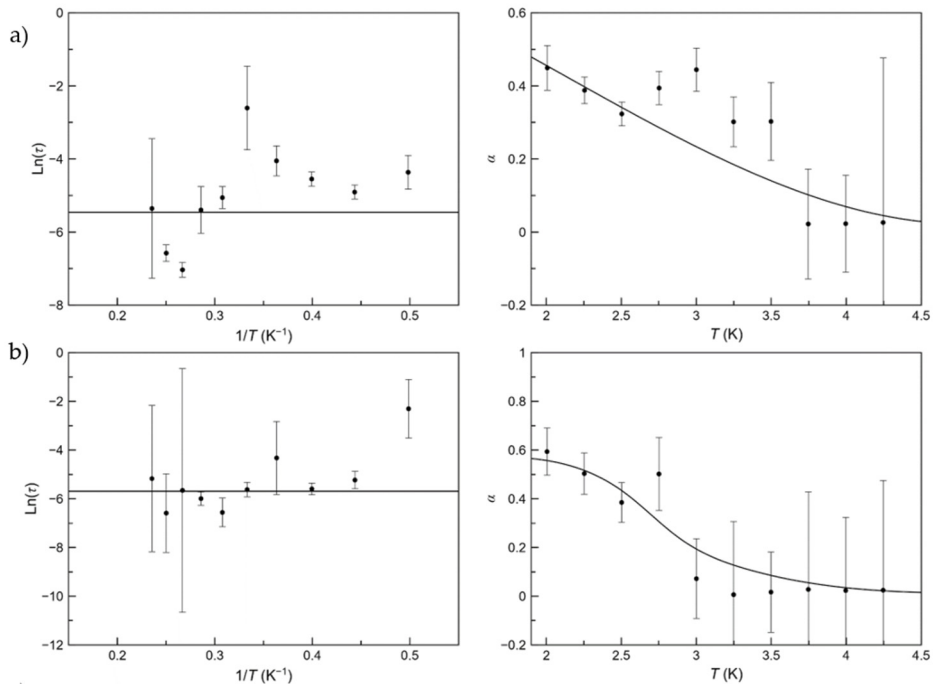

Figure A.112. Arrhenius plots (left) and thermal dependence of α (right) for the second process found in **9-o** at 5.0 (a), 2.5 kOe (b), 1.0 kOe (b) dc-applied static fields with ± 0.005 kOe oscillating field in the temperature range of 2.0–4.5 K. The black line on the $\alpha vs\ T$ plots are eye-guides. Standard deviation appears as vertical error bars.

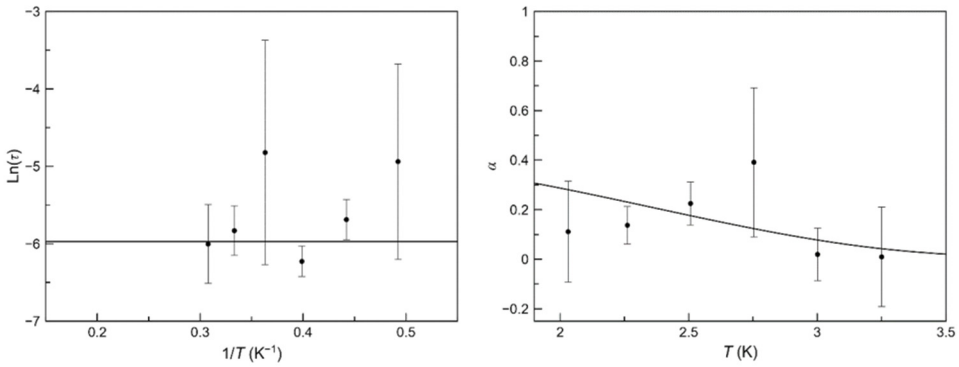

Figure A.113. Arrhenius plots (left) and thermal dependence of α (right) for the second process found in **9-c** at 5.0 kOe (b) dc-applied static fields with ± 0.005 kOe oscillating field in the temperature range of 2.0–3.25 K. The black line on the $\alpha vs\ T$ plots are eye-guides. Standard deviation appears as vertical error bars.

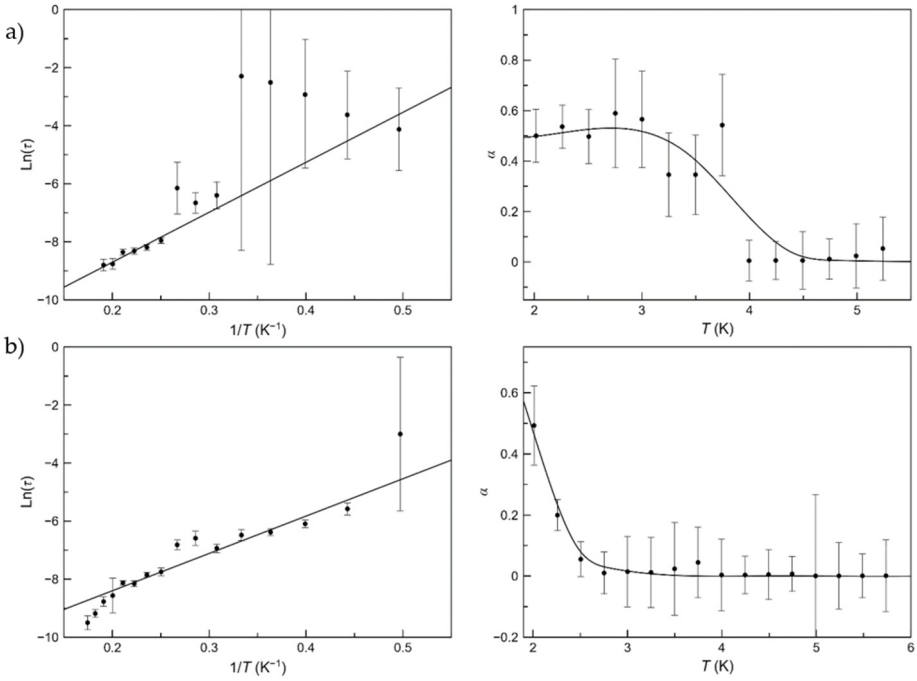

Figure A.114. Arrhenius plots (left) and thermal dependence of α (right) for the second process found in **10-o** at 5.0 (a) and 2.5 (b) dc-applied static fields with ± 0.005 kOe oscillating field in the temperature range of 2.0–5.75 K. The black line on the $\alpha vs\ T$ plots are eye-guides. Standard deviation appears as vertical error bars.

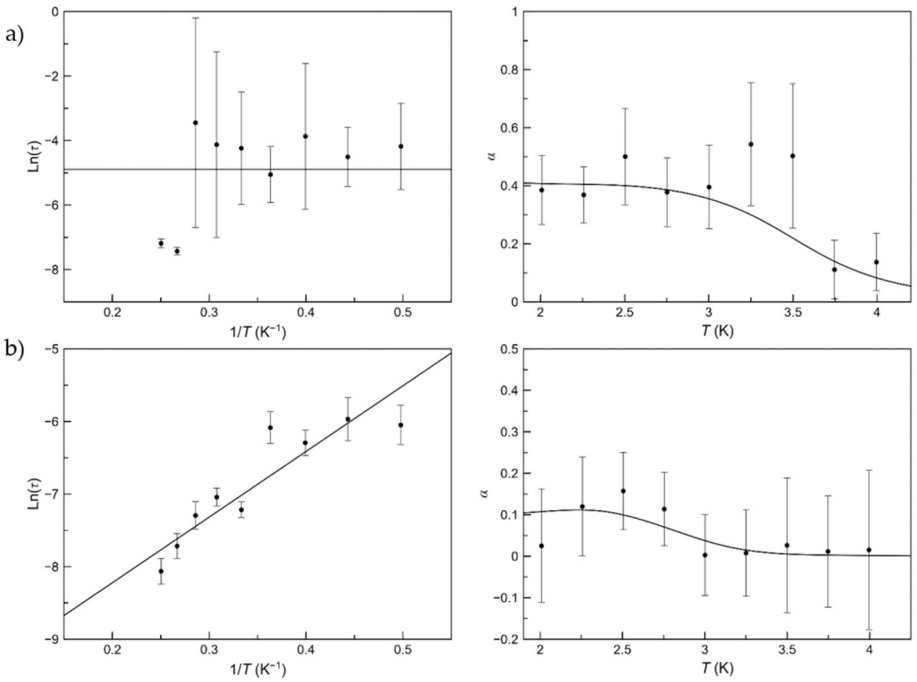

Figure A.115. Arrhenius plots (left) and thermal dependence of α (right) for the second process found in **10-c** at 5.0 (a) and 2.5 kOe (b) dc-applied static fields with ± 0.005 kOe oscillating field in the temperature range of 2.0–4.0 K. The black line on the $\alpha vs\ T$ plots are eye-guides. Standard deviation appears as vertical error bars.

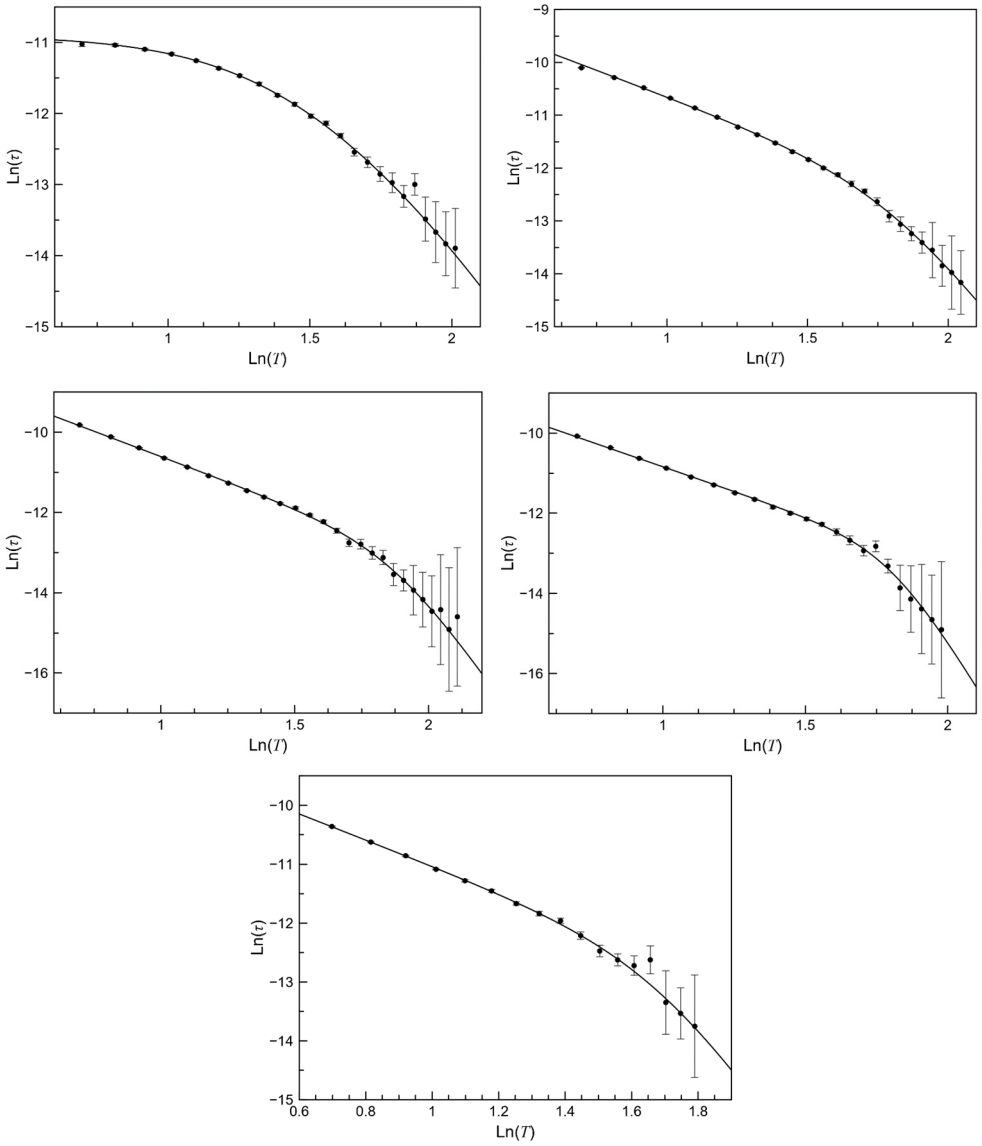

Figure A.116. Ln(τ) *vs* ln(T) plots for the main for the main process of **9-o** under 5.0 (top left), 2.5 (top right), 1.0 (middle left), 0.5 (middle right) and 0.25 kOe (bottom) applied static fields. The solid lines are the best fit-curves (see text). Standard deviations appear as vertical error bars.

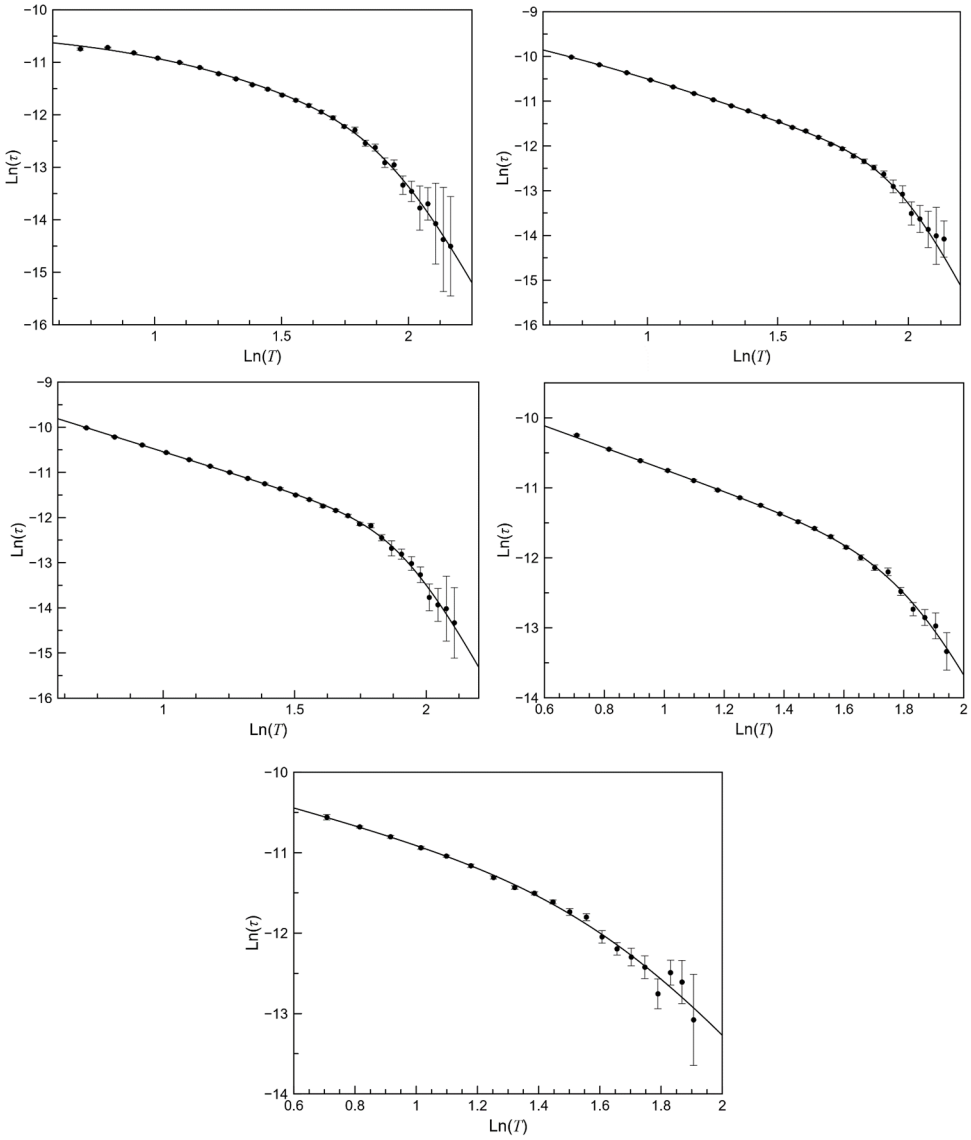

Figure A.117. Ln(τ) *vs* ln(T) plots for the main for the main process of **9-c** under 5.0 (top left), 2.5 (top right), 1.0 (middle left), 0.5 (middle right) and 0.25 kOe (bottom) applied static fields. The solid lines are the best fit-curves (see text). Standard deviations appear as vertical error bars.

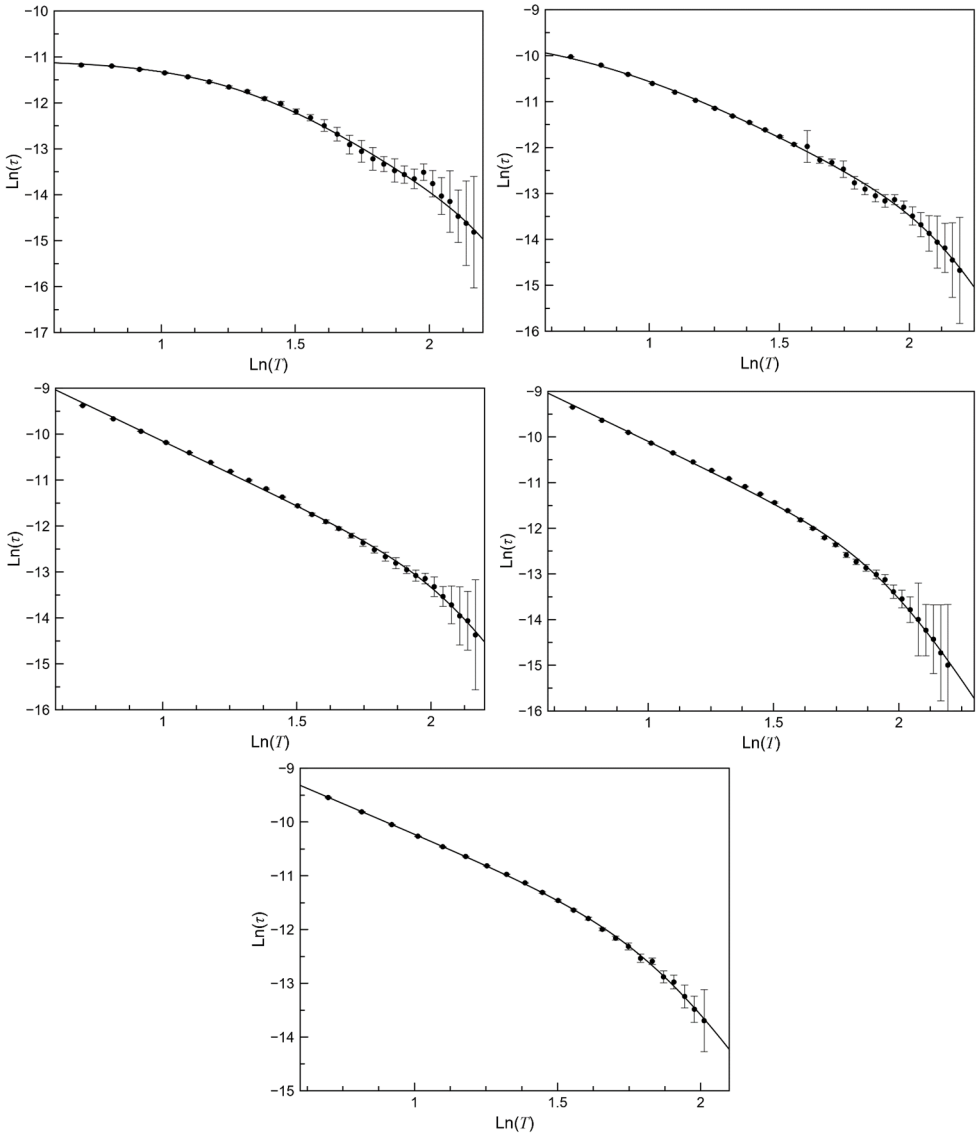

Figure A.118. Ln(τ) *vs* ln(T) plots for the main for the main process of **10-o** under 5.0 (top left), 2.5 (top right), 1.0 (middle left), 0.5 (middle right) and 0.25 kOe (bottom) applied static fields. The solid lines are the best fit-curves (see text). Standard deviations appear as vertical error bars.

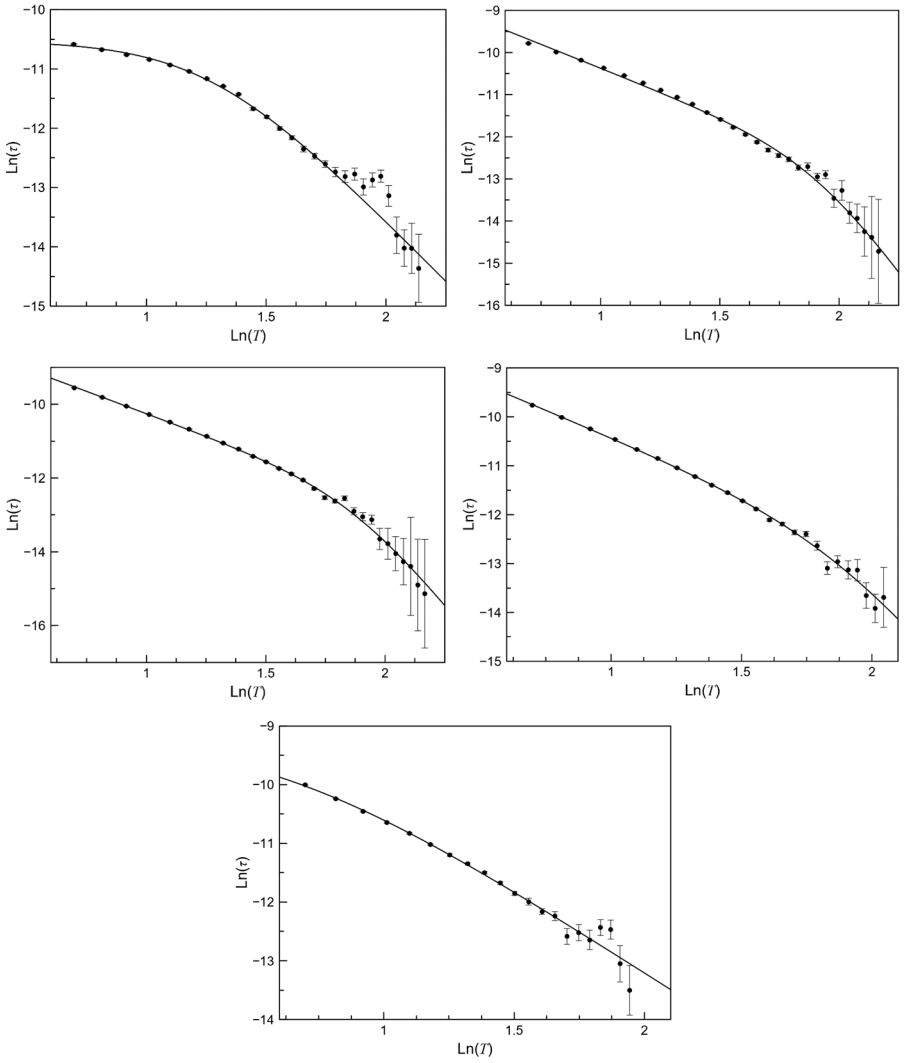

Figure A.119. Ln(τ) *vs* ln(T) plots for the main for the main process of **10-c** under 5.0 (top left), 2.5 (top right), 1.0 (middle left), 0.5 (middle right) and 0.25 kOe (bottom) applied static fields. The solid lines are the best fit-curves (see text). Standard deviations appear as vertical error bars.

Table A.29. Crystal data of compounds **9-o**, **9-c**, **10-o**.

Compound	9-o	10-o	9-c
Formula	$C_{73}H_{62}Cl_2Co_2N_8O_{12}S_2$	$C_{69}H_{54}Cl_2Co_2N_8O_{12}S_2$	$C_{87}H_{78}Cl_2Co_2N_8O_{12}S_2$
Formula weight [g mol^{-1}]	1496.23	1440.08	1680.45
Crystal system	Triclinic	Triclinic	Triclinic
Space group	P–1	P–1	P–1
a [Å]	15.095(8)	14.118(2)	13.514(2)
b [Å]	17.390(9)	16.333(2)	16.246(3)
c [Å]	18.633(9)	17.485(3)	19.950(2)
α [°]	78.044(9)	104.538(3)	71.939(13)
β [°]	78.722(9)	100.192(3)	86.917(13)
γ [°]	89.768(9)	90.673(3)	70.87(w)
V [Å^3]	4689(4)	3834.5(10)	3928.66(11)
Z	2	2	2
D_{calc} [g cm^{-3}]	1.0585	1.247	1.421
Temperature [K]	-	100	100
μ [mm^{-1}]	0.520	0.616	0.613
R (int)	-	0.060	0.0715
Reflections collected	-	81135	17888
Independent reflections	-	17603	
Number of observed reflections ($I_o > 2\sigma(I_o)$)	-	12130	11117
Number of parameters	-	926	1051
Goodness-of-fit *S* on F^2	-	1.02	1.05
R_1[a] [$I > 2.0\sigma(I)$]	-	0.0515	0.0694
wR_2[b] [$I > 2.0\sigma(I)$]	-	0.1466	0.1595

[a] $R_1 = \sum||F_o| - |F_c|| / \sum|F_o|$. [b] $wR_2 = \{\sum[w(F_o^2 - F_c^2)^2]/\sum w(F_o^2)^2\}^{1/2}$.

Table A.30. π−π interactions in **9-o**, **9-c** and **10-o**.

Compound	Cg···Cg[a]	Cg···Cg [Å]	α[b][°]	Cg···Cg[a]	Cg···Cg [Å]	α[b][°]
9-o						
	Cg5···Cg15	3.718(2)	5	Cg13···Cg15	3.6019(19)	1
	Cg7···Cg14	3.874(2)	5			
10-o						
	Cg5···Cg12	3.8731(17)	1.67(13)	Cg12···Cg12	3.7071(17)	0.00(13)
	Cg6···Cg13	3.809(2)	3.13(15)	Cg13···Cg13	3.902(2)	0.02(15)
	Cg8···Cg14	3.571(5)	2.7(4)	Cg14···Cg14	3.561(4)	0.0(4)
	Cg8···Cg17	3.917(6)	2.4(6)	Cg14···Cg16	3.732(7)	5.9(6)
	Cg8···Cg18	3.788(6)	1.1(5)	Cg14···Cg18	3.444(6)	2.7(5)
	Cg10···Cg15	3.5963(18)	1.83(14)	Cg18···Cg18	3.421(7)	0.0(6)
9-c						
	Cg9···Cg15	3.962(3)	4.1(2)	Cg15···Cg18	3.950(4)	16.1(3)
	Cg11···Cg16	3.903(2)	4.35(19)	Cg16···Cg16	3.544(3)	0.03(19)
	Cg15···Cg15	3.717(3)	0.0(2)			

[a] Cg are the six-membered rings: **9-o:** Cg5: N31, C32-C35, C44; Cg7: N51, C52-C55,C64; Cg13: C35-C38, C43, C44; Cg14: C55-C58, C63, C64; Cg15: C75-C78, C83, C84; **10-o**: Cg5: N42, C38-C41, C43; Cg6: N51, C52-C55, C64; Cg8: N71, C72-C75, C84; Cg10: N91, C92-C95, C104; Cg12: C35-C38, C43, C44; Cg13: C55-C58, C63, C64; Cg14: C75-C78, C83, C84; Cg18: C75′-C78′, C83′, C84′; **9-c**: Cg9: N82, C78-C81, C83; Cg11: N102, C98-C101, C103; Cg15: C75-C78, C83, C84; Cg16: C95-C98, C103, C104; Cg18: C501-C506.[b] α is the dihedral angle between each pair of mean ring planes.

Table A.31. Energy of the calculated quartet (D_Q) and doublet (D_D) excited states and their contributions to the *D* value for **9-o**, **9-c** and **10-o** obtained from CASSCF/NEVPT2 calculations.

Compound	*D*	|*E*/*D*|	D_Q[a]	D_D[a]	D_{Q1}	D_{Q2}	D_{Q1} + D_{Q2}
9-o							
Co1	+58.089	0.060	+48.476	+1.787	+27.597	+22.796	+50.393
Co2	+64.101	0.122	+54.220	+1.035	+32.612	+24.009	+56.621
9-c							
Co1	+65.192	0.260	+54.607	+1.486	+37.176	+18.648	+55.824
Co2	+58.537	0.223	+50.612	+1.186	+32.843	+19.550	+53.398
10-o							
Co1	+54.399	0.250	+46.236	+4.964	+30.409	+14.423	+44.832
Co2	+63.472	0.161	+52.525	+3.833	+31.152	+21.859	+53.011
Co2′	+59.934	0.131	+47.882	–2.451	+31.006	+25.157	+56.163

[a] D_Q and D_D are the sum of spin-orbit contributions that comes from quartet and doublet excited states.

Table A.32. Selected fits of ac-magnetic data at different dc-applied field for **9-o/c** and **10-o/c** through the Raman + IK models.

Compound	H^a (kOe)	n^b	C^b (s^{-1} K^{-n})	$\tau_0(1)^b \times 10^5$ (s)
9-o	0.25	2.74 ± 0.16	3483 ± 794	12 ± 5
	0.5	2.83 ± 0.09	2696 ± 386	21 ± 9
	1.0	2.65 ± 0.05	2805 ± 219	14 ± 18
	2.5	2.86 ± 0.03	1719 ± 91	8.5 ± 0.4
	5.0	4.40 ± 0.06	147 ± 17	1.72 ± 0.03
9-c	0.25	2.19 ± 0.11	3885 ± 691	4.9 ± 0.5
	0.5	2.42 ± 0.16	2554 ± 686	6.4 ± 1.2
	1.0	2.62 ± 0.13	1725 ± 376	8.0 ± 1.3
	2.5	2.22 ± 0.05	3142 ± 248	13.5 ± 1.6
	5.0	3.30 ± 0.15	512 ± 131	2.49 ± 0.11
10-o	0.25	2.69 ± 0.09	1600 ± 222	27 ± 7
	0.5	2.99 ± 0.11	1016 ± 164	28 ± 7
	1.0	3.13 ± 0.06	919 ± 86	26 ± 4
	2.5	3.11 ± 0.13	1093 ± 242	7.4 ± 1.1
	5.0	4.03 ± 0.09	321 ± 51	1.55 ± 0.05
10-c	0.25	2.99 ± 0.05	1451 ± 133	8.9 ± 0.8
	0.5	3.08 ± 0.07	1162 ± 136	12.7 ± 1.6
	1.0	2.99 ± 0.06	1136 ± 101	19.1 ± 2.2
	2.5	3.03 ± 0.10	1011 ± 144	10.3 ± 0.9
	5.0	4.19 ± 0.07	179 ± 21	2.66 ± 0.06

Table A.33. Selected fits of ac-magnetic data at different dc-applied field for **9-o** obtained from the ln(τ) *vs* 1/T plots.

H_{dc} (kOe)\Model[a]	$\tau_{0,IK} \times 10^3$ (s)	$\tau_{0,IK} \times 10^5$ (s)	$\tau_{0,LT} \times 10^7$ (s)	E_{aLT} (cm^{-1})	$\tau_{0,MT} \times 10^9$ (s)	E_{aMT} (cm^{-1})
250						
Global	–	5.9 ± 2.0	9 ± 3	6.1 ± 1.0	1.1 ± 0.9	30 ± 3
Process 1	–	–	–	–	–	–
Process 2	–	–	–	–	–	–
500						
Global	–	6.6 ± 1.8	5.8 ± 1.5	7.3 ± 0.8	0.013 ± 0.011	51 ± 4
Process 1	–	–	–	–	–	–
Process 2	–	–	–	–	–	–
1000						
Global	–	8.8 ± 1.8	7.5 ± 1.5	7.2 ± 0.6	0.26 ± 0.11	41.0 ± 2.1
Process 1	–	–	–	–	–	–
Process 2	–	–	–	–	–	–
2500						
Global	–	–	–	–	–	–
Process 1	–	5.1 ± 0.6	8.4 ± 1.5	7.5 ± 0.5	1.3 ± 0.4	35.2 ± 1.6
Process 2	3.6 ± 0.8	–	–	–	–	–
5000						
Global	–	–	–	–	–	–
Process 1	–	1.70 ± 0.54	5.2 ± 2.4	9.7 ± 1.2	5.9 ± 2.1	28.0 ± 2.2
Process 2	7 ± 3	–	–	–	–	–

[a] Global is the analysis considering only one general Debye model, and Processes 1 + 2 are the analyses with the sum of two individual Debye models (equations 5 and 6). All data were analysed by a combination of several TA relaxations plus one IK mechanism.

Table A.34. Selected fits of ac-magnetic data at different dc-applied field for **9-c** obtained from the ln(τ) *vs* 1/T plots.

H_{dc} (kOe)\Model[a]	$\tau_{0,IK} \times 10^3$ (s)	$\tau_{0,IK} \times 10^5$ (s)	$\tau_{0,LT} \times 10^7$ (s)	E_{aLT} (cm^{-1})	$\tau_{0,MT} \times 10^9$ (s)	E_{aMT} (cm^{-1})	$\tau_{0,HT} \times 10^{11}$ (s)	E_{aHT} (cm^{-1})
250								
Global	–	3.4 ± 0.4	20 ± 5	5.4 ± 1.0	9 ± 4	28 ± 3	–	–
Process 1	–	–	–	–	–	–	–	–
Process 2	–	–	–	–	–	–	–	–
500								
Global	–	5.5 ± 1.2	22 ± 5	5.3 ± 0.7	1.2 ± 0.7	37 ± 3	–	–
Process 1	–	–	–	–	–	–	–	–
Process 2	–	–	–	–	–	–	–	–
1000								
Global	–	5.7 ± 0.8	14.0 ± 2.5	6.8 ± 0.6	–	–	9 ± 4	51 ± 3
Process 1	–	–	–	–	–	–	–	–
Process 2	–	–	–	–	–	–	–	–
2500								
Global	–	5.5 ± 0.5	13.1 ± 1.8	7.1 ± 0.5	–	–	33 ± 14	50.3 ± 2.4
Process 1	–	–	–	–	–	–	–	–
Process 2	–	–	–	–	–	–	–	–
5000								
Global	–	–	–	–	–	–	–	–
Process 1	–	2.33 ± 0.14	9 ± 3	8.8 ± 0.9	–	–	24 ± 11	48 ± 3
Process 2	4.3 ± 1.5	–	–	–	–	–	–	–

[a] Global is the analysis considering only one general Debye model, and Processes 1 + 2 are the analyses with the sum of two individual Debye models (equations 5 and 6). All data were analysed by a combination of several TA relaxations plus one IK mechanism.

Table A.35. Selected fits of ac-magnetic data at different dc-applied field for **10-o** obtained from the ln(τ) *vs* 1/*T* plots.

H_{dc} (kOe)\Model[a]	$\tau_{0,IK} \times 10^3$ (s)	$\tau_{0,IK} \times 10^5$ (s)	$\tau_{0,LT} \times 10^7$ (s)	E_{aLT} (cm^{-1})	$\tau_{0,MT} \times 10^9$ (s)	E_{aMT} (cm^{-1})
250						
Global	–	13 ± 3	20 ± 4	6.1 ± 0.6	8 ± 3	28.0 ± 1.8
Process 1	–	–	–	–	–	–
Process 2	–	–	–	–	–	–
500						
Global	–	16 ± 4	18 ± 4	6.4 ± 0.6	8.1 ± 2.2	27.8 ± 1.5
Process 1	–	–	–	–	–	–
Process 2	–	–	–	–	–	–
1000						
Global	–	12.8 ± 1.8	10.7 ± 2.3	7.6 ± 0.6	12 ± 4	27.6 ± 2.0
Process 1	–	–	–	–	–	–
Process 2	–	–	–	–	–	–
2500						
Global	–	–	–	–	–	–
Process 1	–	5.8 ± 1.0	10 ± 3	7.3 ± 1.0	6 ± 3	30 ± 3
Process 2	–	–	133 ± 50	9.5 ± 0.9	–	–
5000						
Global	–	–	–	–	–	–
Process 1	–	1.41 ± 0.06	2.4 ± 1.4	11.2 ± 1.6	3.7 ± 2.1	31 ± 4
Process 2	–	–	78.8 ± 7	10.66 ± 0.24	–	–

[a] Global is the analysis considering only one general Debye model, and Processes 1 + 2 are the analyses with the sum of two individual Debye models (equations 5 and 6). All data were analysed by a combination of several TA relaxations plus one IK mechanism.

Table A.36. Selected fits of ac-magnetic data at different dc-applied field for **10-c** obtained from the ln(τ) *vs* 1/*T* plots.

H_{dc} (kOe)\Model[a]	$\tau_{0,IK} \times 10^3$ (s)	$\tau_{0,IK} \times 10^5$ (s)	$\tau_{0,LT} \times 10^7$ (s)	E_{aLT} (cm^{-1})	$\tau_{0,MT} \times 10^9$ (s)	E_{aMT} (cm^{-1})
250						
Global	–	5.7 ± 1.2	8 ± 3	7.7 ± 1.2	5.7 ± 1.2	33 ± 9
Process 1	–	–	–	–	–	–
Process 2	–	–	–	–	–	–
500						
Global	–	7.8 ± 1.0	8.9 ± 2.3	7.6 ± 0.7	7 ± 4	29 ± 3
Process 1	–	–	–	–	–	–
Process 2	–	–	–	–	–	–
1000						
Global	–	11 ± 3	13 ± 6	7.0 ± 1.3	7 ± 5	29 ± 4
Process 1	–	–	–	–	–	–
Process 2	–	–	–	–	–	–
2500						
Global	–	–	–	–	–	–
Process 1	–	7.0 ± 0.6	11 ± 3	7.6 ± 0.6	5.2 ± 1.5	29.8 ± 1.7
Process 2	–	–	702 ± 63	5.8 ± 1.1	–	–
5000						
Global	–	–	–	–	–	–
Process 1	–	2.50 ± 0.11	4 ± 3	10.6 ± 1.6	7 ± 4	29 ± 4
Process 2	15 ± 3	–	–	–	–	–

[a] Global is the analysis considering only one general Debye model, and Processes 1 + 2 are the analyses with the sum of two individual Debye models (equations 5 and 6). All data were analysed by a combination of several TA relaxations plus one IK mechanism.

Table A.37. Selected fits of ac-magnetic data at different dc-applied field of **9-o** obtained from the ln(τ) *vs* ln(T) plots.

H_{dc} (kOe)\Model[a]	$\tau_{0,IK} \times 10^5$ (s)	$A_{LT} \times 10^{-2}$ (s^{-1} K^{-nLT})	n_{LT}	A_{HT} (s^{-1} K^{-nHT})	n_{HT}
250					
Global	–	68 ± 8	2.21 ± 0.13	0.2 ± 0.3	8.3 ± 0.9
500					
Global	–	44 ± 6	2.46 ± 0.12	0.0002 ± 0.0004	11.9 ± 1.0
1000					
Global	–	32 ± 3	2.54 ± 0.10	0.003 ± 0.006	10.0 ± 1.0
2500					
Global	–	57 ± 5	2.00 ± 0.09	0.5 ± 0.5	7.2 ± 0.5
5000					
Global	1.85 ± 0.14	4 ± 5	3.6 ± 1.2	1 ± 6	7 ± 3

[a] Global is the analysis considering only one general Debye model. All data were analysed by a combination of several Raman relaxations and one IK mechanism.

Table A.38. Selected fits of ac-magnetic data at different dc-applied field of **9-c** obtained from the ln(τ) *vs* ln(T) plots.

H_{dc} (kOe)\Model[a]	$\tau_{0,IK} \times 10^5$ (s)	$A_{LT} \times 10^{-2}$ (s^{-1} K^{-nLT})	n_{LT}	A_{HT} (s^{-1} K^{-nHT})	n_{HT}
250					
Global	–	180 ± 100	1.0 ± 0.7	40 ± 160	4.6 ± 1.7
500					
Global	–	97 ± 8	1.56 ± 0.08	0.013 ± 0.0018	8.9 ± 0.7
1000					
Global	–	61 ± 6	1.82 ± 0.08	0.0003 ± 0.0004	10.7 ± 0.7
2500					
Global	1.7 ± 1.3	37 ± 4	2.12 ± 0.22	0.00004 ± 0.00006	11.5 ± 0.8
5000					
Global	3.1 ± 0.6	22 ± 18	2.3 ± 0.5	0.01 ± 0.01	9.0 ± 0.8

[a] Global is the analysis considering only one general Debye model. All data were analysed by a combination of several Raman relaxations and one IK mechanism.

Table A.39. Selected fits of ac-magnetic data at different dc-applied field of **10-o** obtained from the ln(τ) *vs* ln(T) plots.

H_{dc} (kOe)\Model[a]	$\tau_{0,IK} \times 10^5$ (s)	$A_{LT} \times 10^{-2}$ (s^{-1} K^{-nLT})	n_{LT}	A_{HT} (s^{-1} K^{-nHT})	n_{HT}
250					
Global	–	28.6 ± 1.8	2.26 ± 0.06	0.06 ± 0.05	8.0 ± 0.4
500					
Global	–	17.3 ± 1.4	2.64 ± 0.07	0.009 ± 0.008	8.8 ± 0.4
1000					
Global	–	15.7 ± 1.0	2.79 ± 0.05	0.0014 ± 0.0022	9.4 ± 0.7
2500					
Global	7.6 ± 2.2	12 ± 5	3.05 ± 0.25	0.0001 ± 0.0005	10.5 ± 1.8
5000					
Global	1.56 ± 0.05	3.2 ± 0.5	4.03 ± 0.08	–	–

[a] Global is the analysis considering only one general Debye model. All data were analysed by a combination of several Raman relaxations and one IK mechanism.

Table A.40. Selected fits of ac-magnetic data at different dc-applied field of **10-c** obtained from the ln(τ) *vs* ln(T) plots.

H_{dc} (kOe)\Model[a]	$\tau_{0,IK} \times 10^5$ (s)	$A_{LT} \times 10^{-2}$ (s^{-1} K^{-nLT})	n_{LT}	A_{HT} (s^{-1} K^{-nHT})	n_{HT}
250					
Global	10.4 ± 1.2	18.0 ± 2.0	2.86 ± 0.07	–	–
500					
Global	–	36 ± 9	2.2 ± 0.3	1 ± 3	6.6 ± 1.3
1000					
Global	–	25.6 ± 2.2	2.40 ± 0.08	0.05 ± 0.05	8.1 ± 0.5
2500					
Global	–	33 ± 4	2.26 ± 0.11	0.04 ± 0.06	8.1 ± 0.6
5000					
Global	–	2.0 ± 0.3	4.12 ± 0.12	–	–

[a] Global is the analysis considering only one general Debye model. All data were analysed by a combination of several Raman relaxations and one IK mechanism.

SI Chapter VI

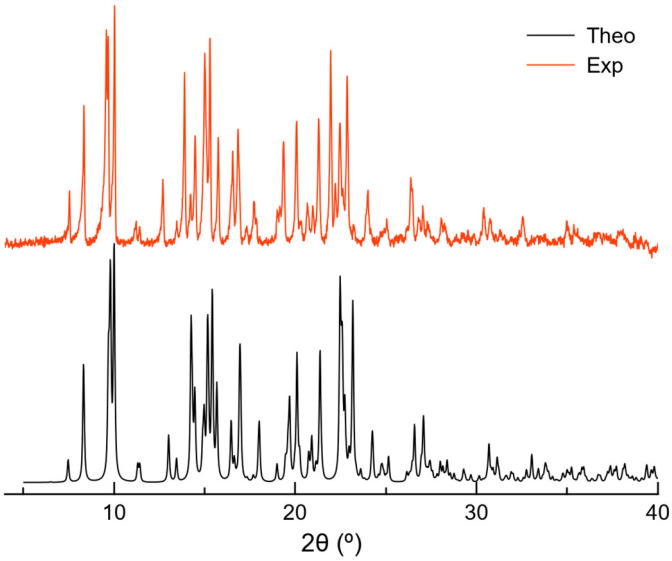

Figure A.120. Experimental and simulated powder X-ray diffraction patterns of **11**.

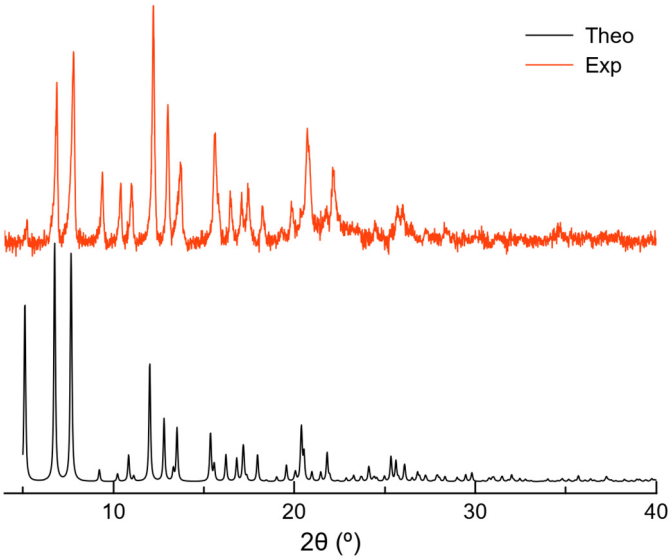

Figure A.121. Experimental and simulated powder X-ray diffraction patterns of **12**.

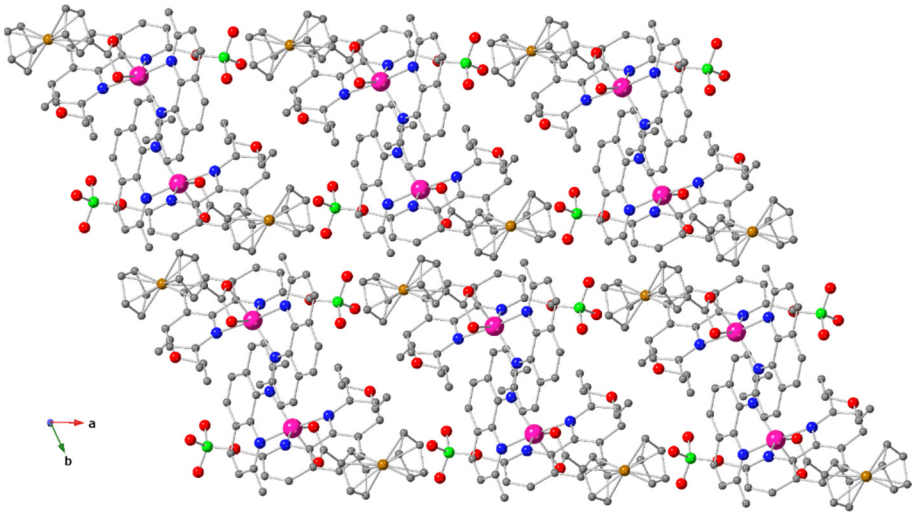

Figure A.122. Perspective view along the *a*-axis of the crystal structure of **11**. Hydrogen atoms are omitted for clarity. Colour code: magenta, cobalt; blue, nitrogen; red, oxygen; grey, carbon; green, chlorine; brown, iron.

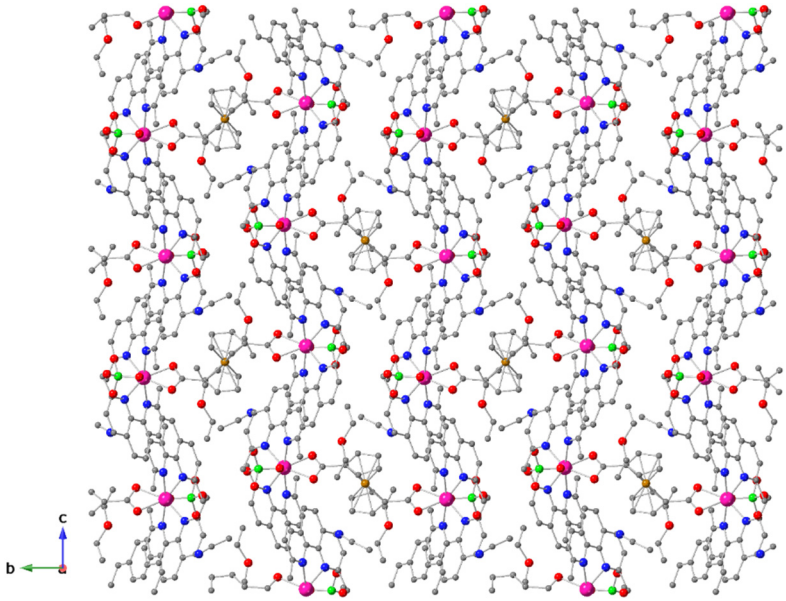

Figure A.123. Perspective view along the *a*-axis of the crystal structure of **12**. Hydrogen atoms are omitted for clarity. Colour code: magenta, cobalt; blue, nitrogen; red, oxygen; grey, carbon; green, chlorine; brown, iron.

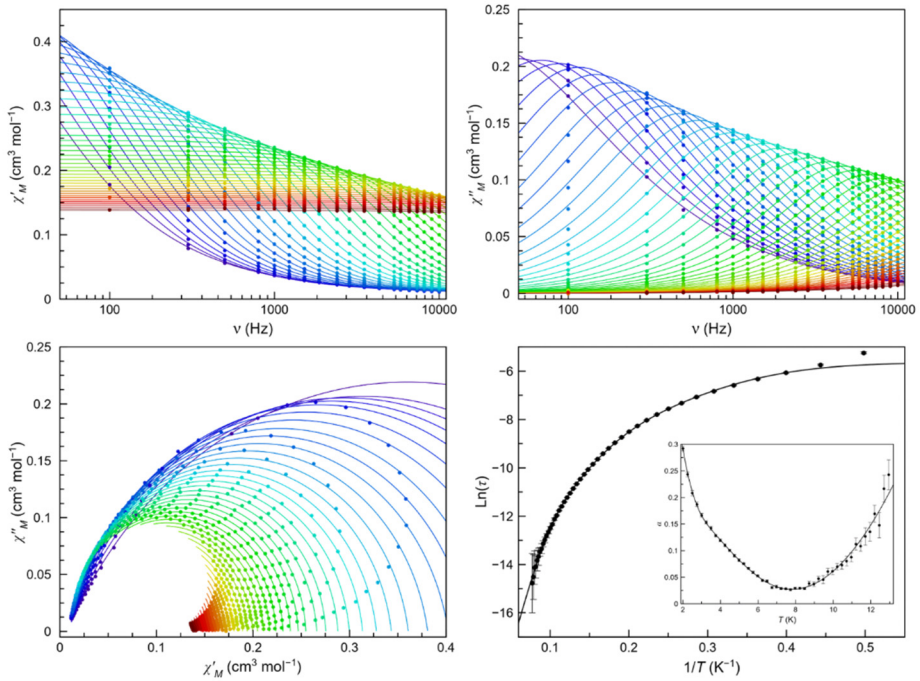

Figure A.124. Frequency dependence of χ_M' (top left) and χ_M'' (top right), Cole-Cole plots (bottom left) and Arrhenius plots of **11** (bottom right) in a dc-applied static field of 2.5 kOe with ± 0.005 kOe oscillating field in the temperature range of 2.0–13.0 K (purple to green gradient). Thermal dependence of α is included on the bottom right figure as an inset, where the black line are eye-guides. Standard deviation appears as vertical error bars.

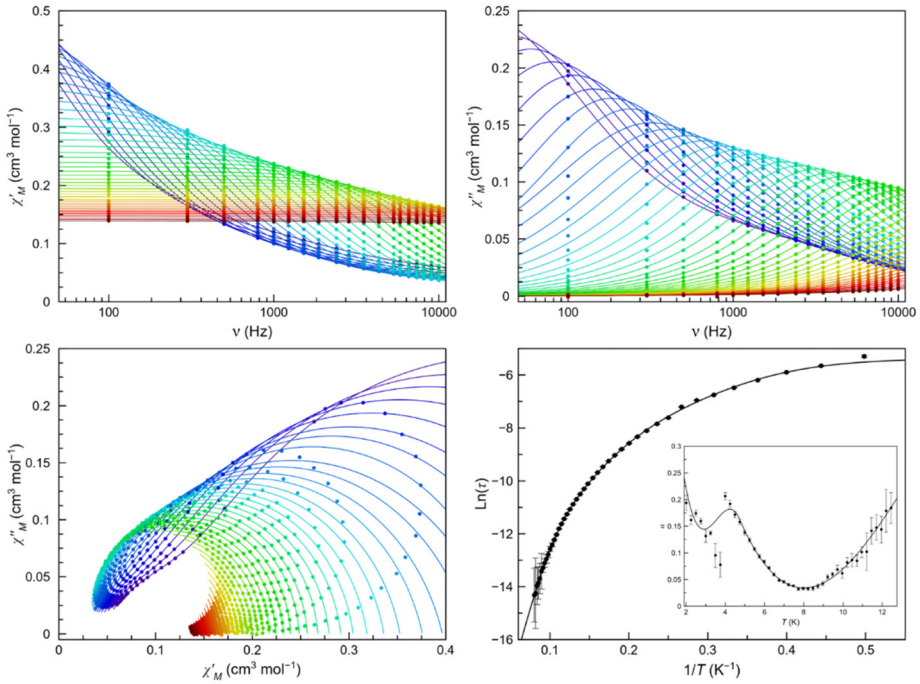

Figure A.125. Frequency dependence of χ_M' (top left) and χ_M'' (top right), Cole-Cole plots (bottom left) and Arrhenius plots of **11** (bottom right) in a dc-applied static field of 1.0 kOe with ± 0.005 kOe oscillating field in the temperature range of 2.0–13.0 K (purple to green gradient). Thermal dependence of α is included on the bottom right figure as an inset, where the black line are eye-guides. Standard deviation appears as vertical error bars.

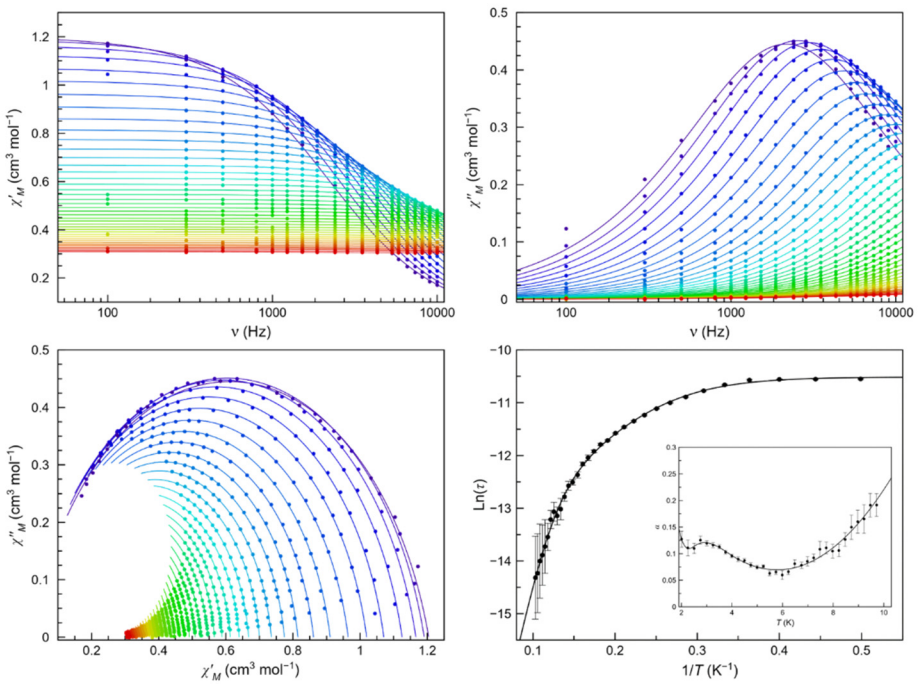

Figure A.126. Frequency dependence of χ_M' (top left) and χ_M'' (top right), Cole-Cole plots (bottom left) and Arrhenius plots of **12** (bottom right) in a dc-applied static field of 2.5 kOe with ± 0.005 kOe oscillating field in the temperature range of 2.0–12.0 K (purple to green gradient). Thermal dependence of α is included on the bottom right figure as an inset, where the black line are eye-guides. Standard deviation appears as vertical error bars.

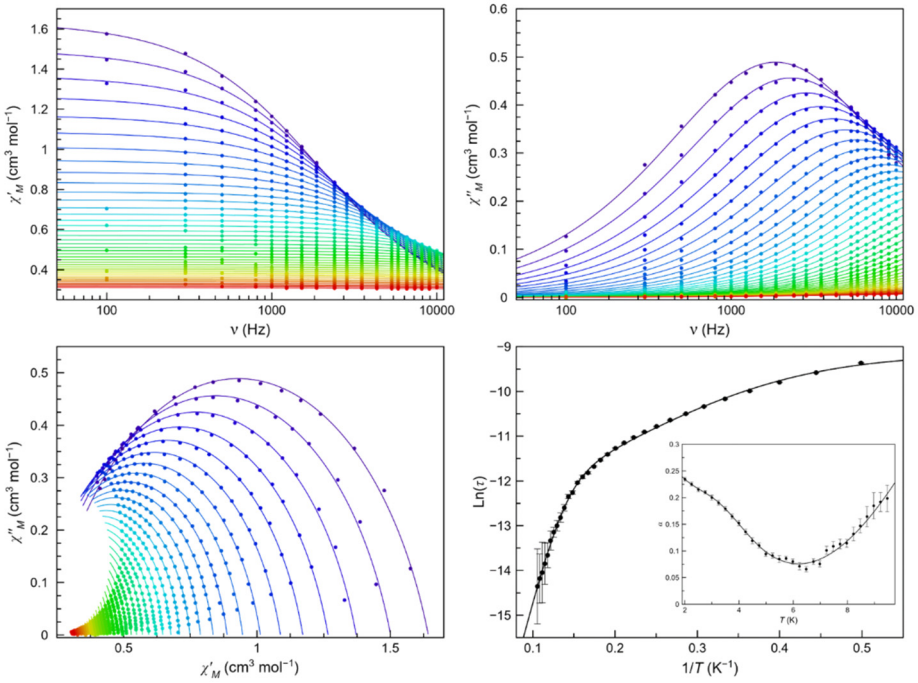

Figure A.127. Frequency dependence of χ_M' (top left) and χ_M'' (top right), Cole-Cole plots (bottom left) and Arrhenius plots of **12** (bottom right) in a dc-applied static field of 1.0 kOe with ± 0.005 kOe oscillating field in the temperature range of 2.0–12.0 K (purple to green gradient). Thermal dependence of α is included on the bottom right figure as an inset, where the black line are eye-guides. Standard deviation appears as vertical error bars.

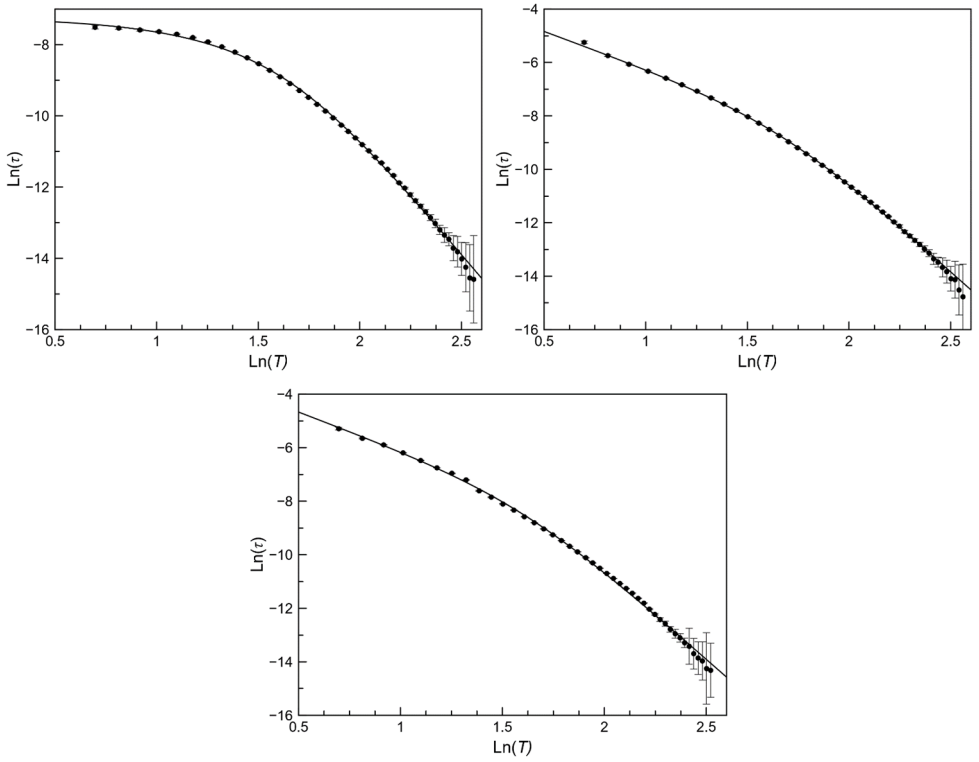

Figure A.128. Ln(τ) *vs* ln(T) plots for the main for the main process of **11** under 5.0 (top left), 2.5 (top right) and 1.0 kOe (bottom) applied static fields. The solid lines are the best fit-curves (see text). Standard deviations appear as vertical error bars.

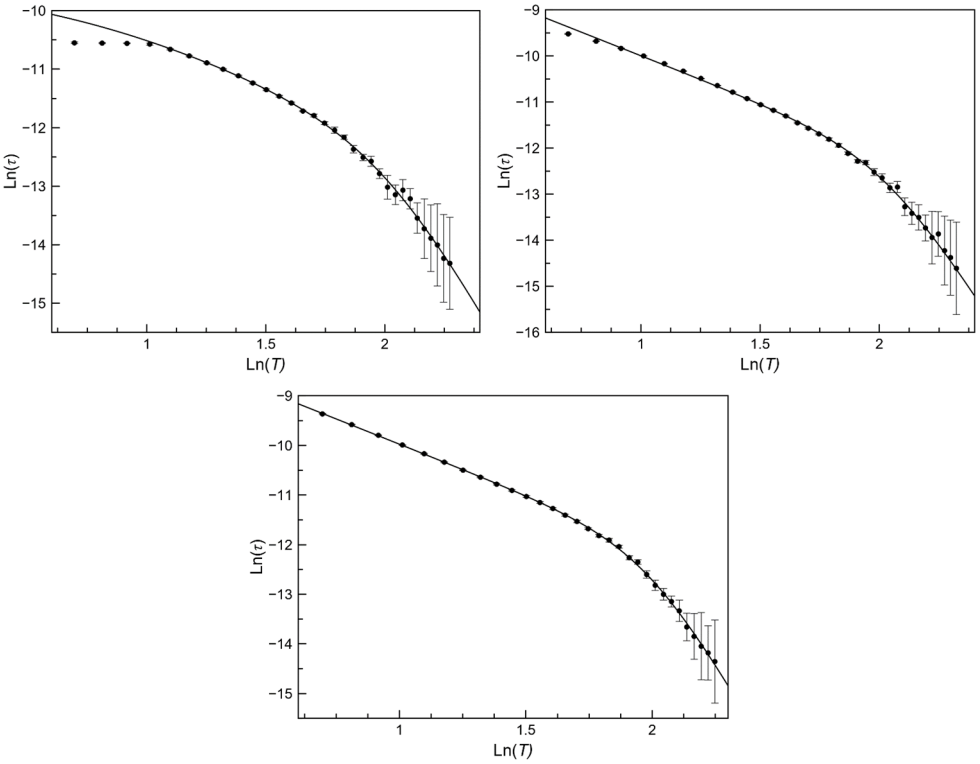

Figure A.129. Ln(τ) *vs* ln(T) plots for the main for the main process of **12** under 5.0 (top left), 2.5 (top right) and 1.0 kOe (bottom) applied static fields. The solid lines are the best fit-curves (see text). Standard deviations appear as vertical error bars.

Table A.41. Crystal data of compounds **11** and **12**.

Compound	11	12
Formula	$C_{43}H_{43}ClCoFeN_4O_7$	$C_{80}H_{82}Cl_2Co_2FeN_{10}O_{14}$
Formula weight [g mol^{-1}]	878.04	1652.17
Crystal system	Triclinic	monoclinic
Space group	P−1	$P2_1/n$
a [Å]	12.0366(7)	13.163(4)
b [Å]	13.2547(8)	18.253(6)
c [Å]	13.8084(8)	16.304(5)
α [°]	84.359(5)	90
β [°]	79.775(5)	104.542(8)
γ [°]	63.097(6)	90
V [Å^3]	1933.0(2)	3792(2)
Z	2	2
D_{calc} [g cm^{-3}]	1.509	1.447
Temperature [K]	293	120
μ [mm^{-1}]	0.932	0.764
R (int)	0.124	0.171
Reflections collected	16383	40385
Independent reflections	6806	4623
Number of observed reflections ($I_o > 2\sigma(I_o)$)	4470	3121
Number of parameters	520	500
Goodness-of-fit *S* on F^2	1.42	1.60
R_1[a] [$I > 2.0\sigma(I)$]	0.0925	0.1393
wR_2[b] [$I > 2.0\sigma(I)$]	0.3815	0.4129

[a] $R_1 = \sum||F_o| - |F_c|| / \sum|F_o|$. [b] $wR_2 = \{\sum[w(F_o^2 - F_c^2)^2]/\sum w(F_o^2)^2\}^{1/2}$

Table A.42. Selected fit of ac-magnetic data at different dc-applied field of **11** obtained from the ln(τ) vs 1/T plots.

H_{dc} (kOe)\Model[a]	$\tau_{0,IK} \times 10^4$ (s)	$\tau_{0,LT} \times 10^5$ (s)	E_{aLT} (cm^{-1})	$\tau_{0,MT} \times 10^7$ (s)	E_{aMT} (cm^{-1})	$\tau_{0,HT} \times 10^{10}$ (s)	E_{aHT} (cm^{-1})
1000							
Global	46 ± 5	1.4 ± 0.5	10.8 ± 0.8	1.1 ± 0.4	29.8 ± 1.9	1.0 ± 0.3	77 ± 3
2500							
Global	36.0 ± 2.2	1.5 ± 0.3	10.6 ± 0.5	0.71 ± 0.15	31.8 ± 1.3	0.65 ± 0.03	82 ± 3
5000							
Global	5.57 ± 0.17	1.35 ± 0.13	10.70 ± 0.10	1.07 ± 0.20	29.0 ± 1.1	0.71 ± 0.03	80.03 ± 0.16

[a] Global is the analysis considering only one general Debye model. All data were analysed by a combination of several TA relaxations plus one IK mechanism.

Table A.43. Selected fits of ac-magnetic data at different dc-applied field of **11** obtained from the ln(τ) vs ln(T) plots.

H_{dc} (kOe)\Model[a]	$\tau_{0,IK} \times 10^4$ (s)	A_{LT} (s^{-1} K^{-nLT})	n_{LT}	$A_{HT} \times 10^2$ (s^{-1} K^{-nHT})	n_{HT}
1000					
Global	–	25.0 ± 3	2.87 ± 0.10	4.62 ± 0.01	6.78 ± 0.08
2500					
Global	–	31.0 ± 1.8	2.79 ± 0.06	3.4 ± 0.4	6.87 ± 0.06
5000					
Global	7.1 ± 0.3	44 ± 3	2.702 ± 0.014	4.3 ± 0.7	6.80 ± 0.08

[a] Global is the analysis considering only one general Debye model. All data were analysed by a combination of several Raman relaxations and one IK mechanism.

Table A.44. Selected fits of ac-magnetic data at different dc-applied field of **12** obtained from the ln(τ) vs 1/T plots.

H_{dc} (kOe)\Model[a]	$\tau_{IK} \times 10^5$ (s)	$\tau_{0,LT} \times 10^6$ (s)	E_{aLT} (cm^{-1})	$\tau_{0,HT} \times 10^{10}$ (s)	E_{aHT} (cm^{-1})
1000					
Global	10.5 ± 0.7	1.65 ± 0.14	7.6 ± 0.3	3.7 ± 0.7	49.2 ± 1.2
2500					
Global	7.8 ± 0.5	1.08 ± 0.16	9.0 ± 0.5	5.8 ± 1.8	48.9 ± 2.1
5000					
Global	2.72 ± 0.10	0.43 ± 0.11	12.1 ± 0.9	5 ± 3	50 ± 4

[a] Global is the analysis considering only one general Debye model. All data were analysed by a combination of several TA relaxations plus one IK mechanism.

Table A.45. Selected fits of ac-magnetic data at different dc-applied field of **12** obtained from the ln(τ) vs ln(T) plots.

H_{dc} (kOe)\Model[a]	$\tau_{0,IK} \times 10^4$ (s)	A_{LT} (s^{-1} K^{-nLT})	n_{LT}	$A_{HT} \times 10^4$ (s^{-1} K^{-nHT})	n_{HT}
1000					
Global	–	2810 ± 120	2.03 ± 0.03	28 ± 13	8.96 ± 0.21
2500					
Global	–	2820 ± 230	2.05 ± 0.07	87 ± 84	8.3 ± 0.4
5000					
Global	7.1 ± 0.3	2880 ± 240	2.1 ± 0.5	796 ± 64	7.3 ± 0.4

[a] Global is the analysis considering only one general Debye model. All data were analysed by a combination of several Raman relaxations and one IK mechanism.

Appendix B

Reader Guidelines

For those who wants to take a brief look into the basics. This way it might be easier to follow the concepts across the dissertation.

Classic Magnetism

What is magnetism?

In classical magnets, magnetism can be seen as a force of attraction or repulsion, which travels through a vacuum, between two objects. The reason of this force is quite peculiar, and it is assigned to atomic composition of the matter and, particularly, to the electrons. These charged particles are moving, thus, they originate a magnetic field and an electrostatic field also.

Inside a material, the electrons are usually paired up, becoming a diamagnetic material, which is repelled by an external magnetic field. However, sometimes the materials are attracted by an external magnetic field, and that is because the electrons within the material are not totally paired up, some of them are unpaired. The force of attraction can be quantified with a balance under a magnetic field, *i.e.*, the variation of mass observed can be related with their magnetic moments. Why there are materials that can be either attracted or repelled by a magnetic field? Well, this is more complex and it is the reason why magnetism is a very active research topic. Nevertheless, the answer is rather simple: magnetic interactions. But first, we will discuss about the atom and the spin first.

B.1.1 The atom and the spin

As a reminder, atoms compose matter and elementary particles compose atoms but these cannot be fully explained with classical models. Light travels in small and quantified packets of energy as Max Plank observed, and Louis De Broglie demonstrated that every particle behave as a particle or as a wave. These facts were stunning in the scientific era.

"It seems as though we must use sometimes the one theory and sometimes the other, while at times we may use either. We are faced with a new kind of difficulty. We have two contradictory pictures of reality; separately neither of them fully explains the phenomena of light, but together they do."

Albert Einstein and Leopold Infeld, The Evolution of Physics, pg. 262-263.

Erwin Schrödinger developed and postulated the first model which could describe both "pictures of reality" in one, the Schrödinger equation, and thus the quantum theory was born. This theory is used for understanding quantum systems and the discrete solutions for the Schrödinger equation describe each one. These solutions are known as *quantum numbers*.

One very important quantum number is called the "spin", which was found to be an intrinsic property for every elementary particle. The spin is a vector that defines the "orbital angular momentum" of the particle and, it can be seen as a "dipolar magnetic moment" that generates a small magnetic field. The spin can be represented by only two

values: $\frac{1}{2}$ and $-\frac{1}{2}$, also called spin up and spin down (Figure B.1). Thus, since its vector nature, two different spins can cancel out (sum of vectors equals to zero) in proper conditions.

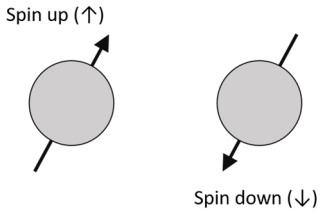

Figure B.1. Classical representation for two electrons with spin up and spin down magnetic moments.

Inside an atom, there is an equal amount of electrons and protons (spin differs from zero), but the electron has a magnetic moment ~1000 to 10000 times greater than the proton, which means electrons are "stronger magnets" than protons. Therefore, the magnetic properties of the matter are directly dependent on their electronic configuration, which can be described with multiple quantum numbers. These define each energy level of the electron in the free atom/ion, or in other words, they describe where the electron is mostly probable to be localised around the nuclei. This means that electrons can be distributed in specific ways, but they have to obey the Hund's Rule and the Pauli's exclusion principle: in a degenerated system (multiple levels with the same energy), electrons are forced to remain unpaired until there are plenty electrons in the same energy level. All these conditions allow us to identify the principal quantum numbers for an electron which defines its energy state (orbital); the principal quantum number ($n > 0$), the orbital angular momentum quantum number ($0 < l < n$), the magnetic quantum number ($-l < m_l < l$), and the electron spin quantum number ($m_s = \pm\frac{1}{2}$).

Free electrons are often located on a paramagnetic atom and less frequently encountered in organic radicals. The magnetic behaviour of the electron depends on the orbital where the electron is located at, being more decisive in the case of paramagnetic atoms. The more free electrons a paramagnetic atom has, the higher the total spin is, which means it might have more remarked properties.

B.1.2 Magnetic interactions

A paramagnetic material contains many unpaired electrons but, if there are not magnetic interactions among them, they do not "feel" each other. This means that every spin (vector like) will be randomly oriented and they will cancel each other out, exhibiting no magnet behaviour. Nevertheless, when the material is placed inside a strong magnetic field, the spins will turn and orient themselves parallel to the external field, giving rise to the appearance of a magnetisation M (Figure B.2). However, when the magnetic field is

removed, the thermal energy of the system will turn the spins back to a random distribution and the magnetisation becomes zero.

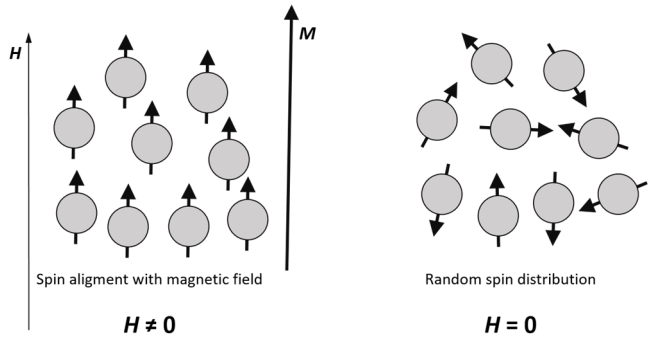

Figure B.2. Representation of spins oriented in a magnetic field that become randomly organised when the field disappears.

When magnetic interactions are present, the spins of different atoms "feel" each other and the system will look for the more stable configuration. Sometimes the stability is reached when the spin momentum of two different atoms lie parallel to each other, known as ferromagnetism. Other times, the stability appears when the spins lie antiparallel to each other, known as antiferromagnetism. Some other times, the stability surges when they lie parallel but a little bit tilted, known as spin canting. In all cases, there is a magnetic ordering when the interactions grown along a 3D network. The parameter that measures the interaction strength is called coupling constant J. Considering the Heisenberg spin Hamiltonian $\widehat{H} = -J\widehat{S_1}\widehat{S_2}$, if J is negative the coupling is antiferromagnetic and if J is positive the coupling is ferromagnetic. Greater values of $|J|$ is related to a stronger exchange coupling.

Usually, the spins of the different atoms are equally balanced so that the local spin momenta in an antiferromagnetic system cancel each other out, giving a total spin of zero. In a ferromagnetic system, the contribution of each momentum adds up, providing an infinite theoretical contribution. There is an exception, known as ferrimagnetism, where different spin momenta lie antiparallel, but they are not equally balanced resembling softer ferromagnetism.

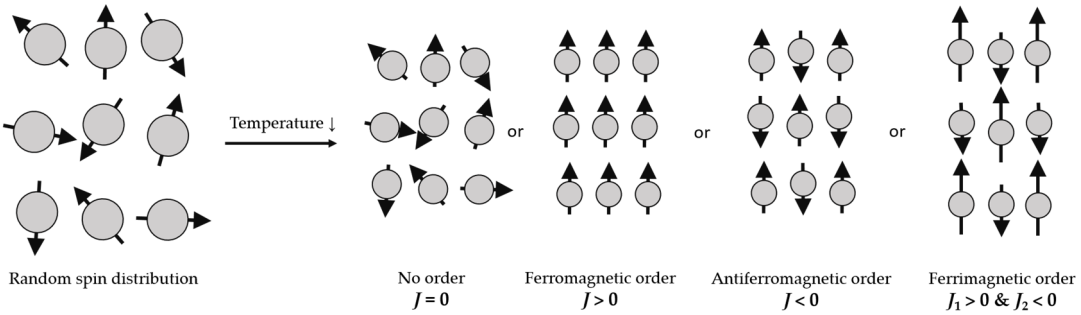

Figure B.3. Representation for the most common magnetic exchange interactions among different spin systems.

Additionally, these interactions have to overcome the thermal agitation, which leads to a non-ordered system, as indicated above. Then, they can be only detected when the effect of the magnetic coupling exceeds to that of thermal energy; only this way a magnetic ordering can be achieved.

Nowadays, these mentioned properties are measured and evaluated in the Super-Quantum Interference Device (SQUID), which measures the total magnetic moment (magnetic response) of the sample at a specific field, sweeping through the temperature domain down to 1.8 K (DC measurements). This way, if there is a sudden increase or decrease of the magnetic susceptibility (deviation of the Curie law), it is almost certain a magnetic interaction is involved (although other phenomena should not be ruled out, *e.g.*, depopulation of Kramers doublets). In some cases, samples at low temperatures under a strong applied magnetic field becomes almost fully magnetised. Then, the magnetisation value remains almost constant while sweeping the magnetic field, causing a drop on the χ value, also known as blockage of the magnetisation ($\chi = \frac{\partial M}{\partial H}$, where χ is the magnetic susceptibility, M is the magnetisation value and H is the external applied magnetic field).

B.1.3 Magnets

The first discovered magnet was the magnetite (Fe_3O_4) which is a ferrimagnetic system. In this case, the entire piece of material works as a magnet, meaning that its size is quite large. Unfortunately, a single-domain magnet is thermodynamically unstable, which leads the system to fragmentation into smaller magnetic domains separated by thin boundaries, reaching an equilibrium. This fragmentation reduces the magnetic strength of the material since each domain is a small and randomly oriented ferromagnet. In the case of multi-domain ferri/ferromagnetic systems, the application of an external magnetic field forces the ordering of the spins in the system, breaking the boundaries and creating a single domain at expenses of energy until the saturation of the magnetisation is reached (Figure B.4).

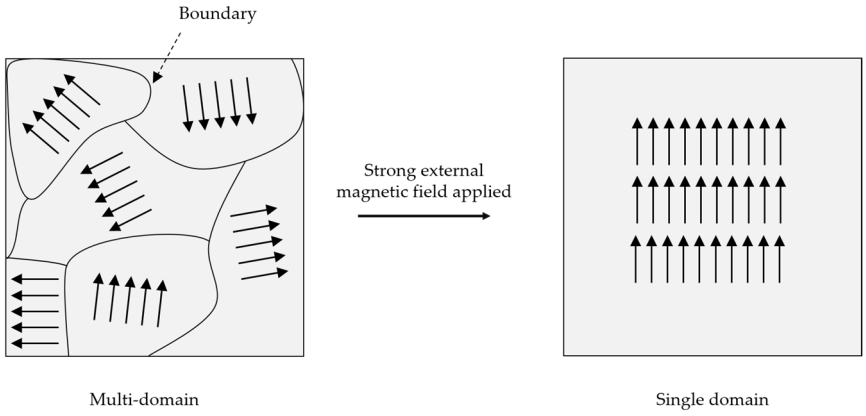

Figure B.4. Multi-domain system under a strong magnetic field breaks the boundaries and forms a single domain.

Nonetheless, not every material exhibits this behaviour. There is an exception, like nanoparticles (nanometric materials), which present a particle size smaller than the magnetic domains. Therefore, no magnetic domains are formed, and the absence of multi-domains characterizes them. In this situation, known as superparamagnetism, all spin momenta within the nanoparticle flip together with the temperature. The magnetic ordering of these systems with a magnetic field cost no additional energy.

In magnetic ordered systems, the magnetisation might not vanish when removed the external field; in other words, the system remains partially ordered in absence of an external magnetic field, known as magnetic retentivity. Is the retentivity the thing that defines a magnet? No, it isn't by its own. Three principal parameters define a magnet, which can be obtained by hysteresis measurements (Figure B.5).[146] These are:

Magnetic retentivity (or remanence): Parameter that defines the maximum strength of the magnetic field generated by the magnet in absence of an external magnetic field. Additionally, when the system retains the magnetisation it is said it displays an "open-loop", and when it does not a "closed-loop".

Coercive force: After removing the external magnetic field, it is the amount of reverse magnetic field that must be applied to the material to reduce the internally generated magnetic field due to the breaking of the magnetic order.

Hysteresis loss: The amount of energy required to invert the magnetisation of a magnet, which can be obtained from the integral of the hysteresis loop.

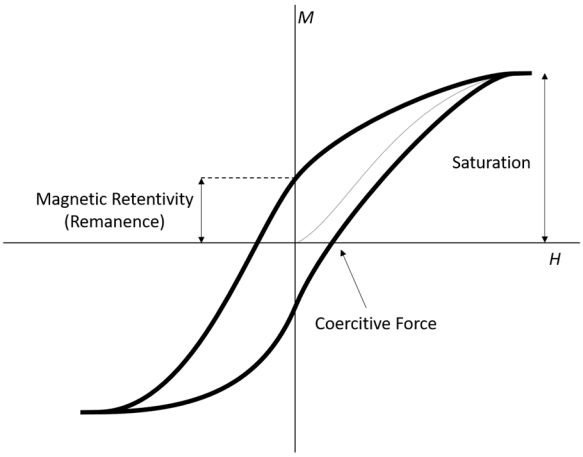

Figure B.5. Representation for a hysteresis loop curve, where *M* is the magnetisation and *H* is the external applied field.

All three parameters are essential for the design of new materials. For example, in data storage devices: a weak coercive force means that the material can be easily disturbed ending in data corruption; a small retentivity could end up in being incapable of "reading" the data. Nevertheless, a compromise between both has to be reached: a large hysteresis

loss means a significant amount of energy is required to invert the magnetisation (or change the stored data). On the contrary, if we seek for a powerful magnet, the magnetic retentivity has to be the greatest. At present, the hardest magnet (not an electromagnet) available in markets is the neodymium magnet, which is widely used together with the ferrite magnet.

Moving forward with more examples, the magnetite has strong magnetic interactions, *i.e.*, only at temperatures above 858 K the magnet behaviour is lost. However, when lowered the temperature back to 293 K the magnet is re-magnetised. When a material exhibits recovery of the magnetisation by itself below a certain temperature (Curie temperature), it is said it has a spontaneous magnetisation.

How are the magnetic measurements being performed nowadays? A sample is placed inside a magnetometer with a static magnetic field in which, as explained above, the free spins of the system will be aligned with the field. Simultaneously, a perpendicular alternating magnetic field is applied with a particular frequency, forcing the spin momenta to tilt/flip each time the magnetic field flips too. The combination of both magnetic fields causes the spin population to oscillate but, when the blocking temperature is reached, the spin population of the system is "locked". The "locking" of the population occurs when the energy barrier for the spin being flipped is greater than the thermal energy required, leaving the population "fixed" in that configuration. The steps are performed by the equipment at different temperatures so that the slow magnetic relaxation as a function of temperature, field strength and frequency is tracked.

B.1.4 Effects on the electronic m_j states for a paramagnetic ion

In an ideal environment without perturbations, neither symmetry, the energy states for a paramagnetic ion would be degenerated. However, in reality, there are interelectron repulsions among the free electrons that change the energy of these levels, stabilising some levels and destabilising some others. Five principal interactions cause the shifts in the energy levels:

Crystal Field: The coordination of ligand molecules changes the electronic density of the paramagnetic ion. Depending on the final geometry of the ion, the involved orbitals shift in energy. Hence, some orbitals are stabilised, and some others destabilised, breaking the degeneracy of the d and f orbitals. Additionally, the ligand nature has also an important role; some ligands cause more shifting than others known as spectrochemical series. These interactions can be explained with the "ligand field theory". In consequence, this situation provokes the emergence of a splitting of the ground (also the excited) terms that describe the electronic structure of the system into lower-symmetry states.

Zeeman Effect: There are different perturbation orders that cause the splitting of energy levels which are part of the spin state. The most relevant are the first- and second-order perturbation.

First-order perturbation: The existence of an external magnetic field causes the splitting of the energy levels for the different orientations, *i.e.*, a positive magnetic field stabilises the negative m_s and destabilises the positive m_s and vice versa. At greater applied fields, the splitting is more significant, and this behaviour follows the formula: $\Delta E = E_{Zeeman} = h\nu = g\mu_B B$, being h the Plank's constant, ν the frequency, B the applied external magnetic field, μ_B is the Bohr magneton, and g is the gyromagnetic ratio (or Landé g-factor).

Second-order perturbation: Smaller perturbation that comes from the interaction of one electron with the induced magnetic field generated by other electrons, causing a small splitting.

SOC (Spin-Orbit Coupling): Relativistic effect originated by the interaction of the electron spin with its orbit. In other words, from the point of view of the electron, the nucleus is orbiting around him, generating a magnetic field that interacts with the electron magnetic moment. This phenomenon is similar to the Zeeman Effect, and it is most likely to happen with electrons from *d* and *f* orbitals, but more with *f* orbitals. From the point of view of the ligand field theory, in high molecular symmetry, the ground term can be described as a set of degenerate states. In such a case, this degeneracy is the cause of the non-zero orbital moment of the term. In cases where the degeneracy is weakly split, the set of emerging states are energetically close. These states interact with each other but, due to the small energy gap between them. If a perturbation theory to describe this interaction is considered, it will respond to a first-order perturbation that is the first perturbation term.

As could be expected, the orbital angular momentum and magnetic quantum numbers (l and m_l) are relevant for this interaction. A new total orbital angular momentum "J" ($J = S+L$) appears and gives rise to new "m_j" states ($|L-S| \leq m_j \leq L+S$).

zfs (Zero-Field Splitting): For systems with more than one free electron, the spin density distribution and SOC cause breaking of the microstate degeneracy of the ground state in the absence of an external magnetic field (Figure B.6). The removal of the microstate degeneracy can be:

Axial: Equal $|m_j|$ states remain degenerated (known as "Kramers doublets") and different $|m_j|$ states are split. The energy of this splitting is defined by the parameter D, and its sign dictates which pair of m_j states conform the ground state. The larger the $|m_s|$, the lower in energy for $D < 0$ systems, and vice-versa. Besides, the energy difference

among the ground state and the last excited state is $-S^2|D|$ for integer spin and $-(S^2 - \frac{1}{4})|D|$ for half-integer spin, causing a natural energy barrier at zero-field (Figure B.6).

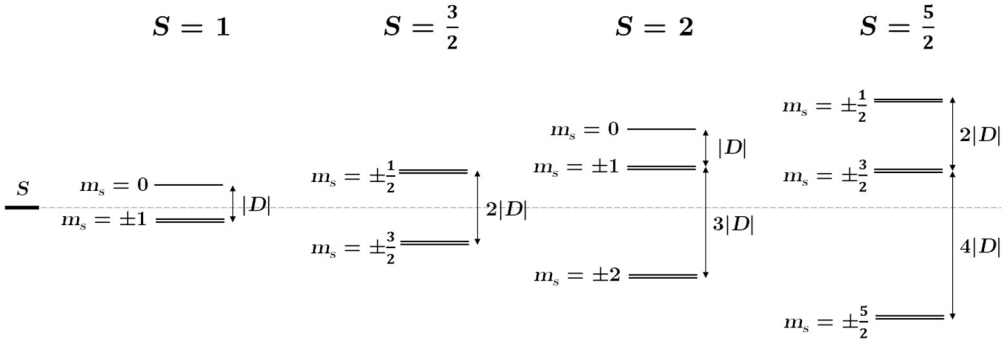

Figure B.6. Scale diagram of the energy level spacing for different S systems with axial zfs ($D < 0$).

Rhombic: Equal $|m_j|$ states are also split, and the parameter E defines the energy of the splitting. The rhombic splitting ($E \neq 0$) only exists if there is an axial splitting ($D \neq 0$) as well.

The interval of values E can attain is limited by D. The $\frac{E}{|D|}$ ratio must be fall within 0 and $\frac{1}{3}$, both included. When $\frac{E}{|D|} > \frac{1}{3}$, the energies for the $|m_j|$ states overlap. Therefore a redefinition of the system is performed, fitting again inside $[0, \frac{1}{3}]$ (Figure B.7). Once again, from the point of view of the ligand field, in a low molecular symmetry system, the energy gap between the states that constitute the fundamental term, in an ideal symmetry, is more significant. Therefore, the interaction between these states is much weaker and is dealt with through the second-order perturbation theory. States from excited terms can also be part of the set of interacting states, but their contribution to zfs is much more limited.

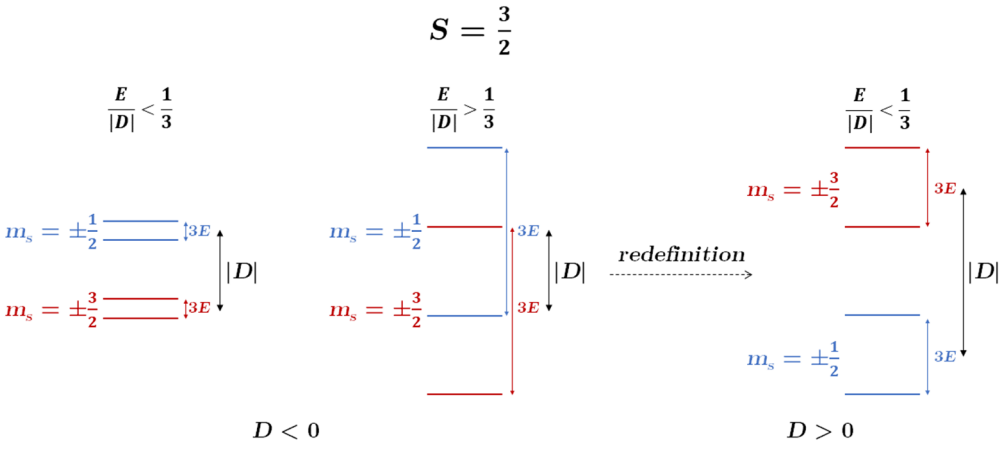

Figure B.7. Energy level spacing for an $S = \frac{3}{2}$ system with zfs and $E \neq 0$. When the ratio $\frac{E}{|D|}$ is larger than $\frac{1}{3}$ the sign of D flips due to a redefinition of the $|m_j|$ states.

Magnetic dipole-dipole interaction: As we already know, electrons have a magnetic moment, but also nuclei may contain a magnetic moment with which the electron can interact. There are a few ones:

Hyperfine interaction: An electron interacts with its nucleus. This interaction depends on two parameters principally: a) how penetrating the orbital is and, b) the magnetic permeability of the nucleus. For example, 4*f* orbitals are innermost than the 5*d*, thus, the interaction with the nucleus is stronger. As another example, the copper atomic nucleus is much more permeable than the cobalt atomic nucleus, then, the interaction with the nucleus is much stronger, being frequently resolved with ease.

Moreover, this interaction can also occur in systems with more than one nuclei interacting with an exchanging coupling (*J*) large enough, *i.e.*, the electron may feel the other nuclei as his own.

Superhyperfine interaction: An electron interacts with the magnetic moment of other nuclei with which *J* is weak or null. This interaction is weaker than the hyperfine.

Spin-spin interaction: An electron interacts with the magnetic moment of another electron from other nuclei. This interaction is almost negligible but takes an important role in spin relaxations mechanisms (explained later on).

The interaction among magnetic moments are the weakest, and they are usually only detectable by EPR measurements. For this reason, the previously mentioned interactions are called the electronic "fine structure", and these are called the "hyperfine structure".